

Investigating how Alzheimer's
Disease risk genes *Spi1* and
Abi3 modulate Macrophage
physiology


Ruth Elizabeth Jones

Thesis presentation for the degree of Doctor of Philosophy
(Medicine)

2019


Declaration

This work has not been submitted in substance for any other degree or award at this university or any other university or place of learning, nor is being submitted concurrently in candidate for any degree or other award.

Signed:  (candidate) Date: 05/04/2019


Statement 1

This thesis is being submitted in partial fulfillment of the requirements for the degree of PhD.

Signed:  (candidate) Date: 05/04/2019


Statement 2

This thesis is the result of my own independent work, except where otherwise stated, and the thesis has not been edited by a third party beyond what is permitted by Cardiff University's Policy on the use of third party editors by research degree students. Other sources are acknowledged by references. The views expressed are my own.

Signed:  (candidate) Date: 05/04/2019

Statement 3

I hereby give consent for my thesis, if accepted, to be available online in the university's open access repository and for inter-library loans **after the expiry of a bar on access previously approved by the Academic Standards and Quality Committee.**

Signed:  (candidate) Date: 05/04/2019

Acknowledgements

I would like to express my deep gratitude to Professor Phil Taylor for his invaluable advice, for sharing his immense knowledge and for all his guidance and support throughout this project. I would also like to sincerely thank my co-supervisors Professor Paul Morgan and Professor Lesley Jones for their insight throughout this work. I would especially like to thank Lesley for her advice regarding the RNA-Sequencing work.

I am particularly grateful for all the bioinformatic assistance given by Dr Robert Andrews with the RNA-Sequencing datasets. I wish to acknowledge the help provided by Dr Matt Hill with the *in-silico* analysis of *Spi1* and Professor Peter Holmans who kindly performed the comparison between the RNA-Sequencing work and the IGAP cohort. I would also like to thank the Data Clinic for their help and advice regarding statistics. I would also like to thank Dr Marcela Rosas for all her help at the start of this project, especially for setting up the initial MØP cell line, enabling me to dive straight in. My sincere thanks to Dr Natacha Ipseiz for the use of her single-cell sequencing dataset and Elena Simonazzi for her assistance with the Abi3 immunohistochemistry data.

I would like to offer my special thanks to the entire Myeloid Cell Biology Group. Thank you all for your support over the last 4 years, for the fun we had at pub lunches, annual meetings and Christmas meals. Special mention to the tuck-shop gang Selinda, Mark and Dina, and to Rob and Leah for answering my endless questions. I would also like to thank those who kindly volunteered to proof-read this work, I promise there is a giant thank-you cake coming your way. To all my colleagues, this project would not have been as great an experience without all your insightful comments or encouragement. As the hippocampus said at his retirement party- Thanks for the memories!

Last but by no means least I would like to thank all my family for supporting me throughout this thesis and my life in general, especially during the past year which has been difficult for all of us. Special thanks to mum for listening to me talk endlessly about brains and to Deborah for her patience and kindness in these last few months.

Summary

Patients with Alzheimer's Disease (AD) represent over 60 % of all dementia cases and current treatments cannot slow disease progression. Multiple AD-risk genes suggest microglia contribute to AD pathophysiology. This thesis investigates two AD-risk genes, *SPI1* and *ABI3*.

SPI1 encodes the transcription factor PU.1, essential in myeloid populations. *SPI1*/PU.1 is thought to affect AD-risk gene expression and an earlier AD-onset is predicted in individuals with high *SPI1*-expression polymorphism. Current literature suggests increased *SPI1*/PU.1 expression alters the transcriptome of microglia and increases AD risk. PU.1 is essential for the survival of macrophages (MØ) raising concerns that treatment reducing PU.1 may affect peripheral MØ in the immunocompromised elderly. This thesis confirmed low PU.1 expression reduced microglial phagocytic capacity.

RNA-Sequencing analysis identified over 162 microglia genes controlled by the amount of PU.1 expressed. Some genes were only detected in a *Spi1* over-expression dataset. 21 genes with significant expression-alterations showed an enriched signal for the IGAP (human AD-risk) dataset. Increased microglial *Spi1* expression did result in increased expression of several AD-risk genes. Microglia *Spi1* RNA-Seq datasets may provide a 'map' for future work to investigate how *Spi1* affects microglia function.

ABI3 is thought to inhibit actin-cytoskeleton reorganisation impacting several MØ functions. Newly developed *Abi3* KO mice were used to investigate the function of *Abi3* in pMØ and in cell lines derived from these mice. *Abi3* appeared to be expressed by a subset of peritoneal MØ (pMØ) and *Abi3* KO pMØ had a moderately-reduced phagocytic capacity *ex vivo*. *In vitro* work suggested that M-CSF induced cell morphology changes are also subtly changed in cells lacking *Abi3*. Therefore, *Abi3* KO did appear to modify the function of the actin cytoskeleton in MØs.

Overall, this thesis demonstrated the AD-risk genes *SPI1* and *ABI3* can impact microglia/MØ physiology and provides some insights into how these changes might contribute to AD pathology.

Contents

Declaration	i
Acknowledgements	ii
Summary.....	iii
Contents	iv
List of Figures.....	x
List of Tables	xv
Abbreviations.....	xvii
Chapter 1 Introduction.....	1
1.1 Overview.....	2
1.2 Alzheimer’s Disease.....	3
1.2.1 Insights from Genetic Association Studies	5
1.2.2 The Immune System in AD	8
1.3 Tissue Resident Macrophages	14
1.4 Microglia	15
1.4.1 Origin and Lifetime of Microglia	15
1.4.2 Important Microglia Receptors	17
1.4.3 Microglial Function	22
1.4.4 How LOAD risk effect Microglial Physiology.....	27
1.5 <i>Spi1</i> /PU.1	29
1.5.1 <i>Spi1</i> Layout and Regulation	32
1.5.2 CNS Function and role in AD.....	34
1.6 ABI3.....	38
1.6.1 ABI3 Layout and Signalling.....	41
1.6.2 CNS Function and proposed role in AD	42
1.7 Project Aims and Hypothesis	43

Chapter 2	Methods	47
2.1	Buffers and Solutions	48
2.2	Mice	51
2.2.1	<i>Spi1</i> -URE floxed Mice	51
2.2.2	ABI3 Knock-Out Mice	52
2.3	Genotyping	53
2.3.1	<i>Spi1</i> URE removal PCR	55
2.3.2	Abi3 Genomic PCR	56
2.4	General Cell Culture and Maintenance	56
2.4.1	Incubation and Media Preparation	56
2.4.2	Cryopreservation and Thawing	57
2.4.3	Cell counting	57
2.4.4	Jurkat Cell Line	58
2.4.5	Human Embryonic Kidney 293T Cells	58
2.4.6	Macrophage Precursor (M ϕ P) Cell lines	58
2.4.7	RAW 264.7 Cell line	59
2.4.8	Bone-Marrow Derived M ϕ (BMDM)	59
2.4.9	Primary Microglia Cultures	60
2.5	Functional M ϕ Assays	61
2.5.1	Adhesion assay	61
2.5.2	pM ϕ Phagocytosis assay	62
2.5.3	Primary Microglia Phagocytosis assay	62
2.5.4	M-CSF Stimulation assay	63
2.6	Microglia Isolation for Flow Cytometry	64
2.7	Peritoneal Lavage	66
2.8	<i>In vivo</i> Intraperitoneal (I.P.) Injections	66
2.8.1	Lentivirus Injection	66

2.8.2	Lipopolysaccharide (LPS) Injection	66
2.9	Flow Cytometry	67
2.9.1	Intra-nuclear Staining	67
2.9.2	Intra-cellular Staining	68
2.9.3	β -Galactosidase Staining	69
2.9.4	Surface Marker Staining	69
2.9.5	NIM-DAPI Staining	69
2.9.6	Imaging Cytometry	70
2.10	Immunohistochemistry Staining for β -Galactosidase	70
2.11	Cloning.....	70
2.11.1	Preparation of Plasmid Stocks	71
2.11.2	Insert Preparation.....	71
2.11.3	Vector Layouts.....	75
2.11.4	Vector Linearisation.....	76
2.11.5	Cloning and Transformation	77
2.11.6	Colony PCR.....	77
2.12	Lentivirus Production.....	78
2.12.1	Transfection.....	78
2.12.2	Sucrose Purification	79
2.12.3	Lenti-X Concentrator	79
2.12.4	Lentiviral Titration	80
2.13	Western Blot.....	80
2.13.1	Cell Lysis.....	80
2.13.2	Bicinchoninic acid (BCA) assay.....	80
2.13.3	Sample Preparation	81
2.13.4	Gel Electrophoresis.....	81
2.13.5	Semi-Dry Gel Transfer.....	82

2.13.6	Antibody Staining.....	83
2.13.7	Stripping and Re-Blotting for Actin	83
2.14	Quantitative PCR (qPCR)	84
2.14.1	RNA Extraction	84
2.14.2	Conversion to cDNA	84
2.14.3	qPCR reaction.....	84
2.15	RNA-Sequencing.....	86
2.16	Statistics and Analysis Software.....	86
2.16.1	IFL Data.....	86
2.16.2	Flow and Imaging Cytometry Data.....	86
2.16.3	qPCR Data.....	88
2.16.4	RNA-Sequencing Data	88
2.16.5	Graphs and Statistics.....	88
Chapter 3	Effects of <i>Spi1</i> -URE removal on PU.1 protein expression.....	90
3.1	Introduction	91
3.2	Results.....	93
3.2.1	Genomic Analyses of <i>Spi1</i> URE.....	93
3.2.2	PU.1 Antibody Specificity	97
3.2.3	<i>In vitro</i> Cre induced removal of -14 kb URE in <i>Spi1</i> -URE floxed MØP Cell Line	101
3.2.4	PU.1 expression in transgenic mice	110
3.2.5	Troubleshooting in the URE KO Model	114
3.3	Discussion.....	124
3.3.1	Conclusions and future work	126
Chapter 4	Development of <i>in vitro</i> microglia model with altered Spi1/PU.1 expression	127
4.1	Introduction	128
4.2	Results.....	131
4.2.1	Validation of Knock-Down and Over-Expression Vectors	131

4.2.2	Optimisation of Primary Microglia Culture System	144
4.2.3	Primary Microglia Cultures used for mRNA Sequencing	162
4.3	Discussion	166
4.3.1	Summary of main findings.....	166
4.3.2	Conclusions and future work.....	168
Chapter 5	Influence of PU.1 dose on Microglia mRNA transcriptome	170
5.1	Introduction.....	171
5.2	Results	174
5.2.1	Differential gene expression changes in both datasets	174
5.2.2	Validation of alterations to Spi1 expression.....	180
5.2.3	Selection & Validation of Other Genes.....	187
5.2.4	Pathway and Clustering analyses	197
5.2.5	Confirmation of functional changes	209
5.2.6	Comparison to human IGAP dataset	224
5.3	Discussion	228
5.3.1	Summary of main findings.....	228
5.3.2	Conclusions and Future Work	233
Chapter 6	Investigating the function of ABI3 in Macrophages	235
6.1	Introduction.....	236
6.2	Results	238
6.2.1	Evaluating Abi3 KO mice breeding	238
6.2.2	Establishing MØP Cell Lines.....	261
6.3	Discussion	294
6.3.1	Conclusions and future work.....	298
Chapter 7	General Discussion	301
7.1	Introduction.....	302
7.1.1	<i>Spi1</i> /PU.1	302

7.1.2	Abi3	303
7.2	Main Findings.....	304
7.2.1	Removal of the -14 kB <i>Spi1</i> -URE did not impact trMØ PU.1 expression	304
7.2.2	<i>In vitro</i> Microglia Model.....	306
7.2.3	<i>Spi1</i> RNA-seq Results and Validation	308
7.2.4	The role of Abi3 in MØ function	316
7.3	Conclusions	317
7.4	Future perspectives	319
	References	322
	Appendices.....	351
	List of 162 Genes Controlled by level of PU.1.....	351

List of Figures

Figure 1.1 The Amyloidogenic APP Processing pathway. APP is cleaved by β -Secretase to release a soluble APP β fragment.	5
Figure 1.2 Summary of key Quiescent and Effector microglia receptors adapted from [169]	17
Figure 1.3 Overview of Effector and Quiescent signalling cues in Microglia.	19
Figure 1.4 An Overview of the Phagocytic Process, adapted from [185].	20
Figure 1.5 Diagram summarising the level of PU.1 in differentiating immune cells adapted from [253]	30
Figure 1.6 Graphic depiction of M-CSF dependent PU.1 Feedback Loop.	31
Figure 1.7 Comparison of protein sequences between mouse and human PU.1	32
Figure 1.8 Overview of distal Spi1 regulatory elements or enhancers, and how the binding of transcription factors at these sites can increase PU.1 protein expression in M \emptyset , adapted from [269]	34
Figure 1.9 Depiction of risk SNPs (rs) associated with SPI1 and how they are thought to impact the level of the PU.1 transcription factor and AD risk	36
Figure 1.10 Abi3 Immgen RNA-seq Gene Skyline database, as normalised by DESeq2 [248].	38
Figure 1.11 Wave Regulatory Complex (WRC) adapted from [292].	39
Figure 1.12 IPA diagram of experimentally observed protein-protein interactions with the Abi3 protein.	40
Figure 1.13 Mouse Abi3 Exon and Protein structure	41
Figure 1.14 Comparison of protein sequences between mouse Abi3 and human ABI3.	42
Figure 1.15 Graphic Summary of the -14 kB Spi1 URE floxed mice model used in this thesis	44
Figure 1.16 Abi3 KO model.	46
Figure 2.1 Graphic depiction of predicted outcome to -14 kB URE following Spi1-ERT and Spi1-CONST transgenic mouse strains in Cx3cr1 ⁺ cells	52
Figure 2.2 Graphic depiction of the Abi3 WT and Abi3 KO mouse strains in all Abi3 expressing cells	53
Figure 2.3 Touchdown PCR program used for genotyping, based on standard Jackson Laboratory protocol	54
Figure 2.4 Diagram indicating the approximate binding sites of each of the primers to measure URE recombination in the Spi1 URE floxed mice	56
Figure 2.5 Schematic diagram summarising the culture protocol used for RNA-sequencing experiments	61

Figure 2.6 Experimental layout of Chamber Slide used in M-CSF stimulation assay.....	63
Figure 2.7 Diagram summarising the 37C_ABDK program on the GentleMACS™.	65
Figure 2.8 Summary of AutoMACS® Myelin Depletion using the ‘DepleteS’ program.....	65
Figure 2.9 An overview of the cloning process	71
Figure 2.10 Summary of shRNA sequence design.	73
Figure 2.11 Summary of Infusion primer design.....	74
Figure 2.12 The 2-step and 3-step Phusion PCR reactions used to generate inserts.	75
Figure 2.13 Summary of basic lentiviral vectors used in this thesis, adapted from [310].....	76
Figure 2.14 Set-up of components in Semi-Dry Transfer Cell.....	82
Figure 3.1 In-Silico ATAC-Seq Analysis suggests the -14 kB Spi1 URE chromatin is accessible in multiple immune cell populations.	95
Figure 3.2 In-Silico Analysis of H3K27ac suggests -14 kB Spi1 URE is an active enhancer in B-cell and MØ populations.	96
Figure 3.3 Comparing the ATAC-Seq and H3K27ac profiles in Microglia and pMØ.....	97
Figure 3.4 Demonstrating PU.1 Antibody Specificity.....	98
Figure 3.5 Initial validation of the Spi1-URE floxed model	102
Figure 3.6 Experiments authenticating the function of Cre pSFEW virus.....	104
Figure 3.7 In Vitro experiments with Cre pSFEW virus in Spi1-URE floxed BMDM or M-CSF differentiated MØPs	106
Figure 3.8 Confirming the Cre pSFEW virus is functional in vivo using a published model.....	109
Figure 3.9 Determining PU.1 expression in Spi1-ERT and Spi1-CONST Heterozygous Mice.....	111
Figure 3.10 Determining PU.1 expression in Spi1-ERT and Spi1-CONST Mutant Mice.	114
Figure 3.11 Confirmation of Cre function in Cx3cr1-Cre ^{CONST} Mice.....	115
Figure 3.12 PU.1 Expression in DM mice compared to Cx3cr1-Cre ^{CONST} and C57BL/6J mice.	117
Figure 3.13 In vivo pilot experiment testing if removal of the -14 kB Spi1-URE impacts pMØ and microglial response to an LPS challenge.....	121
Figure 4.1 Cloning Lentiviruses to Manipulate PU.1 Expression.	132
Figure 4.2 Confirmation of Viral Function in Cell Lines.....	134
Figure 4.3 In Vivo Timecourse to see when Spi1 shRNA knock-down was most effective.....	136
Figure 4.4 In Vivo comparison of Spi1 shRNA lentiviruses.	138
Figure 4.5 Determining if endogenous GFP expression extends lifetime of Spi1 shRNA viruses In vivo.....	139
Figure 4.6 Piloting Spi1 shRNA and PU.1 Over-Expression Viruses in Primary Microglia	141

Figure 4.7 Tmem119 Antibody Staining in Fresh and Cultured Microglia.....	145
Figure 4.8 Pilot Experiment to determine if Microglia should be purified before viral infection...	147
Figure 4.9 The impact of TGF- β addition on microglia gene expression at different times.....	149
Figure 4.10 Determining if TGF- β should be added to cultures before or after lentivirus.	150
Figure 4.11 qPCR analysis of the impact of TGF- β and Virus order on Cultured Microglia Gene Expression. Replicate 1.....	153
Figure 4.12 qPCR analysis of the impact of TGF- β and Virus order on Cultured Microglia Gene Expression. Replicate 2.....	154
Figure 4.13 Pilot to Optimise the best time to add Virus to Microglia Cultures.	156
Figure 4.14 qPCR Analysis of Virus Optimisation Experiment- Replicate 1.....	160
Figure 4.15 qPCR Analysis of Virus Optimisation Experiment- Replicate 2.....	161
Figure 4.16 Final Experimental Design of Cultures used for RNA Sequencing.	163
Figure 4.17 Sorting used for all RNA Sequencing Replicates.....	164
Figure 5.1 Summary of gene changes from RNA-sequencing analyses at different statistical cut-off points.....	175
Figure 5.2 Adjusted P-values in the Spi1 knock-down dataset plotted against the adjusted P-values in the Spi1 over-expression dataset..	177
Figure 5.3 Venn diagrams showing the amount of overlap between the Spi1 knock-down dataset (KD; blue) and the Spi1 over-expression dataset (OE; green) at P<0.01 and P<0.05 cut-offs.	178
Figure 5.4 The 162 'core' genes that were ranked according to the size of the Log ₂ fold-change value.	179
Figure 5.5 Principal Component Analysis (PCA) of the RNA sequencing dataset.....	180
Figure 5.6 Spi1 expression data from both RNA Sequencing dataset and experimental validation of Spi1 mRNA and PU.1 protein.....	182
Figure 5.7 Flow cytometric analysis of PU.1 protein expression in RNA -Seq validation microglia cultures.....	185
Figure 5.8 Summary of RNA sequencing values and qPCR data measuring selected targets in four original samples and the validation culture	189
Figure 5.9 Alterations to Iba-1 protein expression in virally infected cultures by flow cytometry.	193
Figure 5.10 Measuring alterations to P2ry12 protein in infected cultures using flow cytometry. .	195
Figure 5.11 Results of functional pathway analysis in IPA comparing Spi1 knock-down dataset against the Spi1 over-expression dataset with a P < 0.05 cut-off	198

Figure 5.12 Canonical/Biological pathway analysis comparing the Spi1 shRNA to the NS shRNA samples (Knock-Down dataset) using the $P < 0.05$ cut off..	200
Figure 5.13 Canonical/Biological pathway analysis comparing the Spi1 pSIEW to the empty pSIEW samples using the $P < 0.05$ cut off.	201
Figure 5.14 Hierarchical Clustering of Spi1 knock-down (KD) and Spi1 over-expression (OE) \log_2 fold-changes of genes with a P-value of over $\alpha=0.05$	202
Figure 5.15 IPA analysis of potential Upstream Regulators.....	204
Figure 5.16 Hierarchical clustering of the z-scores calculated from the FPKM values ($P<0.05$) from each replicate.....	206
Figure 5.17 The Absolute number of infected (GFP+) microglia.....	210
Figure 5.18 Assessing proliferation using ki67 staining in Spi1 shRNA and control cells.	211
Figure 5.19 Assessing DAPI Nuclear Content of NI, NS shRNA and Spi1 shRNA infected microglia.	214
Figure 5.20 Preliminary work to optimise microglial phagocytosis assay in this model	216
Figure 5.21 Representative gallery images taken from the NS shRNA samples describing the stages of analysis using the internalisation wizard.....	218
Figure 5.22 Plots from the internalisation analysis of the first replicate of the phagocytosis experiment.....	220
Figure 5.23 Final analysis from the second replicate of the phagocytosis experiment.....	221
Figure 5.24 The internalisation ratio and mean zymosan pixel range for the first replicate of the phagocytosis experiment.....	223
Figure 5.25 The internalisation ratio and mean zymosan pixel range for the second replicate of the phagocytosis experiment.....	224
Figure 5.26 Volcano plots comparing distribution of genes in the Spi1 OE dataset.	226
Figure 6.1 Abi3 expression in primary murine Macrophage populations as shown by RNA-Seq. Part I	239
Figure 6.2 Abi3 expression in primary murine Macrophage populations as shown by RNA-Seq. Part II	240
Figure 6.3 PCR to show the lack of ABI3 exons 5-7 in DNA extracted from lavage cells.	241
Figure 6.4 Detection of LacZ reporter in primary pM \emptyset macrophages Part I	244
Figure 6.5 Detection of LacZ reporter in primary pM \emptyset macrophages Part II	246
Figure 6.6 Determining Abi3 mRNA expression by qPCR. In all these experiments Ywhaz was used as an endogenous control gene.....	248

Figure 6.7 pMØ Cell Counts from fresh lavages	249
Figure 6.8 Assessing the impact of ABI3 KO on lavage cell adhesion.....	252
Figure 6.9 Exemplar Images from the ABI3 KO Phagocytosis experiment.....	256
Figure 6.10 Shows the F4/80+Tim ^{high} and F4/80+Tim ^{low} populations in each sample	257
Figure 6.11 Gating used in analysis to identify pMØ that had phagocytosed zymosan, including exemplar images.	258
Figure 6.12 Internalisation ratio calculations and summary	260
Figure 6.13 Confirmation of Abi3 KO in MØP Cell Lines.....	263
Figure 6.14 Determining if the LacZ reporter can be detected in M-CSF differentiated MØP cells..	265
Figure 6.15 Morphological Characterisation of ABI3 WT and KO MØP cell lines.....	267
Figure 6.16 Additional images of M-CSF Differentiated MØPs	268
Figure 6.17 Characterisation of ABI3 WT and KO MØP cell lines Receptor Expression.	269
Figure 6.18 Summary of Receptor Expression in WT and KO MØP Cells	270
Figure 6.19 Colour changes in ABI3 KO and WT media suggest there could be altered proliferation..	272
Figure 6.20 Assessing WT and ABI3 KO MØP cell proliferation by flow cytometric analysis of ki67 and phh3 staining	273
Figure 6.21 Results of EdU stimulation in WT and ABI3 KO MØP cells at multiple timepoints.	276
Figure 6.22 NIM-DAPI analysis of serial MØP cell samples.	278
Figure 6.23 Proliferation as analysed by Ki67 staining in M-CSF differentiated MØP cells.	280
Figure 6.24 WT and ABI3 KO M-CSF differentiated MØP cells treated with EdU.	282
Figure 6.25 M-CSF Depletion Assay Set-up and Analysis..	285
Figure 6.26 Exemplar picture of cell morphology in the M-CSF depletion assay.....	287
Figure 6.27 Summary of parameters analysed in M-CSF depletion assay.	289
Figure 6.28 Experimental pattern of each replicate in M-CSF depletion assay..	292
Figure 6.29 Graphical hypothesis of the impact of Abi3 KO on M-CSF depletion assay based on insights from the literature..	297
Figure 7.1 Z-Score of Cell-Cycle IPA Disease/Function Pathways in the Spi1 Knock-Down dataset.	312
Figure 7.2 Z-Score of Cell-Cycle IPA Disease/Function Pathways in both RNA-Seq dataset.	315

List of Tables

Table 2.1 List of Buffers and Solutions used in this thesis..	48
Table 2.2 Official and abbreviated names of the transgenic mice strains used in this thesis.	51
Table 2.3 Volumes of each GoTaq® G2 Flexi DNA Polymerase kit component needed for one standard 25 µL reaction	54
Table 2.4 All genotyping primer sequences needed for genotyping PCR reactions and the expected product size in base-pairs (bp).....	54
Table 2.5 Primers used to determine if the URE has been excised by Cre.	55
Table 2.6 Primers used to assess the presence of Abi3 exons and predicted band sizes.	56
Table 2.7 The RPMI and DMEM medias used in these experiments..	57
Table 2.8 List of the age and gender of the mice that were used to generate the MØP cell lines. .	58
Table 2.9 Summary table of commonly used antibodies including the clone name, final dilution and the type of permeabilization, if required.....	67
Table 2.10 The shRNA sequences used in this thesis (5'→ 3') direction without the 15 bp overhang sequences.	72
Table 2.11 Final Infusion primer sequences..	75
Table 2.12 The restriction enzymes used to linearise plasmids to open the desired insert site and the primer sequences required for plasmid DNA sequencing.....	77
Table 2.13 The amount of each plasmid required to transfect the lentiviruses using the Effectene® transfection system.	79
Table 2.14 The volumes of each reagent needed to make one 10 % acrylamide separating gel.....	81
Table 2.15 The volumes of each reagent required for one acrylamide stacking gel.	82
Table 2.16 The Primary and Secondary antibodies used to detect proteins in western blotting. ...	83
Table 2.17 qPCR primer sequences used in this thesis.....	85
Table 2.18 The temperature and time cycling times used for to generate the qPCR data.	86
Table 2.19 Definition and Example Images of Features and Masks used in IDEAS® Analysis Software.....	87
Table 3.1 Summary of the ATAC-Sequencing and H3K27ac datasets used in the In-Silico analyses..	93
Table 3.2 Summary of all Raw Cell Counts from Double Mutant (DM) mice experiments..	119
Table 4.1 the table above illustrates some of the main characteristics of the PU.1 lentiviruses. sequence for mouse Spi1 (CCDS 16425.1) into plasmids with a GFP reporter pSIEW..	133

Table 4.2 An Overview of the Percentage of Infected Microglia in each Culture Condition.	158
Table 4.3 Final proportions of Microglia, both non-infected and infected, and results of RNA Quality Checks.	165
Table 5.4 Summary of the number of genes that were regulated, either up (positive fold-change) or down (negative fold-change), when compared to the relevant control at P<0.01 and P<0.05 cut- offs.	176
Table 5.5 Summary of targets selected for validation of RNA sequencing data.	187
Table 5.6 Summary table of MAGMA analysis comparing the RNA-Seq datasets created in this thesis to IGAP data..	225
Table 5.7 The 21 genes that had an adjusted P-value of <math><1 \times 10^6</math> that were significantly associated to the IGAP dataset.	227
Table 6.1 Equations used to calculate the shape descriptor features in ImageJ.	284
Table 7.1 Comparison of papers manipulating PU.1 expression in cultured microglia.	310

Abbreviations

Abi3	Abl Interactor Family Member 3
AD	Alzheimer's Disease
AMPA	α -amino-3-hydroxy-5-methyl-4-isoxazolepropionic acid
A β	Amyloid- β
BDNF	Brain Derived Neurotrophic Factor
BMDM	Bone-Marrow Derived Macrophage
cDNA	complementary DNA
CSF1R	Colony Stimulating Factor Receptor 1
DAM	Disease Associated Microglia
DAPI	4',6-diamidino-2-phenylindole
EOAD	Early-Onset Alzheimer's Disease
FPKM	Fragment reads per
GFP	Green Fluorescent Protein
GM-CSF	Granulocyte Macrophage Colony Stimulating Factor
HDAC	Histone Deacetylase
Iba-1	ionized calcium-binding adapter molecule 1
IFN	Interferon
IGAP	International Genomics of Alzheimer's Project
IL	Interleukin
iNOS	Nitric Oxide Synthase
IRF	Interferon Regulatory Factor
KO	Knock-Out
LOAD	Late-Onset Alzheimer's Disease
LPS	Lippopolysaccharide
M-CSF	Macrophage Colony Stimulating Factor
MDML	Monocyte-Derived Microglia-Like Cells
MHC	Major Histocompatibility
NMDA	N-methyl-D-aspartate receptor
NO	Nitric Oxide
NS	Non-Silencing
P2ry12	Purinergic Receptor p2y12
PGE2	Prostaglandin E2
Phh3	Phosphohistone H3
Pilr β	Paired-Immunoglobulin-Like type 2 Receptor β
pM \emptyset	Peritoneal Macrophage
PRR	Pattern Recognition Receptor
RNA-Seq	RNA-Sequencing
shRNA	short hairpin RNA
SNP	Single Nucleotide Polymorphism
Spi1	Spleen Focus Forming Virus (SFFV) Proviral Integration
TGF- β	Transforming Growth Factor β
TLR	Toll-Like Receptor
trM \emptyset	Tissue Resident Macrophae

URE	Upstream Regulatory Element
WASP	Wiskott-Aldrich Syndrome Protein
WAVE2	WASP-family Verprolin Homologous Protein 2
WRC	WAVE Regulatory Complex
WT	Wild-Type

Chapter 1 Introduction

1.1 Overview

As the most common form of dementia, Alzheimer's Disease (AD) has become a worldwide health concern, affecting over 520,000 people in the UK. Currently dementia care costs the UK over £26 billion every year, and the number of patients has been predicted to increase dramatically within the next century [1]. Thus, there is a drive to find a disease-modifying treatment for AD. Multiple clinical trials have failed to treat AD, likely due to a poor understanding of AD aetiology. As AD pathology is thought to occur up to 20 years before clinical symptoms appear it makes the pathophysiology difficult to investigate. As a result there are multiple theories of and lots of conflicting evidence which has slowed understanding of the disease.

In the past decade genome sequencing has been used to take a more unbiased approach to discover which genes contribute to AD risk. Multiple large-scale genetic studies of AD cases and controls produced a list of AD risk single nucleotide polymorphisms (SNPs). These SNPs were then attributed to genes and mapped onto biological pathways. These Genome Wide Association Studies (GWAS) purported that many of these AD risk genes were linked to immune system function [2,3]. This has led to an increased interest in the immune system of the brain, with a special focus on microglia. There is now a drive to understand how microglia might contribute to AD pathophysiology, but also how these individual AD risk SNPs/genes might alter the function of microglia.

This thesis will focus on two protein-encoding AD risk genes identified by genetic association studies; *SPI1*/PU.1 and *ABI3*/ABI3 [4,5]. *SPI1* encodes PU.1, an essential transcription factor in all macrophage (M ϕ) populations [6–8] that is known to alter the M ϕ transcriptome in a dose-dependent manner [9,10]. Less is known about the functional role of ABI3 but it is suspected to play a role in cell motility and phagocytosis [11]. Thus the aim of this thesis was to investigate these proteins in knock-out/knock-down or over-expression models to determine the impact on microglial/M ϕ function.

1.2 Alzheimer's Disease

The first recorded case of AD was described in 1907 by Alois Alzheimer. The 1995 translation of his work states the case of a 51-year-old woman who suffered memory loss and a lack of awareness of the date or time [12]. The clinical features of AD include impaired spatial navigation, short term memory loss and difficulty making decisions resulting from progressive neuronal loss in brain regions such as the hippocampus and pre-frontal cortex. Despite there being over 112 drugs currently in clinical trials for AD there are only a very few clinical treatments available and these only temporarily manage the symptoms [13]. These treatments are unable to alter disease progression and as increasing numbers of neurones are lost in AD, often making these drugs ineffective as AD progresses.

Other pathological features of AD have been well described in post-mortem where brains commonly have shown enlarged ventricles, a consequence of the erosion of grey matter, Amyloid- β ($A\beta$) plaques and tangles of hyper-phosphorylated Tau [14].

AD cases are normally categorised as early-onset AD (EOAD) or late-onset AD (LOAD). A proportion of EOAD carry familial autosomal dominant mutations (fAD) in the Amyloid Precursor Protein (APP) gene or in the Presenilin 1 (PSEN1) or Presenilin 2 (PSEN2) genes, which form part of the γ -Secretase complex [15–17]. APP is first processed by β -Secretase before being further cleaved by the γ -Secretase into Amyloid- β ($A\beta$). Cleavage by the γ -Secretase enzyme will result in the production of multiple $A\beta$ species but the most abundant isoforms end at position 40 ($A\beta_{1-40}$) or position 42 ($A\beta_{1-42}$) [18]. The PSEN1/ PSEN2 AD-risk mutations are thought to alter the structure of the γ -Secretase complex favouring production of the longer $A\beta_{1-42}$ isoform which are more prone to aggregation [18]. In AD patients the ratio between $A\beta_{1-42}$: $A\beta_{1-40}$ is significantly increased, and the clearance of $A\beta_{1-42}$ is reduced [19]. The discovery of these early-onset AD risk genes led to the development of the Amyloid Cascade Hypothesis (ACH) which prevailed over the field for ~20 years [20,21]. The ACH postulated that an accumulation of the $A\beta$ protein due to an increased production of the stickier $A\beta_{1-42}$ isoform and a reduced clearance, resulted in oligomers which eventually formed neurotoxic plaques [20].

Multiple *in vitro* studies have shown that oligomeric $A\beta$ and Neurofibrillary Tau Tangles (NFTs) are neurotoxic, it is not yet clear why these aggregated proteins appear in AD pathology [22,23]. However, recent evidence suggests that Tau pathology better correlates to AD progression [24–27]. Tau production is increased in active neurones [28]. Mice which over-expressed Tau in the entorhinal cortex showed that NFTs formed here and were transferred to other neurons through

synaptic transmission [26]. As neuronal activity increases the release of Tau [28] excitatory neurones were particularly vulnerable to tau-induced death [29]. A β may also exacerbate this effect by further increasing neuronal activity in the brain [30]. Also hAPP AD model mice had a slower disease progression compared to hAPP mice that also over-expressed Tau [31]. Further studies using optogenetic technology are being done to look at how Tau and A β contribute to these hyper-excitability circuits, and to see if reducing the activity of the circuits has any influence on AD progression [32].

Thus present-day understanding of AD aetiology suggests that dysregulated A β /Tau can result in aberrant excitatory activity within neuronal networks (reviewed in Huang & Mucke 2012). Over 50 % of family members with fAD mutations experienced seizures [34]. Seizures have been observed early on in AD patients [35] and AD patients with epileptiform activity had a steeper decline in cognitive tests [36].

In transgenic mouse models hAPP_{FAD} mice had spontaneous seizure activity in cortical and hippocampal neural networks [37], and in APP/PS1 mice seizures coincided with A β plaque development [38]. Bi-photon imaging of APP23/PS45 mutant mice found all hyperactive neurones were within 60 μ M of an A β plaque [39]. Fu *et al.* (2017) noted that at 30 months of age mice over-expressing Tau in the entorhinal cortex lost excitatory neurones in the entorhinal cortex, and experienced deficits in spatial memory as a consequence of altered neuronal circuitry [29]. Martinez-Losa *et al.* (2018) developed interneuron progenitor cells that had been genetically altered improve regulatory function. When these cells were transplanted into the brains of J20 AD transgenic mice they lessened the abnormal neuronal activity and restored performance in spatial-memory tasks [40]. Consequently, it appeared as though Tau and A β pathology are linked to aberrant neuronal circuits. Interestingly microglia can both influence and be influenced by neurotransmission and are altered by epileptic seizures, reviewed in [41] and [42].

Microglia express receptors for most neurotransmitters and microglial can influence synaptic transmission [43,44]. Loss of two key microglia receptors, Cx3cr1 and CD200, can impair Long Term Potentiation (LTP) which is the molecular mechanism underlying learning and memory [45,46]. Lipopolysaccharide (LPS), part of the outer membrane of gram-negative bacteria, stimulates microglia through Toll-Like Receptor (TLR) 4. LPS stimulated microglia could induce neuronal signalling from excitatory neurones which was not observed in mice lacking microglia [47]. Moreover TNF α , which is released by reactive microglia, inhibited astrocytic-uptake of glutamate in primary human glial cultures potentiating the excitotoxic environment [48]. Thus, it

follows that microglia are able to influence neuronal signalling. As microglia are thought to contribute to AD pathophysiology it is possible reactive microglia add to the hyperexcitable circuitry observed in pathology.

More work is required before our understanding of AD pathophysiology is sufficient to inform drug design. In the last 10 years understanding of the genetic contribution in AD has improved, as well as environmental risk factors such as obesity and gender. Age remains the most significant environmental risk factor, and therefore much effort has gone into researching how aging affects the brain, especially as the immune system is thought to become senescent in the elderly reviewed in [49]. Therefore the following will focus genetically associated risk genes in AD.

1.2.1 Insights from Genetic Association Studies

1.2.1.1 Early onset AD (EOAD) risk genes

The most extreme form of EOAD originates from heritable APP, PSEN1 or PSEN 2 mutations [15–17]. These mutations converge on the APP processing pathway, as shown in Figure 1.1.

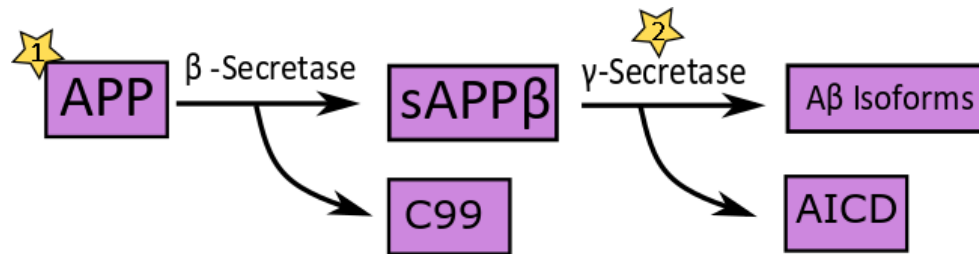


Figure 1.1 The Amyloidogenic APP Processing pathway. APP is cleaved by β -Secretase to release a soluble APP β fragment. The C99 fragment is further cleaved by γ -Secretase to produce various A β isoforms and the APP intracellular domain (AICD). The longer A β 1-42 form is more prone to aggregate in plaques. Mutations in the APP gene normally lie in the cleavage sites for β -Secretase (highlighted by the first star) or γ -Secretase (indicated by the second star) enzymes which results in inappropriate cleavage. PSEN1 and PSEN2 encode parts of the γ -Secretase complex.

PSEN1 and PSEN2 encode parts of the γ -Secretase complex which is responsible for the cleavage of APP into the various A β isoforms. These AD risk mutations are thought to result in the preferential cleavage of the longer A β isoforms which are more prone to aggregation [18]. As reviewed in [50] these mutations have provided insight into the role of the A β pathway in AD pathology. The next sections will discuss LOAD risk genes which are thought to affect a wider range of pathways.

1.2.1.2 Apolipoprotein E risk genes

LOAD risk is thought to be between 65 to 70 % heritable [51]. The *Apolipoprotein E (APOE)* is the most well-known LOAD risk gene and has three allele variants, ϵ 2, ϵ 3 and ϵ 4 which are each associated with a different level of risk as reviewed in [52]. The most common variant is ϵ 3, and ϵ 4

is associated with the highest AD risk. The predicted increase in risk is 2-3 times with one copy of the $\epsilon 4$ allele and up to 12-fold higher if an individual has two copies of the $\epsilon 4$ [53]. The $\epsilon 2$ allele variant is thought to be protective against AD but could result in an increased risk of vascular dementia, which is caused by $A\beta$ deposits in the vasculature. Approximately 12 % of the European population has at least one copy of the $\epsilon 4$ allele, 79 % have an $\epsilon 3$ allele whereas only 7 % have one or more copies of the $\epsilon 2$ allele [54].

Many *in vitro* studies are trying to determine the exact function of ApoE in the brain and believe it to have a role in lipid transport and potentially in microglial phagocytosis [55,56]. Induced Pluripotent Stem Cell (iPSC) cultures have shown each APOE allele alters the physiology of multiple CNS cell types [56,57]. For example, iPSC neurones with the $\epsilon 4$ allele produce far more $A\beta$ compared to iPSC neurones with an APOE $\epsilon 3$ genotype. Moreover, astrocytes and microglia-like cells derived from the APOE $\epsilon 4$ iPSC line tend to a more inflammatory state than the APOE $\epsilon 3$ controls [56].

APOE is thought to act with another AD-risk gene TREM2 to form a molecular trigger for Disease-Associated Microglia (DAM) [58]. Krasemann *et al.* (2017) proposed that apoptotic neurones activate the Trem2-Apoe signalling pathway, which suppresses homeostatic Transforming Growth Factor- β (TGF- β) signalling resulting in a more inflammatory phenotype. Microglia did not respond in this manner to exogenous immune stimuli such as *e. coli* or zymosan [58]. Recent developments in genome sequencing technology have made undertaking large populations screening for AD risk genes feasible.

1.2.1.3 Other Late Onset AD risk genes

Several large-scale studies have investigated genetic loci associated with LOAD risk. *CLU*, *PICALM* and *CR1* [59–62] were quickly identified as LOAD risk loci. Later investigations also identified *MS4A4/MS4A6E*, *CD2AP*, *CD33*, *EPHA1* and *ABCA7* as loci conferring an increased AD risk [63,64].

Lambert *et al.* (2013) performed the largest publicly available genome wide screen of AD patients and controls as part of the International Genomics of Alzheimer's Disease Project (IGAP) [3]. The comparison of the AD patients and controls allowed risk SNPs to be assessed in an unbiased manner. Several novel risk loci were identified in this study including *INPP5D*, *MEF2C* and *HLA-DRB5* which are linked to immune function and three others were validated *CD33*, *CR1* and *TREM2*. Recent work by Sims *et al.* 2017 identified rare coding AD variants in *PLCG2*, *ABI3* and *TREM2* [5]. *ADAM10* and *ACE* have been independently confirmed as AD risk loci [65,66].

Furthermore, the data gained from these large-scale genetic association studies has been interrogated to identify risk genes from these loci. In 2014 Escott-price *et al.* identified *SPI1* as a LOAD risk gene using a mathematical modelling approach [4].

Overall the understanding of the genetic causes underlying LOAD is sufficient that a polygenic risk score can be used to correctly predict over 90% of LOAD cases [67]. This discovery means that studies could now investigate changes in the brain before symptoms appear, and clinical trials could intervene earlier on in AD. Therefore, some focus is moving to align the risk loci to genes link these genes with pathways to improve the biological understanding of AD.

1.2.1.4 Linking Genetics to Biological Understanding

The first *in silico* analyses of these AD risk loci by Jones *et al.* (2010) who used gene ontology databases to try and predict possible biological pathways with a role in AD pathophysiology. The results showed the most significant pathways associated with AD pathology were related to the immune system, endocytosis and cholesterol metabolism [2]. In a later paper the same group combined the GWAS and gene expression data to confirm immunity to be a relevant process in AD pathology, in addition to identifying cholesterol transport and protein ubiquitination as other important processes [68].

Other studies have taken a different approach to link the genetic results to our biological understanding. Karch *et al.* (2012) measured mRNA expression of AD-risk genes in AD and control brains and found there to be alterations in AD brains [69]. However a problem with measuring gene expression in whole-tissue AD samples is the disease pathophysiology results in neuronal loss and microgliosis meaning that the microglia genes are likely over-represented in AD cases compared to controls, so expression of microglia always appears higher. There are several obstacles that make studying these genes in a more biological context including; identifying which cell type these risk SNPs exert their biological effect, developing appropriate *in vitro* and *in vivo* models and determining how these changes might influence the final phenotype of the whole organism.

Gjoneska *et al.* (2015) compared epigenetic data taken from AD patient samples and the CK-p25 AD mouse model. They found an enriched active promoters/enhancer signal in immune-related genes, which was conserved between species. Moreover this study concluded *SPI1/PU.1* may have a role in AD pathology [70]. As many of the AD-risk genes seem to implicate the immune system in AD pathology several *in silico* have looked at the immune-related genes as a network.

The indication that immunity appears to play a role in AD pathology has led to several immunotherapeutic drugs being re-purposed for AD and are currently in phase I/II and III trials [13]. In conclusion LOAD genetic association studies have prompted several new investigative lines of research, including the role of the immune system in AD. The next section will discuss what is presently known about the contribution of the immune system in AD.

1.2.2 The Immune System in AD

Several pieces of evidence suggest microglia are implicit in AD aetiology, as reviewed in [50]. Firstly, immune-related LOAD risk gene networks have been identified [2]. The individual LOAD risk genes will be discussed in section 1.4.4.

Secondly, evidence collected from post-mortem investigations has shown that there is an expanded microglia population (microgliosis) in the brains of AD patients and that these microglia are in a more reactive state compared to controls [72,73]. It is not known if microgliosis is contributing to AD or helps alleviate AD pathology. The 'double-edged sword' theory is most widely accepted, proposing that microglia are beneficial in early AD but become pathogenic after chronic exposure to an inflammatory environment. AD is thought to prime microglia for activation, so a second immune stimulation results in an exaggerated inflammatory response [74]. In AD patients microgliosis has also been observed in some PET imaging studies, though these results have not been consistent [75]. Most studies measure TPSO to infer the status microglia however, immunohistochemical analysis has shown TSPO is expressed on astrocytes and neurones in addition to microglia [76] so is not a suitable marker of microglia activation.

Thirdly, work in transgenic mouse models has indicated microglial have a role in AD pathophysiology [77], as discussed below.

1.2.2.1 Assessing Microglia impact in AD mouse models

Historically the impact of microglia in disease models has been assessed by removing the microglia population. The most common approaches to ablate the native microglia population were irradiation or the thymidine kinase enzyme (TK) gene under the CD11b promoter and treating with ganciclovir to induce death in cells expressing CD11b [78]. When the TK-ganciclovir approach was used to temporarily deplete microglia in the APP/PS1 AD mouse model the A β plaque load was unaltered [78]. This could have been due to the short depletion time (2-4 weeks) that occurred too far into disease progression. However even when microglia were depleted for 1-3 months A β deposition in APP/PS1 mice was unaltered [78]. When microglia were imaged *in vivo* to observe interactions with A β over time it was found that microglia could not prevent A β plaque formation,

but did restrict plaque growth [79]. As previously discussed (section 1.2) A β deposition might not accurately represent the stage of AD, which could make it an inaccurate measure of the outcome in these studies [27]. By depleting the microglia in these models the impact of how microglia contribute to disease progression cannot be assessed. Thus, multiple experiments opted to utilise AD transgenic models where microglia lacked a functional receptor instead. Cx3cr1 and CD200 receptors are expressed on microglia and contribute to a homeostatic phenotype, see section 1.4.2.1 for full discussion [46,80–82].

In 2010 Fuhrmann *et al.* bred mice without the Cx3cr1 receptor to the 5xTg-AD mouse model [83]. Complete removal of Cx3cr1 in 5xTg-AD model prevented the extensive neuronal loss that was observed in 5xTg-AD/Cx3cr1-heterozygous mice. Thus, more responsive microglia helped slow AD progression in this model [83].

Mice lacking CD200, a CNS ligand which signals through the CD200 receptor on microglia, have a higher baseline expression of reactive microglia markers associated with an inflammatory state [84]. While it does not appear that the CD200 KO mice have yet been bred to AD transgenic mice, work in Wistar rats showed microglia activation correlated to a reduced CD200 expression, CD200 was also reduced following A β injections [85]. As CD200 knock-out mice have a higher inflammatory this may also slow disease progression in AD mouse models [46].

Macrophage-Colony Stimulating Factor (M-CSF) and IL-34 signal through the Colony Stimulating Factor 1 receptor (CSF1R) to maintain M ϕ and microglial populations and drive M ϕ /microglial proliferation [86–88]. CSF1R antagonism can prevent microglia in response to an LPS challenge [89]. Recently, CSF1R inhibitors have been used to prevent microgliosis in AD mouse models.

9-month-old APP/PS1 mice had CSF1R inhibitor (GW2580) incorporated in their diet for 3 months. The Csf1R inhibitor treated APP/PS1 mice had a reduced number of microglia due to a lower microglial proliferation compared to APP/PS1 mice on a control diet [73]. This was associated with a reduction in several microglia specific genes, such as *Spi1*, *C/ebpa* and *CSF1R*. Treatment with the CSF1R inhibitor did not alter the A β plaque load, though the synapses of these mice were more preserved than in APP/PS1 mice on a control diet. This likely explains why CSF1R inhibitor treated APP/PS1 mice performed better on several cognitive tests designed to test short-term memory, which was impaired in control APP/PS1 mice [73].

Similar observations were made in 3xTg-AD model mice treated with a different CSF1R inhibitor (PLX5622) for up to 3 months [90]. Treatment with this inhibitor caused a ~30 % reduction in the

number of microglia compared to untreated 3xTg-AD mice [90]. After 3 months of treatment A β pathology was unchanged, though fewer microglia were associated with A β plaques compared to untreated mice. More importantly, CSF1R inhibitor treated 3xTg-AD mice performed better on cognitive tests than untreated mice [90].

When 5xTg-AD model mice were treated with the PLX3397 CSF1R inhibitor at 2 months it reduced A β plaque pathology [91]. These 5xTg-AD mice were treated with the CSF1R inhibitor for 3 months and had a 70-80 % reduction in the number of microglia population which resulted in an improved performance in cognitive tests compared to untreated controls [91]. A shorter CSF1R inhibitor treatment in older 5xTg-AD mice also reduced the number of microglia compared to [92]. While both untreated and treated 5xTg-AD mice had a similar A β plaque load, though CSF1R inhibitor treatment again prevented deficits in cognitive performance that were seen in untreated 5xTg-AD mice [92].

These CSF1R inhibitor experiments suggest that reducing microgliosis ameliorates cognitive-deficits associated with AD pathology, even at later disease stages. However, Cx3cr1 knock-out studies suggests that reactive microglia are beneficial in AD pathology. It could be that microglia become less reactive in AD so the population expands to try and offset the impact of having less reactive microglia. These studies also suggest A β plaque pathology does not accurately represent behavioural changes in these mice (as discussed in section 1.2). However, these microglia depletion experiments do not account for the impact of the peripheral immune system in AD which will be discussed in the following section.

1.2.2.2 Recruitment of Peripheral Immune Cells in health and AD

If the native microglia population has been depleted then peripheral monocytes are thought to be recruited to the brain and differentiate into microglia-like (MDML) cells [8,93–96]. It has been proposed that, in mice, Ly6C^{high} monocytes are preferentially recruited following CNS lesions, in a CCR2-dependent manner [95]. Induction of a peripheral interferon- γ (IFN- γ) response has been shown to increase trafficking of Ly6C^{high}CCR2⁺ monocytes through the choroid plexus, slowing disease progression in both 5xfAD and hTAU expressing mouse models [97–99]. Recent work has proposed that T-cells located in the choroid plexus are able to impact the immune system of the CNS both short-term and long-term [100]. The choroid plexus is the site of the Blood-Cerebrospinal-fluid Barrier (BCSFB), which is slightly different from the rest of the Blood-Brain Barrier (BBB), and is the site of immune-cell trafficking in the brain [101].

Multiple studies have suggested that these MDML cells are present in transgenic mouse models [102] and help slow AD progression [103–105]. It has been observed that MDML have a higher phagocytic capacity than native microglia in AD [78,103] which may be due to MDML having a more inflammatory basal state, observed in APP/PS1 mice [106]. However, others believe that the presence of MDML is dependent on the transgenic mouse model as another study found MDML did not interact with A β plaques in 5XfAD and APP/PS1 mice [107]. The discovery of better microglia specific markers, such as Tmem119, should help determine if MDML are present in all transgenic AD mouse models, and in human AD pathology [108].

As reviewed in [109] the BBB is now thought to be compromised early on in AD pathology. High resolution MRI showed the BBB around the hippocampus begins to breakdown with age, and individuals with Mild Cognitive Impairment (MCI), which precedes most AD cases, had a more overt hippocampal BBB breakdown [110]. Patients with early AD have also been shown to have leakier BBB than healthy controls in multiple brain regions [111]. Moreover, there is some evidence that a compromised hippocampal BBB is independent of A β and Tau pathology changes [112]. A similar breakdown of the BBB has been seen in some transgenic mouse models, as reviewed in [109]. This likely alters monocyte and T-cell CNS entry in AD, especially as the normal entry site, the choroid plexus, is thought to be suppressed in AD [110,113,114].

An age-dependent immunosuppression of the choroid plexus was observed in humans and mice. Increased type-I IFN (IFN-I) was thought to lower peripheral IFN- γ reducing monocyte trafficking and resulting in deficits in hippocampal learning and memory in mice [115,116]. More recent work suggested that IFN-I downregulates the microglial *Mef2C* transcription factor, which is known to collaborate with *Spi1*, and is another LOAD associated risk gene [117,118].

When a mIFN γ expressing virus injected in the cerebral ventricle of 2-day-old APP-TgCRND8 mice the A β load at 5 months was reduced in these mice compared to mice who received a control virus [119]. This was accompanied by an increased number CD11b⁺/Iba-1⁺ cells and increased MHCI/MHCII gene expression and a larger population of non-A β plaque associated MDML [119]. Together this suggests that IFN- γ expression results in immune activation and a reduction in plaque load, though the lack of behavioural testing meant the impact on AD progression could not be determined.

24-month-old APP/PS1 had higher cortical expression of *Cd68*, *I11b* and *Ifny* mRNA and higher phosphorylated (functional) STAT1 than wild-type (WT) littermates [120]. On a cellular level there were a higher number of CD11b/IFN- γ receptor double-positive cells in APP/PS1 transgenic mice.

The BBB was thought to be more permeable in these AD model mice, as assessed by MRI staining and a higher percentage of infiltrating monocytes [120].

Recent work has also shown T-cells, part of the adaptive immune system, enter a healthy CNS through the choroid plexus and may have a beneficial role in immune surveillance and repair [101,115]. This T-cell recruitment is thought to require signalling cues from both the periphery and the brain [121]. In AD pathology the choroid plexus is immunologically suppressed in the 5xfAD mouse model as both peripheral IFN- γ production and ICAM-1 expression were both reduced and FoxP3⁺ regulatory T-cells (T-regs) were present in higher numbers [98]. Both transient depletion of T-regs and PD-1 inhibition, which impairs T-reg signalling through the checkpoint PD-1, restored systemic IFN- γ signalling in 5xfAD and APP/PS1 AD model mice. This restored T-cell trafficking through the choroid plexus, reduced A β load and improved performance on behavioural tests in 5xfAD and APP/PS1 AD model mice [98].

Additionally Marsh *et al.* (2016) bred Rag2/IL2ry knock-out mice to the 5xfAD transgenic model to remove the adaptive immune system (T-cells, B-cells and NK cells) [122]. It was observed that 5xfAD mice with no adaptive immune system had higher levels of A β , which was attributed to impaired A β clearance. Moreover, the microglial gene expression and phagocytic capacity was altered in the 5xfAD mice with no adaptive immune system. Further investigation suggested that this disparity was due in part to a lack of immunoglobulin (IgG) antibody secretion from the adaptive immune arm [122].

However Togo *et al.* (2002) thought T-cells were detrimental as T-cells were present in higher numbers in late stage AD especially in the hippocampus and entorhinal cortex, which are regions affected by AD pathology [123]. Though hippocampal T-cells were also present in the control cases, often at similar levels to the AD cases [123].

Overall these studies suggest multiple AD mouse models have an immunosuppressed choroid plexus and relieving this suppression increases monocyte and T-cell trafficking which is beneficial. While IFN-I has been shown to be higher in aged humans as it was in mice [116], alterations to the choroid plexus in human AD pathology are not as easily assessed. There are several recently developed human *in vitro* BBB models that could be adapted to investigate the choroid plexus (BCSFB) in AD [124,125]. It is not only peripheral cells that have been shown to impact microglia physiology as peripheral infections have been shown to impact AD progression, as discussed below.

1.2.2.3 Microglial response to Peripheral Infection and Inflammation

Clinicians observed AD patients with an infection experienced an acceleration in cognitive decline, supported by evidence that inflammatory proteins were associated with an increased AD-risk [126]. Moreover, PET scans of patients with a high level of peripheral C-Reactive Protein (CRP, denoting inflammation) had an increased TSPO binding potential compared to low-CRP patients, suggesting that systemic inflammation is linked to neuroinflammation [127]. Holmes *et al.* (2009) later demonstrated AD patients with a higher baseline TNF α expression had a faster cognitive decline over 6-months compared low-TNF α patients [128].

Moreover, Rheumatoid arthritis (RA) patients are over 7 times more likely to develop AD than patients without this inflammatory disease [129]. RA patients treated with TNF inhibitors, like Etanercept, had a lower risk of developing AD. Therefore, following successful safety trials [130], Etanercept is being tested as a potential AD therapeutic [131].

In mice peripheral LPS injections induced microglia activation in multiple mouse strains [132]. In a mouse prion disease model a LPS-challenge resulted in a more aggressive CNS inflammatory response and cognitive impairment that was not observed when non-diseased mice were given LPS [133]. It was hypothesised that the neurodegenerative disease primes microglia which then respond in an exaggerated manner to a peripheral immune challenge [133].

1.2.2.4 Non-Microglial CNS M ϕ populations

While microglia are the best characterised population of myeloid cells, other functionally distinct populations such as perivascular M ϕ , meningeal M ϕ , choroid plexus M ϕ and resident monocytes exist in the CNS [134]. Research into the potential role of each CNS myeloid population in AD pathology has only just begun. One study found perivascular M ϕ play an important role in A β ₁₋₄₂ clearance in vessels, which could be beneficial in vascular dementia. The perivascular M ϕ were depleted in TgCRND8 AD mouse model, resulting in an increased deposition of A β ₁₋₄₂ in the vasculature. When the perivascular M ϕ were stimulated this A β ₁₋₄₂ deposition was reduced [135], which was observed in another mouse model (Tg2674-APP^{SWE}) [136]. The advent of single cell sequencing technology should enable these CNS myeloid populations to be studied independently, pending the discovery of identifying markers.

1.2.2.5 Astrocyte Activation in AD

As the brain contains multiple cell types the potential contribution of other glial cells such as astrocytes in AD has also been investigated. Liddelow *et al.* (2017) found that microglia could activate a subset of astrocytes following LPS stimulation via secretion of IL-1a, TNF or C1q. This

subset of astrocytes was not activated in LPS-challenged mice lacking microglia. The activated astrocytes were found to reduce synapse number and became neurotoxic [137].

In 2013 Serrano-Pozo *et al.* found an increased GFAP expression, a marker of astrocyte activation, in AD patients compared to non-demented controls [138]. Activated microglia and astrocytes were found to surround A β plaques in 15-month-old APP/PS1 transgenic mice [139], which has been independently observed in humans [140].

Work in the APP/PS1 model mice suggested that astrocyte activation may surpass microglia activation in AD [139]. It has been proposed that microglia have evolved to quickly shut-off production of inflammatory, to protect neurones, but as astrocytes do not normally contribute to cytokine production they are unlikely to have a well-regulated off-switch [141]. As reviewed in [142] astrocytes support neurones by maintaining the extracellular environment, uptake of neurotransmitters like Glutamate, and the production of various growth factors. Therefore, the astrocytic contribution to AD pathology could severely affect neuronal function.

1.3 Tissue Resident Macrophages

Macrophages (M \emptyset) are part of the leukocyte family and the innate immune system and were first described by Eli Metchnikoff in the late 19th century [143]. M \emptyset have an important role in pathogen defence, clearance of debris and tissue repair as reviewed in [144]. Tissue resident M \emptyset (trM \emptyset) are highly specialised populations of M \emptyset that are mostly seeded in a tissue early on in development [145]. The trM \emptyset were first studied using transgenic mice with GFP or Cre expressed under the *Cx3cr1* promoter, which is expressed on M \emptyset populations [146,147]. The diversity of trM \emptyset populations was investigated by sequencing the mRNA of multiple tissue M \emptyset populations [148].

trM \emptyset have been shown to have a separate transcriptional identity from other M \emptyset , which likely aids their niche-specific functions [148–151]. Lavin *et al.* (2014) profiled multiple trM \emptyset populations using a combination of RNA-sequencing (RNA-Seq), Chromatin Immunoprecipitation-sequencing (ChIP-Seq) and ATAC-sequencing (ATAC-Seq) to try and elucidate epigenomic and transcriptomic differences in these trM \emptyset . In microglia the tissue specific enhancer has been reported to be *Mef2C* [118], though *Sall1* is also considered to be important for microglia identity [152]. Compared to other trM \emptyset populations microglia showed a more distinctive gene expression pattern, suggesting these populations were more distantly related [153]. Moreover, it has been found that tissue specific enhancers collaborate with C/EBP and PU.1 to produce the trM \emptyset transcriptomic signature [153].

Lavin *et al.* (2014) also investigated if the transcriptomic signature is partly determined by the local tissue environment. Irradiated mice that endogenously express CD45.2 received bone marrow transplants from mice expressing CD45.1 and trM \emptyset populations were isolated 4 months later. It was observed that the CD45.1 bone-marrow derived M \emptyset (BMDM) replaced the lost trM \emptyset subset and acquired some of the enhancer landscape of trM \emptyset taken from untreated mice [118]. In another experiment CD45.1+ pM \emptyset were transplanted into the lungs of CD45.2+ mice had a partial loss their old transcriptomic profile to favour of more alveolar M \emptyset specific genes, though a lot of cells were lost in the transplantation and this adaptation was not complete [118]. This was supported by Gosselin *et al.* (2014) who found environmental signals were required to maintain expression of certain genes. When comparing freshly isolated microglia and pM \emptyset to cultured microglia and pM \emptyset they noted the loss of expression in several genes in the cultured M \emptyset .

In the brain environmental signals include M-CSF, cholesterol and TGF- β [153–155]. It is likely other signals are required as once murine microglia are removed from the brain TGF- β dependent genes such as *Tmem119* are halved within a matter of hours [154,155]. Mouse and human microglia transcriptomes have been shown to be largely conserved [156]

Further evidence for the CNS providing specific signals that contribute to microglia identity comes from MDML cells, described in 1.2.2.2. Monocytes adopt a microglia-like phenotype (MDML) in the brain, upregulating expression of *Cx3cr1* and *Iba-1* while reducing *CD45* expression [95]. *Tmem119* is thought to only be expressed *in vivo* by the native microglia population and not on MDML cells, in mice and humans, though some *in vitro* work suggests iPSC cells can also express *Tmem119* [108,157,158].

1.4 Microglia

1.4.1 Origin and Lifetime of Microglia

Microglia were first described by Nissl in 1899 were first referred to as microglia by del Rio-Hortega in 1932, who described them as a potential disposal system within the brain [159]. For many years the developmental origin of the microglia population was a matter of debate, as reviewed in [160]. As the *Cx3cr1* receptor is highly expressed in microglia throughout development Ginhoux *et al.* (2010) were able to trace the development of microglia *in vivo* using *Cx3cr1*^{GFP} reporter mice [146]. As a result of this study microglia are now known to be derived from the embryonic yolk sac and are seeded around day 10.5 in murine embryonic development [88]. Transcriptomic work has determined that microglia have three distinct developmental phases [161]. Recent evidence has suggested microglia density varies between brain regions. Erö *et al.*

2018 produced a cell atlas for the mouse brain and noted more microglia were present in the cortex of these mice compared to the cerebellum or fibre tracts [162]. The microglia density was also found to vary between different parts of the basal ganglia [163].

Microglia are a long lived self-renewing population. In 2015 Bruttger *et al.* found that microglia were able to repopulate the CNS within 4 days after ablation [164]. Askew *et al.* (2017) built on this work to show that microglia number was maintained by a tightly regulated balance between proliferation and apoptosis. The standard rate of microglial proliferation was determined to that 0.69 % of microglia were in the S-phase of the cell cycle at any given time [165]. As the density of microglia was similar in mice aged 4 to 24 months, it was evident that a high rate of apoptosis was required. Two-photon imaging studies showed that after a microglia died the nearest neighbouring microglia proliferated suggesting that microglia turnover was spatially and temporally linked [165].

These findings were confirmed in the “Microfetti” mouse model whose microglia randomly expressed one of four fluorescent proteins, enabling “daughter” microglia cells to be tracked after cell division. In these mice microglia density was stable, though there were regional differences in the rate of microglia turnover [166].

Microglia are thought to be long lived within the mouse CNS, as 26-months later approximately 50 % of the imaged microglia were still present [167]. Following proliferation the daughter cell moves ~40 μ M away from the parent microglia. This distance ensures they are able to interact with the established microglia network while maintaining their own "territory" [167].

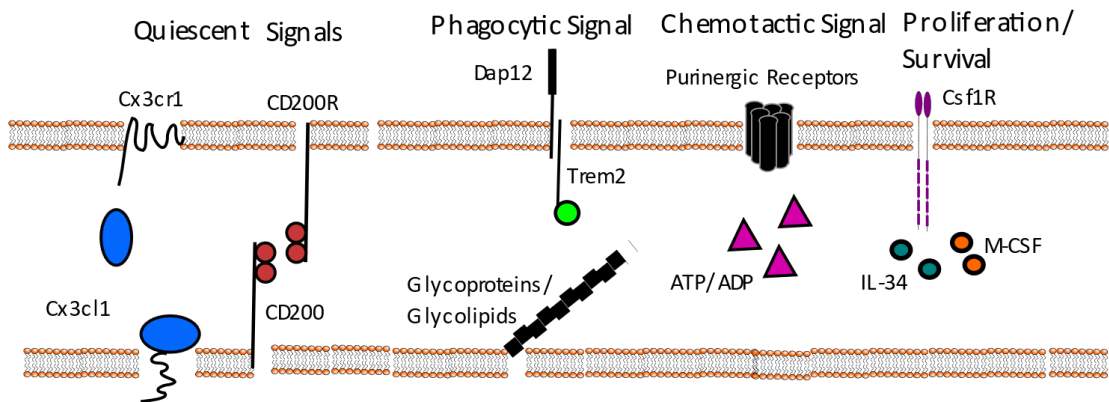
Réu *et al.* (2017) suggested that murine microglia had a much higher turnover than human microglia [168]. They calculated that approximately 0.08 % of human microglia were undergoing division on any given day. This differed from the calculations by Askew *et al.* (2017) who estimated 2 % of human microglia were dividing in post-mortem tissue samples [165]. As human microglia gene expression has been shown to increase with age which could explain the disparity between these studies meaning a greater samples size could improve these calculations.

While the development of new reporter mouse lines has allowed researchers to reliably determine the microglia turnover in murine models, there is a lot of work remaining to gain an accurate microglia proliferation rate in human, in health and disease. It is important to remember that the function of microglia is not solely reliant on the cell number, as discussed in the next section.

1.4.2 Important Microglia Receptors

Microglia identity is controlled by both transcriptional regulator and environmental cues, such as TGF- β (section 1.3). The function of several key receptors, shown in Figure 1.2, will be discussed below, with a focus as to how they are able to influence microglia function. A thorough review of microglia physiology can be found in [43].

Microglia



Neuron/Astrocyte

Figure 1.2 Summary of key Quiescent and Effector microglia receptors adapted from [169]. CD200R and Cx3cr1 receptor signalling maintains microglia in a quiescent state. Trem2/Dap12 signalling is one of the phagocytic signalling receptors. Purinergic receptors aid in microglia chemotaxis and Csf1R signalling promotes microglia survival and proliferation.

1.4.2.1 Quiescent receptors

Microglia help maintain neuronal function and preserve CNS tissue by surveying their territory to detect any damage or debris. As neurones are metabolically active this often means phagocytosing of debris. While some stimuli trigger an inflammatory response, this is promptly resolved under normal physiological conditions. *In vivo* imaging has demonstrated microglia have very motile processes even when they are in a “quiescent” state, so they should not be considered resting [170,171].

Receptors expressed on neurones, astrocytes and oligodendrocytes help maintain microglia homeostasis. There are two principal receptor pairings that are considered to induce a quiescent signalling cascade in microglia, CD200-CD200R and CX3CL1-CX3CR1 (Figure 1.2).

The CD200 ligand is expressed by neurones, astrocytes and oligodendrocytes while the receptor is only found on microglia [81,82] Hoek *et al.* (2000) demonstrated that removing the CD200 ligand prevents microglia from becoming fully quiescent. The microglia were found to have a higher baseline expression of CD11b and CD45 which is known to indicate that the cells are in a more reactive state.

Justin *et al.* (2011) investigated the effect of Cx3cr1 knock-out on CNS physiology under non-pathological conditions. Mice with a complete Cx3cr1 knock-out had impaired several forms of hippocampal dependent learning compared to mice that were heterozygous for Cx3cr1 deficiency [45]. These Cx3cr1-related memory deficits were determined to be caused by an increased expression of the inflammatory cytokine IL-1 β [45].

Cardona *et al.* (2006) found that microglia which are deficient in Cx3cr1 were more sensitive to immune stimuli. Cx3cr1 knock-out mice showed a higher microglial activation following a peripheral LPS injection compared to Cx3cr1 heterozygous mice [172]. The paper does not mention if the Cx3cr1 knock-out microglia had an altered baseline inflammation compared to the heterozygous mice. It was determined that Cx3cr1 suppression of microglia is at least partly mediated by IL-1, preventing a widespread activation [172].

Taken together these experiments demonstrate the importance of maintaining the quiescent signalling pathways in homeostasis that exist between microglia and other CNS cells. The next section will move onto discuss which receptors are involved in enabling microglia to perform functions such as chemotaxis, recruitment of other cells and phagocytosis (Figure 1.3).

1.4.2.2 Effector receptors

In addition to quiescent signalling molecules, there are also several receptors expressed on non-microglial cells that provoke a microglial response, often described as “reactive” or “effector” state. The branched, ramified morphology of quiescent microglia is lost once microglia become reactive. In this conversion the cell processes become shorter and thicker resulting in microglia with a rounder more ameboid morphology (Figure 1.3). These morphological changes were seen by Nissl in 1899, reviewed in [159], and are still used to study microglia activation today.

Reactive microglia express higher levels of CD45, CD68 and MHCII which is often accompanied by a reduction in Iba-1, Tmem119 and P2Y₁₂ receptor (P2ry12). The advent of microglia transcriptomic studies has meant a more unbiased approach can be taken when characterising microglia phenotype.

In 2013 Hickman *et al.* defined a set of proteins that allowed microglia to sense changes in their environment, termed “sosome” [173]. A later transcriptomic study characterised the microglia “reactome” following multiple immune challenges [174]. These studies will enable researchers to accurately identify the profile of microglia, following validation experiments. The following sections will discuss the receptors that are critical in the microglia effector response namely, chemotaxis and phagocytosis (Figure 1.3).

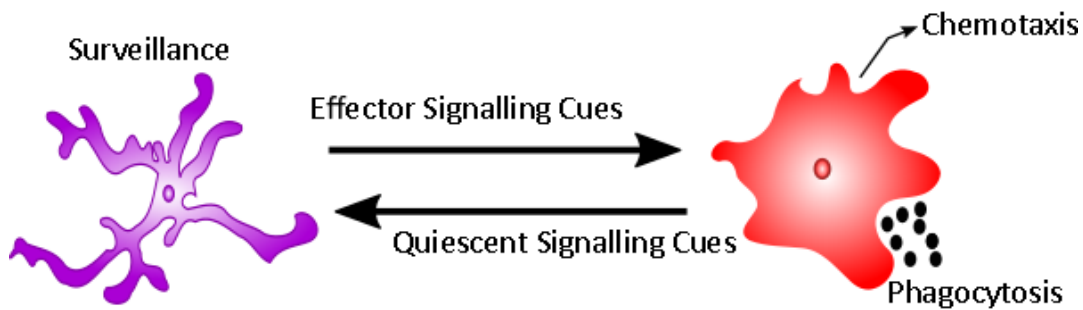


Figure 1.3 Overview of Effector and Quiescent signalling cues in Microglia. Quiescent signals help microglia maintain a homeostatic surveying state (purple). Effector signals such as detection of apoptotic cells results in reactive microglia (red). These effector microglia then migrate to the area of injury and phagocytose apoptotic cells.

1.4.2.2.1 Chemotactic Receptors

Microglial need to quickly migrate to the site of any damage. The development of 2-photon imaging allowed microglia responses to be imaged *in vivo*. In 2005 Davalos *et al.* used a small laser to injure the CNS and observe how microglia respond. Microglia were found to respond to the site of injury within a matter of minutes and remained there for at least 30 minutes [171]. Further investigations confirmed ATP acts as a chemotactic signal to quickly recruit microglia. Microglia detect ATP and other similar stimulants through purinergic receptors such as P2X ion channels and P2Y G-protein coupled receptors (Figure 1.2). These receptors are also found on neurones and the core ligand ATP can be released by both neurones and astrocytes [175].

In 2006 Haynes *et al.* focused on the role of P2ry12 in the microglial activation response. In primary microglial cultures ATP induced an ameboid morphology and cell migration. While *in vivo* studies showed the microglia without P2ry12 were still able to migrate to the site of injury, though there was a greater response time compared to wild-type mice [176] suggesting other cues can initiate microglia chemotaxis. There is some evidence that soluble CX3CL1 [177], neuronal glutamate release [178], the C5a complement protein [179] and TREM2 [180] can also induce chemotaxis in microglia.

While multiple signals can initiate microglial chemotaxis it is thought these signals converge on intracellular calcium signalling pathways, as reviewed in [181]. Intracellular calcium signalling is important in helping microglia move through the extracellular matrix to migrate to the site of injury [182]. Once the reactive microglia arrive at the signal origin respond by the secretion of chemokines and cytokines but also begin to clean up the damage through phagocytosis.

1.4.2.2.2 Phagocytotic Receptors

Phagocytosis is the process by which microglia engulf debris, apoptotic cells or pathogens over 0.5 μM in size [183] (Figure 1.4). Microglia are more sensitive to endogenous damage, detected through danger-associated molecular pattern (DAMP) receptors, than exogenous pathogens detected by pathogen-associated molecular pattern (PAMP) receptors [173]. As microglia are a highly specialised $\text{M}\phi$ population, and it has been proposed that the phagocytic process may be slightly adapted [184].

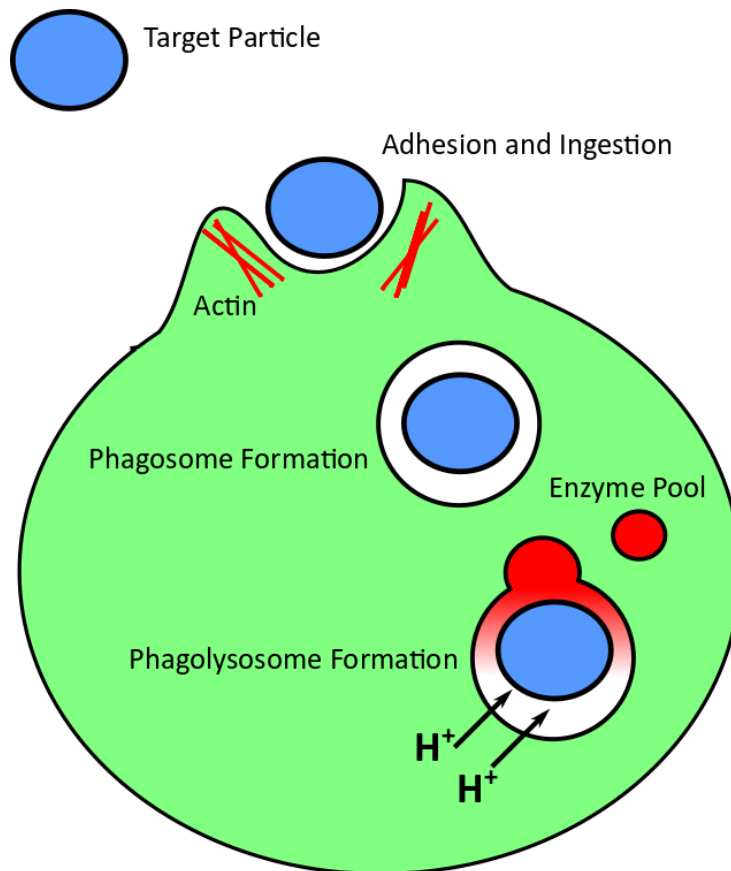


Figure 1.4 An Overview of the Phagocytic Process, adapted from [185]. The target particle (blue) can be opsonised with complement proteins or IgG which aids in detection. The particle is then bound receptors engulfed, which is mediated by the actin cytoskeleton (red lines). The phagosome then detaches from the cell surface where the particle is surrounded. Lysosomal enzymes (red circle) then fuse to the phagosome, which is acidified through hydrogen ion (H^+) to ensure the particle is completely destroyed.

Therefore, it follows that microglia phagocytosis needs to be studied independently and, where possible, *in situ* studies are needed rather than *in vitro*. Known receptors involved in microglial phagocytosis include TREM2, Fc receptors and complement receptors [186].

Microglia in Trem2 knock-down in primary mouse microglia cultures could not phagocytose apoptotic neurones as well as control cultures [187]. When Trem2 was over-expressed in microglia cultures increased the amount of apoptotic neurones that were phagocytosed [187]. TREM2 mediated phagocytosis has received a lot of attention in this field of AD research TREM2 is an AD-risk gene [58].

The TLR family are key to several innate immune processes, including phagocytosis. TLR4 is suspected to alter microglial phagocytosis in neurodegenerative diseases [188]. Work by Fellner *et al.* (2013) observed that TLR4 knock-out microglia cultures were not able phagocytose as efficiently as their WT counterparts [189].

Fc Receptor mediated phagocytosis is more efficient if the target particle has been opsonised, coated with immunoglobulins, IgGs, found in serum. In 1994 Ulvestad *et al.* showed that Fc receptors (FcRs) are expressed at very low levels on microglia under normal conditions, but expression was increased during pathological conditions [190].

The role of the complement system in microglial phagocytosis is known to be important in development and in AD [191]. C1q and C3 accumulate on synapses located near amyloid- β (A β) plaques, tagging these synapses for disposal by microglia [191]. *In vitro* the receptor for C3 (CR3) is key in the phagocytosis of myelin debris [192]. Overall more *in vivo* studies are needed to confirm earlier *in vitro* work, as cultured microglia are exposed to serum which affects phagocytic function [155]. It was demonstrated that cultured rat microglia exposed to serum resulted in a higher expression of complement proteins than microglia cultured without serum. It was concluded that *in vivo* microglia would only be exposed to serum if the BBB had been breached, meaning that *in vitro* microglia exposed to serum may respond differently to *in vivo* microglia [155]. The need for further studies of microglia phagocytosis under physiological conditions has led to the publication of protocols for direct assessment of phagocytosis *in vivo* [193].

1.4.2.3 The Importance of TGF- β signalling

Several studies have confirmed the importance of TGF- β in maintaining a 'quiescent' microglia phenotype. In 2003 Paglinawan *et al.* stimulated microglia with a combination of TNF α /IFN γ stimulation and observed an increased production of inflammatory genes. If the microglia cultures

were pre-treated with TGF- β then a smaller number of genes were up-regulated following TNF α /IFN γ stimulation, suggesting TGF- β lessened the inflammatory response [194].

Butovsky *et al.* (2014) observed a high expression of the genes encoding TGF- β (*Tgfb1*) and its receptor (*Tgfb1r1*) on microglia. By using RNA sequencing they were able to determine a set of genes that form a fresh microglial 'signature' [154]. These signature genes were highly expressed by freshly isolated microglia and reduced on microglia cultured with M-CSF. When microglia cultures were supplemented with both M-CSF and TGF- β the gene expression signature became increasingly similar to freshly isolated microglia [154]. These 'signature' genes included *Tmem119*, *P2ry12* and *Siglech*.

In 2017 Bohlen *et al.* built upon this study by determining what other factors are secreted by astrocytes to maintain microglia *in vitro*. Primary rat microglia cultures identified IL-34, M-CSF, TGF- β and cholesterol [155] as key reagents. They observed that these three factors made serum-supplementation redundant and serum-free cultured cells better represented *in vivo* microglia. However cultured microglia still had a higher expression of inflammatory genes compared to freshly isolated cells, meaning it is most appropriate to study microglia *in vivo* [155].

TGF- β has been known to promote an anti-viral response that reduces the efficacy of some viral infections [195]. In tissue resident M ϕ this anti-viral effect was purported to be due to the immunoregulatory role TGF- β has, as reviewed in [196]. Specific examples of how TGF- β maintains tissue resident M ϕ homeostasis include the regulation of inflammatory cytokines like IL-1 and the suppression of nitric oxide synthase (iNOS) [196].

1.4.3 Microglial Function

The next few sections will provide a brief overview of the primary functions of microglia in physiological and pathological settings, see [43,197] for detailed reviews.

1.4.3.1 *In Health*

Microglia are thought to have indispensable functions within the CNS. Patients with Nasu-Hakola disease have dysfunctional microglia and develop an aggressive form of Frontotemporal Dementia (FTD) leading to a premature death, as reviewed in [198]. The main physiological roles microglia play in both development and in the adult brain will be discussed below.

1.4.3.1.1 Phagocytosis and Synaptic Refinement

During brain development surplus neurones undergo programmed cell death to ensure that only the required number remain. Microglia engulf apoptotic neurones which express activated

caspase-3 [199]. When microglia were removed from *ex vivo* cerebellar slices it was observed that microglia promote neuronal apoptosis in this phase of development [199] thought to be mediated, at least in part, by the release of reactive oxygen species (ROS). Following phagocytosis, microglia have been shown to respond by stimulating phagocyte NADPH oxidase to produce ROS and superoxides in a process termed respiratory burst [200]. The release of these superoxides results in neuronal death, as reviewed by [201]. In development excess synapses are also removed by microglia. Synaptic pruning has been shown to be essential for proper brain development, as without this loss neurones electrophysiology is abnormal [202].

The visual cortex is often used to investigate how microglia influence neurones under physiologically conditions as it is quite plastic, and it is easy to control the input (light). In 2007 Stevens *et al.* found that the complement protein C1q was localised to certain synapses in the retinal neurones of the developing visual cortex, activating the complement system to remove excess synapses [203]. Recent *in vivo* studies of TREM2 knock-out mice have confirmed that TREM2 is also essential for microglia synaptic removal in development [204].

While some synapses are “tagged” for removal by C1q others are protected by CD47 expression which prevents microglial engulfment in visual cortex development [203,205]. The CD47 protective signalling was preferentially found on more active synapses [205]. This suggests that more active synapses are protected from removal and less active synapses are targeted for removal, which has been supported by others [206,207].

The adult CNS is a highly metabolically active tissue which microglia constantly monitor the CNS to ensure any potential damage is quickly removed [170]. There is some debate as to whether microglia maintain the same degree of phagocytosis and synaptic refinement in an adult brain.

Following birth very few areas of the brain constantly produce new neurone, so many studies focus on the sub-ventricular zone of the hippocampus. Here many of these new-born neurones are surplus to requirements so undergo apoptosis and are quickly cleared by microglia [208]. Microglia have been shown to restrict the number of neural precursor cells in the hippocampus through phagocytosis [209]. Further work is needed to see if microglia also quickly clear apoptotic cells in other regions.

1.4.3.1.2 Neurogenesis, Axonal Growth and Neurotransmission

In cortical development microglia ensure survival of particular neurones partially through secretion of Insulin-like Growth Factor [210]. Squarzoni *et al.* (2014) showed microglia moderate

dopaminergic axon outgrowth and some interneuron positioning in forebrain development [211]. Cx3cr1^{GFP} reporter mice show that Cx3cr1 signalling in microglia is critical in recruiting microglia to the appropriate sites of development, reviewed by [212].

Work by Wake *et al.* (2009) demonstrated that in quiescent microglia processes preferentially contact synapses that have a higher basal activity [213]. This was also seen in the visual cortex where microglia processes were near developing dendritic synapses [206].

It has also been suggested that microglia are able to influence neurones through secreted factors. At glutamatergic synapses the neurotransmitter glutamate signals through post-synaptic NMDA-receptors. Microglia conditioned media was able to induce a larger NMDA-receptor post-synaptic, suggesting microglia also secrete factors which are able to alter neurotransmission. In a follow up study glycine was proposed as the main factor in microglia conditioned media which increased NMDA-receptor evoked potentials [214].

In an *in vivo* model microglia depletion was found to alter function at glutamatergic synapses and impair hippocampal-dependent learning [215]. It was later determined that some of these microglial driven changes to synaptic plasticity were mediated by secretion of Brain Derived Neurotrophic Factor (BDNF) [215].

Microglia have also been shown to be necessary for hippocampal LTP, which is thought to be the physiological mechanism underlying learning and memory. When Cx3cr1 expression is absent in microglia mice have impaired LTP and deficits in hippocampal-dependent memory formation [45]. LTP was also impaired in mice where the microglia had a higher baseline inflammatory state [46].

Microglia can also influence neurotransmission via astrocytes [47]. It was observed that LPS-stimulated microglia released more ATP which activated purinergic signalling in astrocytes. These activated astrocytes increased the excitatory post-synaptic current in neurones [47].

1.4.3.1.3 Angiogenesis

Angiogenesis is the process in which new blood vessels develop from the existing vasculature. Most studies explore the role of microglia in angiogenesis in the developing retina. In 2010 Ginhoux *et al.* showed that microglia precursor cells appeared to be closely related to blood vessels [88].

Moreover, microglia closely associate with the vessel tip and that depleting microglia in the developing retina results in a sparse vessel network [216]. The endothelial cell tip is critical to the

formation of a new vessel [216]. *In vitro* studies confirmed that microglia stimulate vessel sprouting, likely through a combination of direct contact and secreted factors. Further investigations showed that microglia secrete several angiogenic factors, though not the most common Vascular Endothelial Growth Factor-A (VEGF-A) [216]. However microglia co-cultured with retinal microvascular endothelial cells can secrete VEGF-A and Platelet Derived Growth Factor-BB (PDGF-BB) [217]

These findings have been independently corroborated. Fantin *et al.* (2010) demonstrated that ramified microglia closely associate with the developing vessel tip. In genetic models where microglia were ablated, mice had a reduction in vascular complexity but the deficiency appeared to be different from VEGF-A mutants [218]. Imaging studies in zebrafish embryos suggest that microglia act as “cellular chaperones” linking different vessel tips and bridging contacts with other cells [218].

As reviewed in [219], there is very little evidence as to what role microglia might play in maintaining the vasculature of the adult brain. It has been suggested microglia may contribute to the maintenance of the BBB [170] but this has yet to be confirmed in a non-pathological setting.

1.4.3.1.4 Immune surveillance

This section will discuss the role of microglia in CNS immune surveillance. Recently it was discovered that *in vivo* microglia monitor a defined territory roughly situated 50-60 μM apart. The soma remains static while the processes rapidly expand and contract, at a rate of ~ 1.47 $\mu\text{M}/\text{minute}$ [170]. Microglia were observed to contact astrocytes, neurones and blood vessels. The more active the neurones the more microglial contact the cells receive, suggesting that microglial surveillance is adaptable.

It has also been suggested that microglia may collaborate with other immune cells. Microglia within the circumventricular organs monitor cerebrospinal fluid and were at higher densities express a higher level of “effector” receptors such as CD86, which is linked to antigen presentation pathways [220]. Other work has suggested microglia may be capable of antigen presentation [221]

In summary, microglia are constantly monitoring the CNS for any perturbations which could result in damage. With technological developments in microglia Imaging these cells can now be studied *in situ* however, many of the studies infer function from the impact of microglia in pathology.

1.4.3.2 In AD Pathology

As previously discussed, microglia are now thought to be connected to AD pathology. The complement system has been shown to mediate synaptic removal by microglia during CNS development [203] and genetic studies have linked multiple complement genes AD risk [3]. This led Hong *et al.* (2016) to investigate the potential role of the complement system in AD pathology. It was discovered that C1q synaptic tagging preceded synaptic loss by several months in the J20 mouse model of AD [191]. Further work showed that oligomeric A β was able to induce synaptic C1q deposition. The complement protein C3 was also shown to be important in mediated microglia-driven synaptic loss [191]. Taken together these results suggest that the complement system may drive microglia to inappropriately prune synapses in AD.

In vitro studies have shown microglia preferentially phagocytosed A β fibrils over oligomeric A β [222]. In this study oligomeric A β caused microglia to expel several pro-inflammatory mediators, including IL-1 β , TNF α , NO and PGE2. This led Pan *et al.* (2011) to conclude that failure to phagocytose oligomeric A β causes perturbs microglia causing them to become more neuroinflammatory, at least *in vitro*.

In a later study Meyer-Luehmann *et al.* (2008) performed longitudinal imaging in APP/PS1 and Tg2576 mice. While microglia did not eliminate A β plaques they prevented the plaques from growing. Individual A β plaques were formed within 24 hours and surrounded by microglia.

Füger *et al.* (2017) imaged APP/PS1 transgenic mice microglia every two weeks for 6 months. It was noted that APP/PS1 mice had a lower microglia number in A β -plaque free areas. However, the non-plaque associated microglia were found to divide approximately 3 times as often as plaque associated microglia, therefore new microglia migrated to A β plaques in APP/PS1 mice [167].

In 2016 Bisht *et al.* observed that there appear to be a subset of highly dystrophic microglia associated with CNS pathology. In the APP/PS1 mouse model this pathological subset of microglia were associated with dystrophic neurites. Later a single cell sequencing study in the 5xFAD transgenic model confirmed the existence of pathological subset of microglia, termed Disease-Associated Microglia (DAM) [223]. DAM microglia were closely associated to A β plaques and had an increased expression of AD-associated genes such as *ApoE* and *TyroB*. This was accompanied by a reduced expression of homeostatic genes such as *Cx3cr1*, *Tmem119* and *P2ry12*. The conversion from healthy microglia to DAM is thought to be a two-part process. In the first stage increased APOE signalling is thought to reduce TGF- β -dependent gene expression [58]. The second stage was

thought to be TREM2 and resulted in an increased activation of lipid metabolism and phagocytosis pathways [223].

The DAM population has also been observed in post-mortem human tissue [224]. Again, plaque-associated microglia had a higher level of inflammatory markers compared to microglia which were not associated with plaques.

It is now thought that the DAM subset of microglia are most harmful in AD pathology and this population expands as the disease progresses [223]. This is in-keeping with the ‘double-edged sword’ hypothesis, which suggest microglia become detrimental in late-stage. As the DAM microglia conversion is mediated by APOE-TREM2 signalling it raises the question of how other LOAD genes might impact the phenotype of microglia.

1.4.4 How LOAD risk effect Microglial Physiology

TREM2 and DAP12 are known to collaborate during signalling [58] (Figure 1.2) and have associated AD risk mutations [225]. The expression data shown in [226] demonstrates that many LOAD risk genes are only expressed by microglia. *CD33*, *PILRA* and *PLCG2* have mutations which are considered to lower AD-risk [227–229]. In a recent review Hansen *et al.* (2018) summarised what is currently known about each LOAD risk gene [226]. The following sections will focus on the impact of transcription factors associated with AD risk and LOAD genes thought to affect the cytoskeleton, which are relevant to this thesis.

1.4.4.1 Transcription Factors

There are two microglial transcription factors associated with LOAD risk, PU.1 and MEF2C [3,4]. Both of these transcription factors establish microglia identity in development, to produce a transcriptomic profile unique to microglia [118,153].

Microglia lacking *Mef2C* had a higher expression of CD45 and CD11b, indicative of inflammation. Moreover, the higher levels of IFN-I associated with age downregulates *Mef2C* expression [117]. Therefore, it is possible that *Mef2C* is reduced as a response to AD-related inflammation which leads to microglia with a “primed” phenotype.

Spi1 encodes the PU.1 transcription factor which likely affects many genes in microglia. When PU.1 was knocked-down in the BV-2 cell line, expression of several genes and the phagocytic capacity of these cells was reduced [230]. Later work in human microglia has suggested there are potential PU.1 binding sites upstream of several other AD-risk genes [231]. In human microglia cultures a reduction in PU.1 also altered the microglia transcriptome and phagocytic capacity [232,233], see

section 1.5.2 for full discussion. Overall alterations to either of these transcription factors appear to alter microglia in a manner associated with AD pathology.

1.4.4.2 Cytoskeletal Dynamic Signalling related genes

Chemotaxis and phagocytosis (Figure 1.4) are two microglial functions which rely on cytoskeletal changes. Several LOAD-risk genes have been linked to pathways regulating the actin cytoskeleton namely, *PICALM*, *SHIP-1*, *CD2AP*, *RIN3*, *BIN1* and *ABI3* [226].

PICALM was one of the first LOAD genes identified through a GWAS approach [60,62,234]. In post-mortem cortical tissue *PICALM* was higher in LOAD and EOAD patients compared to controls and *PICALM* staining was associated with NFTs, a hallmark of AD pathology [235]. In the APP/PS1 mouse model *Picalm* knock-down was found to reduce A β pathology [236], suggesting that a reduction in *Picalm* was beneficial.

SHIP-1, *CD2AP*, *RIN3* and *BIN1* have all been linked to DAP12, the signalling partner for TREM2 (Figure 1.2)[237]. Kamen *et al.* (2007) found that *Ship-1* is recruited to the phagosome during phagocytosis in a reporter M ϕ cell line [238]. In 2012 Bao *et al.* demonstrated that *SHIP-1* binds to another risk gene *CD2AP* and together these proteins complex to potentiate Fc Receptor mediated phagocytosis in Dendritic Cells [239]. The *CD2AP* protein has also been shown to associate with *BIN1*, another AD associated risk gene that is known to have a role in endocytosis.

Primary cortical neuronal cultures with artificially reduced *Bin1* and *Cf2ap* had higher A β 42 levels than controls. These proteins were thought to collaborate with APP and Bace1 at the surface of a phagosome [240]. Another study has suggested that a loss of neuronal *BIN1* increased the speed of Tau deposition *in vitro* [241]. *BIN1* has also been shown to be recruited some vesicles during endocytosis [242].

The frontal cortices of AD patients had an increased expression of *BIN1* compared to non-demented controls [243] and suggested that *BIN1* is primarily expressed by neurons in immunohistochemical analysis of post-mortem human AD and controls brains. This conflicts with transcriptomics data presented in [226] which suggests *BIN1* expression is highest in microglia. These differences could be attributed to detection of different *BIN1* isoforms, but requires further study of both *BIN1* RNA and protein, in a complete system.

In a recent report Sims *et al.* (2017) identified a rare coding variant in *PLCG2* associated with a lower AD risk gene [5]. *PLCG2* is an enzyme linked to intracellular calcium signalling in microglia

and the variant associated with a reduced AD risk, P522R, has a slightly stronger enzyme activity compared to the common form of PLCG2 [229].

The final AD risk gene that will be mentioned in this section is *ABI3*. Again recently a rare coding mutation of *ABI3* was linked to AD pathology [5]. *ABI3* is known to be highly expressed in microglia and preliminary analysis of post-mortem AD brain tissue suggests *ABI3* expression is present on a subset of microglia [244]. The exact function of *ABI3* remains largely unknown, though *ABI3* can form part of the WAVE regulatory complex [245], which suggests *ABI3* may be able to influence actin remodelling in the microglial cytoskeleton. This discussion will be continued in section 1.6.2.

Overall, several LOAD-risk genes suggest there is a deficit in microglial phagocytosis may contribute to AD aetiology. Preliminary work in cell lines supports these findings, though further work is required to fully elucidate the part these proteins play. These studies should focus more on microglia models and, wherever possible, rely on *in vivo* systems to ensure a holistic approach.

1.5 *Spi1*/PU.1

The *Spi1* gene encodes the transcription factor PU.1 which is a member of the ETS family and is conserved between species [246]. PU.1 is highly expressed in myeloid cells such as M \emptyset , and present at a lower level in B-Cells, as ratified by Immgen [247,248]. The level of PU.1 transcription factor is altered in hematopoietic progenitor cells and drives differentiation of multiple immune cells (Figure 1.5). Early *in vitro* experiments have shown that in hematopoietic progenitor cells a lower amount of PU.1 drives B-cell development whereas a high level of PU.1 commits cells to a myeloid lineage [249]. In T-cell and NK-Cell development PU.1 expression is lost early in development [9]. This was confirmed in a *Spi1*^{GFP} reporter mouse where GFP was fused onto exon 1 of the *Spi1* gene [250]. Again a high level of PU.1 activity was needed for myeloid cell differentiation, a lower level of PU.1 resulted in B-cell differentiation [251].

Therefore, the amount of PU.1 within a hematopoietic stem cell helps determine its fate. Recent work by Heinz *et al.* (2010) reviewed the location of PU.1 binding sites throughout the mouse genome in pM \emptyset and splenic B-cells. PU.1 is thought to bind near other lineage-determining factors such as C/EBP in M \emptyset and Oct-2 in B-cells, which suggests that PU.1 works closely with other transcription factors to determine cell lineage [252].

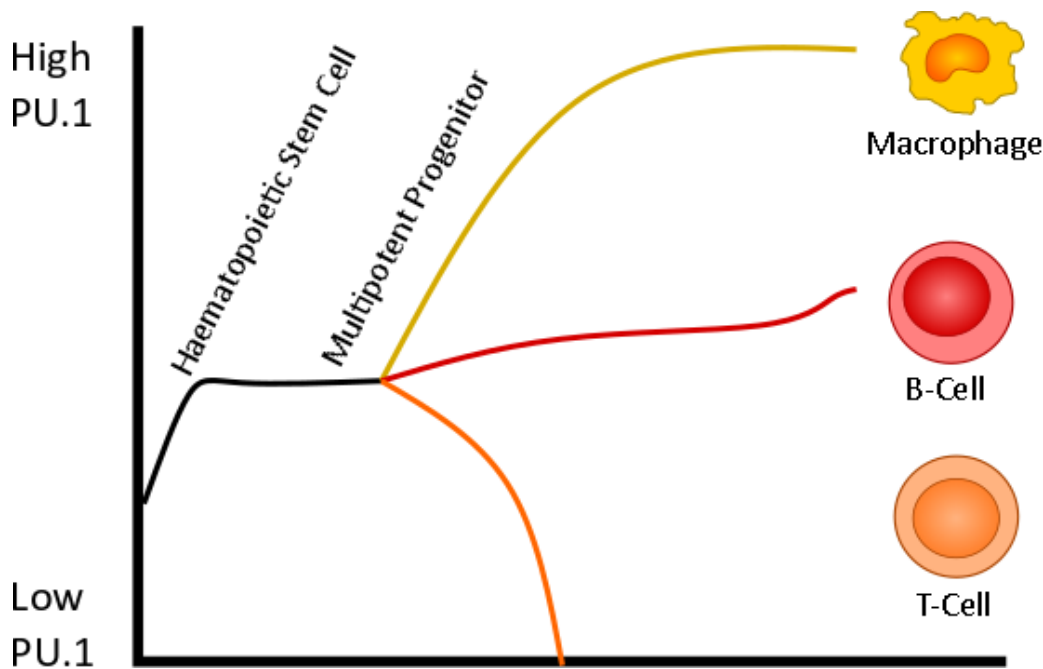


Figure 1.5 Diagram summarising the level of PU.1 in differentiating immune cells adapted from [253]. This highlights that PU.1 is important in both Myeloid/M ϕ and B-Cell differentiation and is suppressed in T-cell differentiation. M ϕ had a larger expression of PU.1 compared to B-Cells.

After development PU.1 contributes to M ϕ proliferation and survival. Microglia strongly express the PU.1 protein, and the pattern of PU.1 binding has been linked with the M ϕ activation [254]. PU.1 also contribute to the epigenetic signature of cells via monomethylation of histone 3 lysine 4 (H3K4) [252].

In 1996 Celada *et al.* found that bone marrow derived-M ϕ (BMDM) transfected with an anti-sense PU.1 had a reduced proliferation when exposed to M-CSF compared to non-transfected controls and PU.1 sense transfected cells [255]. This was attributed to the fact that PU.1 controls the expression of the M-CSF receptor also known as CSF1R (Figure 1.6) [256]. The contribution of PU.1 to microglia proliferation was confirmed when Smith *et al.* (2013) showed that siRNA targeting of PU.1 reduced the viability of cultured microglia. Moreover, Kueh *et al.* (2013) showed there is a positive feedback loop between the level of PU.1 and the length of the cell cycle, once the level of PU.1 passes a critical threshold cells differentiate into M ϕ [257].

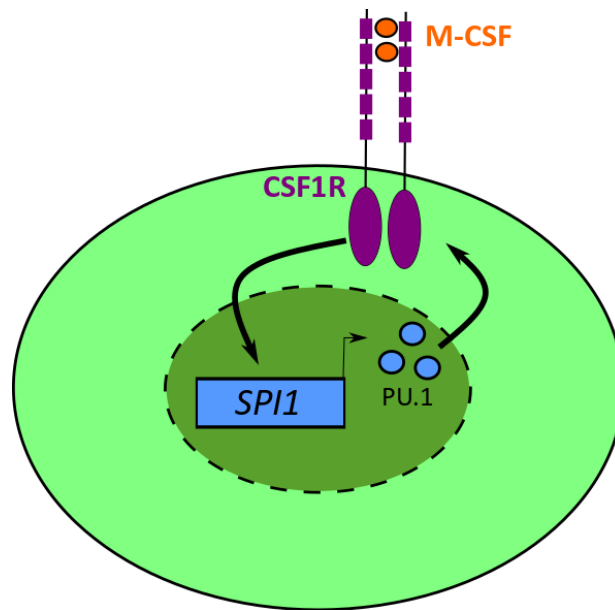


Figure 1.6 Graphic depiction of M-CSF dependent PU.1 Feedback Loop. M-CSF activates the CSF1R and which results in an increased *Spi1* transcription and production of the PU.1 protein. PU.1 has been shown to also increase CSF1R expression [255,256].

Several mouse models of disrupted PU.1 confirm PU.1 is essential for the survival and normal function of myeloid cells. The first reported transgenic models attempted to knockout PU.1 by disrupting exon 5, which contains the DNA binding domain of PU.1 [258]. Scott *et al.* (1994) failed to produce a homozygous PU.1 mutant mouse finding that embryos did not survive past day 18 of development due to severe disruptions to the immune system. Another group did breed homozygous mutant PU.1 mice but these died of septicaemia within 48 hours, though antibiotic treatment prolonged survival for 2 weeks [7]. PU.1 mutant embryos had no M ϕ , neutrophils, B-cells or T-cells. Despite the severe phenotype of PU.1 null mice no phenotypic differences have been reported in PU.1 heterozygous null mice [7]. Another model disrupted *Spi1* by mutating the first coding exon, these mice survived 1-3 weeks post birth though both myeloid and B-cell differentiation was impaired [259]. Beers *et al.* (2000) found that several immune populations, including M ϕ s, were restored in PU.1 mutant mice following wild-type bone-marrow transplants [8]. However, in the brain these cells were likely MDML rather than native microglia.

Rosenbauer *et al.* (2004) discovered that when the -14 kB URE was deleted from the *Spi1* gene PU.1 expression in the bone-marrow reduced by 80 % compared to wild-type cells. These mice were able to breed and appeared to be functionally normal until approximately 3 months of age. Then the mice with reduced PU.1 had an expanded population of progenitor cells and neutrophils compared to wild-type mice. This neoplastic phenotype worsened until the mice eventually died within 8 months, which was compared to Acute Myeloid Leukemia (AML) [260].

Taken together these PU.1 knock-out/mutant mouse models have conclusively shown that PU.1 is essential to a functional immune system, especially in myeloid cells. The next section will focus on how the *Spi1* gene is laid out and regulated.

1.5.1 *Spi1* Layout and Regulation

As previously mentioned PU.1 is a prominent member of the ETS transcription factor family [246]. A general review of the ETS transcription factors can be found here [261]. Due to its essential role in the development of the immune system the *Spi1* gene is highly conserved between mice and humans. Protein sequence alignment shows that mouse and human PU.1 protein sequences were over 85 % identical, as shown in Figure 1.7.



Figure 1.7 Comparison of protein sequences between mouse and human PU.1. The mouse protein sequence (RefSeq ID NP_035485) and human protein sequence (RefSeq ID NP_003111.2) were over 88 % identical, using BLAST analysis, suggesting PU.1 is highly conserved between species.

As this thesis primarily focuses on the *Spi1* gene in mice the rest of this section will focus on murine *Spi1*/PU.1. Early In vitro studies suggested the DNA binding domain of PU.1 was found to be in exon 5 of *Spi1* [247]. PU.1 is now known to bind DNA in a loop-helix-loop manner, as demonstrated by the crystal structure work done by Pio et al. 1996 [262].

A recent report explored how PU.1 can bind in a variety of ways, which likely helps PU.1 act as a master regulator of myeloid cell function [10]. In addition to combining with other transcription factors at PU.1 binding sites it was proposed that there were transcription sites that were dependent on the concentration of PU.1 within the cell [10].

Spi1/PU.1 regulation is complex and contains multiple feedback loops. Zhang *et al.* (1999) found that GATA-1 and GATA-2 can both repress PU.1 activity by blocking other transcription factors binding to the *Spi1* promoter [263]. RUNX1 has also been suggested as forming a negative feedback loop with PU.1 [264–266].

Additionally, there are several distal regulatory elements of PU.1. Li *et al.* (2001) identified 3 potential regulatory elements within 35 kb upstream or downstream of the *Spi1* gene sequence. This included the -14 kb Upstream Regulatory Element (also referred to as URE in this thesis).

The -14 kb URE was inserted into myeloid cell lines the promoter function was enhanced, whereas this URE had no effect when transfected into a T-cell line [267]. The function of this URE was further studied *in vivo* when a GFP reporter was inserted under the URE. This URE was found to have a higher expression in myeloid cells and a lower expression in B-cells [268].

Other *Spi1* regulatory elements have since been discovered (Figure 1.8) including myeloid-cell specific enhancer sites at -10.3 kb and -12.2 kb [269]. Zarnegar *et al.* 2012 found the -10.3 kb and -12.2 kb sites upstream of *Spi1* were specifically utilised by myeloid cells such as MØ whereas -13.7 kb, -14 kb and -17.8 kb regulatory elements were thought to help maintain B-Cell PU.1 protein levels [269].

In T-cell development runx1 is known to suppress PU.1 by binding to the -14 kb *Spi1* URE. However in myeloid cells Runx1 binds both the -14 kb and -10.3 kb *Spi1* URE to induce a high expression of PU.1 [266].

When C/EBPα binds at the -14 kb *Spi1* URE site in myeloid cells it induces reorganisation of chromatin which activates an enhancer at the -12 kb site, allowing other PU.1-driven transcription factors to bind and further increase PU.1 expression [270]. In human microglia cultures M-CSF has been shown to increase the level of C/EBPα [271].

Ikaros has been shown to bind at the myeloid specific *Spi1* regulatory sites -10.3 kb, -12.2 kb and -14 kb which again increases PU.1 expression [269]. Ikaros requires the presence PU.1 to increase *Spi1* expression though this is more essential at the -10.3 kb and -12.2 kb regulatory sites rather than the -14 kb URE. In pre-B-Cells Ikaros and PU.1 binding at the -14 kb URE acts with other unknown factors to suppress *Spi1* expression [269].

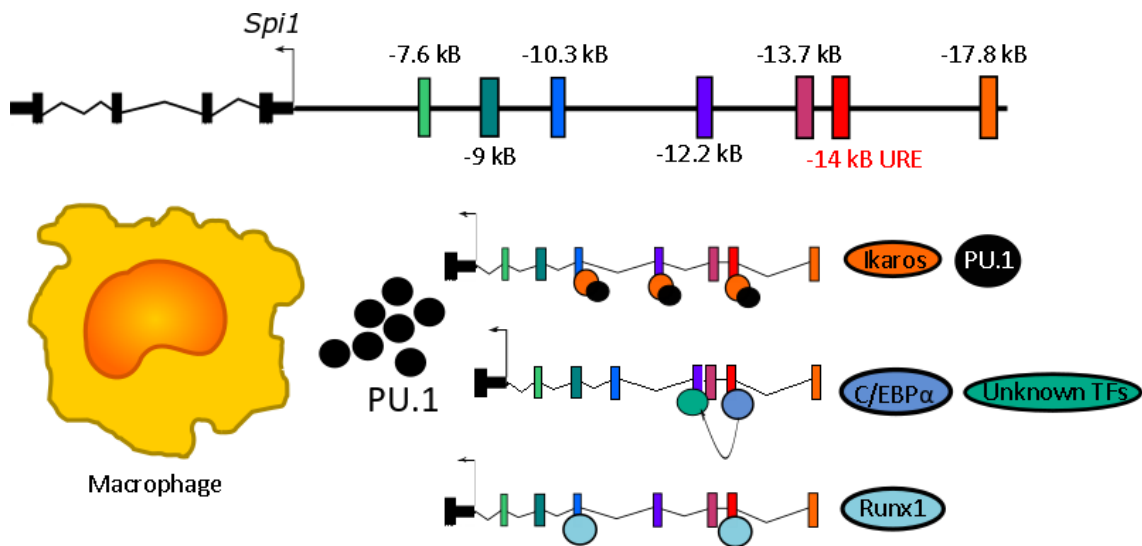


Figure 1.8 Overview of distal *Spi1* regulatory elements or enhancers, and how the binding of transcription factors at these sites can increase PU.1 protein expression in MØ, adapted from [269]. The *Spi1* regulatory elements (top) include the -14 kb Upstream Regulatory Element (URE, red). In myeloid cells, like MØ, when *Runx1* binds the -14 kb and -10.3 kb regulatory sites production of PU.1 protein is increased. PU.1 expression is also increased in myeloid cells via *Ikaros* and PU.1 binding at the -10.3 kb, -12.2 kb and -14 kb URE sites. When *C/EBPα* binds to the -14 kb URE it causes chromatin reorganisation activating another the -12.2 kb enhancer, opening up binding sites for other transcription factors (TFs), further promoting PU.1 protein expression [264,265,268].

Overall multiple mechanisms exist to ensure PU.1 is highly expressed in myeloid cells, many of which involve the -14 kb URE. This led Rosenbauer *et al.* (2004) to investigate if the removal of this URE could lead to a reduced PU.1 expression in the myeloid cell subset, providing a model to study the functional role of PU.1 in MØ [260], which will be discussed in the next section.

1.5.2 CNS Function and role in AD

As previously described the PU.1 transcription factor plays a critical role in MØ identity, and PU.1 controls the expression of several key functional MØ receptors, as reviewed in [246]. This includes expression of CSF1R which is linked to proliferation [255], CD11b which is involved in phagocytosis [272] and the CD45 phosphatase [273].

Primary human microglia cultures treated with M-CSF had an increased expression of the PU.1, which was observed alongside an increase in proliferation and phagocytosis [271]. This was later confirmed to be a direct result of the PU.1 level within the cells after an siRNA targeting PU.1 reduced the viability and phagocytosis of human microglia *in vitro* [232].

In recent years the PU.1 transcription factor has been well studied in the context of AD and other diseases, reviewed in [274]. Walton *et al.* (2000) demonstrated that PU.1 is increased the brain following a hypoxic-ischemia insult, though suspected this was partly due to microgliosis rather

than an increase on the individual cell level [254]. There have been several transcriptomic studies in recent years which have also implicated PU.1 in MØ inflammation. One study performed PU.1 ChIP-seq in LPS-stimulated and unstimulated RAW264.7s, a MØ cell line. Particular enhancers were activated following LPS stimulation, and within many of the enhancer regions PU.1 binding sites were located near the binding site for inflammation-related transcription factors such as NF-κB and IRF [275]. Das *et al.* 2016 performed transcriptome analysis on primary microglia cultures that had been stimulated with LPS and unstimulated controls. The genes expressed after LPS-stimulation were enriched for PU.1 binding sites in the promoter regions, alongside NF-κB, IRF1, IRF2, STAT1 and STAT2 [276]. In a MØ cell line PU.1 binds to the IFN Regulator Factor 4 (IRF-4) and the IFN Consensus Binding Protein (ICSBP) to induce activity at the IL-1β [277]. Taken together these studies show that PU.1 is able to impact several key MØ functions like proliferation, phagocytosis and inflammatory response.

ChiP-Seq of histone modifications in CK-p25 AD mice and hippocampal grey matter of AD patients suggested that the immune response was enriched, and there were more potential PU.1 binding sites in many of the promoter/enhancer regions in this set [70]. This has been supported by others. In 2018 Tansey *et al.* showed that the AD risk SNPs were more commonly found in open chromatin regions in MØ and microglia and that a portion of these open chromatin sites had binding motifs for *SPI1* [231]. Huang *et al.* (2017) showed that several LOAD risk SNPs were thought to affect PU.1 binding motifs and again showed that PU.1 is likely bound to nearby regulator elements in 10 other AD-associated genes in human MØ [230]. Sierksma *et al.* (2019, pre-print only) compared genes altered in APP/PS1 transgenic mice aged 4 and 10 months and a genome wide analysis performed by Marioni *et al.* 2018 [65]. The top 18 genes in the 'species-conserved risk' set were thought to have adjacent *Spi1* binding sites [278].

Genomic studies have shown multiple microglia AD risk variants have upstream promoter regions that are likely to bind *SPI1* [231]. *SPI1* binding accounts for a significant amount of heritability in LOAD [230,231]. Additionally, a rare allele in the *SPI1* locus (rs1057233^B) has been associated with a lower risk of AD, a higher age of onset and an improved clearance of Aβ42 from the brain (Figure 1.9). This rare allele was associated with a lower level of *SPI1* expression [230]. In another *in vitro* study the AD-risk associated SNP (rs1377416^C) was found to increase the luciferase reporter when inserted upstream of PU.1 in the BV-2 cell line [70].

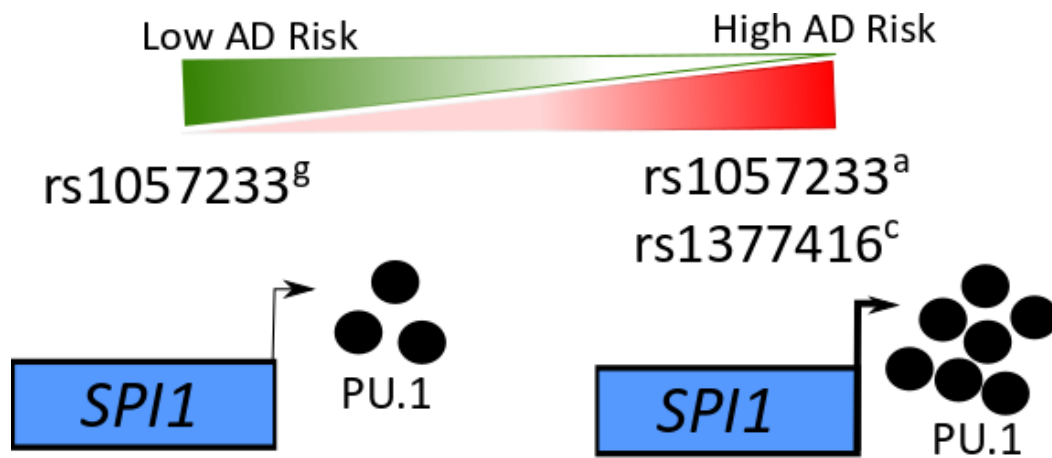


Figure 1.9 Depiction of risk SNPs (*rs*) associated with *SPI1* and how they are thought to impact the level of the *PU.1* transcription factor and AD risk. The rare allele (*g*) of the *rs1057233* SNP is associated with a reduced *PU.1* expression and an increased age of AD onset and the common allele (*a*) was associated with an increased level of *PU.1* [230]. A separate AD-risk SNP *rs1377416*^c was also predicted to increase activity at the *SPI1* promoter site [70].

When *PU.1* was over-expressed and knocked-down in the BV-2 cell line phagocytosis was found to increase and decrease respectively [230]. Moreover there several key inflammatory genes were altered in response to these alterations to *PU.1* including genes implicated in LOAD pathology such as *ApoE*, *Cx3cr1* and *ccl2* [230].

In human microglia cultures a lower *PU.1* reduces the phagocytic capacity of microglia, as well as influencing *DAP12* and *CX3CR1* expression, though some of these results may be as a result of the influence of *PU.1* on microglia viability [232]. A later study performed a microarray on primary cultured microglia where *PU.1* was suppressed by siRNA. The biological processes that were affected by a reduction in *PU.1* include the immune response, and antigen processing and presentation.

When the all the genes were analysed as a network *SPI1* was found to be a central hub gene [233], which was validated in another study [5]. Post-mortem analysis of human tissue has also shown *Spi1* expression to be increased in AD compared to non-demented controls, though it is unknown if this is due to an increased expression within the individual cells or a global increase as a consequence of microgliosis in AD [73].

PU.1 has been implicated in AD pathology and it is thought some of the *Spi1/PU.1* pathology is conserved between mice and humans [70]. As discussed in section 1.2.2.1 CSF1R inhibitors have been successfully *in vivo* to treat AD pathology in mouse models [73,90–92] but there are concerns that these inhibitors would have negative side-effects in the periphery.

The Histone Deacetylase (HDAC) inhibitors Valproic Acid (VPA) can reduce PU.1 levels in both M ϕ [279] and microglia [280,281]. VPA has been shown to act by increasing the acetylation of Histone 3 and Histone 4 and likely blocks the catalytic site in HDAC enzymes [282]. In the mouse BV-2 cell line VPA treatment enhanced phagocytosis of A β [280] though the opposite was seen in human microglia cultures, where VPA reduced the microglial phagocytic capacity [281]. When VPA was trialled in AD patients the progress of the disease was accelerated, suggesting HDAC inhibitors may not be a suitable treatment for AD. Further work in human microglia cultures has proposed another HDAC inhibitor, Vorinostat, also reduces PU.1 and the number of microglia [233]. While Vorinostat is only in phase I clinical trials [283] there are concerns that a similar acceleration of AD pathology will occur. If HDAC inhibitors are going to be used to treat AD more information about the genes and pathways downstream of the PU.1 transcription factor is needed, to ensure reducing PU.1 is beneficial in AD.

1.6 ABI3

The Abl Interactor (ABI) family has three members, Abi1, Abi2 and Abi3. The ABI family are known to bind to the WASP-family verprolin homologous protein 2 (WAVE2) to form part of the Wave Regulatory Complex (WRC) and have a role in actin cytoskeleton remodelling [245,284]. In the brain actin cytoskeleton remodelling is critical for both neuronal plasticity and immune cell activation and chemotaxis, reviewed in [285].

The ABI family has been shown to have a role in membrane ruffling, podosome and lamellipodia formation which are critical to the process of cell motility [286]. As mentioned in section 1.4.2.2.1 the ability of microglia to migrate towards chemotactic signals is an essential part of the microglia response. *In vitro* work has shown podosomes are on the leading edge of the cell and contribute to cell migration by adhering to the extracellular matrix and partially degrading the extracellular matrix [182,287]. Following a M-CSF signalling cue WAVE2 contributed to the formation of small actin protrusions called podosomes which aid in M \emptyset migration [288,289]

ABI3 was first identified by Miyazaki *et al.* (2000) alongside its binding protein [290]. The Immgen RNA-Seq database suggests *Abi3* is highly expressed in murine microglia, though *Abi3* mRNA expression was still detected in peritoneal M \emptyset (pM \emptyset , Figure 1.10).

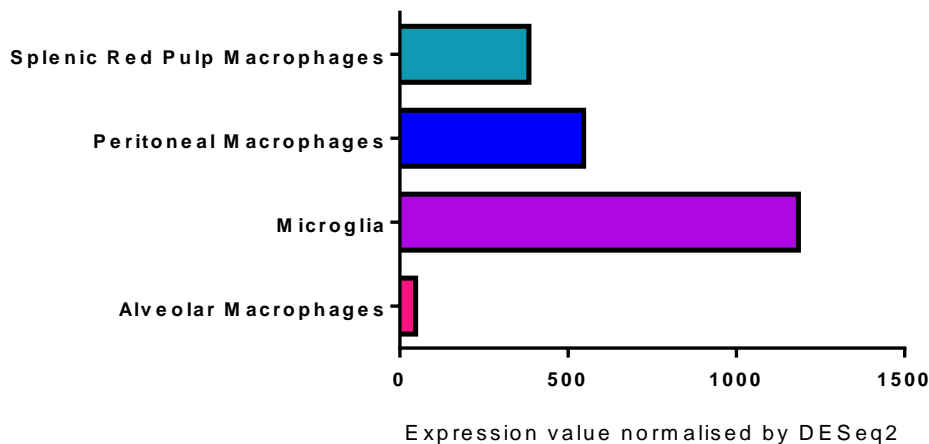


Figure 1.10 *Abi3* Immgen RNA-seq Gene Skyline database, as normalised by DESeq2 [248]. *Abi3* is highly expressed in microglia, though is still expressed by pM \emptyset and splenic M \emptyset populations. *Abi3* expression is barely detectable in Alveolar M \emptyset .

Work by Sjöstedt *et al.* (2015) confirmed ABI3 was strongly expressed in both microglia and lymph nodes, with a lower expression in bone marrow [291]. In post-mortem human brain sections ABI3

protein expression appears to be restricted to microglia and is detected in the cytoplasm near the cell membrane [244].

While little has been discovered about the role of ABI3 in microglia there are a few clues that suggest ABI3 might be involved in microglial function. One study demonstrated that ABI3 is dependent on TGF- β signalling which as discussed in section 1.4.2.3 is important in maintaining a surveying microglial phenotype [154]. *In vitro* work in the human microglia cell line HM06 have shown that TGF- β will increase ABI3 expression, but ABI3 is not induced by any inflammatory mediators such as LPS or IFN γ .

ABI3 and ABI1 have been shown to have mutually exclusive roles within the WAVE2 complex, as summarised in Figure 1.11. Sekino *et al.* (2015) forcibly over-expressed Abi3 in the murine fibroblast cell line NIH3T3 and found that this reduced endogenous levels of Abi1 [245]. Moreover, it was observed that when ABI3 was ectopically expressed WAVE2 did not translocate to the cell membrane and lamellipodia formation was disrupted [245].

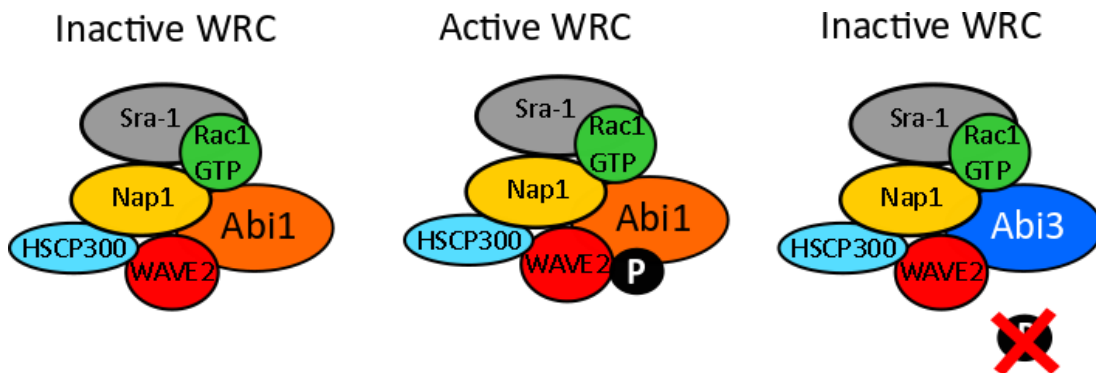
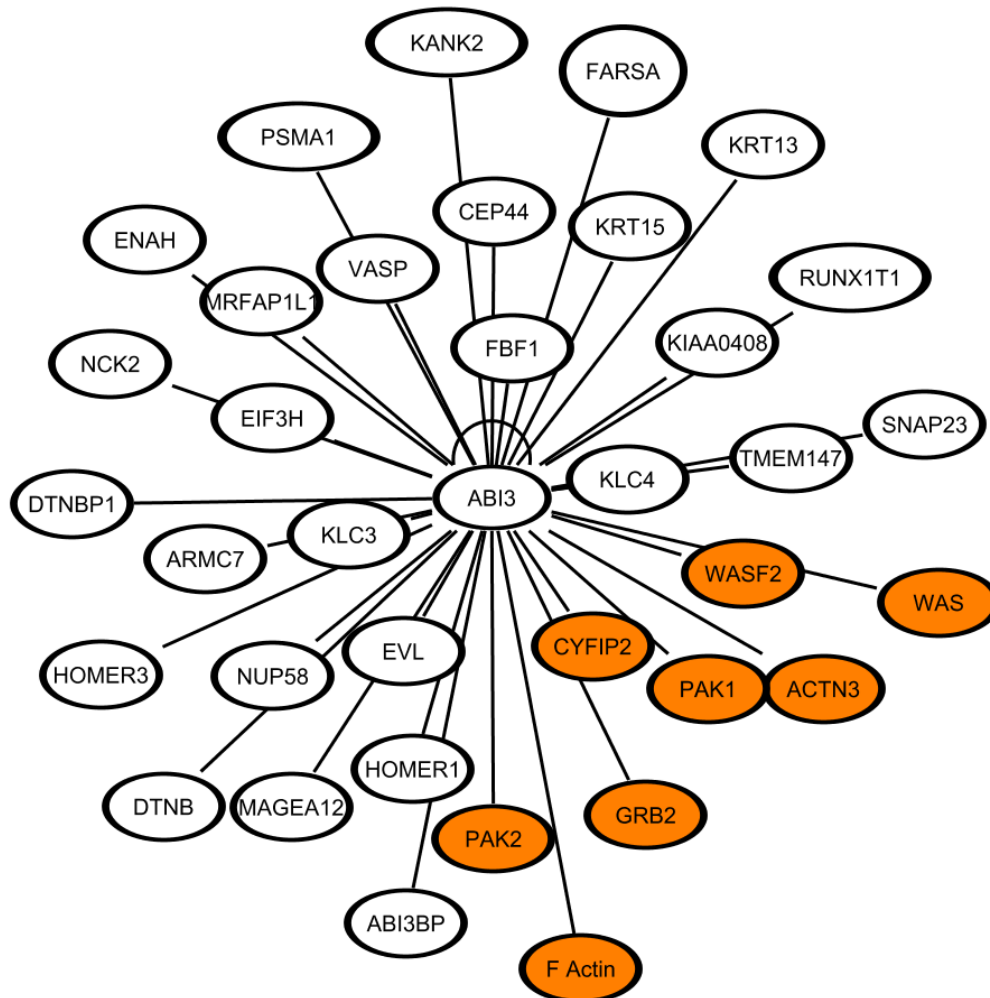


Figure 1.11 Wave Regulatory Complex (WRC) adapted from [292]. The WRC is made up of Rac1-GTP (green), Rac1-associated protein 1(Sra-1, grey), Nck-associated protein 1 (Nap1, yellow), WAVE2 (red), Haematopoietic Stem/Progenitor Cell Protein 300 (HSCP300, light blue) and Abi1 (orange) or Abi3 (blue). The Abi1-WRC is activated by phosphorylation (P, black). Once activated the WRC translocate to the cell surface and alters the actin cytoskeleton. As Abi3 cannot phosphorylate WAVE2 it is thought that an Abi3-WRC complex is inhibitory and does not result in alterations to the actin cytoskeleton [245,293].

This could explain earlier observations by Hirao *et al.* (2006) in comparison of all three ABI family members localised with the WAVE2 complex. Both ABI1 and ABI2 were able to phosphorylate the WAVE2 complex whereas ABI3 could not. Once phosphorylated ABI1/WAVE2 complexes localised to the leading edge where the lamellipodia form [284]. Later work showed that ABI3 could be phosphorylated through the PI3K/AKT pathway, though phosphorylated ABI3 was not able to form a WRC complex with WAVE2 and CYFIP-1 [294]. The PI3K/AKT signalling pathway has been

associated with cell growth, proliferation and cytoskeleton remodelling. Figure 1.12 shows that Abi3 likely interacts with multiple proteins in the actin cytoskeletal pathway.



© 2000-2019 QIAGEN. All rights reserved.

Figure 1.12 IPA diagram of experimentally observed protein-protein interactions with the Abi3 protein. Proteins highlighted in orange are linked to actin cytoskeleton signalling.

Most of the knowledge regarding ABI3 function has come from cancer cell models. In 2011 Latini *et al.* found that the ABI3 protein was reduced in malignant thyroid cancer cells. When ABI3 was re-introduced into these cells proliferation was reduced and cells appeared to become more senescent [295]. This validated earlier work by the same group which showed similar results but with the ABI3-BP [296]. In other cancer cell lines ABI3 was found to inhibit cancer cell migration [11]. *In vivo* work has demonstrated that the presence of ABI3 within tumours prolonged mouse survival, compared to those who were given wild-type tumours [11]. Latini *et al.* 2011 also demonstrated that forced expression of ABI3 reduced tumour growth *in vivo* [295]. The structure

of the ABI3 protein and what is known about its intracellular signalling pathways will be the focus of the next section.

1.6.1 ABI3 Layout and Signalling

The functional domains within the ABI3 protein are detailed in Figure 1.13. The layout of the other members of the ABI family has been reviewed here [286]. In both mice and humans ABI3 is an 8-exon protein and the SH3 is thought to be the critical signalling domain through which most of ABI3 functions are mediated.

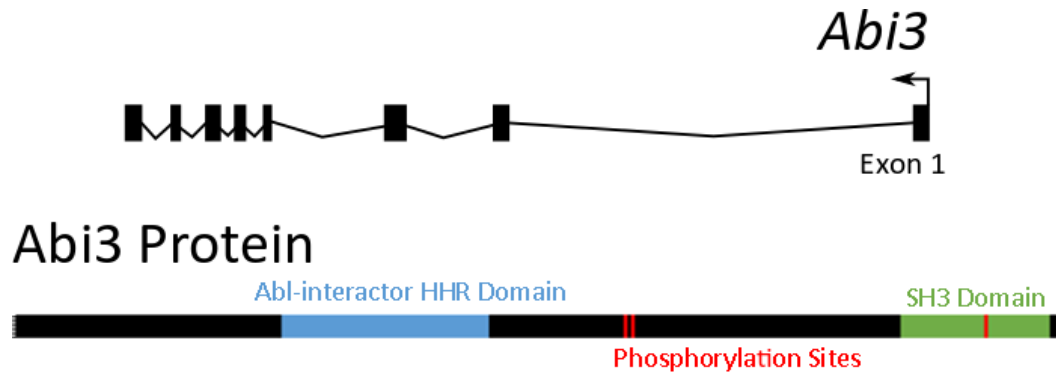


Figure 1.13 Mouse *Abi3* Exon and Protein structure. The 8-exon structure of *Abi3* is and the *Abi3* protein structure (RefSeq ID NP_079935.1) where the Abl-interactor HHR domain (blue) and Src Homology 3 (SH3) domain (green) and the known phosphorylation sites (red) at position 216, 219 and 343.

The ABI3 protein does appear to be well conserved between mice and humans. BLAST comparison of the protein sequences demonstrated that the sequence homology between mice *Abi3* and human ABI3 is over 80 % (Figure 1.14).

	4	LQQIQQLQEFDIPTGREALRGNHSALLRVANYCEDNYLQATDKRKALEETMAFTTQALAS	63
	1	MAELQQQLQEFEIPTGREALRGNHSALLRVADYCEDNYVQATDKRKALEETMAFTTQALAS	60
	64	VAYQVGNLAGHTLRMLDLQGAALRQVEAKMSTLGQMVNMHMEKVARREIGTLATVVRLPS	123
	61	VAYQVGNLAGHTLRMLDLQGAALRQVEARVSTLGQMVNMHMEKVARREIGTLATVQRLPP	120
	124	NQKVIPPESLPSLTPYHRKPLNFACLDDIGHGVKDLSTQLSRTGTLRKSIAKAPATPVSA	183
	121	GQKVIAPENLPLTPYCRRLNFGCLDDIGHGKDLSTQLSRTGTLRKSIAKAPATPASA	180
	184	TLGRPPRIPEPVQLPAVPDGKLSAASSASSLASAGSAEGASGIPQSKGQVAPATPPPPPV	243
	181	TLGRPPRIPEPVHLPVVPDGRLSAASSAFSLASAGSAEGVGGAPTPKGQAAPPAPPLPSS	240
	244	APVTPPPPPLSAEVFLPPPPL-EVSQPPLEAELPLPPPPALEGDELG---LLPPPPPGFG	299
	241	LDPPPPPA--AVEVFQRPPMLEELSPPPPDEELPLPLDLPPPPPLDGLPPLPPPPGFG	298
	300	PDEPSWVPASYLEKVVTLYPYTRQKDNELSFSEGTVICVTRRYSDBGWCEGVSSEGTGFFP	359
	299	PDEPSWVPASYLEKVVTLYPYTSQKDNELSFSEGTVICVTRRYSDBGWCEGVSSEGTGFFP	358
	360	GNVVEPSC	367
	359	GNVVEPSC	366

Figure 1.14 Comparison of protein sequences between mouse *Abi3* and human *ABI3*. The mouse protein sequence (RefSeq ID NP_079935.1) and human protein sequence (RefSeq ID NP_057512.2) were over 82% identical, using BLAST analysis.

As mentioned in the previous section PI3K/AKT signalling is responsible for the phosphorylation and dephosphorylation of ABI3 [294]. *In vitro* work has shown ABI3 signalling is mediated through its Src Homology 3 (SH3) domain via the binding of PAK [11].

1.6.2 CNS Function and proposed role in AD

In 2017 Sims *et al.* discovered a missense mutation in ABI3 that conferred LOAD risk. The AD risk mutation, recorded as SNP rs616338, is at position 209 where a serine residue was mutated into a phenylalanine residue (S209F) [5].

In silico analyses of a 151 network of AD-related proteins included ABI3 [5]. Little experimental work has been done to elucidate the role of ABI3 in microglia, other than to confirm it is expressed specifically in microglia [244,291]. In a small pilot study the area of ABI3 staining was not significantly altered in post-mortem human sections taken from 10 AD cases and 4 non-demented controls [244].

However a study by Bae *et al.* (2012) suggested that ABI3 may also have a role in synaptic remodelling due to its interactions with F-actin. During learning and memory, alterations to the actin cytoskeleton is required at the dendritic synapses. In this instance both ABI3 over-expression and knock-down prevented synapse formation in the hippocampus [297]. Taken together this suggests that ABI3 may play a role in neuronal function.

1.7 Project Aims and Hypothesis

The broad objective of this thesis was to better understand how two individual GWAS AD risk genes can impact microglia or macrophage physiology to better elucidate how they may impact AD pathophysiology. As a transcription factor *Spi1* is known to modulate many pathways including phagocytosis, a key function of macrophages and microglia. While relatively little is known about the role of *Abi3* in the MØ function, evidence from other family members such as *Abi1* and *in silico* pathway analysis suggest that *Abi3* likely has a role in actin cytoskeleton formation or reformation. As an example, both *Spi1* and *Abi3* have been suggested to alter phagocytosis which is an effector macrophage response. It is likely that *Spi1* is one of the first steps in the phagocytic pathway and *Abi3* one of the last. It was predicted that both *Spi1* and *Abi3* would be able to impact microglia/macrophage physiology individually, though *Spi1* likely has a variety of downstream effects given the extensive number PU.1 transcription factor binding sites in MØs. As previously mentioned *Spi1*/PU.1 is essential to survival of the myeloid cell population and therefore complete removal of PU.1 is not feasible to investigate PU.1 function in MØ. However the impact of *Spi1*/PU.1 levels on MØ function can be studied established transgenic models with reduced *Spi1*/PU.1 in MØs or *de novo* lentiviral manipulations. Recently *Abi3* KO mice have been derived as part of the KOMP² mouse consortium to allow research into the function of *Abi3* in myeloid cells. The individual results chapter objectives and rationale behind the approach will be discussed in the following sections.

Chapter 3. To see if removal of the -14 kB URE of *Spi1* results in an altered PU.1 expression in microglia and peritoneal macrophages.

Multiple mouse models have shown that complete PU.1 knock-out is not possible as this mutation is lethal to several myeloid populations [7,8,258,259]. Consequently, for this project the model developed by Rosenbauer *et al.* (2004) was utilised. In this model removal of the -14kB URE (URE) resulted in a 80 % PU.1 knockdown in total bone marrow cells [260] and later URE function was suggested in splenic MØ [298]. This model meant that PU.1 expression should be lower in microglia without having a great reduction in cell number. As the URE was floxed in the transgenic mouse line (B6;129-*Spi1*^{tm1.2Dgt}/J) Cre-recombinase expression was required. This thesis aimed to restrict any off-target effects using mice where the Cre-recombinase (Cre) gene under control of a *Cx3cr1* promoter, thus restricting Cre to cells of a myeloid lineage. Figure 1.15 provides a summary of the -14 kB *Spi1* URE floxed mice used in this thesis.

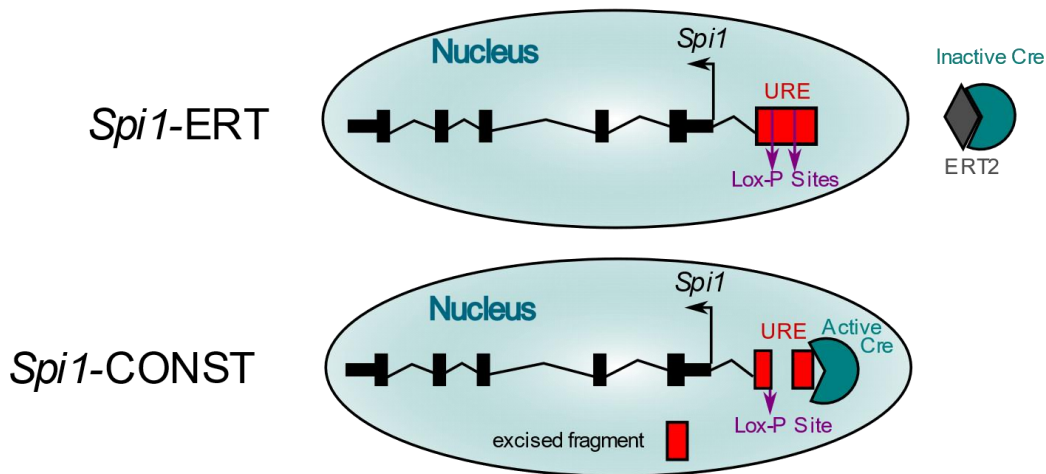


Figure 1.15 Graphic Summary of the -14 kB *Spi1* URE floxed mice model used in this thesis. These *Spi1* floxed mice were bred to one of two mouse lines where Cre recombinase expression was restricted to *Cx3cr1* expressing cells. In the *Spi1*-ERT mice the Cre was tamoxifen-inducible and in the *Spi1*-CONST mice the Cre was constitutively expressed. It was predicted that in the absence of tamoxifen the *Spi1*-ERT mice would retain all their PU.1 expression. In the *Spi1*-CONST mice PU.1 expression was thought to be reduced by 80 % in *Cx3cr1* expressing cells, based on work published by Rosenbauer et al. 2004.

It was predicted that mice which perpetually express an active Cre would lack the *Spi1* – 14 kB URE and should have a reduction in PU.1 protein expression when compared to mice that require tamoxifen to activate Cre expression (and therefore have an intact URE). Any reduction to PU.1 had the potential to diminish the microglial population, so during this experiments cell number was assessed.

Chapter 4. To develop an accurate *in vitro* system where microglia could be cultured and manipulated with customised lentiviruses to knock-down and over-express PU.1 protein.

As there were no suitable transgenic models available, then a primary microglia culture model can be utilised in combination with custom lentiviruses to manipulate protein levels. As mentioned in section 1.4.2.3 TGF- β can improve the transcriptome of cultured microglia ensuring a greater similarity to freshly isolated microglia [154,155]. Therefore one aim of this chapter was to optimise a primary microglia culture model that incorporates TGF- β and lentiviruses to allow for manipulation of primary microglia. Another aim was to develop and test lentiviruses designed to knock-down or over-express *Spi1* and to incorporate these into the primary microglia culture model. Once developed the microglia cultures with altered *Spi1* would be processed for RNA-Sequencing analyses to assess the impact of *Spi1* dose on the microglia transcriptome.

Chapter 5. To utilise RNA-sequencing data gained from *Spi1* *in vitro* manipulations to elucidate which genes are differentially expressed following a reduction or over-expression of *Spi1*.

Exploring which signalling pathways are under the control of *Spi1*/PU.1 could improve understanding of how microglia physiology may be altered in AD where an increased *Spi1* expression is thought to result in an earlier age of disease onset [230]. Therefore this chapter aimed to analyse two RNA-Seq datasets where *Spi1* has been either reduced or over-expressed. Genes altered following a reduction in *Spi1* may provide some insight as to how drugs reducing *Spi1*/PU.1 expression impact the microglia transcriptome.

The second RNA-Seq dataset focused on increasing *Spi1*/PU.1 in microglia to mimic the microglia phenotype associated *Spi1* AD risk SNPs. One AD risk SNP (rs1377416c) is thought to cause increased *SPI1* expression in microglia [70], thus it seemed prudent to observe how increases to PU.1 alone may affect microglial phenotype without the added complexity of AD pathology. Currently there are no commercially available transgenic mice over-expressing PU.1, so it became necessary to develop a lentiviral vector to over-express *Spi1*/PU.1.

Transcriptomic analysis using RNA-sequencing data was predicted to show which genes were relatively unaffected by the amount of PU.1 but more importantly which genes, if any, were only expressed when PU.1 expression was considerably augmented or reduced. However, it was also anticipated that there might be genes whose expression depended on the amount of PU.1 in the microglia, termed *Spi1* dose-sensitive genes. It was expected that some of the altered pathways would influence microglia functions such as proliferation and phagocytosis, which could then be measured experimentally.

Chapter 6. To assess the usefulness of the *Abi3* knock-out mice and perform basic phenotyping on conditionally-immortalised bone marrow MØ precursor cells and exploratory functional experiments on *ex vivo* peritoneal macrophages.

More needs to be understood about the function of ABI3 in MØ, especially microglia, to better understand how alterations to ABI3 may contribute to AD pathophysiology. Recently an *Abi3*^{tm1.1(KOMP)Vlcg}/J (ABI3 KO) mouse line was made by the Jackson Laboratory [299]. As detailed in the Figure 1.16 a 9515 base pair (bp) fragment of *Abi3* was removed and instead inserting a *LacZ* reporter gene.

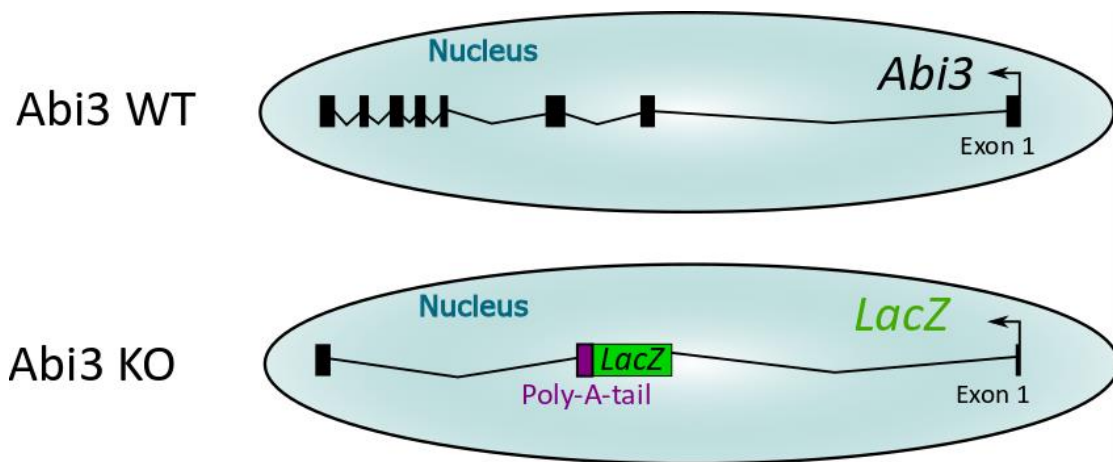


Figure 1.16 *Abi3* KO model. These mice were made by replacing exons 2-7 and part of exon 1 (9515 bp fragment) with a *LacZ* sequence (green) terminated by a Poly-A-tail (purple). The sequence for the *Abi3* KO mice is ENSMUST00000059026.

These novel *Abi3* knock-out mice provide an unparalleled opportunity to study the function of ABI3 both *in vitro* and *in vivo*. From the studies mentioned above it was predicted that MØ that lacking ABI3 may have an altered proliferation and response to M-CSF cytokine stimulation, resulting from alterations to the actin cytoskeleton.

Chapter 2 Methods

2.1 Buffers and Solutions

Table 2.1 List of Buffers and Solutions used in the thesis. Unless otherwise stated all reagents were provided by Fisher Scientific or Sigma Aldrich.

Buffer/Solution Name	Ingredients
Mammalian Cell Lysis Buffer	100 mM Tris pH 8.5
	5 mM EDTA
	200 mM NaCl
	0.2 % (v/v) Sodium Dodecyl Sulphate (SDS)
	Nuclease free water
Tris-Acetate-EDTA (TAE) Buffer	50X TAE stock solution
	Distilled water
MUSE Staining Solution	625 ng/mL Propidium Iodide (PI)
	500 ng/mL LDS 751 (Thermofisher)
	1X DPBS (Gibco)
Freezing Media	10 % (v/v) Dimethyl Sulfoxide (DMSO)
	90 % (v/v) Heat-Inactivated filtered FBS (Gibco)
Ammonium-Chloride-Potassium (ACK) Lysis Buffer (pH 7.2)	150 mM NH ₄ Cl
	10 mM KHCO ₃
	0.1 mM Na ₂ EDTA
2 % Formaldehyde	36.5-38 % Formaldehyde solution with methanol
	1X DPBS (Gibco)
4 % Paraformaldehyde	4 % (w/v) Paraformaldehyde powder
	1X PBS
0.1 % Triton-X-100 Buffer and 0.3 % Triton-X-100 Buffer	Triton-X-100
	1X DPBS (Gibco)
RIPA Buffer	1 % NP-40
	0.5 % Deoxycholate (DOC)
	0.1 % SDS
	150 mM NaCl
	50 mM Tris-Cl pH 8.0
Sodium Bicarbonate Buffer (pH 8.3)	0.2 M Sodium Bicarbonate
	Distilled water
FACS Block	5 % (v/v) filtered Rabbit Serum
	4 µg/mL Rat Anti-Mouse FcγRII/III (2.4G2 clone)

	FACS Wash
FACS Wash	0.5 % (w/v) BSA
	5 mM EDTA
	2 mM NaN ₃
	1X DPBS (Gibco)
MACS Buffer	0.5 % (w/v) BSA
	1X DPBS (Gibco)
MACS Buffer with EDTA	0.5 % (w/v) BSA
	2 mM EDTA
	1X DPBS (Gibco)
MACS Block	5 % (v/v) filtered Rabbit Serum
	4 µg/mL Rat Anti-Mouse FcγRII/III (2.4G2 clone)
	MACS Wash
MACS Wash	0.5 % (w/v) BSA
	5 mM EDTA
	1X DPBS (Gibco)
0.5 % Saponin FACS Block	5 % (v/v) filtered Rabbit Serum
	4 µg/mL Rat Anti-Mouse FcγRII/III (2.4G2 clone)
	0.5 % Saponin FACS Wash
0.5 % Saponin FACS Wash	0.5 % (w/v) Saponin
	0.5 % (w/v) BSA
	5 mM EDTA
	2 mM NaN ₃
	1X DPBS (Gibco)
Staining Medium (pH 7.2)	5 % (v/v) Heat-Inactivated filtered FBS (Gibco)
	10mM HEPES
	1X DPBS (Gibco)
Lavage Fluid	5 mM EDTA
	1X DPBS (Gibco)
10 % APS	10 % (w/v) Ammonium Persulphate
	Distilled water
10 % SDS	10 % (w/v) SDS
	Distilled water
1.5 M Tris-HCl	1.5 M Tris base

	Sufficient HCl to get pH 8.8
	Distilled water
0.5 M Tris-HCl	0.5 M Tris base
	Sufficient HCl to get pH 6.8
	Distilled water
Laemmli Buffer	250 mM Tris pH 6.8
	4 % (v/v) SDS
	40 % (v/v) Glycerol
	20 % (v/v) β -Mercaptoethanol
	0.02 % (w/v) Bromophenol Blue
	Distilled water
Running Buffer	10X Tris/Glycine/SDS Stock Solution (Biorad)
	Distilled water
Transfer Buffer	10X Tris/Glycine Stock Solution (Biorad)
	20 % (v/v) Methanol
	Distilled water
10X TBS (pH 7.6)	200 mM Tris base
	1.5 M NaCl
	Sufficient HCl to get pH 7.6
	Distilled water
1X TBST	0.1 % (v/v) Tween 20
	1X TBS
Blocking Buffer	5 % (w/v) Skimmed Milk Powder (Tesco)
	0.1 % (v/v) Tween 20
	1X TBS
Stripping Buffer	62.5 mM Tris-HCl pH 6.8
	10 % (w/v) SDS
	100 μ M β -Mercaptoethanol
	Distilled water

2.2 Mice

All mice used in this thesis were maintained at Cardiff University's JBIOS facility in accordance with the 1986 Animals (Scientific Procedures) Act Guidelines [300]. All experiments were performed under the UK Home Office licenses 30/2938 (2015-2016) or PO5D6A456 (2017-2019). Mice were culled via asphyxiation with a slow rising level of CO₂ and death was confirmed via dislocation of the neck. Mice were matched in experiments by age and gender whenever possible. Details of the age, gender and number of mice used in each experiment can be found in the figure legends. Most experiments were performed using mice aged 8-16 weeks and involved a mix of male and female mice.

The pilot *in vivo* studies carried out in this thesis were performed using the minimum number of mice (usually 1-2 mice per group) to gain insight into the biological effect size providing justification for any potential follow up studies. All mice were group housed in conventional cages according to genotype and were provided chow and water *ad libitum*. The only exception to this involved any *in vivo* experiments involving lentiviruses. In lentivirus experiments mice were injected in a biological safety cabinet and housed in scintainers where each cage was individually ventilated, chow/water were still provided *ad libitum*.

The transgenic mice strains used in this thesis, listed in Table 2.2, were purchased from Jax Laboratory and bred in house. C57BL/6J wild-type mice were ordered from Charles River as required. All microglia cultures used for RNA-sequencing (See chapter 4) were derived from 8-week-old female C57BL/6J mice order from Charles River to try and minimise variation between cultures.

Official Strain Name	Thesis Abbreviation
B6;129-Spi1 ^{tm1.2Dgt} /J	<i>Spi1</i> URE floxed
B6J.B6N(Cg)-Cx3cr1 ^{tm1.1[cre]Jung} /J	Cx3cr1 ^{CONST}
B6.129P2(C)-Cx3cr1 ^{tm2.1[cre/ERT2]Jung} /J	Cx3cr1 ^{ERT}
B6N(Cg)-Abi3 ^{tm1.1[KOMP]vicg} /J	Abi3 KO
B6.129(Cg)-Foxp3 ^{tm3[DTR/GFP]Ayr} /J	FoxP3 ^{GFP}

Table 2.2 Official and abbreviated names of the transgenic mice strains used in this thesis.

2.2.1 *Spi1*-URE floxed Mice

An active Cre recombinase (Cre) is required to remove a 3.4 kB fragment of the -14 kB *Spi1* URE in B6;129-Spi1^{tm1.2Dgt}/J (*Spi1* URE floxed) mouse line [260,267]. It was decided the best method to adopt in this investigation was to restrict Cre expression to cells expressing Cx3cr1, which is

primarily expressed by myeloid cells [146,147]. Microglia are lost in models where PU.1 was knocked out or disrupted, and there were concerns removing the -14 kB *Spi1* URE would also reduce the population [7,8,258]. To abate these concerns the *Spi1* URE floxed mice were bred to two mouse strains. The B6J.B6N(Cg)-Cx3cr1^{tm1.1(cre)Jung/J} (Cx3cr1^{CONST}) strain constitutively expressed an active Cre whereas the B6.129P2(C)-Cx3cr1^{tm2.1(cre/ERT2)Jung/J} (Cx3cr1^{ERT}) strain express an tamoxifen-inducible Cre recombinase [147].

The experiments in this thesis did not expose the *Spi1* URE floxed-Cx3cr1^{ERT} (*Spi1*-ERT) mice to tamoxifen but were instead used to control in experiments using the *Spi1* URE floxed-Cx3cr1^{CONST} (*Spi1*-CONST) mice to negate any effects resulting from the transgenic background of these mice. Figure 2.1 summarises predicted differences between the *Spi1*-ERT and *Spi1*-CONST mouse strains.

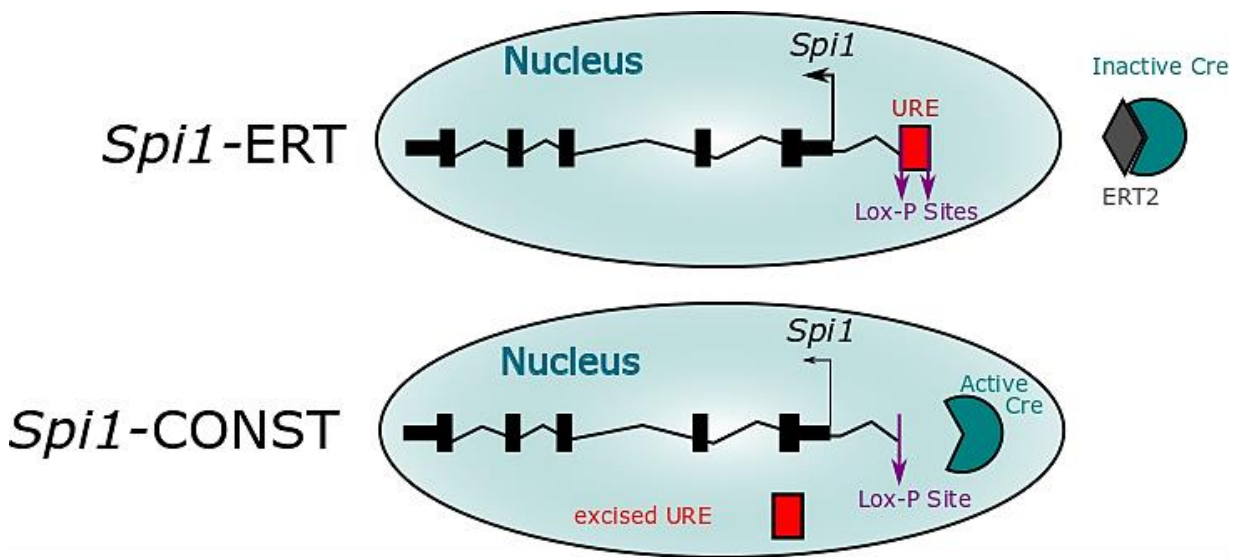


Figure 2.1 Graphic depiction of predicted outcome to -14 kB URE following *Spi1*-ERT and *Spi1*-CONST transgenic mouse strains in *Cx3cr1*⁺ cells. The *Spi1*-ERT mice express a tamoxifen inducible Cre that cannot enter the nucleus (blue) in the absence of tamoxifen, so the -14 kB URE (red) is intact and *Spi1* expression should not be altered. In the *Spi1*-CONST mice Cre can enter the nucleus where it causes recombination of the loxP sites (purple) and removal of ~3.4 kB of the -14 kB URE reducing expression of the *Spi1* gene. This Cre mediated loxP recombination is restricted to the nuclei of *Cx3Cr1* expressing cells which express Cre.

2.2.2 ABI3 Knock-Out Mice

The *Abi3* B6N(Cg)-*Abi3*^{tm1.1(KOMP)Vlcg/J} (*Abi3*-KO) mouse colony was generated by the Jackson Laboratory [299]. In the *Abi3* KO mice exons 2-7 were replaced with a *LacZ* gene encoding β -Galactosidase as a reporter, as depicted in Figure 2.2 [299]. Mice that were heterozygous for the *Abi3* KO mutation were used to establish separate *Abi3* KO and *Abi3* WT colonies which were derived on a C57BL/6NJ background.

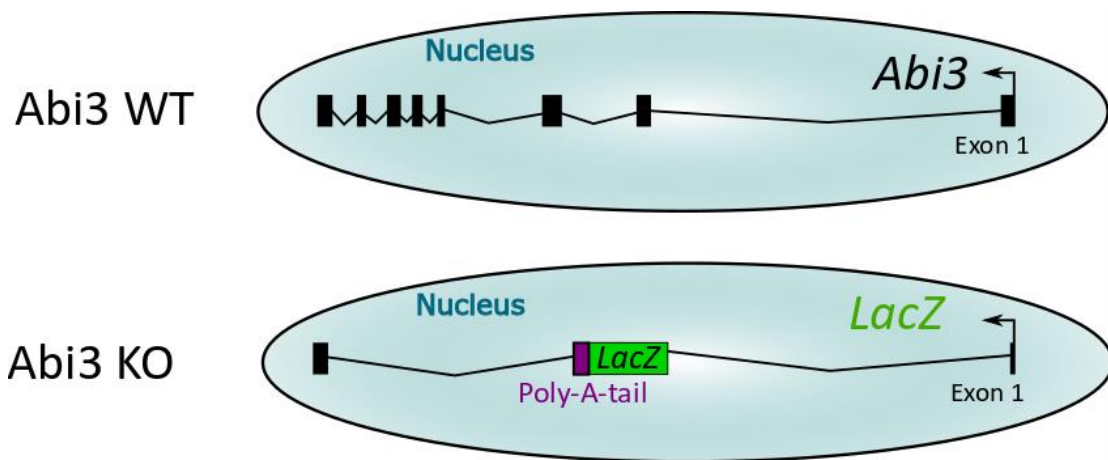


Figure 2.2 Graphic depiction of the *Abi3* WT and *Abi3* KO mouse strains in all *Abi3* expressing cells. The *Abi3* WT mice have all 8 exons intact and will express *Abi3* mRNA. In the *Abi3* KO mice exons 2-7 have been replaced with an *Escherichia coli* (*E. coli*) *LacZ* gene (green) and a poly-A-tail (purple) to terminate transcription. Therefore, in the *Abi3* KO mice *LacZ* mRNA is expressed in the place of *Abi3*, which is translated into a detectable β -galactosidase reporter.

2.3 Genotyping

Genomic DNA (gDNA) was isolated from individual ear-punch biopsies taken by JBIOS staff for genotyping purposes. Biopsies were digested with 50 μ L of mammalian lysis buffer and 100 μ g/mL of proteinase K (from *Tritirachium album*, Sigma P4850) in a 1.5 mL microcentrifuge tube (STARLAB) at 52 $^{\circ}$ C for 1 hour being shaken in a Thermo-Shaker at 1200 rpm (Grant-bio, PSC24N). The proteinase K was deactivated after heating to 72 $^{\circ}$ C for 30 minutes. Tubes were cooled before 400 μ L of nuclease free water (Life Technologies) was added to each sample and briefly vortexed. The GoTaq[®] G2 Flexi kit (Promega) was used for genotyping per manufacturers direction, the volumes for one reaction are summarised in Table 2.3. Each reaction was placed in a 0.2 mL PCR tube (STARLAB) before the addition of 1 μ L of gDNA. These tubes were then placed in a Mastercycler[®] Nexus Gradient (Eppendorf) PCR machine and run using the PCR protocol detailed in Figure 2.3.

Component	Volume (μL)
5x Green GoTaq® Flexi buffer	5
25 mM MgCl ₂	3.6
10 mM dNTPs	0.5
Forward primer (500 nM)	0.125
Reverse primer (500 nM)	0.125
GoTaq DNA polymerase	0.1
Nuclease-free water	14.55
Total Reaction Volume	24

Table 2.3 Volumes of each GoTaq® G2 Flexi DNA Polymerase kit component needed for one standard 25 μL reaction. 1μL of genomic DNA was added to this reaction mix. dNTPs were purchased separately from Promega and all primers were provided through Sigma.

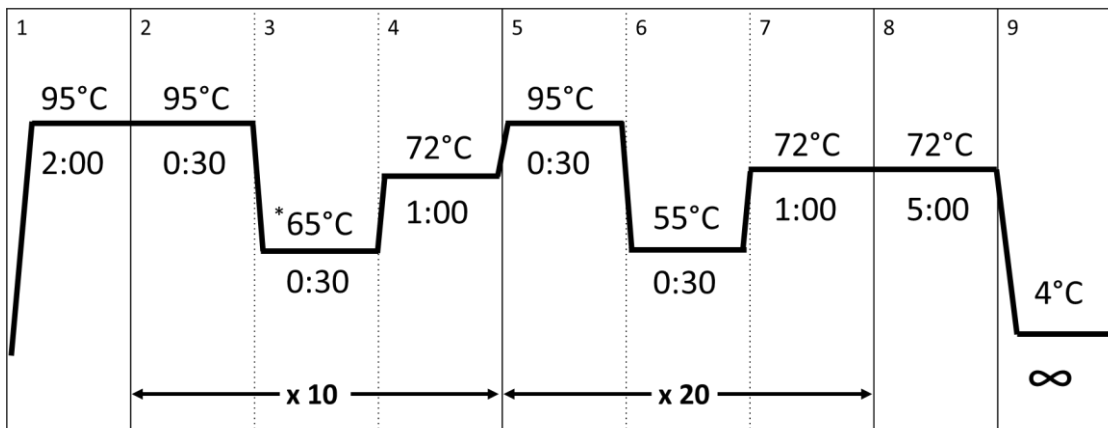


Figure 2.3 Touchdown PCR program used for genotyping, based on standard Jackson Laboratory protocol. The temperature is shown in °C above the black line and the duration given in minutes and seconds below the line. *During the touchdown cycles (steps 2-4) the annealing temperature was decreased by one degree in each cycle.

All genotyping primer sequences, listed in Table 2.4, were provided by the Jackson Laboratory and were purchased through Sigma Aldrich.

Mouse		Forward Primer (5' to 3')	Reverse Primer (5' to 3')	Product Size (bp)
Spi1- URE floxed	Wild-Type	GGCCTCAGTTTTCTCACCTG	CCTTCCTGGTTGGGAGAAT	250
	Mutant			480
Cx3cr1^{ERT}	Wild-Type	AGCTCACGACTGCCTTCTTC	ACGCCCAGACTAATGGTGAC	151
	Mutant	GTTAATGACCTGCAGCCAAG	ACGCCCAGACTAATGGTGAC	230
Cx3cr1^{CONST}	Wild-Type	AGCTCACGACTGCCTTCTTC	GCAGGGAAATCTGATGCAAG	816
	Mutant	GACATTTGCCTTGCTGGAC	GCAGGGAAATCTGATGCAAG	380
Abi3	Wild-Type	ACCCAGATCCCTGAGAATTT	CAAGTCTGAAGGGAGAACG	334
	KO	CGGTCGCTACCATTACAGT	CAGCCCAAGAGGTAGACAGG	473

Table 2.4 All genotyping primer sequences needed for genotyping PCR reactions and the expected product size in base-pairs (bp).

The resulting PCR reaction was electrophoresed on a 2 % agarose gel. The gels were made by dissolving an appropriate amount of agarose powder (Thermofisher) in 1X TAE buffer with heat and gentle agitation. To visualise the DNA approximately 0.5 µg/mL of Ethidium Bromide (one drop) or 1:20, 000 dilution SYBR™ Safe (from 10,000X stock in DMSO) was added to the dissolved agarose and gently mixed before the mixture was poured into an appropriate Fisherbrand™ mould, and a comb (Thermofisher) was inserted to form individual wells once the gel had set. The samples were then loaded alongside the 100 bp DNA ladder (Promega) and run using the Fisherbrand™ gel system (Thermofisher) at 100 V until for ~45 minutes. The gels were then transferred to a UV transilluminator where they were imaged.

2.3.1 Spi1 URE removal PCR

To ensure the -14 kB URE was removed, as depicted in Figure 2.1, genomic PCR was used to assess the presence or absence of the -14 kB *Spi1* URE. Briefly genomic DNA was isolated in accordance with the instructions of the GenElute™ Mammalian Genomic DNA Miniprep Kit and eluted in nuclease-free water. The PCR reactions were performed as described in Section 2.3, using all three primers listed in Table 2.5. These primers were used to genotype the *Spi1*^{tm1.3Dgt/J} transgenic mice, a slightly altered version of the mice used in this project that lack the -14 kB URE and the neomycin cassette [298,301].

Name	Primer Sequence (5'→3')	Target
<i>Spi1</i> ^{tm1.3Dgt/J} Primer 1	GCCAACTCAGCACTCAGGCA	Before URE
<i>Spi1</i> ^{tm1.3Dgt/J} Primer 2	CTGGATACTGACCAATTTGT	In floxed URE region
<i>Spi1</i> ^{tm1.3Dgt/J} Primer 3	ACTGAGTGCCACGGGTCATC	After URE

Table 2.5 Primers used to determine if the URE has been excised by Cre.

As indicated in Figure 2.4 the -14 kB URE was intact then a PCR band would only form between primer 1 and primer 2, as the extension time would not allow the larger band between primer 1 and primer 3 to form. If the -14 kB URE has been removed by Cre then the distance between primer 1 and primer 3 would be short enough to allow a PCR band to form. As primer 2 binds to the sequence in floxed URE region it would have been lost in the Cre mediated recombination, ensuring only one PCR fragment would be formed in each reaction. As the exact sequences for this region of the *Spi1*-URE floxed or the *Spi1*^{tm1.3Dgt/J} mouse strains have not been published [260,298] the exact fragment size of the PCR fragment generated by primers 1 and 2 could not be predicted. However due to the design of the PCR reaction it was determined that the PCR fragment generated by primers 1 and 3 in the absence of the -14 kB URE would be ~200 bp larger.

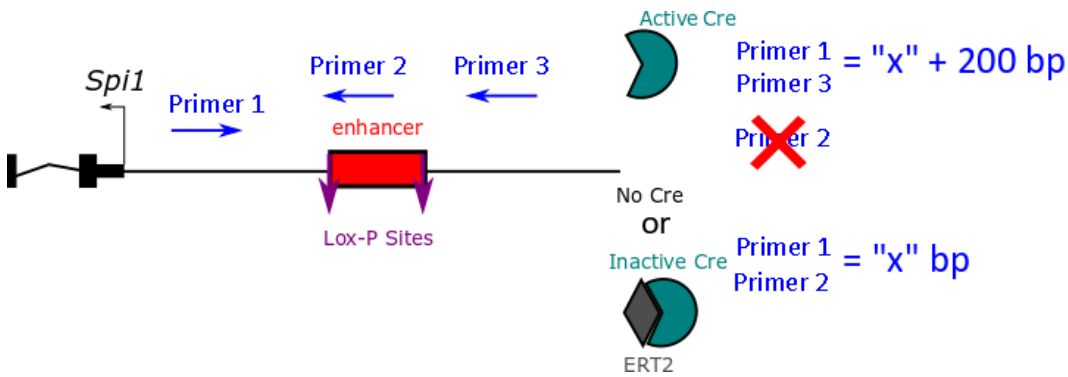


Figure 2.4 Diagram indicating the approximate binding sites of each of the primers to measure URE recombination in the *Spi1* URE floxed mice. As described in the text above the *Spi1*^{tm1.3Dgt/J} genotyping primer 1 and 2 combine to form a PCR product of “x” bp in the *Spi1*^{tm1.2Dgt/J} mice used in this thesis, which are slightly different meaning the band size was unknown. When these mice were in the presence of an activated Cre causes recombination of the LoxP sites, meaning the site binding primer 2 was lost, though primer 1 and 3 were now able to form the larger PCR band in the extension time (“x”+ 200bp).

2.3.2 *Abi3* Genomic PCR

The *Abi3* KO mice should lack exons 5-7 of the *Abi3* gene. To assess this genomic DNA was isolated in accordance with the instructions of the GenElute™ Mammalian Genomic DNA Miniprep Kit and eluted in nuclease-free water. Two separate PCR reactions were then performed as described in Section 2.3, using either the primers targeting *Abi3* exon 5-7 or exon 8, listed below in Table 2.6.

Target	Forward Primer Sequence (5'→3')	Reverse Primer Sequence (5'→3')	Predicted Band Size (bp)
<i>Abi3</i> Exon 5-7	GATCCCTGAGCCGGTG	GGGCAACTCTGCTT	766
<i>Abi3</i> Exon 8	TCTTCAGCACCTGTTGC	AGCACGATTAAGTGAAGAGA	962

Table 2.6 Primers used to assess the presence of *Abi3* exons and predicted band sizes.

2.4 General Cell Culture and Maintenance

2.4.1 Incubation and Media Preparation

Cells were incubated at 37°C in a humid incubator with 95% air 5% CO₂ unless otherwise stated. Dulbecco's Modified Eagle Medium (DMEM) and Roswell Park Memorial Institute 1640 (RPMI) were supplemented with heat-inactivated Foetal Bovine Serum (FBS) and Penicillin-Streptomycin antibiotics (100X), as described in Table 2.7. All the reagents listed above were produced Gibco® (Thermofisher). Unless stated otherwise the cell lines were maintained in Nunc™ T75 or T175 flasks with filters (Thermofisher).

Culture Media	Contents
Standard RPMI	2 g/L D-glucose
	2 mM L-Glutamine
	10 % (v/v) FBS
	100 (v/v) units/mL Penicillin
	100 (v/v) µg/mL Streptomycin
Standard DMEM	4.5 g/L D-glucose
	4 mM L-Glutamine
	10 % (v/v) FBS
	100 (v/v) units/mL Penicillin
	100 (v/v) µg/mL Streptomycin
Microglia DMEM	4.5 g/L D-glucose
	GlutaMAX™
	15 % (v/v) FBS
	100 (v/v) units/mL Penicillin
	100 (v/v) µg/mL Streptomycin

Table 2.7 The RPMI and DMEM medias used in these experiments. The reagents show in blue were added to the media separately.

2.4.2 Cryopreservation and Thawing

Cells were centrifuged at 350 x g for 5 minutes, the supernatant discarded and the pellet resuspended 1 mL of in freezing media per 3-5 x 10⁶ cells. The media was divided into 1 mL aliquots and frozen down in either a Mr. Frosty™ (Thermofisher) or a CoolCell® LX (Biocision) overnight at -80 °C. Aliquots were then stored at - 80 °C or moved into liquid nitrogen for longer term storage.

Cells were thawed by transferring the aliquots into a 37 °C water bath until the ice crystals disappeared. The defrosted aliquots were quickly transferred into 10 mL of the appropriate media and centrifuged at 350 x g for 5 minutes. The supernatant was removed and the cells resuspended in the correct culture media, as detailed below.

2.4.3 Cell counting

Cells were counted with the Muse® Cell Analyzer (Merk Millipore) per manufacturer's instructions. Briefly, samples were prepared by diluting cells between 1:10 and 1:40 with MUSE staining solution. Following a 5-minute incubation at room temperature (RT) these samples were run on the Muse® Cell Analyzer. Cells were also counted using a 4 x 4 haemocytometer, cells were first diluted 1:1 ratio with 0.4 % Trypan Blue solution (Gibco).

2.4.4 Jurkat Cell Line

The Jurkat immortalised human T-lymphocyte line was established from the peripheral blood of an acute T-cell Leukaemia patient [302]. These non-adherent cells were maintained in standard RPMI media were passaged twice-weekly at a 1:20 or 1:40 dilution pre requirements.

2.4.5 Human Embryonic Kidney 293T Cells

The Human Embryonic Kidney 293T cell line (293T) was originally derived from human embryonic kidney cells that were virally transformed to stably express the SV40 large T-antigen [303]. The 293T cells were cultured in standard DMEM media and passaged every 4 days. These cells were passaged after the old media was aspirated and the cell monolayer was gently washed with Dulbecco's Phosphate Buffered Saline (DPBS). The cell monolayer was then covered with 0.05 % Trypsin-EDTA (Thermofisher) and incubated at 37°C for 5 minutes to detach the cells. The detached cells were then collected into a 50 mL falcon tube and ~10 mL of standard DMEM was added to neutralise the trypsin. The cells were then centrifuged for 5 minutes at 350 x *g*, the supernatant was removed before the cells were resuspended and diluted 1:20 in standard DMEM before being added to a new culture flask.

2.4.6 Macrophage Precursor (MØP) Cell lines

The polyclonal conditionally immortalised Macrophage Precursor (MØP) cell lines were derived from transfecting CD117⁺ mouse bone marrow cells with a retrovirus carrying an oestrogen inducible *HoxB8* gene, as previously described [304]. Table 2.8 lists the origin of the MØP cell lines used in this thesis. My thanks to Dr Marcela Rosas for producing the *Spi1* URE floxed MØP cell line.

Mouse Strain	Age	Gender
<i>Spi1</i> URE floxed	10 weeks	Female
ABI3 KO	8 weeks	Female
ABI3 WT	8 weeks	Female

Table 2.8 List of the age and gender of the mice that were used to generate the MØP cell lines. The *Abi3* KO and *Abi3* WT lines were made in parallel to minimise the risk of experimental differences.

The MØP cells were maintained in standard RPMI media supplemented with 1 µM oestrogen (10 mM β-estradiol (w/v) in absolute ethanol; Sigma) and 10 ng/mL recombinant murine Granulocyte-Macrophage Cytokine Stimulating Factor (GM-CSF; Peprotech) and were passaged every 3-4 days at a 1:20-1:40 dilution as required.

2.4.6.1 Differentiation of MØP Cells

Following oestrogen withdrawal these MØP cells could be differentiated with GM-CSF or recombinant Macrophage Cytokine Stimulating Factor (M-CSF; Peprotech). Oestrogen was depleted from the cultures by washing the cells in 10 mL standard RPMI media three times where the 50 mL falcon tubes were centrifuged at 350 x *g* for 5 minutes to pellet the cells between washes. After the final wash cells were counted (see section 2.4.3) and resuspended in standard RPMI media containing either M-CSF or GM-CSF, as required. To get differentiated cells like bone-marrow derived MØ (BMDM) 1x10⁶ MØP cells were resuspended in 3mL of RPMI with 20 ng/mL of M-CSF per well of a 6-well-plate. To differentiate DC-like cells 3x10⁵ MØP cells were differentiated in 3 mL of RPMI media supplemented with 10 ng/mL GM-CSF. These differentiating MØP cells were incubated 3-4 days, where the M-CSF or GM-CSF differentiation media was replenished on day 2/3. The differentiated MØP cells were harvested using Accumax™. The media was discarded, and cells were washed with DPBS before sufficient Accumax™ was added to cover the bottom of the well. The 6-well-plates were then incubated for 5 minutes at 37 °C before the wells were gently scraped with a plastic scraper. The cell suspension was then transferred to a 50 mL falcon tube containing ~10 mL standard RPMI and centrifuged at 350 x *g* for 5 minutes to pellet the cells before downstream applications.

2.4.7 RAW 264.7 Cell line

The RAW 264.7 (RAW) cell line was originally derived from murine tumours BALB/C mice transformed with Abelson leukaemia virus [305]. RAW cells were cultured in standard DMEM and were passaged twice-weekly by gently scraping with a plastic cell scraper. Cell suspension was then transferred to a 50 mL falcon tube and centrifuged at 350 x *g* for 5 min. Supernatant was discarded, and cells were resuspended in at a 1:20 dilution in standard DMEM before being transferred to a new culture flask.

2.4.8 Bone-Marrow Derived MØ (BMDM)

The femur and tibia bones were harvested from sacrificed mice and placed into 50 mL falcon tube containing ice-cold DPBS. The bones were then sterilized in 70 % absolute ethanol (in DPBS) for 1 minute before being washed twice with DPBS. The ends of each bone were removed. The marrow was flushed out using a 25G needle on a 10 mL syringe filled with standard DMEM media onto a 40 µM strainer placed in a 50 mL falcon tube. Cells were centrifuged at 350 x *g* for 5 minutes. At this point cells were either cryopreserved, as described in Section 2.4.2 for a few months or underwent a red-blood-cell (RBC) lysis step if being directly cultured. The cell pellet was resuspended in 1 mL

of ACK lysis and incubated for 1 minute before 9 mL of DPBS was added. An FBS layer was carefully added below the cell suspension before centrifuged at 350 x *g* for 5 minutes. Frozen bone-marrow aliquots did not require this step as freeze/thawing results in lysed the RBCs. The bone-marrow cells were resuspended in 5 mL of standard DMEM and counted as described in Section 2.4.3. Cells were plated in 100 mm x 20 mm (diameter x height) Cellstar® plate (Greiner Bio-one) at 1x10⁷ per plate in DMEM with 20 ng/mL of M-CSF. 25 mL of the cell-media suspension was transferred to a and incubated for 7 days at 37 °C. Differentiation media was refreshed after 3-4 days before being harvested with Accumax™ (Sigma) as described in section 2.4.9.

2.4.9 Primary Microglia Cultures

The brains were digested to obtain a single-cell suspension, as described in Section 2.6. The cells suspension was washed in 10 mL of microglia DMEM media and centrifuged at 300 x *g* for 7 minutes. The supernatant was carefully removed, and the pellet was resuspended in 6 mL per brain of microglia DMEM media supplemented with 10 ng/mL M-CSF. The resulting cell suspension was then transferred to a 6-well-plate at 3 mL per well and incubated overnight at 37 °C to allow the microglia to adhere. The myelin debris from the brains was resuspended in the culture media on the subsequent day following gentle agitation. The myelin-media was then removed before the well was washed with 3 mL of microglia DMEM. Following the removal of this wash 4 mL of microglia DMEM supplemented with 10 ng/mL M-CSF was added to each well. Microglia were maintained in culture for 7-21 days with M-CSF supplemented media replaced every 3 days. To harvest the media was removed and enough Accumax™ was added to cover the bottom of the well before being incubated at 37 °C for 20 minutes. The bottom of the plate was gently scraped with a plastic cell scraper (Greiner) to ensure all cells were dislodged. The cell suspension was transferred to a 50 mL falcon tube and centrifuged at 300 x *g* for 7 minutes before the cells were used in other applications. When necessary this protocol was scaled up in 100 mm x 20 mm (diameter x height) plates, T-25cm² and T-75cm² flasks where the culture volumes were increased proportionally.

2.4.9.1 Addition of TGF-β and Lentivirus

When required microglia culture media was supplemented with 50 ng/mL recombinant murine transforming growth factor β1 (TGF-β, eBioscience™). In Chapter 4 any pilot experiments using TGF-β have been clearly labelled and all microglia cultures in Chapter 5 were supplemented with TGF-β. An schematic overview of the optimised microglia culture protocol used for RNA-Sequencing (RNA-Seq) experiments and in Chapter 5 is shown in Figure 2.5.

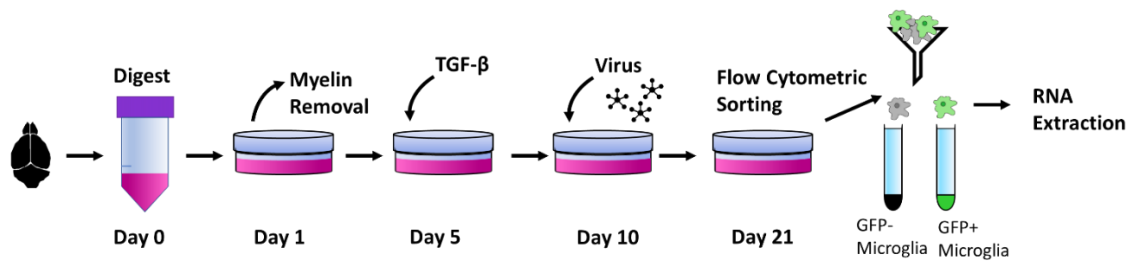


Figure 2.5 Schematic diagram summarising the culture protocol used for RNA-sequencing experiments. On Day 0 brains were digested and plated as described in 2.4.9. On Day 1 in culture the myelin was removed by gentle agitation to re-suspend the myelin in the media. After 5 days in culture the microglia DMEM media was supplemented with 50 ng/mL TGF- β in addition to 10ng/mL M-CSF. On day 10 lentiviruses were added to the cultures. On day 21 the cells were harvested and stained ready for flow cytometric sorting with BD FACS Aria II. Finally RNA was extracted from the sorted cells, as described in section 2.14.1.

After Day 1 media was replenished every 2 days, and 5 days after the cultures were established the media was supplemented with 50 ng/mL TGF- β in addition to 10 ng/mL M-CSF (supplemented microglia DMEM). Microglia cultures in a 6-well-plate were infected with lentivirus on Day 10 of culture. The media was removed and replaced with 3 mL supplemented microglia DMEM lentivirus was then added at a 1:10 dilution and incubated for 6 hours. Following this incubation an additional 3 mL of supplemented microglia DMEM was added to each culture well. This was scaled-up in larger flasks when required according to the surface area of the culture dish. The culture media was changed every 2 days, until Day 21 when microglia were harvested as described in the preceding section.

2.5 Functional M ϕ Assays

2.5.1 Adhesion assay

Lavages (described in Section 2.7) were counted (see section 2.4.3) before tubes were centrifuged at 350 x g for 5 minutes at room temperature. Cells were plated at a density of 0.5×10^6 per well in 1 mL standard DMEM media. Plates were incubated at 37°C to allow the cells to adhere, incubation times are indicated in results. At the end of each time-point the wells were washed three times with 1 mL DPBS before the cells were fixed with 2 % formaldehyde for 10 minutes at RT. Following incubation the fixative was aspirated and cells were permeabilised with 1 mL 0.1 % (v/v) Triton-X-100 in DPBS for 3 minutes cells at RT. The wells were then stained with 25 ng/mL of 4',6-Diamidino-2-Phenylindole Dilactate (DAPI; ThermoFisher) in 1 mL of DPBS for 5 minutes before the DAPI staining was imaged using the 10X magnification lens on the EVOS™ FL Imaging System (Life Technologies).

2.5.2 pMØ Phagocytosis assay

Lavages were counted (section 2.7) before being centrifuged at 350 x g for 5 minutes. Following this lavage cells were resuspended at 1x10⁶ cells per mL in standard DMEM and 500 µL was transferred to each well of a 24-well Costar® Ultra-low attachment plate (Corning) with an additional 1.5 mL of standard DMEM. FITC labelled Zymosan (Life Technologies) was added at a concentration of 20 µg per well (~4.5x10⁶ particles) before plates were incubated for 30 minutes at 37 °C. Zymosan is a cell wall extract of the yeast *Saccharomyces cerevisiae* (*S. Cerevisiae*). Media was removed from the plate before cells were recovered with 1 mL of Accumax™ and a 20-minute incubation. The detached cells were then transferred to 1.5 mL microcentrifuge tubes before centrifugation at 350 x g for 5 minutes at 4 °C. Samples were kept on ice until they were run on the Amnis Imagestream®X Mark II Imaging Cytometer, as described in section 2.16.2.

2.5.3 Primary Microglia Phagocytosis assay

Microglia were cultured in T-25cm² flasks for 21 days prior to the assay (section 2.4.9.1). Media was removed and the cells were gently washed in DMEM containing 2 % FBS. As described in 2.5.3.3 30 µg (approximately 6.75x10⁶ particles) of zymosan was opsonised and resuspended in 15 mL of 2 % FBS DMEM media supplemented with 10 ng/mL M-CSF and 50 ng/mL TGF-β. Each T-25cm² flask was incubated with 5mL of this zymosan-media for 1 hour at 37 °C. The media was removed and the cell monolayer was carefully rinsed three times with ice-cold DPBS before microglia were harvested with Accumax™ as described in section 2.4.9. The harvested cells were then fixed with 2 % formaldehyde for 20 minutes on ice. The cells were centrifuged at 350 x g for 5 minutes to remove the fixative. The cells were stained for surface markers, as described in section 2.9.4 prior to being resuspended in 50 µL FACS wash and run on the Amnis Imagestream®X Mark II Imaging Cytometer.

2.5.3.1 Collection of Mouse Serum

Mice were cardiac punctured using 1 mL syringe with a 23G needle. The collected blood was then transferred to a 1.5 mL microcentrifuge tube and transported on ice. The tubes were centrifuged at 2000 x g for 20 minutes at 4 °C and the serum was carefully removed from the cell pellet. The serum was aliquoted and stored at – 80 °C until required.

2.5.3.2 Fluorescent Labelling of Zymosan

Unlabelled zymosan was resuspended at 20 mg/mL (Life Technologies). One 10 mg aliquot was then diluted at a 1:1 in 0.2 M Sodium Bicarbonate buffer. In accordance with kit guidelines 1 mg of AlexaFluor™ 405 NHS Ester (Life Technologies) was dissolved in 35 µL of Dimethyl Sulfoxide

(DMSO) and added to the zymosan- and incubated at RT for 1 hour on a tube roller before the roller was moved to 4 °C and incubated overnight. The zymosan was then washed by adding 30 mL DPBS and centrifuged at 3000 x g for 5 minutes. The supernatant was then discarded. This wash step was repeated an additional 3 times before the AF405 labelled zymosan was resuspended at a 4 mg/mL concentration (~9x10⁸ particles by MUSE counts) and aliquoted before storage at -80 °C until needed.

2.5.3.3 Opsonisation of labelled Zymosan

Labelled zymosan was opsonised using mouse serum. Briefly, 30 µg (approximately 6.75x10⁶ particles) of zymosan was added to FBS-free DMEM supplemented with 30 % (v/v) mouse serum to give a total volume of 200 µL in a 1.5 mL microcentrifuge tube. The tube was then incubated at 37 °C for 20 minutes in the dark. The zymosan particles were then washed by the addition of 1 mL of DPBS and centrifuging the tubes at 1000 x g for 5 minutes. This wash step was repeated twice more to ensure unbound serum was removed.

2.5.4 M-CSF Stimulation assay

The M-CSF stimulation assay was adapted from published work [289] to use M-CSF differentiated MØP cells. Briefly, following the protocol outlined in section 2.4.6.1, 5x10³ MØP cells were differentiated in 200 µL of standard RPMI supplemented with 20 ng/mL M-CSF in Nunc™ Lab-Tek™ II 8-well Chamber Slide™ (Thermofisher). Another 200 µL of this media was added on the second day of culture. In accordance with the experimental layout shown in Figure 2.6, M-CSF was depleted from all experimental chambers except the ‘original’ control samples by gently washing the cell monolayer with standard RPMI before adding 200 µL of standard RPMI. The slide was then returned to the incubator for 3 hours.

Abi3 WT	M-CSF Stimulated	M-CSF Stimulated	Unstimulated	Original
Abi3 KO	M-CSF Stimulated	M-CSF Stimulated	Unstimulated	Original

Figure 2.6 Experimental layout of Chamber Slide used in M-CSF stimulation assay. *Abi3 WT and Abi3 KO MØP cells were differentiated on the same slide in separate wells. Both the M-CSF stimulated and unstimulated samples were depleted of cytokines and serum, whereas ‘original’ samples were left untouched until fixation.*

Media was carefully removed, and the cell monolayer was then washed once with serum-free RPMI and replaced with 100 µL of serum-free RPMI and incubated for a further hour. At this point M-CSF stimulated samples received 50 µL of serum-free RPMI supplemented with 60 ng/mL M-

CSF, to give a final dilution of 20 ng/mL, for 5 minutes. Following stimulation the media was removed from all chambers and washed twice with DPBS. Cells were fixed with 100 μ L 4 % paraformaldehyde for 10 minutes at RT. The fixative was aspirated and each chamber was washed twice with DPBS. Cells were then permeabilised with 100 μ L of 0.1 % Triton-X-100 in DPBS for 4 minutes at RT and washed twice more in DPBS. The cells were then stained for phalloidin in accordance with manufactures directions (Invitrogen). Methanolic phalloidin stock was diluted 1:40 in 0.5 % BSA in DBPS and 100 μ L of this staining solution was placed in each chamber. The solution was incubated on the slides for 20 minutes at RT in the dark. The staining solution was removed and 100 μ L of DPBS containing 0.5 ng/mL of DAPI (1:100 from 50 μ g/mL stock) was incubated in each chamber for 5 minutes. The DAPI solution was removed and the chamber were detached from the slide, as per manufacturer's instructions (Thermofisher). The slides were then mounted with ProLong[®] Gold reagent (Thermofisher) and covered with a 24 x 50 mm Menzel™ coverslip (Thermofisher). These slides were then imaged using the 20X magnification lens on the Zeiss Apotome Axio Observer microscope using the AxioCam506 camera (Carl Zeiss Microscopy GmbH). Exemplar images to demonstrate cell morphology changes were taken using the 63X magnification lens on the Zeiss Cell Observer Spinning Disk Confocal Microscope, taken with the AxioCam 503. Images were captured as Z-stacks, whereby upper and lower limits were manually set and the optimal number of slides determined by Zen software. Following capture the Z-stacks were processed using the orthogonal projection feature and exported as TIFF files, thus ensuring fine processes were not lost by focusing on one plane. The 20X images were used for all ImageJ analyses.

2.6 Microglia Isolation for Flow Cytometry

Mice were culled before the brains were removed and kept in 1 mL Hank's Balanced Salt Solution without Ca^{2+} and Mg^{2+} (HBSS w/o; Gibco) on ice. The brains were then digested using the Neural Tissue Digest Kit P (NTDK; Miltenyi Biotec) as per manufacturer's guidelines. Briefly, the weight of the brains was used to calculate the volume of buffers and enzymes required, the specific contents of which are proprietary knowledge. Buffer X and Enzyme P (confirmed to contain papain) were then added to a GentleMACS™ C-tube (Miltenyi) followed by the brain and 1 mL HBSS (w/o) followed by addition of Buffer Y and Enzyme A. The C-tubes were then placed in the GentleMACS™ OctoDissociator with heaters (Miltenyi) and run on the program 37C_ABDK, summarised in Figure 2.7.

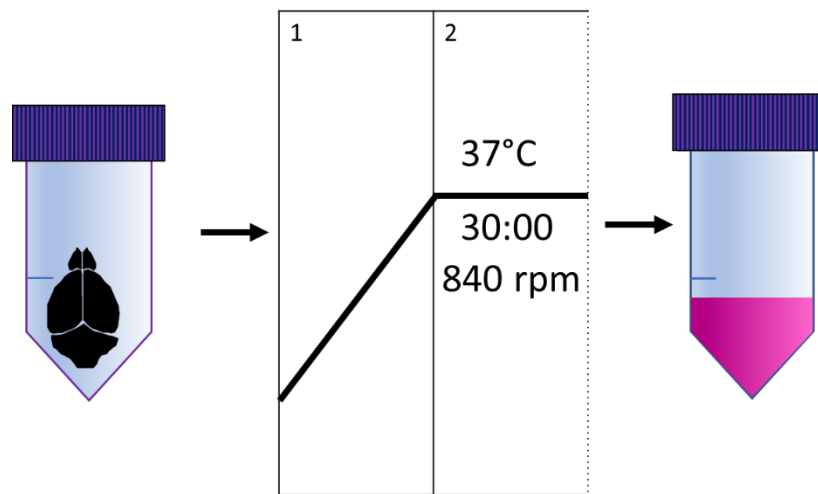


Figure 2.7 Diagram summarising the 37C_ABDK program on the GentleMACS™. Briefly, the C-tube was inverted and placed in the GentleMACS™ OctoDissociator with a heater. The program guide states that the C-tube was then heated to 37 °C for 30 minutes while being gently rotated at 840 rpm.

The resulting single-cell suspension was passed through a 70 µM strainer on a 50 mL falcon tube containing 10 mL HBSS with Ca²⁺ and Mg²⁺ (with), before being centrifuged at 300 x g for 7 min. The supernatant was carefully removed, and the pellet was resuspended in 1800 µL MACS buffer before the addition of 200 µL of myelin removal beads per brain (Miltenyi). These samples were incubated at 4°C for 15 minutes. Unbound beads were removed with the addition of 20 mL of MACS buffer and centrifugation at 300 x g for 7 min. After the supernatant had been removed each sample was resuspended in 2 mL MACS buffer and then run on the AutoMACS® Pro-Separator using the 'DepleteS' program to remove the myelin, as shown in Figure 2.8 (Miltenyi).

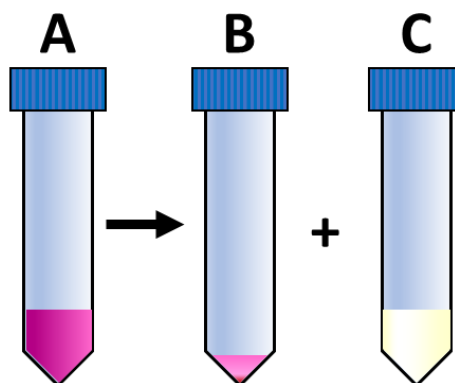


Figure 2.8 Summary of AutoMACS® Myelin Depletion using the 'DepleteS' program. The sample containing magnetic beads bound to myelin were placed in row A of the sample rack. Empty tubes were placed in rows B and C to collect the myelin 'negative' and myelin 'positive' fractions respectively. The myelin negative fraction contains the microglia among other cell types. The 'DepleteS' program has been optimised to remove myelin from the other cells to give a negative fraction with a high purity.

When required an additional bead separation was performed to purify CD11b⁺ cells. In this instance a small sample of the myelin-negative cell fraction was taken to calculate the cell number (see 2.4.3). The remaining cell fraction was centrifuged at 300 x g for 7 min. The supernatant was aspirated and the cells were resuspended in 90 µL per 10⁷ total cells of MACS buffer with EDTA. Then 10µl per 10⁷ total cells of CD11b (Microglia) MicroBeads (Miltenyi) were added to the samples before they were incubated at 4 °C for 15 minutes. The samples were washed by adding 1-2 mL of MACS buffer with EDTA and centrifuged at 300 x g for 7 min. Following this the supernatant was aspirated and the cells were resuspended in 1 mL MACS buffer with EDTA before being run on the 'Possel' program of the AutoMACS® Pro-Separator. This program is used to isolate cells with a robust CD11b expression that make up more than 5 % of the cell population. As in the 'DepleteS' program the labelled fraction was collected in row C.

2.7 Peritoneal Lavage

Mice were sacrificed and the peritoneum was exposed. Following this 5 mL of ice-cold lavage fluid was carefully injected into the peritoneal cavity using a 21-gauge hypodermic needle (BD Bioscience), avoiding any organs. The needle was withdrawn ensuring the injection site was blocked with abdominal fat. The mice were then gently rocked to ensure a maximum cell harvest and the needle re-inserted to withdraw cell-containing fluid. Following this recovery, the needle was removed and the fluid was transferred to a 15 mL falcon tube and placed on ice. Any lavages containing excessive blood or other contamination were discarded from further analysis.

2.8 *In vivo* Intraperitoneal (I.P.) Injections

All I.P. injections were performed by injecting mice in the lower right quadrant at a 45 ° angle.

2.8.1 Lentivirus Injection

Lentiviruses were produced as described in section 2.12. The resulting lentiviruses were thawed on ice before up to 300 µL was drawn into a 29-gauge insulin needle (Fisher Scientific). The injection site was gently washed with Hydrex Surgical Scrub (4 % (w/v) Chlorhexidine Gluconate; Ecolab) diluted 1:1 in water.

2.8.2 Lipopolysaccharide (LPS) Injection

LPS is found on the peripheral membrane of gram-negative bacteria and can thus, in appropriate doses, be used to provide a mild immune challenge. A recent meta-analysis purported that an I.P. injection of 100 µg/kg LPS was sufficient to elicit an immune response microglia [132]. The average

weights of C57BL/6 mice were used to calculate the LPS dose for male and female mice [306] and injections were carried out with a 29-gauge insulin needle (Fisher Scientific).

2.9 Flow Cytometry

Samples were run on either a 3-colour Cyan ADP Analyser (Beckman-Coulter), Fluorescence-activated cell sorting (FACS)-Fortessa or FACS-Canto (BD Biosciences), although the majority of samples were run on the Attune NxT flow cytometer (Thermo Fisher Scientific). Each experiment used internal single colour controls and where possible photo multiplier tube (PMT) voltage settings were kept constant between experiments.

Target	Clone	Company	Fluorochrome Colour	Final Dilution	Permeabilisation
CD11b	5C6	In-house	FITC	8 µg/mL	N/A
CD11b	M1/70	Biolegend®	Brilliant Violet™ 421	2 µg/mL	N/A
CD11b	M1/70	BD Biosciences	PerCP-Cy5.5	2 µg/mL	N/A
CD45	30-F11	eBioscience™	eFlour® 450	2 µg/mL	N/A
CD45	30-F11	eBioscience™	PE-Cyanine7	2 µg/mL	N/A
Dectin-1	2A11	AbD Serotec/Biorad	Alexa Fluor™ 647	10 µg/mL	N/A
F4/80	BM8	Biolegend®	Pacific Blue	5 µg/mL	N/A
F4/80	BM8	Biolegend®	Alexa Fluor™ 700	5 µg/mL	N/A
FcyRII/III	2.4G2	In-house	N/A	4 µg/mL	N/A
Iba-1	polyclonal	Wako	Alexa Fluor™ 635	0.01 µg/mL	0.3 % Triton-X-100
Ki67	SolA15	eBioscience™	PE-Cyanine7	2 µg/mL	0.5 % Saponin
P2ry12	S16007D	Biolegend®	Alexa Fluor™ 647	5 µg/mL	N/A
phosphohistone H3	D2C8	Cell Signalling Technology®	Alexa Fluor™ 647	1:80	0.5 % Saponin
PU.1	7C2C34	Biolegend®	Alexa Fluor™ 647	5 µg/mL	Methanol
PU.1*	9G7	Cell Signalling Technology®	Alexa Fluor™ 647	1:50	Methanol
Tim4	RMT4-54	Biolegend®	Alexa Fluor™ 647	5 µg/mL	N/A
Tmem119**	106-6	abcam	N/A	0.5 µg/mL	N/A
Staining Kit					
LIVE/DEAD®	N/A	Thermofisher	Near-IR	1:1000	N/A
Click-iT™ Edu Kit	N/A	Thermofisher	Alexa Fluor™ 647	Specified in kit	Provided in kit
Secondary Antibodies					
Goat anti-Rabbit	N/A	Jackson ImmunoResearch	DyLight™405	1:100	N/A

Table 2.9 Summary table of commonly used antibodies including the clone name, final dilution and the type of permeabilization, if required. *This Cell Signalling Technology® (CST) antibody was used in preliminary experiments in the *Spi1* floxed MØP cell lines. This was replaced with the Biolegend® anti-PU.1 antibody which was used in all subsequent experiments. Any experiments that used the CST anti-PU.1 antibody will clearly state it in the figure legend. **This Tmem119 antibody did not work on brains digested with papain and required a customised FACS block with 5 % Goat serum instead of Rabbit serum, due to the secondary antibody. If primary conjugated antibodies were also used in this staining panel then a second FACS block step with 5 % rabbit serum was performed after incubation with the secondary antibody but before the primary conjugated antibodies were applied.

2.9.1 Intra-nuclear Staining

Cells (0.2×10^6 per well) were fixed with equal volumes of 8 % formaldehyde in DPBS (to give a final concentration of 4 %) for 30 minutes at RT. The fixative was then removed by centrifuging samples at $350 \times g$ for 5 min and removing the supernatant. The cell pellet was resuspended in 90% ice cold methanol (Fisher Scientific) and left on ice for 30 minutes. Following this samples were centrifuged

at 350 x *g* for 5 minutes and the supernatant was carefully removed. The cells were then resuspended in 50 µL FACS wash before being transferred to one well of a V-bottom 96 well plate (Greiner). The plate was then centrifuged at 350 x *g* for 5 minutes and the supernatant was carefully removed. The cells were then resuspended in 50 µL of FACS block and incubated for 20-30 minutes on ice. During this incubation desired antibodies were diluted in FACS wash at twice (2X) the required final concentration, the final concentration of the most commonly used antibodies can be seen in Table 2.9. 50 µL per well of 2X concentrated antibodies were added to the FACS block in appropriate wells, resulting in a 1X final concentration, and incubated for 30-60 minutes in the dark on ice. For unstained samples 50 µL of FACS wash were added per well. The plate was then centrifuged at 350 x *g* for 5 minutes. The supernatant was removed and cells were resuspended in 100 µL FACS wash per well before being centrifuged again at 350 x *g* for 5 minutes. This washing step was repeated twice more. The cells were then centrifuged at 350 x *g* for 5 minutes one final time before being resuspended in ≥ 300 µL FACS wash and transferred to the appropriate microtiter tubes (Biorad). If DAPI staining was required, for example in Ki67 staining, then before the final re-suspension 100 µL of DAPI diluted 1:100 from a 50 µg/mL stock (Life Technologies) was added to each well and incubated in the dark for 20 minutes. The contents of each well were then transferred to a separate microtiter tube cell and ≥ 200 µL of FACS wash was added to each tube.

2.9.2 Intra-cellular Staining

For each sample 0.2 x10⁶ cells were fixed in equal volumes of 2 % formaldehyde, to give a final concentration of 1 % formaldehyde for 20 minutes at RT before being centrifuged at 350 x *g* for 5 minutes. The fixative was removed before the pellet was resuspended in 50 µL of 0.5 % Saponin FACS wash. The suspension was then transferred to a single well of a V-bottom 96-well-plate. The plate was then centrifuged at 350 x *g* for 5 minutes. The supernatant was discarded and the pellet resuspended in 50 µL of 0.5 % Saponin-FACS block before incubation on ice for 30 minutes. During this incubation the antibodies were prepared in 50 µL Saponin-FACS wash at 2X the desired concentration. 50µl of 2X antibodies were then added to the desired wells to give a 1X concentration in a final volume of 100 µL per well, before being incubated on ice in the dark for 30-60 minutes. The plate was then centrifuged at 350 x *g* for 5 minutes. The cells were then washed three times with standard FACS wash as described in the previous section, before samples were resuspended in ≥ 300 µL FACS wash and transferred to microtiter tubes. If desired DAPI staining was performed as described in section 2.9.1. Some antibodies required permeabilization

with 0.3 % Triton-X-100 in which case this protocol was used with 0.3 % Triton-X-100 in DPBS in place of 0.5 % Saponin FACS wash, as highlighted in Table 2.9.

2.9.3 β -Galactosidase Staining

To confirm *LacZ* reporter activity the FluoReporter™ *LacZ* flow cytometry kit was used to detect β -galactosidase activity as per manufacturers direction (ThermoFisher). Nonfluorescent FDG is sequentially hydrolysed by β -galactosidase to highly fluorescent fluorescein. To summarise, 1×10^6 cells were resuspended in 100 μ L of staining medium containing 3 mM Chloroquine diphosphate (SM+C) which inhibits lysosomal β -galactosidase [307]) and transferred into a 5 mL polypropylene tube (Greiner). Each tube was then incubated in a 37 °C water-bath for 20 minutes.

The fluorescein di β -D-galactopyranoside (FDG) substrate was diluted to 2 mM in de-ionised water and warmed at 37 °C for 10 minutes. To start the FDG loading 100 μ L of the warmed FDG substrate was added per tube, and the tubes were returned to the water-bath for 1 minute. The tubes were quickly placed on ice and 1.8 mL of ice-cold SM+C with 1.5 μ M propidium iodide (SM+C+PI) was added to each tube, trapping the loaded FDG via osmotic shock. The tubes were left on ice for at least 5 minutes before cell marker stains were added, as described in the section below. The samples were resuspended in 500 μ L of SM+C+PI and kept cold before being promptly analysed on the flow cytometer to avoid premature processing of the FDG substrate.

2.9.4 Surface Marker Staining

Tubes were centrifuged at 350 $\times g$ for 5 minutes at 4 °C and the supernatant removed. The cell pellets were resuspended in 50 μ L of FACS Block and incubated on ice for 10-20 minutes. As previously described, antibodies were diluted to a 2X concentration in 50 μ L FACS wash and 50 μ L was added to each sample. The samples were then incubated on ice for 15-30 minutes and washed three times in the 5 mL tubes using centrifugation as described in 2.9.1. After the wash steps each sample was resuspended in ≥ 500 μ L of FACS wash. If this staining was performed on live cells then MACS block and MACS wash, without sodium azide (NaN_3), were utilised in place of FACS block/wash respectively. This was mainly required for fluorescence-activated cell sorting on the FACS Aria TM III (BD Biosciences) and β -Galactosidase staining protocols.

2.9.5 NIM-DAPI Staining

Cells were counted and transferred to 1.5 mL microcentrifuge tubes and centrifuged at 350 $\times g$ for 5 minutes. The suspension was discarded and the pellet was thoroughly resuspended in 400 μ L of Nuclear Isolation Media containing DAPI (NIM-DAPI; Beckman Coulter) before a 30 minute

incubation in the dark at 4°C. The top 350 µL was carefully removed from each tube and placed into a clean 1.5 mL microcentrifuge tube before being analysed through flow cytometry.

2.9.6 Imaging Cytometry

Certain experiments benefitted from visual assessment such as phagocytosis assays. These experiments were analysed on the Amnis ImageStream®X Mark II (Merck) imaging cytometer. Samples were resuspended in a small volume of 30 µL in 1.5 mL microcentrifuge tubes. The magnification used in the data collection will be clearly stated in the necessary figure legends.

2.10 Immunohistochemistry Staining for β-Galactosidase

The expression of *LacZ* β-galactosidase was also confirmed by immunohistochemistry (IHC). The M-CSF differentiated MØP cells were generated as described in 2.4.6.1, where 5×10^5 MØP cells were differentiated onto 50 mm glass-bottomed tissue-culture dishes (MatTek corp). β-galactosidase staining was also assessed in lavage cells by another PhD student (Elena Simonazzi). Briefly mice were lavaged (section 2.7) and 5×10^5 cells were incubated on autoclaved 13 mm Circular Coverslips (VWR) overnight in standard RPMI media to allow the pMØ to adhere.

The β-galactosidase staining kit IHC staining was used per manufacturer's directions (Sigma). In short, the media was removed, and the cell monolayer was washed twice with DPBS. The cells were then covered with 1X fixative solution which was incubated for 10 minutes at RT. This solution was removed and the cells washed twice more with DPBS. The cells were covered with sufficient staining solution to cover the dish; 10 µL reagent-A, 10 µL reagent-B, 10 µL reagent-C, 50 µL of 20 mg/mL X-gal solution in 920 µL DPBS per mL and incubated at 37 °C for a minimum of 1 hour. The exact time used will be stated in the figure legend for each experiment. Staining solution was removed and the cells were rinsed once with DPBS. The bottom of the 50 mm glass-bottomed tissue culture dishes (MatTek corp) were covered with 70 % glycerol (Thermofisher) in DPBS. Alternatively, coverslips were mounted onto SuperFrost™ Plus™ glass slides (Thermofisher) with ~10 µL of Pro-long anti-fade gold mounting medium (Thermofisher) and secured using clear nail varnish. Brightfield images were taken using the 20X magnification lens on the Zeiss Apotome Axio Observer microscope using the AxioCamIC (Carl Zeiss Microscopy GmbH).

2.11 Cloning

A visual summary of the entire cloning process can be seen in Figure 2.9. The steps will be discussed in detail in the subsequent sections. All DNA concentrations were measured using the Nanodrop™ 2000 Spectrophotometer (Thermofisher Scientific).

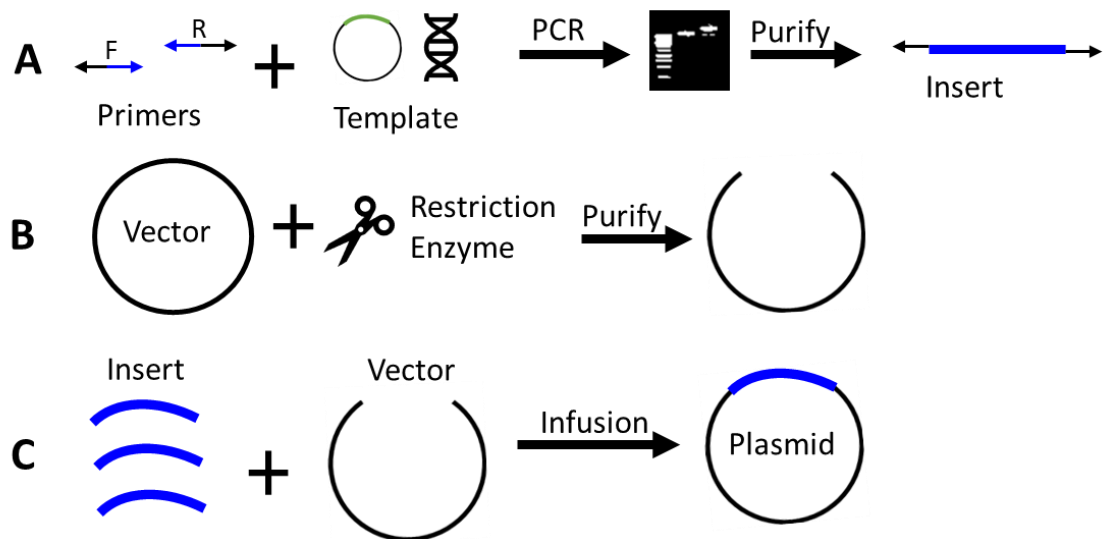


Figure 2.9 An overview of the cloning process. A Custom primers were used to amplify DNA from a template, namely another plasmid or directly from cDNA, using PCR. The resulting product was electrophoresed on an agarose gel and purified. B The plasmid vector was linearised with the appropriate restriction enzymes and purified. C In the final step the insert and linearised vectors were combined using the infusion enzyme to generate a new plasmid.

2.11.1 Preparation of Plasmid Stocks

Prior to cloning vector plasmids containing an ampicillin resistance gene were grown-up overnight. For each plasmid a Luria Bertani (LB) broth tablet (Lennox; Sigma) was added to 48.3 mL distilled water and autoclaved. Once cool the LB broth was transferred to a 250 mL conical flask (Fisher Scientific) and 100 µg/mL of Ampicillin (Sigma) was added to ensure only the desired vector plasmid was grown. A clean pipette tip was used to scrape a small amount of the plasmid glycerol stock into the flask which was then loosely covered with foil and incubated overnight at 37 °C with 225 rpm in an S1500 orbital shaking incubator (Stuart). The following day each amplified plasmid was prepared using the Maxiprep Kit per manufacturer's direction (Qiagen). Plasmids were eluted in nuclease-free water (Thermofisher) and stored at -20 °C until required.

2.11.2 Insert Preparation

2.11.2.1 shRNA Construction

Target *Spi1* shRNA sequences were designed against the principle isoform shown on the Ensemble genome browser (release version 95) using the primer Basic Local Alignment Search Tool (BLAST; National Institute of Health) in accordance with previously published guidelines [308] as shown in Figure 2.10. In short, each selected sequence started with a guanine residue which is optimal for the U6 promoter and was terminated with five thymine nucleotides to ensure RNA polymerase III disassociation. Specificity was confirmed using BLAST. The non-silencing (NS) control shRNA had

already been tested and developed by a previous lab member [309]. The final shRNA sequences can be seen in Table 2.10.

<i>Spi1</i> shRNA Insert Sequence (5'→3')	
shRNA 1	GAGCTATACCAACGTCCAATGCTCGAGCATTGGACGTTGGTATAGCTCTTTT
shRNA 2	GATGTGCTCCCTTATCAAACCTCGAGGTTTGATAAGGGAAGCACATCTTTT
Non-Silencing shRNA Insert Sequence (5'→3')	
GTCTCGCTTGGGCGAGAGTAAGTAGTGAAGCCACAGATGTACTTACTCTCGCCCAAGCGAGACTTTT	

Table 2.10 *The shRNA sequences used in this thesis (5' → 3') direction without the 15 bp overhang sequences. The Non-Silencing (NS) shRNA sequence was designed and tested by a previous lab member [309].*

This shRNA insert was ordered along with a reverse complement shRNA sequence, 25 µL of each primer pair were mixed (100 µM; Sigma) in a 0.2 mL PCR tube (STARLAB) and heated to 95 °C for 5 minutes. After the reaction mixture had cooled 10 µL was diluted 1:100 with nuclease-free water.

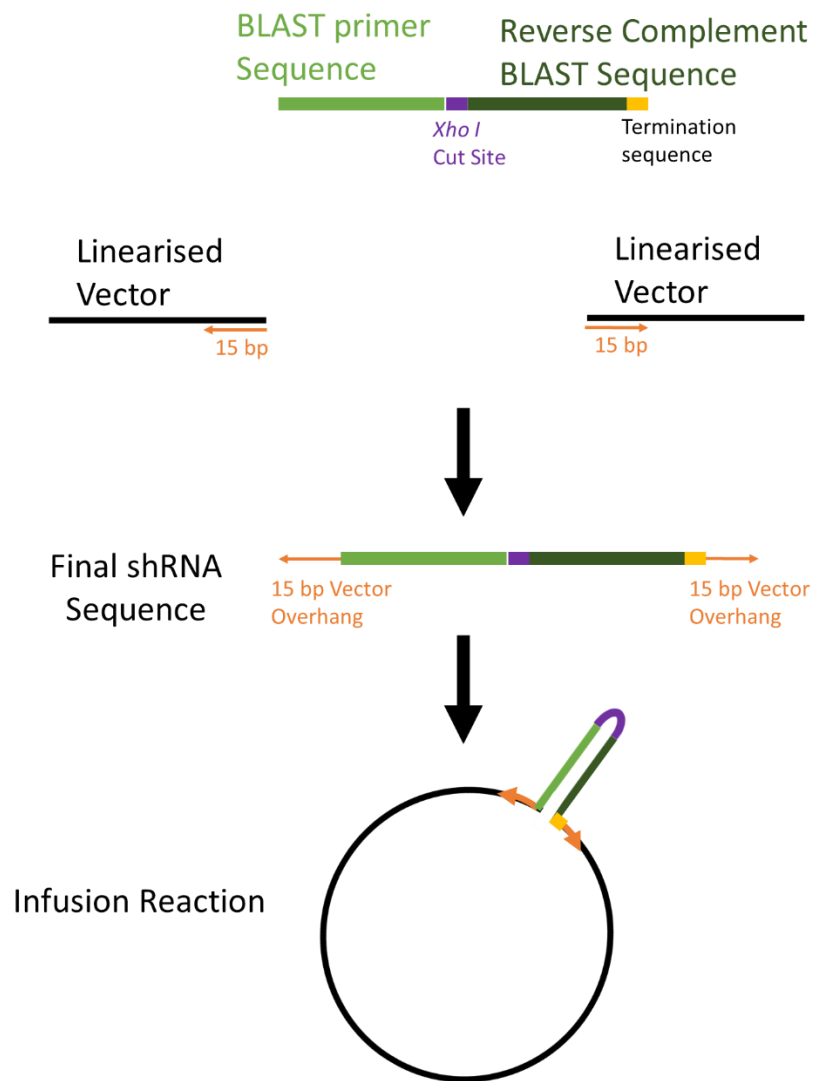


Figure 2.10 Summary of shRNA sequence design. The BLAST primer sequence (light green) against the desired mRNA target was aligned to a reverse complement sequence of the BLAST primer (dark green) with an *Xho* I cut site sequence (purple) inserted between the two primer sequences, with a termination sequence (TTTTT; yellow) appended to the second primer sequence. Finally the shRNA sequence was flanked with a 15 bp sequence homologous to the region upstream and downstream of the restriction enzyme cut site (orange) on the vector plasmid. This sequence should allow the shRNA to be easily inserted into the vector during the infusion reaction.

2.11.2.2 From complementary DNA (cDNA) or plasmid DNA

Inserts were also amplified from other plasmids or cDNA. Firstly Infusion primers were designed with a 15 base-pair (bp) overlap between the vector and insert, as per manufacturer's direction (Clontech) and shown in Figure 2.11.

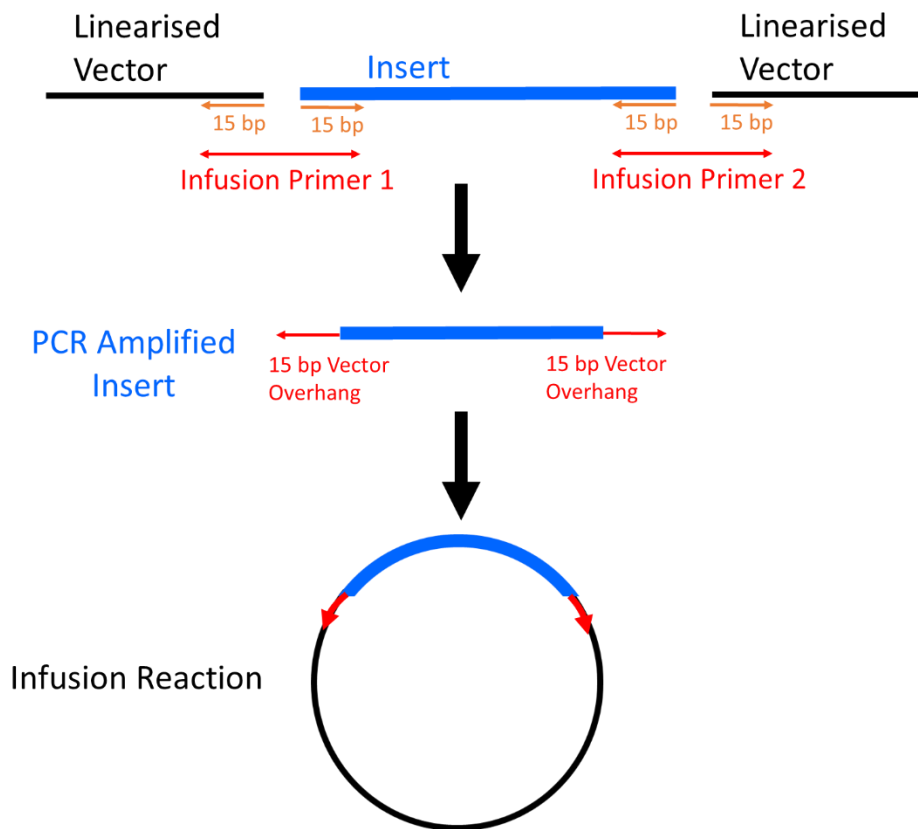


Figure 2.11 Summary of Infusion primer design. Infusion Primer 1 (red) was made by taking the final 15 bp sequence preceding the restriction enzyme cut site (black) and the first 15 bp of the insert sequence (blue). The second Infusion Primer (2; red) was made of the final 15 bp sequence of the insert (blue) and 15 bp immediately downstream of the restriction enzyme cut site (black). Thus when the insert was amplified by PCR using these primers the insert sequence would be flanked by 15 bp of the vector sequence either side of the restriction site. These flanking sequences enable an easier insertion into the vector during the infusion reaction.

As the Cre sequence was amplified from another plasmid the sequence did not need to be altered, as it already was preceded by a Kozak sequence (CCACC) before the start codon to improve translation and the stop codon had been removed to ensure both Cre and GFP were produced. The murine *Spi1* (see Ensemble CCDS 16425.1 for sequence) was amplified from cDNA from the pMØ of C57BL/6 mice using Infusion primers designed to add the 15 bp overhang and a Kozak sequence before the start codon. The stop codon was maintained in the SIEW plasmid to ensure GFP was produced separately from the insert protein. The final Infusion primer sequences can be seen below in Table 2.11.

<i>Spi1</i> pSIEW Primer Sequences (5'→3')	
Forward	GGATCCCGGGCTCGAGCCACCATGTTACAGGCGT
Reverse	TACCAGGCCTCTCGAGCTATCAGTGGGGCGGGAG
Cre pSFEW Primer Sequences (5'→3')	
Forward	GGATCCCGGGCTCGAGCCACCATGTCCAATTTACTG
Reverse	CGCTGCCGCTCTCGAGCAAGTCTTCTCAGAAATAAG

Table 2.11 Final Infusion primer sequences. The regions that overlapped with the plasmids are shown in black, the Kozak sequence and start codon in green and the regions overlapped with the insert sequences in blue.

Multiple PCR reactions were performed using the high fidelity Taq Phusion® enzyme in accordance with manufacturer’s recommendations (NEB) to amplify the insert. Each insert required different annealing temperatures to generate the optimal PCR band. Figure 2.12 below shows the 2-step and 3-step PCR protocols that were used to generate the inserts in this thesis.

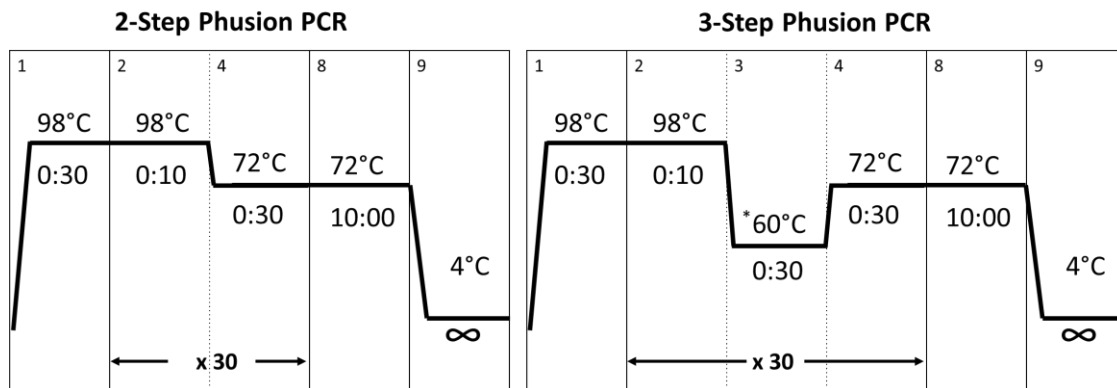


Figure 2.12 The 2-step and 3-step Phusion PCR reactions used to generate inserts. The 2-step PCR was used to generate inserts where the predicted annealing temperature of the primers was 72 °C or higher. The 3-step PCR was most commonly used to generate inserts. *Indicates the annealing temperature which was adjusted based on the primers.

The resulting PCR reactions were pooled and electrophoresed on a 1 % agarose gel, as described in 2.3. The gel was then placed on a UV transilluminator and the correct sized band was carefully excised from the gel then purified using the NucleoSpin™ PCR clean-up kit (Macherey-Nagel) and eluted in nuclease-free water.

2.11.3 Vector Layouts

All vectors were made by a previous PhD student in the lab, Dr Luke Davies [151,310]. Figure 2.13 summarises the main features between the long terminal repeats of the three vectors used in this thesis, adapted from [310], the key functional features are described below. In the SU6EW-plasmid (pSU6EW) vector the shRNA sequence is inserted under a U6 promoter which ensures the sequence is transcribed by a RNA polymerase III [308]. The pSFEW vector is a fusion plasmid,

meaning both the inserted protein and the eGFP reporter are under the same promoter but the proteins are produced separately due to the T2A site in-between the coding sequences which causes ribosomal skipping. In the final plasmid, pSIEW, expression of the desired protein is controlled by the Spleen Focus Forming Virus (SFFV) promoter and the eGFP expression by the Internal Ribosome Entry Site (IRES) sequence which binds ribosomes to initiate transcription of the eGFP. The IRES sequence is fairly inefficient at recruiting the ribosomal complex compared to the SFFV promoter so when another protein is inserted under the SFFV promoter there is a reduction in the transcription of the eGFP reporter [311].

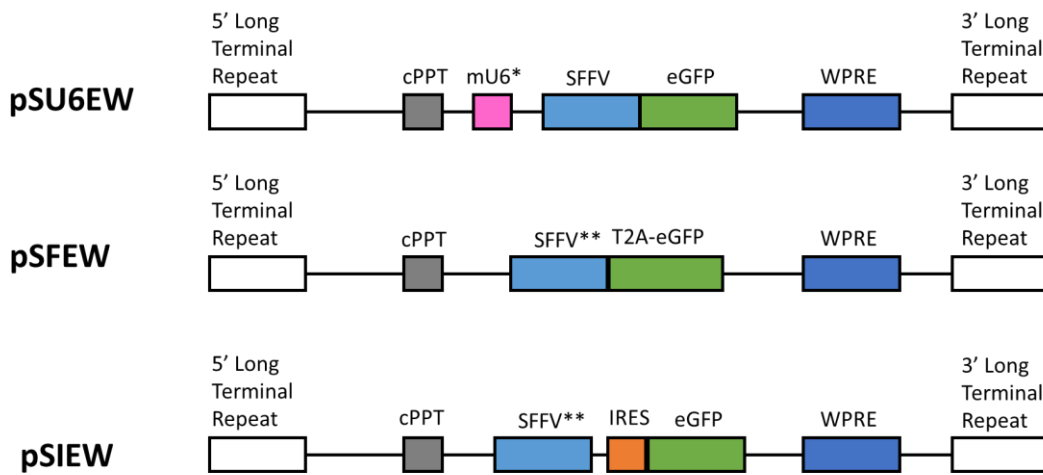


Figure 2.13 Summary of basic lentiviral vectors used in this thesis, adapted from [310]. The features between the two long terminal repeats are as follows: The cPPT (grey) denotes the central polypurine tract sequence. The mU6 (pink) is the mouse U6 promoter exclusively used for promoting shRNA sequences. The SFFV (light blue) is the spleen focus forming virus promoter. eGFP (green) is the GFP reporter sequence. The pSFEW plasmid has a T2A fusion sequence which precedes the eGFP sequence. WPRE (dark blue) is the sequence for a woodchuck post-transcriptional regulatory element, which enhances post-transcriptional gene expression. The IRES (orange) is the internal ribosome entry site sequence promoter. The location of the insert/enzyme restriction sites are also shown, where *denotes a PmeI restriction site and **a XhoI cut site.

2.11.4 Vector Linearisation

The vector was linearised by the addition of 3 µg of the desired plasmid to the appropriate amount of restriction enzyme, as listed in Table 2.12, and 1X CutSmart® buffer adjusted to give a final reaction volume of 50 µL as per manufacturer's direction (NEB) in a 0.2 mL PCR tube (STARLAB). The reaction mixture was incubated at 37°C for at least 1 hour before the enzyme was inactivated at 65 °C for 15 min in a Mastercycler® Nexus Gradient PCR machine (Eppendorf).

Vector	Restriction Enzyme	Enzyme per Reaction	Forward Primer Sequence (5'→3')	Reverse Primer Sequence (5'→3')
SU6EW	* <i>Pme I</i>	50 Units	TGCCCCGGTTAATTTGCAT	CAAACCTACAGGTGGGGTCT
SFEW	* <i>Xho I</i>	100 Units	CTCCGACAGACTGAGTC	GACACGCTGAACTTGTGGCCGTTT
SIEW	* <i>Xho I</i>	100 Units	CTCCGACAGACTGAGTC	GACACGCTGAACTTGTGGCCGTTT

Table 2.12 The restriction enzymes used to linearise plasmids to open the desired insert site and the primer sequences required for plasmid DNA sequencing. Including the amount of enzyme used per reaction in Units. As per manufacturers instructions "1 Unit equates to the amount of enzyme to digest 1 µg of λ DNA fragments in 1 hour at 37 °C in 50 µL" (NEB).

The successfulness of the linearisation was confirmed by comparing the linearised PCR product to the circular plasmid on a 1 % agarose gel, as described in section 2.3). The remaining reaction mix was purified using the NucleoSpin™ PCR clean-up kit (Macherey-Nagel) and eluted in nuclease-free water. The linearised vector was then be stored at -20 °C until required.

2.11.5 Cloning and Transformation

The insert and vector were combined according to the Infusion Cloning kit (Clontech). Briefly, 200 ng of the linearised vector and the calculated molar ratio of 3:1 amount of insert, 61.8 ng for the plasmids generated in this thesis, were added to 2 µL of the Infusion enzyme premix in a 0.2 mL PCR tube. Nuclease-free water was used to make the total reaction volume 10 µL. The resulting reaction mix was incubated at 50 °C for 15 minutes before being cooled on ice and stored at -20 °C. The newly generated plasmid was transformed into the NEB® 10-β Competent *Escherichia coli* (*E. coli*; 10-β) cells in accordance with manufacturer's instructions (NEB). In short, 1 µL of the cloning reaction mix was added to one 50 µL aliquot of 10-β cells and gently mixed before being incubated on ice for 30 minutes. The 10-β cells were heat shocked at 42 °C for 30 seconds before being put back on ice for 5 minutes. Once cooled 950 µL of stable outgrowth media (NEB) was added to each reaction which was then incubated at 37 °C while being shaken at 250 rpm for 1 hour in a Thermo-Shaker (Grant-bio, PSC24N). LB broth was then used to serially-dilute the transformed 10-β cells. Following this 100 µL of each 10-β dilution were spread onto pre-warmed LB agar plates (Sigma) containing 100 µg/mL Ampicillin with a plastic spreader. These plates were incubated at 37 °C for 20 minutes before the plates were inverted and incubated at 37 °C overnight. The following day the resulting bacterial colonies were screened using colony PCR.

2.11.6 Colony PCR

Colonies were selected using individual clean pipette tips and added to a 1X KAPA2G Fast Ready-Mix PCR reaction (Sigma) containing primers designed to target either side of the insert site (Table 2.12), as per manufactures' instructions. Over 15 colonies were screened for each transformation

and the resulting PCR products were electrophoresed on a 2 % agarose gel, as described in section 2.3. Colonies that resulted in a PCR band of the predicted size, and thus contained the insert, were again selected with a clean pipette tip and incubated overnight in 10 mL of LB broth with 100 µg/mL of Ampicillin while being shaken at 225 rpm at 37 °C in a SI500 orbital shaking incubator (Stuart). On the subsequent day if colonies had been successfully grown then the LB broth would appear cloudy. At this point glycerol stocks of each colony were made by adding 400 µL of the cloudy LB broth to 600 µL of autoclaved glycerol (Fisher Scientific) and thoroughly mixed before the stocks were stored at – 80 °C until required. The plasmid present in the remaining broth was purified using the PureLink® Quick Plasmid Miniprep Kit according to manufacturer’s instructions (Invitrogen). The plasmid was eluted in nuclease-free water and sent to Eurofins Genomics (Wolverhampton, UK) for Sanger sequencing using primers specific to the vector located on either side of the insert site. The resulting sequences were checked against the predicted template. Once confirmed the plasmids were prepared as detailed in 2.11.1.

2.12 Lentivirus Production

All lentivirus work was performed in a category II laminar flow hood and all waste was bleached as per safety requirements. The protocol used has been scaled up from a previously published protocol [309].

2.12.1 Transfection

Firstly 12x10⁶ recently passaged 293T cells were seeded in a T175 cm² flask in 15 mL standard DMEM media and incubated overnight to ensure a confluency of 70-80 %. The following day the cells were transfected using the Effectene® transfection reagent (Qiagen). In short, the required amount viral packaging/envelope plasmids were added to the custom lentivirus plasmid in a 1.5 mL microcentrifuge tube, as shown in Table 2.13, using a previously published method [151,310]. Buffer EC was added to give a total volume of 600 µL in each tube 36 µL of the enhancer buffer was then thoroughly mixed into each tube, and incubated for 5 minutes at RT. Following this 120 µL of the Effectene reagent was added to each tube, which was then vortexed for 10 seconds and incubated at RT for 10 minutes.

Plasmid	Amount (µg)
pCMV-δ8.91 packaging plasmid (containing Gag/Pol virus structural proteins, Tat and Rev viral regulatory proteins)	1.5
pMD2.G viral envelope plasmid (encoding VSV-G coat)	1
Lentiviral plasmid (e.g. SU6EW)	2

Table 2.13 The amount of each plasmid required to transfect the lentiviruses using the Effectene® transfection system.

During this incubation the 293T media was aspirated, then the cells were carefully washed with DPBS, to avoid disturbing the cell monolayer, before being replaced with 15 mL of standard DMEM. The final Effectene mix was added to 4.2 mL standard DMEM in a 15 mL falcon tube and the 1.5 mL tube was rinsed with an additional 1 mL of standard DMEM. The Effectene-DMEM mix was then added dropwise to the T-175cm² flask, avoiding disrupting the cells, before the flasks were incubated for 48 hours. The following two methods were used to harvest the virus, the Lenti-X concentrator (Clontech) was mainly used to test newly sequenced plasmids and sucrose purification for *in vivo* and RNA-Sequencing experiments.

2.12.2 Sucrose Purification

The virus-infected media was carefully removed from the culture flask and passed through a 0.45 µM filter (Sartorius) and serum-free DMEM was added to give a final volume of 25 mL. If a second virus harvest was required then 15 mL of standard DMEM was added to the culture flask, without disturbing the cell monolayer, and returned to the incubator for another 24 hours. The 25 mL of virus-containing media was transferred into a 28 mL thin-walled polypropylene konical tube (Beckman Coulter) and 3 mL of RT 20 % (w/v) sucrose solution in DPBS was carefully underlaid. The konical tubes were then centrifuged at 26,000 rpm for 90 minutes at 4 °C in a SW28Ti swinging-bucket ultracentrifuge rotor assembly in a Optima XPN-80 Ultracentrifuge (Beckman Coulter). Following ultracentrifugation liquid was carefully poured-off into bleach and the tubes were inverted on paper-towels for 10 minutes. Any remaining medium was carefully removed before the addition of 1 mL Aim V™ media (Gibco). Following a 20-minute incubation the viral pellet was gently resuspended with a pipette and the virus was then aliquoted and stored at -80 °C for up to 3 months. For the second virus harvest then the pellet was resuspended in 0.5 mL of Aim V™ media.

2.12.3 Lenti-X Concentrator

The virally infected media was transferred to a 50 mL falcon tube and centrifuged at 500 x g for 10 minutes to remove any cells. Sufficient lenti-X concentrator was added to a clean 50 mL falcon tube to give a final concentration of 1-part lenti-X concentrator to 3-parts viral supernatant. The supernatant was carefully poured into the falcon tube containing Lenti-X concentrator and gently mixed by inversion. These tubes were stored at 4 °C for at least 4 hours, normally the incubation was overnight. The virus/concentrator mixture was centrifuged at 1500 x g for 45 minutes at 4 °C.

The supernatant was poured into bleach and the viral pellet was resuspended in 1mL AimV media. The virus was then aliquoted and stored at -80 °C for a maximum of 3 months.

2.12.4 Lentiviral Titration

To assess the efficiency of each batch of virus small amounts were used to infect Jurkat cells [310]. Firstly, Jurkat cells were counted (see Section 2.4.3) and 2×10^5 cells were added to each well of a 24-well-plate in 200 μ L of standard RPMI. Following this 0.5 μ L, 1 μ L, 2.5 μ L, 5 μ L or 10 μ L of lentivirus was added to individual wells and standard RPMI media was added to give a total volume of 400 μ L per well. One well on each plate contained no lentivirus to provide a non-infected baseline control. The plates were incubated overnight before the addition of another 600 μ L standard RPMI per well. The plates were then returned to the incubator for a further 2-3 days before the infection was stopped by the addition of an equal volume (1 mL) of 2 % formaldehyde plates were incubated for 20 minutes at room temperature. From each well 1.5 mL was transferred to a microcentrifuge tube and the tubes were centrifuged at $350 \times g$ for 5 minutes. The supernatant was carefully removed and the cell pellet resuspended 400 μ L of FACS wash and the percentage of infected (GFP+) cells was determined via flow cytometric analysis. The original volume of lentivirus was then plotted on a graph alongside the percentage of infected cells to determine the strength of lentivirus, an example can be seen in Figure 4.16B (Section 4.2.3.1).

2.13 Western Blot

2.13.1 Cell Lysis

Cells were pelleted in a 1.5 mL microcentrifuge tube after centrifugation at $350 \times g$ for 5 minutes. The supernatant was removed and the cells were lysed with RIPA buffer and a 1:100 dilution of Halt™ Protease and Phosphatase Inhibitor Cocktails (100X; Thermo) and thoroughly mixed with a pipette. The tubes were then centrifuged at $12,000 \times g$ for 10 minutes at 4 °C. The supernatant was carefully removed and transferred to a new 1.5 mL microcentrifuge tube and stored at - 80 °C.

2.13.2 Bicinchoninic acid (BCA) assay

Total protein levels were calculated for each sample using the Pierce BCA assay (ThermoFisher). First 5 μ L of each protein sample and BSA standard, seven serial dilutions from 2 mg/mL to 15.625 μ g/mL were added to individual wells of a 96 well flat-bottomed ELISA plate (Corning®). Next the working BCA solution was made by adding one part of reagent B to 50 parts of reagent A, which was then distributed across at 100 μ L per well. The plate was sealed with clingfilm before being incubated at 37 °C for 30 minutes. The plate was then read at 562 nm using a Multiskan®

Spectrum Microplate reader (Thermo). The standard curve was used to interpolate the protein concentration of the samples in PRISM software (see 2.16.5).

2.13.3 Sample Preparation

For each sample 40 µg of protein was added to 10 µL of reducing sample buffer (4X Laemmli buffer with β-Mercaptoethanol) and DPBS was added to give a final volume of 40 µL. These samples were then heated at 70 °C for 10 minutes.

2.13.4 Gel Electrophoresis

First a 10 % acrylamide SDS-Polyacrylamide Gel Electrophoresis (SDS-PAGE) separating gel was made using the components and volumes stated in Table 2.14. The 1.5 M Tris-HCl (pH8.8), water, 30 % (Poly-) Acrylamide and 10 % SDS were added to a 50 mL falcon tube. The 10 % APS and N,N,N,N'-Tetra-methyl.ethylenediamine (TEMED) were the last ingredients added to the 50 mL falcon tube as they catalyse the polymerisation reaction. The resulting gel mixture was quickly poured into 1.5 mm gel cassette (Biorad) were filled up leaving an approximate gap of ~1.5 cm and the top of the gel was covered with distilled water (dH₂O) saturated butanol to level the gel before it was left to set for 30 minutes.

10 % Separating gel	
1.5 M Tris-HCl pH8.8	2.6 mL
30 % (Poly-) Acrylamide	3.4 mL
dH ₂ O	3.8 mL
10 % SDS	100 µL
10 % APS	100 µL
TEMED	10 µL

Table 2.14 The volumes of each reagent needed to make one 10 % acrylamide separating gel.

The butanol was removed from the top of the gel and the gel was rinsed with distilled water. The stacking gel was made as before using the components listed in Table 2.15 before the mixture was carefully pipetted on top of the set separating gel and the comb was inserted. This was left to set for an hour.

Stacking Gel	
0.5 M Tris-HCl pH6.8	1.25 mL
30 % (Poly-) Acrylamide	0.670 mL
dH ₂ O	3 mL
10 % SDS	50 µL
10 % APS	50 µL
TEMED	5 µL

Table 2.15 The volumes of each reagent required for one acrylamide stacking gel.

The final set gel was transferred to the running chamber (Mini-PROTEAN® Tetra Cell System; Biorad) which was then filled with running buffer before the comb was carefully removed. The previously prepared samples (as shown in section 2.13.3) were loaded into the wells alongside 4 µL of the Amersham™ Rainbow™ marker ladder (GE Healthcare). Any spare wells were filled with 40 µL of 1X non-reducing Laemmli buffer (without β-Mercaptoetanol). The gel was electrophoresed at 90 V for 10 minutes, to allow the samples to reach the separating gel. The voltage was then increased to 120 V and the gel was run until the loading dye was ~1cm from the bottom of the cassette. Each protein was detected using a separate gel.

2.13.5 Semi-Dry Gel Transfer

Gels were transferred onto a PVDF membrane using the semi-dry method. First two pieces of thick blotting paper (Biorad) were soaked in transfer buffer for 5 minutes. The gel was briefly rinsed in water before being left in transfer buffer to 5 minutes. The Immun-Blot® PVDF membrane (Biorad) was dipped in 100 % methanol before being soaked in transfer buffer for 5 minutes.

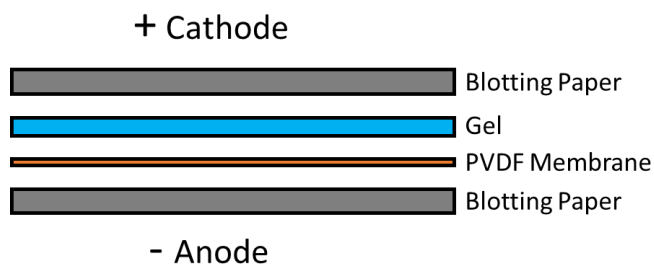


Figure 2.14 Set-up of components in Semi-Dry Transfer Cell. One transfer-buffer soaked piece of blotting paper was placed on the Anode, followed by the prepared PVDF Membrane. The gel was carefully placed on top of the membrane and another piece of soaked blotting paper put on top. All air bubbles were removed from these layers before the Cathode was replaced.

As shown in Figure 2.14 the Trans-Blot® Semi-Dry Transfer Cell (Biorad) set-up was as follows; a pre-soaked piece of blotting paper was placed on the anode and topped with the PVDF membrane. The gel was then carefully placed onto the membrane and a second piece of soaked blotting paper and after ensuring there were no air bubbles the cathode was replaced. The gel was then transferred onto the membrane by setting the Trans-Blot® Semi-Dry Transfer Cell (Biorad) at 20 V for 45 minutes. The PVDF membrane was briefly washed in 1X Tris-Buffered Saline (TBS).

2.13.6 Antibody Staining

The PVDF membrane was transferred to a 50 mL falcon tube, so that the proteins faced the inside of the tube. The membrane was then blocked by adding 10 mL of blocking buffer to the 50 mL falcon tube before it was placed on a mechanical tube-roller for 60 minutes at rt to minimise background staining. During this incubation time the primary antibodies were diluted in 5 mL of blocking buffer, using the concentrations shown in Table 2.16.

	Antibody	Clone/Catalog Number	Company	Dilution
Primary	Rabbit anti-Cre Recombinase IgG	D3U7F	CST	1:4000
Primary	Purified Rat anti-GFP IgG2a, κ	FM264G	Biolegend	1:1000
Secondary	Goat anti-rat IgG HRP	AP183P	Merck	1:2500
Secondary	Donkey anti-rabbit IgG HRP	NA934	GE Healthcare	1:10000

Table 2.16 *The Primary and Secondary antibodies used to detect proteins in western blotting.*

Following blocking buffer was removed and replaced with the primary antibody buffer. The 50 mL falcon was then incubated overnight on the tube-roller at 4 °C. The following day the membrane was transferred to a clean 50 mL falcon tube and washed three times with 5 mL of blocking buffer at rt for 10 minutes per wash. The primary antibody was stored at – 20 °C for future use. During these wash steps the secondary antibody was diluted to the desired concentration, as stated in table 11, in 5 mL blocking buffer. After the last wash had been discarded the secondary antibody was added to the 50 mL falcon tube and incubated for 60 minutes on the mechanical roller at rt. The membrane was then transferred to a new 50 mL falcon tube washed for 10 minutes with 5 mL of TBS-Tween 20 (TBST) at rt on the tube-roller. This wash step was repeated twice more before a brief wash in TBS. The ECL™ prime (GE Healthcare) detection reagent was prepared as per manufacturer's instructions by mixing equal parts of reagent A and B in a 50 mL tube. The membrane was added to the 50 mL tube containing the ECL™ prime and incubated in the dark for 5 minutes. After this incubation the membrane was transferred to a exposure cassette covered with clingfilm before all air bubbles were removed. The exposure cassette was then taken into the dark room where a piece of RX NIF X-ray film (Fujifilm) was placed on top of the membrane for 1 minute. The exposed film was then developed using the Compact X4 imaging system (Xograph). The exposure time was adjusted based on the strength of the signal detected at 1 minute.

2.13.7 Stripping and Re-Blotting for Actin

Each membrane was re-blotted at least once to probe for actin to confirm an equal loading of protein. Firstly the membrane was briefly washed in 1X TBS to remove any remaining ECL. The

membrane was then transferred to a clean 50 mL falcon tube and incubated with 10 mL of stripping buffer for 30 minutes at 50 °C with gentle agitation. The stripping buffer was discarded and the membrane was moved into a new 50 mL falcon tube where it was washed three times with 5 mL TBST for 10 minutes per wash. The membrane was then blocked again with 5 mL blocking buffer for 60 minutes described in the previous section. The blocking buffer was then discarded and replaced with the anti-mouse β -actin-HRP conjugated antibody (clone 8H10D10; Cell Signalling Technology®) at a 1:2000 dilution in 5 mL blocking buffer which was incubated on the tube-roller overnight at 4 °C. The following day the membrane was washed in TBST before incubation with ECL™ prime and detection using film, as described in the previous section.

2.14 Quantitative PCR (qPCR)

2.14.1 RNA Extraction

Samples were prepared accordance with the Qiagen RNeasy Mini kit (Qiagen), most the cell pellet was thoroughly resuspended in the correct amount of RLT buffer. RNA extracted directly from brain tissue was homogenised in the correct amount of RLT being transferred to a QIAshredder (Qiagen) and centrifuged at $\times 13,000 g$ for 2 minutes to ensure a maximum yield of RNA. At this point samples were often stored at $-80\text{ }^{\circ}\text{C}$ for a few days before the RNA was extracted. The samples were then defrosted on ice were mixed then processed in accordance with manufacturers instructions (Qiagen). The RNA was eluted in 30 μL of nuclease-free water in a 1.5 mL microcentrifuge tube and kept on ice. The concentration of RNA was measured using the Nanodrop™ 2000 (Thermofisher Scientific). Following this the RNA tubes were stored at $-80\text{ }^{\circ}\text{C}$ or were directly converted to complementary DNA (cDNA).

2.14.2 Conversion to cDNA

The RNA was converted to cDNA using the Precision™ Reverse-Transcription Premix 2 kit (PrimerDesign LTD). As per manufacturer's directions 20 μL of the Premix was added to a 0.2 mL PCR tube between 1-10 μL of RNA was then added to each tube. In each experiment the amount of RNA, in ng, was kept consistent. These samples were then heated in the Mastercycler® Nexus Gradient (Eppendorf) PCR machine to 42 °C for 20 minutes and then 72 °C for 10 minutes. If required, nuclease-free water was added to make a total volume of 30 μL before samples were stored at $-20\text{ }^{\circ}\text{C}$.

2.14.3 qPCR reaction

All qPCR reactions were performed using the 2X Precision®FAST qPCR Master Mix (with SYBR-green and low ROX) according to manufacturers instructions (PrimerDesign LTD). To summarise 5

μL of the Precision®FAST master mix was added to 300 nM of forward and reverse primers and 12.5 ng cDNA. Nuclease-free water was used to ensure the reaction mix had a total volume of 10 μL, which was transferred to one well of a 0.1 mL MicroAmp™ Fast Optical 96-well reaction plate (Applied Biosystems™). The qPCR primer sequences can be seen in Table 2.17.

Target	Species	Forward Primer Sequence (5'→3')	Reverse Primer Sequence (5'→3')
<i>Abi3</i>	mouse	TCAAAACCCAGCAGGCTCCC	CTGTCTGTGGCCTGCAAGTAGT
<i>Aif1</i>	mouse	GGAAAGTCAGCCAGTCCTCC	TCCACATCAGCTTTTGAAATCTCC
<i>Apoe</i>	mouse	AGATGGGGTTCTCTGGGTGG	TAGGCATCCTGTCTAGCAATGT
<i>Cd34</i>	mouse	GGAGTTCTGCTGGCCATCTT	TAAGGGTCTTCACCCAGCCTT
<i>Csf3r</i>	mouse	CTGTCAATTAACGACGGGGCT	TGTCTCAGCAATGACTGGGG
<i>Fcrls</i>	mouse	GTCGCTGGGGCACTGTATGT	GCACAGGCAGAGCTTCATCAA
<i>Gapdh</i>	mouse	TGGCAAAGTGGAGATTGTTGCC	AAGATGGTGTATGGGCTTCCCG
<i>Il-6</i>	mouse	TCCGGAGAGGAGACTTCACA	TTGCCATTGCACAACCTTTTCT
<i>P2ry12</i>	mouse	CATTGCTGTACACCGTCCTG	GGCTCCCAGTTTAGCATCAC
<i>Pilrb</i>	mouse	AGGCATGAAGTTGTGGCAGT	CATGGTGGTGTGAGTGCTTG
<i>Sall1</i>	mouse	TAAGCCGAGGACCAAGCCTC	ACATCAGCCGCTCACGG
<i>Siglech</i>	mouse	TGTGCATGTGACAGACCTCA	GTAGGACGACCAAGCTCCAG
<i>Spi1</i>	mouse	GATGGAGAAGCTGATGGCTTGG	TTCTTCACCTCGCTGTCTTGC
<i>Tmem119</i>	mouse	GTGTCTAACAGGCCCCAGAA	AGCCACGTGGTATCAAGGAG
<i>Tnf</i>	mouse	TAGCCCACGTCGTAGCAAAC	ACAAGGTACAACCCATCGGC
<i>Ubc</i>	mouse	*Not Available	
<i>Ywhaz</i>	mouse	TTGAGCAGAAGACGGAAGGT	GAAGCATTGGGGATCAAGAA
<i>YWHAZ</i>	human	CCCAGAGAAAGCCTGCTCT	CCGATGTCCACAATGTCAAGT

Table 2.17 qPCR primer sequences used in this thesis. *This sequence is proprietary knowledge as the primer was taken from the GeNorm endogenous control comparison kit (PrimerDesign LTD).

Each qPCR reaction was run in triplicate where possible or duplicate if this was not possible. Primer pairs targeting an endogenous control gene were also included in each qPCR plate and were either mouse UBC, GAPDH or YWHAZ, or human YWHAZ and will be clearly stated in the figure legend. Control samples without a cDNA template were also included on each plate. Plates were then sealed with an adhesive PCR plate seal (Thermo) and centrifuged at 350 x g for 1 minute. The plates were run on the ViiA™ 7 Real-Time PCR system (Applied Biosystems™) using the 40-cycle ΔΔCT method, according to the Precision®FAST guidelines, described in Table 2.18.

Step	Time	Temperature	Cycle Number
Enzyme Activation	2 minutes	95 °C	N/A
Denaturation	5 seconds	95 °C	x 40
Data Collection	20 seconds	60 °C	
Melt Curve	15 seconds	95 °C	N/A
	1 minute	60 °C	
	15 seconds	95 °C	

Table 2.18 The temperature and time cycling times used for to generate the qPCR data.

2.15 RNA-Sequencing

RNA was extracted using the RNeasy Mini kit (Qiagen), as described in section 2.14.1. The RNA quality control checks and sequencing analyses were performed by an external agency, the Welsh Gene Park. Briefly, the RNA integrity (RIN) values and RNA concentration was assessed using the Agilent 2100 Bioanalyser (Aligent), these values can be seen in Chapter 3. The cDNA libraries were then generated using the Illumina® Truseq® stranded total RNA with Ribo-Zero GOLD kit. The paired-end sequencing was performed using the Illumina® HiSeq 2500 sequencer to a depth of 30-40 million paired reads. The resulting fastq files were processed using the STAR-DESeq2 pipeline [312] by the department bioinformatician, Dr Rob Andrews, using the mm10 reference genome.

2.16 Statistics and Analysis Software

2.16.1 IFL Data

All images taken on the Zeiss Apotome Axio Observer microscope (Carl Zeiss Microscopy GmbH) were converted into TIFF files using ZEN software (version 2.0.0.0; Carl Zeiss Microscopy GmbH). All images taken on the EVOS™ FL Imaging System (Life Technologies) were ready for analysis. ImageJ was then used for further analysis (version 1.51k; Wayne Rasband), the method use to analyse the pictures will be stated within the chapter.

2.16.2 Flow and Imaging Cytometry Data

All flow cytometry files were analysed using FlowJo software (version 10; FlowJo LLC). Data generated through imaging cytometry was analysed using the analysis wizards in the IDEAS® software (version 6.2; Merck). A summary of the key features of the IDEAS® software are listed below in Table 2.19.

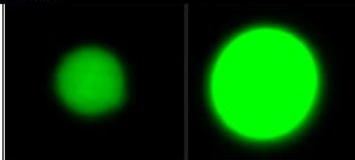
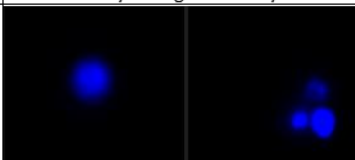
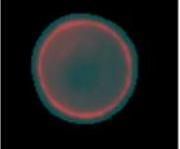
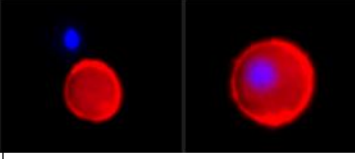
Mask/Feature	Description	Image
Intensity	The intensity is the sum of the pixel values in the masked area, minus the background signal.	 Low Intensity → High Intensity
Max Pixel	This is the intensity of the brightest pixel (1 pixel = 0.25µM ²). A smaller brighter zymosan particle will have a higher value than a larger particle with more diffuse staining.	 Low Max Pixel → High Max Pixel
Cell Mask	Cell boundary is determined using a Mask over a selected channel, shown in grey, which can be used in other analyses.	 Cell Mask using CD11b Staining
Internalisation Ratio	This is the ratio between the intensity of the zymosan within the CD11b cell mask and the overall intensity (unmasked).	 Negative Ratio → Positive Ratio

Table 2.19 Definition and Example Images of Features and Masks used in IDEAS® Analysis Software.

2.16.2.1 Calculating Normalised PU.1 Expression

Normalised PU.1 expression was calculated using equation 1. Briefly the isotype background was subtracted from the sample before being divided by the average control PU.1 MFI. This calculation controlled for variation between experiments.

$$\text{Normalised PU.1 Expression} = \frac{(\text{PU.1 MFI} - \text{Isotype MFI})}{\text{Average Control PU.1 MFI}}$$

Equation 2.1 The calculation used to determine the normalised PU.1 protein expression from the raw median fluorescent intensity (MFI) values.

2.16.2.2 Calculating Absolute Cell counts

The absolute cell counts were determined using the calculation outlined in equation 2. For example the percentage of pMØ was calculated from flow cytometric staining. This was then multiplied by the number of viable cells in each sample, as determined by the Muse® Cell Analyzer (Merk Millipore).

$$\text{Absolute Counts} = \frac{\% \text{ Cell type}}{100} \times \text{Total Viable Cell Number}$$

Equation 2.2 *The calculation used to determine the absolute pMØ number. The percentage of pMØ was calculated from flow cytometry data using MØ markers, and the total viable cell number from the cell counts obtained using the MUSE® Cell Analyzer.*

2.16.3 qPCR Data

Data was collected using QuantStudio™ Real-Time PCR software (version 1.3; ThermoFisher Scientific) and the relative gene expression was determined using a template created by Dr Simone Cuff, based on work published by Livak and Schmittgen in 2001 [20].

2.16.4 RNA-Sequencing Data

RNA-Seq data was analysed using a combination of Ingenuity® Pathway Analysis (version 0.-10; Qiagen), the Database for Annotation, Visualization and Integrated Discovery (DAVID) (version 6.8 Laboratory of Human Retrovirology and Immunoinformatics [313]). Heat-maps were generated with the Morpheus software (The Broad Institute [314]). Single cell sequencing data was analysed using the Loupe Cell Browser (version 3.0.1; 10X Genomics).

2.16.4.1 Enrichment of Genetic Risk Factors for AD in the Spi1 RNA-Seq data

Sets of differentially expressed genes from the *Spi1* RNA-Seq datasets were tested for enrichment of an AD association signal using the International Genomics of Alzheimer's Project (IGAP) GWAS study. The IGAP dataset is the largest publicly available LOAD GWAS study [3]. Briefly, the gene lists generated by the *Spi1* knock-down and *Spi1* over-expression datasets were converted to human orthologs using the BioMart feature in Ensemble, as detailed in [315]. The *Spi1* knock-down dataset was split into 8 different gene sets using different adjusted P-value thresholds for differential expression and the *Spi1* over-expression dataset split into 6 different gene sets. Each gene set was then tested for enrichment of a signal in the IGAP GWAS using Multi-marker Analysis of GenoMic Annotation (MAGMA) [316]. MAGMA first combines the association statistic across all SNPs in a gene to get a gene-wide measure of the association. Then, the gene-wide association measures within the gene set were then compared to those outside of the gene set. This analysis corrects for correlations in gene-wide association measures in neighbouring genes due to linkage disequilibrium. The enrichment analyses of IGAP association signal in the *Spi1* RNA-Seq dataset were kindly performed by Professor Peter Holmans.

2.16.5 Graphs and Statistics

All graphs and statistical analyses were performed using GraphPad PRISM® 6 (version 3.07; GraphPad Software, Inc.). The most appropriate statistical test was selected based on the following criteria and the chosen test was stated in each figure legend. In all figure legends 'n'

refers to the number of independent experiments, and data presented as the mean \pm the standard deviation unless otherwise stated.

When comparing two groups an unpaired two-tailed t-test was often the most appropriate test. Paired tests were utilised when data from each replicate had been normalised to the control group, thus removing variation in the control group and making a paired comparison more suitable, for example in chapter 6 when comparing the normalised cell numbers in Abi3 WT and KO experiments. In instances where the data was not normally distributed or the variances between groups were uneven a Welch's unequal variance t-test was used.

Datasets with three or more groups were compared using One-Way ANOVAs followed by a post-hoc multiple comparison test. Either Tukey's test was used to compare all means, Dunn's multiple comparison test to compare all means against a selected control or Sidak's test where the means of selected pairs were compared. In cases where a One-Way ANOVA was unsuitable, for example if the variance of the groups or the group sizes were unequal, then a non-parametric Kruskal-Wallis Test was used in lieu. In one experiment a Friedman's test was used as a repeated-measures test to compare the number of Abi3 KO and WT MØP cells taken from culture samples collected over three days (Figure 6.22).

P-values of ≥ 0.05 were taken as non-significant (ns). P-values of ≤ 0.05 will be denoted with a single asterisk*, P-values of ≤ 0.01 will be written as **, P-values of ≤ 0.001 by *** and P-value of ≤ 0.0001 as ****.

Chapter 3 Effects of *Spi1*-URE removal on PU.1 protein expression

3.1 Introduction

The past ten years have seen increasingly rapid advances in understanding the aetiology of AD. Insights from genetic association studies has resulted in a focus on the impact of the immune system on pathology [2]. The *SPI1* gene, which encodes the transcription factor PU.1, is of particular interest in AD for the following reasons. Firstly *SPI1* is an AD-risk gene [317] and an allele that confers a high *SPI1* expression (rs1057233^a) has been linked to a younger AD onset [230]. Another *SPI1* AD-risk SNP (rs1377416^c) was spliced into *Spi1* enhancer region of BV-2 cells resulted in an increased production [70]. Secondly several studies have also proposed that *SPI1* may act in the promoter region of other AD-risk genes, potentially increasing expression of multiple AD-risk genes [230,231]. In a network analysis of 151 proteins thought to mediate AD-risk *SPI1*/PU.1 was found to interact with multiple other proteins [5].

What is not yet clear is the impact that PU.1 protein levels have on biological processes in AD. The transcription factor PU.1 has long been known to influence myeloid cell differentiation and M-CSF dependent proliferation [246]. Recently, *in vitro* studies have shown that an altered PU.1 expression can effect critical microglia functions like phagocytosis in both the BV-2 mouse cell line [230] and in primary human microglia cultures [232]. *In vivo* CSF1R inhibitor experiments suggest that a partial reduction in AD microgliosis is beneficial [73,90–92] and are thought to partially block the M-CSF/PU.1 proliferation pathway [89].

HDAC inhibitors like Valproic Acid have also been shown to reduce PU.1 protein expression [280,281] and a clinical trial testing VPA in AD patients accelerated AD progression [318]. While HDAC inhibitors likely alter more genes than PU.1, Valproic Acid reduced the phagocytic capacity of human microglia *in vitro*, similar to a forced reduction of PU.1 [232,281].

Given that the elderly are immunocompromised [49] there are concerns peripheral MØ may be further compromised by a reduction in PU.1, as a consequence of peripheral drug administration.

Currently much uncertainty still exists about the relationship between the amount of PU.1 and biological pathway changes within microglia. It has been suggested that PU.1 can control gene expression in a dose-dependent manner [9,10] and in in the mouse BV-2 microglia cell line there were over 5,000 PU.1 binding sites [319]. Recent *in vitro* work has shown that reducing PU.1 in the BV-2 cell line or in primary human microglia cultures affected the expression of multiple genes [230,233]. Cultured microglia might not fully represent the complex *in vivo* environment [155].

Therefore, investigating how a low PU.1 alters the transcriptome of freshly isolated microglia may provide more accurate insight than *in vitro* work.

Recently a mouse model was developed that reduced PU.1 expression in total bone marrow by approximately 80 % compared to control mice [260]. This was done by Cre-LoxP mediated removal of a well characterised upstream regulatory element (URE) ~14 kB upstream of the *Spi1* promoter (-14 kB *Spi1* URE, [268]). The pups appeared phenotypically normal until 8-10 weeks of age, but then developed an Acute-Myeloid Leukemia-like pathology and died within 3 months. It was hypothesised that these *Spi1*-URE knock-out mice could be used to reduce PU.1 expression in microglia and pMØ based on *in silico* analysis (discussed in section 3.2.1).

Overall the purpose of this chapter was to observe the effects of removing the -14 kB URE of *Spi1* alters the level of PU.1 protein in microglia and pMØ. This was achieved by:

- Deleting the -14 kB *Spi1*-URE in myeloid cells by breeding *Spi1*-URE floxed mice to another mouse strain that expressed Cre recombinase under the control of the *Cx3cr1* promoter. This has been previously described in sections 1.7 and 2.1.
- Evaluating the level of PU.1 knock-down in microglia and pMØ in this mouse model.
- Monitoring for any impact on *in vivo* function or behaviour.

3.2 Results

3.2.1 Genomic Analyses of *Spi1* URE

In silico analyses were performed to confirm the -14 kB *Spi1* Upstream Regulatory Element (URE) was likely to participate in maintaining PU.1 expression in microglia with the help of Dr Matthew Hill. Publicly available ATAC-Sequencing (Assay for Transposase-Accessible Chromatin using sequencing) datasets allowed assessment of DNA accessibility across the genome [320]. Acetylation of histone 3 lysine residue 27(H3K27ac) datasets determined if there were likely to be enhancers or promoters in this region [321]. Datasets for various immune cells were gathered through the “Gene Expression Omnibus” database provided by the National Institute of Health (NIH) and were collated in the Cistrome database which assessed the quality of these datasets [322]. The datasets used in these analyses are listed in Table 3.1.

ATAC-Seq		
Cell Type	GEO Reference	Additional Information
Microglia	GSM2692293	C57BL/6*
pMØ	GSM2692320	C57BL/6*
Splenic B-cell	GSM2692261	C57BL/6*
Splenic CD8 ⁺ Naïve T-Cell	GSM2692188	C57BL/6*
Splenic CD4 ⁺ Naïve T-Cell	GSM2692186	C57BL/6*
Splenic CD4 ⁺ regulatory T-Cell	GSM2692347	C57BL/6*
BMDM	GSM2845671	C57BL/6 differentiated with M-CSF**
H3K27ac		
Cell Type	GEO Reference	Additional Information
Microglia	GSM1545963	C57BL/6†
pMØ	GSM1545985	C57BL/6†
Splenic mature B-cell	GSM1463441	C57BL/6††
Splenic naïve CD4 ⁺ T-cell	GSM2538960	C57BL/6†††
BMDM	GSM2845607	C57BL/6 differentiated with M-CSF**

Table 3.1 Summary of the ATAC-Sequencing and H3K27ac datasets used in the *In-Silico* analyses. The ATAC-Seq and H3K27ac datasets were collated using the Cistrome Project database [322], where they were checked to ensure quality. The Gene Expression Omnibus (GEO) reference numbers for each sample have been provided. All of the datasets had been previously published in the following papers *[323] **[324] †[118] ††[325] †††[326].

The ATAC-Seq and H3K27ac profiles were compared using the UCSC genome browser [327] focusing on the region upstream of the *Spi1* transcription start site, where the URE was defined

using the BLAT tool [328]. In the ATAC-sequencing datasets each peak denoted a region of open chromatin that is more available to interact with DNA binding proteins, such as transcription factors. In Figure 3.1, peaks in the -14 kb *Spi1* URE region (indicated by the black bar) intimated that the chromatin was more accessible in this region, which suggested that the URE could contribute to *Spi1* gene regulation in this cell type.

At the *Spi1* transcription start site (indicated with an arrow) there were only open chromatin peaks in cell types that are known to express PU.1 namely, microglia (green), pM \emptyset (purple) and BMDM (teal). There was a reduced signal in the B-lymphocytes (B-cells) taken from the spleen. As described in 1.5.1, PU.1 protein level is downregulated during B-cell development, but the transcription factor was still detectable in these cells [251]. The regulatory T-lymphocyte population (T-reg; grey) did not appear to have much open chromatin at the locus of the *Spi1* transcription start site, again fitting with the literature that has confirmed a lack of PU.1 protein in most T-cell populations [329]. As shown in Figure 3.1 both the microglia (green) and pM \emptyset (purple) datasets there were multiple ATAC-Seq peaks that align with the -14 kB URE site, suggesting that the enhancer may function in both these myeloid cell populations. While peaks were still observed in splenic B-cells (blue) they do not appear to be as substantial, indicating that this region of chromatin is not as open in this population. Very little open chromatin was detectable in multiple splenic T-cell populations (grey), at both the -14 kB URE and *Spi1* transcription start site, which suggests neither the URE does not function in these cells. The final ATAC-Seq plot (teal) demonstrates the -14 kB open chromatin pattern detected in myeloid cells is maintained even in *in vitro* Bone-Marrow Derived M \emptyset (BMDM) cultures.

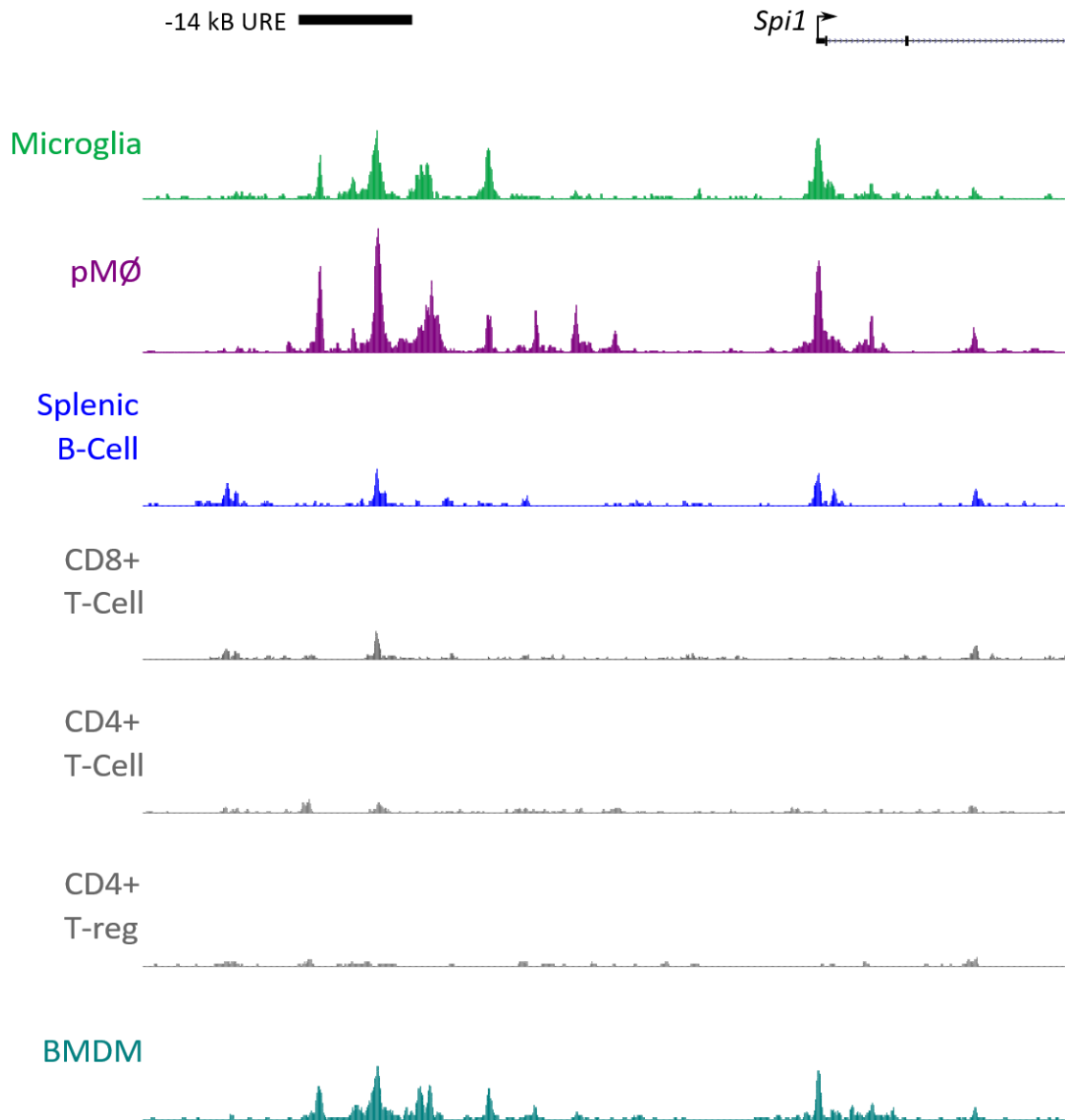


Figure 3.1 In-Silico ATAC-Seq Analysis suggests the -14 kB *Spi1* URE chromatin is accessible in multiple immune cell populations. Publicly available ATAC-sequencing datasets for different immune cell populations were compared to investigate where regions of open chromatin lie upstream of the *Spi1* transcription start site (indicated by the arrow). The region of the -14 kB URE is denoted by the black bar and all datasets were equivalently scaled. ATAC-Seq datasets are shown for microglia (green), pMØ (purple), splenic B-cells (blue), splenic T-cell populations (grey) and BMDM cultures (teal).

Analysis of the H3K27ac profiles suggested that the URE acts as an enhancer. In Figure 3.2 below the peaks indicated the presence of the H3K27ac histone modification which is indicative of enhancers [321]. The pattern of H3K27ac is similar in the immune cell populations to the ATAC-Seq data, meaning that there are more peaks in the MØ populations compared to the splenic B-cells. Again, there was very little H3K27ac detected in the T-Cell subset. The acetylation of H3K27 suggests that the -14 kB URE is acting as an enhancer of *Spi1* expression in microglia, pMØ and BMDM, and to a lesser extent in the splenic B-cell population.

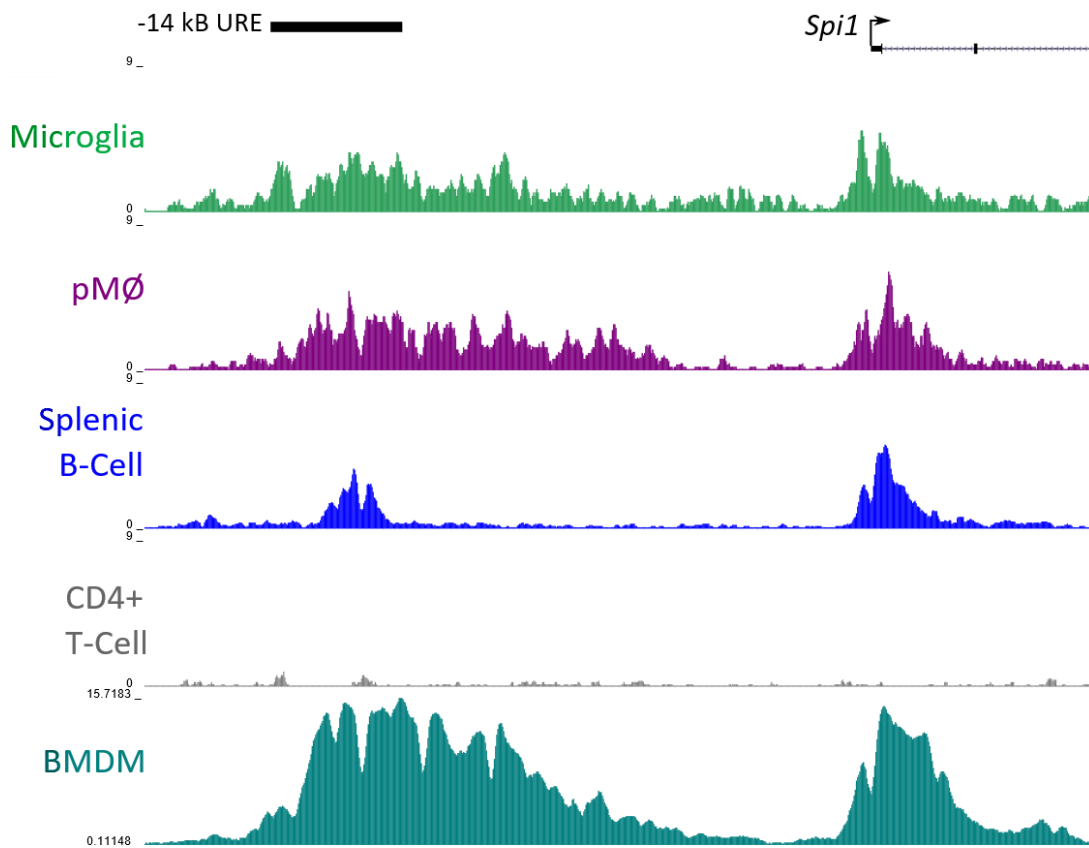


Figure 3.2 In-Silico Analysis of H3K27ac suggests -14 kb Spi1 URE is an active enhancer in B-cell and MØ populations. Again the -14 kb URE region is denoted by the black bar and all datasets were equivalently scaled, except for the BMDM dataset, hence the scale is denoted by the numbers on the left. Microglia (green), pMØ (purple) and BMDM (teal) datasets there are multiple H3K27ac peaks within the -14 kb URE site, suggesting that this enhancer active in these MØ populations. Again the splenic B-cell dataset (blue) had smaller peaks compared to the pMØ and microglia populations. The H3K27ac modification was barely detectable in the T-cell population (grey), at both the -14 kb URE and Spi1 transcription start site.

Figure 3.3 compares the ATAC-Seq and H3K27ac profiles of the microglia and pMØ populations. Together this indicates that in the -14 kb region of Spi1 there are large regions of open chromatin surrounded by histones modified in a manner that are associated with enhancer activation. Additionally, this comparison confirms the accuracy of these profiles as open chromatin regions are known to lie in the H3K27ac troughs.

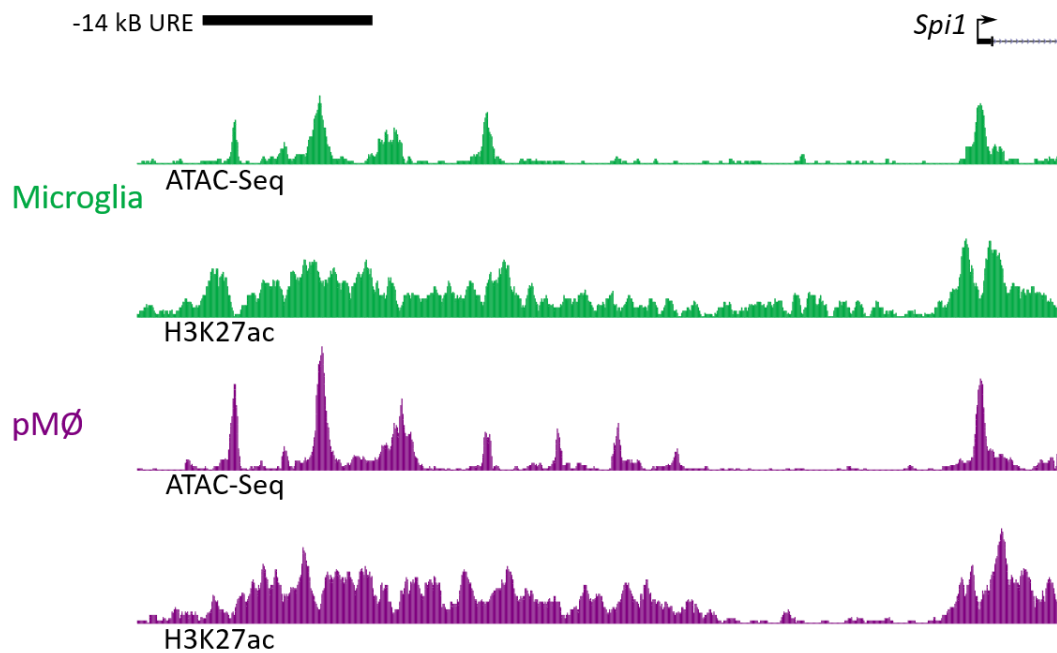


Figure 3.3 Comparing the ATAC-Seq and H3K27ac profiles in Microglia and pMØ. As expected, the peaks in the ATAC-Seq and H3K27ac datasets were mutually exclusive. Taken together these datasets indicate that at the -14 kb URE the open chromatin regions are surrounded by regions where the histones are modified in a manner which is indicative of an enhancer.

To sum-up this section ATAC-Seq and H3K27ac datasets show that chromatin in the -14 kb *Spi1*-URE region is likely active in pMØ and microglia and may be promoting *Spi1* expression. This supports the hypothesis that removing the URE in these cells will result in an alteration to *Spi1* gene regulation and likely the PU.1 protein expression, though this needed to be confirmed experimentally.

3.2.2 PU.1 Antibody Specificity

This thesis needed to accurately measure PU.1 protein even after a potentially large protein reduction, hence it was necessary to validate the chosen antibody for specificity and signal strength.

The anti-Spi1 (PU.1) antibody (Biolegend; clone 7C2C34) was first tested in the RAW cell line where PU.1 stained cells were run on the Amnis ImagestreamX MkII imaging cytometer. Figure 3.4A showed that PU.1 staining (red) was co-localised to the nuclear DAPI stain and not the CD11b membrane stain (green). Moreover RAW cells stained with PU.1 staining had a higher signal intensity than RAW cells stained with the isotype control (Figure 3.4B). The PU.1 nuclear localisation was assessed using the IDEAS® software, where PU.1 staining was determined to have 100 % overlap to the 'nuclear' template made using DAPI staining (Figure 3.4C). The steps used as

part of the “nuclear localisation analysis wizard” in the IDEAS® software. From left to right, the first histogram demonstrates how focused cells were selected, anything with a gradient RMS value of over 50 was taken as focused. Following this, single cells were gated, as shown in blue. The next plot compared DAPI staining intensity to PU.1 signal intensity in both the isotype (grey) and PU.1 antibody (red). These double positive (DAPI and PU.1 positive) cells were selected. The DAPI nuclear staining was set as an outline or “mask” that the PU.1 staining was compared against. When the same analysis was performed against the CD11b membrane marker the staining was dissimilar to the DAPI template, with only a 6.47 % similarity. Taken together this confirms that the PU.1 antibody staining was restricted to the nucleus.

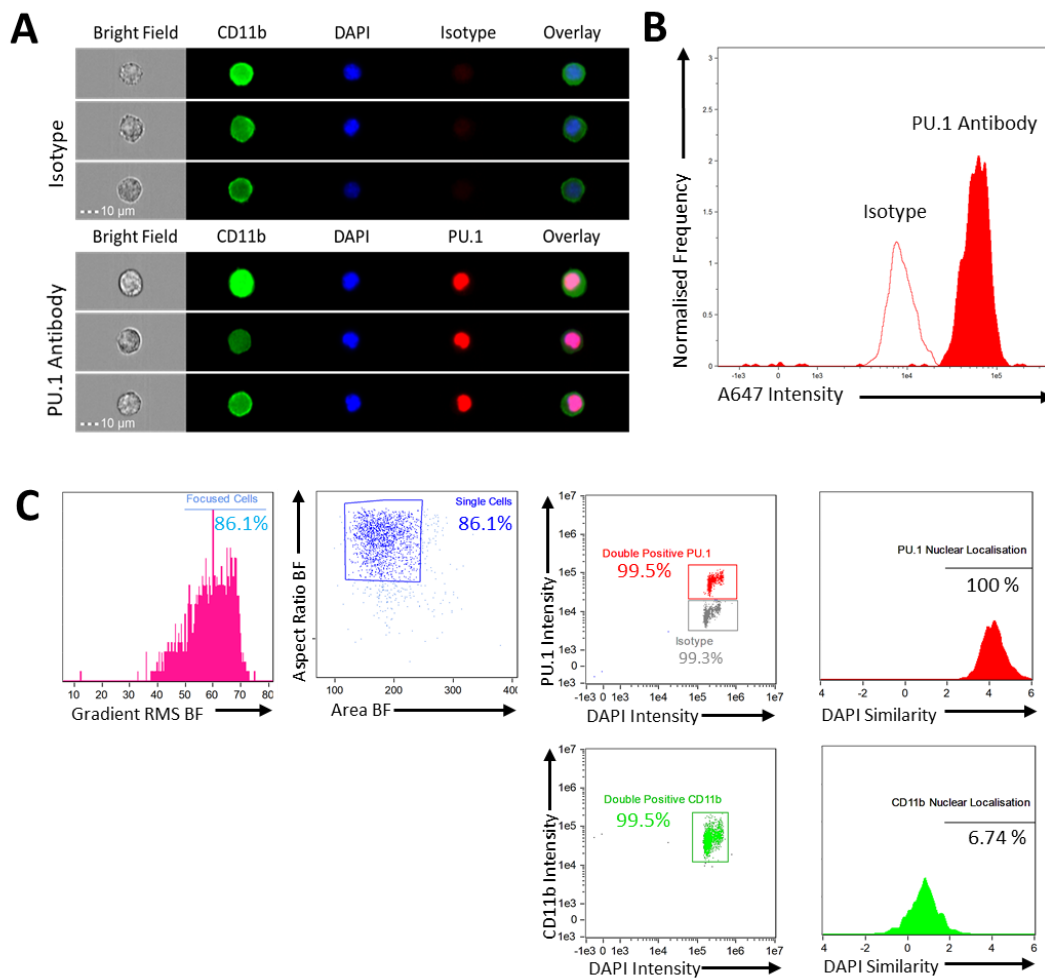


Figure 3.4 Demonstrating PU.1 Antibody Specificity-part I **A** Images from representative RAW cells stained with CD11b (green), DAPI (blue) and either the PU.1 antibody or an isotype control (red). The bottom panel with antibody staining shows that PU.1 staining overlapped with the nuclear marker DAPI (magenta), rather than the CD11b surface stain. **B** Histogram denoting PU.1 staining intensity compared to isotype control. The PU.1 antibody (filled red peak) produces a much higher A647 channel intensity compared to the isotype control (unfilled peak). Therefore in RAW cells PU.1 expression was fairly uniform across the population. **C** PU.1 staining was shown to be highly similar to DAPI when the images are linearly correlated in a nuclear

'masked' region (100 % similar), which was not seen when CD11b staining was compared in the same way. CD11b did not correlate well to DAPI staining (6.74 % similarity). The data used here is the result of one experiment (n=1) though other immunofluorescence experiments in RAW cells have confirmed this localisation (n=2, data not shown).

Antibody specificity was further confirmed by using lentiviruses targeting *Spi1* mRNA or a non-silencing control. In this experiment peritoneal lavage cells (1×10^6 per condition) were infected either with a *Spi1* shRNA pSU6EW (*Spi1* shRNA) or a non-silencing shRNA control pSU6EW virus (NS shRNA) and cultured for 4 days in M-CSF cytokine supplemented media. These cells were harvested and stained for pM \emptyset surface markers and PU.1 and run through the imaging cytometer.

Figure 3.4D showed the method used to gate pM \emptyset (F4/80^{high}MHCII^{low}) cells. The next sets of plots (Figure 3.4E) show the GFP and PU.1 expression following infection with these lentiviruses. Here it was observed that PU.1 expression was reduced in pM \emptyset infected with *Spi1* shRNA pSU6EW virus, as determined by GFP expression. This reduction in PU.1 antibody staining was not observed in the NS shRNA pSU6EW infected cells nor in non-infected (NI) pM \emptyset . Figure 3.4F displays the PU.1 signalling intensity in the infected GFP+ cells. Here PU.1 signalling was reduced in the *Spi1* shRNA (blue) compared to the NS shRNA infected pM \emptyset (grey). Exemplar images shown in Figure 3.4G confirmed that pM \emptyset with a strong GFP expression, meaning a high NS shRNA infection, had a strong PU.1 signal. Exemplar images taken from the *Spi1* shRNA sample the PU.1 expression decreases as the GFP expression increases. This shRNA mediated reduction in PU.1 was comparable to other validation experiments performed with these shRNA viruses which can be found in section 4.2.1. Collectively these results further confirm the PU.1 antibody specificity, showing that the antibody is able to detect PU.1 even after it has been artificially reduced.

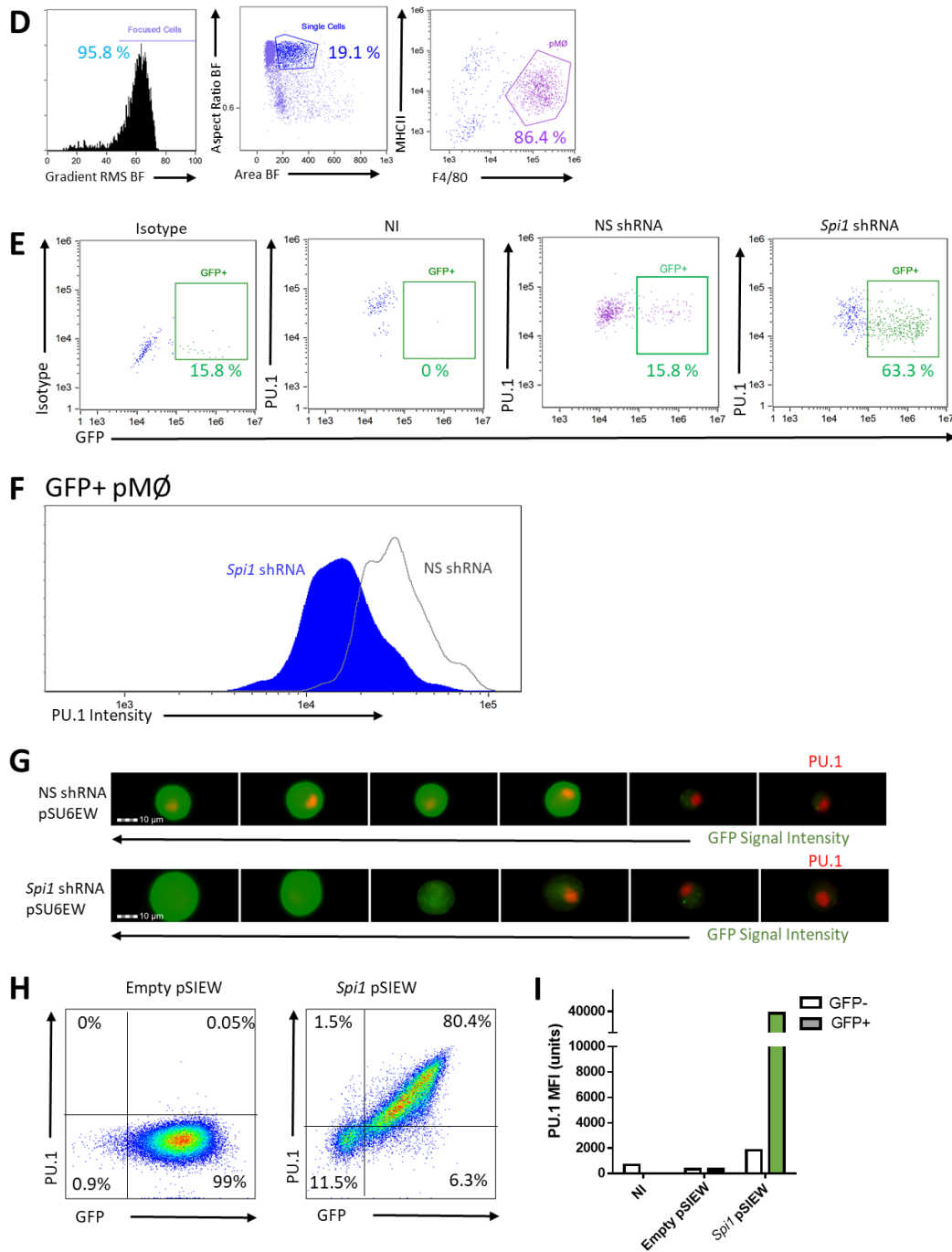


Figure 3.4 Demonstrating PU.1 Antibody Specificity- part II **D** This first set of plots made using the IDEAS® software demonstrates the gating approach taken to identify focused cells, single cells and pMØ (identified as F4/80^{high} MHCII^{low}). pMØ were isolated from 4 female *Spi1*^{tm1.2dgt} mice aged 32 weeks. The cells were cultured with M-CSF and infected with lentiviruses for 4 days before analysis. **E** Plots showing GFP expression, a marker of lentiviral infection, against PU.1 antibody or Isotype staining in the NS shRNA sample.. The pMØ infected with *Spi1* shRNA virus have a lower PU.1 signal than the uninfected cells, this was not seen in the NS shRNA control sample. **F** A histogram comparing PU.1 intensity in both the NS shRNA and *Spi1* shRNA samples. These cells were pre-gated on GFP+ pMØ, using the gate shown in part **D**. Here the PU.1 antibody signal was lower in the PU.1 shRNA infected pMØ compared to the NS shRNA positive pMØ. **G** Selected images from the NS shRNA and *Spi1* shRNA samples, pre-gated on pMØ. The images confirm that PU.1 signal

is detected in highly GFP positive NS shRNA cells (orange indicates overlap) whereas in the *Spi1* shRNA cells PU.1 antibody staining is lost as GFP expression increases. **H** Investigating PU.1 antibody staining in Jurkat cells infected with either an empty vector virus (pSIEW) or the *Spi1* over-expression virus (*Spi1* pSIEW). The plots show GFP signalling intensity against PU.1 antibody staining. **I** Provides a graphical summary of this experiment, showing that the MFI from the PU.1 antibody staining was only increased in Jurkat cells infected with the *Spi1* pSIEW virus. The analyses for this data were either performed using the IDEAS[®] software (**D-G**) or using FlowJo (**H-I**). Both these experiments are n=1 though similar results were obtained from experiments performed on other cell types (as discussed in 4.2.1).

The final evidence supporting the specificity of this PU.1 antibody specificity came from experiments using a *Spi1* over-expressing lentivirus (*Spi1* pSIEW). This virus was used to infect Jurkats which are an immortalised human T-lymphocyte cell line which do not endogenously express PU.1 [329]. Moreover, as the *Spi1* coding sequence inserted into the pSIEW vector was the murine sequence and therefore would not be endogenously expressed in a human cell line. As shown in Figure 3.4H, no PU.1 staining is seen in Jurkats infected with an empty pSIEW virus or in uninfected cells within the *Spi1* pSIEW sample. *Spi1* pSIEW infected Jurkats show an increased PU.1 expression, and those with a higher expression of the GFP reporter have a higher PU.1 signal. When the intensity of this PU.1 antibody staining is plotted on a graph alongside additional controls (Figure 3.4I) it shows that the PU.1 protein is greatly increased in *Spi1* pSIEW infected cells. Therefore, these results confirm that the antibody is specifically detecting murine PU.1 and is sensitive enough to still show PU.1 protein levels even when expression has been exogenously reduced.

3.2.3 *In vitro* Cre induced removal of -14 kb URE in *Spi1*-URE floxed MØP Cell Line

To ensure that the *Spi1*^{tm1.2Dgt}/J (*Spi1*-URE floxed) model was functioning correctly in our facility we began by confirming the removal of the URE using PCR. Genomic DNA was isolated from a conditionally-immortalised *Spi1*-URE floxed MØ precursor (*Spi1*-MØP) cell line generated by retroviral infection of CD117+ macrophage precursor cells from the bone marrow of *Spi1*-URE floxed mice. DNA was also extracted from peritoneal lavages taken from *Spi1*-URE floxed mice bred to either B6J.B6N(Cg)-Cx3cr1^{tm1.1(cre)Jung}/J (*Spi1*-CONST) or B6.129P2(C)-Cx3cr1^{tm2.1(cre/ERT2)Jung}/J (*Spi1*-ERT). Together these samples provided the full range of Cre recombinase states, from not present (*Spi1*-MØP cells), to tamoxifen-inducible (*Spi1*-ERT) or constitutively-active (*Spi1*-CONST).

Figure 3.5A graphically represents the where the primers bind in the PCR reaction that was designed to detect URE removal following loxP recombination. As described in section 2.3.1 primers 1 and 3 can only form the larger band when the URE has been removed. This was used in conjunction with the genotyping PCR (section 2.3) that detects the mutant form of the *Spi1* URE. These PCRs confirmed that the URE was only removed in cells where the Cre is active (*Spi1*-CONST)

and is not found in any of the other samples, which had formed the smaller PCR band formed by primers 1 and 2. These results show that on the genomic level the URE is removed in the presence of an active Cre in the Spi1-CONST mice.

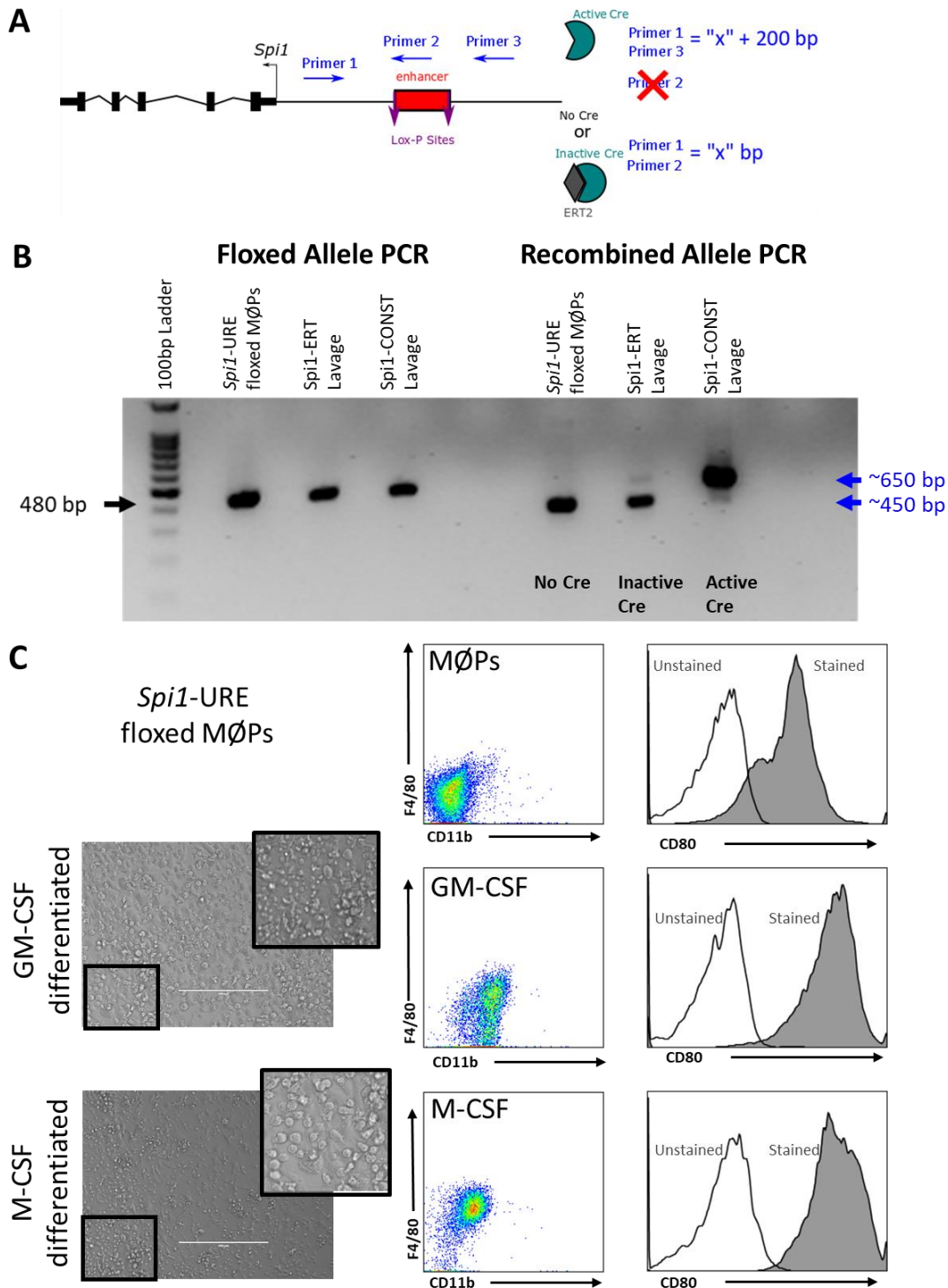


Figure 3.5 Initial validation of the *Spi1-URE* floxed model. **A** Schematic diagram showing the approximate binding sites of the three primers used to determine if the Cre-LoxP recombination event has occurred in the

URE. The larger ("x" + 200 bp) band that forms between primers 1 and 3 can only form if URE has been lost following recombination of the LoxP sites. **B** PCR confirming Cre-mediated removal of the URE the first lane contains the Promega 100 bp ladder. The DNA used in this analysis was obtained from the Spi1-URE floxed MØP cell line, a Spi1-ERT DM or a Spi1-CONST DM peritoneal lavage. The left-hand side of the gel shows the bands produced by the primers used to genotype the Spi1-URE floxed mice (see 2.3). The right-hand side of the gel used primers developed to genotype the URE KO Spi1^{tm1.3Dgt}/J mice. As mentioned in section 2.3.1 the larger band was ~650bp and only present in the Spi1-CONST lavage genomic DNA. The other samples which either had no Cre (Spi1-URE floxed MØPs) or an inactive Cre (Spi1-ERT lavage DNA) had the lower DNA band ("x") which was ~450 bp and associated with an intact URE. This PCR experiment was performed twice (n=2) using the same samples. **C** Basic characterisation of Spi1-URE floxed MØP cell line. The first column shows brightfield images of these cells following 4 days of differentiation with either GM-CSF or M-CSF. These images were taken using the EVOS using the 20X magnification lens. The data shown here is representative of two independent experiments (n=2).

Figure 3.5C also shows the basic phenotyping of the Spi1-MØP cell line. The microscope images show that the morphology of the cells following differentiation with either GM-CSF or M-CSF was as expected. Moreover, expression of several key marker such as CD11b, F4/80 and CD80 were measured using flow cytometry. As previously published by Rosas *et al.* (2011) CD11b, CD80 and F4/80 expression increased following cell differentiation compared to unstained controls [304]. This work suggested that the phenotype of the Spi1-URE MØP cell line follows established work.

The *in vitro* removal of the Spi1-URE was achieved using a combination of the bone-marrow derived MØ (BMDM) or M-CSF differentiated MØPs and a custom Cre-pSFEW lentivirus vector, using the plasmids described in section 2.11.3. In short, the Cre and GFP are expressed under the same promoter expression separated by a T2A sequence that induces ribosomal skipping thus the levels of both proteins should resemble each other in an infected cell.

Figure 3.6A and Figure 3.6B display the initial titrations of this Cre pSFEW and confirm that the GFP virus reporter increases in a dose dependent manner for both viruses. As colony 10 produced higher infection rates the colony 10 Cre pSFEW plasmid was exclusively used for virus production and will henceforth be referred to as Cre pSFEW. At lower titres (<5 µL) the empty vector pSFEW virus is more effective than the Cre pSFEW virus which is not unexpected due to the additional effort required to produce Cre recombinase in addition to the GFP reporter. These difference in viral effectiveness can be lessened by using an excessive dose, as shown when Jurkats are given 10 µL of virus.

Co-expression of the Cre recombinase enzyme (Cre) was confirmed using a reducing western blot in RAW cells that were sorted on GFP expression to ensure a pure infected population. Figure 3.6C confirms that Cre protein is only expressed in RAW cells infected with the Cre pSFEW virus, and not in either the pSFEW or non-infected (NI) RAW cells. While the the anti-Cre plot produced several bands this could be due to an ineffective T2A ribosomal skipping, meaning that the Cre and

GFP were produced as one larger protein, or these bands the result of other modifications. The right-hand western blots shows that GFP was detected in both the pSFEW and Cre pSFEW infected samples but not in NI cells. The GFP blot did suggest that the ribosomal skipping, resulting in a separate Cre and GFP, was not completely efficient as there were some higher bands that were only present in the Cre pSFEW sample.

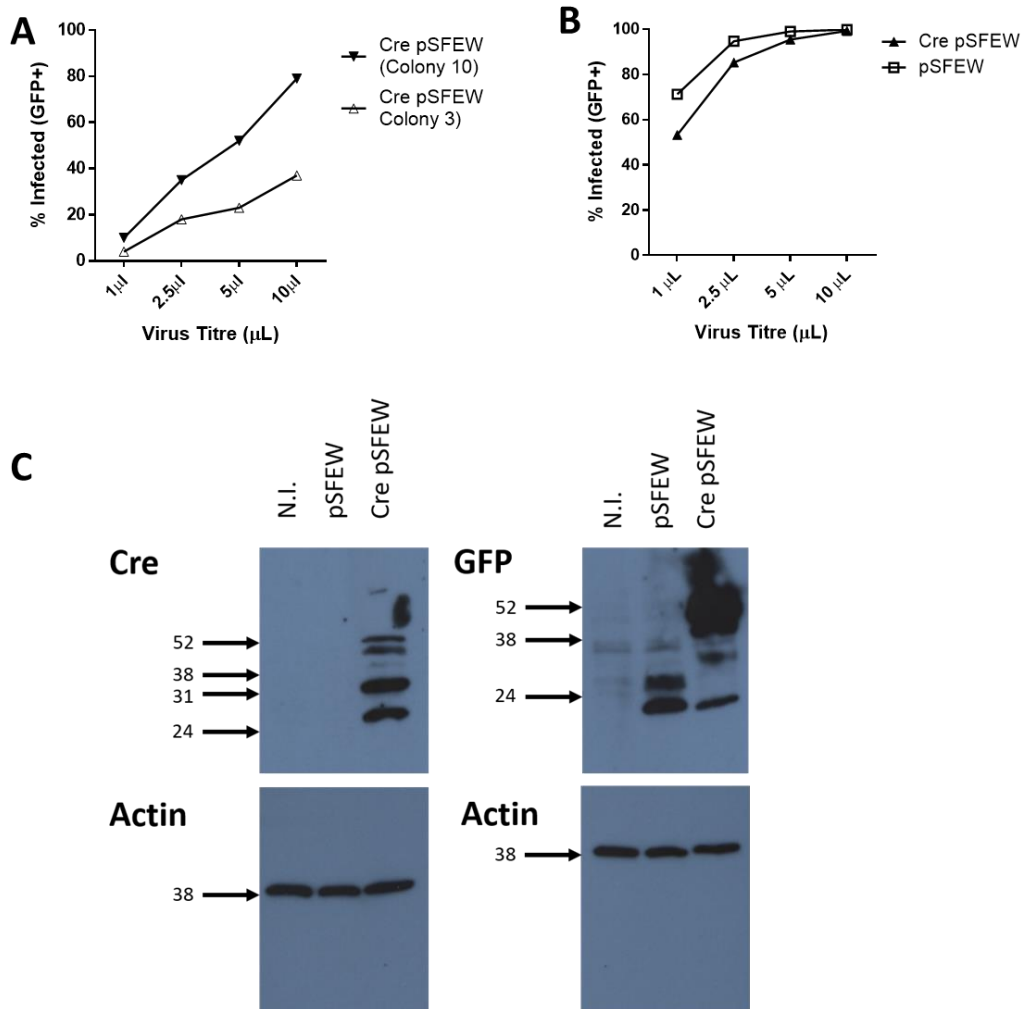
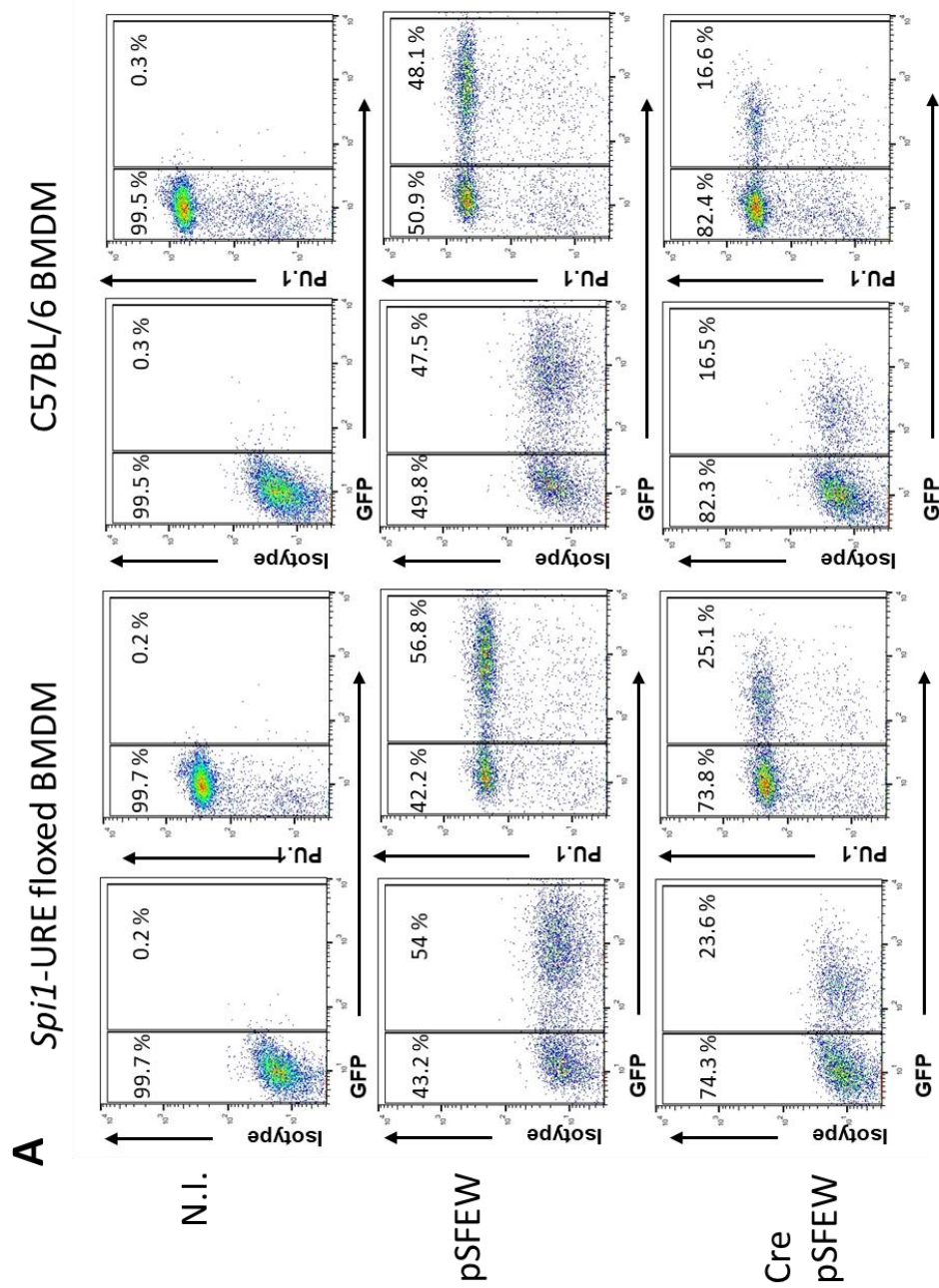


Figure 3.6 Experiments authenticating the function of Cre pSFEW virus. **A** Jurkat viral titrations of two Cre pSFEW plasmids grown from separate colonies, as described in section 2.12.4.. **B** A similar viral titration experiment was used to compare the effectiveness of Cre pSFEW to pSFEW. **C** Confirming that both Cre recombinase (Cre) and GFP are produced separately in RAW cells that were either uninfected or infected with either the pSFEW virus or Cre pSFEW virus. These RAW cells were sorted following viral infection so that only GFP+ cells were used in these western blots. The left-hand blots show the results of anti-Cre staining (top, predicted molecular weight 38 kDa). The lower plot shows actin antibody staining performed to confirm loading. The two right-hand blots show the results of the blot detecting GFP, expected band 27 kDa, including the actin control. The data presented **A** and **B** were representative of two (n=2) and five (n=5) experiments respectively. The blots shown in part **C** are from one experiment (n=1) though similar observations were made in infected Jurkat cells (data not shown).

Having confirmed the function of the Cre-pSFEW virus, it was then used to infect 1×10^6 BMDMs differentiated from either *Spi1*-URE floxed or C57BL/6 wild-type mice. Non-infected and empty vector virus (pSFEW) were used as additional controls. BMDM were harvested 7 days after infection and processed for flow cytometric analysis. Figure 3.7 shows that, as predicted, PU.1 protein levels were not different between the uninfected and infected (GFP+) cells in the pSFEW and Cre pSFEW WT BMDM. The *Spi1*-URE floxed BMDM did not have a reduction in PU.1 expression, compared to either the NI BMDM or the control pSFEW virus infected BMDM. Surprisingly, it appeared that Cre pSFEW viral infection did not impact PU.1 protein levels in *Spi1*-URE floxed BMDM. This was unexpected as previously published work showed that Cre-mediated loss of the URE resulted in a reduction in PU.1 protein in the total bone-marrow of mice [260].

Figure 3.7 In Vitro experiments with Cre pSFEW virus in Spi1-URE floxed BMDM or M-CSF differentiated MØPs- Part I
A The flow plots show PU.1 and GFP expression in BMDM infected with pSFEW or Cre pSFEW. These plots show that PU.1 expression is not reduced in GFP+ BMDM infected with Cre pSFEW in either the Spi1-URE floxed BMDM or in C57BL/6 control mice. In every sample the infection of the BMDM (inferred from GFP expression) did not affect the PU.1 staining when compared to the non-infected cells in each



As summarised in Figure 3.7B below, the expression of PU.1 did not appear to be changed in the *Spi1*-URE floxed BMDM infected with the control virus (pSFEW, lined grey bars) or the Cre pSFEW virus (lined blue bars). It is likely that the slight reduction compared to the non-infected sample (white) is likely because of the effect lentiviral infection has on BMDM. In the WT BMDM samples PU.1 expression is not altered in the infected cells when compared to the uninfected within their respective samples, though there is variation between each condition.

Cre expression in both BMDM genotypes infected with Cre pSFEW virus was also confirmed using flow cytometry (Figure 3.7C). In both the *Spi1*-URE and WT BMDM Cre expression appeared to be equally robust (blue bars). The findings of this BMDM experiment were replicated in several experiments performed in M-CSF differentiated MØP cells which have been shown to be phenotypically like BMDM (n=3; Figure 3.7D). These MØP cells were differentiated with M-CSF and used another version of the Cre fusion plasmid where a truncated form of rat CD2 replaces the GFP reporter (Cre pSFRW). In these experiments PU.1 expression, as determined by the CST PU.1 antibody, in M-CSF MØP cells was normalised by removing the isotype background then dividing by the MFI of the uninfected cells within each sample. Again, no clear changes were seen in PU.1 expression in *Spi1*-URE floxed M-CSF differentiate MØPs infected with Cre pSFRW or an empty pSFRW control virus.

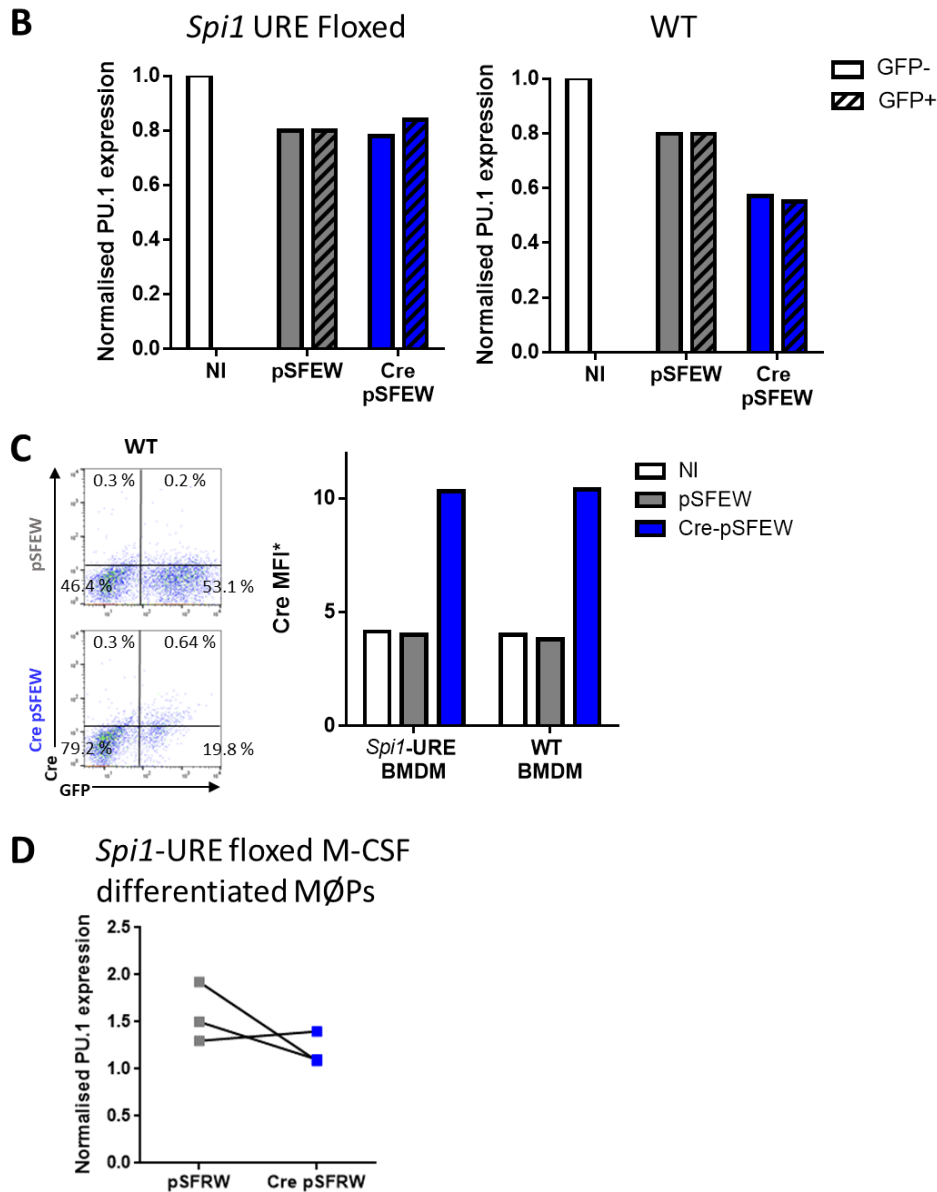


Figure 3.7 In Vitro experiments with Cre pSFEW virus in *Spi1*-URE floxed BMDM or M-CSF differentiated MØPs- Part II **B** Graphs showing the normalised PU.1 expression in *Spi1*-URE floxed BMDM infected with pSFEW (grey) or Cre pSFEW (blue). Here the PU.1 protein expression was normalised to the non-infected BMDM sample for each genotype. **C** Detection of Cre recombinase protein via flow cytometry. The flow plots show that Cre could be measured in WT cells infected with Cre pSFEW compared to pSFEW infected cells. When represented graphically a moderate amount of Cre protein was detected in both the *Spi1*-URE and WT BMDM. **D** A summary of preliminary experiments in M-CSF differentiated MØP cells. The BMDM data shown here was only repeated once (n=1) but similar results were observed in the *Spi1*-URE floxed M-CSF differentiated MØPs (n=3).

Given the unanticipated lack of a change in PU.1 expression there were concerns that the Cre recombinase was expressed but not functioning correctly. To ensure the Cre expressed from the pSFEW plasmid was able to translocate to the nucleus of the cells and recombine the loxP sites the Cre pSFEW virus was tested in a previously published *Gata6*^{tm2.1Sad}/J mouse model [151].

The presence of Cre in the peritoneal cavity of these mice removes the tissue specific transcription factor *Gata6*. This *Gata6* knock-out results in several phenotypic changes to the pMØ population including a reduced F4/80 expression, which was used to assess the functionality of the Cre recombinase. Three *Gata6*^{tm2.1Sad}/J mice received an intraperitoneal injection of either pSFEW or Cre pSFEW lentivirus. One week after injection these mice were sacrificed and lavaged to retrieve the pMØ cells. These peritoneal lavage cells were then stained for F4/80 and Tim4, another pMØ surface marker, and analysed using flow cytometry. Figure 3.8A (left) shows no difference was observed in F4/80 staining between cells infected with control pSFEW (green) compared to non-infected cells from the same sample (black outline). *Gata6*^{tm2.1Sad}/J mice who received an injection of Cre pSFEW (Figure 3.8A, right) the infected cells (green) had a reduced F4/80 expression compared to non-infected cells (outline). The percentage F4/80 knock-down was calculated using the method described in section 2.16.2.1. The percentage reduction of F4/80 expression was higher pMØ infected with Cre pSFEW compared to those infected with control pSFEW (Figure 3.8B). The percentage Cre expression was also confirmed in those pMØ infected with Cre pSFEW (Figure 3.8C).

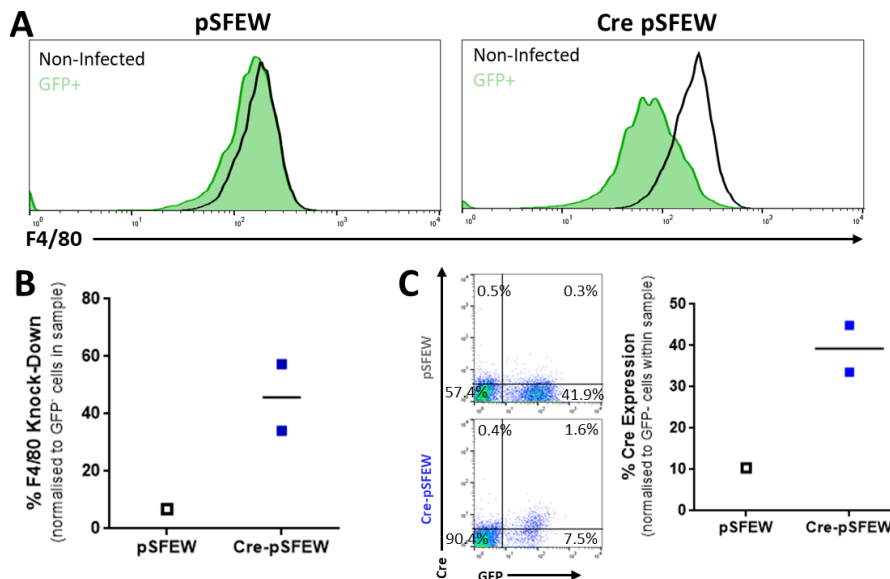


Figure 3.8 Confirming the Cre pSFEW virus is functional in vivo using a published model. One *Gata6*^{tm2.1Sad}/J male mouse aged 8 weeks received an injection of pSFEW virus and two mice received Cre pSFEW injections. One week later pMØ were harvested and stained for flow cytometric analysis. Cre mediated *Gata-6* removal in the peritoneal cavity results in a reduced F4/80 expression on pMØ. **A** These exemplar flow plots show that no reduction of F4/80 was detectable in pMØ infected with pSFEW virus (Green) when compared to uninfected cells within the sample (black outline). **B** Graphical summary of the % F4/80 knock-down (normalised to GFP+ cells within the sample) from virally injected *Gata6*^{tm2.1Sad}/J mice. F4/80 expression was reduced in mice infected with Cre-pSFEW **C** Percentage Cre protein expression (normalised to GFP- cells within the sample). Following intra-nuclear staining for Cre recombinase, can see that Cre was present in Cre pSFEW

GFP+ cells only from flow plots (left) and graph (right). The results shown here represent one experiment ($n=1$) containing three mice total and replicate the findings of previously published work [151]. The horizontal bar denotes the mean and the error bars show the standard deviation.

These findings corroborate the previously reported observations by Rosas *et al.* [151] and suggest that the Cre pSFEW virus is functioning correctly. It was therefore surprising that no reduction in PU.1 expression was noted when Spi1-URE floxed cells were treated with Cre pSFEW. The next section moves onto describe the changes seen *in vivo* when *Spi1*-URE floxed mice were bred to multiple transgenic lines expressing Cre.

3.2.4 PU.1 expression in transgenic mice

As discussed in section 1.5.3 *Spi1* URE floxed mice were bred to mice where Cre recombinase was expressed under the *Cx3cr1* promoter. There were two *Cx3cr1*-Cre mouse lines used in this chapter, previously described in 1.5.3. The first expressed an active Cre (*Cx3cr1*-Cre^{CONST}) and the other a tamoxifen-inducible Cre (*Cx3cr1*-Cre^{ERT}). Henceforth these mice shall be referred to as Spi1-ERT for the conditional Cre and Spi1-CONST for mice with an active Cre.

3.2.4.1 Double-Heterozygous *Spi1*-ERT and *Spi1*-CONST Mice

Previously published work has shown PU.1 expression was reduced by 80 % in bone marrow of mice lacking the *Spi1* URE [260]. Initially this experimental model assessed the impact on PU.1 expression in double-heterozygous (DH) mice, which had one *Spi1*-URE Floxed allele and one Cre. These mice were referred to as Spi1-ERT DH and Spi1-CONST DH.

Given this information a reduction of <40 % of PU.1 expression was estimated in the presence of an active Cre, as mice would have wild-type *Spi1*-URE site. However this was not expected to be direct relationship, as there may be other intrinsic mechanisms that act with the URE expression to compensate for this partial loss. Therefore the reduction in PU.1 was not expected to be more than 40 % in Spi1-CONST DH mice compared to Spi1-ERT DH mice. In this thesis all Spi1-ERT mice were not treated with tamoxifen as they were used as controls to account for any variation in results caused by the background of the transgenic strains.

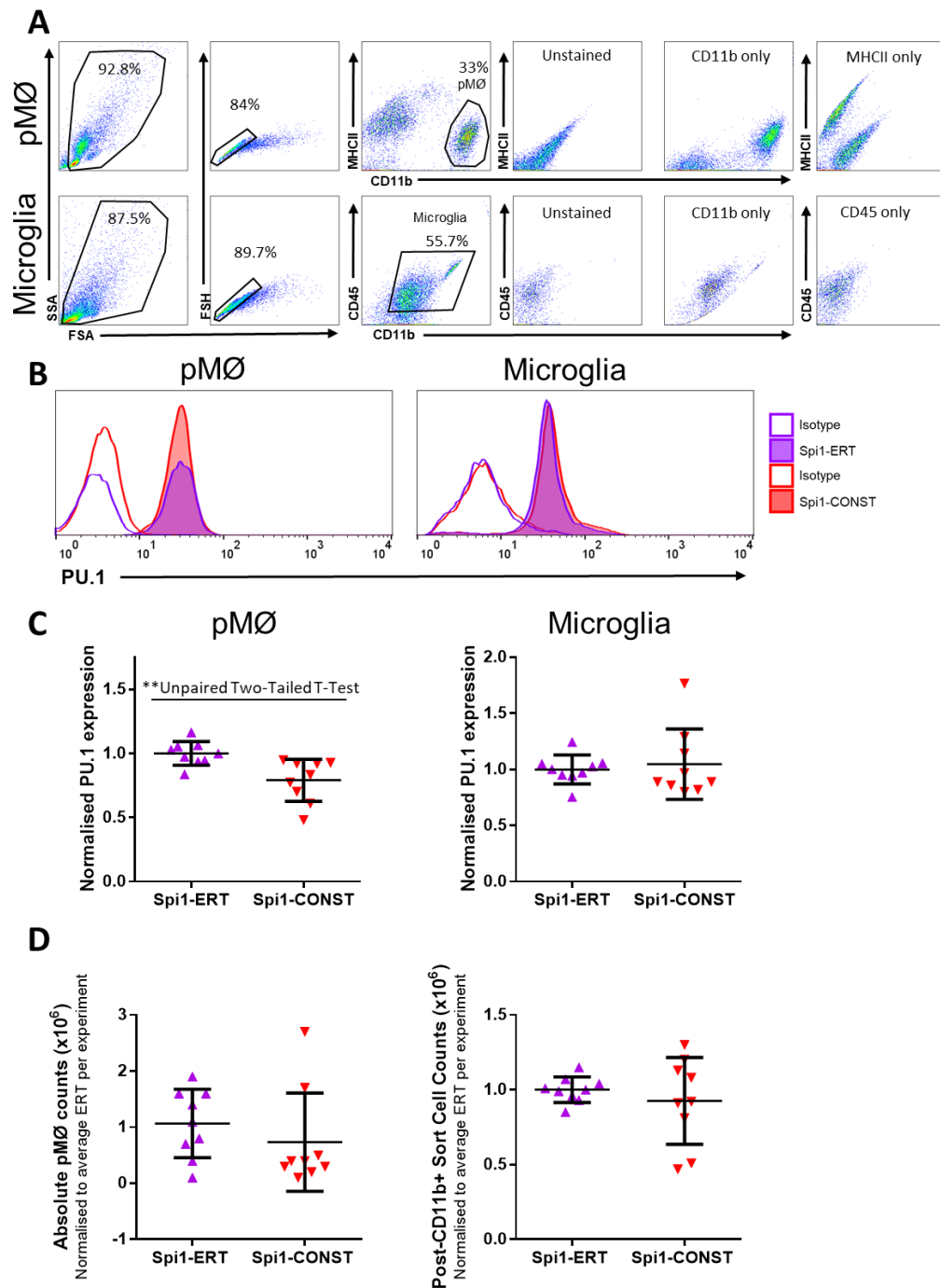


Figure 3.9 Determining PU.1 expression in Spi1-ERT and Spi1-CONST Heterozygous Mice. The mice in each experiment were matched as closely as possible by age (range 5-19 weeks) and gender (Spi1-CONST- 5 males and 4 females and Spi1-ERT- 3 males and 6 females). A total of 9 mice were assessed for each genotype. **A** Gating approach used in flow cytometric analyses to determine PU.1 protein expression in pMØ and microglia, including unstained and single stained controls. Debris and doublets were removed, pMØ were selected as CD11b^{high}MHCII^{low}. Microglia were selected on CD11b⁺ CD45^{ow}, though microglia CD11b expression was lower due to bead purification. **B** Example histograms of PU.1 staining in pMØ and Microglia. Isotype controls (outlines) are shown next to PU.1 stained cells (filled). **C** PU.1 expression was normalised to the average MFI values from the Spi1-ERT mice pMØ or microglia from each experiment. In pMØ samples

there was a significant reduction in PU.1 expression in the *Spi1*-CONST DH mice (Unpaired Two-Tailed T-Test, $**P=0.0043$). There was no significant difference between the PU.1 expression microglia (Unpaired Two-Tailed T-Test, $P=0.6801$). **D** Absolute counts in DH mice. There was no difference found in ERT normalised cell counts in pM \emptyset or in the cell counts of brains after CD11b+ bead selection (Microglia) between both genotypes (Unpaired Two-Tailed T-Test, $P=0.3624$ and $P=0.4714$ respectively). The results shown here are the results of 5 independent experiments ($n=5$). The means are denoted by the horizontal line and the error bars show the standard deviation.

To enable an accurate comparison equal numbers of *Spi1*-CONST and *Spi1*-ERT mice were matched as closely as possible for age/sex and processed in parallel. Figure 3.9A provides an example of the gating strategy used to select pM \emptyset (top) and microglia (bottom) populations before measuring PU.1 expression. A combination of CD11b and CD45 or MHCII surface stains were used to identify both trM \emptyset populations the single stain controls for both are also shown in Figure 3.9A.

The results obtained from the preliminary analyses of PU.1 expression in DH mice suggest that there is no difference between the *Spi1*-ERT (purple) and *Spi1*-CONST (red) genotypes (Figure 3.9B). Figure 3.9C shows the normalised PU.1 expression of all 5 independent experiments calculated as described in 2.16.2.2. pM \emptyset had a significantly lower level of PU.1 protein in *Spi1*-CONST mice compared to *Spi1*-ERT mice, determined by an Unpaired Two-Tailed T-Test ($P=0.004$). Conversely no significant reduction in PU.1 protein was seen in the target microglia population between DH *Spi1*-ERT and *Spi1*-CONST mice (Unpaired Two-Tailed T-Test $P=0.68$).

The absolute pM \emptyset counts and post-CD11b+ selection cell counts, set out in Figure 3.9D, suggested there were no meaningful differences in the number of pM \emptyset or microglia between the two DH genotypes (Unpaired Two-Tailed T-Test, $P=0.362$ and $P=0.471$ respectively). In summary, the reduction in PU.1 expression observed in the pM \emptyset was ~24 % lower in *Spi1*-CONST DH mice compared to *Spi1*-ERT pM \emptyset . The results of these experiments suggest that URE removal does not reduce the amount of PU.1 protein in microglia. However as one copy of the wild-type *Spi1*-URE was present in these mice it was not possible to yet conclude the success of this model.

3.2.4.2 Double-Mutant Mice

The impact of both *Spi1*-URE sites being removed double mutant (DM) mice, where both *Spi1*-URE sites were floxed and both *Cx3cr1* sites express Cre. The histograms below (Figure 3.10A) show that in DM mice PU.1 expression did not appear to largely differ between *Spi1*-ERT or *Spi1*-CONST mice in either the pM \emptyset or in microglia.

Figure 3.10B shows the normalised PU.1 expression in all samples across both genotypes determined from all 13 independent biological replicates. Again, PU.1 expression was not

significantly reduced in the pMØ of Spi1-CONST mice compared to Spi1-ERT mice (Unpaired Two-Tailed T-Test, $P=0.8682$). No significant reduction in PU.1 expression was found in the Spi1-CONST microglia compared to the Spi1-ERT control microglia (Unpaired Two-Tailed T-Test, $P=0.2479$).

The results of the absolute cell counts are set out in Figure 3.10C and did not differ between the genotypes in either the pMØ or microglia (Unpaired Two-Tailed T-Tests $P=0.2899$ and $P=0.1879$ respectively).. There was some variation in cell counts between the experiments, though this was likely due to the age range across the cohort (3-14 weeks). Taken together these results suggest that *Spi1*-URE removal in the *Cx3cr1* expressing pMØ and microglia does not appear to reduce PU.1 expression.

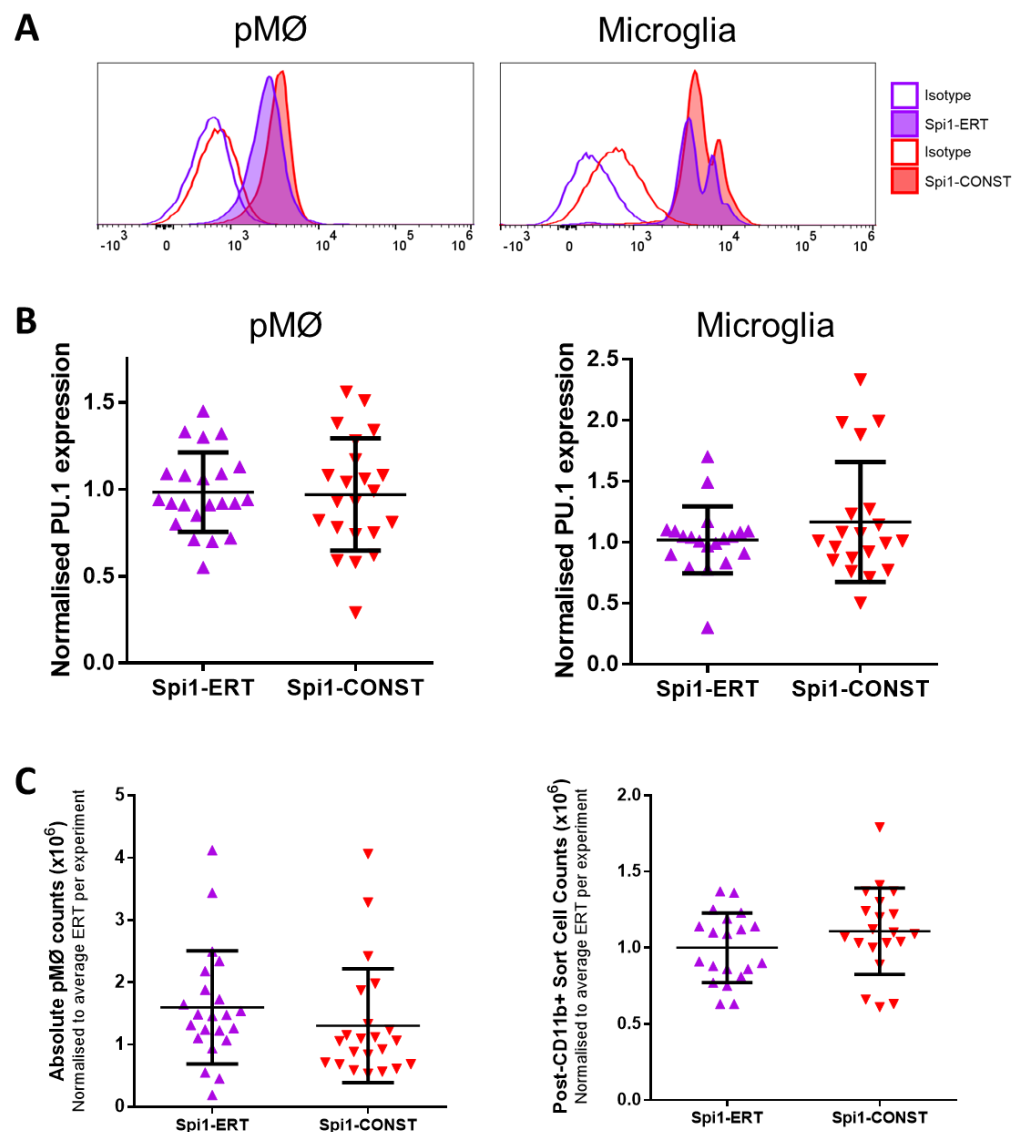


Figure 3.10 Determining PU.1 expression in Spi1-ERT and Spi1-CONST Mutant Mice- Part I In all experiments mice were matched according to age (ranging from 3-14 weeks) and gender (Spi1-CONST- 9 males and 12 females, Spi1-ERT- 9 males and 12 females). **A** Representative histograms showing PU.1 expression in pM \emptyset and Microglia. Here PU.1 expression does not appear to differ between Spi1-ERT and Spi1-CONST mice. **B** PU.1 expression in all Double-Mutant (DM) Mice Sampled. Normalised expression was calculated as previously described (section 2.16.2.1). In these pM \emptyset samples PU.1 expression did not differ between the Spi1-ERT or Spi1-CONST genotypes (Unpaired Two-Tailed T-Test, $P=0.8682$). There was also no observed difference between genotypes in the microglia samples (Unpaired Two-Tailed T-Test, $P=0.2479$). **C** Absolute pM \emptyset cell counts and Post-CD11b+ selection (microglia) cell counts in DM mice. No significance difference was seen between Spi1-ERT and Spi1-CONST mice in either tissue resident M \emptyset population. The statistical results of an Unpaired Two-Tailed T-Test were as follows in pM \emptyset ($P=0.2899$) and in microglia ($P=0.1879$). The results presented here are the cumulation of 11 separate experiments ($n=11$). The means are shown by the horizontal line alongside the standard deviation error bars.

3.2.5 Troubleshooting in the URE KO Model

Several steps were taken to try and elucidate why PU.1 protein was not being reduced in pM \emptyset and microglia following removal of the URE. The URE removal had been previously confirmed by PCR (Figure 3.5). The following section will focus on the experiments that suggest this URE may not be as important in trM \emptyset subsets.

3.2.5.1 Confirming Cre activity in Cx3cr1-Cre^{CONST} mice

Cre activity was confirmed in the microglia of these Cx3cr1-Cre^{CONST} mice by breeding them to the B6J.129(B6N)-Gt(ROSA)26Sor^{tm1(CAG-cas9*,-EGFP)Fezh}/J mouse strain (Cas9), commonly known as the CRISPR-Cas9 strain [330]. These mice were chosen as they produce Cas9 and a GFP reporter in the presence of an active Cre [330]. Therefore, it was expected that if Cre in the Cx3cr1-Cre^{CONST} mice functioned correctly then microglia from the Cas9-Cre^{CONST} strain should express GFP expression. Spi1-ERT mice were used as a background control for M \emptyset auto-fluorescence. Following brain digestion and myelin removal the cells were stained for M \emptyset markers CD11b and CD45 in addition to a LIVE/DEAD™ stain. The gating used to analyse the microglia is displayed in Figure 3.11A.

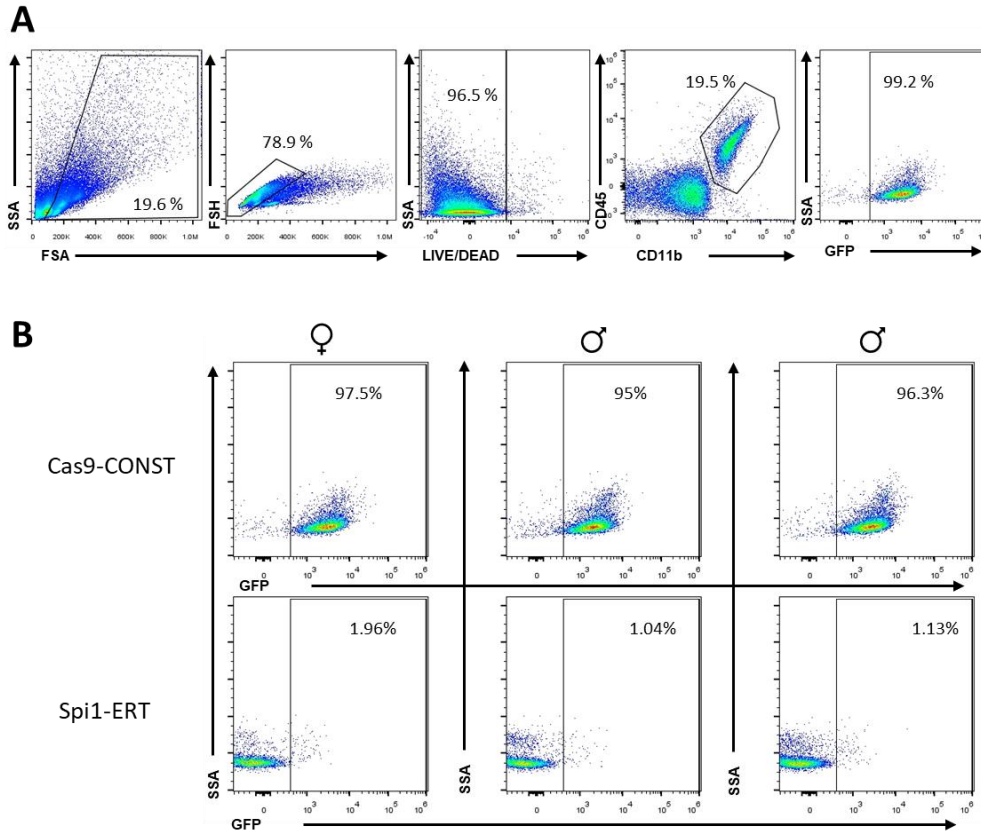


Figure 3.11 Confirmation of Cre function in *Cx3cr1-Cre^{CONST}* Mice. *Cx3cr1-Cre^{CONST}* mice were bred to *B6J.129(B6N)-Gt(ROSA)26Sor^{tm1(CAG-cas9*,-EGFP)Fezh/J}* mice, ensuring that a GFP reporter was expressed when Cre was expressed. All mice used here were aged 13 weeks, and each group contained 1 female and 2 male mice. **A** Gating strategy used in flow cytometric analysis. Once debris was removed from the sample, single cells were selected. Of these single cells the live cells were taken further. Cell viability in these samples were all over 97% (data not shown). Microglia were then gated as *CD11b⁺CD45^{low}*, before GFP expression was observed. **B** GFP Expression in *Cas9-CONST* and *Spi1-ERT* samples. The top panel shows the GFP expression in microglia cells in female (*n*=1) and male (*n*=2) mice. In comparison to the *Spi1-ERT* control mice (bottom panel) the GFP expression was clearly detectable in all *Cas9-CONST* samples, and was over 95 % of all microglia (*CD11b⁺CD45⁺*) were GFP+. The data presented here was gathered from one independent experiment (*n*=1).

The data collected from *Cas9-CONST* mice confirms that there is a strong GFP expression in microglia (Figure 3.11) and as expected, there was no GFP expression in the *Spi1-ERT* control mice. Thus, it was concluded that Cre is active in the microglia of *Cx3cr1-Cre^{CONST}* mice. As discussed in the next section there was potential issue with the *Spi1-ERT* mice that meant they may not provide an accurate baseline expression of PU.1 in microglia.

3.2.5.2 Confirming *Spi1-ERT* mice as suitable controls

Recently the Cre-activation of the *Cx3cr1-Cre^{ERT}* mice in absence of tamoxifen has been questioned following observations that *Cre^{ERT}* was active even when tamoxifen was not present in the brain [331]. In this report *Cx3cr1-Cre^{ERT}* mice saw a tamoxifen-independent Cre activation in microglia in

mice from 4 weeks, supposedly due to the high microglial Cx3cr1. As the Spi1-ERT mice used to give a baseline PU.1 expression were older 4 weeks it was possible that they had an active Cre. Hence a Cre mediated reduction to PU.1 protein levels may be present in both the Spi1-ERT and Spi1-CONST mice, which could explain the similarity in PU.1 expression between the two genotypes.

To ensure this was not the case PU.1 protein was measured in Spi1 mutant mice, Cx3cr1-Cre^{CONST} and C57BL/6J mice. The results of these comparisons can be viewed in Figure 3.12.

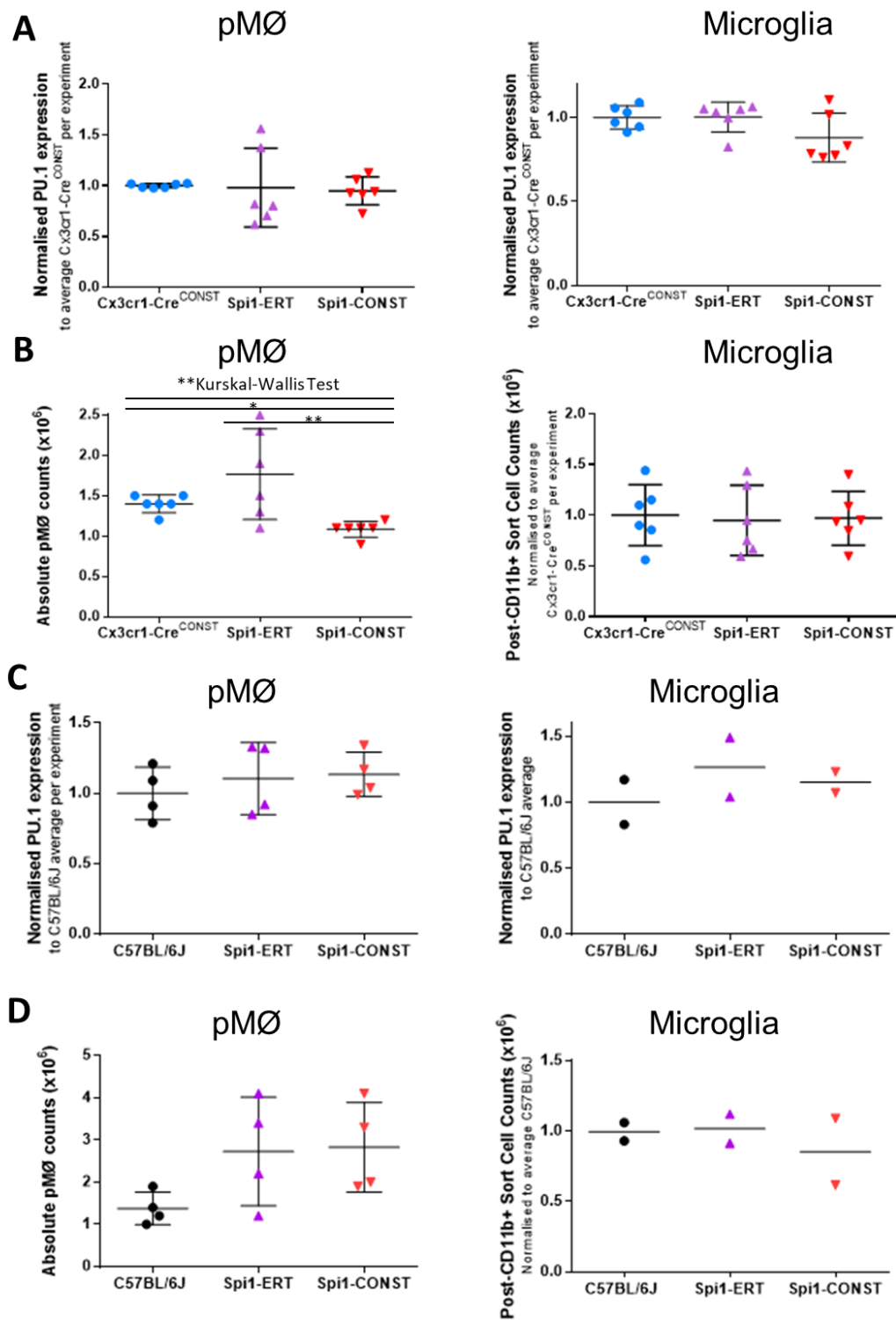


Figure 3.12 PU.1 Expression in DM mice compared to Cx3cr1-Cre^{CONST} and C57BL/6J mice. All mice were used in these experiments were female and aged 10-14 weeks. **A** Normalised PU.1 expression suggests the lack of change in PU.1 was not due to a 'leaky' Cre in Spi1-ERT Mice. In pMØ there was no significant difference in PU.1 expression across all three genotypes (Kruskal-Wallis Test, $P=0.5118$). No difference in PU.1 expression was observed in Microglia across any genotype. (One-way ANOVA, $P=0.1045$). **B** Absolute pMØ cell counts and normalised post-CD11b+ sort cell counts. There was a difference in the pMØ counts

across all three genotypes (Kruskal-Wallis Test, $P=0.0032$), the difference between the *Spi1*-ERT mice and *Spi1*-CONST mice were different (Dunn's Multiple Comparison $P\leq 0.01$ as were the *Cx3cr1*-CreCONST and *Spi1*-CONST mice pMØ number (Dunn's Multiple Comparison $P\leq 0.05$). The microglia counts were not significantly different between the genotypes (One Way ANOVA $P=0.9571$). The data presented here resulted from 3 independent experiments ($n=3$). The mice were again matched by age (range 7-14 weeks) and gender (4 male and 2 female per group). **C** pMØ and microglial PU.1 expression was compared between C57BL/6J mice (black), *Spi1*-ERT mice (purple) and *Spi1*-CONST mice (red). There were no meaningful changes in PU.1 protein levels across all three genotypes in either pMØ (One-Way ANOVA, $P=0.6315$) nor microglia. **D** The absolute pMØ counts in the C57BL/6J mice were not significantly different from either *Spi1* mutant mouse strain (One-Way ANOVA, $P=0.1215$) and no difference was seen in the microglia counts. There was a technical issue prevented experiment from being repeated a second time in microglia, while $n=2$ experiments in pMØ. The mean is indicated by a horizontal line and the standard deviation is denoted by the error bars. *denotes a P-Value of ≤ 0.05 and ** ≤ 0.01 .

Figure 3.12A shows there were no changes to the PU.1 expression between pMØ harvested from the *Cx3cr1*-Cre^{CONST} mice compared to either *Spi1* mutant strain (Kruskal-Wallis Test, $P=0.5118$). The microglia PU.1 expression was also similar across all genotypes (One-way ANOVA, $P=0.1045$). The absolute pMØ cell number did slightly differ between the assessed genotypes as shown in Figure 3.12B (Kruskal-Wallis Test, $P=0.0032$), though the variation in the *Spi1*-ERT counts suggest this 'increase' might be lost if the experiment was repeated (Figure 3.10). The number of microglia did not differ between the *Cx3cr1*-Cre^{CONST} mice and *Spi1* mutant mice (One Way ANOVA $P=0.9571$). The *Spi1* mutant mice were also compared to C57BL/6J mice. Again no meaningful differences were seen in the PU.1 protein levels in either the pMØ (One-Way ANOVA, $P=0.6315$) or the microglia between the genotypes (Figure 3.12C). The trMØ cell counts did not differ between the C57BL/6J mice and the *Spi1* mutants (Figure 3.12D), pMØ (One-Way ANOVA, $P=0.1215$). The average cell counts for the pMØ and microglia in all of the PU.1 comparison experiments are shown in Table 3.2 below.

As PU.1 expression measured in *Cx3cr1*-Cre^{CONST} mice (blue) very closely resembled expression seen in microglia of *Spi1*-ERT mice (purple), suggesting that even if the Cre is 'leaky' in the *Spi1*-ERT mice PU.1 expression was unaffected. Together these experiments indicate that PU.1 pMØ/microglia expression was not altered in the *Spi1*-CONST or *Spi1*-ERT mice compared to strains with a wild-type *Spi1* URE (*Cx3cr1*-Cre^{CONST} and C57BL/6J mice).

C57BL/6J Comparison	Post-CD11b+ Cell Counts (Microglia)			
	Genotype	Mean Count (1x10 ⁶)	n	
	Spi1-ERT	1.00	2	
	Spi1-CONST	0.85	2	
C57BL/6J	0.99	2		
Peritoneal Lavage Cell Counts				
Genotype	Mean Count (1x10 ⁶)	Standard Deviation	n	
Spi1-ERT	3.43	1.60	4	
Spi1-CONST	4.04	1.74	4	
C57BL/6J	1.84	0.56	4	

Cx3cr1-Cre ^{CONST} Comparison	Post-CD11b+ Cell Counts (Microglia)			
	Genotype	Mean Count (1x10 ⁶)	Standard Deviation	n
	Spi1-ERT	0.67	0.28	6
	Spi1-CONST	0.68	0.20	6
CX3CR1-Cre ^{CONST}	0.71	0.23	6	
Peritoneal Lavage Cell Counts				
Genotype	Mean Count (1x10 ⁶)	Standard Deviation	n	
Spi1-ERT	3.15	0.87	6	
Spi1-CONST	2.55	0.05	6	
CX3CR1-Cre ^{CONST}	2.61	0.36	6	

All Experiments	Post-CD11b+ Cell Counts (Microglia)			
	Genotype	Mean Count (1x10 ⁶)	Standard Deviation	n
	Spi1-ERT	0.72	0.22	20
	Spi1-CONST	0.79	0.20	20
Peritoneal Lavage Cell Counts				
Genotype	Mean Count (1x10 ⁶)	Standard Deviation	n	
Spi1-ERT	2.72	1.10	22	
Spi1-CONST	3.20	2.15	22	

Table 3.2 Summary of all Raw Cell Counts from Double Mutant (DM) mice experiments. Mean counts were calculated using the viable MUSE cell counts from Spi1-ERT, Spi1-CONST, Cx3cr1-Cre^{CONST} and C57BL/6J mice peritoneal lavages and Post-CD11b+ brain selection. The experiments where Spi1 mutant mice were compared to either C57BL/6J mice (black outline), or Cx3cr1-Cre^{CONST} (blue outline) have been shown separately as there was a narrower age range within these experiments. Here 'n' denotes the number of individual mice used to determine the averages.

3.2.5.3 LPS challenge in mice lacking -14 kB Spi1-URE

Another proposition was that in differentiated MØ the URE may not play a role in maintaining PU.1 protein levels in homeostasis, but might during an inflammatory challenge. The PU.

Expression was assessed with a pilot study where Spi1-CONST mice and C57BL/6NJ mice received a peritoneal LPS injection. As discussed in [132] a peritoneal injection of LPS can cause microglia

activation. C57BL/6NJ mice were used as controls due to lingering concerns about the suitability of Spi1-ERT mice as appropriate controls. As summarised in Figure 3.13A male and female mice were given either an intra-peritoneal injection of approximately 100 µg/kg LPS in 100 µL PBS or 100 µL of PBS as a vehicle only control. The 100 µg/kg dose of LPS was calculated according to the average C57BL/6J weight as 2.56 µg/100 µL for the male mice and 1.98 µg/ 100 µL for the females. There was one male and one female mouse in each experimental group. Two hours later microglia and pMØ were extracted from these mice and *Spi1* expression was assessed by qPCR and PU.1 levels via flow cytometry.

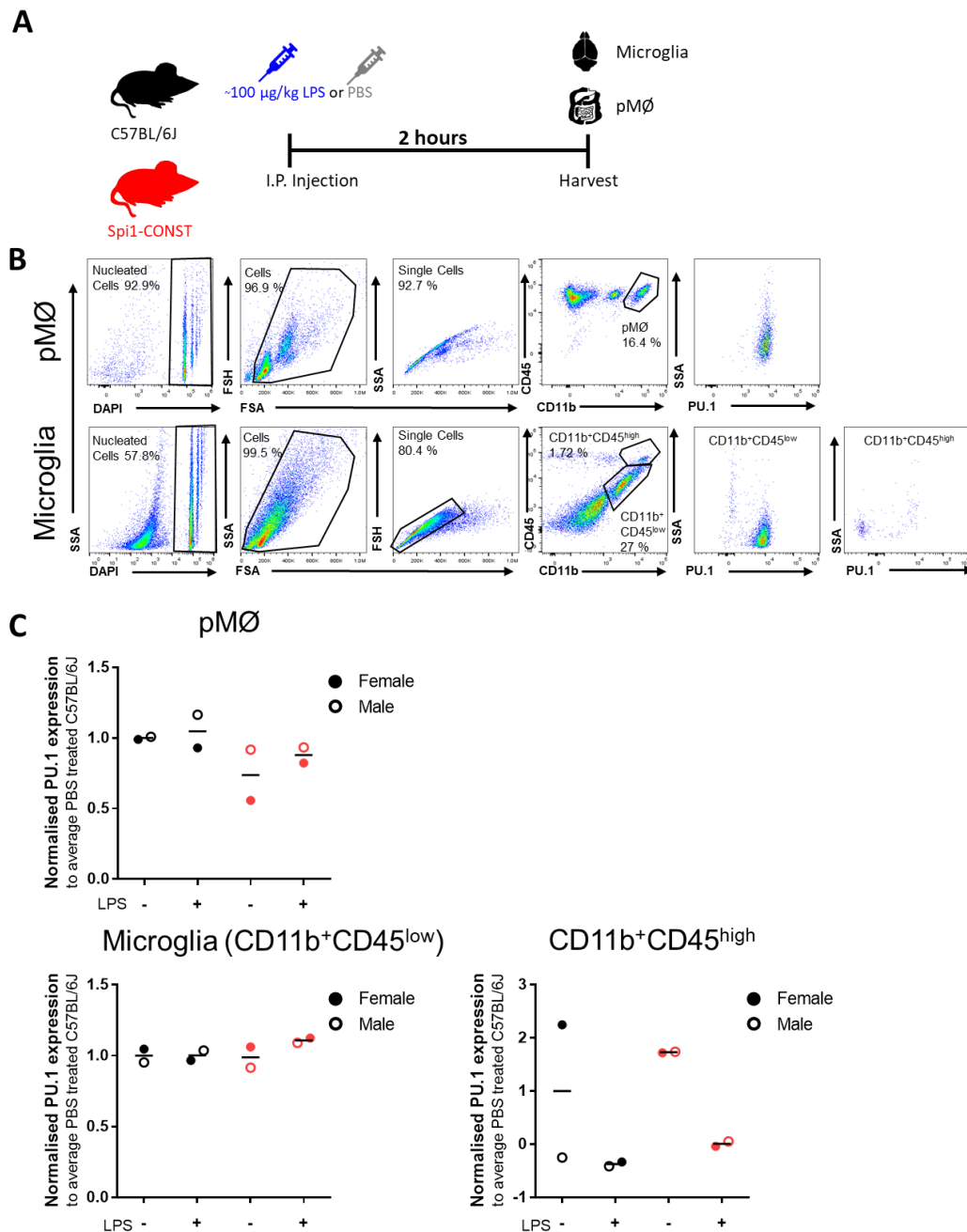


Figure 3.13 In vivo pilot experiment testing if removal of the -14 kB Spi1-URE impacts pMØ and microglial response to an LPS challenge- Part I. **A** Summary of the approach taken in this experiment. Briefly, C57BL/6J (black) or Spi1-CONST (red) mice aged 10-11 weeks received ~100 µg/kg of LPS and were sacrificed after 2 hours. **B** DAPI staining was included in flow cytometric analysis to aid in the separation of cells from debris and CD11b and CD45 staining was used to gate on the myeloid populations. In the brains CD11b⁺CD45^{high} and CD11b⁺CD45^{low} populations were analysed separately **C** PU.1 protein expression was normalised to the average expression between both C57BL/6J PBS control mice (2 mice per group, one of each gender). The horizontal bars in the plots denote the mean value. The results presented here were from one experiment $n=1$, where male mice were injected in the morning and female mice in the afternoon of the experiment.

The trM ϕ populations were gated as shown in Figure 3.13B. Briefly, single-cells were gated on CD11b and CD45 expression to select M ϕ populations before calculating the MFI of PU.1 antibody staining. The graphs in Figure 3.13C show the PU.1 protein levels in the pM ϕ and microglia of mice following this LPS challenge. There were no substantial changes in PU.1 protein expression in either the C57BL/6J mice (black) or Spi1-CONST mice (red) following LPS stimulation when compared to PBS controls. Spi1-CONST mice pM ϕ populations did appear to have a slightly lower baseline PU.1 expression in pM ϕ compared to the C57BL6/J control mice though it is hard to definitively conclude given the small group sizes (n=2 per group). Again, little difference in PU.1 protein levels were observed across the experimental conditions in the microglia (CD11b⁺CD45^{low}). LPS stimulation did appear to impact PU.1 expression in the CD11b⁺CD45^{high} cells, potentially a mix of monocytes and slightly activated microglia, but again the genotype of the mice did not appear to alter the results though the number of mice in each group would need to be increased before this could be definitively concluded. Nevertheless, these results suggested that PU.1 protein was not greatly reduced in mice lacking the *Spi1*-URE even following a mild immune challenge. However, as the tissue was harvested only 2 hours after the LPS challenge it was likely that this did not allow enough time to see any changes at the protein level.

As the tissue harvest the samples were split to assess *Spi1* mRNA expression by qPCR and other inflammatory markers. RNA was extracted from unsorted lavages or extracted from whole-brain tissue to try and preserve the *in vivo* mRNA expression.

Figure 3.13D presents the data from these qPCR analyses. *Spi1* mRNA does not appear to be affected following LPS stimulation, though there does appear to be a difference in the baseline expression between the genotypes. In the peritoneal lavage samples *Tnf* expression does seem to increase following LPS stimulation in the C57BL/6J mice (black), though this change was not seen in the Spi1-CONST genotype (red), though the variation in the Spi1-CONST PBS samples make it hard to definitively conclude this. Despite the immune stimulus being given in the periphery and the relatively short interval between challenge and harvest an increase in brain *Tnf* expression was still observed in the C57BL/6J mice. It is possible this also occurred in the Spi1-CONST mice though the small sample size would need to be increased before this could be ascertained with certainty. *Ii-6* mRNA expression was also measured in the brain samples and seems to be moderately increased following LPS stimulation in both genotypes, though further repetitions would be required to confirm this change was consistent.

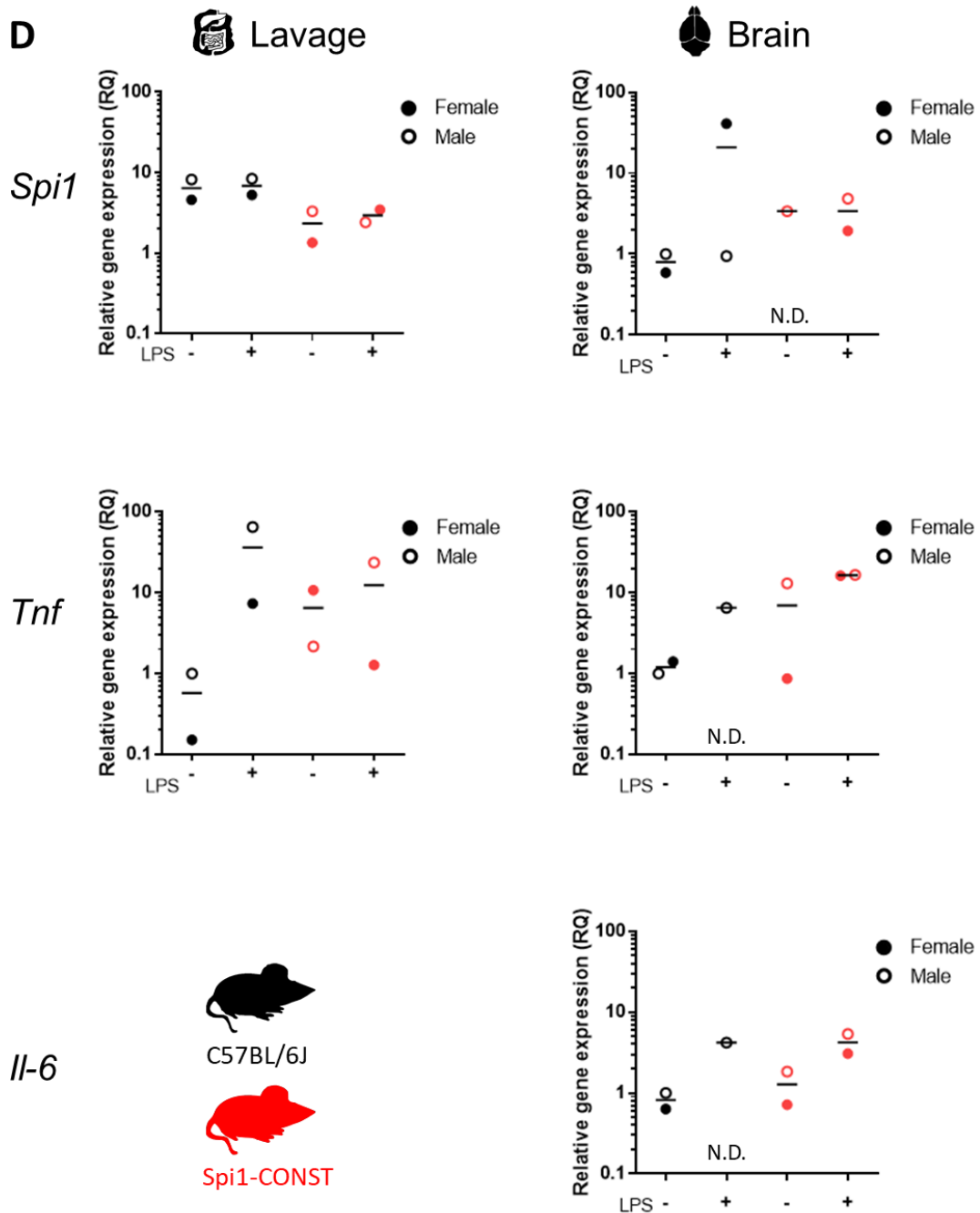


Figure 3.13 *In vivo* pilot experiment testing if removal of the -14 kbp *Spi1*-URE impacts pMØ and microglial response to an LPS challenge- Part II. **D** RNA was extracted from half of the peritoneal lavage or one brain hemisphere. The expression of each gene was presented as relative to the GAPDH endogenous control gene and *Spi1* (PU.1, top), *Tnf* (middle) and *Il-6* (bottom) were normalised to the male C57BL/6J mouse that received PBS. *Spi1* mRNA did not appear to change with LPS stimulation in the lavage samples, though the *Spi1*-CONST mice (red) seem to have a lower baseline expression compared to C57BL/6J (black) controls. Again, the horizontal bars in the plots denote the mean value. N.D. indicates no available data as gene expression was beyond the limit of detection.

While this is a small pilot study there are several inferences that can be made. Firstly, a peritoneal injection of 100 µg/kg appeared to induce some inflammation, though a higher dose may elicit a

more defined microglial response. Secondly, this pilot LPS challenge suggested that inflammation is unlikely to alter *Spi1* mRNA or PU.1 protein in mice lacking the *Spi1*-URE (Spi1-CONST) compared to wild-type control mice. However further repeats with a stronger stimulus would be needed to definitively conclude if the *Spi1*-URE is required to regulate PU.1 protein in an inflammatory setting in trMØs.

3.3 Discussion

SPI1 is an AD risk gene encoding PU.1, a critical transcription factor for survival of the cells in the myeloid and lymphoid lineage. This chapter set out to establish if the *Spi1*-URE floxed mice could be used to knock-down PU.1 expression in microglia *in vivo*. This was done to better understand how a reduction in PU.1 may alter microglia physiology.

The experiments in this chapter show that removal of the -14 kB *Spi1*-URE in Cx3cr1⁺ cells did not alter the level of the PU.1 transcription factor in conditionally-immortalised CD117⁺ bone marrow macrophage precursors (MØPs), BMDM, pMØ or microglia. Subsequent experiments demonstrated the lack change to the PU.1 levels were not as a result of inappropriate Cre expression. Finally, it was confirmed that removal of the URE did not reduce the level of the PU.1 transcription factor in an inflammatory setting. The impact of these results will now be discussed in detail.

The genomic recombination as a result of URE removal has been demonstrated by PCR (Figure 3.5) where only the Spi1-CONST cells showed the recombination. No significant PU.1 reduction was observed in the target microglia population, when Spi1-CONST mice were compared to either the Spi1-ERT or Cx3cr1-Cre^{CONST} mice. While no *Spi1*-URE floxed mice were available to use as a background control for any effects that floxing the *Spi1*-URE may have on PU.1 expression, the Cx3cr1-Cre^{CONST} mice were an equally appropriate control. C57BL/6J mice were used to investigate the impact that the background strain of these mice might have on PU.1 protein levels again no alterations were seen between the genotypes. The findings of the current study do not support the previous research, where PU.1 expression was shown to be 80 % reduced in total bone marrow cells using a western blot [260].

Together the experiments in section 3.2.5 demonstrated that even if Cre was activated independently of tamoxifen in the microglia of the Spi1-ERT mice, as seen in other models [331], there was no alteration to PU.1 expression in mice that lacked a *Spi1*-URE (Spi1-CONST) or mice with a wild-type *Spi1*-URE (C57BL/6J or Cx3cr1-Cre^{CONST}, Figure 3.12).

The lack of PU.1 reduction is not likely to be because the Cre in this model was not functional. The functionality of the Cre expression in the Cx3cr1-Cre^{CONST} and that it is present in *ex vivo* microglia has been shown by flow cytometric analysis of the Cas9-CONST mice, which express GFP in the presence of an active Cre, as shown in Figure 3.11.

One argument might be that pMØ/microglia with a large PU.1 reduction present *in vivo* and the lack of PU.1 in these cells makes them vulnerable to cell death, as PU.1 is important for cell survival. However, this is unlikely as *in vitro* there was a similar number of GFP+ cells in Cre-pSFEW infected *Spi1*-URE floxed BMDM compared to BMDM from C57BL/6J mice (Figure 3.7A). Furthermore, no differences were observed in the cell counts when mice with an active Cre (*Spi1*-CONST) compared to inactive Cre controls (summarised in Table 3.2).

As PU.1 can regulate the expression of CD11b [272], was possible that during the CD11b⁺ selection step microglia with a lower PU.1 expression had a lower CD11b expression making the magnetic bead sorting biased. To ensure this was not the case the CD11b negative fractions were analysed for PU.1 expression. In the “CD11b negative” fraction there were very few cells that were stained with microglia markers, and in the small percentage that were not positively selected the PU.1 expression did not differ from the CD11b positive fraction (data not shown).

Analysis of ATAC-Seq and H3K27ac ChIP-Seq data (Figure 3.3) suggested the URE was likely operational in the pMØ and microglia. Li *et al.* (2001) have also suggested that this URE is needed for high PU.1 expression in pMØ, bone-marrow and spleen [267]. However these datasets only show the chromatin accessibility or the indicates the presence of an enhancer element it does not show what other factors may bind at this URE.

It was also proposed that the *Spi1*-URE may not play a role in PU.1 protein levels in a normal environment, but only have an effect during inflammation. Following an LPS challenge the no changes to PU.1 protein expression in pMØ or microglia were observed, though the two-hour time-point may be too soon to detect these changes (Figure 3.13A-C). However several other papers suggest that LPS can increase PU.1 protein within this time frame *in vitro* [332,333]. This pilot experiment measured *Spi1* mRNA production in total brain tissue and peritoneal lavages and indicated that this was unlikely. Even though there are other cell types present in these analyses all of the *Spi1* expressing cells should be targeted by the Cx3cr1 restricted Cre expression (Figure 3.13D).

The discrepancy between our results and the published work [260,298] is most likely to the difference in Cre recombinase delivery. The Rosenbauer papers ubiquitously expressed Cre to ensure the -14 kB *Spi1*-URE was lost in all tissues, including germline cells and thus hematopoietic stem cells [298].

In this model Cre expression was restricted to Cx3cr1⁺ cells which includes monocytes, M ϕ and a subset of NK cells [146]. Consequently, it is likely that the reduction in PU.1 protein in the bone marrow following URE removal in the paper is due to the B-cell population. In fact, another paper published shortly after showed that the B2 lymphoid population was depleted in these URE knock-out mice [298], though little is mentioned about cells derived from the myeloid lineage. This discussion will be continued in 7.2.1.

Collectively these data demonstrate that PU.1 expression is largely unaffected by the removal of the URE, and therefore this model is unsuitable to investigate the effects of a reduced PU.1 expression in microglia.

3.3.1 Conclusions and future work

The present results are significant in at least one major respect. Firstly, that deletion of the -14kB *Spi1*-URE in microglia and pM ϕ did not produce a reduction in PU.1 protein, contrary to expectations. Several questions remain unanswered at present, including why PU.1 was not reduced in either trM ϕ subset. Further work would be required to if establish this is because the URE mainly regulates PU.1 expression in B-cells after development.

While low PU.1 transgenic mice could be developed using CRISPR-Cas9 system to reduce PU.1, possibly by the removal of other *Spi1* myeloid regulatory elements at -12.2 kB and -10.3 kB upstream of the *Spi1* promoter [269,330]. As heterozygous PU.1 knock-out could be given *in vivo* injections of an shRNA lentivirus targeting *Spi1* expression, though this would require a high infection efficiency. These experiments were not within the scope of this project as targeting microglia in this manner would take considerable time and expertise.

In summary, the *Spi1*-URE floxed model developed by Rosenbauer *et al.* (2004) could not be used to investigate the impact of a low PU.1 expression on microglia behaviour. Therefore, the following chapter moves onto to manipulating PU.1 expression using custom lentiviruses, which were tested *in vitro* and *in vivo* in M ϕ populations

Chapter 4 Development of *in vitro* microglia model with altered Spi1/PU.1 expression

4.1 Introduction

The primary aim of this chapter was to alter the level of the PU.1 transcription factor in microglia and determine transcriptomic changes. Previous evidence indicated that a moderate reduction in PU.1 protein would be required. In foetal liver cells there were different transcriptional “thresholds” dependent on PU.1 levels being 80 % reduced or 98 % lower than controls [9]. Similarly, in the BV-2 cell line several key microglia genes were altered by an 80 % reduction in PU.1 protein [230]. However, a 60 % reduction in PU.1 was sufficient to cause transcriptional changes in a human mixed glia culture system [233]. Therefore a physiological relevant knock down of PU.1 protein, between 60-70 % was desired.

To reiterate, the aim of this thesis was to be able to manipulate PU.1 expression in microglia with the purpose of observing gene expression changes and the possibility of providing insight into AD pathology. It has been demonstrated the human SNP (rs1057233^B) associated with a lower PU.1 expression meant that the age of onset in AD was delayed [230]. Therefore, by diminishing PU.1 to the minimum level required for cell survival could provide insight into which biological pathways are most affected in these “low PU.1” individuals whom have a prolonged disease-free state. Moreover, this would highlight pathways that would most likely be affected by any therapeutic treatment affecting PU.1 expression such as M-CSF inhibitors or HDAC inhibitors [73,89,233,334,335].

A deficiency in much of the work quantifying *SPI1* expression in post-mortem human brain tissue is the failure to normalise the expression to the cell number [73]. As PU.1 is known to regulate proliferation in general MØ populations [257], and in microglia specifically [73,271] it is important to investigate PU.1 expression on a single cell level.

As previously discussed PU.1 levels are highly regulated in myeloid cells, which includes several endogenous feedback loops [267,268,336]. There were therefore concerns that these endogenous pathways might offset any virally-induced increases to PU.1 protein. An ectopically induced 40 % increase in *Spi1* expression had been reported, suggesting it was possible [230]. At the time of writing there were no commercially available transgenic mice over-expressing PU.1 in microglia though they were in development. Therefore, the subsequent chapter shows the development and optimisation of an *in vitro* culture system where PU.1 protein was reduced or over-expressed using custom lentiviruses.

Lentiviruses are a class of retrovirus that can be used to infect multiple cell types, including non-dividing cells, to give a stable expression of the desired construct and can be utilised *in vitro* and *in vivo* [337,338]. In addition lentivirus systems can incorporate a co-expression of a reporter of infection, such as enhanced Green Fluorescent Protein (eGFP) or the T-cell surface antigen from a rat-CD2 (rCD2), can be used to tag the infected cells. These reporter genes enable infected cells to be specifically gated on during flow-cytometry analysis and even separated out using flow-cytometric sorting. While use of these viruses may result in an inflammatory response, the effects of the virus carrier can be separated from any functional effects of altered PU.1 expression with the use of appropriate control viruses.

Accurately modelling microglia *in vitro* is challenging. Much like any tissue resident M ϕ , microglia rely heavily on the local tissue microenvironment and once cells are removed from the tissue the microglial phenotype is considerably altered. A recent study has shown that expression of microglia specific markers like Tmem119 can be halved within hours of being removed from the brain [155].

The use of mixed glial cultures was preferred, as this enabled microglia to retain some trophic support from other cell types, including regulatory signals from astrocytes [155]. Mixed glial cultures are often supplemented with M-CSF (M ϕ -colony stimulating factor) to encourage microglia proliferation and survival [271,339]. Two recent studies highlighted the addition of Transforming Growth Factor β (TGF- β) in microglia cultures results in a gene expression profile more similar to freshly extracted microglia [154,155]. TGF- β is thought to have an immunoregulatory role in M ϕ TGF- β [196] and TGF- β has also been shown to have an anti-viral effect on Langerhans cells [195].

Given the flexibility of a lentiviral approach a *Spi1* over-expression model could now be studied in parallel. It was predicted that valuable information could be gleaned by over-expressing the PU.1 transcription factor, such as how the *Spi1* risk SNP might contribute to the pathogenic phenotype of microglia observed in AD [70].

Therefore the work in this chapter investigated the utility of lentiviral vectors to both reduce PU.1 *in vivo* and knock-down/ over-express PU.1 protein in cultured primary microglia. An improved culture model was developed throughout the course of these investigations to ensure the microglia were as representative of their *in vivo* counterparts as possible. Finally, these PU.1 “high” and PU.1 “low” microglia were sorted and processed for downstream mRNA Sequencing. Previous studies reducing PU.1 utilised either quantitative PCR (qPCR) or microarray to assess PU.1

changes to the transcriptome [230,233]. RNA-Seq analysis would provide a more complete map of genes and biological pathway changes affected by an altered PU.1 expression.

Thus, this chapter aimed to develop a primary microglia culture model that combined both TGF- β and lentiviruses designed to knock-down and over-express *Spi1* mRNA. This was achieved by:

- Cloning lentiviral plasmids that would express an shRNA targeting the *Spi1* mRNA or over-express the *Spi1* coding sequence.
- Validating these lentiviruses *in vitro* and *in vivo* in the peritoneal cavity by measuring PU.1 expression after infection.
- Optimising a primary murine microglia culture that can incorporate both TGF- β and lentiviruses.
- To utilise this optimised *in vitro* model and lentiviruses to knock-down and over-express *Spi1* in primary microglia, and prepare these cells for RNA-Seq.

4.2 Results

4.2.1 Validation of Knock-Down and Over-Expression Vectors

The first set of analyses in this chapter examined the impact of the effectiveness of the newly derived lentiviral vectors.

4.2.1.1 Cloning custom lentiviral plasmids

Spi1 knock-down shRNA sequences were designed as described in 2.11.2.1. Both the *Spi1* shRNA 1 (red) and *Spi1* shRNA 2 (blue) sequences were designed to target different parts of the *Spi1* coding sequence (Figure 4.1A). An example of vector linearization is illustrated in Figure 4.1B, where the linearised vector was electrophoresed faster. After transformation individual bacterial colonies were PCR screened using primers designed around the *PmeI* insert site, see methods (2.11) for further detail. A selection of positive colonies (blue) would then be taken and grown-up before lentiviral plasmids were extracted Figure 4.1D.

Over-expression viral vectors were made using the *Spi1* consensus coding sequence (CCDS16425.1) taken from Ensemble. Due to the size of this fragment (>800 nucleotides) a gradient PCR was used to optimise the temperature at which the primer annealing was most efficient. Figure 4.1E shows the gradient PCR for *Spi1* insert where the optimum annealing temperature was determined to be 63 °C.

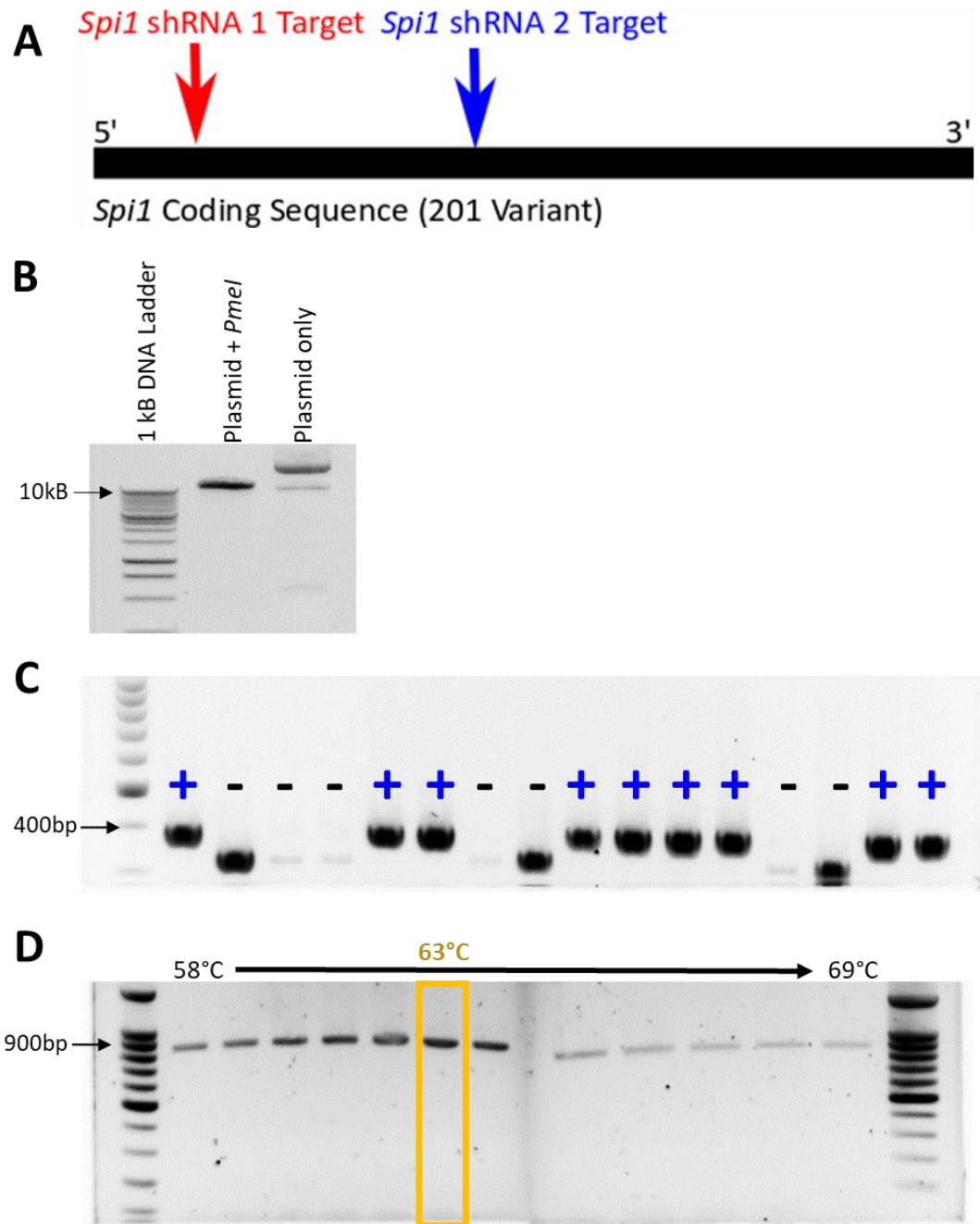


Figure 4.1 Cloning Lentiviruses to Manipulate PU.1 Expression. **A** Predicted shRNA binding sites on *Spi1* mRNA. Two separate *Spi1* shRNAs were designed to target different parts of the *Spi1* coding sequence. The predicted binding sites are highlighted in red (*Spi1* shRNA 1) and blue (*Spi1* shRNA 2). **B** pSU6EW Vector Linearization. Lane 1 shows the 1 kB ladder (Promega) used to determine approximate size. The undigested plasmid is shown in Lane 3, whereas the plasmid linearised with the a *PmeI* restriction enzyme is shown in Lane 2. As expected, the linearised plasmid (Lane 2) runs through the agarose gel quicker than the uncut control. **C** Colony PCR for *Spi1* shRNA 2. Bacterial colonies were screened using PCR primers designed to bind to either side of the insert. Here positive colonies give an expected band size of 380 bp labelled (+) and negative colonies (-) with an estimated 320bp band, based on 100 bp ladder (Promega). Individual colonies were then grown up in LB broth and sequenced. **D** Temperature Gradient PCR for *Spi1* coding sequence insert. The temperature of the PCR reaction was optimised to ensure one clear strong band of the correct size for *Spi1* was produced (819bp). From the agarose gel 63°C was determined to be the optimum temperature for these primers.

A summary of the final cloned lentiviral vectors used in this chapter can be seen in Table 4.1, including the predicted changes to PU.1 protein expression, infection reporter, and the appropriate control virus.

Plasmid Name	Predicted Change	Reporter	Control
<i>Spi1</i> shRNA 1 pSU6EW	↓ PU.1	eGFP	Non-Silencing shRNA pSU6EW
<i>Spi1</i> shRNA 2 pSU6EW	↓ PU.1	eGFP	
<i>Spi1</i> pSIEW	↑ PU.1	eGFP	Empty pSIEW

Table 4.1 the table above illustrates some of the main characteristics of the PU.1 lentiviruses. The two *Spi1* shRNA vectors were designed to reduce PU.1 and were used with the Non-Silencing shRNA virus as a control. All shRNA viruses were designed with a GFP reporter to allow for cell sorting of infected cells. The over-expression viruses were made by inserting the consensus coding sequence for mouse *Spi1* (CCDS 16425.1) into a plasmid with a GFP reporter (pSIEW). For this over-expression viruses an empty vector control virus was used.

4.2.1.2 Validation of expression in Cell Lines

The effectiveness of the *Spi1* shRNA viruses was first tested in the murine MØ RAW cell line, which have a high PU.1 expression (see Figure 3.4). Figure 4.2 shows the results of RAW cells after infection with *Spi1* shRNA virus or Non-Silencing (NS) shRNA virus and underwent flow-cytometric sorting by GFP expression after 7 days of infection. Figure 4.2A showed PU.1 protein was reduced in RAW cells infected with *Spi1* shRNA virus when compared to the NS shRNA control virus, as assessed by flow cytometry. *Spi1* expression was also assessed by qPCR analysis of RNA extracted from *Spi1* shRNA 2 infected RAW cells, which confirmed that *Spi1* mRNA was reduced in comparison to the NS shRNA virus (Figure 4.2B). PU.1 protein expression was normalised as described in 2.16.2.1. Figure 4.2C shows there was a reduction in PU.1 expression in *Spi1* shRNA infected RAW cells compared to NS shRNA control samples.

The *Spi1* pSIEW over-expressing virus was tested in Jurkats, which do not typically express PU.1 protein [268]. The flow plots in Figure 4.2D show there was an increase in PU.1 expression in Jurkats infected with *Spi1* pSIEW (Right) which was not seen in Jurkats infected with the empty vector pSIEW virus (Left). *Spi1* mRNA was analysed by qPCR in these infected Jurkat cells, and the results (Figure 4.2E) reflected changes to PU.1 protein expression (Figure 4.2F).

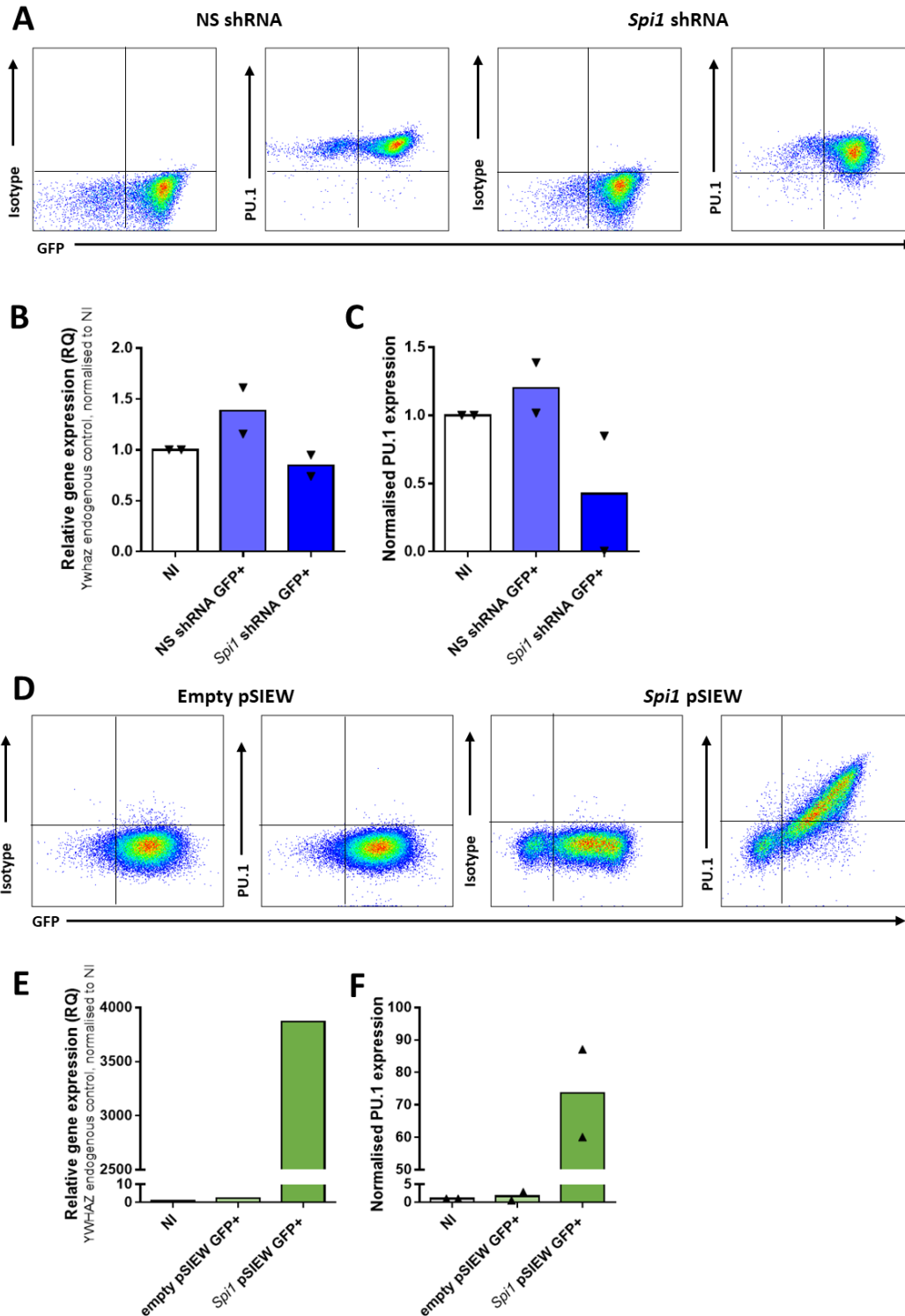


Figure 4.2 Confirmation of Viral Function in Cell Lines. **A** *Spi1* shRNA reduced PU.1 expression in the RAW Cell Line. RAW cells were infected with either NS shRNA virus or *Spi1* shRNA virus 2 and sorted by GFP expression after 1 week. Some cells were then fixed and stained for PU.1 and run through a flow cytometer. **A** The two left panels show that in infected cells (GFP+) PU.1 expression was unaltered in NS shRNA infected RAW cells. As expected RAW cells infected with the *Spi1* shRNA 2 virus had a reduced PU.1 expression compared to GFP- cells within the sample. **B** Summary of *Spi1* mRNA Infected RAW cells were sorted by GFP

expression. RNA was then isolated from these cells for qPCR analysis of *Spi1* mRNA, where *Ywhaz* was used as an endogenous control gene. *Spi1* mRNA was reduced in *Spi1* shRNA infected RAW cells compared to RAW cells infected with NS shRNA control virus. **C** PU.1 protein expression in GFP+ RAW Cells. Protein expression was also determined in these cells using anti-PU.1 antibody. Here it can be seen that *Spi1* shRNA protein was reduced when compared to the NS shRNA. The results in part B and C are the result of two independent experiments $n=2$, individual replicates are denoted by black symbols and the bars represent the mean values **D** Over-expression *Spi1* pSIEW lentivirus induces PU.1 protein in Jurkat cell line. Here the Jurkat cell line was infected with either a *Spi1* pSIEW over-expression virus or an empty vector control virus. As Jurkat cells do not naturally express PU.1, no PU.1 was detectable in cells infected with the empty pSIEW virus. **E** *Spi1* mRNA was increased in Jurkats infected with *Spi1* pSIEW. The results here are from one experiment where *YWHAZ* was used an endogenous control. **F** PU.1 protein was increased by *Spi1* pSIEW virus but not empty pSIEW. PU.1 protein can be detected in Jurkats infected with the '*Spi1*' pSIEW virus, showing that the virus was indeed functioning to over-express PU.1 in these cells. The results are the result of two independent experiments $n=2$, individual replicates are denoted by symbols and the bars represent the mean values.

Overall these results indicate that the *Spi1* shRNA viruses could partially knock-down PU.1 protein and the *Spi1* over-expression virus was able to exogenously express PU.1 levels in cell lines. This chapter now turns to the data showing on how the *Spi1* shRNA viruses performed in an *in vivo* context.

4.2.1.3 Validation of knock-down viruses In Vivo

Several pilot studies were performed *in vivo* as $\text{trM}\emptyset$ phenotype is better maintained in the local environment [118,153]. As the peritoneal cavity was easier to access than the brain the effectiveness of the *Spi1* shRNA lentiviruses was assessed in $\text{pM}\emptyset$.

The first *in vivo* experiment, shown in the figure below, was done to investigate the time required between injection of virus and $\text{pM}\emptyset$ harvest to gain the largest reduction in PU.1 protein. Figure 4.3A provides an overview of the experiment design. Briefly C57BL/6J mice were divided into three groups; Non-Injected, NS shRNA and *Spi1* shRNA injected. At both timepoints, 4 days and 7 days after injection, 2 mice from each group were sacrificed and lavaged to retrieve the $\text{pM}\emptyset$. Any lavages contaminated with blood were removed from analysis ($n=1$, non-injected control at the day 4 timepoint). From the flow plots in Figure 4.3B and the graphs in Figure 4.3C it was apparent that infection with the *Spi1* shRNA results in a moderate PU.1 protein reduction compared to NS shRNA infected $\text{pM}\emptyset$ at both timepoints. However, Figure 4.3D suggested the proportion of infected $\text{pM}\emptyset$ was slightly higher at the later timepoint. Given that the reduction in PU.1 seemed similar at both timepoints the 7-day timepoint was selected, which would give a greater delay between the physical trauma caused by the injection and $\text{pM}\emptyset$ harvest. The results from this experiment confirm that a mild PU.1 protein knock-down occurred *in vivo* following lentivirus

administration, therefore the next experiment was to compare the effectiveness of both *Spi1* shRNA viruses.

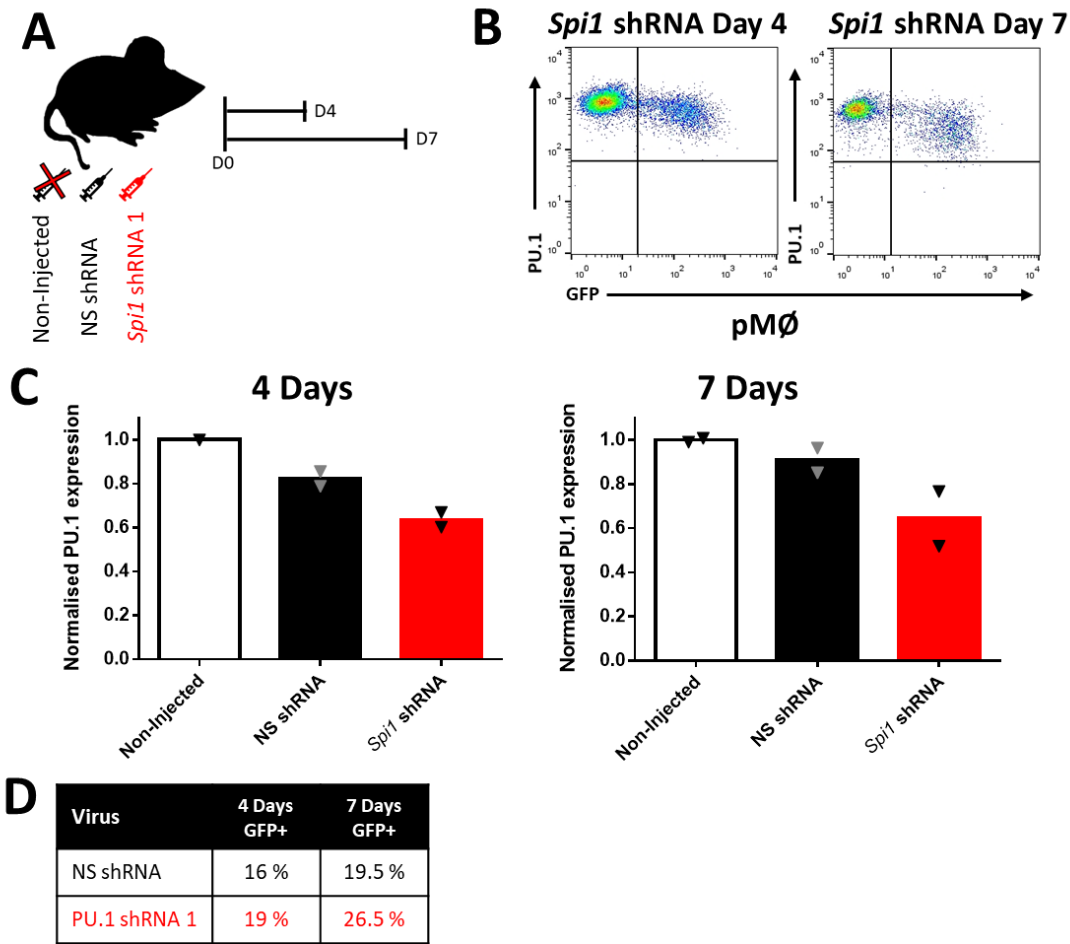


Figure 4.3 In Vivo Timecourse to see when *Spi1* shRNA knock-down was most effective. **A** The experimental setup to determine when PU.1 expression was most reduced by *Spi1* shRNA, using *Spi1* shRNA 1 as a guide. 7-week-old Female C57BL/6J mice were divided into three groups. On Day 0 these mice were either put in the non-injected group or in the NS shRNA or *Spi1* shRNA 1 virus injected groups ($n=4$ per group). At both timepoints, day 4 and day 7 post-injection, 2 mice from each group were sacrificed and lavaged to retrieve the pMØ. These two timepoints were chosen following insight gained from in vitro studies. **B** Flow cytometry plots for *Spi1* shRNA infected pMØ. Here pMØ were pre-gated as CD11b⁺F4/80⁺ cells and the plots show PU.1 antibody staining plotted against GFP expression. This figure shows that PU.1 protein expression was reduced in *Spi1* shRNA infected pMØ, and the stronger the GFP expression the more apparent the reduction in PU.1 protein. **C** Summary of PU.1 expression changes in infected (GFP+) pMØ at day 4 and day 7 post-injection. Expression was normalised to the average PU.1 expression in non-injected mice. *Spi1* shRNA knock-down appears to be slightly more effective at 7 days compared to 4 days. At the 4-day timepoint one non-injected control was removed from analysis following a blood contaminated lavage. In the graphs the bars represent the mean values and the individual datapoints are indicated by the symbols. **D** Average percentage of GFP+ pMØ at both timepoints. Again 7 days appears to result in a larger number of infected pMØ compared to 4 days.

As outlined in Figure 4.4A, C57BL/6J mice were given I.P. injections of either NS shRNA, *Spi1* shRNA 1, *Spi1* shRNA 2, or *Spi1* shRNA 1 and 2 combined in a 1:1 ratio (n=2 per group). One week after injection all mice, including non-injected controls (n=2) were sacrificed and pMØ retrieved and analysed by flow-cytometry. Figure 4.4B provides an example of the reduction in PU.1 expression seen in GFP+/infected pMØ from a mouse injected with *Spi1* shRNA virus (Right) compared to pMØ from a mouse injected with NS shRNA virus (Left). The results of the entire experiment are set out in Figure 4.4C.

While it appeared that the NS shRNA virus increased pMØ PU.1 expression in relative to non-injected controls, this could be an experimental artefact from the one mouse in this group, and this effect was not observed in the previous experiment (Figure 4.3). Both shRNA viruses produces shRNA molecules that could initiate an immune response [340], which could increase PU.1 expression [277]. On average mice injected with *Spi1* shRNA lentiviruses had a moderately reduced level of PU.1 protein, 50-60 % lower, compared to non-injected controls and though the reduction was ~80 % when compared to the NS shRNA control sample.

The PU.1 reduction between the two *Spi1* shRNA suggested *Spi1* shRNA 2 might be marginally more effective. Figure 4.4 suggests that the *Spi1* shRNA viruses did not work better together than when they were injected independently. In summary, these results suggest that the *Spi1* shRNA 2 virus might provide a slightly better PU.1 knock-down than the *Spi1* shRNA 1 virus, and that combining the *Spi1* shRNA viruses did not result in a greater reduction of PU.1 protein. However, the proportion of infected pMØ in all experiments were quite low, suggesting that further optimisation was required, to ensure lentiviral infection was efficient.

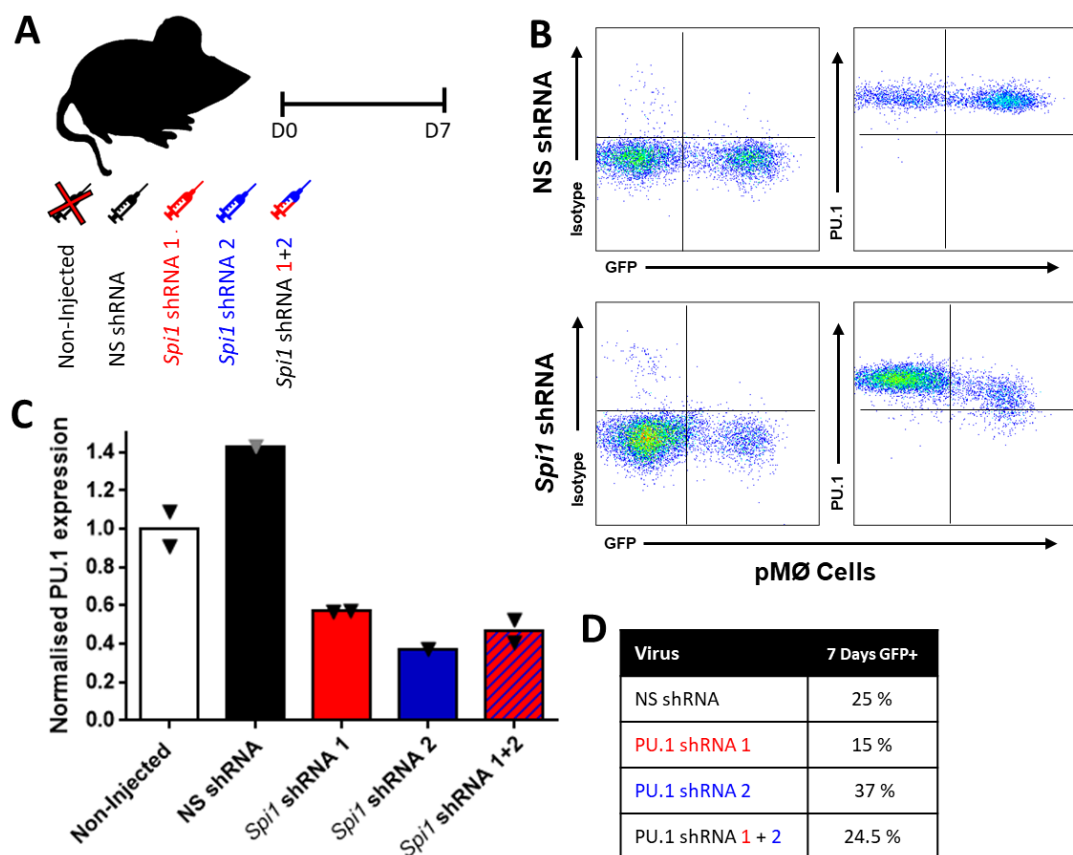


Figure 4.4 In Vivo comparison of Spi1 shRNA lentiviruses. **A** Experimental setup to compare Spi1 shRNA Viruses. On day 0 C57BL/6J female mice, aged 7 weeks, were divided into the following groups; non-injected, NS shRNA, Spi1 shRNA 1, Spi1 shRNA 2 or Spi1 shRNA 1 and 2 combined ($n=2$ per group). After 7 days these mice were sacrificed and lavaged to harvest pMØ. **B** Flow cytometry plots comparing NS shRNA and Spi1 shRNA viruses. pMØ were gated as CD11b⁺F4/80⁺ cells before PU.1 staining was determined. Spi1 shRNA infected pMØ have a reduced PU.1 expression when compared to NS infected controls, or even the non-infected pMØ within the sample. **C** Summary of PU.1 expression across all conditions. PU.1 expression was normalised to the average PU.1 expression in the non-injected control mice. PU.1 expression is reduced in both Spi1 shRNA 1 (red) and Spi1 shRNA 2 (blue) when compared to NS shRNA virus (black). Yet it does not appear that combining the Spi1 shRNAs 1 and 2 (blue/red stripes) produces any greater reduction in PU.1 protein expression compared to Spi1 shRNA 2 alone. Two lavages were excluded from further analysis ($n=1$ non-silencing, $n=1$ Spi1 shRNA 2). The error bars indicate the standard deviation about the mean. The normalised PU.1 expression from each mouse are shown with symbols. **D** Average percentage of GFP⁺/Infected pMØ.

It was proposed that transgenic mice that endogenously express GFP would better the shRNA viruses, extending the efficacy of this virus as GFP would not trigger an immune response. This was thought to be beneficial as it would help separate the impact of Spi1 shRNA PU.1 knock-down from any lingering effects of injection and would be useful if an immune-challenge was added to the experimental design. Therefore, B6.129(Cg)-Foxp3^{tm3(DTR/GFP)Ayr/J} (FoxP3^{GFP}) mice which express GFP in FoxP3⁺ T-cells were injected with the Spi1 shRNA 2 lentivirus before pMØ were harvested at

one of three timepoints (n=2 per group; as pictured in Figure 4.5A). As endogenous GFP was only present in the T-Cells any GFP+ pMØ were the result of viral infection and was thus assessed in these mice at 7 days, 10 days and 14 days after the initial virus injection. Representative flow plots from each timepoint are displayed in Figure 4.5B, where GFP+ pMØ harvest had the expected reduction in PU.1 expression as a result of *Spi1* shRNA 2 infection. Figure 4.5C shows the PU.1 expression at each timepoint, normalised to the average non-infected (GFP-) pMØ. Interestingly, PU.1 protein was ~50 % lower at day 7 and day 10 but only a ~40 % reduction was seen at day 14, suggesting the *Spi1* shRNA virus still became less effective over time. Moreover, the proportion of infected pMØ was smaller at each timepoint but was highest at the first timepoint (day 7, Figure 4.5D). Taken together these results suggest that mice with endogenous GFP still experience a decline of *Spi1* shRNA virus performance over time.

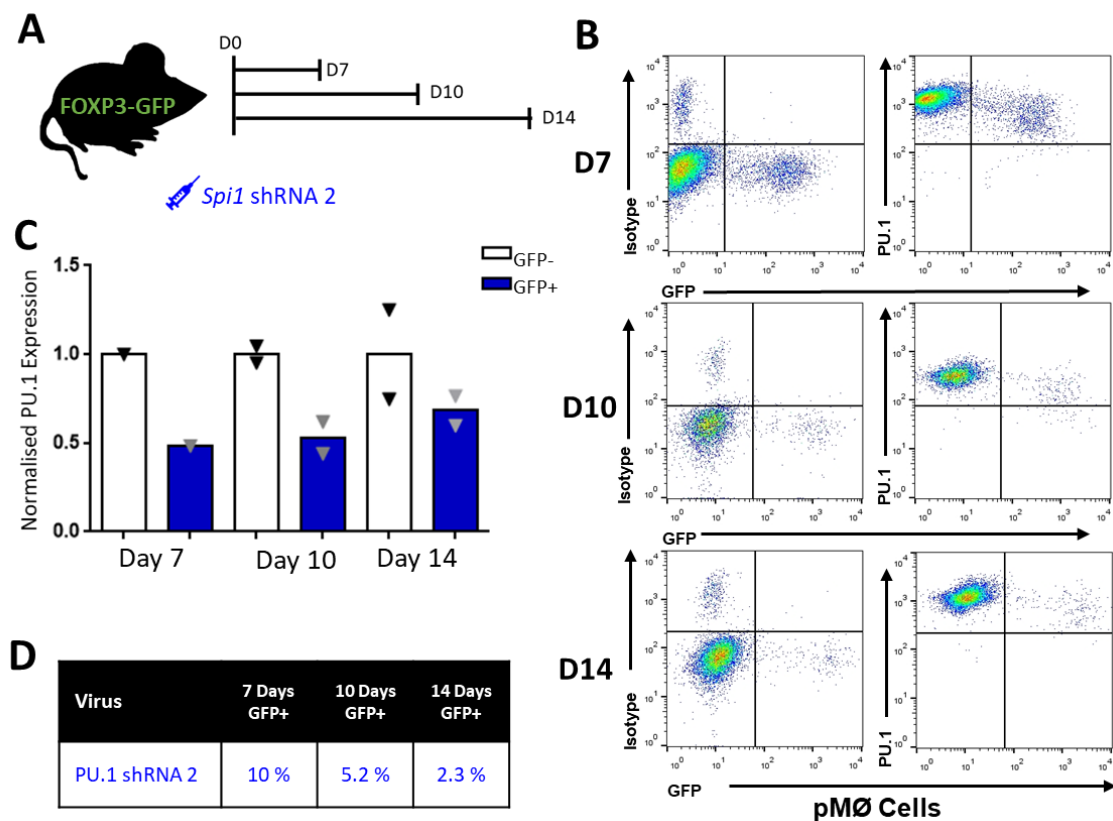


Figure 4.5 Determining if endogenous GFP expression extends lifetime of *Spi1* shRNA viruses In Vivo. **A** Experimental plan. The purpose of this experiment was to establish if *Spi1* shRNA virus knock-down could be prolonged with *FoxP3*^{GFP} mice which express GFP endogenously. It was hypothesised that mice expressing GFP under the *FoxP3*^{GFP} promoter would tolerate the viral GFP for longer and therefore maintain a reduced PU.1 expression for longer. 6-week-old *FoxP3*^{GFP} mice were injected with *Spi1* shRNA 2 pSU6EW virus (n=6, 3 Female and 3 male). One male and one female mouse were sacrificed at each timepoint; 7 days, 10 days and 14 days post-injection. **B** PU.1 flow cytometry staining in pMØ cells at each timepoint. pMØ were gated using CD11b⁺F4/80⁺ expression. There seem to be a larger proportion of infected cells at day 7 compared to day 10 or day 14. PU.1 expression was reduced in pMØ infected with *Spi1* shRNA 2 virus at all time points. **C** Level of PU.1 reduction seen at each timepoint. PU.1 protein expression was normalised to the average MFI of the

non-infected cells at each timepoint. The average PU.1 protein knock-down was ~50% at both day 7 and day 10, whereas by day 14 the reduction in PU.1 protein was ~40%. The mean is shown by the bar. The individual values are denoted by symbols. **D** Average proportion of GFP+ pMØ at each timepoint. There are a larger number of infected cells at day 7 compared to the other timepoints. By day 10 the number of infected cells was almost halved and was further reduced at 14 days post-injection.

Overall these pilot experiments provided meaningful insight into the feasibility of using *Spi1* shRNA to reduce PU.1 protein *in vivo*. Achieving a high infection rate and a large PU.1 knock-down proved challenging. Given that pMØ are far more accessible than microglia it suggested that stereotaxic injection of *Spi1* shRNA viruses into the brain was not a feasible approach for this thesis to take. A primary microglia culture system can still be used to model *in vivo* microglia with some accuracy, especially when supplemented with TGF- β , as discussed in section 1.3.2.3 [154,155]. Hence a primary microglia culture model was established, incorporating both TGF- β and lentiviral infection.

4.2.1.4 Validation in Primary Microglia

To assess the potential of the knock-down and over-expression lentiviruses *in vitro* established primary microglia cultures were infected with either *Spi1* shRNA virus or *Spi1* pSIEW virus. Figure 4.6A shows microscope images of primary microglia cultures taken after NS shRNA or *Spi1* shRNA 2 viral infection. There was no great difference observed in cell number or microglia morphology between the NS shRNA and *Spi1* shRNA 2 infected cultures. In the representative flow plots in Figure 4.6B there were virally infected microglia in both the NS shRNA and *Spi1* shRNA 2 cultures. As expected, there was a reduction in PU.1 expression in microglia infected with the *Spi1* shRNA 2 virus. The graph below (Figure 4.6C) shows the PU.1 expression in all virally infected microglia, normalised to the non-infected microglia. On average, all cultures infected with *Spi1* shRNA virus had a reduction in PU.1 protein of over 80 % compared to NS shRNA or non-infected controls. There was no substantial further decrease in the quantity of PU.1 protein when the *Spi1* shRNA viruses were combined compared to either *Spi1* shRNA virus separately. Going forward only the *Spi1* shRNA 2 lentivirus was used to target *Spi1* mRNA, and shall henceforth be referred to as *Spi1* shRNA.

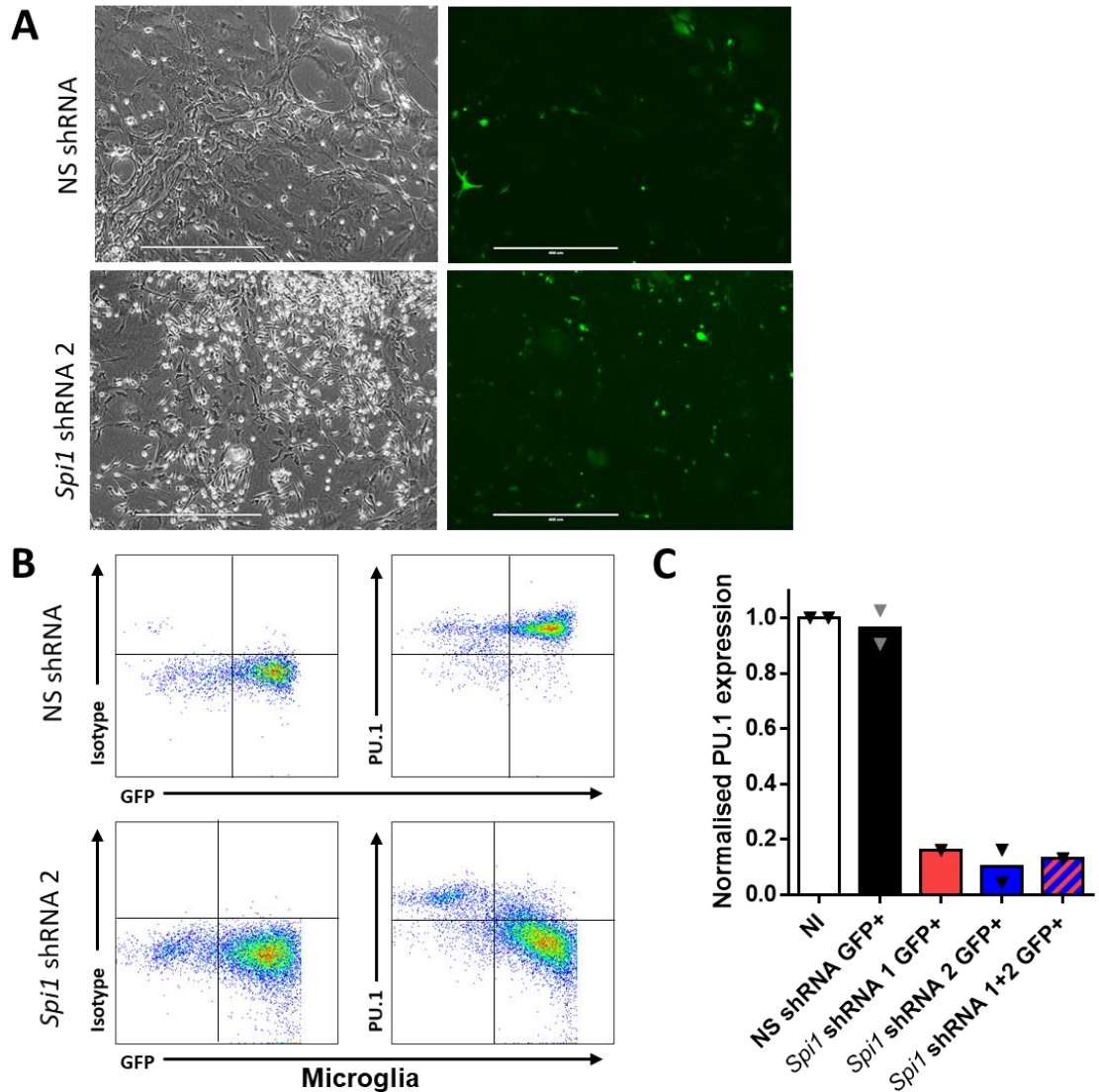


Figure 4.6 Piloting *Spi1* shRNA and PU.1 Over-Expression Viruses in Primary Microglia- Part I **A** Images of cultured microglia infected with shRNA virus. Both Bright-Field (Left) and GFP channel (Right) images were taken of each culture on the EVOS microscope at 10X magnification. There were no obvious differences in the morphology of microglia infected with NS shRNA or *Spi1* shRNA 2 virus. Scale bar shows 400 μ M. **B** Representative PU.1 and GFP expression in infected microglia. Microglia were pre-gated as CD11b⁺CD45⁺ cells. As expected PU.1 protein was reduced in microglia infected with *Spi1* shRNA 2 virus compared to microglia infected with the NS shRNA control. **C** Comparison of *Spi1* shRNA viruses in primary microglia. The PU.1 protein expression for the GFP⁺ cells in each virus sample was normalised to the MFI of the non-infected (NI) microglia. PU.1 expression was reduced by over 80 % in microglia infected with *Spi1* shRNA 1 or *Spi1* shRNA 2, though combining both *Spi1* shRNA's did not appear to produce any additional reduction. The results presented here are taken from two independent experiments, the bar shows the average for NI, NS shRNA and *Spi1* shRNA 2 samples (all n=2) and the individual experiment results are shown by symbols. One experiment used 9-week-old *Spi1*-ERT female mice and the other *Gata-6* WT 18-week-old females.

The next set of analyses examined the impact of infecting primary microglia cultures with the *Spi1* pSIEW over-expression virus. There was no discernible difference in the appearance of microglia cultures infected with either the *Spi1* pSIEW virus or the empty vector control pSIEW (Figure 4.6D). The strength of the GFP expression in pSIEW infected microglia appeared weaker than in shRNA-pSU6EW viruses. This was confirmed when the infected microglia were analysed through flow cytometry (Figure 4.6E). Both pSIEW viruses utilise an IRES, which is known to result in a lower expression of the a viral reporter [311] and can be down-regulated by primary cultured MØ [309]. Despite the low percentage of infected cells, PU.1 expression was still increased in the *Spi1* pSIEW infected microglia when compared to the empty pSIEW virus (Figure 4.6E). The over-expression of PU.1 protein in *Spi1* pSIEW and pSIEW infected microglia was presented in Figure 4.6F. It was apparent that *Spi1* pSIEW infected microglia had > 50 % increased PU.1 protein expression in comparison to pSIEW infected microglia or non-infected microglia. As PU.1 is a critical transcription factor in myeloid cells even a minor increase in PU.1 protein could lead to sizeable alterations to gene expression. Overall, these results indicate that both the PU.1 knock-down and over-expression viruses performed well in primary microglia cultures.

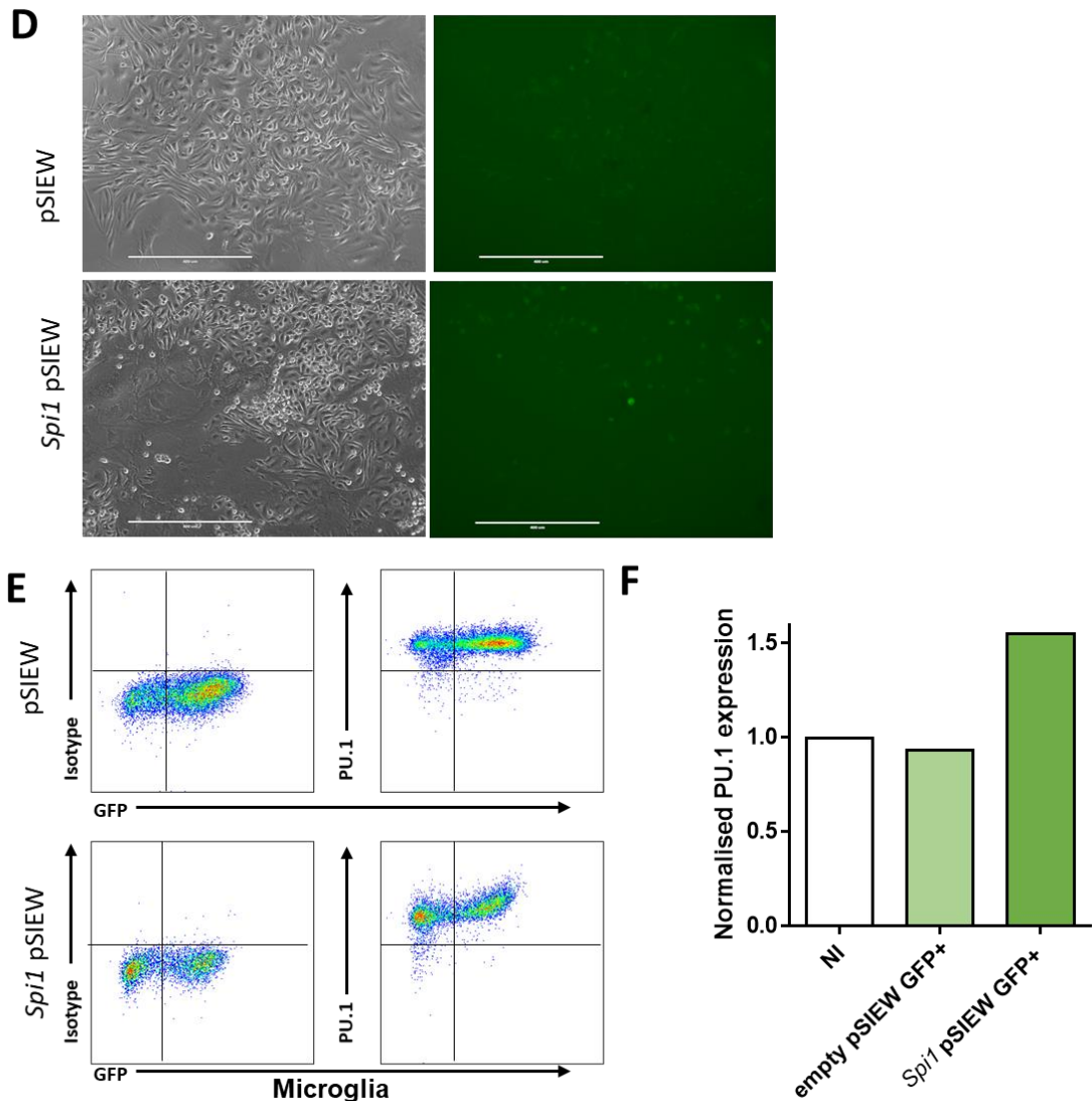


Figure 4.6 Piloting *Spi1* shRNA and PU.1 Over-Expression Viruses in Primary Microglia- Part II **D** Images taken of primary microglia cultures infected with *Spi1* over-expression virus or control (pSIEW) virus. There were no observable differences in the morphology or number of cultured cells (Bright field images- Left), and there were GFP positive infected cells (pictured Right), though GFP expression did appear to be weaker compared to the shRNA viruses. Again these images were taken at 10X magnification on the EVOS and the scale bar denotes 400 μ M. **E** Flow cytometry analysis of PU.1 and GFP expression in cultured microglia. Infected cells were harvested and stained for flow-cytometric analysis. The PU.1 and GFP expression are shown for microglia (CD11b⁺CD45⁺ cells) infected with either *Spi1* pSIEW or empty vector control pSIEW virus. An increase in PU.1 expression was observed in *Spi1* pSIEW cells with a higher GFP expression compared to control virus infections. **F** Normalised PU.1 expression in microglia infected with pSIEW or *Spi1* pSIEW. PU.1 protein expression in *Spi1* pSIEW infected cells was 50 % higher than control microglia. These results are from one experiment in 9-week-old *Spi1*-ERT female mice.

4.2.2 Optimisation of Primary Microglia Culture System

The next section of this chapter was concerned with improving the *in vitro* culture of microglia to better simulate microglia in an *in vivo* context. Briefly this included determining if lentiviral infection in mixed cultures was more beneficial than if purified microglia were infected, and at what points TGF- β and lentiviruses should be added to the culture.

4.2.2.1 *Tmem119 as a Marker for Cultured Microglia*

Tmem119 was recently shown to discriminate between native microglia from any monocytes that have adopted a “microglia-like” phenotype [108]. However, as shown in Figure 4.7 there were some difficulties that prevented the inclusion of Tmem119 staining in the flow cytometric sorting panel. Firstly Papain, an enzyme in the NTDK (Miltenyi), has lots of potential cleavage sites in Tmem119 (Figure 4.7A). As shown in Figure 4.7B if papain (blue) was present in the digestion mix then Tmem119 expression could not be detected, whereas brains that were digested without papain (red) Tmem119 was present. Moreover, Tmem119 expression was found to be downregulated in cultured cells (Figure 4.7C) even in the presence of TGF- β , as confirmed by qPCR analysis (Figure 4.7D). Therefore Tmem119 was not used to sort cultured microglia in flow-cytometric based sorting.

A Tmem119

Translation (280 aa):

MVPWF^SLSLL^LARPVPGVAYSVS^LPAS^FEDVAGSGEAE^GSSASSPS^LPPP^GTPAFSPTP
 ERQP^TALDGPVPP^TN^LEGIMDFFRQYVM^LI^AVVGS^LTF^LIMFIV^CAA^LITRQKHKATA
 YYPSSFPEKKYVDQRDRAG^GPRTFSEVPDRAPDSRHEEG^LDTSHQ^LQADI^LAATQNLRS
 PARAL^PGN^GEGAKPVK^GGGSEEEEEV^LSGQEEAQEAPV^CGVTEEK^LGVPEESVSAEAE
 GVPATSE^GQGEAE^GSFS^LAQESQ^GATG^PPPESP^CACNRVSPSV

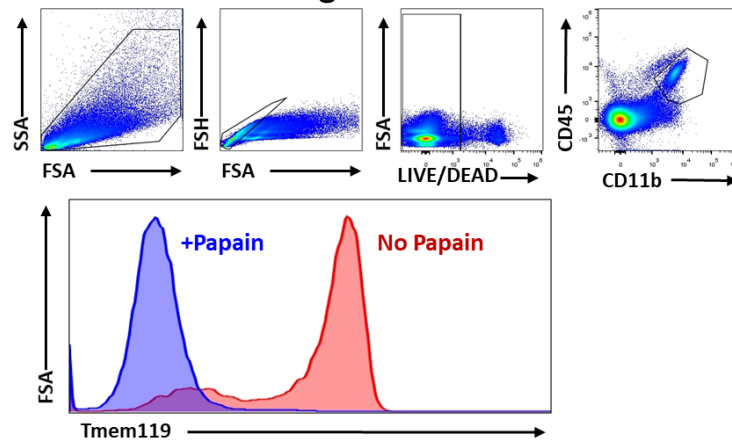
Cysteine

Leucine

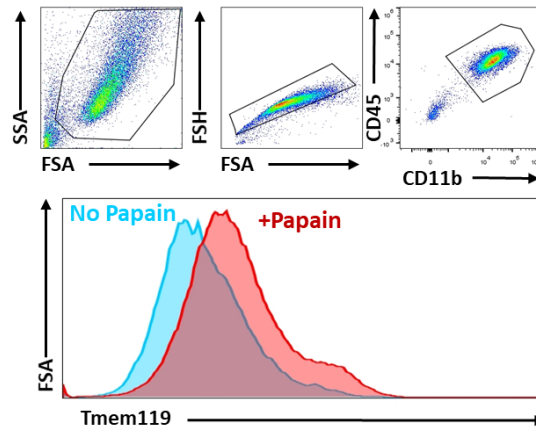
Glycine

All cut by Papain

B Fresh Ex Vivo Microglia



C Cultured Microglia



D Tmem119 Expression (UBC Endogenous Control)

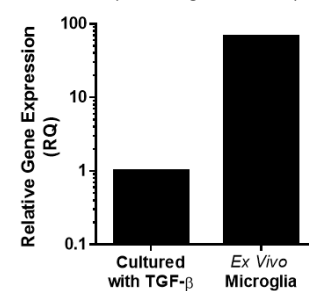


Figure 4.7 Tmem119 Antibody Staining in Fresh and Cultured Microglia. **A** Translation sequence of Tmem119. All potential Cysteine (pink), Leucine (green), and Glycine (blue) sites where the Papain enzyme could cleave the Tmem119 receptor. **B** Tmem119 Receptor Expression in Brains digested with and without Papain. Debris was removed from the samples. Live singlet cells were then selected before CD11b⁺CD45^{low} Microglia were gated on. Extracellular Tmem119 antibody staining was then observed (Histogram). The addition of Papain (blue) to the digestion mixture appears to cleave the Tmem119 receptor, as when Papain was removed from the initial brain tissue digest protocol (red) Tmem119 expression was easily detected. **C** Tmem119 Receptor Expression Appears to be Reduced in Cultured Microglia. Brains that were digested with and without the papain enzyme were cultured for 14 days (with TGF- β added from day 5 onwards) before being stained for analysis by flow-cytometry. The gating strategy has selected single microglia cells (CD11b⁺CD45⁺) before Tmem119 expression was observed (Histogram). In the cultured cells there does not seem to be as high expression of extracellular Tmem119 irrespective of the presence (red) or absence (blue)

of papain in the tissue digest, compared to primary cells (B). D Tmem119 mRNA Expression in Cultured and Freshly Isolated Microglia. Relative gene expression (RQ) was calculated relative to the UBC endogenous control. A much higher level of Tmem119 mRNA was detected in freshly isolated Ex Vivo than was detected in cultured microglia, even in the presence of TGF- β . The microglia used in this experiment came from 9-week-old female CD45.1 C57BL/6J mice.

4.2.2.2 Is viral Infection more effective in mixed-glia cultures or isolated Microglia

The efficiency of lentivirus infection was tested in primary mixed cell cultures and mixed cultures that had been CD11b⁺ bead purified before infection. As can be seen from the flow plots (Figure 4.8A) microglia (CD11b⁺F4/80⁺) were present in both cultures. Figure 4.8B illustrates the percentage of microglia seen in both culture conditions. At lower lentiviral titres a higher proportion of microglia were present in the mixed glia cultures. The percentage of GFP⁺ infected microglia for each viral dose in each culture are set out in Figure 4.8C. Irrespective of the amount of virus added a higher proportion of infected cells measured in mixed cell cultures compared to pre-purified cultures. From this data it appeared microglia benefitted from trophic support provided by other cells in culture, such as astrocytes, during the viral infection.

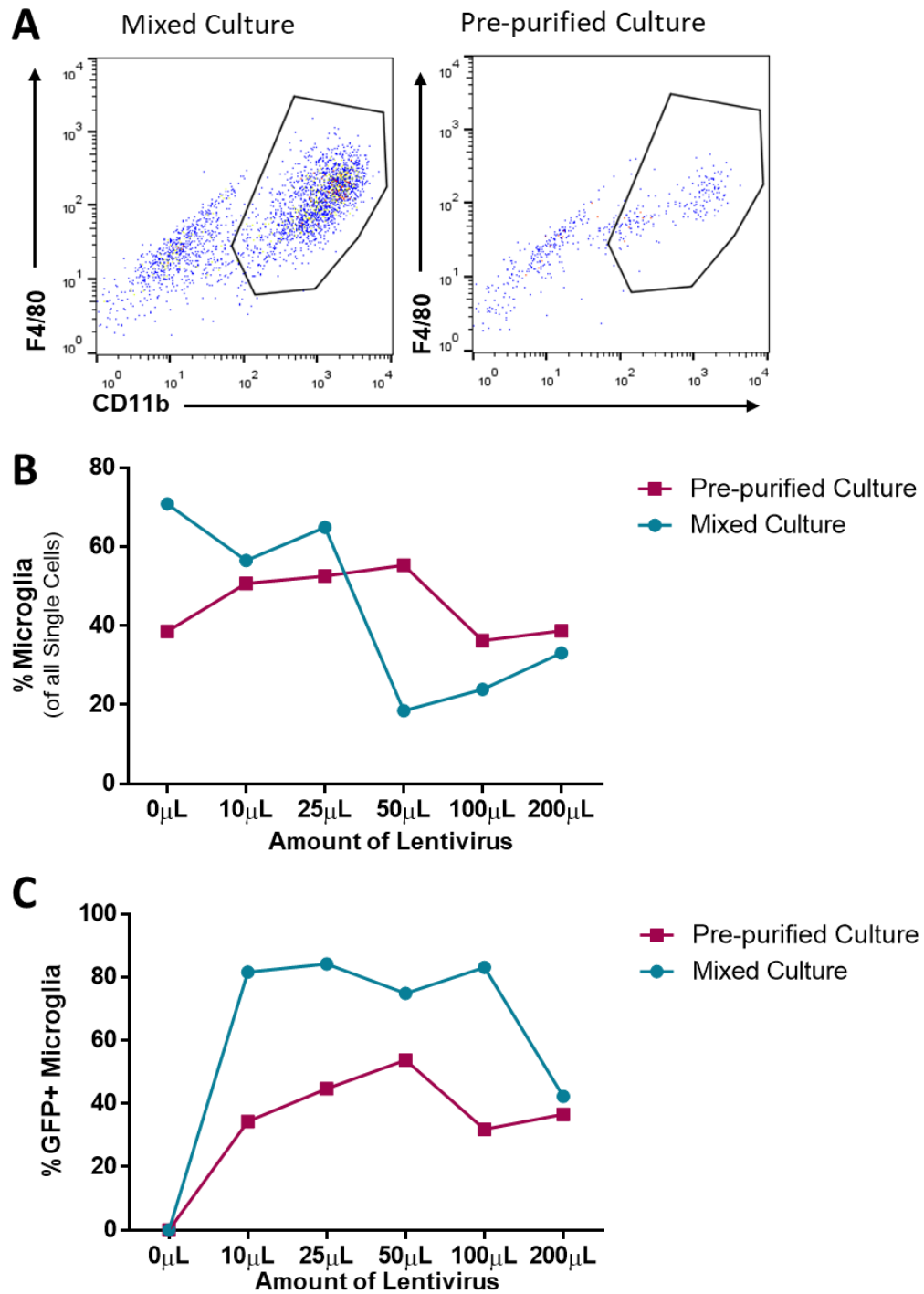


Figure 4.8 Pilot Experiment to determine if Microglia should be purified before viral infection. **A** Flow-Cytometry plots of stained cultured microglia. Microglia were cultured for 10 days. At the point either microglia remained as mixed glia cultures or underwent a CD11b+ purification before viral infection. Both primary microglia cultures were then infected with NS shRNA virus for 3 days. There appears to be a higher cell number in mixed cultures. **B** Percentage of Microglia in each culture system. At lower viral infections there were a higher percentage of microglia (CD11b⁺F4/80⁺ cells) in the mixed glia cultures, though this does not seem to be accurate at higher viral doses where there was a slightly higher proportion of microglia in the CD11b purified cultures. **C** Proportion of Infected Microglia gained from each culture method. The percentage of infected microglia was also assessed at each viral dose. Each viral dose had a larger percentage of infected

microglia was seen in mixed cell cultures compared to pre-purified cultures. The microglia were cultured from 13-week-old GATA-6 WT male mice.

4.2.2.3 Determining when to start TGF- β supplementation

Recent reports have shown the addition of TGF- β *in vitro* contributes to a phenotype more characteristic of resting *in vivo* microglia [154,155]. Thus, it was proposed that TGF- β would improve the physiological relevance of this *in vitro* model. To determine when TGF- β should be included in the microglia culture media an initial experiment was designed where 50 ng/mL TGF- β was added to microglia on D0, D5 and D7 of culture alongside an M-CSF only control. On day 14 qPCR was used to assess to the expression of 6 homeostatic microglia genes, that have been reported to be increased by TGF- β expression [154]. Figure 4.9 shows the results of this analysis. The first replicate (Figure 4.9A) suggested that adding TGF- β on day 0 of culture did not appear to be as beneficial as adding TGF- β at day 5 or day 7. The second replicate (Figure 4.9B) showed TGF- β induced high expression of these microglia genes irrespective of what stage it was added to the culture media, which was expected from the literature [154]. In both replicates *Siglech* mRNA was the most robustly changed by TGF- β expression, suggested it could be a good measure to assess the impact of TGF- β on cultures. Overall these experiments suggest that the addition of TGF- β at day 5 or day 7 will still result in the expression of these genes. Given that TGF- β has the potential to inhibit microglia proliferation [341,342] these later timepoints were chosen to give microglia time to proliferate.

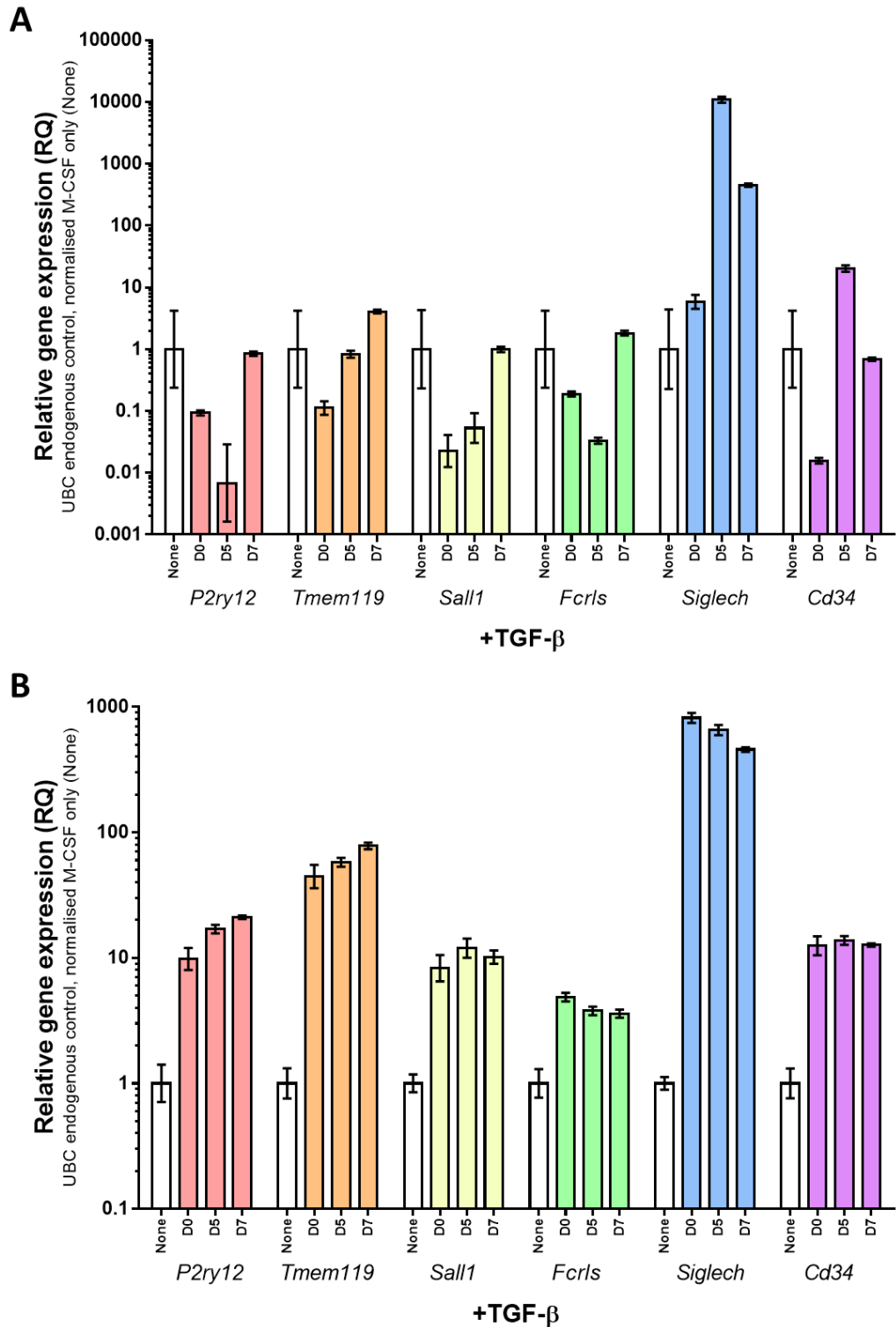


Figure 4.9 The impact of TGF-β addition on microglia gene expression at different times. **A** The first replicate of this experiment. In this replicate TGF-β did not have the large impact on gene expression that was expected, except for Siglech which was increased when TGF-β was added at day 5 and day 7 of culture. Overall day 5 and day 7 seemed to provide the most changes to gene expression, compared to D0. **B** In the second replicate, TGF-β caused robust increases in gene expression irrespective of the time at which TGF-β

was included in the culture media. The results presented here are the result of two independent experiments. All microglia were cultured for 2 weeks from the brains of female C57BL/6J mice aged 8 weeks. The error bars denote the upper and lower limits between technical replicates.

4.2.2.4 Determining order TGF- β and virus in Microglia cultures

The second set of experiments were performed to distinguish whether TGF- β should be added before viral infection with an empty vector pSFEW plasmid or after. Moreover, this assessment will indicate if giving TGF- β two weeks into culture will still result in robust gene expression changes.

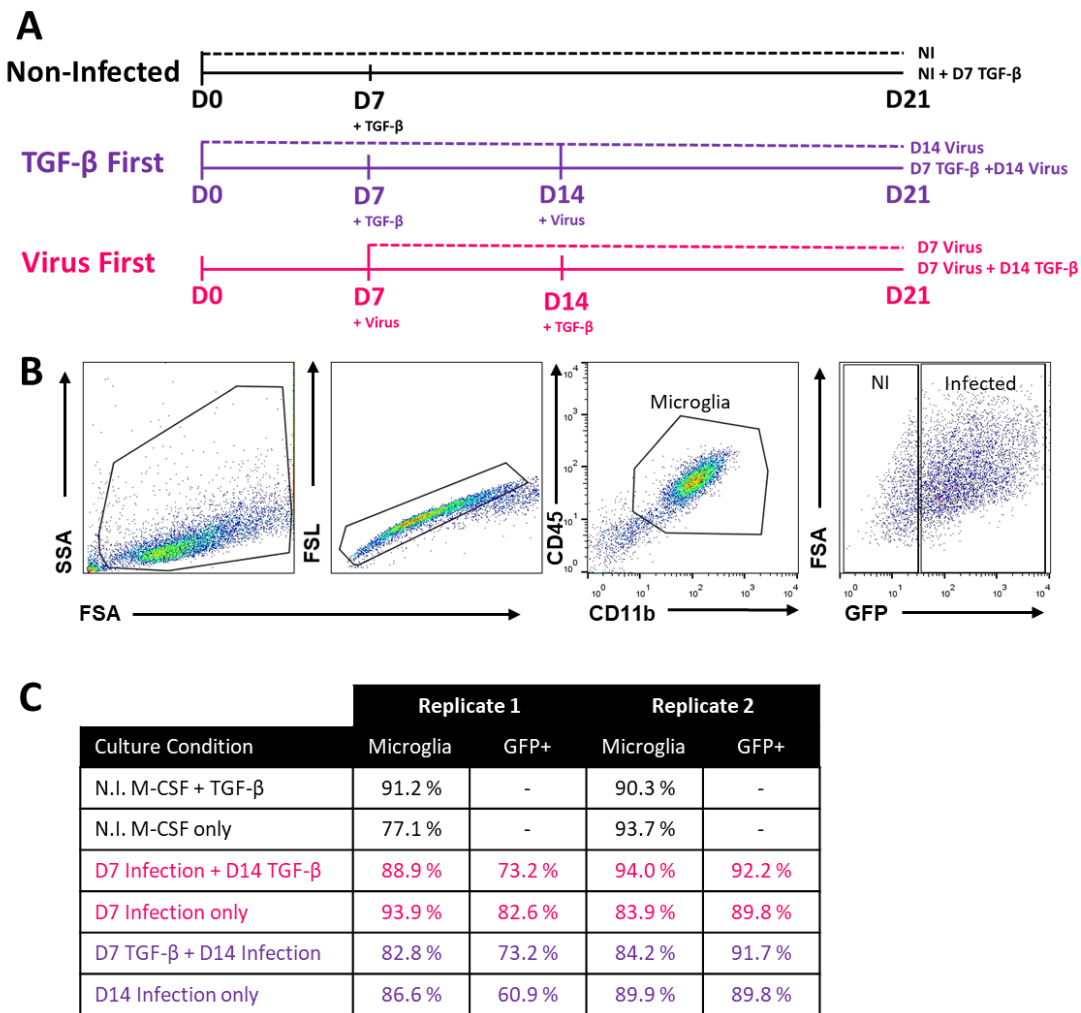


Figure 4.10 Determining if TGF- β should be added to cultures before or after lentivirus. **A** Experimental Plan. Cultures were established on day 0. On day 7 either TGF- β (purple) or empty vector pSFEW virus (pink) was added to the appropriate mixed cell cultures, as indicated in the timeline. On Day 14 TGF- β (pink) and virus (purple) were added to the desired samples. All cultures were harvested after 21 days in culture. Some cells were taken for flow analysis and RNA was extracted from the remaining sample. **B** Gating Strategy used in flow-cytometric analysis. Cells were first separated from debris and doublet cells excluded from each sample. CD11b⁺CD45⁺ surface staining was then used to select the microglia. The final flow plot shows the GFP expression in microglia, allowing the number of infected microglia (GFP+) to be calculated. **C** Summary

the distribution of Microglia, and Infected Microglia in each Culture Condition. All culture conditions resulted in a high proportion of microglia, over 70 % of all single cells and a large number of these microglia were infected. Non-infected (N.I.) cells were also found to have a high percentage of microglia. The data in this figure were taken from two independent replicate cultures made from C57BL/6J female mice aged 8 weeks.

Figure 4.10A (above) illustrates the experimental timelines used in this experiment. All cultures were maintained with M-CSF supplemented media alone until day 7. On day 7 TGF- β was added to the appropriate non-infected (black) and “TGF- β first” (purple) cultures. The “virus first” cultures (pink) were infected with empty pSFEW virus at this timepoint. On day 14 of culture pSFEW virus was added to all the “TGF- β first” cultures (purple) and one “virus first” culture infected on day 7 was supplemented with TGF- β cytokine (pink). The flow-cytometry gating strategy used to determine the percentage of infected microglia in each sample is shown in Figure 4.10B. Following debris and doublet exclusion, microglia were selected using the M \emptyset surface expression markers CD11b and CD45. Finally, the percentage of pSFEW infected cells was determined by comparing the GFP expression to the non-infected samples. The values determined from flow-cytometric analysis are displayed in Figure 4.10C. All samples had a high proportion of infected microglia. These results indicate that infecting microglia before supplementing media with TGF- β might provide better results, but this analysis does account for changes to the selected homeostatic genes. Figure 4.11 and Figure 4.12 show that the addition of TGF- β and virus affected the relative gene expression of several fundamental microglia genes.

In the first repeat of this experiment (Figure 4.11) *Siglech*, *Tmem119* and *Cd34* gene expression were higher when microglia cultures were infected with virus before TGF- β (pink lined) compared to the relative M-CSF only control (pink). When microglia cultures were given TGF- β supplementation before viral infection (purple) only *Cd34* mRNA expression was increased in the first replicate. In the second replicate of this experiment (Figure 4.12) TGF- β increased expression of all the measured genes compared to their M-CSF only controls, though in *Cd34* gene expression this increase was modest. The “TGF- β first” cultures (purple) *Tmem119* and *Fcrls* gene expression was higher than “virus first” cultures (pink). While TGF- β *Sall1* mRNA expression was lower in the cultures supplement with TGF- β before viral infection than cultures given TGF- β post-infection, *Fcrls* expression was equally impacted by TGF- β irrespective of the order TGF- β and virus were added. Despite having less available data, the second replicate suggests that giving TGF- β before viral infection resulted in more beneficial gene changes. This was supported by *Cd34* and *Siglech* gene expression data from the first replicate, though *Tmem119* was higher in “virus first” (pink) cultures than “TGF- β first” (purple) cultures. Biologically the expression of several key microglia

genes, such as *Tmem119*, have been shown to decrease once removed from the brain [155]. Additionally, the previous section (4.2.1.3) suggested the *Spi1* shRNA viruses become less effective after 7 days. Taken together this suggested TGF- β should be administered before virus to try and partially maintain homeostatic microglia gene expression.

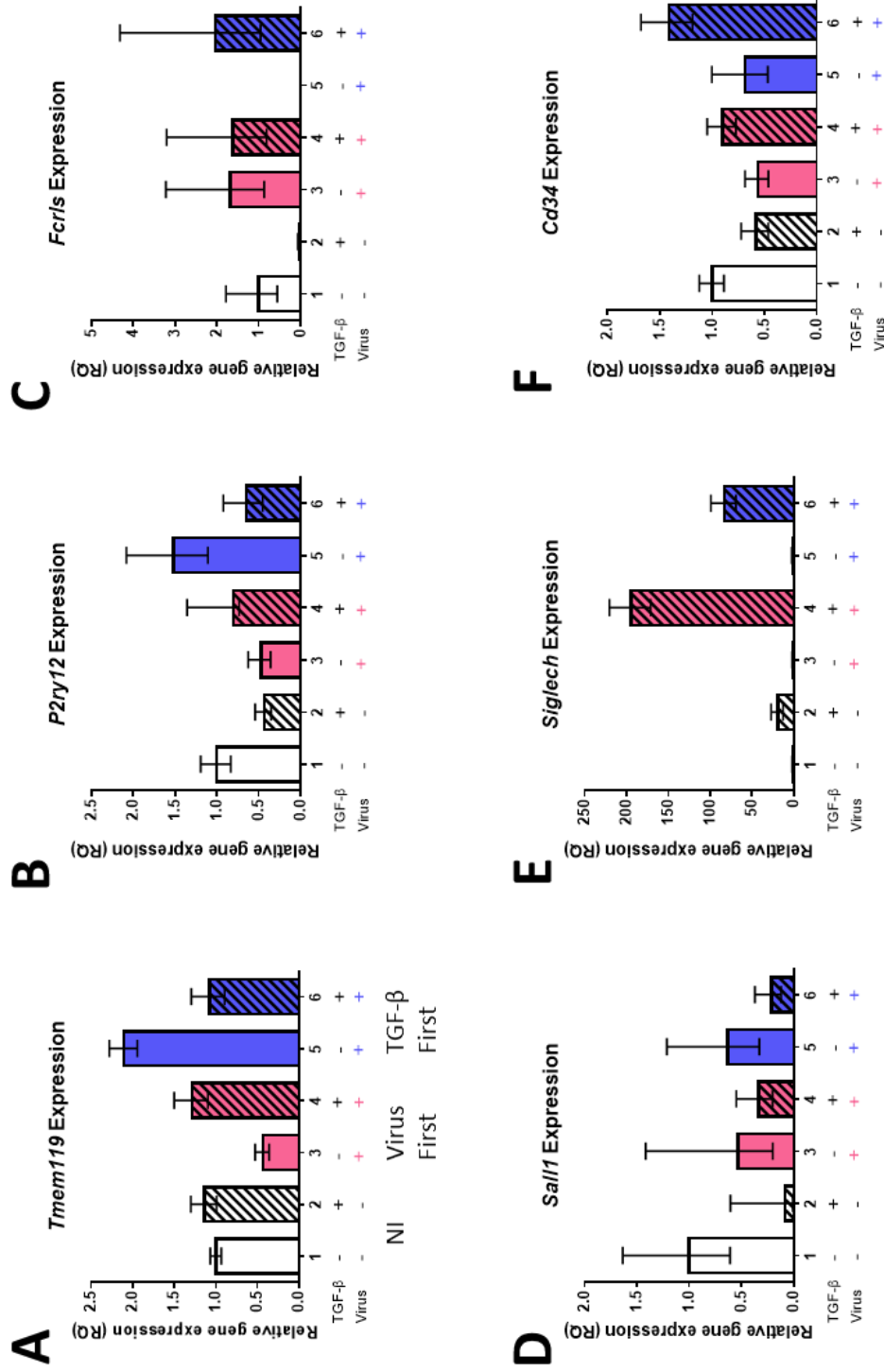


Figure 4.11 qPCR analysis of the impact of TGF- β and Virus order on Cultured Microglia Gene Expression. Replicate 1. Relative gene expression (RQ) for each microglia specific gene was calculated relative to the Ubiquitin C (UBC) endogenous control gene expression. Tmem119, P2ry12 and CD34 expression (A, B and F), all seem to benefit from receiving TGF- β before virus (purple lined bars). Siglech expression (E) was higher in samples that received virus before the addition of TGF- β (pink lined bars). Neither Sall1 or Fcrls gene expression (C and D) seem to be affected by the order in which TGF- β or virus were added to the culture, though the addition of TGF- β does seem to have an effect on mRNA expression of these genes. The microglia were cultured from 8-week-old female C57BL/6J mice. The error bars indicate the upper and lower limits between the technical replicates.

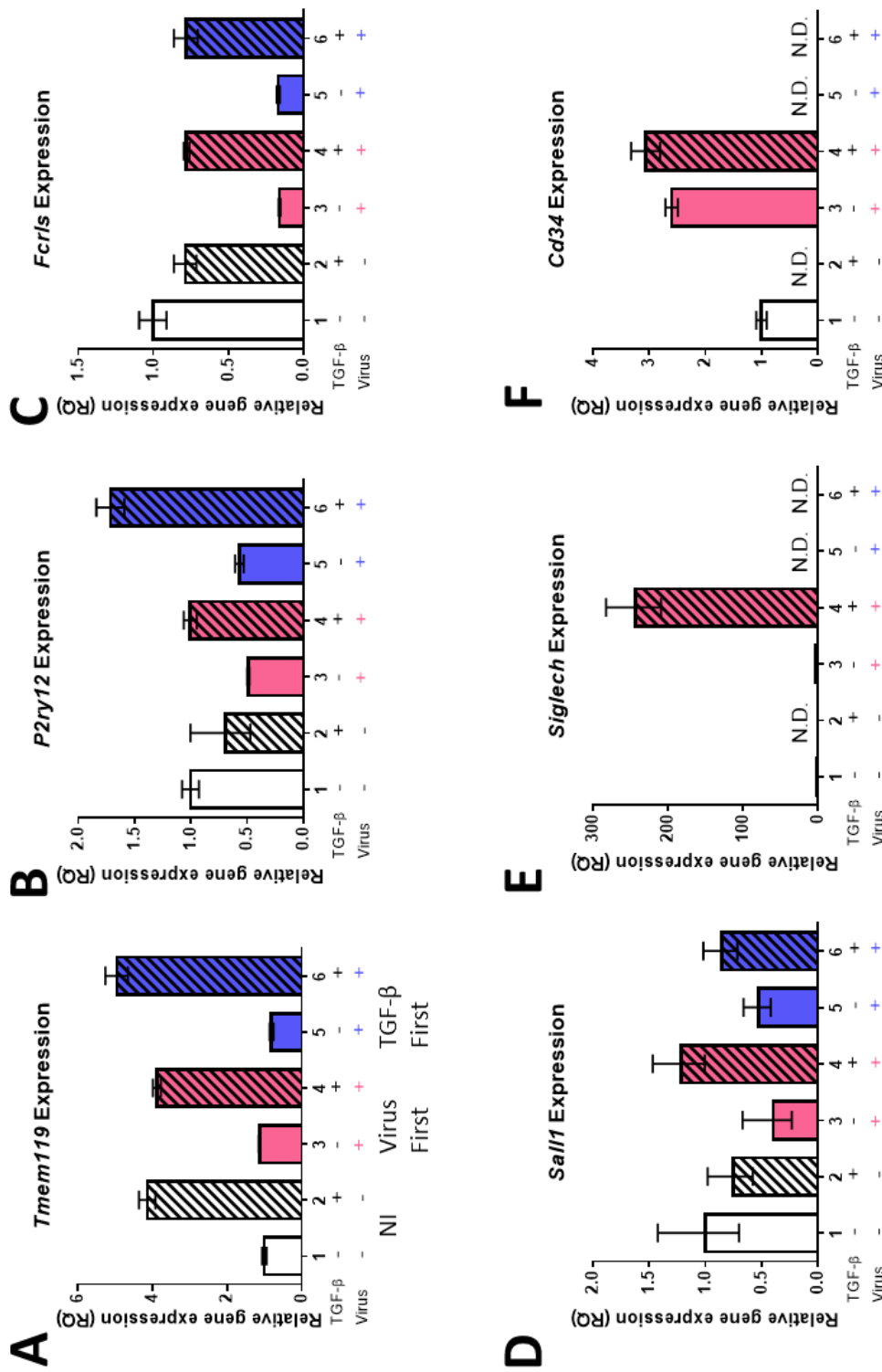


Figure 4.12 qPCR analysis of the impact of TGF- β and Virus order on Cultured Microglia Gene Expression. Replicate 2. Relative gene expression (RQ) for each microglia specific gene was calculated relative to the Ubiquitin C (UBC) endogenous control gene expression. *Tmem119*, *P2ry12*, *Fcrls* and *Sall1* expression (A-D), all seem to benefit from receiving TGF- β before virus (purple lined bars). *Tmem119*, *P2ry12*, *Fcrls*, *Sall1* and *Siglech* expression (A-E) was higher in samples that received virus before the addition of TGF- β (pink lined bars). *CD34* gene expression did not appear to be hugely impacted by the addition of TGF- β (F). The microglia were cultured from 8-week-old female C57BL/6J mice. The error bars indicate the upper and lower limits between the technical replicates.

4.2.2.5 *Determining optimal timepoint for addition of virus*

The final optimisation experiment aimed to ascertain the optimal time for lentivirus to be included in these cultures. As laid out in Figure 4.13A TGF- β was added to half the cultures on day 5 and cultures were then infected with equal volumes of empty vector pSFEW virus at 7, 10 and 14 days after initial plating. Microglia cultures that were infected 7 days after plating were harvested after 14 days, alongside non-infected control microglia. Cultures infected at the later timepoints were maintained for 21 days. The results obtained from the 14-day cultures are presented in Figure 4.13B. Microscope images taken of M-CSF only and M-CSF/TGF- β cultures before harvest indicate that the addition of virus and TGF- β in close proximity results in a reduced cell number (Figure 4.13B2). No overt changes in cell number were observed in non-infected cultures with M-CSF alone or M-CSF/TGF- β (Figure 4.13B1) or in virally infected cultures where microglia media was supplemented with only M-CSF. Microglia infection was then analysed using flow cytometry. The proficiency of viral infection was not altered by the addition of TGF- β to the microglia cultures. There was an indication that the strength of GFP expression was slightly higher in infected microglia cultured with M-CSF alone compared to cells cultured with M-CSF/TGF- β combined. However, it was hard to draw meaningful conclusions at this timepoint due to the small number of cells in these cultures. Figure 4.13C compares the results from the cultures harvested at 21 days. When the virus was added to M-CSF/TGF- β cultures at the later timepoints, day 10 and day 14, it did not appear to have any substantial effect on the number of cells in culture (Figure 4.13C). The images presented below propose that percentage of GFP+/infected cells was comparable across all virally infected cultures. Analysis of flow-cytometry data still appeared to demonstrate a minor increase in the strength of viral infection of M-CSF viral cultures when compared to M-CSF/TGF- β viral cultures (Figure 4.13C).

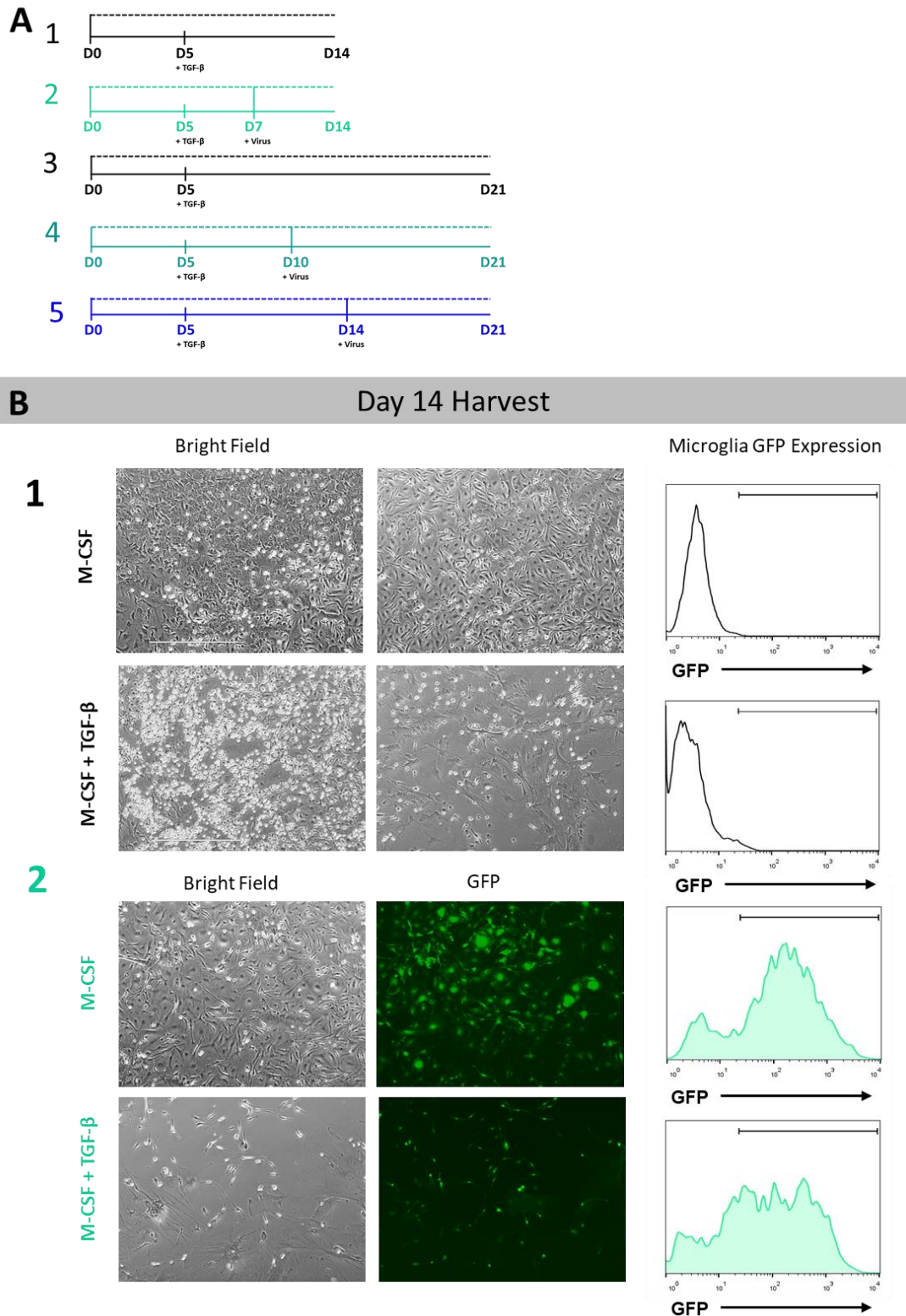


Figure 4.13 Pilot to Optimise the best time to add Virus to Microglia Cultures- Part I **A** Experiment design Cultured cells were harvested after either 14 days (1 and 2) or 21 days (3-5). Both 1 and 3 were non-infected controls, while 2, 4 and 5 had virus added after 7 days, 10 days and 14 days respectively. **B** Data from Cultures Harvested after 14 days. Pictures were taken of each culture well, Non-Infected with and without TGF-β (1) as well as mixed cell cultures which received virus on day 7 (2). In culture 2 where TGF-β and virus

were added two days apart there appears to be a reduced number of cells. The flow plots, gated on microglia first ($CD11b^+CD45^+$), show the distribution of infected cells across both M-CSF only and M-CSF + TGF- β cultures.

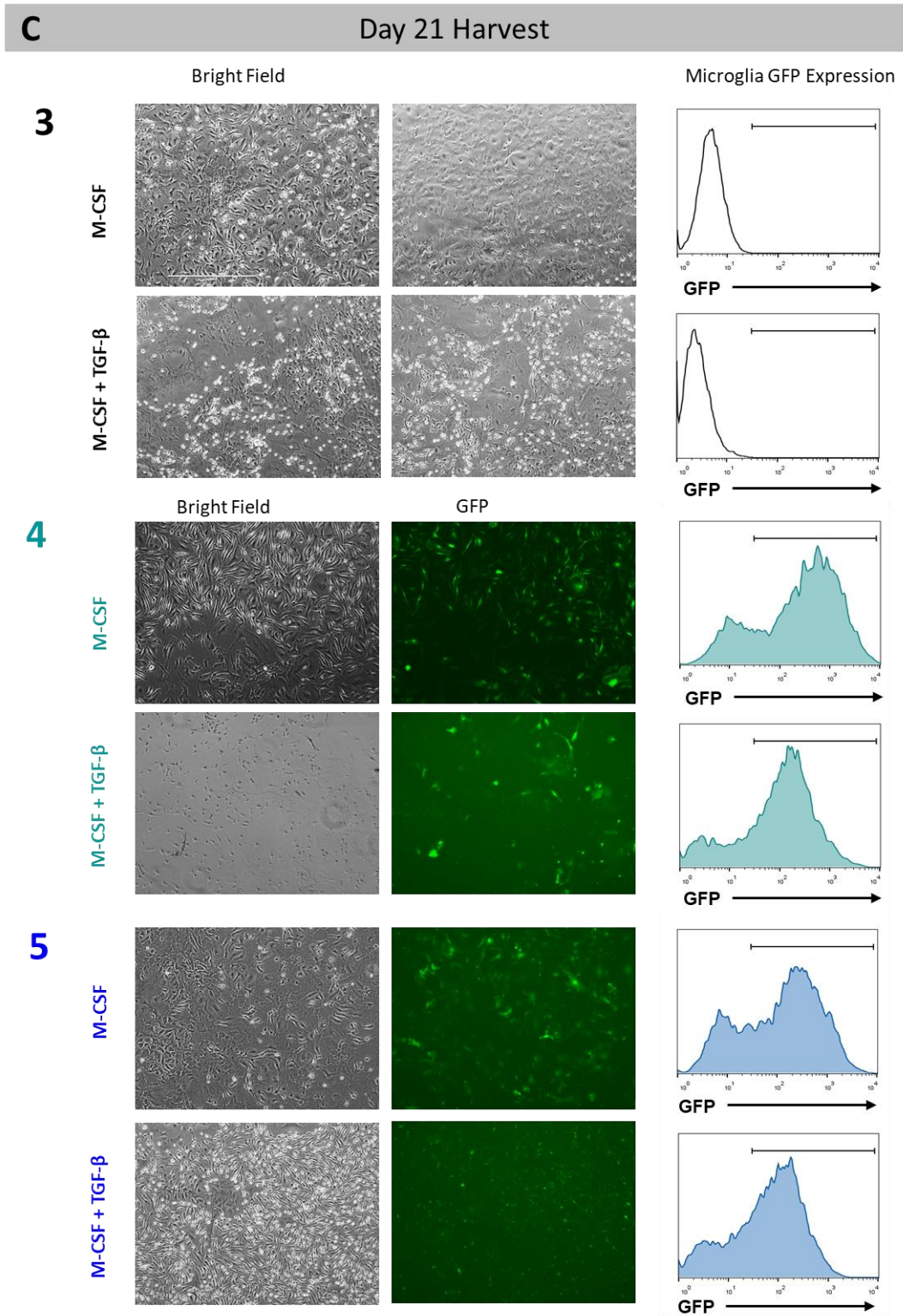


Figure 4.13 Pilot to Optimise the best time to add Virus to Microglia Cultures- Part II Results following the 21 day harvest. C Pictures and flow-cytometry plots taken from cultures 3-5 after 21 days in culture. Bright-

field images show no apparent difference in cell morphology or number between M-CSF and M-CSF + TGF- β non-infected cultures (3). The distribution of GFP expression in cultures infected after 10 days (4) appear to be slightly higher in microglia cultured with M-CSF alone compared to cultures supplemented with M-CSF + TGF- β . A similar trend was seen in cells infected 14 days after initial plating (5). The cell number in M-CSF + TGF- β cultured cells (4 and 5) does not appear to be drastically different when compared to the relative M-CSF cultured cells. The data presented here are from one culture experiment using were cultured from 8-week-old female C57BL/6J mice.

It can be seen from the data in Table 4.2 that the percentage of microglia was quite consistent across all culture conditions, excluding the infected microglia harvested at day 7 in the second repeat. The proportion of GFP+ infected microglia was slightly lower in cultures with TGF- β at each timepoint. This was not unexpected as TGF- β has been previously shown to reduce the efficiency of viral infections [195,196]. As the objective was to determine the influence of TGF- β on microglial gene expression in combination with lentivirus it was concluded that the level of infection was satisfactory for future experiments, especially when the virus was added 10 days into the cultures.

Culture Conditions 14-Day	Replicate 1		Replicate 2	
	Microglia	GFP+	Microglia	GFP+
Non-Infected M-CSF only	88.7 %	-	85.3 %	-
Non-Infected M-CSF + TGF- β	90.1 %	-	87.4 %	-
D7 Virus Infection M-CSF only	93.4 %	80.6 %	51.6 %	91.2 %
D7 Virus Infection M-CSF + TGF- β	82.1 %	71.0 %	38.0 %	97.7 %
Culture Conditions 21-Day	Microglia	GFP+	Microglia	GFP+
Non-Infected M-CSF only	86.9 %	-	83.9 %	-
Non-Infected M-CSF + TGF- β	92.4 %	-	99.0 %	-
D10 Virus Infection M-CSF only	81.4 %	80.6 %	96.2 %	76.9 %
D10 Virus Infection M-CSF + TGF- β	96.8 %	76.4 %	91.2 %	67.4 %
D14 Virus Infection M-CSF only	92.3 %	73.2 %	91.9 %	83.5 %
D14 Virus Infection M-CSF + TGF- β	91.1 %	69.3 %	95.0 %	71.1 %

Table 4.2 An Overview of the Percentage of Infected Microglia in each Culture Condition. The percentage of microglia was determined from the number of CD11b⁺CD45⁺ single cells in each sample, along with the proportion of GFP+/Infected microglia as appropriate. The data presented here are from two independent replicates where microglia were cultured from 8-week-old female C57BL/6J mice.

The qPCR analysis from the 14-day and 21-day cultures can be seen from the bar graphs detailed below (Figure 4.14-Figure 4.15). It was apparent from these graphs that the expression of most of these microglia genes were responsive to the addition of TGF- β . In the first replicate (Figure 4.14) these genes included *Tmem119*, *P2ry12*, *Siglech* and *Cd34* which all showed increased gene

expression in the presence of TGF- β (lined bars) compared to microglia cultures only supplemented with M-CSF (empty bars). In the second replicate (Figure 4.15) only *Fcrls* and *Siglech* were increased in cultures with TGF- β in the 21-day harvest. A more unexpected finding in this qPCR data was in the effect viral infection had on expression of these microglia genes. This was especially evident in the 14-day cultures, where cells were infected 2 days after TGF- β supplementation began. In there was a clear reduction in gene expression in *Tmem119*, *P2ry12*, *Fcrls*, *Siglech* and *Cd34* in TGF- β + microglia cultures infected one week into culture (Lane 4) when compared to the relative non-infected control (Lane 2). This same pattern was also seen in the second repeat of this experiment (Figure 4.15) in all genes except *P2ry12*.

In 21-day TGF- β supplemented cultures that were infected with virus at later timepoints, day 10 (Lane 8) and day 14 (Lane 10), no substantial alterations to gene expression were noted in the first repeat (Figure 4.14). However, in the second repeat while both *Fcrls* and *Siglech* expression were increased as a result of TGF- β expression this increase was more moderate in virally infected cells (Figure 4.15). In the second repeat the expression of the other genes was either unchanged by TGF- β in infected cells, *P2ry12* and *Cd34*, or were higher in M-CSF only samples at one of the timepoints (*Tmem119* and *Sall1*).

Taken together these results suggest that adding virus to microglia cultures two days after the first TGF- β supplementation (day 7) was not the best approach. Broadly speaking neither the percentage of infected or the qPCR gene expression profiles appeared to be similar whether microglia were infected at day 10 or day 14. While the full implications of these experiments will be discussed in section 4.3.1, it was decided that a 21-day where microglia were given TGF- β on day 5 and lentivirus on day 10 was a good approach to ensure a large proportion of infected microglia with an improved gene expression profile. These were the conditions used for the *in vitro* cultures sent for mRNA sequencing.

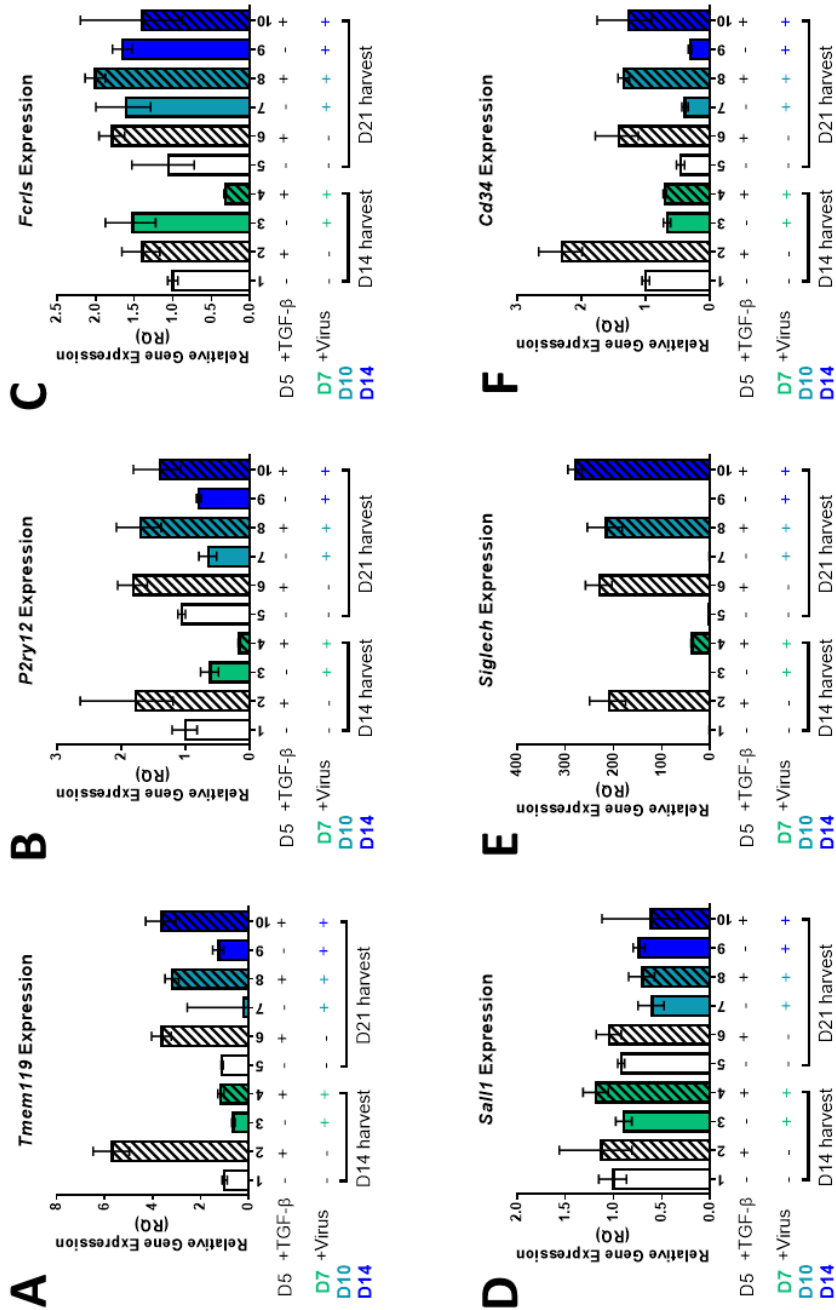


Figure 4.14 qPCR Analysis of Virus Optimisation Experiment- Replicate 1. Relative gene expression (RQ) was calculated with reference to gene expression from the UBC endogenous control. All lined bars represent cultures treated with M-CSF + TGF- β whereas unfilled bars show gene expression in cultures supplemented with M-CSF alone. The addition of TGF- β to these primary microglia cultures appears to increase the expression of these microglia specific genes across all samples (A-F). The increase in TGF- β induced gene expression was especially prominent in Tmem119 (A), P2ry12 (B), Siglech (E) and CD34 (F). The addition of virus to these cultures has had an effect on expression of certain genes, especially when virus was added at day 7 (green) when compared to 14 day non-infected cultures (white). In cultures that were infected at day 10 (light blue) and day 14 (dark blue) of culture the largest impact appears to be on Sall1 (D) and Fcrls (C) gene expression, compared to the 21-day non-infected culture (white). The error bars indicate the upper and lower limits between the technical replicates. The microglia were cultured from 8-week old C57BL/6J mice.

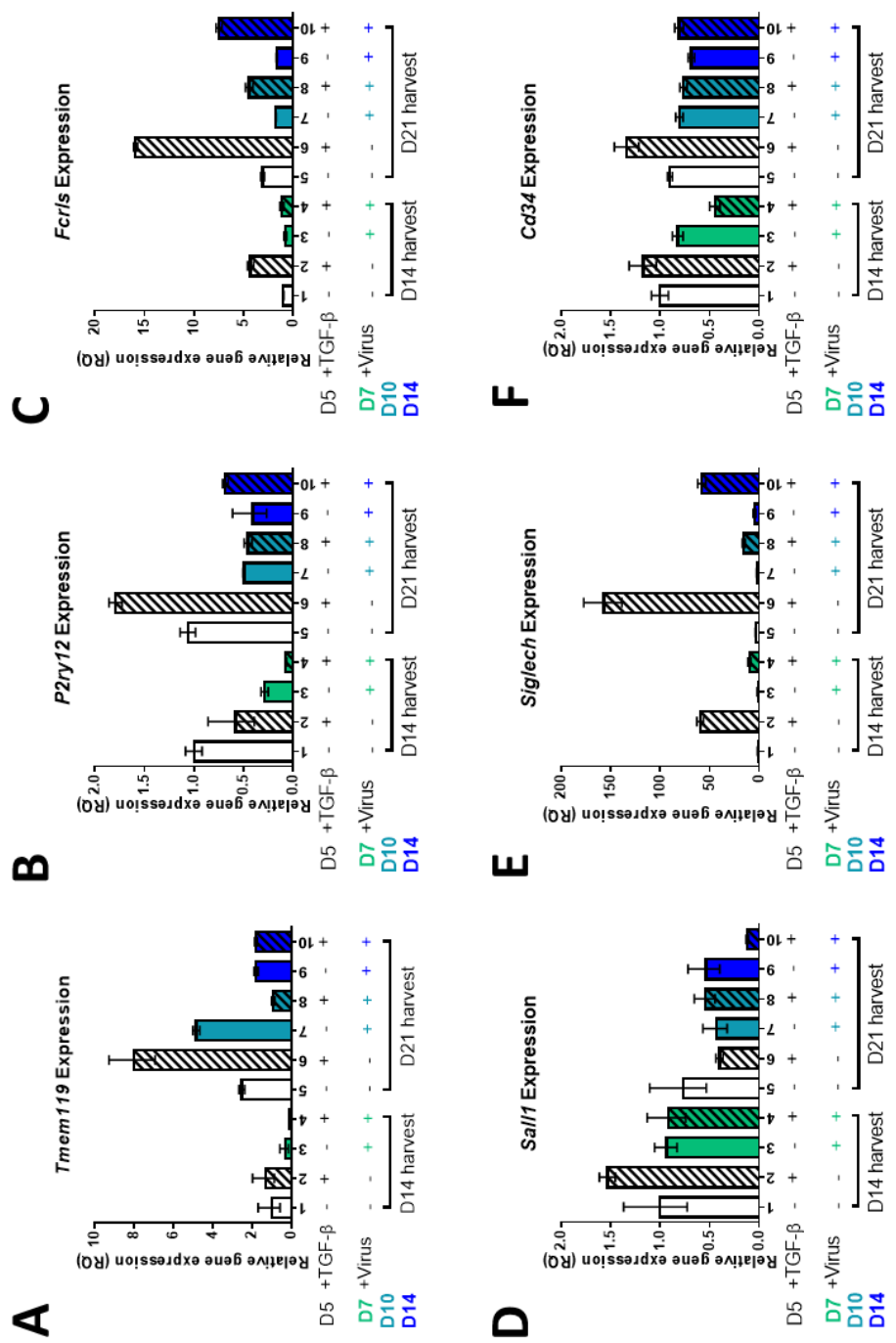


Figure 4.15 qPCR Analysis of Virus Optimisation Experiment - Replicate 2. Relative gene expression (RQ) was calculated with reference to gene expression from the UBC endogenous control. All lined bars represent cultures treated with M-CSF + TGF-β whereas unfilled bars show gene expression in cultures supplemented with M-CSF alone. Here the highest TGF-β induced gene expression changes were seen in the NI cells of the 21-day harvest (A-C, E, F). Again viral infection appeared to reduce the impact of TGF-β on gene expression in all genes, though increases were still observed in C Fcrl5 (21-day harvest) and E Siglech (21-day harvest). The error bars indicate the upper and lower limits between the technical replicates. The microglia were cultured from 8-week old C57BL/6J mice.

4.2.3 Primary Microglia Cultures used for mRNA Sequencing

The final part of this chapter sets out the implementation of the *in vitro* culture system optimised in the preceding section to gain the samples for RNA sequencing, described in 2.4.9.1.

4.2.3.1 Microglia Cultures

Figure 4.16A summarises the experimental timeline used in these microglia cultures. On day 0 brains from 8-week-old female C57BL/6J mice were digested and plated. Ten mice were used for each experiment to ensure there were sufficient sorted microglia to get enough mRNA for RNA-Seq. All cultures were supplemented with TGF- β at day 5, which was replenished when the media was changed every 2-3 days. After 10 days in culture the plates were infected appropriate *Spi1* knock-down or over-expression lentiviruses, except for the non-infected control plate which received media instead. After 3 weeks in culture cells were harvested and stained for flow-cytometric sorting. This experiment was repeated to give at least three separate biological replicates in each condition. Several precautions were taken to ensure these replicates were as consistent as possible. Firstly, all the brains were pooled following digestion to minimise the impact of variation between individual mice. Secondly, where possible the lentiviruses used in the cultures were from the same batch. The first three replicates were infected from one batch, though the final biological replicate utilised a different batch of lentivirus, the viral titration experiments performed on both lentivirus preps suggest the efficiency of the second lentivirus batch was roughly equivalent to the first (Figure 4.16B). Thirdly, in each replicate all microglia cultures were sorted and processed in parallel on the same day.

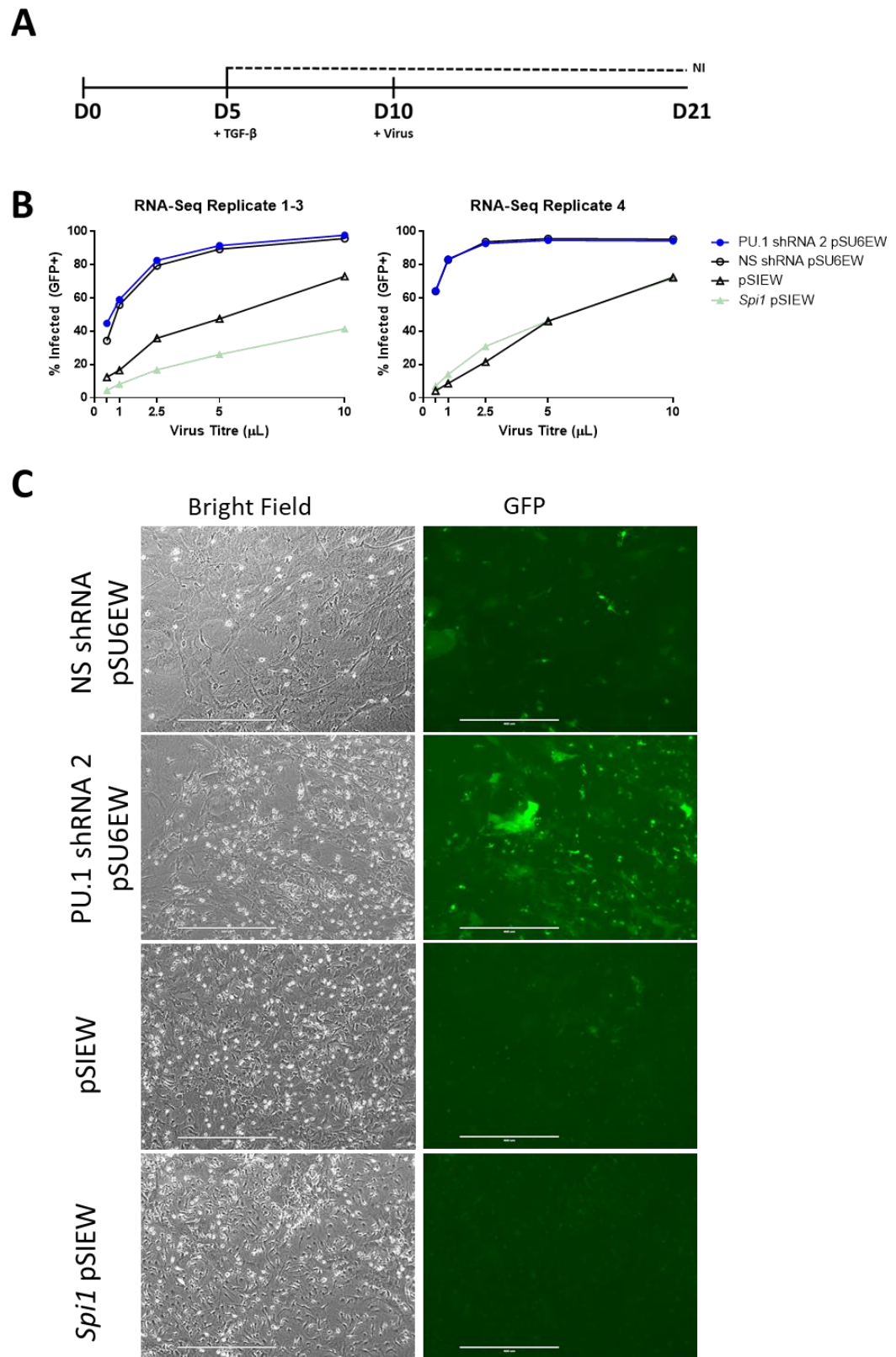


Figure 4.16 Final Experimental Design of Cultures used for RNA Sequencing. **A** Timeline used for each Replicate. Brains were digested and plated on Day 0, TGF- β was added to all cultures on day 5. Viruses were added to cultures on Day 10, excluding non-infected plates, and cultures were harvested after 21 days. The

media was changed on these cultures every 2-3 days, the final media change was on day 20. **B** Titrations of viruses used in RNA Sequencing Experiments. Jurkat cells (2×10^5) were infected with an increasing amount of virus and cultured for 3 days before cells were harvested and run through a Flow Cytometer to determine the percentage of GFP+/Infected cells. An additional batch of virus was required and titrated for the fourth replicate of this experiment. **C** Microscope images taken from one replicate of the RNA sequencing experiment. A similar cell number was observed across all four virus conditions, and in non-infected microglia (not pictured). GFP expression appeared higher in cultures infected with non-silencing/Spi1 shRNA pSU6EW virus compared with the pSIEW/Spi1' pSIEW infected cells. This experiment was repeated 4 times using 8-week-old female C57BL/6J mice.

As can be seen from the above pictures of one representative biological replicate (Figure 4.16C), taken before the cells were harvested, there were no obvious differences in the morphology or number of cells in the cultures. When pictures of the viral GFP reporter were taken it was apparent that GFP expression was stronger in pSU6EW based viruses compared to pSIEW viruses, as expected from previous results (section 4.2.1.4).

4.2.3.2 Cell Sorting

Once the microglia cultures had been harvested the cells were stained with CD11b and CD45 antibodies, as well as the LIVE/DEAD™ marker (Thermofisher). These cells were kept on ice throughout sorting to minimise cell death. Each sample was sorted on the BD FACSAria™ III using the gating strategy set out in Figure 4.17A.

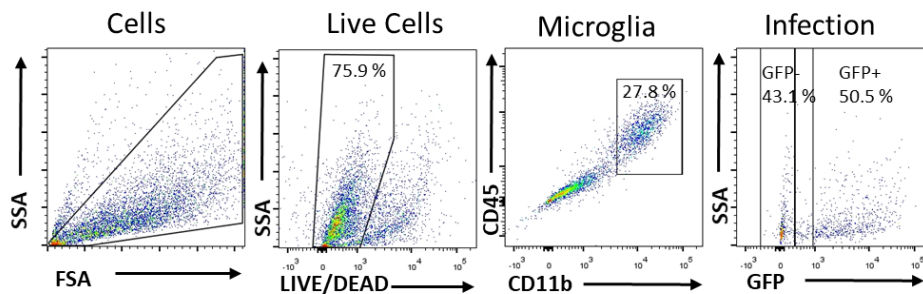


Figure 4.17 Sorting used for all RNA Sequencing Replicates. The gating strategy used in flow-cytometric sorting to select non-infected and infected microglia. The first gate was used to gate out debris, the second gate selected live single cells. The third gate used CD11b and CD45 staining to select microglia cells. The final uninfected (GFP-, left) and infected gates (GFP+, right) were sorted into separate tubes. In the non-infected samples only the uninfected microglia were sorted.

In brief, debris and doublets were removed and CD11b/CD45 surface stains used to identify microglia. The uninfected (GFP-) and infected (GFP+) microglia were sorted into separate tubes. In each non-infected sample only microglia were sorted. After flow-cytometric sorting the cells were pelleted before being lysed to extract RNA.

4.2.3.3 RNA extraction and Quality Checks

The results obtained from all the cell sorting and subsequent RNA extractions are compared in Table 4.3. All infected microglia samples RNA Integrity (RIN) value of over 7.5 met the Welsh Gene Park minimum required RNA concentration of 100 ng in 10 μ L. There were four biological replicates for each condition except for *Spi1* shRNA virus which had only three biological replicates. The microglia sorted from the non-infected microglia cultures were not sent off for RNA sequencing.

Sample	% Microglia (of live cells)	% GFP-	% GFP+	RIN	BioAnalyser RNA Concentration (ng/ul)
Non-Infected	83	95.3	-	-	-
Control pSIEW	90.7	24.4	47.6	9.8	17
<i>Spi1</i> pSIEW	77.8	25.3	50.6	10	59
NS shRNA	50	24.3	74.5	8	9
<i>Spi1</i> shRNA	68.7	59.4	30.9	7.6	13
Non-Infected	83.5	88.2	-	-	-
Control pSIEW	36.1	15.3	65.6	10	90
<i>Spi1</i> pSIEW	39.4	35.5	57	9.8	101
NS shRNA	27.6	29.6	65.6	10	32
Non-Infected	59.9	30.7	-	-	-
Control pSIEW	48.2	14	67.1	10	104
<i>Spi1</i> pSIEW	50.5	20.7	46.2	10	45
NS shRNA	31.6	39.9	51.8	9.6	19
<i>Spi1</i> shRNA	27.8	39.4	34.1	8	8
Non-Infected	69.5	31.3	-	-	-
Control pSIEW	67.1	6.6	79.1	10	145
<i>Spi1</i> pSIEW	83.1	8.4	76.7	10	23
NS shRNA	30.6	6.8	88	7.7	12
<i>Spi1</i> shRNA	23.3	30.1	41.5	9.7	18

Table 4.3 Final proportions of Microglia, both non-infected and infected, and results of RNA Quality Checks. For each sample the percentage of microglia were calculated. Only samples infected with virus (GFP+) were taken forward for further analysis. The RNA Integrity Number (RIN) and BioAnalyser were provided for all infected microglia samples used in RNA sequencing. The results here are from 4 biological replicates where all mice were 8-week-old female C57BL/6J.

4.3 Discussion

The present chapter was designed to optimise an *in vitro* microglia culture where PU.1 protein expression was manipulated with lentiviruses. This primary culture model needed to be suitable for mRNA sequencing, to better understand the influence of PU.1 protein level on gene expression.

4.3.1 Summary of main findings

In summary the results showed *Spi1* shRNA and *Spi1* pSIEW lentiviruses were able to reduce and increase PU.1 protein respectively in primary microglial cultures. Moreover, these experiments suggest that TGF- β helped maintain the mRNA expression of several key microglia genes in culture. Another important finding was that the interval between virus infection and TGF- β supplementation of media appears to be critical to the efficacy of the cultures.

The first set of experiments clearly show the custom PU.1 knock-down and over-expression lentiviruses were functional. *Spi1* shRNA viruses were able to reduce PU.1 protein expression in the RAW M ϕ cell line while the *Spi1* over-expression viruses could induce *de novo* PU.1 protein in Jurkat T-cell line. The *Spi1* shRNA lentiviruses were also shown to be partially effective *in vivo* in the pM ϕ population. Stereotaxic injections were not within the scope of this project due to the increased complexity of injecting lentiviruses into the brain to infect microglia *in vivo*. Therefore, the decision was made to move forward with an *in vitro* microglia model in M-CSF only cultures. PU.1 protein expression could be manipulated in primary microglia cultures with relative ease. The reduced efficacy of GFP expression the *Spi1* pSIEW virus compared to the *Spi1* shRNA virus was likely due to the use of an IRES sequence to express GFP [311]. Another interesting finding was that the *Spi1* shRNA virus appears to work in a dose-dependent manner to reduce PU.1, where microglia strongly expressing GFP have greater reduction in PU.1 expression. The current study found that viral infections were more effective in mixed cell cultures than in cultures where the cells were pre-purified with CD11b selection beads. It is probable that the higher infection rate was a result of microglia having more trophic support from other cell types such as astrocytes, which are known to provide several key factors to aid microglia [155].

An interesting observation was that the proportion of infected (GFP+) microglia in Table 4.3 appeared to be slightly lower in *Spi1* shRNA samples compared to NS shRNA samples. Given that previous work using *Spi1* siRNAs to reduce PU.1 in human microglia has also resulted in a lower cell number [232], it was possible that reducing *Spi1*/PU.1 results in activation of apoptotic pathways. that when differentiated M ϕ s were depleted of CSF-1 this resulted in apoptotic cells,

and were found to have reduced levels of PU.1 [343]. Moreover in pre-leukaemic cells *Spi1* was found to provide resistance to apoptosis [344]. However loss of functional PU.1 did not always seem to contribute to apoptosis in terminally differentiated MØs [345]. Therefore, it was possible that the reduced levels of *Spi1*/PU.1 did result in the microglia being more vulnerable to apoptosis and a lower number of *Spi1* shRNA infected microglia compared to NS shRNA microglia, though further investigations would be needed to confirm this. Live cell imaging after lentiviral infection, potentially incorporating an apoptotic cell marker such as Annexin V, could be used to assess the impact of reducing *Spi1* on microglia apoptosis.

The addition of the TGF- β cytokine to the microglia cultures was done in an effort to preserve receptor expression seen *in vivo* microglia and lost when cells are cultured with M-CSF alone. The first experiment explored if TGF- β needed to be added to culture media immediately following digest to maintain expression of genes identified by Butovsky *et al.* (2014) [154]. As the qPCR results (Figure 4.9) did not provide a clear preference and TGF- β can inhibit microglia proliferation [341,342] the later timepoints (day 5 and day 7) were chosen to give microglia time to proliferate. The second experiment aimed to determine if it was better to supplement media with TGF- β before or after viral infection with an empty vector pSFEW. The results suggested that the order in which TGF- β and virus were administered to cultures had little bearing on the proportion of microglia cells or the efficiency of lentivirus infection. No major expression changes were observed in five out of the six genes analysed by qPCR (Figure 4.10-Figure 4.12). This finding, while preliminary, proposed that TGF- β should be added to the culture media slightly earlier. In the third experiment (Figure 4.13-Figure 4.15), one unanticipated finding was that the temporal proximity of TGF- β and virus had a moderate effect on the percentage of GFP+ microglia and gene expression. While viral infection did reduce expression of some genes compared to uninfected controls, there did not appear to be a large difference to gene expression whether pSFEW virus was added 10 days or 14 days into the culture. As TGF- β is thought to promote a homeostatic phenotype in microglia which could prevent virus from entering the cells as efficiently. This has been seen in Langerhans cells [195]. While the exact biological mechanism underlying this TGF- β /virus interaction remains unknown [196], it is possible that viral infection was causing a down regulation of these homeostatic genes. In the end the final *in vitro* model added TGF- β to the cultured media at day 5 and lentiviruses on day 10.

While the TGF- β induced expression of some genes such as *Siglech* and *Cd34* were consistent between experiments the expression of other genes varied between replicates. There are several

potential explanations for the variation seen in the qPCR cultures. Firstly, these are mixed glia cultures meaning that astrocytes could be releasing TGF- β into the culture media impacting gene expression [154,155]. Secondly, as these are cultures of primary cells and qPCR analysis is very sensitive meaning that small changes caused by the brains can potential skew results, though it is possible that the use of additional reference genes might help negate some of the variation [346,347]. Despite the variation, overall these experiments suggest that the addition of TGF- β in the microglia culture media was beneficial.

This study also found that Tmem119 protein was not expressed on cultured microglia at a high enough level to be used in flow cytometric sorting, confirming work in the literature showing microglia Tmem119 expression following extraction from the brain [155]. Though Tmem119 was not used in the sorting panel to help exclude any monocytes that have adopted a macrophage-like phenotype [108] a pilot experiment suggested perfusion had little effect on the percentage of Ly6C⁺ cells, likely monocytes, in freshly isolated CD11b⁺ cells but did diminish the viability [data not shown] and was therefore a perfusion step was not included in these cultures. Given that this study showed *Siglech* mRNA was robustly expressed in TGF- β cultured microglia it is possible that Siglec-H could be a better target for flow cytometric sorting, as it has already been confirmed as a specific microglia marker [348].

4.3.2 Conclusions and future work

While this culture system is open to some criticism it is it is comparable to previous studies and offers several advantages over other culture protocols used to investigate the reduction of PU.1 [230,233], as discussed in section 7.2.3. While the impact of the amount of PU.1 protein on microglia transcriptomics may be best observed in the freshly isolated cells [155] or *in vivo* [349] there are currently no transgenic mice over-expressing *Spi1* and the current PU.1 knock-out/null mouse models have too many global deficits to determine the impact of a reduced PU.1 on adult microglia in isolation [6–8], mainly due to the reduction in the M \emptyset populations, and as shown in the previous chapter the Rosenbauer *et al.* 2004 was also unsuitable [260]. From a translational perspective these studies could be beneficial as PU.1 is highly conserved in evolution, as it is critical for the survival of the myeloid cell lineage [6–8]. In addition to the work done investigating a reduced PU.1 in human microglia cultures [233] it is possible these findings could be bolstered by investigating AD-risk *Spi1* polymorphisms [230] in induced Pluripotent Stem Cells (iPSC)-microglia. This idea will be discussed in full in section 7.4.

In conclusion, these investigations have confirmed the *Spi1* lentiviruses can manipulate PU.1 expression both *in vitro* and with some success *in vivo*. The present study provides some additional evidence with respect to the usefulness of TGF- β in microglia culture media, especially in combination with viral infection. The primary microglia culture system developed for mRNA sequencing in this chapter will serve as the basis for future work. The next chapter therefore moves onto analysing the RNA sequencing data to verify that the alterations to the expression of the PU.1 transcription factor influence microglial gene expression

Chapter 5 Influence of PU.1 dose on Microglia mRNA transcriptome

5.1 Introduction

As previously discussed, PU.1 is an essential $M\phi$ transcription factor encoded by *Spi1* gene. *In vitro* human microglia cultures with a reduced PU.1 results had a lower rate of A β phagocytosis and an altered transcriptome [232,233]. In myeloid cell development the amount of PU.1 reaches can induce transcription of differential sets of genes [9]. *Spi1* has been recently been suggested to be a central node in a protein AD risk network [5,230,231]. A PU.1 ChIP-Seq experiment indicated there are over 5,000 binding sites for the PU.1 transcription factor in the BV-2 microglial cell line [319] it is probable that there are similar “dose-dependent” transcription differences exist in microglia [10]. The minor allele at rs1057233^g is thought to confer a low *SPI1* expression has been linked to a delayed age of AD onset [230]. This poses the following questions, is the microglia transcriptome altered by changes to PU.1 protein expression? Could transcriptomic data generated from microglia with altered doses of PU.1 provide a clearer understanding of how microglia impact on AD? Moreover, could this provide better therapeutic targets downstream of PU.1?

Several pharmacological compounds being tested therapeutically in AD are thought to partly act by reducing PU.1 levels in microglia [73,89,279,318], though the success of this approach has yet to be determined. While CSF1R inhibitors are successfully treating AD-like pathology in transgenic mouse models (as described in section 1.2.2.1), there have yet to be any results from clinical trials showing if these CSF1R inhibitors translate therapeutically to humans. As these drugs have been shown to reduce the number of microglia [73,89,91] there are concerns that CSF1R inhibitors could diminish the peripheral pool of myeloid cells as well, rendering patients more susceptible to infection.

A better approach may be to understand which genes are directly regulated by PU.1 to try and elucidate a more microglial specific target. In microglia cultured with M-CSF alone the reduction in PU.1 protein in *Spi1* shRNA infected microglia was over 80 % compared to Non-Silencing (NS) shRNA infected microglia. In the previous chapter (section 4.2.3) a primary murine microglia culture model was set-up where PU.1 was both reduced and over-expressed by custom made lentiviruses. As shown in section 4.2.1.4 in M-CSF/TGF- β cultured microglia the reduction in PU.1 protein resulting from *Spi1* shRNA infection was between 60-70 %, again compared to NS shRNA infected microglia. In both M-CSF and M-CSF/TGF- β cultures microglia infected with *Spi1* pSIEW virus had an increased PU.1 protein expression of ~50 % when compared to pSIEW control viruses, though in one experiment PU.1 expression was 2-fold higher in *Spi1* pSIEW infected microglia. Therefore, the RNA-Seq datasets generated in the previous chapter likely have relatively modest

changes to PU.1 protein expression. The purpose of this chapter was to compare gene expression changes between microglia with a lower PU.1 expression to a higher level of PU.1.

During the course of this thesis a report investigating this in the BV-2 cell line demonstrated that several key AD GWAS genes were dysregulated when PU.1 was over-expressed or knocked-down [230]. Multiple genes that were changed as a result of altering the PU.1 transcription factor were associated with phagocytotic process. These changes were verified with a functional assay showing zymosan phagocytosis in the BV-2 cell line depended on the expression of PU.1 protein within the cells. When PU.1 was ectopically increased the rate of phagocytosis increased while reducing the levels of PU.1 also decreased the phagocytic rate. Moreover, several genes mediating inflammation were also downregulated as a result of PU.1 protein reduction [230].

A principal component analysis compared the expression of genes in the BV-2 cell line, cultured primary microglia and freshly isolated cells. It was found that the BV-2 cell line does not represent *in vivo* microglia with enough accuracy to be a reliable model [154]. Despite the advantages of investigating microglia *in vivo* [155], a lack of suitable transgenic mice and difficulties with lentivirus efficacy *in vivo* (see section 4.2.1.3) meant that an *in vivo* approach was beyond the scope of this thesis.

Therefore, in these experiments an *in vitro* culture system of primary microglia supplemented TGF- β was utilised, which has been noted to maintain partial expression of several homeostatic microglia genes [154,155]. The final model described in section 4.2.3, allowed PU.1 protein to be reduced and increased by lentiviral manipulations with TGF- β supplementation.

In summary, this chapter will explore changes to the mRNA transcriptome of primary murine microglia cultures where PU.1 levels have been forcibly downregulated or upregulated. These sequencing data was collected using steps outlined in section 2.16.4. The “knock-down” dataset refers to the comparison between the *Spi1* shRNA and NS shRNA samples. A separate “over-expression” dataset was generated by comparing the *Spi1* pSIEW and empty pSIEW vector samples. While PU.1 protein was not measured in the RNA-sequencing samples the experiments in section 5.2.2 suggest PU.1 was reduced by 60-70 % in the *Spi1* shRNA sample and increased between 50-200 % compared to their respective control viruses.

This Chapter aimed to investigate which microglia genes were differentially expressed depending on low or high *Spi1* expression, and mapping these altered genes onto biological pathways. This was specifically assessed by:

- Scrutinising how the increased and decreased quantities of the PU.1 transcription factor differentially affected subsequent gene transcription.
- Discerning if changes to the mRNA expression level of selected genes in these experiments were reflected at the protein level.
- Utilising Gene-Ontology databases to identify biological pathways affected in these datasets and validate some of the highest-ranking processes *in vitro* using functional assays.
- The comparison of both datasets to the International Genomics of Alzheimer's Project (IGAP) dataset, which was generated from a previously mentioned GWAS study [3].

5.2 Results

5.2.1 Differential gene expression changes in both datasets

As mentioned in the previous section the first aim of this chapter was to examine how gene expression was altered in both the *Spi1* knock-down and *Spi1* over-expression datasets. The exact numbers of up- and downregulated genes in both datasets can be found in Table 5.4.

Figure 5.1A summarises the proportion of genes that were upregulated, denoted by a positive fold-change, or downregulated (negative fold-change) relative to the appropriate controls. Comparisons between the *Spi1* shRNA and NS shRNA samples (shown on the left) show that the proportion of genes with a positive fold-change (dark blue) or a negative fold-change (pale blue) were roughly equal. The number of significantly altered genes in the *Spi1* knock-down dataset was sizeable at both the cut-off thresholds $P < 0.01$ and $P < 0.05$, as summarised in Table 5. The volcano plots shown in Figure 5.1B indicated that most of these changes were relatively small, with a \log_2 fold-change value of less than ± 2 (as indicated by the dashed lines). Most of the largest changes to gene expression with a fold-change over 30 (\log_2 value $> \pm 5$) were downregulated in the *Spi1* shRNA samples compared to the NS shRNA. Therefore artificially reducing PU.1 in primary microglia resulted in gene expression changes. There was a slightly larger proportion of genes with a downregulated expression.

In the *Spi1* over-expression dataset a much larger proportion of the genes were upregulated, over 80 % (dark green) at both $P < 0.01$ and $P < 0.05$ significance thresholds (Figure 5.1A). The volcano plots in Figure 5.1B confirm that when *Spi1* expression was increased and resulted in the upregulation of many genes. This was especially applicable to the greater fold-changes (\log_2 value $> \pm 5$). In summary these initial observations suggested that forcibly increasing *Spi1* expression predominantly results in upregulation of gene expression.

Both the *Spi1* knock-down and *Spi1* over-expression datasets had differing patterns of expression. The overlap between the datasets was further evaluated by comparing the total number of genes that were common to both datasets.

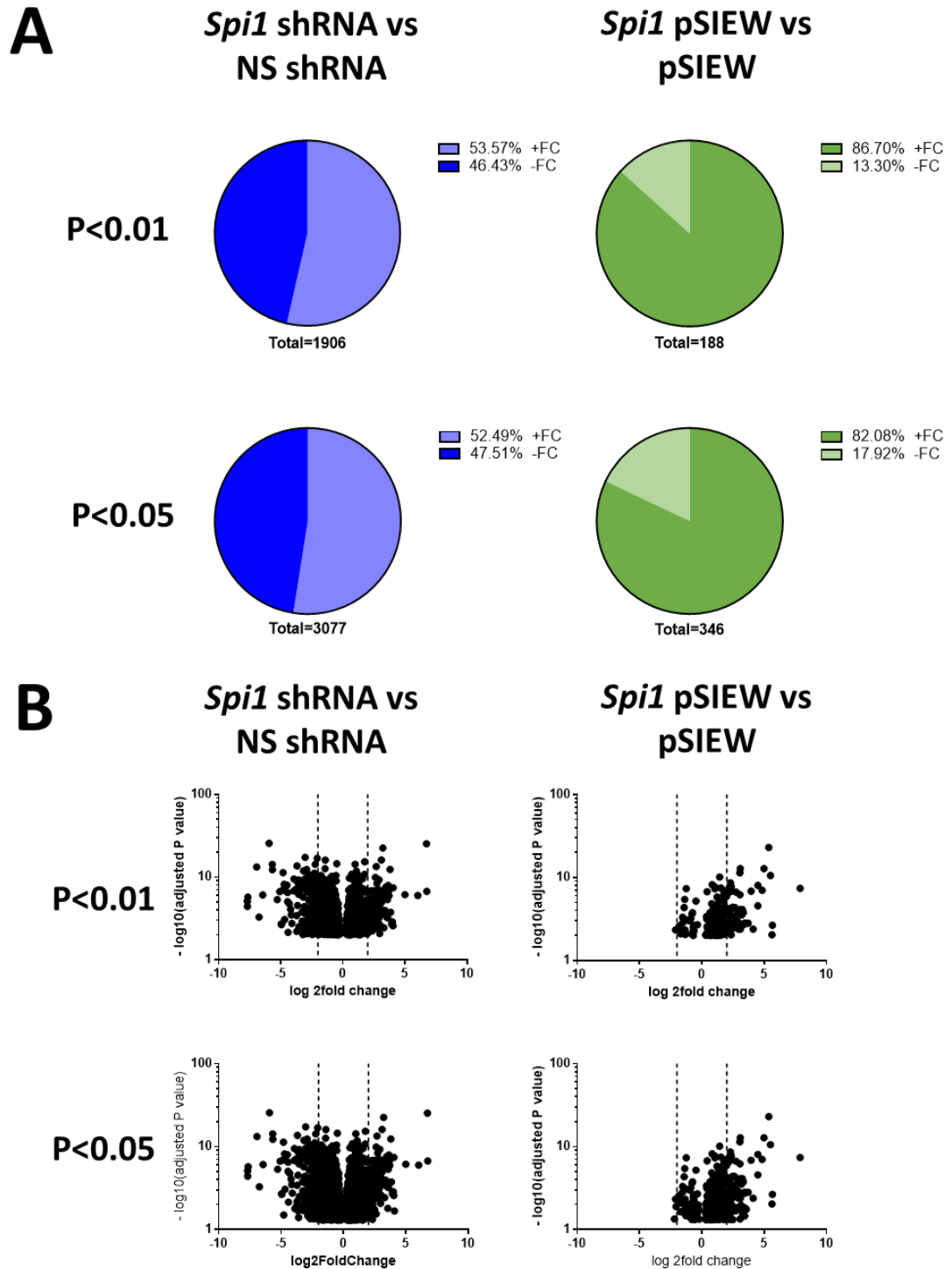


Figure 5.1 Summary of gene changes from RNA-sequencing analyses at different statistical cut-off points. **A** Pie Charts illustrating the proportion of genes with a positive fold-change (+FC) or a negative fold-change (-FC) from all genes that reached the adjusted p-value cut off of $P < 0.01$ (top charts) or $P < 0.05$ (bottom charts) in both the *Spi1* knock-down samples (blue) and *Spi1* over-expression samples (green) compared to their respective controls. **B** Volcano plots presenting the spread of gene fold changes at $P < 0.01$ and $P < 0.05$ as cut-off points.

Gene number	<i>Spi1</i> shRNA vs NS shRNA		<i>Spi1</i> pSIEW vs pSIEW	
	+ FC	- FC	+ FC	- FC
P<0.01	1021	885	163	25
P<0.05	1615	1462	284	62
Gene number	> 2 FC	< -2 FC	> 2 FC	< -2 FC
P<0.01	160	174	50	1
P<0.05	188	230	71	4

Table 5.4 Summary of the number of genes that were regulated, either up (positive fold-change) or down (negative fold-change), when compared to the relevant control at P<0.01 and P<0.05 cut-offs.

The adjusted P-values for the *Spi1* knock-down and *Spi1* over-expression dataset were plotted, as shown in Figure 5.2. Again, this showed there was a higher number of genes with an adjusted P-value of ≤ 0.05 in the *Spi1* knock-down dataset (to the left of the blue line) compared to the *Spi1* over-expression dataset (below the green line). Interestingly there were 196 genes that had adjusted P-values under the $\alpha=0.05$ cut-off in both the *Spi1* RNA-Seq datasets. Therefore, the next step was to look at the expression of the genes that were significantly altered in both datasets to see if the gene expression was diametrically opposed.

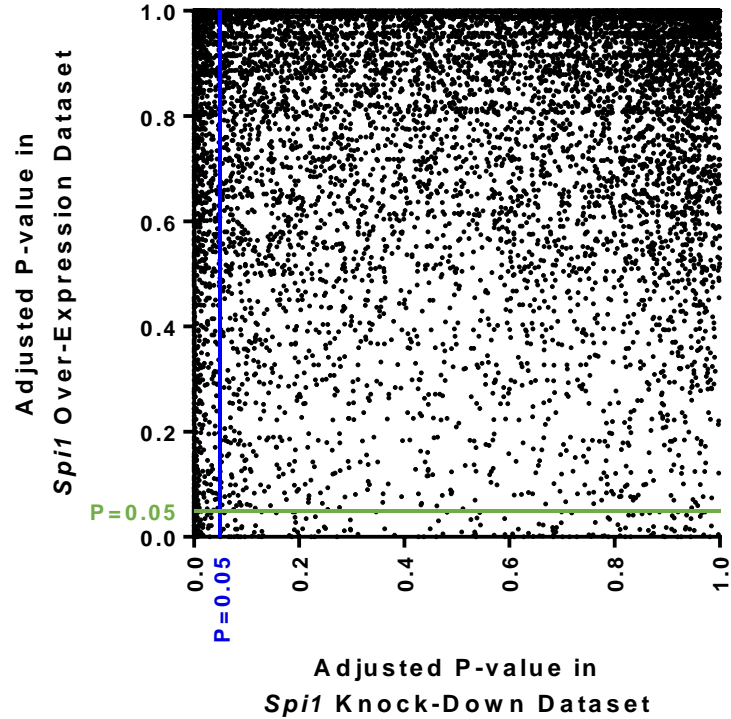


Figure 5.2 Adjusted P-values in the *Spi1* knock-down dataset plotted against the adjusted P-values in the *Spi1* over-expression dataset. Any genes that reached the $P \leq 0.05$ significance threshold in the *Spi1* knock-down dataset are shown to the left of the blue line. Genes that reached the $P \leq 0.05$ cut-off in the *Spi1* over-expression dataset are below the green line. There were 196 genes which had a P-value of ≤ 0.05 , which are contained within the blue and green lines. Any P-values that did not have a numerical value and were returned as N/A by the squash algorithm performed as part of the RNA-Seq pipeline by Dr Robert Andrews were excluded from this analysis.

The Venn diagrams below highlight that the reduction or overexpression of *Spi1* mRNA seemed to affect common genes (Figure 5.3A). There were more genes in the *Spi1* knock-down dataset (blue) that reach the $\alpha=0.01$ significance threshold than in the *Spi1* over-expression dataset (green). As expected, there was a larger number of genes downregulated in the *Spi1* knock-down dataset and a higher proportion were upregulated in the *Spi1* over-expression gene list (Figure 5.3B). The largest proportion of common genes were reduced in the *Spi1* knock-down dataset and increased in the *Spi1* over-expression dataset (Figure 5.3C). The overlapping region in the final set of Venn diagrams shows the number of genes that were upregulated in the *Spi1* knock-down gene list and down-regulated in the *Spi1* over-expression gene list.

These Venn diagrams suggested that when the level of *Spi1* expression was altered in microglia a 'core' set of genes, either 98 or 162 depending on the P-value cut-off, were differentially expressed. In addition to this common core set of genes, there seem to be genes that were only detected in either the *Spi1* knock-down or *Spi1* over-expression dataset. It was possible that more

genes were expressed in both datasets but were not detected due to the read-depth used in the RNA-Seq.

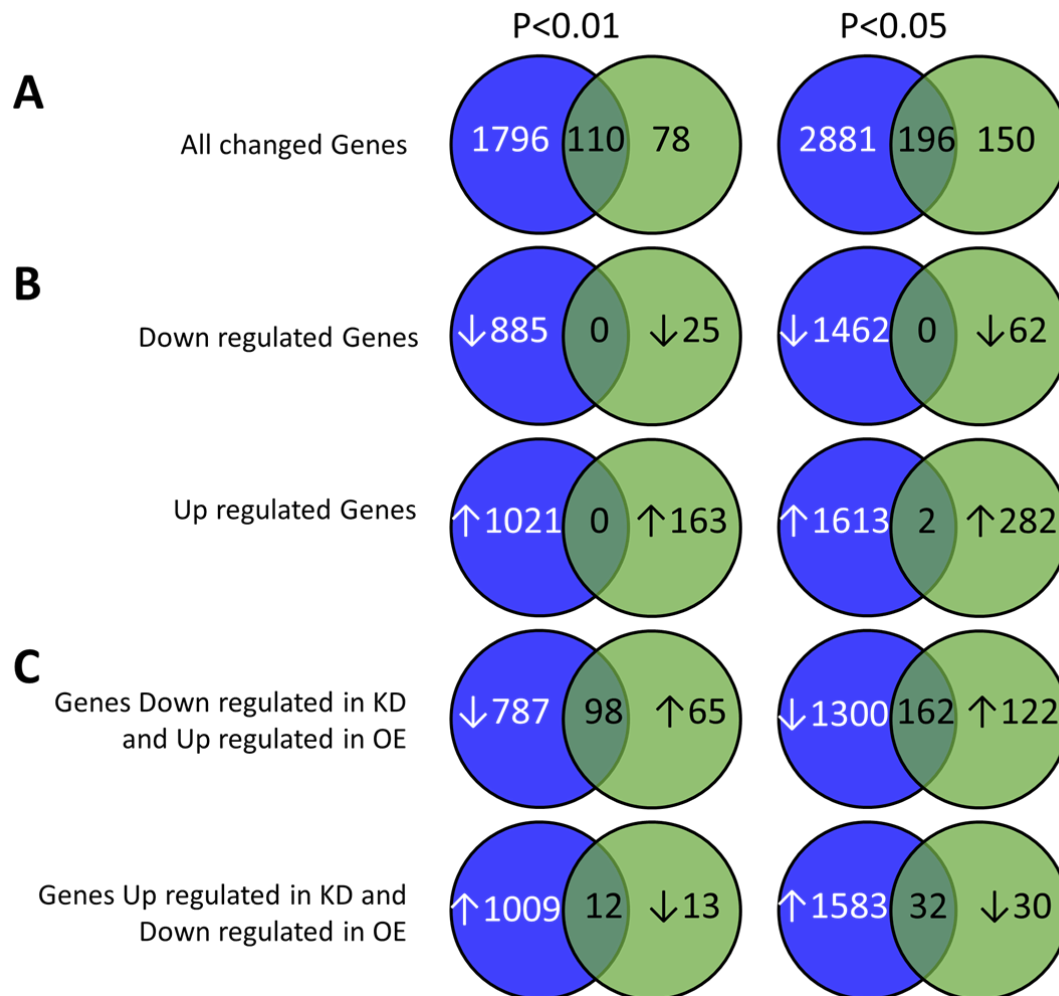


Figure 5.3 Venn diagrams showing the amount of overlap between the Spi1 knock-down dataset (KD; blue) and the Spi1 over-expression dataset (OE; green) at P<0.01 and P<0.05 cut-offs. **A** The first set of diagrams show the proportion of genes which had an altered in either dataset, at both significance thresholds there were a high number of genes in common. **B** The next set of diagrams measures the overlap between genes that were downregulated in the Spi1 knock-down gene list and the Spi1 over-expression gene list or upregulated in both datasets. As expected, there were a higher number of genes that were downregulated in the Spi1 knock-down dataset and a much higher proportion of genes upregulated in the Spi1 over-expression dataset. There were very few genes in common in these Venn diagrams. **C** The next set of diagrams show the overlap between the gene lists when the datasets were diametrically opposed. The top diagrams show the genes that were downregulated in the Spi1 knock-down gene list and upregulated in the Spi1 over-expression gene list. These diagrams had the largest proportion of genes in common out of any comparison. The final set of plots show the overlap between genes that were upregulated in the knock-down dataset and downregulated in the over-expression dataset. Here there seem to be genes uniquely altered in the knock-down or over-expression datasets there were still a number affected in both experimental conditions.

The Venn diagrams show that there were 162 genes that were significantly ($P \leq 0.05$ threshold) downregulated in the Spi1 knock-down set and upregulated in the Spi1 over-expression dataset.

To further assess these *Spi1*-dependent gene changes, the genes were ranked according to the magnitude of the Log₂ Fold-Change in both *Spi1* RNA-Seq datasets. These ranked values were then compared on a scatter plot, shown in Figure 5.4, and seem to indicate most genes had a similar rank in both datasets. This suggests that genes which were largely downregulated in the *Spi1* knock-down dataset were highly upregulated in the *Spi1* over-expression dataset. Overall it appears that the expression of the 162 'core' genes was influenced by the amount of *Spi1* present in the microglia.

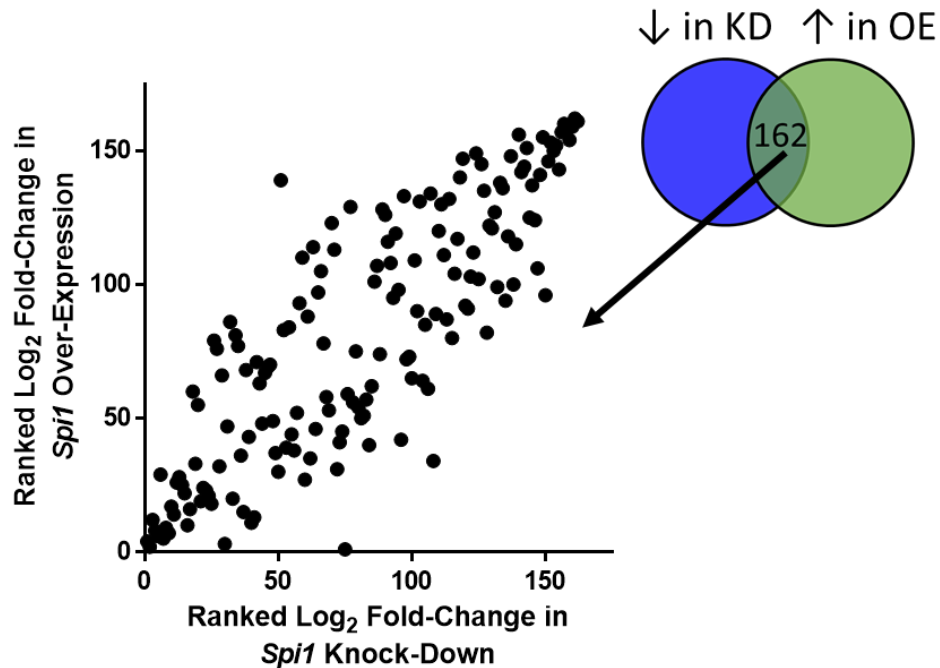


Figure 5.4 The 162 'core' genes that were ranked according to the size of the Log₂ fold-change value. All of these genes were downregulated in the *Spi1* knock-down dataset and upregulated in the *Spi1* over-expression dataset, therefore on the size of the fold-change was compared and not the direction. There seems to be a correlation between the ranks, suggested that for most genes the size of the fold-change was similar whether *Spi1* was knocked-down or over-expressed.

The variation between each experimental replicate (n=4, except *Spi1* shRNA where n=3) was investigated using Principal Component Analysis (PCA). A PCA is often used to summarise the variance between RNA-Seq samples to see if there was clustering of samples which may be due to biological or technical differences in the experiment, in Figure 5.5 each dot represents an experimental sample. In Figure 5.5 the closer the dots were to each other on the plot the more similar the samples were to each other. This PCA plot highlights the reproducibility within each experimental group, as well as the difference between the four culture conditions. Each viral group was circled to highlight the distribution pattern.

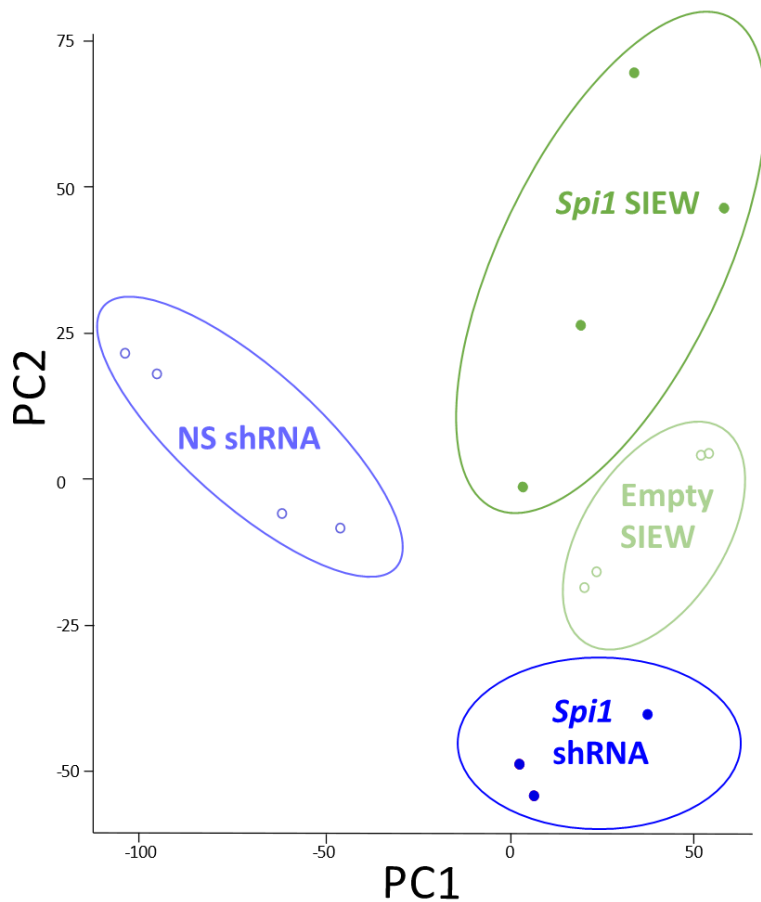


Figure 5.5 Principal Component Analysis (PCA) of the RNA sequencing dataset. The PCA plot assigns each sample co-ordinates based on their similarity, each replicate seem to associate closely with its own experimental group. The *Spi1* SIEW over-expression samples (dark green) seem to show the largest amount of variation between replicates. Each experimental group seems to be fairly distinct NS shRNA (pale blue), *Spi1* shRNA (dark blue), empty SIEW (pale green) and *Spi1* SIEW (dark green), showing that there were consistent differences between the groups. There were 4 replicates in each group, except the *Spi1* shRNA group where there were only 3 replicates.

The largest variation was observed in the *Spi1* pSIEW replicates. As anticipated the different *Spi1* lentiviral groups did not closely associate with their respective control viruses. The *Spi1* shRNA and *Spi1* pSIEW sample groups were also spatially separated, which was unsurprising considering the diametrically opposed *Spi1* manipulations. There was a difference between the control lentiviruses, NS shRNA and empty pSIEW, which was likely due to the different plasmid design as discussed in section 5.3.1.

5.2.2 Validation of alterations to *Spi1* expression

The next analyses looked at the *Spi1* mRNA expression across all virally-transduced microglia that were sent for RNA-Seq analyses. In the over-expression dataset the *Spi1* gene expression levels were significantly altered in the *Spi1* pSIEW samples compared to the empty vector control

(pSIEW; adjusted P-value < 0.001). The *Spi1* gene expression in the knock-down dataset did not reach the P = 0.05 significance threshold (adjusted P-value = 0.089).

Figure 5.6A shows the Fragments per Kilobase Million (FPKM) values for the *Spi1* gene from each replicate. The FPKM value was determined by dividing the number of reads mapping to one mRNA fragment by a million and normalising this number to the length of the gene. It was clear that the FPKM values were increased in the *Spi1* pSIEW samples compared to the pSIEW control samples (One-way ANOVA F=10.91, P=0.0013). In addition to this the NS shRNA and pSIEW control viruses seemed to have similar levels of *Spi1* gene expression. The *Spi1* shRNA FPKM values were only marginally lower than the control NS shRNA values. This had been previously noted in Chapter 4 (Figure 4.2) where the reduction to *Spi1* mRNA seemed fairly mild compared to the PU.1 protein levels in RAW cells. It was hypothesised that this difference was because the *Spi1* shRNA was interfering with the translation machinery rather than directly degrading the mRNA.

To confirm that PU.1 expression was altered at the protein level the RNA-Seq culture experiment (section 4.2.3) was repeated and both *Spi1* and PU.1 expression was assessed. As *Spi1* expression was assessed using qPCR cells were sorted to select CD11b⁺CD45⁺GFP⁺ cells. Figure 5.6B shows the results of measuring PU.1 protein expression in this validation culture using flow cytometry. The MFI between all the uninfected cells within the samples (NI; white) and microglia infected with either the NS shRNA or pSIEW control viruses was fairly similar.

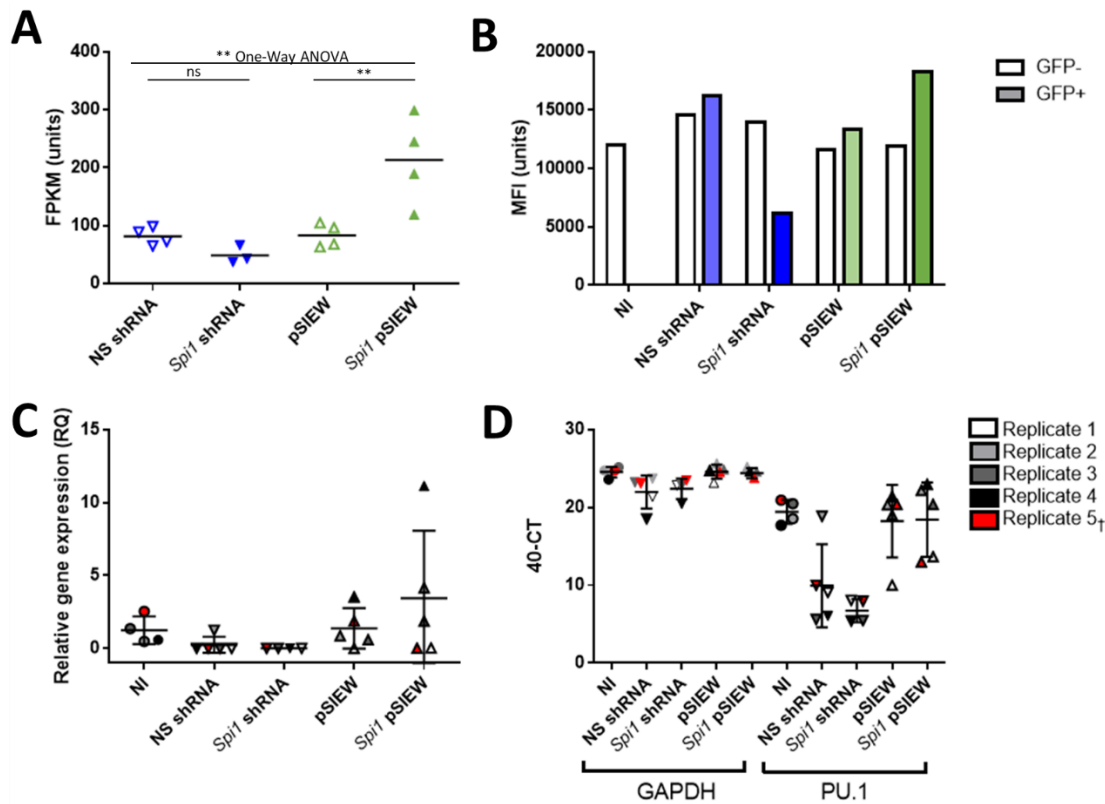


Figure 5.6 *Spi1* expression data from both RNA Sequencing dataset and experimental validation of *Spi1* mRNA and *PU.1* protein. **A** Normalised FPKM (Fragments Per Kilobase Million) values from the RNA sequencing. There did not appear to be a large reduction in mean reads, as indicated by the black line, between *Spi1* shRNA compared to NS shRNA control. The *Spi1* pSIEW over-expression replicates were all higher than the empty control pSIEW, though there seemed to be a large variation in FPKM reads. One-way ANOVA $F=10.91$ (3,11), $P=0.0013$. Sidak's multiple comparison test used to separately compare both shRNA viruses (non-significant/ns) and pSIEW viruses ($P<0.05$). **B** *PU.1* protein expression in validation culture. Median Fluorescent Intensity (MFI) values calculated from removing isotype background from the *PU.1* antibody staining in primary microglia. Unfilled bars represent the non-infected cells. The *Spi1* shRNA (dark blue) compared to both the NS shRNA infected microglia (pale blue) and the non-infected microglia within the sample. The over-expression vector also confirmed that *PU.1* protein was higher in *Spi1* pSIEW infected cells (dark green) compared to both the empty vector control infected cells (pSIEW, light green) and non-infected cells within the sample. **C** Relative *PU.1* mRNA expression for each RNA sequencing replicate (greyscale) and the validation cultures (highlighted in red) alongside mean values for each group ($n=4-5$ per group; \pm Standard Deviation). *GAPDH* was used as the endogenous control gene and values were normalised to the average NI value calculated from all replicates. The graph illustrates that the *Spi1* shRNA virus did not appear to have a large effect at the mRNA level whereas the *Spi1* pSIEW virus had a much higher *Spi1* mRNA compared to the empty vector control (pSIEW). **D** 40-CT values for the qPCRs measuring *Spi1* mRNA in all samples ($n=4-5$ per group). Mean *GAPDH* values were plotted on the left and *Spi1* on the right \pm standard deviation. † Replicate 5 was the validation culture and not part of the original group of samples sent for RNA-Seq analysis. In all plots the mean was indicated by a horizontal line and the error bars denote the standard deviation. ** indicates a P -value of ≤ 0.01 and ns denotes a non-significant result.

As predicted the MFI of microglia infected with the *Spi1* shRNA virus (dark blue) had a reduced level of *PU.1* antibody staining compared to NS shRNA positive microglia (pale blue) or even

uninfected cells within the *Spi1* shRNA sample (white). Meanwhile microglia that were infected with the *Spi1* pSIEW virus (dark green) had a higher PU.1 protein expression than either the non-infected cells (white) or microglia infected with the empty vector control (pSIEW; pale green). This confirmed that in the validation culture PU.1 protein expression was modified by the *Spi1* lentiviruses as expected.

This validation culture was compared to the samples that were sent for RNA-Seq analysis by qPCR assessment of *Spi1* expression. Figure 5.6C shows the relative *Spi1* gene expression in each RNA-Seq replicate (greyscale) and in the validation culture (red). The qPCR data was normalised to the average expression from all non-infected microglia cultures.

The expression of the *Spi1* gene did not appear to vary between the NI, NS shRNA or *Spi1* shRNA samples. The variation between the NI and shRNA-based viruses was minimal as shown by the standard-deviation error bars. There was a larger variation between the pSIEW virus-based replicates, especially the *Spi1* pSIEW replicates, though the average *Spi1* gene expression was higher in the *Spi1* pSIEW samples compared to the empty pSIEW infected microglia. Figure 5.6D shows the 40-CT values for both *Spi1* gene expression and the expression of the endogenous control gene (GAPDH). GAPDH mRNA expression seemed to be consistent between all samples, though did seem to be affected in the shRNA-based viruses. The *Spi1* mRNA CT value were also robust in the NI, pSIEW and *Spi1* pSIEW replicates, though did appear to be lower in both the NS shRNA and *Spi1* shRNA replicates. There was more variation between the *Spi1* gene expression between the replicates.

The slight reduction in *Spi1* mRNA in the *Spi1* shRNA samples compared to NS shRNA samples was not reflected at the protein level, using these validation cultures as an example (Figure 5.6B-C).

Alterations to PU.1 protein were taken to be more meaningful than changes to *Spi1* mRNA expression. Therefore, the experiment was repeated once more to confirm PU.1 protein levels were consistently changed. Figure 5.7 summarises the data gleaned from these two validation cultures (n=2). The plots shown in Figure 5.7B were pre-gated on microglia, defined as single CD11b⁺CD45⁺ cells, using the gates shown in Figure 5.7A. As anticipated, there were no GFP⁺ cells in the NI microglia sample and the PU.1 antibody staining (Figure 5.7B; right plot) was appreciably higher than the isotype control staining (left plot). Microglia infected with the NS shRNA virus had no change in the PU.1 protein expression compared to uninfected cells with the sample, and again the *Spi1* shRNA infected microglia reduced the amount of PU.1 protein. The *Spi1* shRNA infected

microglia with the highest GFP expression had a notably greater reduction in PU.1 staining than those microglia with a lower GFP signal.

A similar virus-dose related change was observed in the *Spi1* pSIEW infected microglia, the higher the expression of the GFP reporter the higher the level of PU.1 protein. This increase to PU.1 expression becomes more apparent when compared to the pSIEW control virus. When the PU.1 expression from both validation cultures were represented graphically (Figure 5.7C) there was little variance in PU.1 protein changes between these two repeats, confirming that these virally-mediated alterations were quite consistent. Overall the non-infected microglia (empty bars) in each sample appeared to have fairly consistent expression of the PU.1 protein. *Spi1* shRNA infected microglia (dark blue) had about a ~60 % reduction compared to cells infected with the NS shRNA virus (pale blue). Microglia infected with the *Spi1* pSIEW virus (dark green) had approximately a 50 % higher PU.1 protein expression compared to microglia infected with the pSIEW control virus (pale green). However these values were calculated based on all GFP+ cells, whereas cells with a higher GFP expression had greater changes to the amount of PU.1.

To investigate if the cells with the highest GFP levels (GFP++) had even greater changes to PU.1 expression the 10 % of cells with the highest GFP levels were analysed separately. Figure 5.7D shows the gates that were used in this analysis, though the GFP++ gate (shaded green) was adjusted to only include to top 10 % of infected cells. The results of this analysis were presented in Figure 5.7E and show that the microglia with the highest level of GFP had more extreme changes to the amount of PU.1 protein. For example, *Spi1* pSIEW infected microglia have an average PU.1 expression of ~150 % whereas the GFP++ microglia had approximately a 200 % increased PU.1 expression.

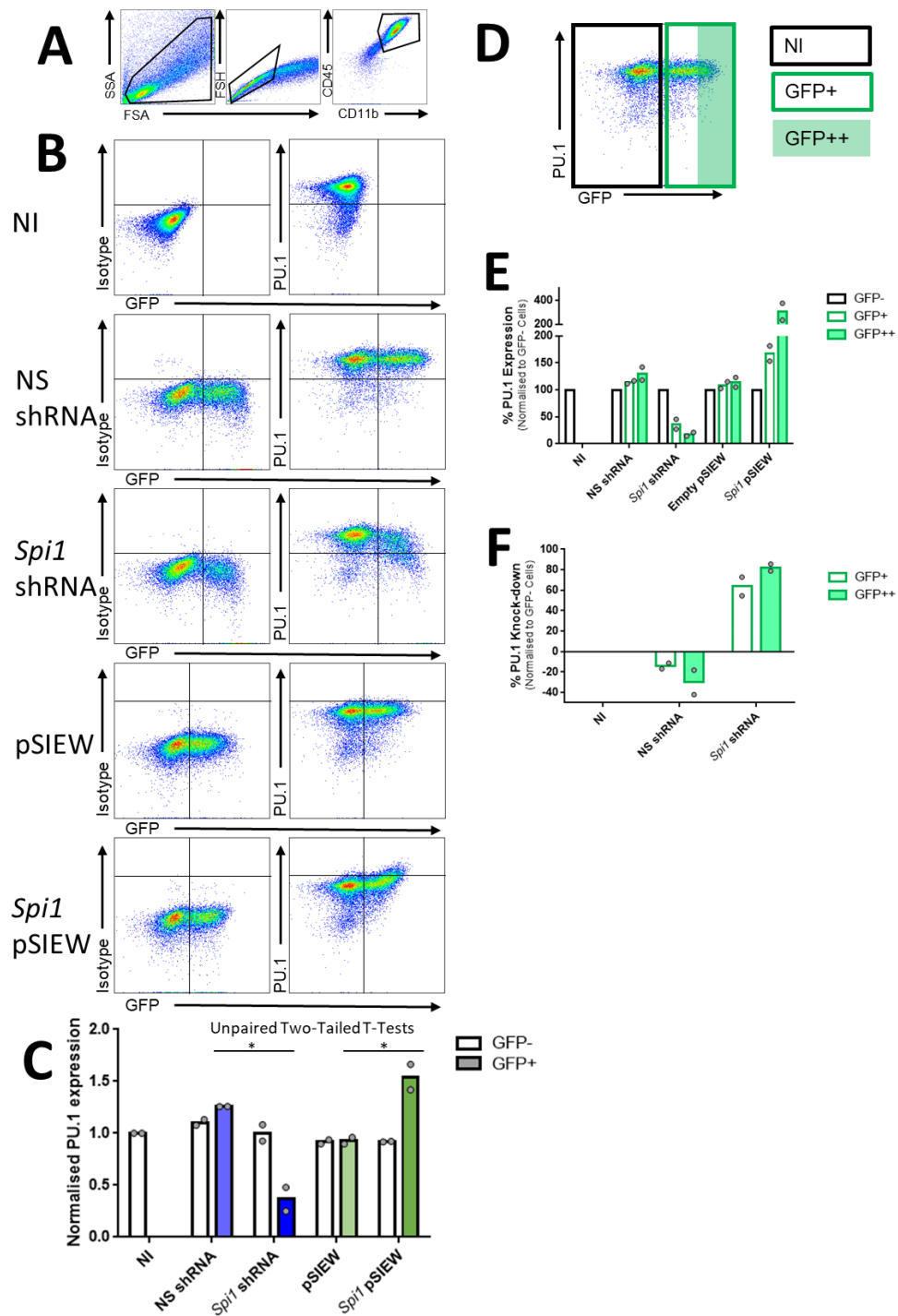


Figure 5.7 Flow cytometric analysis of PU.1 protein expression in RNA -Seq validation microglia cultures. A Gating strategy used in the analysis. From left to right cells were first separated from debris before doublets were excluded. Finally the microglia population were separated as being CD11b⁺CD45⁺. **B** GFP and PU.1 expression in each sample in the validation experiment. The plot gates were based on the PU.1 expression in non-infected cells and the GFP expression for each sample. Isotype staining controls were also used in each experimental condition. **C** Graphical representation of normalised PU.1 expression in these samples. PU.1 expression was normalised after removing any background staining signal, determined using the isotype controls, and the expression was then determined relative to the Non-Infected (NI) sample. PU.1 expression was moderately reduced in the Spi1 shRNA infected microglia (dark blue) in comparison to microglia infected

with the Non-Silencing (NS) shRNA control (pale blue). The *Spi1* pSIEW over expression vector has an increase in PU.1 protein signal (dark green) compared to the empty vector control (pale green). Each bar represents the mean normalised PU.1 expression and the error bars denote the standard deviation. A Two-Tailed unpaired T-Test showed NS and *Spi1* shRNA infected microglia had significantly different PU.1 expression ($P=0.0157$). An unpaired Two-Tailed T-Test between the *Spi1* pSIEW and pSIEW infected microglia was also significant $P=0.0398$. **D** Gating used to separate out 10 % of microglia with the highest infection microglia (GFP++; shaded green) to analyse PU.1 expression alongside all infected (GFP+; green outline) and non-infected (NI; black outline) microglia. **E** Percentage PU.1 protein expression calculated using the gates described in section D and were normalised to the MFI of PU.1 staining in the non-infected cells of each sample. Microglia that had a stronger GFP expression (GFP++) had a larger effect on the PU.1 protein expression, indicating a larger viral load. Therefore the percentage PU.1 expression was more extreme in the GFP++ populations compared to the infected population as a whole. **F** Percentage of PU.1 knock-down using the same analysis described in part D. There was a higher reduction on PU.1 protein expression in the *Spi1* shRNA GFP++ cells, ~80 % compared to non-infected and NS shRNA control cells. However when the whole population of *Spi1* infected cells (GFP+) the reduction in PU.1 protein expression was much more moderate, with these microglia having approximately half of the PU.1 protein compared to controls. *MFI minus the isotype background staining, divided by NI MFI. The data used in this figure was the result of two independent biological repeats ($n=2$), except for sections A and B where only representative flow plots were shown. The mean values were represented by horizontal bars and the standard deviation denoted by the error bars. *Indicates a P-value of ≤ 0.05 .

Spi1 shRNA infected microglia with the highest expression of the viral reporter had a further reduction in the amount of PU.1 protein. The percentage PU.1 knock-down in these cells was calculated and displayed in Figure 5.7F. The entire population of microglia infected with the *Spi1* shRNA virus have a 60 % reduction in PU.1 protein (green outlined bars) compared to uninfected cells. The microglia with the highest GFP expression (GFP++; green filled bars) had an average 80 % knock-down in PU.1 protein. Surprisingly infection with the NS shRNA virus seemed to increase the amount PU.1 protein in microglia by about 10 % overall in all GFP+ cells and roughly 30 % in the microglia with the highest GFP expression (GFP++).

In conclusion, the results presented in this section show that the *Spi1* FPKM values (Figure 5.6A) were supported by PU.1 protein changes (Figure 5.7C). There was some alignment between *Spi1* mRNA expression data from qPCR and RNA-Seq, though there was more variation in the qPCR assessment of *Spi1* mRNA (Figure 5.7A,C-D). The implications of this will be discussed in section 5.3. The alterations to PU.1 protein seemed to be more extreme in microglia that had a higher expression of the GFP viral reporter (Figure 5.7). The *Spi1* shRNA virus the reduction in *Spi1* mRNA expression was subtle, assessed by either qPCR or RNA-Seq, when compared to the PU.1 protein knock-down relative to the NS shRNA control virus. This confirmed the importance of validating mRNA gene changes at the protein level. The next section will move onto discuss other genes that were selected to validated in the *Spi1* knock-down and over-expression RNA-Seq datasets.

5.2.3 Selection & Validation of Other Genes

The validation genes were selected by comparing significantly altered genes from the *Spi1* knock-down dataset (using a P <0.05 threshold) to the genes presented in the Huang *et al.* (2017) paper where *Spi1* was reduced in the BV-2 microglia cell line [230]. This approach was taken as any genes which were altered in both the BV-2 cell line and in primary microglia datasets were thought to be reliably changed by the level of *Spi1*/PU.1..

P2ry12, *Aif1*, *Apoe* and *Pilrb1* were validated by qPCR and, when possible, by flow cytometric analysis. The table below (Table 5.5) shows the fold-change and P-values associated with these transcripts in both *Spi1* RNA-Seq datasets. The next section will provide a brief overview of the potential functions of each protein including any known changes in related AD pathology.

Target name (Gene/Protein)	<i>Spi1</i> Knock-down		<i>Spi1</i> Over-expression		Measured mRNA	Measured protein
	Log ₂ Fold-Change	Adjusted P-Value	Log ₂ Fold-Change	Adjusted P-Value		
<i>Spi1</i> /PU.1	-0.740	0.089	1.356	<0.001	Yes	Yes
<i>P2ry12</i> / <i>P2ry12</i>	-1.265	0.004	0.123	0.999	Yes	Yes
<i>Aif1</i> / <i>Iba-1</i>	-0.998	0.002	0.566	0.321	Yes	Yes
<i>Apoe</i> / <i>Apoe</i>	0.969	0.003	0.330	0.812	Yes	No
<i>Pilrb1</i> */ <i>Pilrβ</i>	-1.339	<0.001	-0.336	0.849	Yes	No
<i>Pilrb2</i> */ <i>Pilrβ</i>	-0.818	0.032	-0.205	0.990	No	No

Table 5.5 Summary of targets selected for validation of RNA sequencing data. *In the mouse genome *Pilrb1* and *Pilrb2* resulted from a gene duplication event. These two sequences were thought to have 87.5 % identical amino acid sequence [350].

The *P2ry12* gene encodes the purinergic receptor *P2ry12* which was highly expressed on homeostatic “surveying” microglia [173]. Purinergic receptors are thought to be vital to microglia chemotaxis, enabling the surveillant microglia to quickly localise to the site of damage in an ATP-dependent manner [171]. *P2ry12* is one of many homeostatic microglia genes that were downregulated in AD pathology, which is thought to coincide with microglia gaining a Disease-Associated (DAM) phenotype [223]. Microglia also suppress *P2ry12* gene expression after LPS or IFN-γ stimulation [58]. In humans *P2RY12* expression is reduced in inflammatory disease like multiple sclerosis and AD. In fixed hippocampal tissue sections taken from 3 patients with AD pathology *P2RY12* was only detected on microglia further from the Aβ-plaque site and became undetectable in plaque-associated microglia [351].

The second validation target was *Aif1* which encodes *Iba1*, a commonly used microglia marker [352]. Functionally *Iba-1* has been shown to interact with the actin cytoskeleton [353] and is

localised to membrane ruffles and aids in phagocytic cup formation [354,355]. Therefore Iba-1 has suspected to play a role in microglia chemotaxis and phagocytosis [356]. One study looked at the strength of Iba-1 staining in cortical sections (middle frontal gyrus) and compared this to the relative level of AD pathology. Here Iba-1 staining was higher in cortical sections taken from the 130 dementia free controls, when compared to 83 samples from patients with AD pathology [357]. However, a recent systematic review of Iba-1 staining in AD showed that this is not consistent between studies. Four of these papers noted an increased Iba-1 in AD frontal cortex compared to controls, three papers where no difference was found and one paper noted Iba-1 was reduced in the frontal lobe of AD samples [358].

The third gene *ApoE* is a well-known AD risk gene, with three variants denoting varying levels of risk. Individuals that were homozygous for the APOE- ϵ 4 variant have a higher AD risk than individuals that were homozygous for the APOE- ϵ 3 variant [53] as discussed in 1.2.1.2. *In vitro* studies exploiting the differences in the APOE variants show that in microglia with the APOE- ϵ 4 variant have a more activated morphology than the APOE- ϵ 3 variant. These changes are associated with an increase in inflammatory genes and a reduction in A β phagocytosis [56]. Moreover *ApoE* has been shown to be part of the biological switch that turns healthy microglia into disease-associated microglia [58].

The fourth and final gene *Pilrb1* encodes the paired immunoglobulin-like type 2 receptor β (PILR β). Mice have two *Pilrb* homologue genes, *Pilrb1* and *Pilrb2* which have a similar amino acid identity, over 87.5 % [350]. In the immune system qPCR analysis has shown PILR β is highly expressed in multiple myeloid cell populations, including M ϕ s. PILR β has been shown to signal through DAP12 (associated with AD risk) to activate immune cells [359]. In a peritoneal parasite infection model *Pilrb* knock-out mice had improved survival compared to C57BL/6 control mice, which was attributed to a downregulated immune response in the gut and also associated with a smaller number of monocytes infiltrating the CNS. It was proposed that PILR β activates Antigen presenting cells, where the other family member PILR α inhibits signalling [360]. A recently identified AD-risk SNP (rs1476679) is thought to be associated with PILRB expression [3,361]. In human monocyte-derived microglia-like cells expression of the T allele in this SNP (rs1476679^T) was associated with increased *PILRB* gene which was also reflected at the protein level [362]. Moreover, another paper suggested that a reduced PILR α inhibitory response, associated with a protective AD mutation, likely results in an increased activation of the PILR β /DAP12 signalling pathway [228].

Figure 5.8A shows the \log_{10} transformed FPKM values for these ‘validation’ genes taken from the *Spi1* knock-down and *Spi1* over-expression datasets. Statistical analysis of the \log_{10} transformed data showed all genes were significantly different between the NS and *Spi1* shRNA groups (empty/filled blue respectively) but were not significantly changed in the over-expression dataset (green). Figure 5.7A shows that *Aif1*, *P2ry12*, *Pilrb1* and *Pilrb2* were all lower in the *Spi1* shRNA samples compared to the NS shRNA control samples. *ApoE* expression was higher in the *Spi1* shRNA samples compared to the NS shRNA controls.

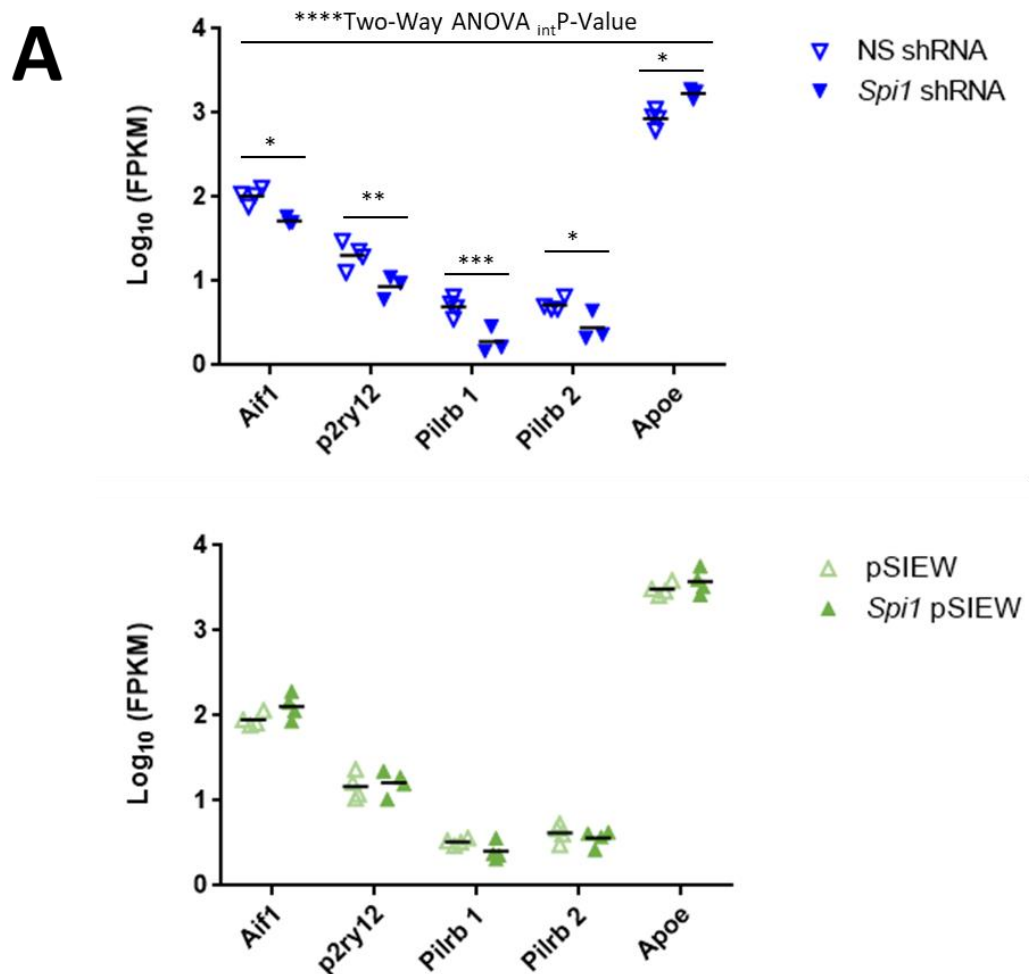


Figure 5.8 Summary of RNA sequencing values and qPCR data measuring selected targets in four original samples and the validation culture- Part I. A Log transformed FPKM values taken from RNA sequencing data to show how the targets selected for validation change. The top plot shows the changes in the knock-down replicates, $n=4$ for NS shRNA (blue outline) and $n=3$ for the *Spi1* shRNA (blue filled) groups respectively. ****Two-Way ANOVA performed on log transformed data, Interaction P-Value ($_{int}$ P-Value) <0.0001 . Sidak's Multiple Comparison Tests showed there were significant differences in gene expression; *Aif1* ($*P\leq0.05$), *P2ry12* ($**P\leq0.01$), *Pilrb1* ($***P\leq0.001$), *Pilrb2* ($P\leq0.05$) and *ApoE* ($*P\leq0.05$) between *Spi1* shRNA and NS shRNA groups. None of these validation genes were significantly different in the *Spi1* over-expression dataset (bottom plot $n=4$ per group; Two-Way ANOVA $_{int}$ P-Value=0.1537). FPKM values taken from the *Spi1* pSIEW

dataset were shown by the filled green shapes and the control pSIEW values were indicated by the empty green shapes. The mean FPKM values were denoted by the horizontal black lines.

The next sections will discuss how expression of these four genes were altered when *Spi1* was reduced or over-expressed, and steps that were taken to validate these findings using qPCR and, where possible, flow cytometric analysis.

5.2.3.1 mRNA Validation

The expression of each validation gene was measured using a second method, qPCR, in addition to the mRNA expression data gathered from RNA-Seq analysis (Figure 5.8). The NS shRNA and *Spi1* shRNA samples had a limited amount of RNA remaining, and therefore qPCR validation could not be performed for every gene. However, the expression of each gene was measured in at least two replicates of the *Spi1* shRNA cultures and three NS shRNA replicates. The 'original' RNA-Seq replicates were shown in greyscale and samples from the validation cultures were indicated by red datapoints.

The first set of plots (Figure 5.8B) show the relative *Aif1* gene expression in addition to the 40-Cycle Threshold (CT) values for each replicate. The 40-CT value demonstrates the total number of cycles (40) used in each qPCR minus the number of cycles taken for the gene expression to surpass the detection threshold. The mean *Aif1* gene expression did appear to be lower in *Spi1* shRNA samples compared to NS shRNA samples. In the samples where *Spi1* was over-expressed (*Spi1* pSIEW) the mean *Aif1* seemed slightly higher than the control pSIEW sample. These changes were reflected in the 40 – CT plots, though it did suggest that there was variation in the *Spi1* shRNA samples.

Expression of the *P2ry12* gene was similar across all samples (Figure 5.8C). The 40-CT plots suggest that the NS shRNA and *Spi1* shRNA samples had lower CT values and higher variation than other samples. *Pilrb1* gene expression appeared to be reduced in microglia infected with *Spi1* shRNA compared to cells infected with the NS shRNA virus, though the variation in these samples made it hard to definitively conclude this (Figure 5.8D). *Pilrb1* expression did not appear to be affected by *Spi1* gene over-expression. The 40-CT values suggested *Apoe* expression (Figure 5.8E) was slightly lower in the *Spi1* pSIEW samples compared to the pSIEW replicates, though the small number of datapoints make it hard to definitively conclude there was a difference.

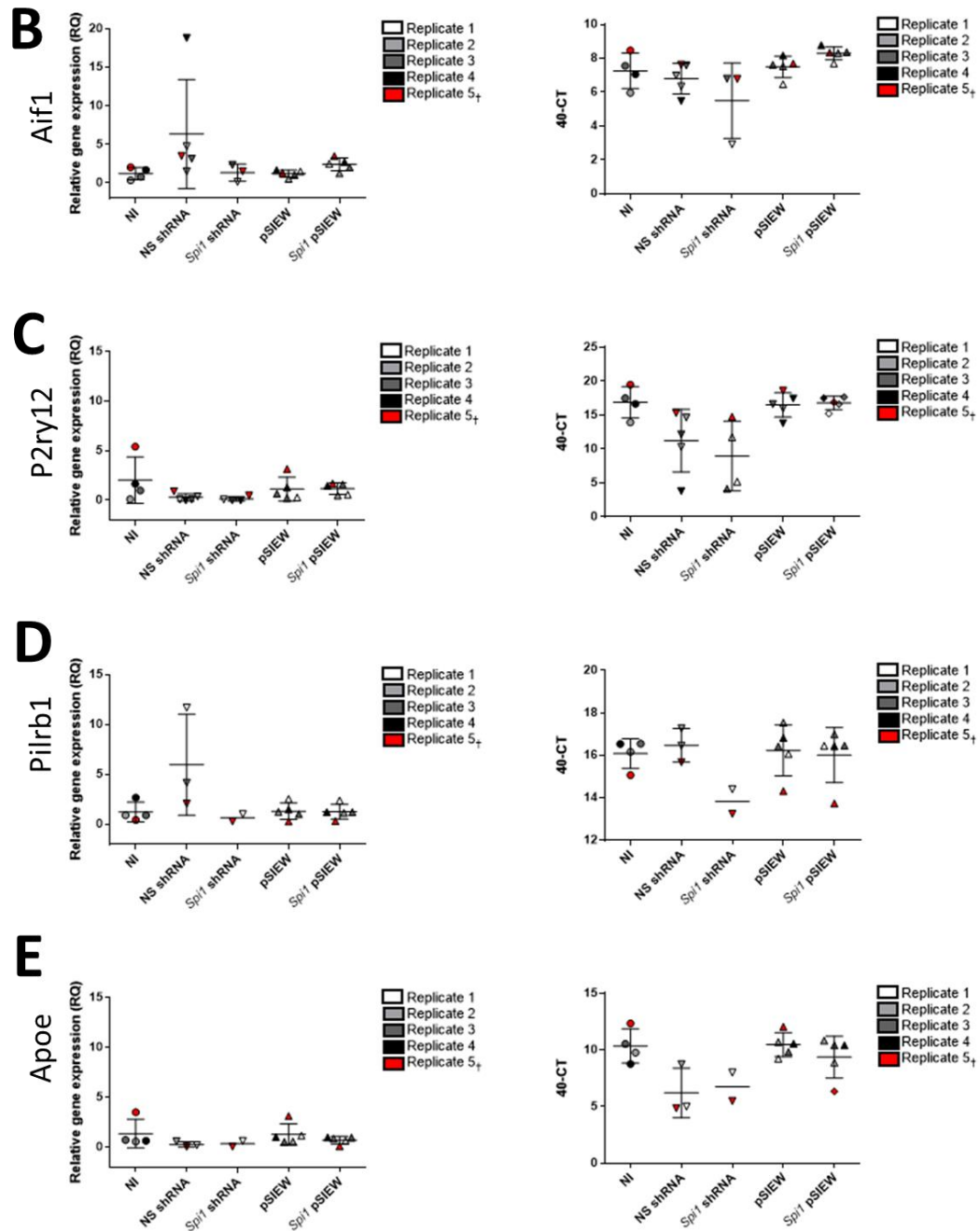


Figure 5.6 Summary of RNA sequencing values and qPCR data measuring selected targets in four original samples and the validation culture- Part II. B-E qPCR results for each gene expression in the original 4 replicates sent for RNA sequencing (greyscale) and the post-RNA sequencing validation replicate (red). In all plots the mean mRNA expression was indicated by the horizontal line and the error bars show the standard deviation around the mean. All genes were missing some datapoints in the NS shRNA and Spi1 shRNA samples due to a lack of available cDNA. The relative gene expression was shown on the left plot and the 40 – CT plots on the right. GAPDH was used as the endogenous control gene and was consistent in all samples (data not shown). Samples were normalised to the average NI value calculated from all replicates. **B Aif1 gene expression does seem to subtly decrease between NS and Spi1 shRNA samples and increase between pSIEW and Spi1 pSIEW samples. The 40 – CT plot shows the changes to Aif1 expression appears to be reflected here. These changes were not significant (One-way ANOVA; $P=0.1585$). **C** P2ry12 expression did not**

appear to be largely changed in the *Spi1* shRNA or over-expression samples, though there was some variation in the NI samples. The 40 – CT plots suggest that *P2ry12* expression was lower in the *Spi1* shRNA samples, though there does appear to be a similar trend in the NS shRNA replicates. One-way ANOVA showed these changes were not statistically significant ($P=0.1646$) **D** *Pilrb1* mRNA expression appears to be fairly similar in all experimental groups, except for the NS shRNA replicates where there was more variation. A One-way ANOVA had a P-value of $P=0.0371$. The 40 – CT plot suggests there may be lower expression in the *Spi1* shRNA samples compared to NS shRNA replicates. **E** *Apoe* expression also remains fairly stable at the mRNA level across the experimental groups, though there was a trend towards a decrease in *Spi1* pSIEW replicates compared to the pSIEW controls. One-way ANOVA confirmed there were no significant differences ($P=0.4033$).

In summary many of the changes seen in *Aif1*, *P2ry12*, *Pilrb1* and *Apoe* expression by qPCR reflect the FPKM values in the RNA-Seq datasets (Figure 5.8A). *Aif1* and *Pilrb1* gene expression seemed to be reduced in the *Spi1* shRNA replicates compared to NS shRNA samples. In the *Pilrb1* plots infection with the NS shRNA virus seemed to impact gene expression, which was not seen in microglia infected with the pSIEW virus. There were some very slight changes to mRNA expression across the experimental *Spi1* pSIEW and pSIEW samples. Biologically changes to protein levels were thought to be more meaningful than changes to mRNA expression.

5.2.3.2 Protein Validation

Iba-1 (encoded by *Aif1*) and *P2ry12* were measured at the protein level as there were commercially available antibodies suitable for flow cytometric analysis. The expression of these proteins was measured alongside PU.1 protein expression, which can be seen in Figure 5.7.

The *Spi1* virus mediated changes to Iba-1 protein expression are summarised in Figure 5.9. First microglia were selected using the gating strategy outlined in Figure 5.9A. The flow plots in Figure 5.9B show the GFP expression compared to the Iba-1 or isotype antibody staining taken from one biological replicate. The NI plots show Iba-1 antibody staining was clearly higher than the isotype control. Microglia infected with *Spi1* shRNA virus had a reduced amount of Iba-1 compared to uninfected cells within the samples or NS shRNA infected microglia. These Iba-1 antibody changes were quantified by normalising the Median Fluorescent Intensity (MFI) values as described in section 2.16.2 (Figure 5.9C). This data suggested Iba-1 was reduced in the *Spi1* shRNA infected cells compared to NS shRNA infected microglia. However, Figure 5.9C suggested that *Spi1* over-expression does not appear to strongly impact Iba-1 protein expression in either experiment.

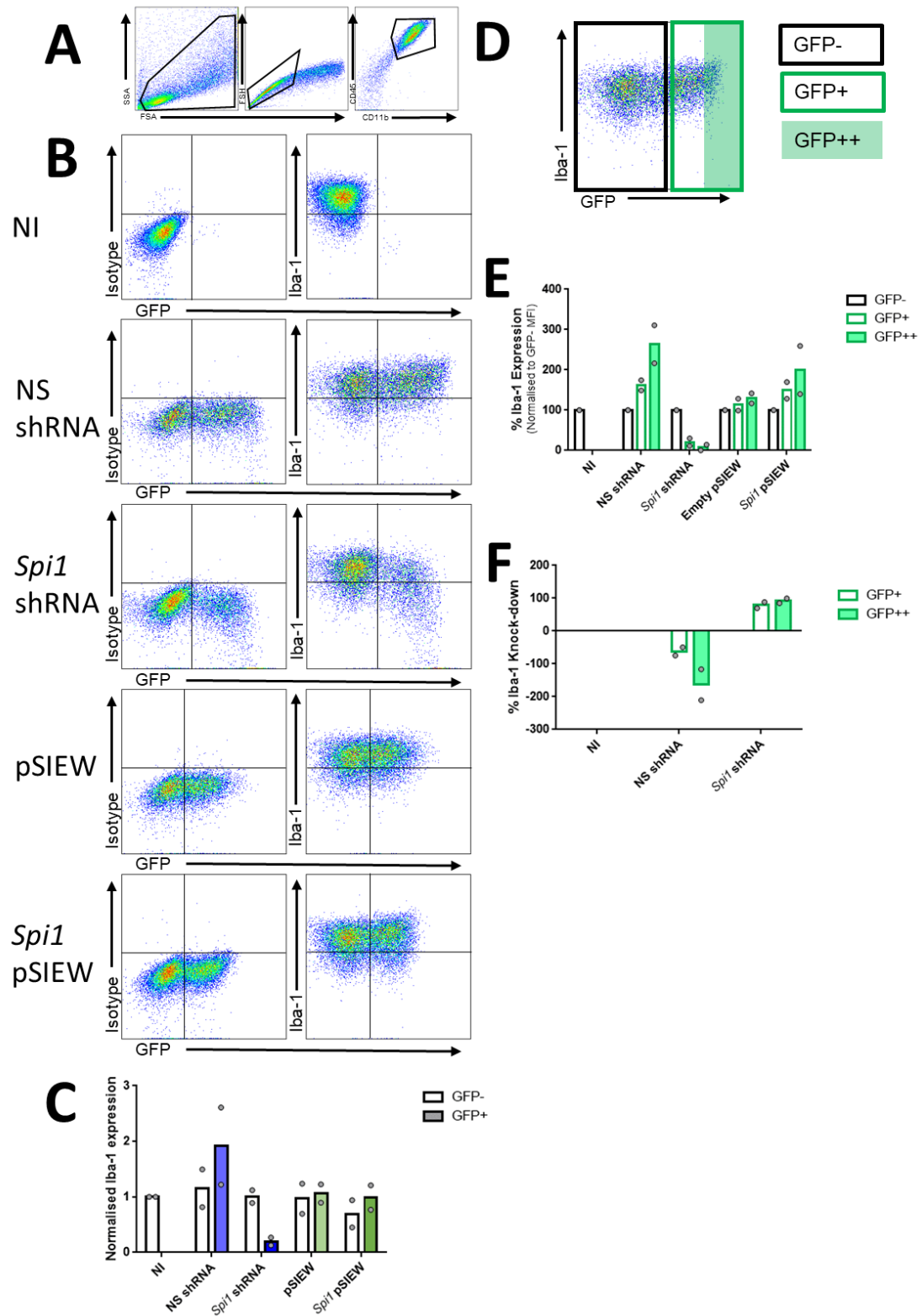


Figure 5.9 Alterations to Iba-1 protein expression in virally infected cultures by flow cytometry. **A** Specific gating used to remove debris, doublets and non-microglial cells ($CD11b^+CD45^-$) from further analyses. **B** Representative flow plots for each sample showing isotype staining (left plots) compared to Iba-1 antibody staining (right plots). Gates were based on the non-infected isotype control MFI. Iba-1 was easily detected in

these cultured microglia as evidenced by the shift in staining between the isotype and Iba-1 specific antibody stains in the NI sample. Iba-1 staining was reduced in Spi1 shRNA infected microglia when compared to both the non-infected cells within the sample and the infected cells of the NS shRNA control. However in the Spi1 forced expression vector (Spi1 pSIEW) there does not appear to be a visible increase in GFP+ infected cells compared to microglia infected with the empty vector virus (pSIEW). **C** Normalised expression values were calculated as described in methods (2.16.2) for the uninfected (GFP-) and infected (GFP+) cells of each sample. Here the Spi1 shRNA infected microglia were shown to have a large reduction in Iba-1 protein expression compared to either the non-infected or NS shRNA controls. When observing the data in this manner there appears to be a slight increase in Iba-1 expression in microglia over-expressing Spi1 compared to the empty vector control. **D** Shows the percentage changes to Iba-1 expression in the NI, and infected (GFP+) cells as well as the highly infected (GFP++) microglia. **E** The MFI data was normalised to the non-infected cells within each sample, which were set at 100 % Iba-1 expression. This graph shows that the Iba-1 expression was greatly reduced in Spi1 shRNA infected microglia there also appears to be an increase in Iba-1 protein resulting from infection with the NS shRNA virus. It could be argued that there was a slight increase in Iba-1 protein expression in the Spi1 over-expression vector, though this increase was also seen in the empty vector control suggesting it was a result of viral infection rather than a biological effect exerted by increasing Spi1 mRNA expression. **F** Iba-1 protein expression expressed as a percentage knock-down, where un-infected cells were considered to have a 0 % reduction. Here it shows that Iba-1 was greatly reduced in the Spi1 shRNA samples, though Iba-1 expression appears to go up hugely in NS shRNA infected microglia. The data used in this figure was the result of two independent biological repeats (n=2), except for sections A and B where representative flow plots are shown. In each graph the bars indicate the mean value and the values from each replicate are overlaid (grey dots).

Figure 5.9D shows the approach taken to separately analyse the 10 % microglia with the highest GFP expression (GFP++), indicating a higher virus infection, against the entire infected (GFP+) and uninfected (GFP-) microglia. The results of this analysis showed that microglia with the highest infection rate have more extreme changes to Iba-1 expression. NS shRNA infected microglia with the highest GFP expression (GFP++) have a higher Iba-1 level than uninfected microglia. The Spi1 shRNA GFP+ and GFP++ microglia have a very low expression compared to uninfected cells within the sample and the equivalent NS shRNA bar. This analysis suggested that Spi1 pSIEW infected microglia with a high GFP expression (GFP++) may have an increased amount of Iba-1 protein compared to the pSIEW GFP++ microglia. The percentage knock-down of Iba-1 was further examined in Figure 5.9F. Iba-1 was approximately 80 % lower in Spi1 shRNA infected microglia compared to NS shRNA infected microglia.

The P2ry12 expression was assessed by flow cytometry using an identical approach. Figure 5.10A demonstrates the approach used to gate on microglia, which were used to create the GFP/P2ry12 plots displayed in Figure 5.10B. These flow plots indicated that the CD11b⁺CD45⁺ microglia population there were separate P2ry12^{low} and P2ry12^{high} sub-populations. These flow plots suggested both P2ry12^{low} and P2ry12^{high} populations were present in all experimental conditions. This was investigated using the gates in Figure 5.10C.

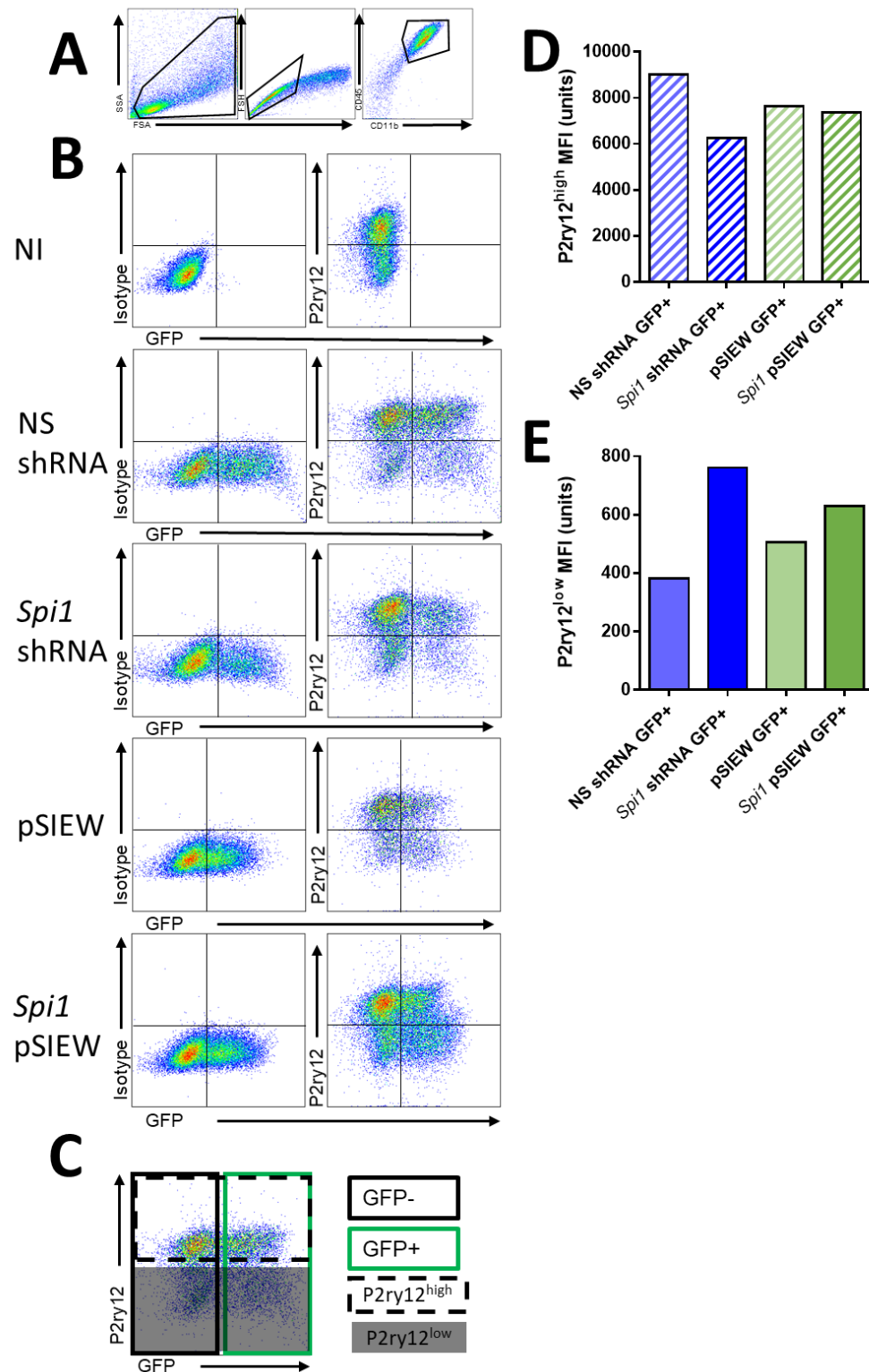


Figure 5.10 Measuring alterations to P2ry12 protein in infected cultures using flow cytometry. **A** Gates used to select single microglia cells. Again, microglia were considered to be CD11b⁺CD45⁺ for the purpose of this analysis. **B** Flow plots displaying GFP expression along the x-axis against P2ry12 antibody staining along the y-axis. Gates were set based on the isotype control for the non-infected sample. In all samples there was a clear shift in the non-infected cells, suggesting the antibody was able to detect P2ry12 though there does

appear to be a subset of microglia that were P2ry12 negative in each sample. The plots show a slight reduction in the P2ry12 staining in the *Spi1* shRNA infected cells compared to the NS shRNA control sample, which was especially visible in those microglia with the strongest GFP expression. However there does not appear to be any change to P2ry12 expression in the *Spi1* over-expression vector compared to the empty vector control. **C** The gating used to analyse P2ry12^{low} and P2ry12^{high} populations in non-infected (GFP-) and infected (GFP+) microglia. **D** MFI of P2ry12^{high}GFP+ microglia (striped), minus the isotype background staining. Here the MFI of the P2ry12^{high} *Spi1* shRNA cells was lower than the NS shRNA infected microglia. There was no obvious difference in the MFI of *Spi1* pSIEW infected microglia compared to microglia infected with an empty control virus. **E** In the P2ry12^{low} (filled) subset of infected microglia the *Spi1* shRNA GFP+ cells (dark blue) appear to have a higher MFI (with isotype background removed) than NS shRNA GFP+ cells (light blue). The MFI of the *Spi1* pSIEW infected microglia (dark green) was slightly higher than microglia infected with the control virus (pSIEW; light green). The P2ry12 antibody staining shown in this figure was only performed on one set of microglial cultures, n=1.

Isotype Median Fluorescent Intensity (MFI) values were removed from the P2ry12 MFI values to quantify P2ry12 expression for each fraction (Figure 5.10D-E). Here the *Spi1* shRNA infected microglia appeared to have a lower MFI in the P2ry12^{high} cells and a higher MFI in the P2ry12^{low} cells, compared to the NS shRNA infected control microglia. Combined with the flow plots in Figure 5.10B this suggests that the *Spi1* shRNA was reducing P2ry12 expression in the P2ry12^{high} microglia, potentially moving these cells into the P2ry12^{low} gate. The MFI of the P2ry12^{high} infected microglia did not appear to be altered in the *Spi1* pSIEW cells. There was a slight increase in the P2ry12 MFI of P2ry12^{low} *Spi1* pSIEW GFP+ microglia compared to pSIEW control cells.

In conclusion reducing *Spi1* appeared to reduce Iba-1 by approximately 80 % and P2ry12^{high} expression by ~30 % at the protein level. The over-expression of *Spi1* in these cultures did slightly increase Iba-1 protein expression when compared to the empty vector control. The P2ry12 protein was increased in the P2ry12^{low} *Spi1* pSIEW infected microglia compared to pSIEW infected microglia.

These protein changes mostly mRNA measurements. Figure 5.8A-B shows *Aif1* (encoding Iba-1) was also reduced in the *Spi1* shRNA samples. The *Spi1* pSIEW related increases to Iba-1 protein (Figure 5.9) appeared to be larger than the slight increase in the *Aif1* mRNA. *Spi1* shRNA infected microglia appeared to have reduce P2ry12 protein in the P2ry12^{high} population (Figure 5.10E) and *P2ry12* gene expression (Figure 5.8A) compared to NS shRNA infected microglia. qPCR analysis of the *P2ry12* expression did not seem to be altered in any of the experimental conditions, though this could be as the P2ry12^{low} and P2ry12^{high} populations were both included. In the *Spi1* pSIEW infected microglia P2ry12 protein expression was increased in the P2ry12^{low} population. Overall, this suggested that the FPKM values in the *Spi1* RNA-Seq datasets were representative of gene changes at the mRNA/protein level, using *Spi1*/PU.1, *Aif1*/Aif1 and *P2ry12*/P2ry12 as examples.

5.2.4 Pathway and Clustering analyses

Having validated several gene expression changes in the previous sections the *Spi1* knock-down and *Spi1* over-expression datasets were then analysed using Ingenuity® Pathway Analysis (IPA) software. The 'comparison' function allowed the *Spi1* knock-down dataset to be directly compared to the *Spi1* over-expression dataset. Figure 5.11A shows the names of the 20 most significantly affected pathways, though the first 17 were more affected in the *Spi1* knock-down dataset (blue) and the other 3 pathways which had a much higher significance in the *Spi1* over-expression dataset (green).

In this list seven pathways were related to cancer and six pathways to cell cycle regulation were most visibly changed in the *Spi1* knock-down dataset. This suggested that reducing microglial *Spi1* may alter the cell cycle. The 3 pathways that were more significantly affected in the *Spi1* over-expression dataset were related to interferon signalling and viral response. Genes in these pathways were also enriched in the *Spi1* knock-down dataset.

Figure 5.11B again compares both datasets but instead using the Z-score calculated by IPA. The Z-score compares the IPA database to the gene changes in *Spi1* knock-down and *Spi1* over-expression datasets. A positive Z-score predicts that a pathway was activated and a negative Z-score predicts a pathway was less active, scores over -2 and 2 were taken to be more meaningful. Interestingly most of these pathways the *Spi1* over-expression and *Spi1* knock-down expression datasets were diametrically opposed. This included changes to several key signalling pathways including interferon, NFκB and IL-8. There were four pathways which were mainly affected by a reduction in *Spi1* which include two metabolic pathways and once cell cycle pathway.

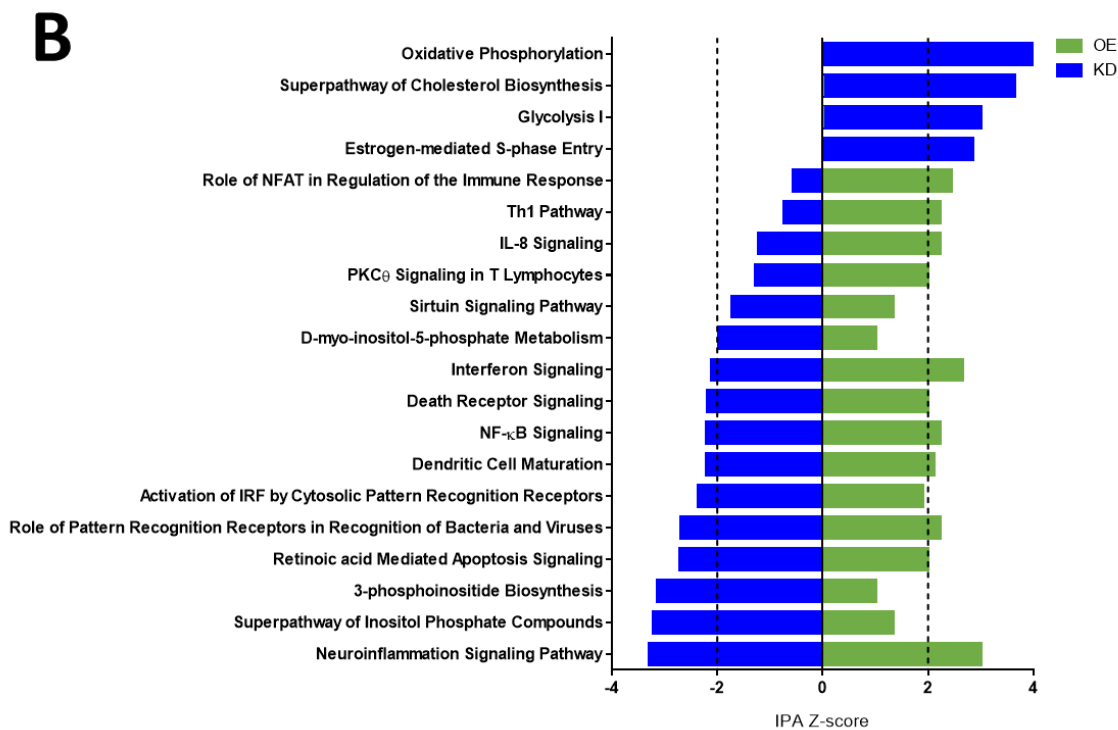
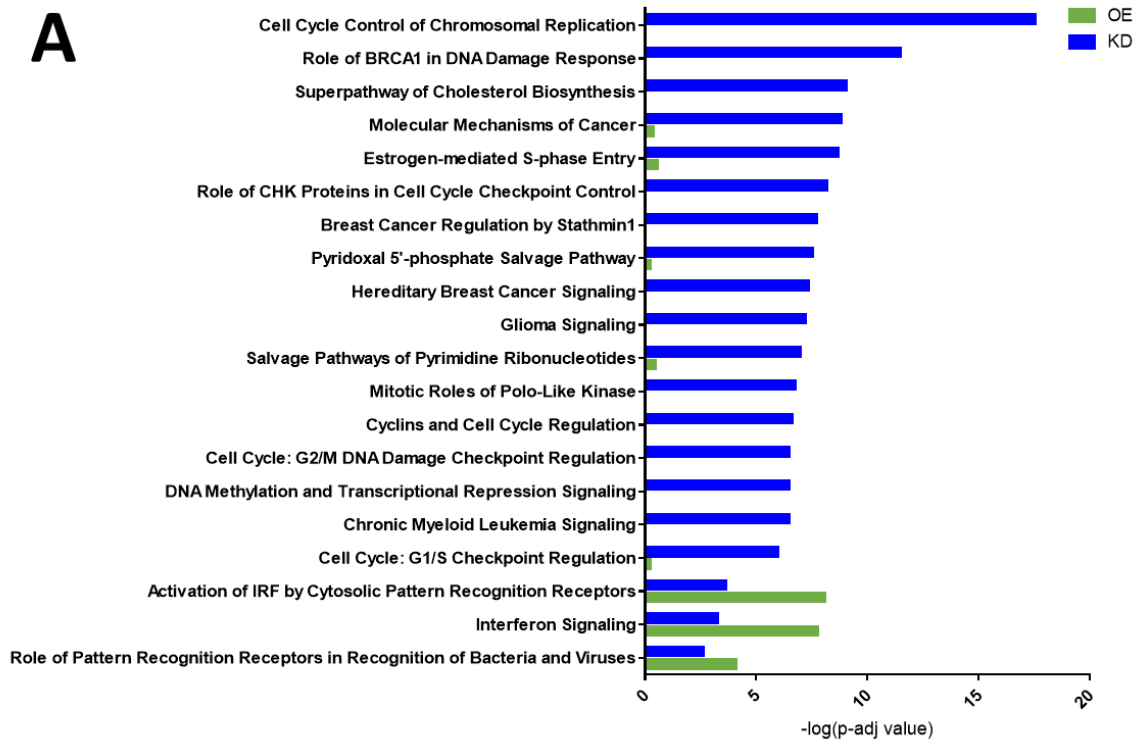


Figure 5.11 Results of functional pathway analysis in IPA comparing *Spi1* knock-down dataset against the *Spi1* over-expression dataset with a $P < 0.05$ cut-off. A This graph shows the canonical pathways that had the 20 lowest P values, which features a lot of DNA and cell cycle related pathways. The inverted log of the P

values are displayed for both the *Spi1* shRNA knock-down dataset (KD; blue) and *Spi1* over-expression dataset (OE; green). **B** The 20 most opposed Z scores resulting from comparing the knock-down and over-expression datasets. The Z-score uses knowledge derived from the literature (IPA database) to determine if genes were upregulated or downregulated in certain conditions. This database was then compared to the gene changes in *Spi1* knock-down and *Spi1* over-expression datasets. The resulting Z-score compares the database prediction with the observed changes from each dataset. A positive score indicates pathway changes were consistent between predicted and observed changes, indicating an activation, and a negative score indicates the pathway was downregulated. Z-scores <-2 and >2 were taken as significant and are indicated by black dotted lines. In this analysis the knock-down showed an enrichment in oxidative phosphorylation and super-pathway of cholesterol metabolism. As you can see for most pathways the Z-scores were diametrically opposed, having a reduced pathway activation in the knock-down dataset, compared to expected and increase in pathway activation in the *Spi1* forced expression replicates. Both these analyses included multiple cell types and species.

Figure 5.12 compares the adjusted P-values on Gene Ontology (GO) pathways that were over-represented when *Spi1* was reduced performed in IPA (Figure 5.12A) and in the Database for Annotation, Visualisation and Integrated Discovery (DAVID version 6.8; Figure 5.12B). While there were some differences in the exact pathways both analyses suggested a reduction in *Spi1* results in changes to multiple pathways relating to the cell cycle. Therefore section 5.2.5.1 assessed changes to microglial proliferation following a reduction in *Spi1*.

An identical pathway analysis was performed on the *Spi1* over-expression dataset using IPA canonical pathways (Figure 5.13A) and DAVID biological processes (Figure 5.13B). In both analyses an increased *Spi1* expression was associated with a viral immune response, including antigen presentation pathways, and interferon signalling pathways.

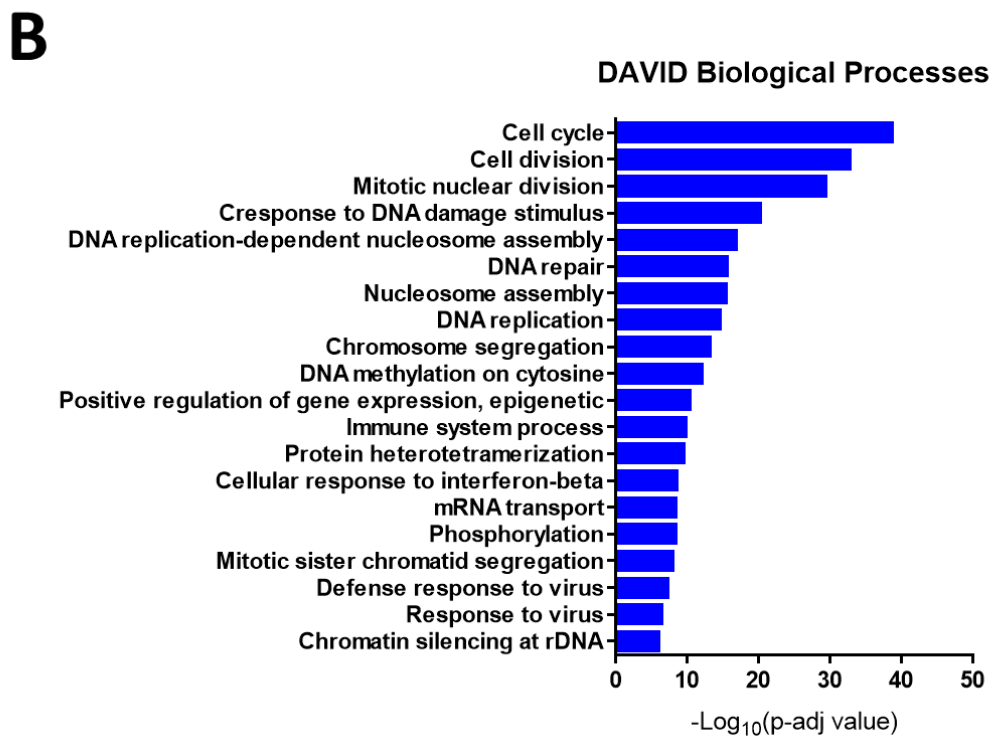
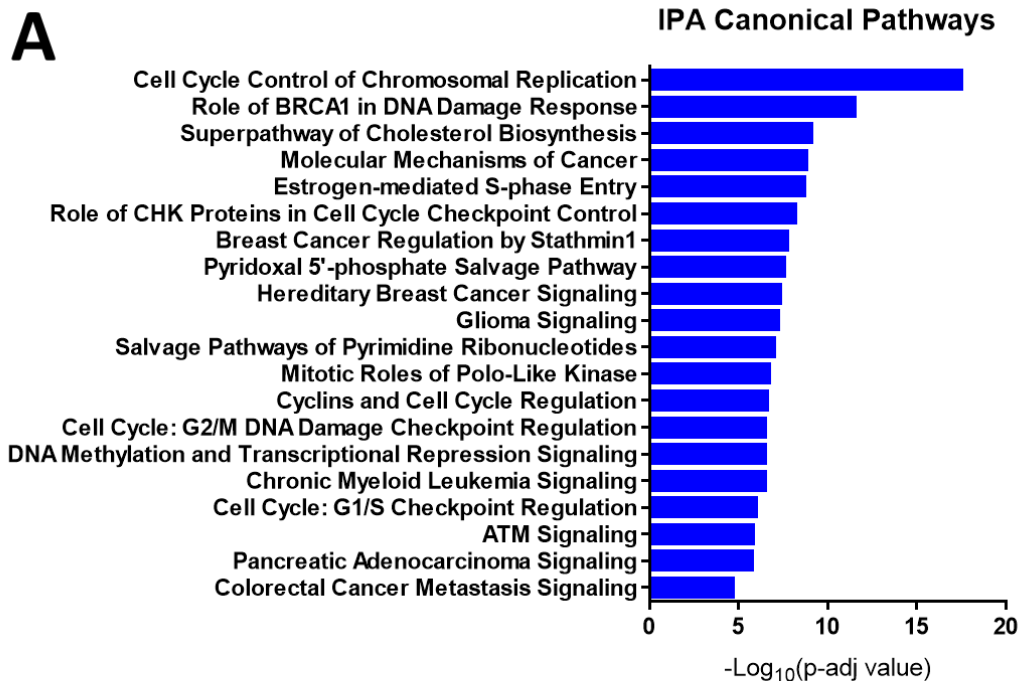


Figure 5.12 Canonical/Biological pathway analysis comparing the Spi1 shRNA to the NS shRNA samples (Knock-Down dataset) using the $P < 0.05$ cut off. A The top 20 canonical pathways identified by IPA software. The inverted log values show that there were a large number of cell cycle related pathways affected by Spi1 shRNA knock-down. **B** The top 20 canonical pathways identified using the DAVID algorithm which again seems to mainly consist of cell cycle related genes.

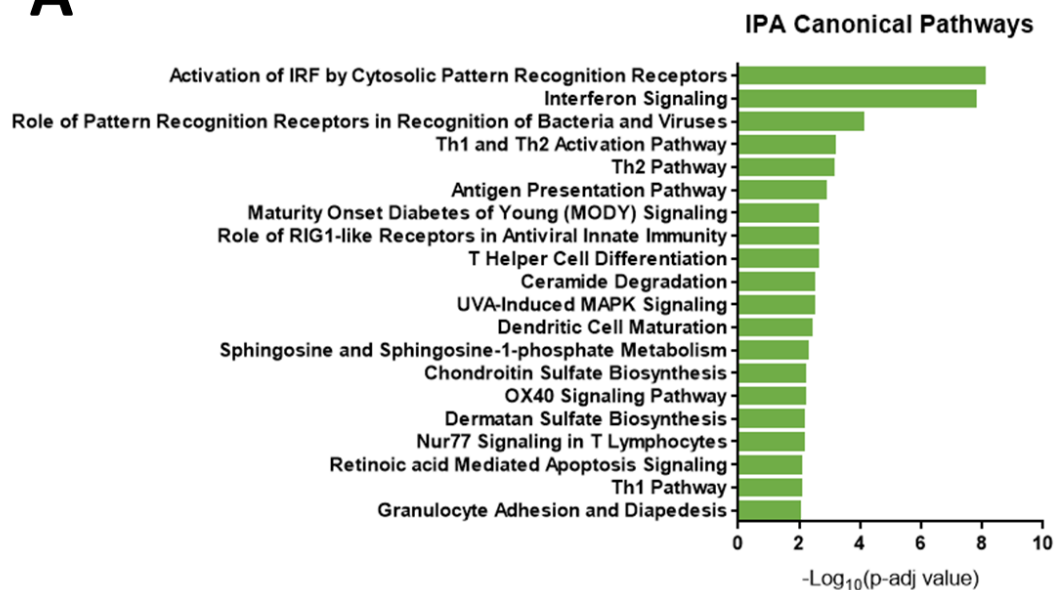
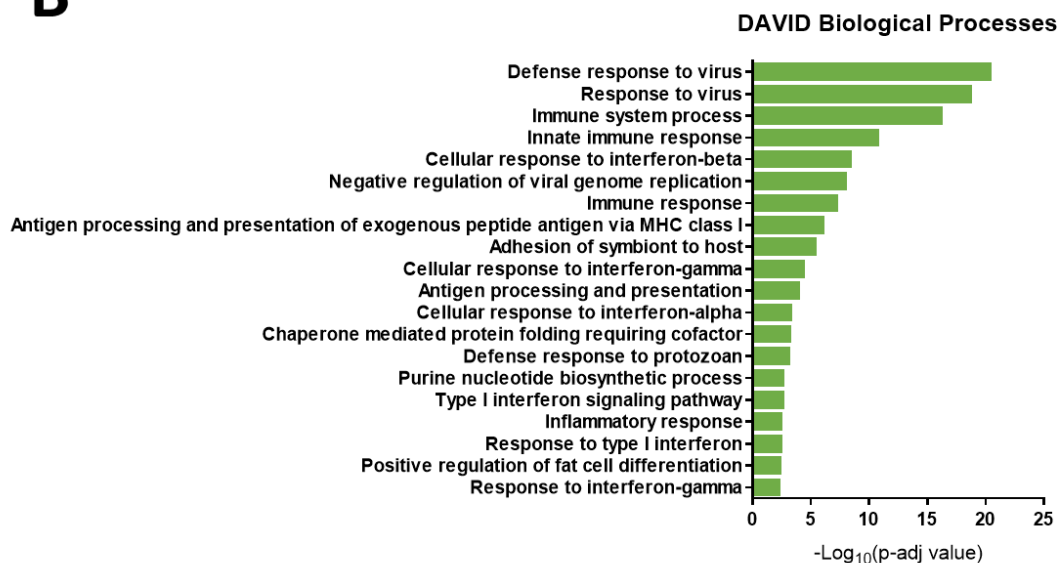
A**B**

Figure 5.13 Canonical/Biological pathway analysis comparing the *Spi1* pSIEW to the empty pSIEW samples using the $P < 0.05$ cut off. **A The top 20 canonical pathways identified by IPA software. The inverted log values show that there were a large number of viral immune response pathways affected by *Spi1* pSIEW over-expression. **B** The top 20 canonical pathways identified using the DAVID algorithm which again seems to mainly consist of immune response pathways including antigen presentation, and interferon genes.**

The *Spi1* knock-down and *Spi1* over-expression datasets were further analysed via hierarchical clustering using the Morpheus software [314]. The first analysis presented below in Figure 5.14A show clustering analysis performed on the on the \log_2 fold-change values which summarise the

gene expression changes in the *Spi1* over-expression and *Spi1* knock-down dataset. Here the genes formed two distinct clusters with diametrically opposed expression patterns. For example, in the first cluster the genes had an increased \log_2 fold-change value in the *Spi1* knock-down dataset and the *Spi1* over-expression data on average had lower \log_2 fold-changes. The opposing pattern was seen in the second cluster. These results support the Venn diagram analysis seen in Figure 5.3C, that genes were diametrically expressed in the *Spi1* knock-down and *Spi1* over-expression datasets.

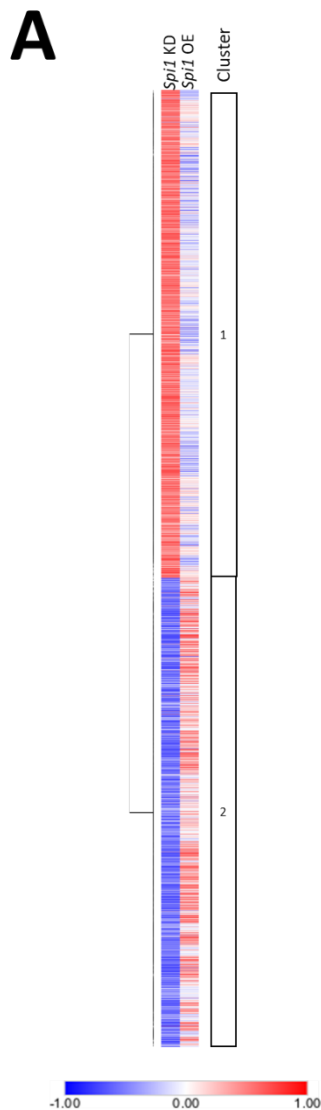


Figure 5.14 Hierarchical Clustering of *Spi1* knock-down (KD) and *Spi1* over-expression (OE) \log_2 fold-changes of genes with a P-value of over $\alpha=0.05$. A The data presented was the \log_2 fold-changes calculated from all *Spi1* shRNA samples and *Spi1* pSIEW samples compared to their relative controls. The genes were clustered by rows. Here it appears that genes form two discrete clusters from following this analysis. The colour key at the bottom of the plot indicates what the colour changes represent. Negative values are shown in blue and positive values in red.

Potential upstream regulators that could result in the pattern of experimental gene expression based on the IPA database. The top three potential regulators were Irf3, Irf7 and Stat1. The predicted activation scores (Z-scores) were thought to be diametrically opposed depending on *Spi1* expression. As shown in Figure 5.15A all of these transcription factors were reduced in the *Spi1* knock-down dataset but increased in the *Spi1* over-expression dataset. Figure 5.15B-C demonstrates the genes in the interferon-7 (Irf7) pathway that were downregulated or upregulated in the *Spi1* knock-down or over-expression datasets respectively. These displays were made by taking the Log₂ fold-changes from each dataset and overlaying them on the Irf7 pathway and show the extent of the changes to this pathway resulting from changes to the amount of *Spi1*/PU.1.

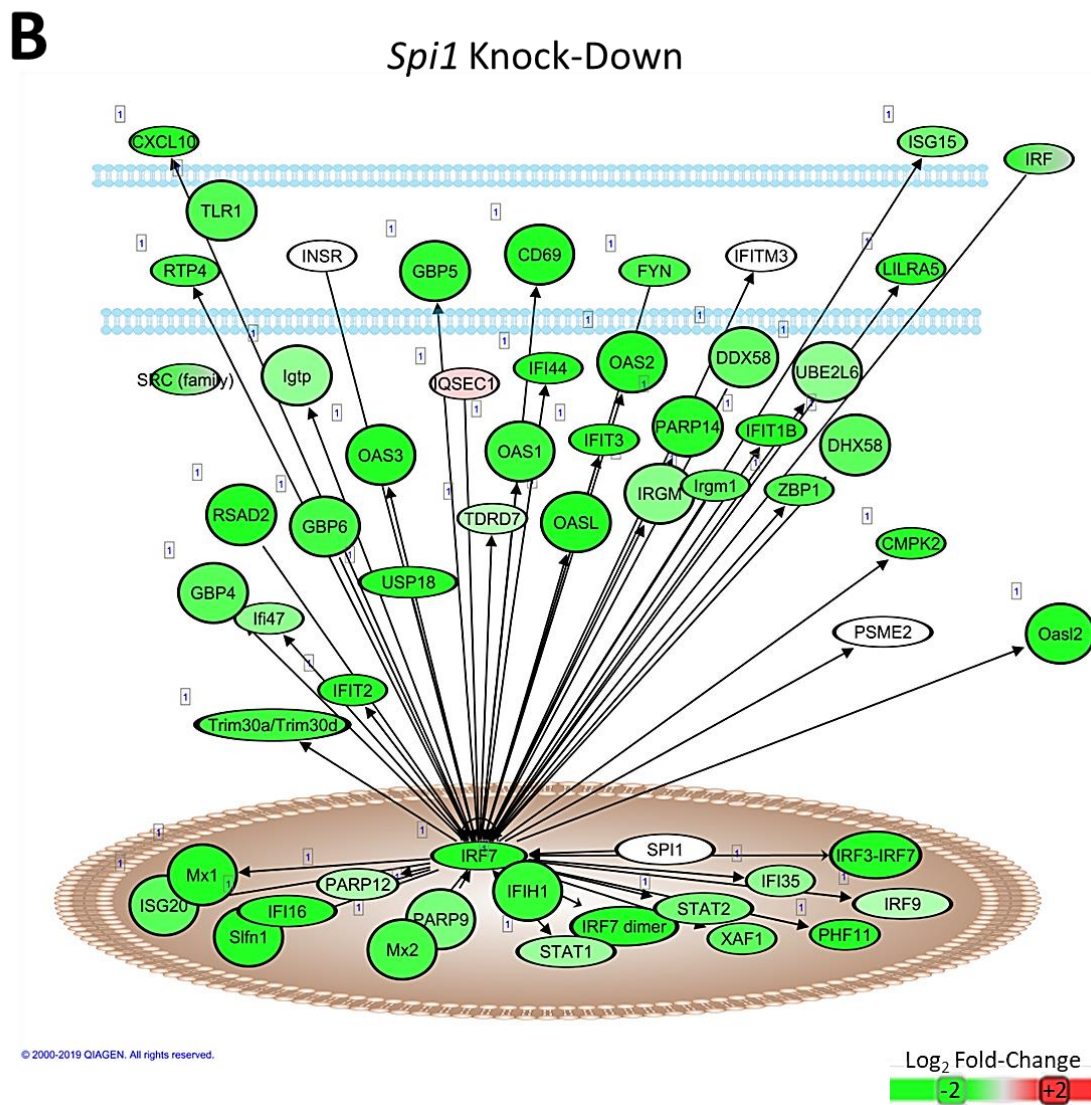
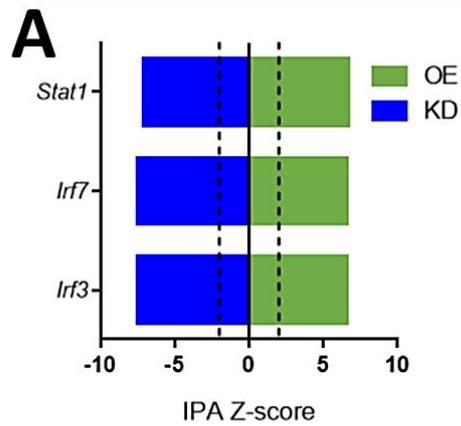


Figure 5.15 IPA analysis of potential Upstream Regulators. **A** The top-three upstream regulators with their Z-scores predicting activation when *Spi1* was over-expressed and a reduction when *Spi1* expression was reduced. **B** The Interferon-7 pathway overlaid with genes where the experimental Log₂ Fold-Change Values

were altered using genes with a P -value of ≤ 0.05 . In the *Spi1* knock-down dataset both *IRF7* and other related genes, including *STAT1* and *IRF3*, were reduced.

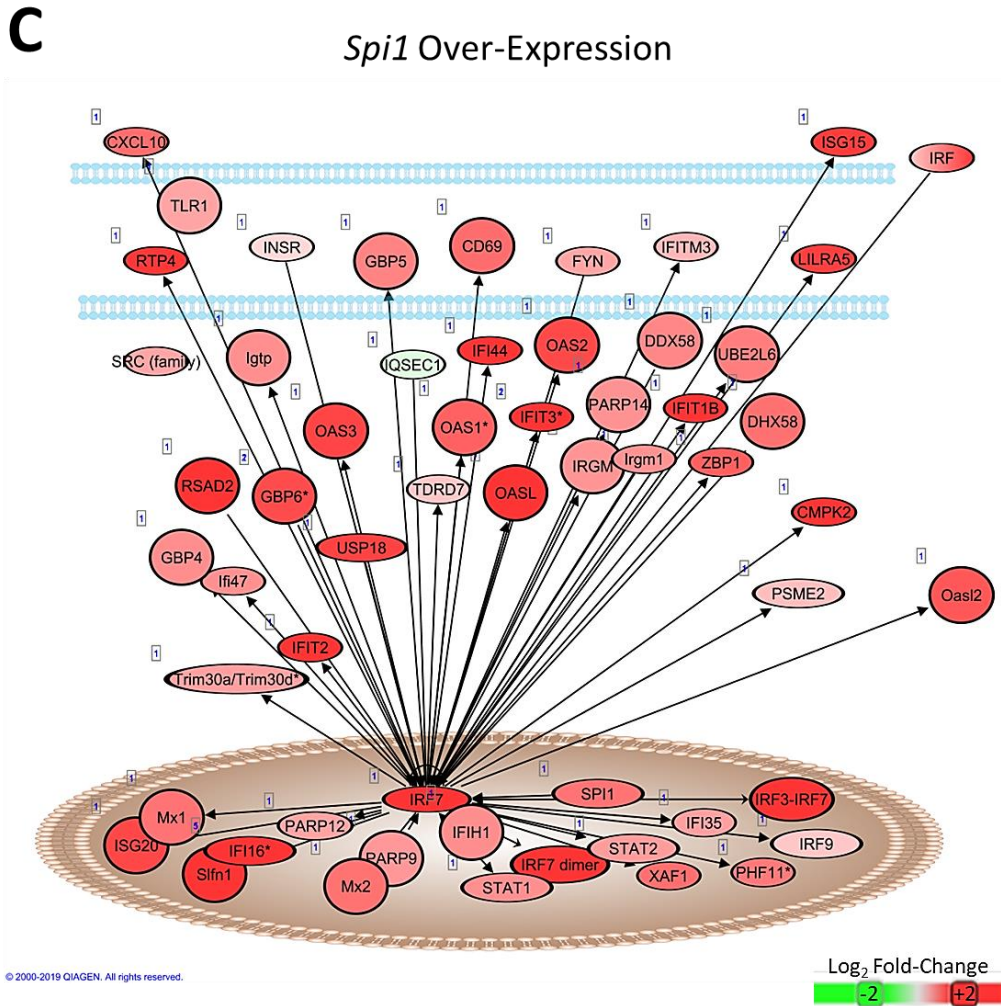


Figure 5.13 IPA analysis of potential Upstream Regulators. C The reverse was seen in the *Spi1* over-expression dataset. When Log₂ Fold-Change Values using genes with a P -value of ≤ 0.05 from the *Spi1* over-expression dataset were overlaid on the *Irf7* pathways, *Spi1* and *Stat1* were both increased. The only exception in this pathway analysis was *QSEC1* which was higher in the knock-down and lower in the over-expression. This diagram was restricted to genes downstream of *Irf7* that were altered in the dataset. The colour scale is indicated below. Transcription factors were all contained within the nucleus (brown). The cell membrane is indicated in blue and can be used to separate cytosolic factors from membrane bound/external proteins.

Given the experimental design these diametrically opposed changes were not unexpected, though more information was gleaned from clustering the FPKM values (Figure 5.16A). In this analysis the FPKM values were first normalised by row to calculate the z-score to ensure that the expression of each gene was within the minimum/maximum range shown at the bottom of Figure 5.16A. The dendrogram on the left of Figure 5.16A was used to separate the data into 6 discrete clusters, which were visually confirmed and displayed to the right of the figure below.

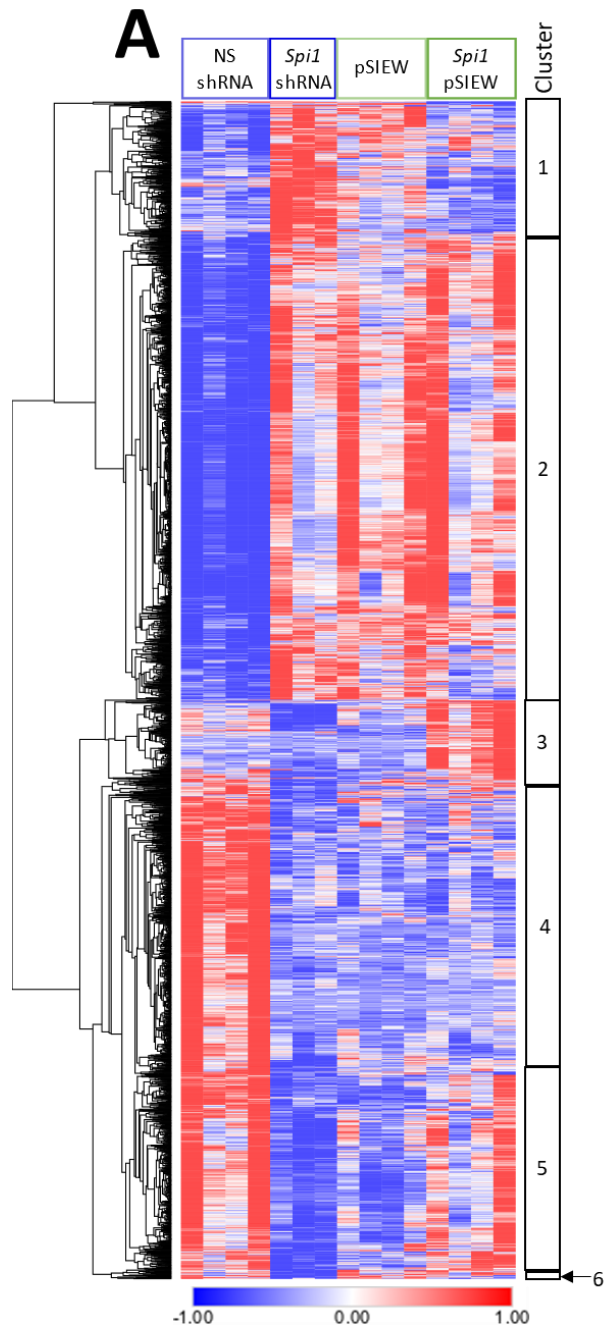


Figure 5.16 Hierarchical clustering of the z-scores calculated from the FPKM values ($P < 0.05$) from each replicate. A The colour key at the bottom of the figure indicate how the colour range relates to the minimum (blue) and maximum (red). This data was separated into 6 discrete clusters (right) based on the dendrogram shown on the left. This data combines all the replicates that were sent for RNA-Seq analysis ($n=4$ for all groups but *Spi1* shRNA where $n=3$).

In the first gene cluster, defined in Figure 5.16A, the genes appeared to be upregulated in *Spi1* shRNA samples compared to NS shRNA controls and *Spi1* pSIEW samples appeared to be slightly downregulated compared to control pSIEW samples. When the gene list in this cluster was run

through IPA and DAVID several signalling pathways were found to be over represented. As shown in Figure 5.16B1, the top five pathways in cluster 1 included Opioid, Gαq and Androgen signalling pathways (following IPA analysis) and metabolic process pathways (DAVID analysis). The pattern in this cluster suggested that reducing *Spi1* activated this set of genes and increased *Spi1* expression reduces the expression in this cluster, relative to the appropriate control virus. The NS shRNA and pSIEW control viruses do not appear to correlate each other, which was not unexpected given they originate from different plasmids.

The second gene cluster contained genes linked to the cell cycle and DNA replication by both IPA and DAVID analysis (Figure 5.16B2). The genes in this cluster had a higher expression in the *Spi1* shRNA samples compared to NS shRNA infected microglia but did not appear to be largely different between the pSIEW and *Spi1* pSIEW samples.

The third gene cluster contained a small number of genes mainly expressed in the *Spi1* pSIEW sample cohort. The expression of these genes was mostly reduced in most of the NS shRNA samples and in the *Spi1* shRNA and pSIEW samples. The genes listed in this cluster appear to be related to antigen presentation pathways and helper T-cell activation (Figure 5.16B3). It was unlikely that these genes were upregulated due to the experimental design as these genes were not upregulated in all samples, see section 5.3 for further discussion. Therefore this analysis suggests that the increased *Spi1* expression resulted in an upregulation of genes in antigen presentation pathways.

The genes in the fourth gene cluster suggested a reduction in *Spi1* impacted several cancer signalling pathways and pathways related to chemotaxis (Figure 5.14B4). This cluster was activated in the NS shRNA samples and largely reduced in the *Spi1* shRNA samples.

The fifth gene cluster contained genes related to interferon signalling pathways and other viral defence pathways (Figure 5.14B5). These genes were downregulated in the *Spi1* shRNA samples and upregulated in the *Spi1* pSIEW samples compared to their respective controls. This suggested that the genes in this cluster were dependent on the level of *Spi1*/PU.1. The variation in the level of gene activation in the *Spi1* pSIEW replicates was likely due to the level of *Spi1* over-expression. For example, the fourth replicate (far right) had the highest *Spi1* FPKM value, which can be viewed in Figure 5.6A.

The sixth and final gene cluster contained genes which did not fit into the other clusters and was the smallest. On average the genes in this cluster appeared to be activated in both the NS shRNA

and pSIEW control samples, but strongly reduced in the *Spi1* shRNA samples. The *Spi1* pSIEW samples appeared to contain a mix of downregulated and over-expressed genes. The pathways associated with this cluster included a DNA damage pathway and pathways involving cell adhesion and lysosome organisation (Figure 5.16B6).

B

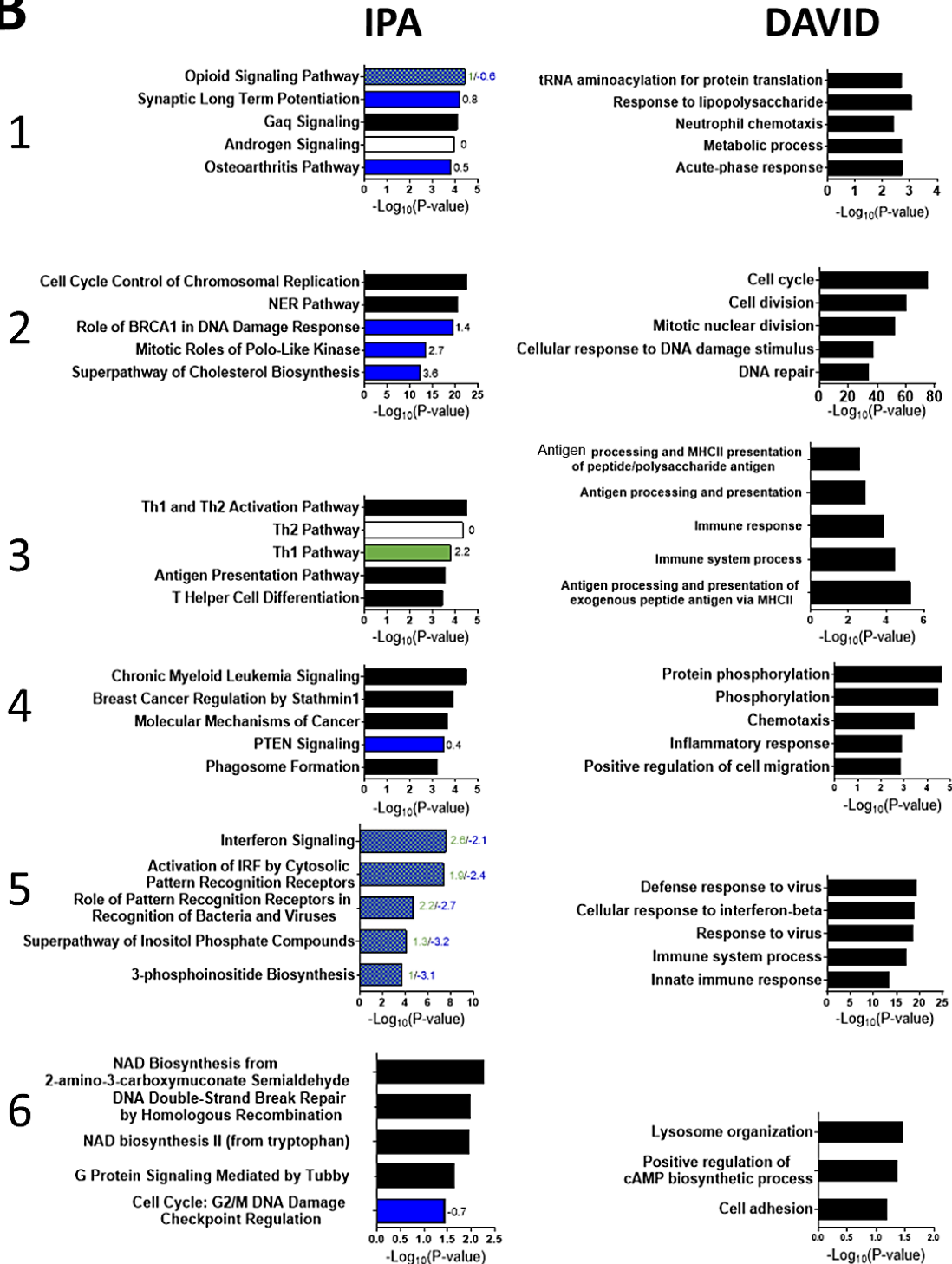


Figure 5.12B The top 5 pathways following analysis in IPA or in DAVID in the gene clusters, based on the P-values. The graphs on the left were generated using the canonical pathway analysis after the cluster gene lists were uploaded to IPA. Where possible these pathways were compared to the original datasets to get Z-score information suggesting the pathway activation state. This data was overlaid on the bars using colour, and the Z-score was listed to the right of the bar. Blue bars means the Z-score was from the *Spi1* knock-down dataset, green bars denote Z-score values taken from the *Spi1* over-expression dataset, hatched blue/green where Z-scores were calculated in both datasets. If there were Z-scores for both datasets the *Spi1* over-expression Z-score is shown first in green and the *Spi1* knock-down Z-score is shown second in blue. If the Z-scores was zero then bars were coloured white. The graphs to the right of the plot show the results of Biological Processes analysis performed using the DAVID website for the same gene list. The cluster number is indicated on the far left.

The pathways identified in these clusters were then compared to the original datasets to obtain a predicted pathway activation state (Z-score). The largest gene cluster, 2, contained genes involved in controlling the cell cycle, which appear to be activated in the *Spi1* knock-down dataset. Cluster 3 appeared to be activated in *Spi1* pSIEW over-expression samples alone, and pathways linked these genes to activation of the adaptive immune response via antigen presentation pathways. The changes in Cluster 5 seemed to correspond to the experimental pattern, and the Z-scores were all negative in the *Spi1* knock-down dataset indicating pathways were activated in a *Spi1*/PU.1 dependent manner. Overall both the pathway and clustering analysis suggested that the cell cycle was disrupted when *Spi1* expression was altered, especially when *Spi1* was reduced, though IPA was not able to offer an insight to the activation state of all the cell-cycle related pathways.

5.2.5 Confirmation of functional changes

The insights provided by the pathway analyses combined with previous reports suggested both proliferation and phagocytosis were affected by *Spi1* expression.

5.2.5.1 Proliferation

The absolute number of microglia was assessed (Figure 5.17A) to show microglia infected with *Spi1* shRNA virus did not have a largely different cell number than NS shRNA controls. This suggested that a lower *Spi1* expression in microglia did not reduce the number of microglia in culture and therefore any impact on proliferation was likely to be subtle.

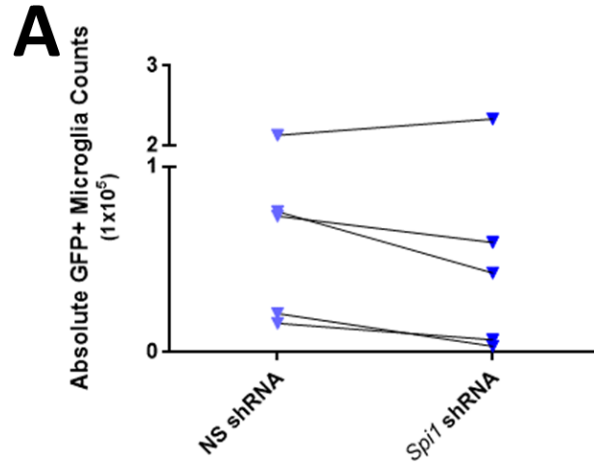


Figure 5.17 The Absolute number of infected (GFP+) microglia. A The absolute counts were determined as described in 2.16.2.2. There were no significant differences in the number of infected microglia in NS shRNA samples (pale blue) compared to *Spi1* shRNA samples (dark blue) in each experiment (Two-tailed Unpaired T-test $P=0.8524$).

Microglia proliferation was assessed using ki67 antibody staining in the culture model described in sections 2.4.9.1 and 4.2.3.1. Given a number of the cell cycle pathways that had positive Z-scores it was predicted that microglia with a reduced level of *Spi1*/PU.1 may have an altered level of proliferation. The ki67 antibody is known to stain cells in the G₁, S, G₂ and M phases of the cell cycle, but not cells in G₀, as highlighted by the top right diagram in Figure 13A. The flow plots in Figure 5.18A were pre-gated on microglia. The first dot plot shows GFP and PU.1 expression in these microglia, followed by isotype and ki67 antibody staining against DAPI nuclear stain.

In the rest of the samples, which were virally infected, ki67 staining was analysed in the uninfected cell (black outline) and infected cell (green outline) populations. The flow plots were representative of three independent experiments. The representative plots show that there were no obvious changes to the ki67 positive population caused by PU.1 knock-down (*Spi1* shRNA GFP+, n=3) or PU.1 over-expression (*Spi1* pSIEW GFP+, n=1). Though in this example the number of microglia in the *Spi1* shRNA sample was lower than the other experimental conditions. The data from these experiments has been summarised for *Spi1* knock-down samples (Figure 5.18B-C) and the one *Spi1* over-expression experiment (Figure 5.18D-E).

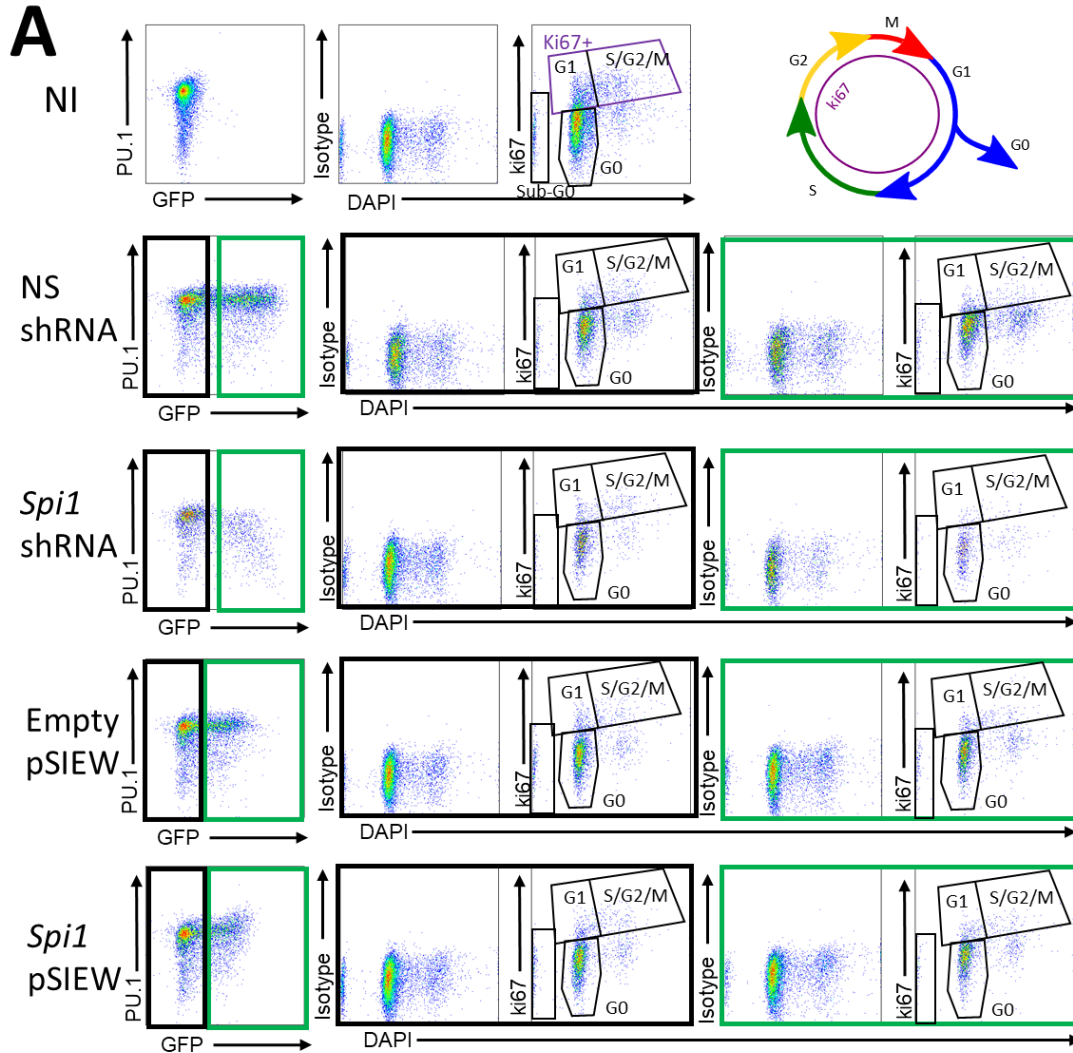


Figure 5.18 Assessing proliferation using *ki67* staining in *Spi1* shRNA and control cells- Part I A Microglia were pre-gated using *CD11b* as a positive marker. The far-left plots show GFP expression against PU.1 where the samples were then gated and divided as NI (black outlines) or GFP+ (green outlines). The middle plots represent the isotype and *ki67* staining against DAPI nuclear staining for NI cells and the far-right plots are the same layout showing the GFP+ gated cells. In each *ki67* plot the *ki67*+ cells were first identified using the isotype control. Any cells below this cut off were considered G₀. *Ki67*+ cells were then further sub-divided in to G₁ and S/G₂/M populations.

Figure 5.18B shows that in these microglia cultures a large proportion (~80 %) of microglia were in the G₀ phase of the cell cycle and were not undergoing cell division. Though there was a significant difference in the percentage of microglia in the G₀ gate (One-Way ANOVA $P=0.0287$) Sidak's Multiple Comparison Test confirmed there were no significant changes between the NS shRNA or *Spi1* shRNA infected microglia ($P \geq 0.05$). During the flow cytometric analysis, the *ki67*+ population could be further subdivided into G₁ or S/G₂/M phases using DAPI expression (shown in Figure 5.18A). The reduction of PU.1 protein (*Spi1* shRNA GFP+) in these microglia did not significantly

alter the percentage of cells in the G₁ or S/G₂/M phases of cell division (One-Way ANOVA, P=0.0535 and P=0.2716 respectively), when compared to the NS shRNA infected microglia populations. There does appear to be a slight reduction in the overall percentage microglia in the G₁/S/G₂/M phase of cell division in the NS shRNA (Figure 5.18C) compared to *Spi1* shRNA infected microglia, this was not significant (One-Way ANOVA, P=0.1502).

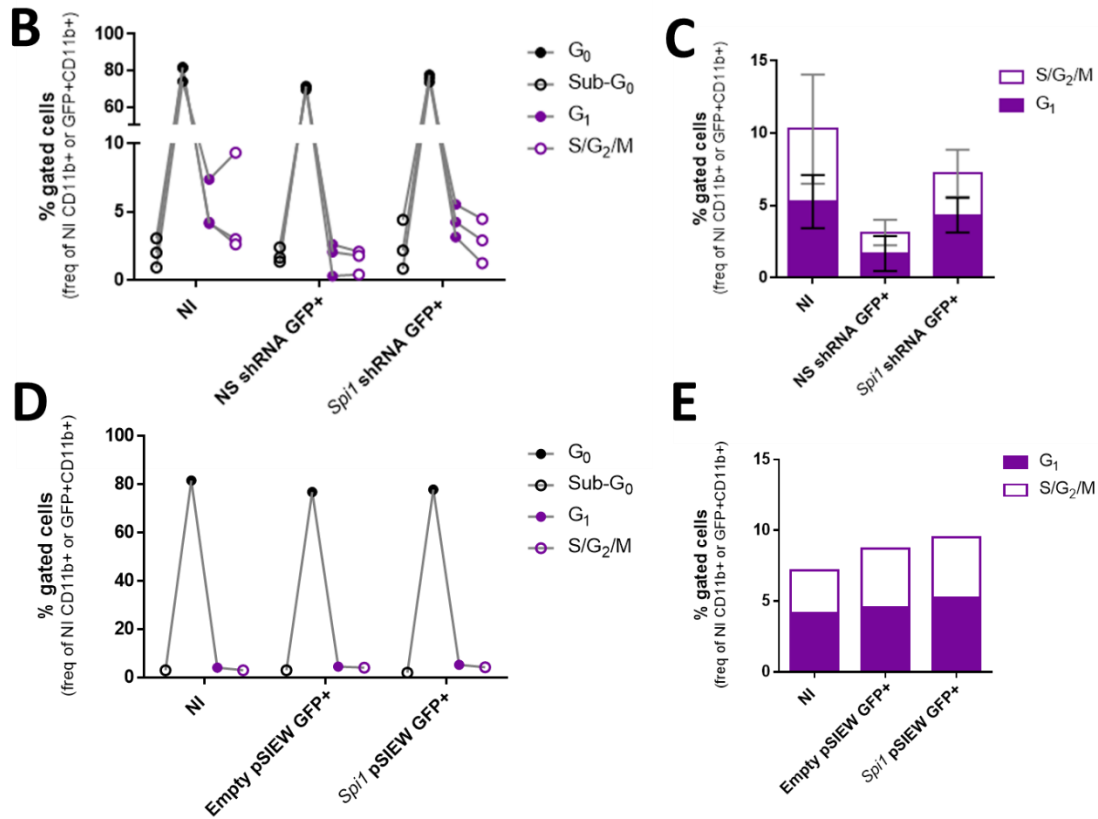


Figure 5.17 Assessing proliferation using ki67 staining in *Spi1* shRNA and control cells- Part II B A comparison of the proportion G₀ and ki67⁺ gated cells in NI, NS shRNA and *Spi1* shRNA samples, of all CD11b⁺ DAPI⁺ cells. There did not appear to be a large difference between the proportion of ki67⁺ (G₁/S/G₂/M) and G₀ cells across the experimental conditions. A One-way ANOVA showed the while there was a significant change in the G₀ population (P=0.0287) Sidak's Multiple Comparison Test showed the only significant difference was between the NI and NS shRNA groups (P≤0.05). Separate One-Way ANOVAs showed there was no significant differences in the Sub-G₀, G₁ or S/G₂/M populations (P=0.8013, P=0.0535 and P=0.2716 respectively). **C** The percentage of cells in G₁ and S/G₂/M gates from parent gates (CD11b⁺ or GFP⁺CD11b⁺). There does not appear to be a suggestion that *Spi1* shRNA GFP⁺ microglia have a higher overall percentage of G₁/S/G₂/M population compared to NS shRNA GFP⁺ microglia, though this difference did not reach significance (One-Way ANOVA, P=0.1502). In **B-C** NI, NS shRNA and *Spi1* shRNA samples have horizontal bars to display the means taken from 3 independent experiments (n=3) and the error bars show the standard deviation. **D** Again there was no observed difference in the G₀ and ki67⁺ cell percentages in NI, pSIEW and *Spi1* pSIEW samples. **E** The proportion of G₁ and S/G₂/M cells were similar across all samples. The data shown in plots **D-E** are the result of one experiment (n=1).

This experiment was only carried out once in cultures where *Spi1* was over-expressed (*Spi1* pSIEW) as shown in Figure 5.18D-E. In this experiment there were no overt differences in the percentage of cells in each stage of the cell cycle in either the NI, empty pSIEW or *Spi1* pSIEW microglia (Figure 5.18D). The percentage of ki67+ microglia that were in the G₁ or S/G₂/M was similar across all conditions (Figure 5.18E).

Taken together these results suggest that in this *in vitro* system microglia proliferation was not majorly affected the changes to PU.1 as shown in Figure 5.18A. However, there was a small proportion of ki67+ cells in these cultured cells and some variation between the replicates. It is possible that measuring proliferation with a more sensitive assay could better quantify the percentage of S/G₂/M cells, see section 5.3 for further discussion.

Following the pathway analysis (section 5.2.4) there were concerns that the *Spi1* shRNA infected microglia may be failing to correctly undergo cytokinesis. If these cells were failing to undergo cytokinesis then the microglia would be polyploid and have a higher nuclear DAPI stain. Therefore, the flow cytometric data gathered to assess ki67 staining in these microglia samples was re-analysed using DAPI staining alone to see if there were any changes to the DNA content of these cells (Figure 5.19).

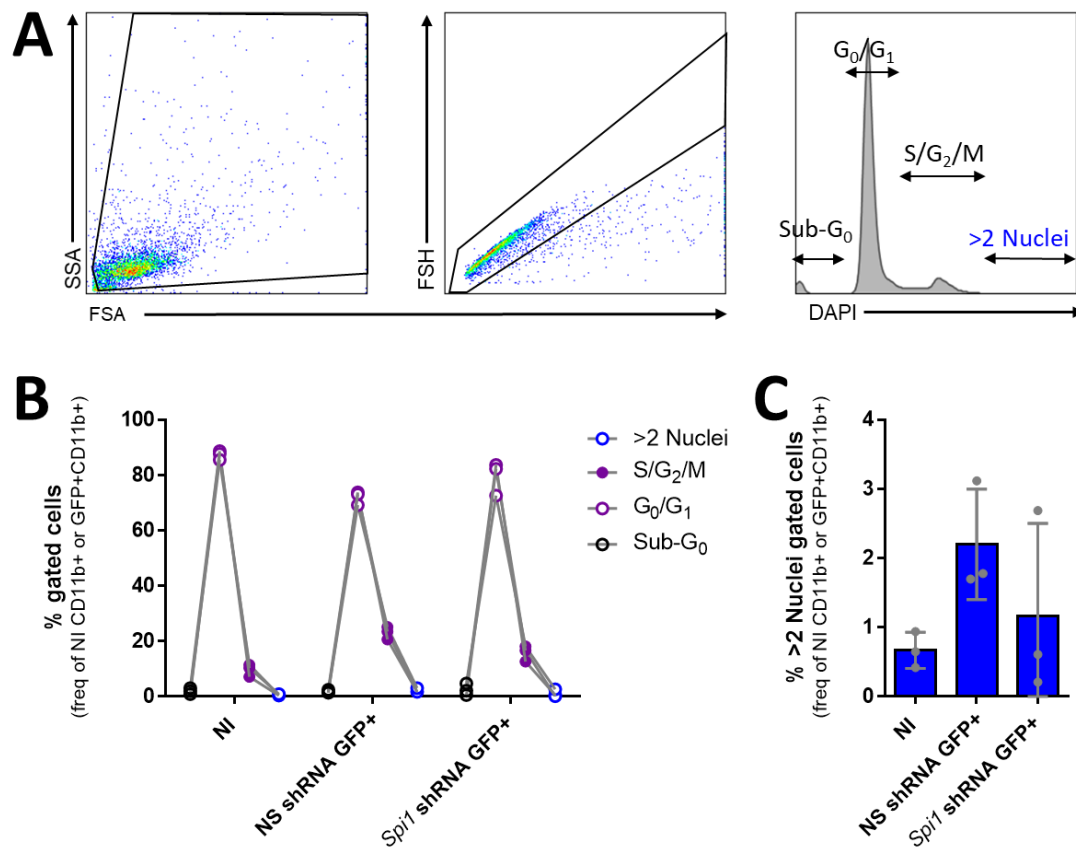


Figure 5.19 Assessing DAPI Nuclear Content of NI, NS shRNA and *Spi1* shRNA infected microglia. **A** The gating approach used in this analysis. When selecting single cells the gates were extended to the edge of the plots to ensure all cells were included, as polyploid cells tend to be larger and more complex they have a higher FSA and SSA. The final was a histogram of DAPI staining and shows the gates used to measure each part of the cell cycle. **B** Graphical summary of showing the percentage of cells in each part of the cell cycle, determined by DAPI staining. **C** Graph only showing the percentage of cells in the polyploid gate (> 2 Nuclei). These graphs show the results of 3 independent experiments (n=3), the bars indicating the mean value and the error bars showing the standard deviation. One-way ANOVA confirmed no significant difference in the >2 Nuclei gated cells (P=0.1908).

Again, Figure 5.19B suggest there were no obvious cytokinesis defects in the *Spi1* shRNA infected microglia, compared to the NS shRNA infected or NI microglia. There appeared to be a slight reduction in the percentage of S/G₂/M phase in the *Spi1* shRNA samples compared to the NS shRNA samples. While it might seem to conflict with the results in the previous analyses (Figure 5.18), this was likely because the polyploid cells directly beneath the S/G₂/M gate (Figure 5.18A) cannot be removed from the analysis when using DAPI staining alone. The percentage of polyploid cells in all samples (Figure 5.19C) was very small, and did not significantly differ between the groups (One-Way ANOVA, P=0.1908), which suggests *Spi1* shRNA cells have no major cytokinesis defect.

The ki67 staining results of the proliferation analyses in this section suggest that microglia with a moderate *Spi1* knock-down and over-expression did not have overt changes to the cell cycle. This was unexpected given the amount of cell cycle pathways that were affected in the *Spi1* knock-down RNA-Seq pathway analyses. Potential reasons for this disparity will be discussed in section 5.3.

5.2.5.2 *Phagocytosis*

Other studies have demonstrated that alterations to the PU.1 protein level impacts microglia phagocytosis [230,232]. Therefore, phagocytosis was investigated in microglia infected with NS shRNA and *Spi1* shRNA by measuring the ability of the cells to phagocytose zymosan particles, as described in section 2.5.3.

Firstly, the expression of Dectin-1, a key phagocytic receptor [183], was confirmed on cultured microglia (Figure 5.20A). Secondly, it was determined if microglial phagocytosis of zymosan was more efficient with opsonisation. Opsonisation was done using mouse serum and enabled complement proteins to bind to zymosan particles, tagging them in a way which ensures preferential microglial phagocytosis via the CD11b receptor [183]. As detailed in section 2.5.3.3 zymosan particles were either opsonised with mouse serum, or left un-opsonised, before being mixed with microglia and incubated for an hour. Following this the cells were fixed and stained with the microglia marker CD11b and run through the flow cytometer. Figure 5.20B shows the gating strategy used to isolate single microglia and determine the proportion of zymosan positive cells. This pilot experiment showed that a larger proportion of opsonised zymosan were phagocytosed by microglia than un-opsonised zymosan.

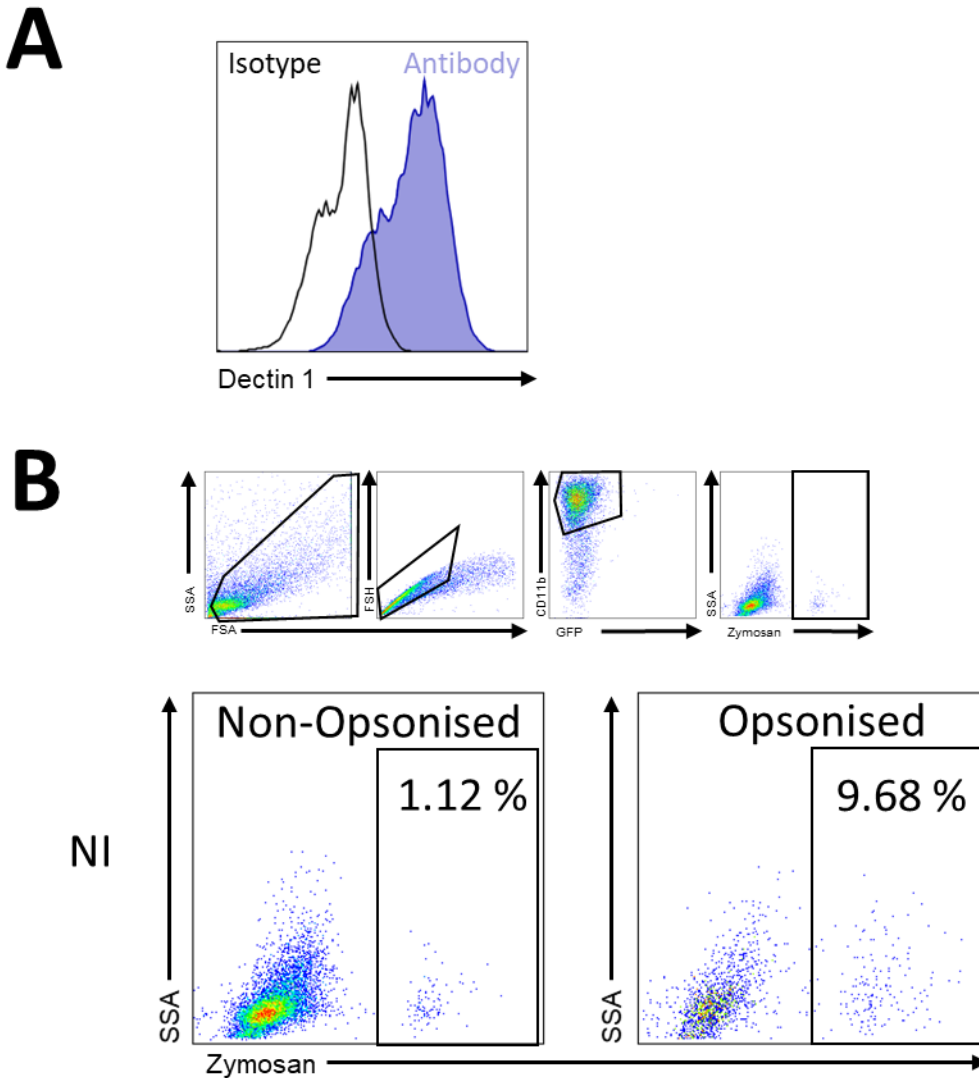


Figure 5.20 Preliminary work to optimise microglial phagocytosis assay in this model. **A** The phagocytic receptor Dectin-1 was expressed on these cultured microglia. Dectin-1 staining is shown in blue, and the isotype control in black. **B** Comparing the proportion of zymosan that was phagocytosed following opsonisation with mouse serum compared to a non-opsonised control. The first row of plots show the gating strategy used in this analysis. Following debris and doublet exclusion NI and infected microglia (CD11b+GFP- and CD11b+GFP+ respectively) were separately selected. Cells that had phagocytosed the AF405 labelled zymosan could be detected by Flow. The plots below the gating outline shown the proportion of zymosan positive microglia in the non-opsonised and opsonised samples. There were a larger proportion of zymosan positive cells in the samples that were treated with the zymosan that was opsonised with mouse serum.

Therefore, zymosan was opsonised all experiments from this point forward and phagocytosis was assessed using the Amnis Imagestream® MKII imaging cytometer. This approach was chosen as phagocytosed zymosan could be differentiated from zymosan bound to the surface of the microglia, which is not easily possible with standard flow cytometry. This experiment aimed for 10:1 ratio of zymosan to total cultured cells. Based on previous experiments the cell number was

estimated to be between 1×10^5 and 2×10^5 . Therefore, 2×10^6 opsonised zymosan particles were diluted in microglia culture media supplemented with M-CSF and TGF- β and added to each culture flask. These cells were then harvested, washed to remove excess zymosan, fixed and stained for CD11b before being run on the imaging cytometer. These results were analysed using the internalisation wizard on the IDEAS[®] software. For detailed descriptions of the parameters used in the IDEAS[®] software refer to section 2.16.2.

Figure 5.21 demonstrates the steps taken in this analysis, including representative images from each subset. The first plot shows how cells were separated from debris such as unbound zymosan and cells undergoing apoptosis (Figure 5.21A). The unfocused cells were then removed from this analysis (Figure 5.21B). Figure 16C shows the gates that were used to separate uninfected microglia (CD11b+GFP-; orange) from infected microglia (CD11b+GFP+; red). As there was a range of GFP expression there was a mixed population of cells in the middle (CD11b+GFPlow; pink) which consists of unlabelled cells and uninfected/low GFP expressing microglia.

As suggested in Figure 5.7E *Spi1* shRNA infected microglia with a higher GFP expression (GFP++) had a lower amount of PU.1 protein compared to the rest of the infected population (GFP+) or uninfected cells within the sample. Therefore, the internalisation analysis was repeated in microglia with the highest infection (GFP++; green) using the gate shown in Figure 5.21. This analysis suggested that microglia with a higher *Spi1* shRNA infection had a large reduction in phagocytosis compared to GFP++ NS shRNA infected cells. Following this zymosan positive microglia were then separated from cells without zymosan, and they were further split into high, mid and low levels of zymosan by the maximum pixel size. Figure 5.21C shows the gates used in this analysis using CD11b+GFP- cells as an example.

The final stage of the internalisation wizard determined the internalisation ratio, which was determined to be the ratio of the zymosan intensity within the cell boundary compared the intensity of the entire cell. A positive ratio indicates zymosan has been internalised and a negative ratio that zymosan was outside of the cell boundary. Examples can be seen in Figure 5.21D. Therefore, this analysis could be used to successfully determine the percentage of uninfected and infected microglia that have internalised zymosan particles.

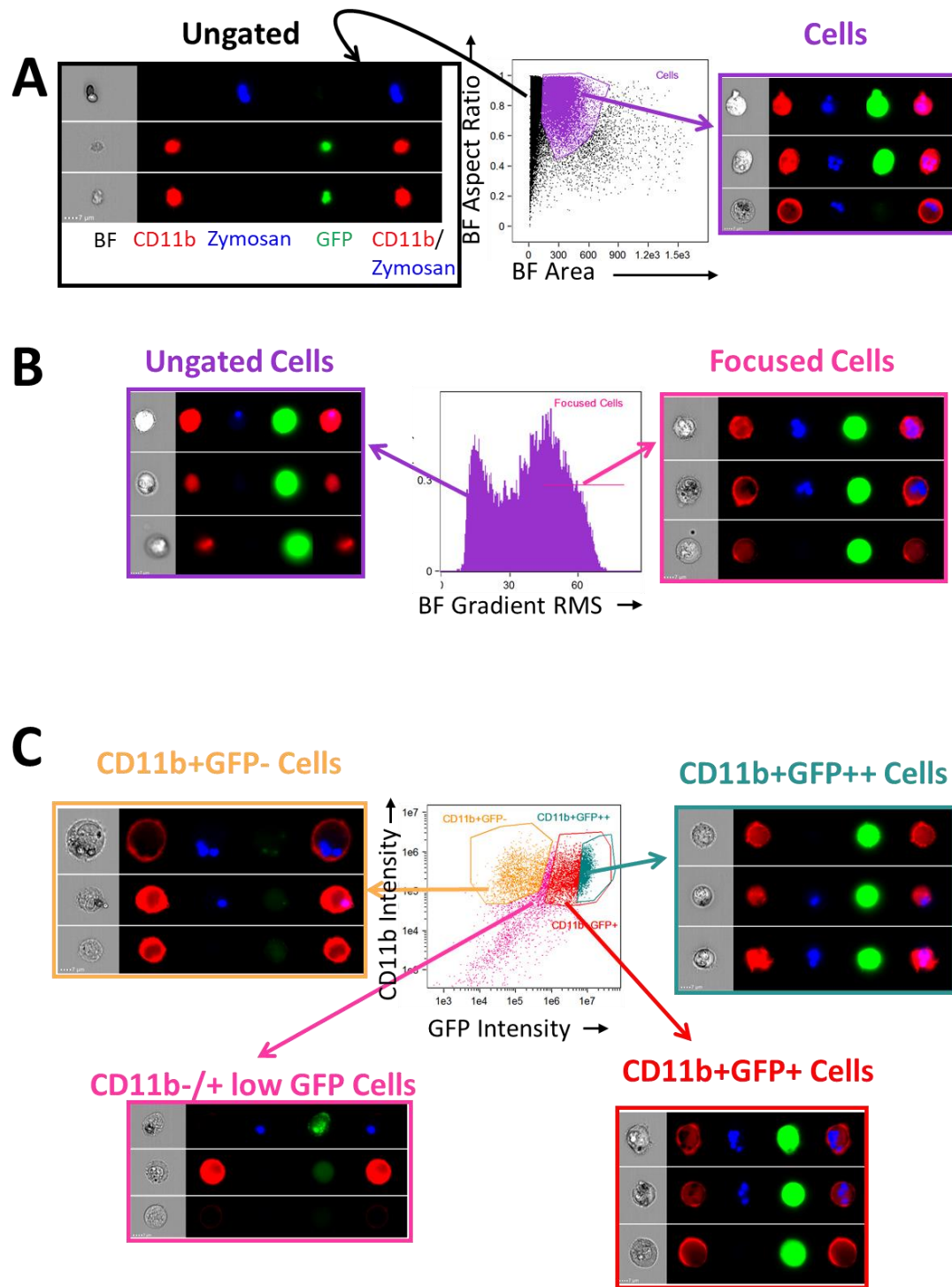


Figure 5.21 Representative gallery images taken from the NS shRNA samples describing the stages of analysis using the internalisation wizard- Part I. All the gallery images all show BF, CD11b (red), Zymosan (blue), GFP (green) and CD11b/Zymosan overlaid (left to right). All of these pictures were taken using the 60x magnification lens. The scale bars in the bottom left corner of the images are 7 μ M long. **A** The first gate was used to separate cells (right) from unbound zymosan and apoptotic microglia (left). **B** the next gate was used to separate cells that were in focus (right), with a BF gradient RMS value of over 50, from unfocused cells (left). **C** The plot shown here was used to separate infected microglia (CD11b+GFP+; right) from non-infected microglia (CD11b+GFP-; left). The ungated portion of this plot (CD11b+GFP^{low}) contained a mixture of NI and GFP^{low} microglia.

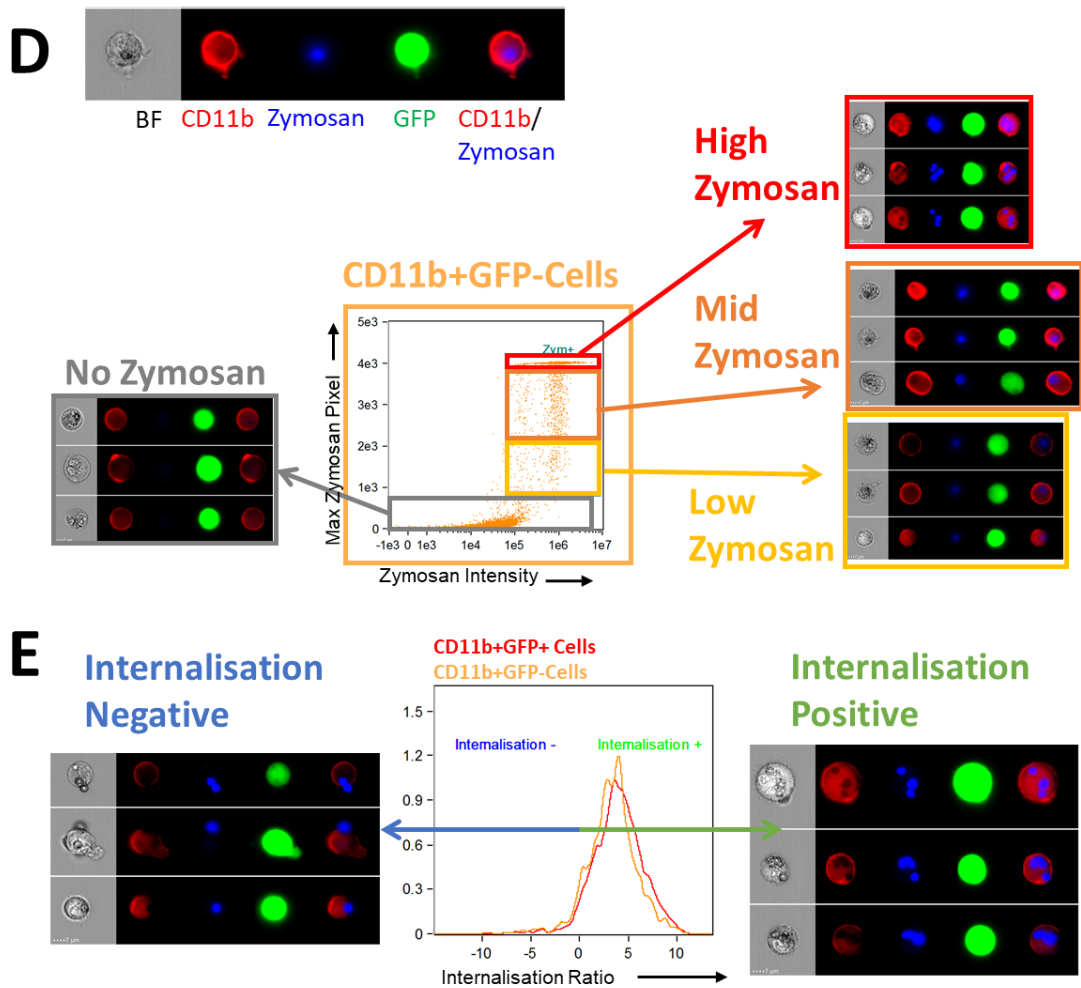


Figure 5.21 Representative gallery images taken from the NS shRNA samples describing the stages of analysis using the internalisation wizard- Part II. D Assessing the number of zymosan+ cells in the CD11b+GFP- microglia fraction. Cells without zymosan had a lower signal intensity and pixel size in this channel (left). Microglia that were associated with zymosan could be further separated into having low, mid and high levels of zymosan according to the maximum pixel size (right). **E** The final step in this internalisation wizard was to calculate the internalisation ratio. This is defined as the ratio of zymosan intensity inside the cell compared to the intensity of the entire cell, the CD11b surface stain was used to denote this in this analysis. A positive score indicates zymosan has been internalised (right) and a negative score suggests zymosan is outside the cell boundary (left).

The following figures will present the results of this internalisation analysis from two independent experiments. Figure 5.22A show the CD11b/GFP plots generated from first replicate in addition to the zymosan positive cell gates and the gates used to determine the level of zymosan associated with the cells. The results of these analyses are summarised graphically in Figure 5.22B. The percentage of Zymosan- and Zymosan+ (low, mid and high) microglia are summarised in Figure 5.22B. Here it appeared that NS shRNA viral infection increased the rate of zymosan uptake when compared to the non-infected sample. This was not seen in microglia infected with the *Spi1* shRNA infected microglia which had a higher percentage of zymosan- cells compared to both NS shRNA

GFP+ microglia and uninfected cells within the sample. The reduction in zymosan+ cells was more apparent in cells with a very high GFP intensity (GFP++), though in the *Spi1* shRNA sample there was only a small number of cells in this gate. Most zymosan positive cells had a high uptake of zymosan.

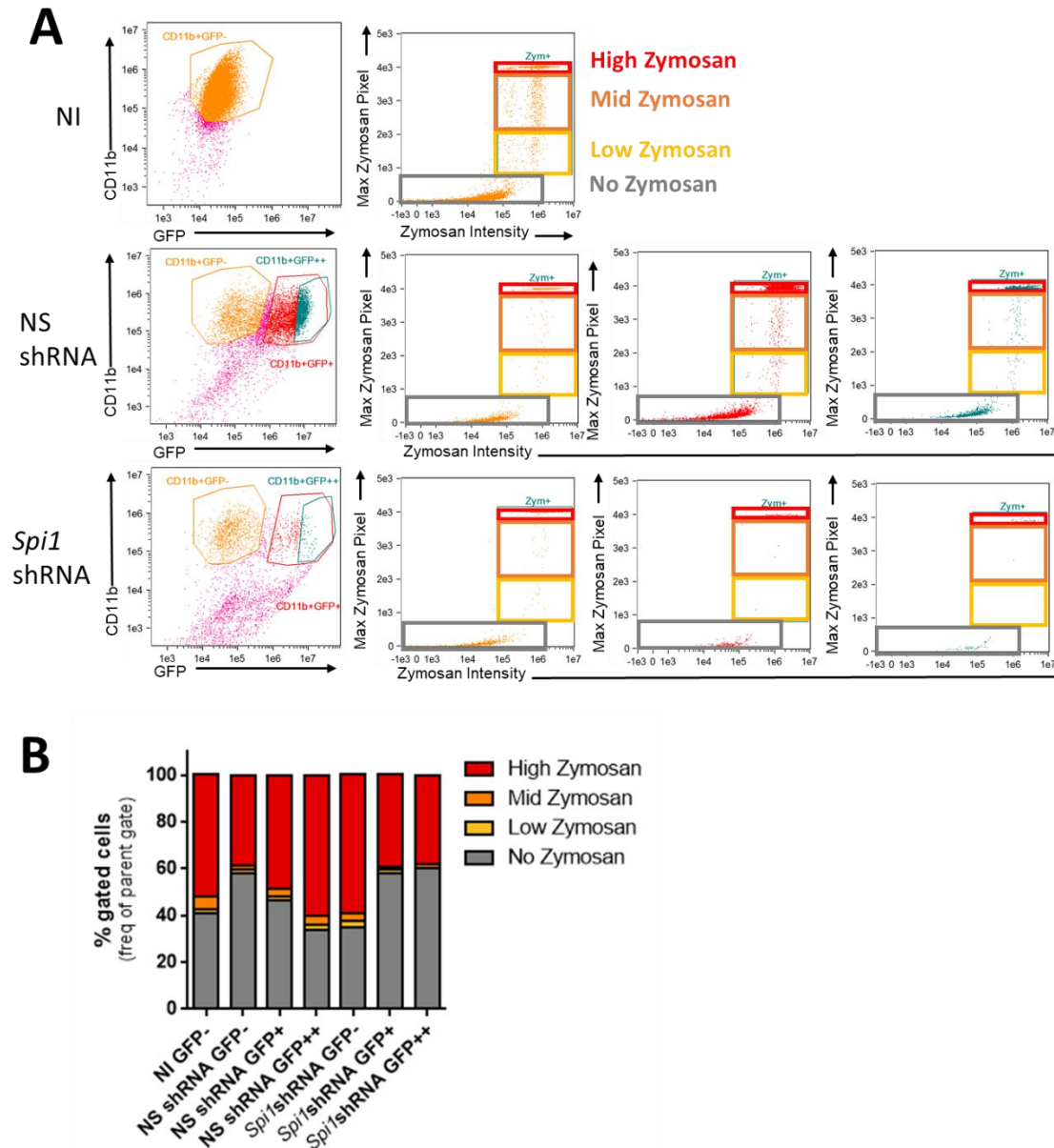


Figure 5.22 Plots from the internalisation analysis of the first replicate of the phagocytosis experiment. **A** the CD11b/GFP plots used to select separate microglia by GFP expression followed by the gates used to select zymosan positive cells, which could then be further subdivided into low, middle and high levels of zymosan. **B** The proportion of zymosan negative (grey) and zymosan+ cells that were considered to have high (red), middling (orange) and low (yellow) levels of zymosan in each condition. In all experimental conditions most of the zymosan+ cells contain a large amount of zymosan.

A similar pattern was observed in the second replicate (Figure 5.23A), where there was a higher proportion of zymosan negative cells in the *Spi1* shRNA GFP+ microglia compared to the NS shRNA GFP+ infected microglia. However in this replicate there did not appear to have such a large difference between *Spi1* GFP- and *Spi1* GFP+ cells. Again, in this zymosan positive population of microglia the majority of cells had a high level of zymosan uptake. When the zymosan positive cells were pooled together (Figure 5.23B), it confirmed that there were significantly fewer *Spi1* shRNA microglia that have internalised zymosan, compared to NS shRNA microglia ($P < 0.0001$).

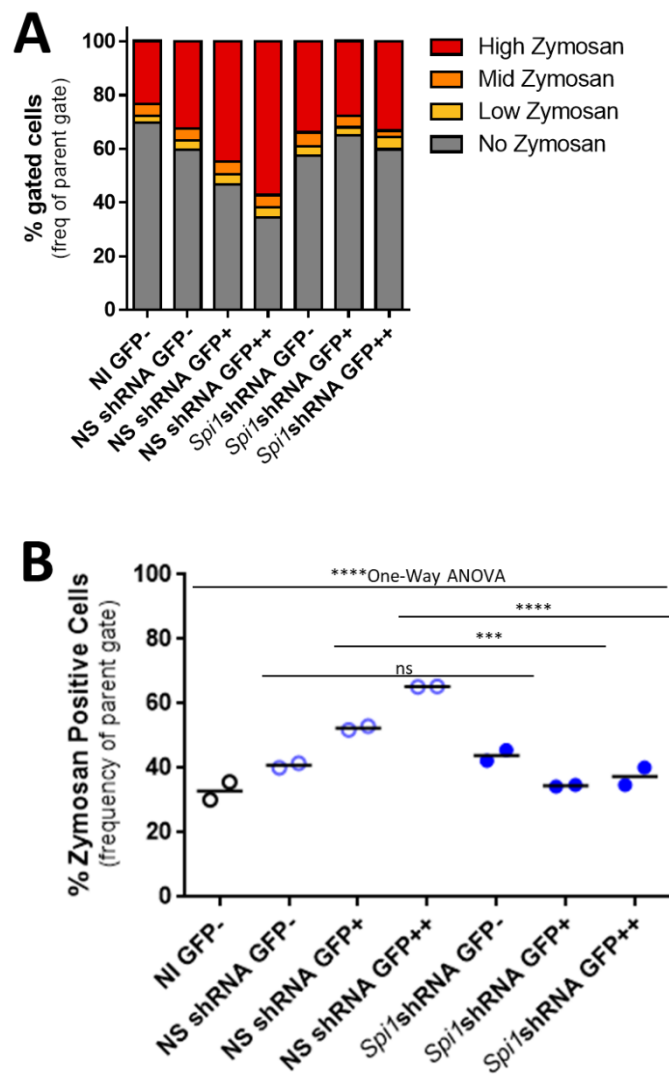


Figure 5.23 Final analysis from the second replicate of the phagocytosis experiment. A Again the percentage of zymosan+ microglia appears to be higher in microglia that were infected with virus compared to non-infected cells. Moreover the NS shRNA GFP+ microglia have a higher proportion of zymosan positive cells compared to microglia infected with the *Spi1* shRNA virus. A large proportion of these zymosan positive cells contained high levels of zymosan. **B** The percentage of Zymosan positive cells from both replicates ($n=2$),

*this confirmed the mean, indicated by the horizontal bar, proportion of cells that internalised zymosan was significantly different (One-way ANOVA, $P < 0.0001$). Sidak's multiple comparison test confirmed this was significant in all infected cells (GFP+ $***P < 0.001$) and became more significant in highly infected cells (GFP++ $****P < 0.0001$). There were no significant differences between the uninfected (GFP-) NS shRNA and Spi1 shRNA microglia, denoted by ns.*

To ensure these zymosan positive events were in-fact the result of a zymosan particles being phagocytosed and not just zymosan being bound to the surface of the microglia the internalisation ratio was calculated for each sample. As described in section 2.16.2 this was done by dividing the intensity of the zymosan signal within the cell boundary by the intensity of the entire cell. If microglia have successfully phagocytosed zymosan then the ratio was positive. Figure 5.24A shows the internalisation ratios for each sample, as you can see these values were mainly positive and therefore suggest much of the zymosan has been internalised. When the percentage of positive and negative cells were compared in Figure 5.24B it confirms that the majority of microglia associated with zymosan have phagocytosed it. The average internalisation ratios were similar in all samples (Figure 5.24C).

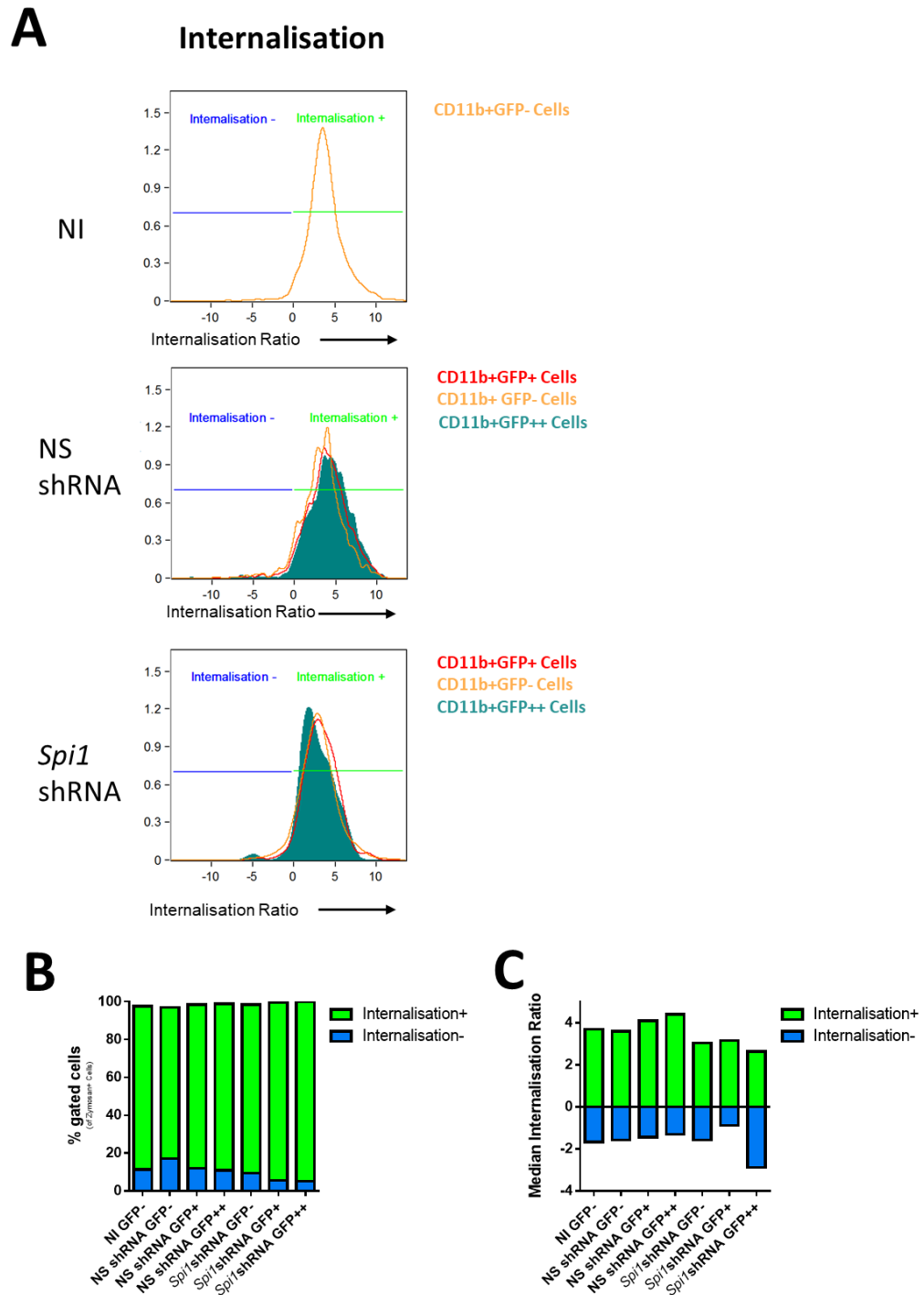


Figure 5.24 The internalisation ratio and mean zymosan pixel range for the first replicate of the phagocytosis experiment. **A** Example plots from the first experiment showing the positive and negative internalisation ratio values (left) and the mean zymosan pixel range for all the samples. **B** Graphical summary of the proportion of internalised zymosan. Over 90 % of all zymosan+ events were a result of internalised zymosan. **C** The median internalisation ratio value for each experimental condition. The ratio value does not appear to be altered by viral infection.

Similar observations were made in the second repeat of the experiment (Figure 5.25) where the majority of zymosan-associated microglia had internalised particles, though neither this or the median value of internalisation (positive) appeared to be meaningfully altered between samples. When these results were pooled (data not shown) it confirmed there were no significant differences between the experimental viruses or NI samples (Two-way ANOVA, $P=0.7542$).

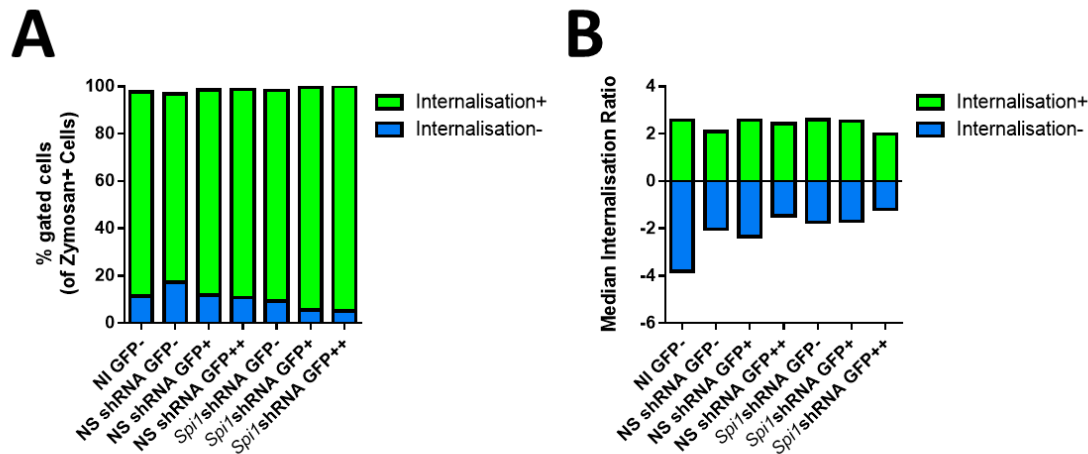


Figure 5.25 The internalisation ratio and mean zymosan pixel range for the second replicate of the phagocytosis experiment. **A** The majority of zymosan positive events were internalised in all samples. **B** The average internalisation ratio values for each sample were similar across all experimental conditions, expected the NI sample where there appeared to be a moderately higher amount on extracellular zymosan.

Taken together these results suggest that during the incubation time microglia were able to internalise opsonised zymosan. *Spi1* knock-down did not completely prevent microglia from being able to engulf zymosan or limit the number of internalised particles. However there was a smaller proportion of zymosan positive *Spi1* shRNA infected microglia compared to NS shRNA infected cells, approximately 10 % lower in each replicate. Thus, it appeared that in this assay *Spi1* knock-down may have impacted the ability of microglia to effectively detect or bind zymosan particles, but did not impact the rest of the phagocytotic process.

5.2.6 Comparison to human IGAP dataset

The aim of this part of the thesis was to determine the impact of altering PU.1 protein levels on microglia gene expression. As discussed in section 1.4.2.2 of the introduction *Spi1* was one of several LOAD genes have been shown to impact microglia gene expression and physiology [230,232,233]. Others have proposed that *Spi1* likely binds upstream of other AD-related risk genes [230,231]. Therefore it was proposed that sets of differentially-expressed genes from the

Spi1 knock-down and *Spi1* over-expression datasets generated in this thesis should be tested for enrichment of association signal in the International Genomics of Alzheimer’s Project (IGAP) dataset [3], this work was carried out by Dr Peter Holmans as described in section 2.15.4.1. The *Spi1* RNA-Seq datasets were split into different gene sets according to the adjusted P-value for differential expression and Table 5.6 summarises the results of this analysis.

Experiment	P-adj Threshold	Number of genes	Enrichment Effect (β)	P-value	Corrected P-value†
<i>Spi1</i> knock-down	0.05	2380	-0.011	0.72564	0.9971
	0.01	1499	-0.00731	0.62718	0.9921
	0.001	812	-0.0236	0.7864	0.9983
	1.00E-04	476	-0.0284	0.7677	0.9981
	1.00E-05	271	-0.0811	0.94442	1
	1.00E-06	166	-0.0441	0.75068	0.9978
	1.00E-08	71	0.000693	0.49713	0.9718
	1.00E-10	33	-0.0205	0.55633	0.983
<i>Spi1</i> over-expression	0.05	267	0.124	0.012724	0.1126
	0.01	145	0.0999	0.090943	0.4903
	0.001	78	0.149	0.067339	0.3985
	1.00E-04	43	0.245	0.035644	0.2526
	1.00E-05	28	0.42	0.006785	0.0632
	1.00E-06	21	0.51	0.003295	*0.0355

Table 5.6 Summary table of MAGMA analysis comparing the RNA-Seq datasets created in this thesis to IGAP data. The P-adj Threshold is the adjusted P-value cut-off used in the analysis of the RNA-Seq datasets. The number of genes in the analysis following these cut-offs are also shown here. The enrichment effect/ β value states if the gene sets (each row) have more significant genes in the IGAP dataset. A positive value means yes and a negative value no. †Corrected for multiple of multiple overlapping gene sets using MAGMA. *Indicates a corrected P-value of <0.05.

For this analysis the null hypothesis stated that the association between the *Spi1* RNA-Seq gene lists, determined by a P-adj threshold, did not have a stronger association than an average gene list containing genes outside of these sets. The question this analysis asked was if the genes from the *Spi1* KD and OE datasets were considered to be enriched in the IGAP dataset. The IGAP dataset contains lists of variants and other genes that have been associated with AD pathology. Table 5.6 demonstrates that the set of 21 genes in the *Spi1* over-expression P-adj 1×10^{-6} gene set were enriched in this AD association gene set.

The positive enrichment effect (β) suggested that the *Spi1* over-expression data appears enriched in signal from the IGAP data, whereas the *Spi1* knock-down data was not. This IGAP association was strongest when the most stringent threshold ($\alpha = 1 \times 10^{-6}$) was applied to the *Spi1* over-

expression data, giving a list of 21 genes, and was significant after correcting for multiple testing of 14 gene sets in MAGMA (corrected for multiple testing P-Value = 0.0355). However, nominally-significant associations were also observed at other thresholds. When these genes are plotted on a volcano plot (Figure 5.26) it shows that these 21 highly significant genes also appear to contain several genes with high \log_2 fold-change values, and these tended to show increased expression.

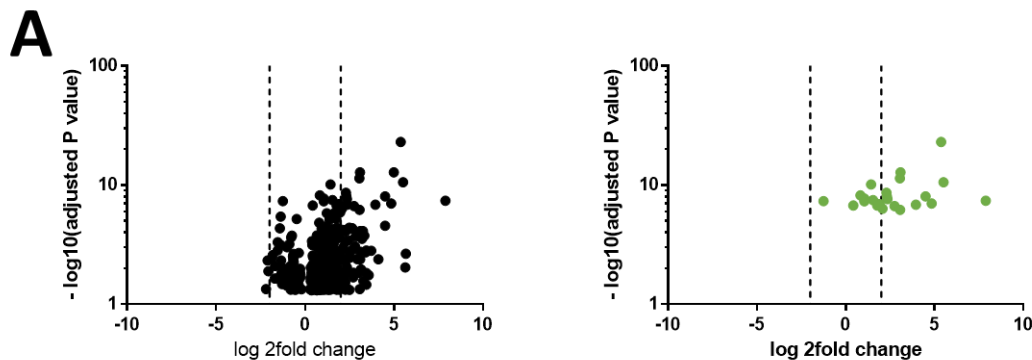


Figure 5.26 Volcano plots comparing distribution of genes in the *Spi1* OE dataset. The left plot indicates all data with an adjusted P value of < 0.05 and the right plot indicates the gene distribution when using threshold of $P\text{-adj} < 1 \times 10^6$. This data shows that the most significant genes ($P\text{-adj} < 1 \times 10^6$) also seem to contain some genes with the highest fold changes.

The complete list of the 21 gene-set that was significantly associated with the IGAP dataset can be seen in Table 5.7. These 21 genes were differentially expressed in the *Spi1* over-expression dataset and had an AD risk SNP that was contained within the IGAP dataset. Not all of the genes listed reached GWAS significance in the IGAP dataset, normally defined as a P-value of $< 5 \times 10^{-8}$ [3], though there were still several genes with moderately significant P-values. The \log_2 fold-change values were provided from the *Spi1* OE RNA-Seq dataset to see how an increased *Spi1* impacted the expression of these genes.

Of the 21 genes listed in Table 5.7 *Ifit2*, *Oas1* and *Oas2* were linked to interferon signalling and the immune response to virus, perhaps unsurprisingly considering the *Spi1* over-expression pathway analysis [363,364]. Interestingly the *Ptger2* gene, which was the only gene in this list with a negative fold-change, encodes the Prostaglandin E Receptor 2 (PGE2) and has been linked to AD pathology. *In vivo* mouse experiments have shown that the Pge2 receptor is involved in the microglia damage response [365] and AD model mice that were Pge2 deficient had a reduced lipid peroxidation and amyloid- β load [366]. Given that a higher *Spi1* expression is associated with an increased AD risk [4,230] it seems odd that *Spi1* over-expression would result in a reduction of the Pge2 receptor which has been linked to pathophysiological changes in AD. This could be investigated by quantifying Pge2 protein expression and comparing this to mRNA changes in the

Spi1 knock-down dataset. With regards to antigen presentation and the adaptive and innate immune responses there were three linked genes *PECAM1*, *RNF144B* and *TREML4* [367–369]. Another gene, ZNF366 which had a log₂ value of over 5, is known to recruit histone-deacetylases to repress gene transcription [370]. Taken together these results suggest that increasing *Spi1* mRNA/PU.1 protein expression in microglia results in a wide range of effects on microglia phenotype.

Human Gene Name	p-value in IGAP	Mouse Gene Name	Log ₂ Fold Change in <i>Spi1</i> OE	P-adj in <i>Spi1</i> OE
EFNB3	5.64E-01	Efnb3	5.3697	8.49E-24
TMEM44	5.88E-01	Tmem44	3.0809	1.61E-13
BTBD11	4.95E-01	Btbd11	3.0482	3.85E-12
ZNF366	1.07E-02	Zfp366	5.508	2.63E-11
ST7	N/A	St7	1.4258	7.47E-11
NAPEPLD	2.84E-01	Napepld	2.2926	2.36E-09
CKB	8.34E-04	Ckb	0.8262	6.26E-09
IFIT3	3.07E-01	Ifit3	2.3135	8.67E-09
TMEM229A	4.66E-01	Tmem229a	4.4963	8.67E-09
DDX19B	7.11E-04	Ddx19b	1.0481	1.93E-08
TREML4	3.43E-03	Trem14	2.3458	2.33E-08
OAS1	3.24E-05	Oas1b	1.5365	3.35E-08
SLC6A4	4.14E-02	Slc6a4	7.8789	4.08E-08
PTGER2	5.02E-01	Ptger2	-1.2546	4.48E-08
RAP1GAP2	1.24E-01	Rap1gap2	1.055	4.71E-08
DNASE1L3	6.73E-01	Dnase1l3	4.837	1.00E-07
ISG15	3.01E-01	Isg15	1.9079	1.15E-07
RNF144B	7.05E-01	Rnf144b	3.9508	1.44E-07
ARHGEF40	6.34E-01	Arhgef40	0.4305	1.77E-07
OAS2	5.25E-05	Oas2	1.7721	1.84E-07
RTN1	3.36E-01	Rtn1	2.7493	2.10E-07
KCND1	N/A	Kcnd1	2.0755	4.49E-07
PECAM1	7.25E-01	Pecam1	3.0653	6.45E-07

Table 5.7 The 21 genes that had an adjusted P-value of $<1 \times 10^{-6}$ that were significantly associated to the IGAP dataset.

In conclusion this comparison demonstrated that forcing *Spi1* over-expression in this *in vitro* model, to a level where PU.1 protein was approximately doubled, caused gene expression changes that aligned to several genes in the human LOAD genetic risk dataset. The expression of most of these genes was increased by *Spi1* over-expression. This analysis demonstrated that even moderate increases to *Spi1* expression levels can cause meaningful changes to microglia gene expression. Moreover, this confirmed that *Spi1*/PU.1 was a good target to study in AD

pathophysiology as the changes seen in this *in vitro* murine study seem to correlate to human genetic data, suggesting this model could be used to mimic changes to microglia in human AD pathophysiology.

5.3 Discussion

In this chapter it has been demonstrated that alterations to the level of the PU.1 transcription factor changes the expression of lots of genes. In this experimental model the aim was to moderately change PU.1 protein levels to try and better model physiological changes to gene expression that might occur as a result of expressing a risk SNP.

5.3.1 Summary of main findings

Firstly, it was confirmed that PU.1 protein expression was reduced in microglia by an average of 60-70 % by the *Spi1* shRNA virus and increased between 50-200 % by the *Spi1* pSIEW virus. While there were changes to gene expression appeared to smaller in *Spi1* shRNA samples. In contrast, alterations at the protein level were often larger, especially in the *Spi1* knock-down dataset, which was seen for both the PU.1 and Iba-1 proteins. There were also changes to the P2ry12^{high} subset of microglia that matched the *Spi1* shRNA samples. In the *Spi1* example it was possible that the *Spi1* shRNA knock-down did not have as large an impact at the mRNA level because the shRNA acts to block translation rather than transcription. As previously discussed qPCR is a sensitive technique that is vulnerable to being skewed by small changes to the measured gene or endogenous control genes [346,347]. However mRNA was also measured with RNA-Seq which is known to be a more robust technique [371] and these results correlated to protein changes.

While the mRNA data includes all infected (GFP+) microglia it has been determined that microglia that had a higher expression of the GFP viral reporter had more extreme changes to the protein levels (Figure 5.7 and Figure 5.9). Thus, if the mRNA expression profiles could also be categorised according to their GFP expression there may also be larger changes at the mRNA level. This could be measured experimentally by splitting these microglia cultures into GFP^{low} and GFP^{high} subsets using flow cytometric sorting and then performing qPCR analysis on the separate fractions. However, this approach would have been more demanding technically, requiring many more infected microglia to ensure there were enough cells to gain a sufficient RNA for this analysis.

The PCA (Figure 5.5) showed that that while the *Spi1* experimental viruses were different, as expected, there were differences between the NS shRNA and pSIEW control viruses. This was likely due to the differences in the plasmid, the NS shRNA virus still results in the production of an

shRNA which can be interpreted as a viral stimulus [372]. Given that each *Spi1* virus was always compared to its own relative control virus the difference between the control plasmids was not considered to meaningfully impact the results. It was found that there were a large proportion of genes that had altered expression values in both *Spi1* RNA-Seq datasets.

The work in this thesis identified 162 *Spi1* dose-sensitive 'core' genes which appeared to be expressed by microglia in a PU.1 dose dependent manner (Figure 5.3-Figure 5.4). This was supported by clustering analyses. The fold-change clustering analyses in Figure 5.14 demonstrated genes that were upregulated in one dataset were downregulated in the other dataset. Moreover the FPKM clustering analyses identified a 'core' gene cluster that was reduced in the *Spi1* knock-down dataset and increased in the *Spi1* over-expression dataset (Cluster 5; Figure 5.16). Pathway analyses of this gene cluster suggests these genes map onto interferon signalling and the immune response to viruses. Taken together this suggests was a 'core' set of immune defence genes that were changed according to the dose of *Spi1*/PU.1.

While this could be due to the experimental approach taken to increase and knock-down *Spi1* expression with viruses this was unlikely to be the sole cause for these differences. Firstly, for both the *Spi1* knock-down and *Spi1* over-expression datasets were assessed relative to their own control viruses to try and minimise any effects that were due to viral infection alone. Also these pathways were not as significantly associated in the *Spi1* knock-down data which suggests these pathways might not be solely due to the experimental design. Upstream analyses of both datasets (Figure 5.15) suggests *IRF3*, *IRF7* and *STAT1* were all upregulated in the *Spi1* over-expression dataset but downregulated in the *Spi1* knock-down dataset. Moreover PU.1 has been shown to link to directly link to member 4 of the interferon regulatory family (IRF) [373] to induce production of the IL-1 β cytokine [277] which is known be secreted from virally infected cells [374]. Recent work has shown that *IRF7* is critical to the type I interferon response, and is increased in post-mortem tissue of AD patients [375]. Therefore the upregulation of these pathways could be due to an increased *Spi1*/PU.1 expression rather than the viruses used in the experiment.

Both Figure 5.3 and Figure 5.16 (Cluster 3) suggested that some genes were only detected in the *Spi1* over-expression dataset. When this gene list was analysed using IPA and DAVID it appears that the pathways activated in this cluster were likely involved in the activation of helper T-cells and antigen presentation. Further IPA investigation suggests a lot of these changes were mediated through MHCII complex and IRF3/IRF7 signalling. Another study human glia-cultures also found genes under the control of the PU.1 transcription factor were also found to be linked to the

antigen presentation pathway [233]. However the tissue used for these cultures came from patients undergoing operations for another condition, such as a brain-tumour or epilepsy, both of which are known to impact microglia function (reviewed in [376] and [42] respectively). Therefore, the microglia in these cultures were likely already altered before PU.1 protein levels were artificially reduced. In addition to this microarray analyses are known to have several disadvantages over RNA-sequencing. RNA-sequencing data is not limited to known transcripts, as microarrays are, and can therefore be re-visited again and again. Additionally, RNA-sequencing studies have been found to better associate with protein changes than microarray studies [377].

Work by Gjoneska *et al.* has advocated that AD mouse models provide useful genomic information about AD pathology in humans, especially when concerning a highly conserved transcription factor like PU.1 [70]. In conclusion, the RNA-Seq data gained from this thesis still have merit despite the aforementioned studies which undertook similar approaches to investigate the role of PU.1 in microglia [230,233]. Given PU.1 has a known role in chromatin remodelling in multiple immune cell types [31–33; reviewed in 33] it is possible that macrophage PU.1 levels link both the innate and adaptive immune system.

The largest gene cluster (Cluster 2, Figure 5.16) consisted of genes that were upregulated in the *Spi1* shRNA samples compared to NS shRNA control but were unchanged in the *Spi1* over-expression dataset. Both IPA and DAVID biological pathway analyses identified a large proportion of the genes were related cell cycle control, DNA replication, DNA damage and cancer-related pathways. While IPA analysis was unable to predict if the cell cycle pathways were changed, DNA damage/repair pathway activation was predicted to be activated in the *Spi1* knock-down dataset. These *in silico* results were unsurprising as it has been previously published that a short interfering RNA (siRNA) targeting PU.1 could reduce protein levels by ~70 % and reduced the cell number in human microglia cultures [232]. Therefore, ki67 antibody staining was used to investigate if there were any changes to the proliferation when the PU.1 transcription factor was reduced (Figure 5.18). There were no obvious changes to the proportion of cells in each phase of the cell cycle following infection with the *Spi1* shRNA or *Spi1* pSIEW virus. However, the NS shRNA infected cultures did seem to indicate there could be a reduction in the percentage of S/G₂/M microglia, possibly resulting from viral infection, which was lost in *Spi1* shRNA infected microglia. While these changes did not reach statistical significance, there are several potential explanations. As the reduction in PU.1 protein was moderate (averaging 65 %) it was possible that this was not enough to alter microglia proliferation. Moreover the addition of TGF- β to the culture media may

have an impact on microglia proliferation, as previous studies have shown that TGF- β can suppress M-CSF/IL-34 induced proliferation *in vitro* in a dose dependent manner [341,342]. In all experimental conditions there were a small number of ki67+ microglia suggesting TGF- β may be causing a lower rate of microglia proliferation, masking the impact of a *Spi1* reduction. Given that TGF- β was added to these cultures to help mimic *in vivo* microglia phenotype [154] which have relatively low rate of proliferation, as discussed in section 1.3.1 of the introduction. Thus, if microglia proliferation was already limited by the presence of TGF- β then *Spi1* shRNA infection may not be able to further reduce the rate of proliferation. However, given that the RNA-Seq analysis following *Spi1* knock-down suggests a multitude of cell cycle related genes were altered it is likely that investigating proliferation including other stains, such as 5-ethynyl-2'-deoxyuridine (EdU) staining which specifically stains cells in S-phase, could clarify these changes [380].

As the clustering analysis also implicated DNA damage and repair pathways several times the amount of DNA within each cell was investigated to ensure that the *Spi1* shRNA infected microglia DNA was not being damaged through a cytokinesis failure, reviewed in [381]. Figure 5.19 shows there was no evidence of increased numbers of microglia containing large amounts of nuclear material, assessed by DAPI staining. However, several papers support the role of PU.1 in proliferation [232,255,257] and survival of M \emptyset populations including microglia [7,8,258]. Also as previously discussed in section 4.3.1 *Spi1* shRNA infected microglia may fail to undergo correct cytokinesis, or have an altered expression of survival/apoptotic factors and were lost before harvesting. Future experiments observing microglial proliferation and apoptosis following infection *Spi1* shRNA infection could be assessed using temporal tracking/time-lapse microscopy.

The phagocytic ability of the *Spi1* shRNA infected microglia was also assessed by imaging cytometry as reductions to PU.1 protein have been shown to reduce the phagocytic ability of microglia multiple times [230,232]. On average microglia infected with the *Spi1* shRNA virus had a 10 % larger population of zymosan negative cells than NS shRNA infected samples (Figure 5.22 and Figure 5.23). Given the differences observed between the non-infected and NS shRNA infected samples it could be that shRNA viral infection activates/primes microglia for phagocytosis and the *Spi1* shRNA prevents this activation.

While still present, the *Spi1* shRNA mediated reduction in phagocytosis appeared to be smaller than those presented in the literature [230,232]. This is likely due to the different experimental approaches. Smith *et al.* (2013) investigated the phagocytosis of A β over a 24-hour period in human cultured microglia with a 70 % reduction of PU.1 [232]. Another paper also used labelled

zymosan in BV-2 mouse microglia cells and exposed the cultures for a longer time, 3 hours [230]. As shown in the preliminary work (figure 15B) opsonised zymosan is quickly internalised by microglia and therefore a 1-hour incubation is more than sufficient time for phagocytosis to have occurred.

An imaging cytometer approach combines the advantages of assessing proliferation by either immunofluorescence [232] and flow cytometry [230] meaning these results may provide a more accurate assessment of impact of *Spi1* reduction on phagocytosis *in vitro*. Another advantage of this approach is that phagocytosis could be assessed over time in live microglia. It could be a useful to determine if *Spi1*/PU.1 knock-down affects the ability of microglia to detect zymosan, continuously engulf zymosan or if any fluorochrome signal is lost following phagocytosis.

The final part of this chapter tested sets of genes differentially expressed in the *Spi1* knock-down and *Spi1* over-expression RNA-Seq datasets for enrichment of AD association signal in the IGAP consortium GWAS data [3]. The *Spi1* knock-down data did not show enrichment of signal in the IGAP data, whereas a significant enrichment of IGAP signal was observed in a set of 21 genes with highly significant expression-alterations in the *Spi1* over-expression dataset.

Of particular interest were the genes linked to interferon signalling, such as *Oas1*, *Oas2* and *Ifit2*. The *Oas* family are induced by both interferon and double-stranded DNA as part of a viral immune response [382]. In APP/PS1 model mice the type-I interferon signalling response is thought to be activated and result in neuroinflammation [375]. *Ifit2* has been shown to be upregulated, alongside other genes related to the type-I interferon response, in APP/PS1 mice compared to wild-type controls [383]. Moreover, a single-cell sequencing analysis of microglia isolated from APP^{NL/G/F} model mice identified a cluster of interferon responsive microglia which were enriched for genes like *Ifit2*, *Oasl2* and *Irf7* [384].

The possibility remains that the induction of type-I interferon genes such as *Oas 1* [385], were induced as a result of the use of lentiviruses in these cultures. However as the pathways appeared to be significantly changed by *Spi1* over-expression but not *Spi1* knock-down this suggests that increases in *Spi1* may result in the activation of an interferon-response gene network and thus could contribute to neuroinflammation, though further experiments would be required to confirm this is accurate.

In addition, the correlation between *Spi1* over-expression in mice and GWAS data from humans, suggests this experimental model could be used to understand more about AD disease biology.

The suggestion that there may be a common pathway in microglia resulting in AD pathology has been previously proposed by [386] where PU.1 is one of three transcriptional effectors. This analysis suggests that increased levels of *Spi1*/PU.1 may also result in the transcription of several other LOAD risk genes.

5.3.2 Conclusions and Future Work

To conclude this chapter has validated the experimental model set-up in Chapter 4 and shown that physiologically relevant changes *Spi1*/PU.1 levels has meaningful impact on gene transcription. The changes to several of these genes was confirmed at protein level. Pathway analysis of these two RNA-Seq datasets led to pilot experiments examining the impact of *Spi1* knock-down on proliferation and phagocytosis. The effects seen in these assays were quite mild though, and several improvements could be made to the experiments. The proliferation assay could be repeated with EdU staining, with a lower level of TGF- β to see if this was a limiting factor in determining the effect of PU.1 knock-down on proliferation.

Phagocytosis could be assessed in a temporal manner with live microglia using fluorescently labelled A β , which is a more endogenous stimuli for microglia and would therefore provide a more physiologically relevant measure of the phagocytic response of these microglia.

Analysis of the *Spi1* over-expression dataset suggested that higher levels of PU.1 trigger a viral-like immune response in microglia. Using a higher expression of *Spi1* by either increasing the amount of *Spi1* pSIEW virus used or inserting the *Spi1* sequence into a fusion plasmid could help determine if these pathways are being activated by the virus or increases to PU.1. This would provide a *Spi1*^{high} dataset into addition to the *Spi1* over-expression dataset already generated.

Given how the level of virus infection can impact PU.1 protein levels in this culture system (Figure 5.7) could be assessed using a single-cell approach. When this thesis was undertaken Drop-seq single-cell sequencing platforms, such as the 10x Genomic system, could not sequence microglia to the depth desired for this analysis. However, since then these single-cell analysis platforms have been improved, and Drop-seq approaches could be combined with the RNA-Seq datasets generated in this thesis to form a more complete picture of *Spi1* mediated changes.

However, the main focus of future work should involve adapting this culture system to measure *Spi1* expression changes caused by the *Spi1* risk SNPs discussed in section 1.5.3 of the introduction to see if there are alterations to PU.1 protein. It would be interesting to compare the SNP related

changes to PU.1 expression to the changes artificially generated by the *Spi1* shRNA and *Spi1* pSIEW viruses to see if they are on the same level.

As there are several *Spi1* over-expression transgenic mice in development at the moment and a longer-term goal would be to use single-cell sequencing study freshly isolated microglia from these mice, as it would negate any potential transcriptome changes resulting from viral infections or from culturing microglia. These *Spi1* over-expression mice could also be bred to AD models to see if AD pathology is accelerated when *Spi1* is increased in microglia, and potentially to see at what point within the disease progression a higher level of *Spi1* has an impact. More specifically to this thesis, these *Spi1* over-expression mice could provide a more accurate model in which to study how increased microglial *Spi1*/PU.1 levels may impact the adaptive immune system, which was highlighted in the *Spi1* over-expression dataset created in this thesis.

Chapter 6 Investigating the function of ABI3 in Macrophages

6.1 Introduction

Recently a rare mutation in ABI family member 3 (ABI3), also known in the literature as NESH, was associated with an increased risk of developing LOAD [5]. RNA-sequencing data from mice and humans confirmed that *ABI3* expression is high in some MØ populations, especially high in microglia [248,387]. This has been ratified by ABI3 immunohistochemical staining, which confirmed a high expression in human microglia [244,291].

As previously discussed in section 1.4.2.2 chemotaxis and phagocytosis in microglia and MØs rely on actin cytoskeleton reformation. The WASP and WAVE family are known to regulate many of these rapid actin cytoskeletal changes, as reviewed in [288]. Multiple studies have shown that stimulation of the mouse MØ cell line BAC1.25F with M-CSF resulted in podosome formation, which are small actin rich protrusions that aid cell motility [388,389]. In Bone-Marrow Derived MØ (BMDM) a reduction in WASP prevented M-CSF-induced podosome formation and chemotaxis [390]. In 2005 Kheir *et al.* measured all three WAVE proteins in BMDM and the mouse MØ RAW cell line by qPCR and found WAVE-2 was predominantly expressed in MØs, though some WAVE-1 was also measured. Immunohistochemical staining confirmed that WAVE-2 localised to the f-actin protrusions produced by M-CSF stimulation [289]. Blocking WAVE-2 function with antibodies or RNA interference prevented the formation of these podosomes and migration. No deficits were seen in Fcγ-R mediated phagocytosis which suggests that another WASP/WAVE family member may also mediate this function [289].

The Abi family consists of 3 members; Abi1, Abi2 and Abi3 which individually bind to WAVE2 to form part of the WAVE Regulatory Complex (WRC) [284]. Abi3 has been shown to have a functionally exclusive role compared to Abi1 within the WRC [245]. Abi1 phosphorylates the WRC allowing translocation of the protein complex to the cell surface, where actin reformation is induced [245,284]. Reducing Abi1 via shRNA within BMDM and the RAW cell line had a similar effect, that down-regulating WAVE-2, a reduction in actin protrusions and migration following M-CSF stimulation [289].

In contrast Abi3 is not thought to phosphorylate the WRC and therefore prevents WRC from translocating to the surface of cells [245,284]. However very little is known about how Abi3 functions when expressed at physiological levels in MØ and microglia. Some insight has been gained from reports in cancer research where forced over-expression of Abi3 was found to be reduced in malignant cancer cells [295] and forced over-expression of ABI3 reduced motility and cancer cell growth [11,295].

It is possible that a high Abi3 expression in MØs may lead to a similar phenotype to cells with a reduced Abi1 expression, where WAVE2 is not able to translocate to the cell surface resulting in a lack of F-actin protrusions and migration following an external stimulus. It was hoped that investigating MØs in the recently developed B6N(Cg)-*Abi3*^{tm1.1(KOMP)Vlcr}/J (Abi3 KO) mouse colony would enable a better understand the functional role of Abi3 in MØ.

Hence the purpose of this chapter was to investigate phenotypic alterations in of peritoneal MØs (PMØ) and custom *HoxB8* conditionally-immortalised CD117+ bone marrow precursor (MØP) cell lines derived from the Abi3 KO mice. When these MØP cell lines are differentiated by withdrawal of oestrogen and the addition of M-CSF they phenotypically resemble BMDM [304]. As summarised in Figure 2.2 Abi3 KO mice were generated by removing exons 2-8 of the Abi3 gene and inserting a β -galactosidase coding sequence from the *E.coli LacZ* gene to act as a reporter to confirm Abi3 deletion [299].

Therefore, this chapter aimed to assess the usefulness of the Abi3 knock-out mice and perform basic phenotyping and exploratory functional experiments on MØ populations. This was achieved by:

- Confirming the loss of Abi3 by PCR and expression of *LacZ* reporter in pMØ and conditionally-immortalised MØP cell lines.
- Comparing the number of pMØ in Abi3 KO mice compared to controls and pilot experiments assessing pMØ adhesion and phagocytosis.
- Performing initial assessment of undifferentiated and differentiated Abi3 KO and Abi3 WT MØP cells, including:
 - Measuring Abi3 expression in these cell lines
 - Measuring expression of key MØ surface receptors CD11b, CD45 and MHCII
 - Assessing proliferation in MØP cells and M-CSF differentiated MØP cells
 - Assessing impact of Abi3 on M-CSF depletion and stimulation in M-CSF differentiated MØP cells.

6.2 Results

The first results will focus on the work done in freshly isolated pMØ from mice before moving onto discuss the MØP cell lines in the second results Section.

6.2.1 Evaluating *Abi3* KO mice breeding

The original B6N(Cg)-*Abi3*^{tm1.1(KOMP)*Vl*cg}/J (*Abi3* KO) mice purchased from the Jackson Laboratory were newly generated by the JAX KOMP² program and were heterozygous (HT) null for *Abi3*. Therefore, the offspring from the first HT-HT breeding pairs were closely observed for any physical abnormalities. Having confirmed that *Abi3* KO mice appeared phenotypically normal and were indistinguishable from *Abi3* HT and *Abi3* WT mice the mice were then bred as separate *Abi3* KO and *Abi3* WT lines to prevent excessive culling. Throughout these experiments the *Abi3* WT and KO mouse colonies were maintained for over 8 months and during this time only one pup was culled due to a physical abnormality (hydrocephalus; genotype unconfirmed). Therefore, a lack of *Abi3* did not obviously impact the ability of the mice to breed, though many these mouse experiments there were no *Abi3* WT mice available so other mice were used as controls. In these experiments the control strain will be clearly stated. While the C57BL/6NJ mice are recommended control with control mice it was not cost effective to order in these mice [299]. Therefore C57BL/6J mice, another C57BL/6 substrain, were often used as controls in these experiments, whilst waiting for the *Abi3* WT colony to stabilise.

6.2.1.1 Confirming *Abi3* KO in pMØ

Abi3 expression data collected from the Immgen GeneSkyline RNA-Seq database [248] showed the *Abi3* mRNA was expressed in pMØs and microglia (Figure 6.1A). Additional support for *Abi3* being expressed in pMØ came from a single-cell sequencing study performed on a peritoneal lavage by another group member (Dr Ipseiz, 2018 unpublished). The t-SNE plots in Figure 6.1B-C show that a proportion of pMØ, identified by *F4/80* and *Tim4* mRNA expression, express *Abi3* with a log₂ fold-change of over 2. As single-cell sequencing is not very in-depth with approximately 2,000 genes detected in each cell it is possible that *Abi3* is expressed in all pMØ but the technology is not sensitive enough to detect this. Despite this, the single-cell sequencing results suggest that *Abi3* should be detectable in lavages. Therefore the *Abi3* KO model was first assessed in pMØ which are an accessible population and have a reasonably high despite *Abi3* gene expression.

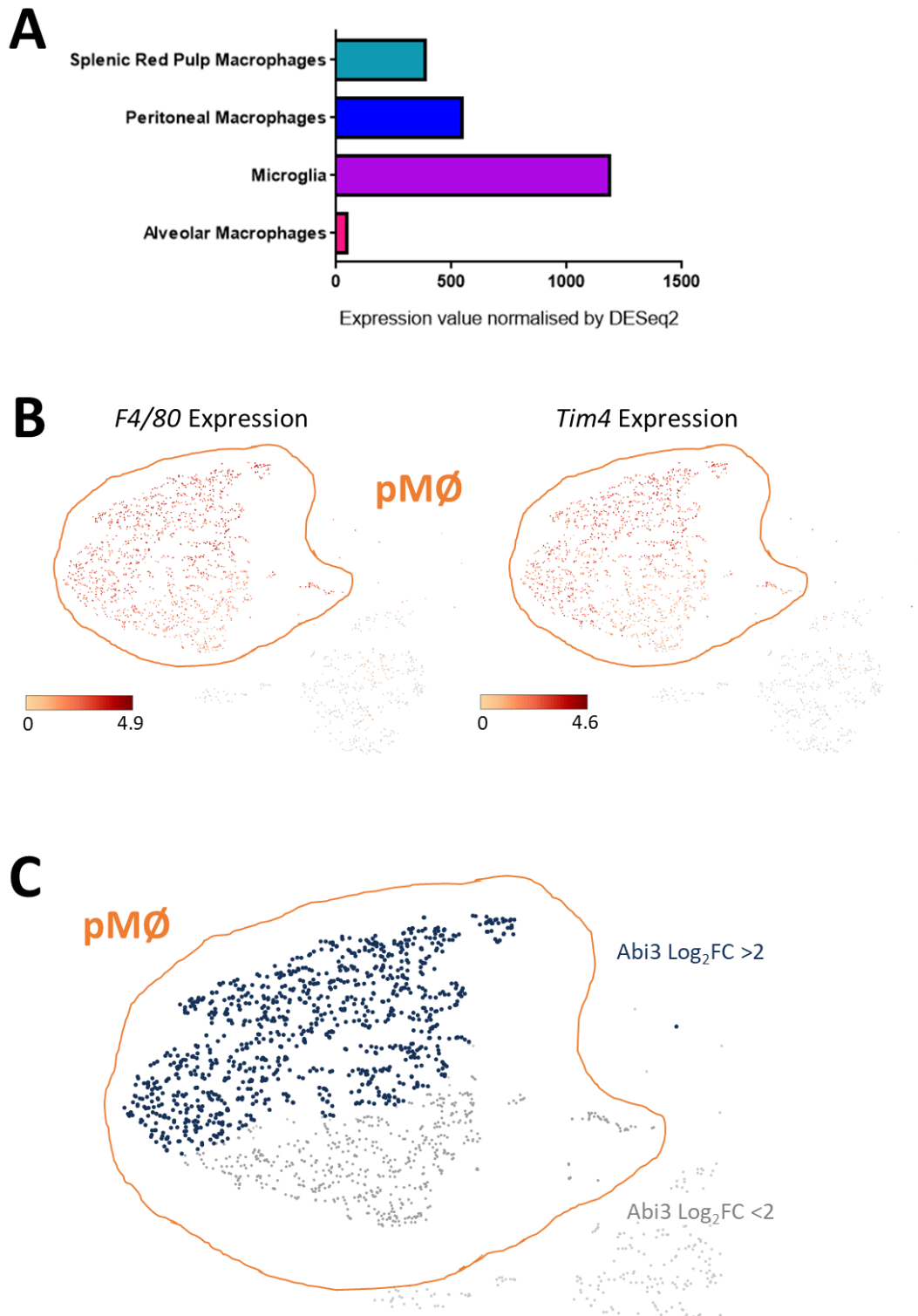


Figure 6.1 *Abi3* expression in primary murine Macrophage populations as shown by RNA-Seq. **Part I-** **A** *Abi3* expression values taken from the Immgen RNA-seq Gene Skyline database, as normalised by DESeq2. This graph clearly shows that while *ABI3* is expressed in most macrophage tissues, including peritoneal macrophages (pMØ) it is most highly expressed in microglia. **B** Single cell sequencing of a lavage taken from a Wild-Type *Gata6^{tm2.1Sod/J}* male aged 8-10 weeks performed on the 10x Genomics Single Cell Sequencing platform by another group member Dr Ipseiz. *F4/80* and *Tim4* mRNA expression was used to determine the

resident *pMØ* population. The colour scale for each plot were indicated below. C *pMØ* separated into cells with an *Abi3* mRNA expression \log_2 fold change of >2 and <2 . The *t*-SNE plots in part B and C were generated using the Loupe Cell Browser. The results presented in B and C were from one experiment and $n=1$ mouse.

To determine if *Abi3* was sensitive to the level of *Spi1* expression the *Abi3* FPKM values from each experiment in the RNA-Seq datasets were plotted in Figure 6.1D. There was no observed difference in *Abi3* expression between the *Spi1* experimental groups (filled) compared to the respective experimental controls (outline). This suggests that the changes to *Spi1* expression resulting from these lentiviruses did not alter the level of *Abi3* gene expression. However further experiments would be required to determine if the level of *Abi3* is completely independent of *Spi1*/PU.1.

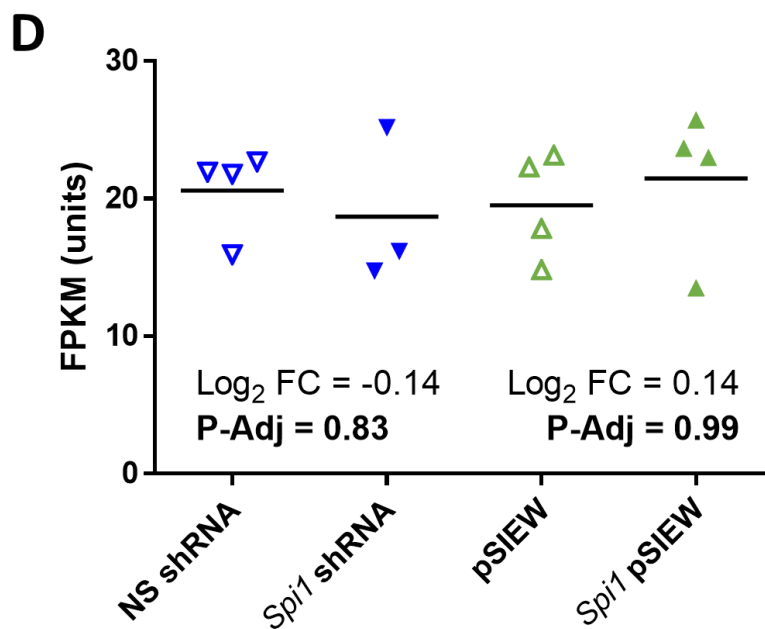


Figure 6.2 *Abi3* expression in primary murine Macrophage populations as shown by RNA-Seq. Part II- D *Abi3* expression FPKM values from both the *Spi1* knock-down (blue) and *Spi1* over-expression (green) RNA-Seq datasets. There were no significant differences between the *Spi1* lentiviral manipulations and the respective control viruses.

Thus, genomic DNA was extracted from peritoneal lavages taken from *Abi3* WT, HT and KO mice. This DNA was used as a template for two PCR reactions. Figure 6.3A shows that the first set of primers were designed to target exon 8 of the *Abi3* gene which was intact in the *Abi3* KO mice, while the second PCR reaction utilised primers targeting exons 5-7 which was expected to be removed in *Abi3* KO mice.

Figure 6.3B shows the bands resulting from these PCR reactions using genomic DNA. All three samples produced a strong band for exon 8 whereas the band produced by exons 5-7 was only

present in the *Abi3* WT and *Abi3* HT samples. This PCR confirmed that exon 5-7 appeared to be absent in the *Abi3* KO mice. Despite exon 8 being detectable at the genomic level in the *Abi3* KO mice it was unlikely to result in the formation of a truncated protein as the poly-A-tail was inserted after the β -galactosidase sequence should terminate transcription before exon 8.

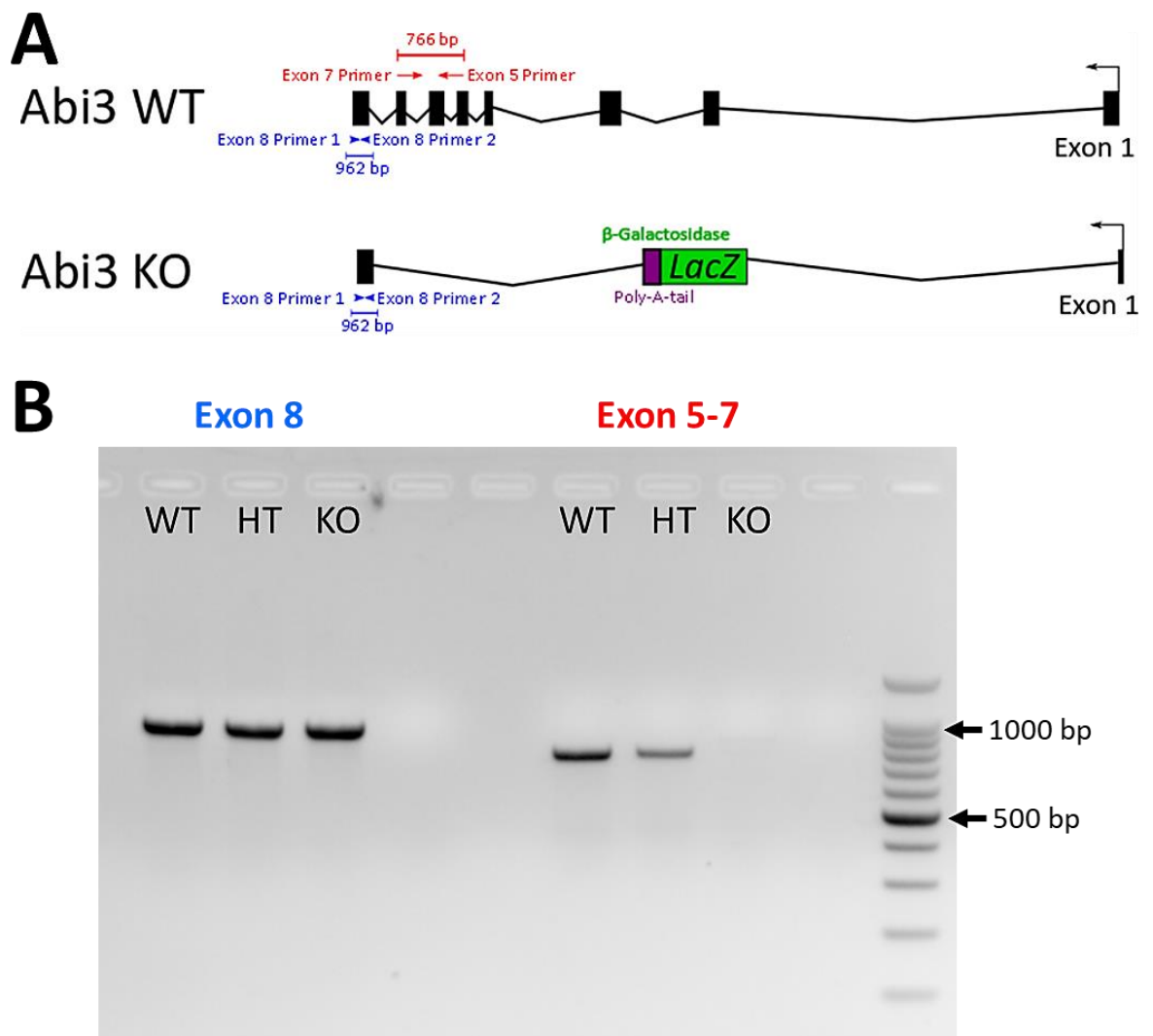


Figure 6.3 PCR to show the lack of *ABI3* exons 5-7 in DNA extracted from lavage cells. A Diagram summarising the layout of the *Abi3* KO gene in comparison to the WT *Abi3* gene. In the *Abi3* KO mice exon 1 is partially deleted and exon 2-7 were completely removed. The *LacZ* coding sequence for the β -galactosidase gene (green) was inserted in this space, followed by a Poly-A-tail (purple) to terminate transcription. To measure this removal one set primers were designed to target exon 8 (blue) which should be intact in both *Abi3* KO and WT mice, while the second set of primers (red) were targeting exons 5-7 which should not be present in the *Abi3* KO mice. **B** Genomic DNA was used in both these reactions. Exon 8 was detected by PCR in the WT, heterozygous mutant (HT) and *ABI3* KO (KO) samples producing a band of the expected size of ~296 bp. Meanwhile the band denoting the presence of exon 5-7 (~766 bp) was only present in the WT and heterozygous (HT) samples. The strength of the band also appears to be weaker in the HT sample, most likely

due to their being half the template available. The 100 bp DNA ladder can be seen on the far-right lane (Promega). Taken together this further confirms ABI3 was successfully knocked-out in the peritoneal cavity of these mice.

The expression of *LacZ* β -galactosidase in the *Abi3* KO mice was confirmed in pM \emptyset by both immunohistochemistry (IHC) and flow cytometry. Flow cytometric analysis of β -galactosidase activity in lavages taken from these *Abi3* KO mice suggested not all pM \emptyset express *Abi3* under resting conditions. In this assay β -galactosidase positive cells processed the fluorescein di-V-galactoside (FDG) substrate into fluorescein which was detected by flow cytometric analysis. To reduce any signal from endogenous lysosomal β -galactosidase activity the cells were pre-treated with chloroquine diphosphate as per manufacturers instruction (Molecular Probes). As the FDG substrate was loaded onto the cells through hypotonic shock propidium iodide (P.I.) was used to remove dead cells from the analysis.

Figure 6.4A shows the gating used in this experiment to select $F4/80^+Tim^+$ or $F4/80^+Tim^4^-$ pM \emptyset subsets to discriminate cells with processed fluorescein, which required cleavage by β -galactosidase. The flow plots shown in Figure 6.4B show that β -galactosidase processed fluorescein was detected in a proportion of *Abi3* KO pM \emptyset . Figure 6.4C shows that FDG is mainly processed in *Abi3* KO mice, where C57BL/6J control mice had very little β -galactosidase activity.

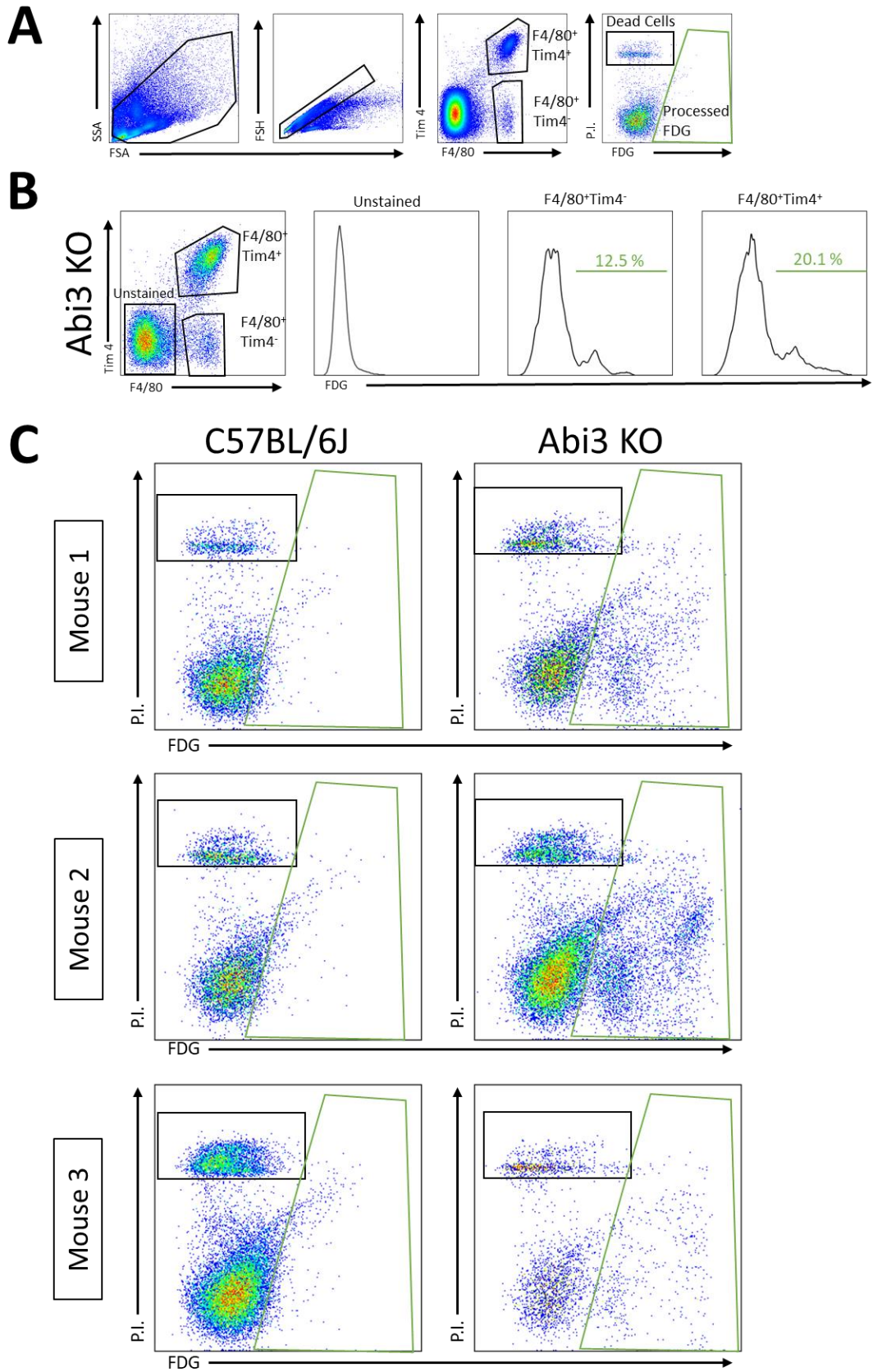


Figure 6.4 Detection of LacZ reporter in primary pMØ macrophages – Part I **A** LacZ activity was also detected through the use of Flow-cytometry. The cells were loaded with the FDG substrate which is processed by LacZ/B-galactosidase to give a fluorescent signal. The plots shown here were pre-gated on F4/80 and Tim4 antibody staining to isolate pMØ and show this lacZ activity (x-axis) against the dead cell marker propidium iodide (y-axis). The LacZ expressing population was easily identifiable, though there does appear to be a small population of macrophages in the WT samples which express endogenous B-galactosidase or have a high level of autofluorescence. Due to the sensitivity of the flow cytometry assay chloroquine diphosphate was used to try and minimise detection of endogenous galactosidase activity. **B** A representative plot showing that Tim4-F4/80- (unstained) cells lack processed FDG signal, whereas pMØ both have strong FDG signalling. Data from one mouse. **C** Plots showing the signal from processed FDG (green gate) against the live/dead cell marker P.I. for the Tim4⁺F4/80⁺ pMØ populations from all mice used in this experiment (n=3 per group) 6-week males. This experiment was performed once in Abi3 KO mice, though similar observations were made with older experiments using Abi3 HT mice (data not shown).

The proportion of pMØ with processed FDG, indicating β -galactosidase activity, were quantified (Figure 6.4D). In both pMØ subsets the average percentage of cells with β -galactosidase activity was ~15 %. The percentage of processed FDG+ cells was significantly higher in both the F4/80⁺Tim4⁻ (Unpaired Welch’s Two-tailed T-Test P=0.0044) and F4/80⁺Tim4⁺ (Unpaired Two-tailed T-Test P=0.0007) pMØ populations. An independent experiment confirmed FDG was processed in the pMØ of two female Abi3 KO mice, and not in matched C57BL/6J control mice (Figure 6.4E).

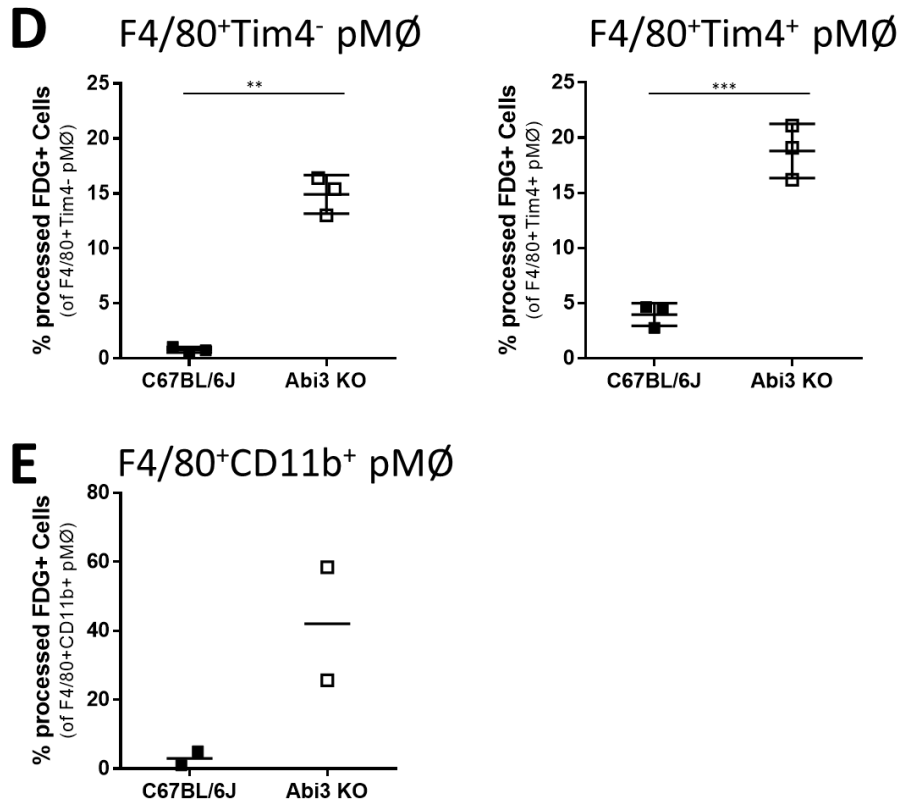


Figure 6.4 Detection of LacZ reporter in primary pMØ macrophages – Part II D The percentage of fluorescein positive cells resulting from processing of FDG in both C57BL/6J and Abi3 KO samples of the $Tim4^-$ (Two-tailed unpaired t-test with Welch's correction $P=0.0044$) and $Tim4^+$ (Two-tailed unpaired t-test $P=0.0007$) respective pMØ gate. Each experimental group contained 3 mice ($n=3$; 6-week-old males) the mean is indicated by the horizontal black line and the error bars denote the standard deviation. **E** A separate experiment assessing the percentage of pMØ with processed FDG+ cells. Each group contained $n=2$ 10-week-old female mice. The horizontal bar indicates the mean. The results presented in part **D** and **E** were from two independent experiments. ** $P<0.005$ and *** $P<0.001$.

LacZ β -Galactosidase expression was also assessed by immunohistochemistry. The LacZ staining experiment performed by Elena Simonazzi, though all images and analyses were performed by myself.

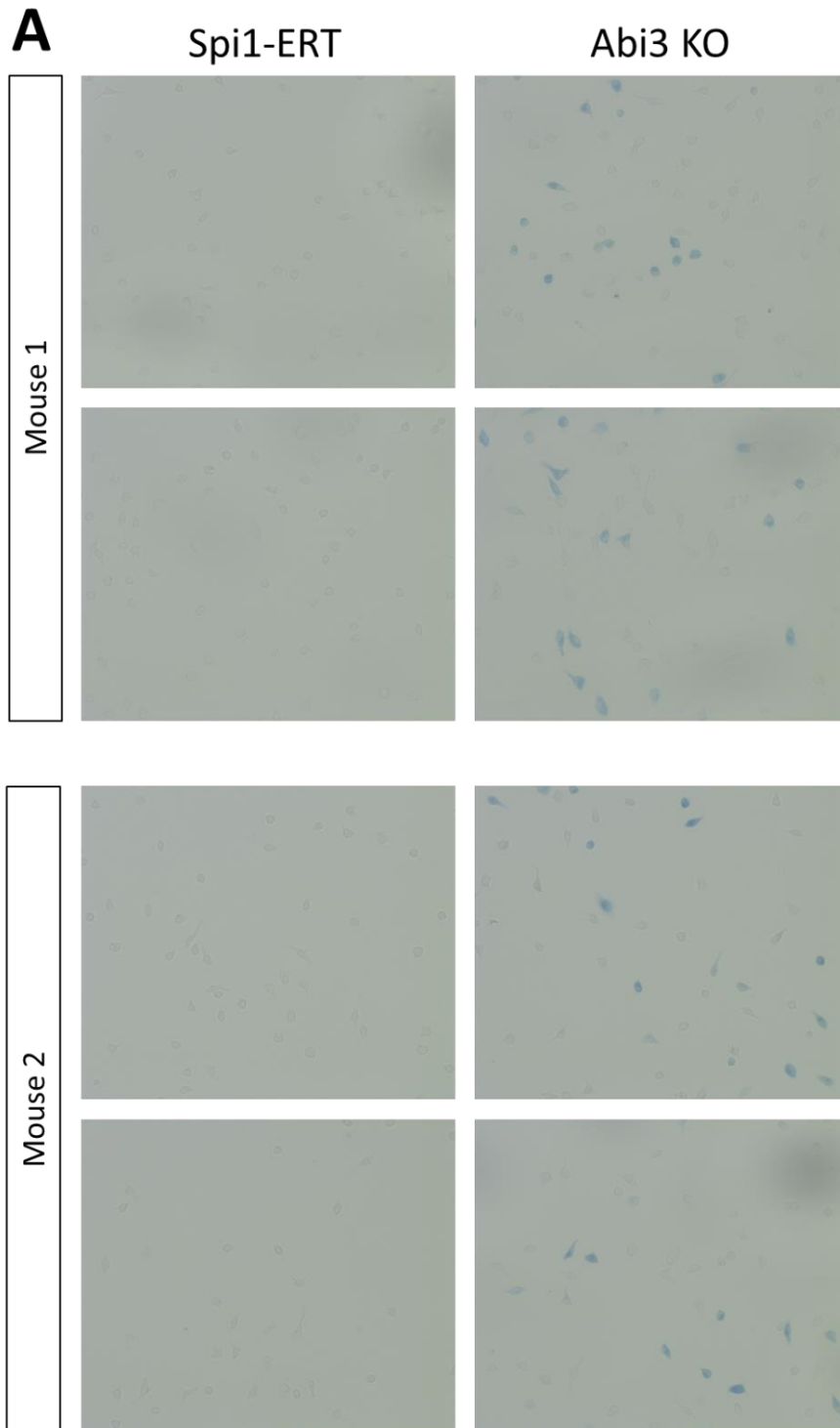


Figure 6.5 Detection of LacZ reporter in primary pMØ macrophages – Part I A *ABI3* KO cells should express *LacZ* in the place of *Abi3* exons 2-7. Images taken after staining with the β -galactosidase detection kit (Sigma). Lavage cells were isolated from mice and cultured in RPMI media overnight to allow cells to adhere onto coverslips before fixation and staining with the detection substrate for 2 hours. The presence of *LacZ* is indicated by a blue colour, cells with a darker blue having a higher expression. The dark blue *lacZ* staining was only present in the *Abi3* KO mice (right images) and not in the age and sex matched *Spi1*-ERT controls (left images). As mentioned in Chapter 4 *Spi1*-ERT mice were generated by breeding $B6;129-Spi1^{tm1.2Dgt}/J$ to

the B6.129P2(C)-Cx3cr1^{tm2.1(cre/ERT2)Jung/J} mouse colony and only had endogenous β -galactosidase expression. The presence of LacZ does not appear to be ubiquitous in all these cells. The pictures above were taken from 2 female Spi1-ERT mice were 12 weeks old and 2 female Abi3 KO mice were 10 weeks old at 20X magnification using the Zeiss Apotome Axio-Observer Microscope. The staining for this experiment was performed by Elena Simonazzi.

Figure 6.5A shows that β -galactosidase was present in the Abi3 KO mice which was represented by a blue stain. No blue cells were observed in the control Spi1-ERT mice (Figure 6.5A; left). In both these images the adhered cells had a morphology indicative of pM \emptyset . However not all the cells in the Abi3 KO mice were stained for β -galactosidase activity. When the number of blue cells (β -galactosidase+) in the Abi3 KO mice was quantified it was observed that an average of 30% of the cells were stained blue (Figure 6.5B).

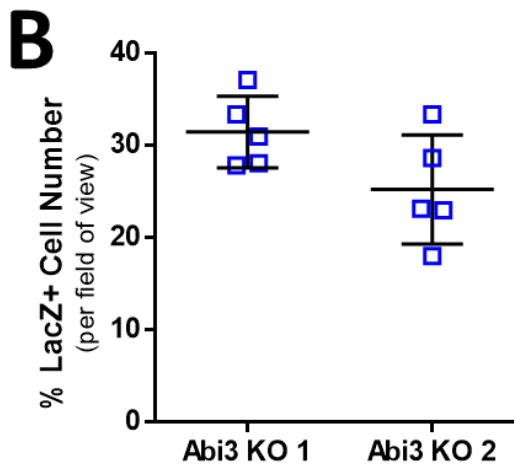


Figure 6.5 Detection of LacZ reporter in primary pM \emptyset macrophages – Part II B The percentage of β -Galactosidase stained (blue) cells calculated from the field of view. 5 pictures were taken from each Abi3 KO mouse sample to give 5 technical replicates per mouse (n=2; 10-week-old females). The horizontal lines indicate the mean value and the error bars show the standard deviation.

The next experiments measured *Abi3* using qPCR to confirm *Abi3* mRNA was not produced in the Abi3 KO mice. The qPCR primers were designed to bind at the exon 1/exon 2 boundary site, meaning that *Abi3* expression could not be detected in Abi3 KO mice lacking exons 2-7. As shown in Figure 6.6A *Abi3* expression was detected in some lavages taken from Abi3 WT mice but was low/undetectable in peritoneal cells from the Abi3 KO mice. Similar results were gathered from experiments with C57BL/6J mice (Figure 6.6C). As shown in Figure 6.6B and Figure 6.6D the variation in gene expression were likely due to the low CT values for *Abi3* mRNA in Abi3 WT and C57BL/6J control mice. This suggested that *Abi3* mRNA was near the limit of detection by qPCR, though this qPCR could be improved by purifying the pM \emptyset population before qPCR or increasing

the amount of cDNA in each reaction. However this data suggested there was no *Abi3* mRNA expressed in the peritoneal lavage cells of these mice.

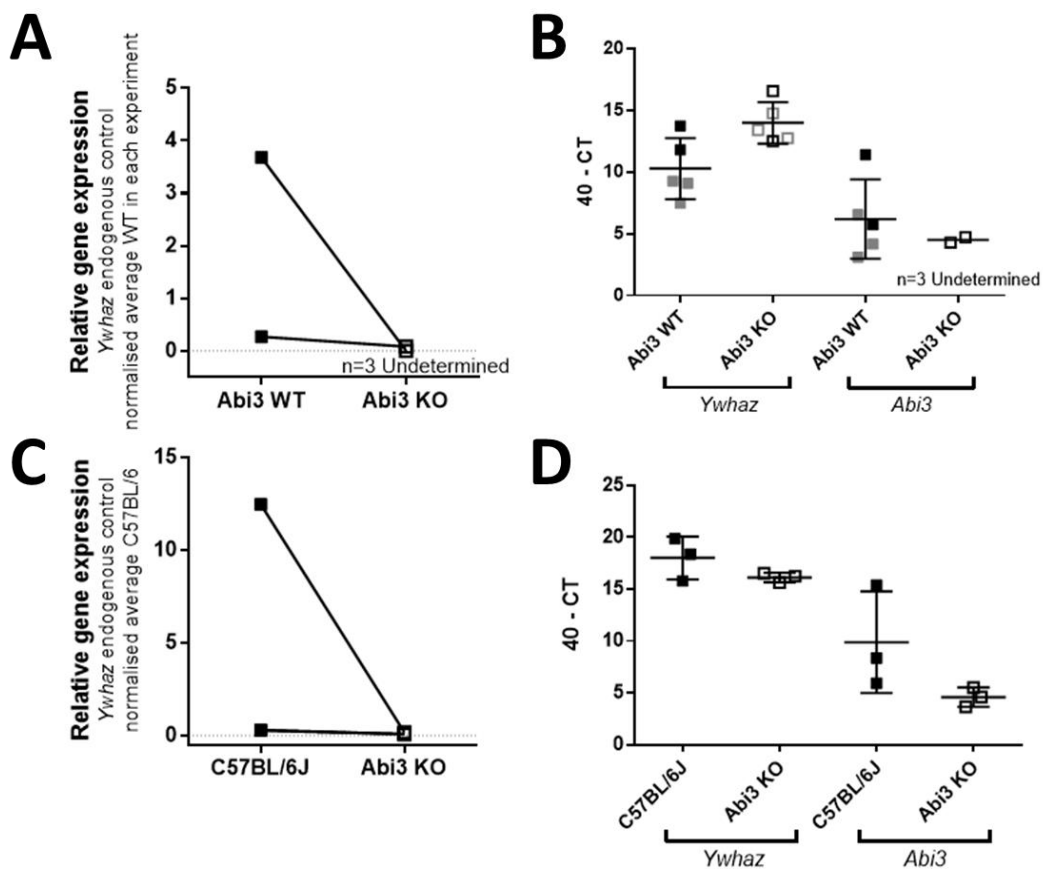


Figure 6.6 Determining *Abi3* mRNA expression by qPCR. In all these experiments *Ywhaz* was used as an endogenous control gene. **A** Relative gene expression of *Abi3* mRNA in lavages taken from *Abi3* WT and *Abi3* KO mice. Three *Abi3* KO mice had undetermined *Abi3* expression, likely due to level of *Abi3* mRNA. **B** The 40-CT expression values from this qPCR analysis. Again there seemed to be lower average *Abi3* expression in *Abi3* KO mice. There were n=3 undetermined results, likely due to the low expression of the gene in the *Abi3* KO mice as the 40-CT plot shows the *YWHAZ* mRNA was detectable and was unlikely to be caused by degraded cDNA (shown in grey). The data presented here were the results of 2 independent experiments. The age range shown here 13-19 weeks, a mix of female and male mice (n=3 female and n=2 male per group). **C** The gene expression values from another experiment where *Abi3* was measured in C57BL/6J and *Abi3* KO mice. **D** The 40-CT values from this experiment for *Ywhaz* and *Abi3*. There mice used in this experiment were 6-week-old males, n=3 per group. The horizontal bar shows the mean and the error bars the standard deviation.

Taken together these results confirm that the *LacZ* reporter was expressed in a subset of pMØ in the *Abi3* KO mice. When combined with the genomic PCR that suggests exon 5-7 had been removed, and the qPCR data suggested *Abi3* mRNA was not highly expressed in *Abi3* KO peritoneal lavages. Overall this indicated that the *Abi3* KO model was performing as expected. The loss of

Abi3 protein could not be confirmed due to a lack of specific commercially available antibodies, though antibodies are being developed in-house (data not shown).

6.2.1.2 Basic Phenotyping in *Abi3* KO of pMØ

To ensure there were no obvious deficits to the pMØ population caused by *Abi3* KO in the number of cells or proportion of pMØs in the peritoneal cavity was assessed in *Abi3* KO and *Abi3* WT mice. When no *Abi3* WT mice were available C57BL/6J mice were used instead as they had a similar genetic background. Data taken from the *Abi3* KO and *Abi3* WT mice were directly compared to ensure there were no overt differences in the pMØ populations (Figure 6.7A-D). In summary there did not appear to be any differences in the number of pMØ between the *Abi3* WT and *Abi3* KO mice.

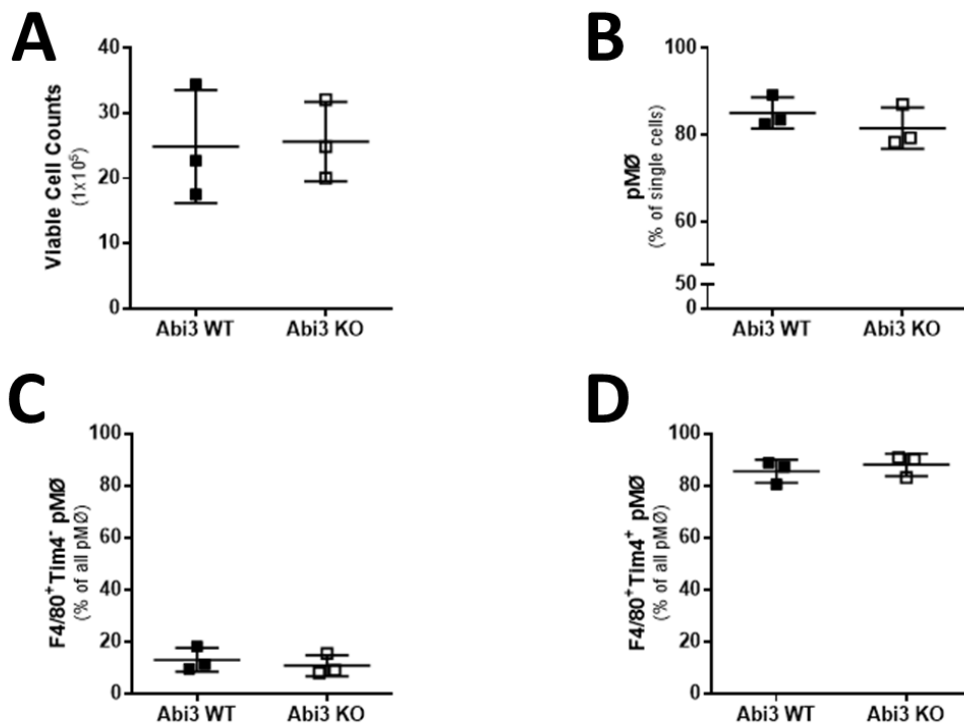


Figure 6.7 pMØ Cell Counts from fresh lavages- Part I **A** The viable cell counts between the age and gender matched mice. There were no differences caused by genotype (Two-tailed T-Test $P=0.9064$) **B** The percentage of pMØ in *Abi3* WT and KO mice of all single cells did not significantly differ (Two-tailed T-Test $P=0.3638$). The proportion of $F4/80^+Tim4^-$ (**D**) and $F4/80^+Tim4^+$ (**C**) cells of all pMØ was also similar in both the *Abi3* WT and *Abi3* KO cells (Two-tailed T-Tests $P=0.5610$ and $P=0.5322$ respectively). In this analysis all mice were 13-week-old females, and $n=3$ per group. Again, horizontal bars denote the mean and error bars show the standard deviation. The data presented here are from one experiment.

The number of viable cells from each lavage did not significantly vary between the genotypes (Kruskal-Wallis Test, approximate $P=0.1207$; Figure 6.7E). The percentage of pMØ was also similar

in Abi3 WT, Abi3 KO and C57BL/6 mice (Kruskal-Wallis Test, approximate $P=0.0488$). Statistically there was a difference in the percentage of $F4/80^+Tim4^-$ pMØ (Figure 6.7G; Kruskal-Wallis Test, approximate $P=0.0335$) though Dunn's multiple comparison test showed the significant difference was between the Abi3 WT and C57BL/6J mice ($P\leq 0.05$) which is likely due to the small Abi3 WT group size. Further comparisons between the Abi3 WT and Abi3 KO mice would be needed to determine if this was a true biological difference. There were also differences in the percentage of $F4/80^+Tim4^+$ cells (Figure 6.7H) between the genotypes (Kruskal-Wallis Test, approximate $P=0.0149$), though again multiple comparisons analysis confirmed this was a difference in the WT and C57BL/6J groups (Dunn's; $P\leq 0.05$). The difference between the C57BL/6J and Abi3 WT mice is likely due to the age of the mice. The mean age of the C57BL/6J experiments was 11.24 weeks (\pm standard deviation of 2.93) whereas the one Abi3 WT experiment all mice were 13-weeks-old. As the percentage of peritoneal macrophages is known to decrease with age [391] it was possible that age had an impact on the results though the possibility remains that these differences were a result of differences between C57BL/6 sub-strains.

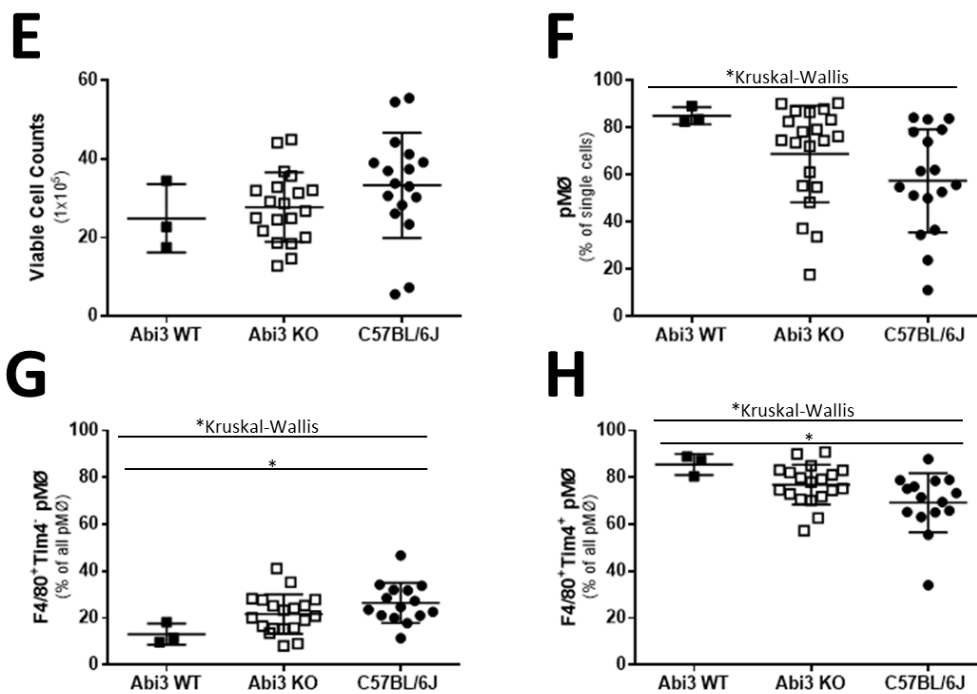


Figure 6.7 pMØ Cell Counts from fresh lavages- Part II **E** The cell counts taken from each peritoneal lavage, as determined by the MUSE cell counter. Here the viable cell counts for ABi3 KO (empty square), ABi3 WT (filled square) and C57BL/6J (filled circle) did not differ (Kruskal-Wallis approximate $P=0.1207$). **F** The proportion of macrophages ($F4/80^+$) harvested from the lavages, expressed as a proportion of all single cells. Though there was a difference between the groups (Kruskal-Wallis approximate $P=0.0488$) this P -Value was approximate, Dunn's multiple comparison test concluded no one groups was significantly different from the other. **G** The percentage of pMØ that were $F4/80^+$ and did not express Tim4. A Kruskal-Wallis test

(approximate $P=0.0335$) with a Dunn's multiple comparison test showed that the only differences were between the *Abi3* WT and C57BL/6J groups ($P\leq 0.05$). **H** The graph shows the percentage of F4/80+Tim4+ pMØ subset in the same mice. C57BL/6J mice seem to have a slightly lower proportion of F4/80+Tim4+ pMØ compared to *Abi3* KO mice though a Kruskal-Wallis test (approximate $P=0.0149$) with a Dunn's multiple comparison showed there were only significant differences in the *Abi3* WT and C57BL/6J groups ($P\leq 0.05$). Each datapoint indicates one mouse out of *Abi3* KO $n=19$, *Abi3* WT $n=3$ and C57BL/6J $n=14$. Mice were matched as closely as possible for gender and age (all mice were aged between 10 and 17 weeks). C57BL/6J mice were used as additional controls as few *Abi3* WT mice were available at the time of these experiments. Means are denoted by horizontal lines while the error bars show the standard deviation. *indicates a P -value of ≤ 0.05 .

As discussed in section 1.6 the WAVE-2 Regulatory Complex containing *Abi1* or *Abi3* has been implicated in formation of lamellipodia [245]. Therefore, it was proposed that the ability of pMØ to adhere to surfaces might be affected in cells lacking *Abi3*. Figure 6.8 shows the results of a pilot experiment where equal numbers of peritoneal lavage cells were allowed to adhere for between 1-6 hours, before the plates were washed and stained with the nuclear marker DAPI.

Representative images for each timepoint can be seen in Figure 6.8A and there were no obvious differences between the morphology of C57BL/6J or *Abi3* KO pMØ. The cells that remained attached were quantified using DAPI staining. The graphs in Figure 6.8B were no significant differences between the number of adhered *Abi3* KO and *Abi3* WT pMØ at 1 hour, 3 hours or 6 hours (Unpaired two-tailed t-test; $P=0.0521$, $P=0.2957$ and $P=0.5129$ respectively). Therefore, at these timepoints a lack of *Abi3* did not appear to obviously affect the ability of pMØ to adhere.

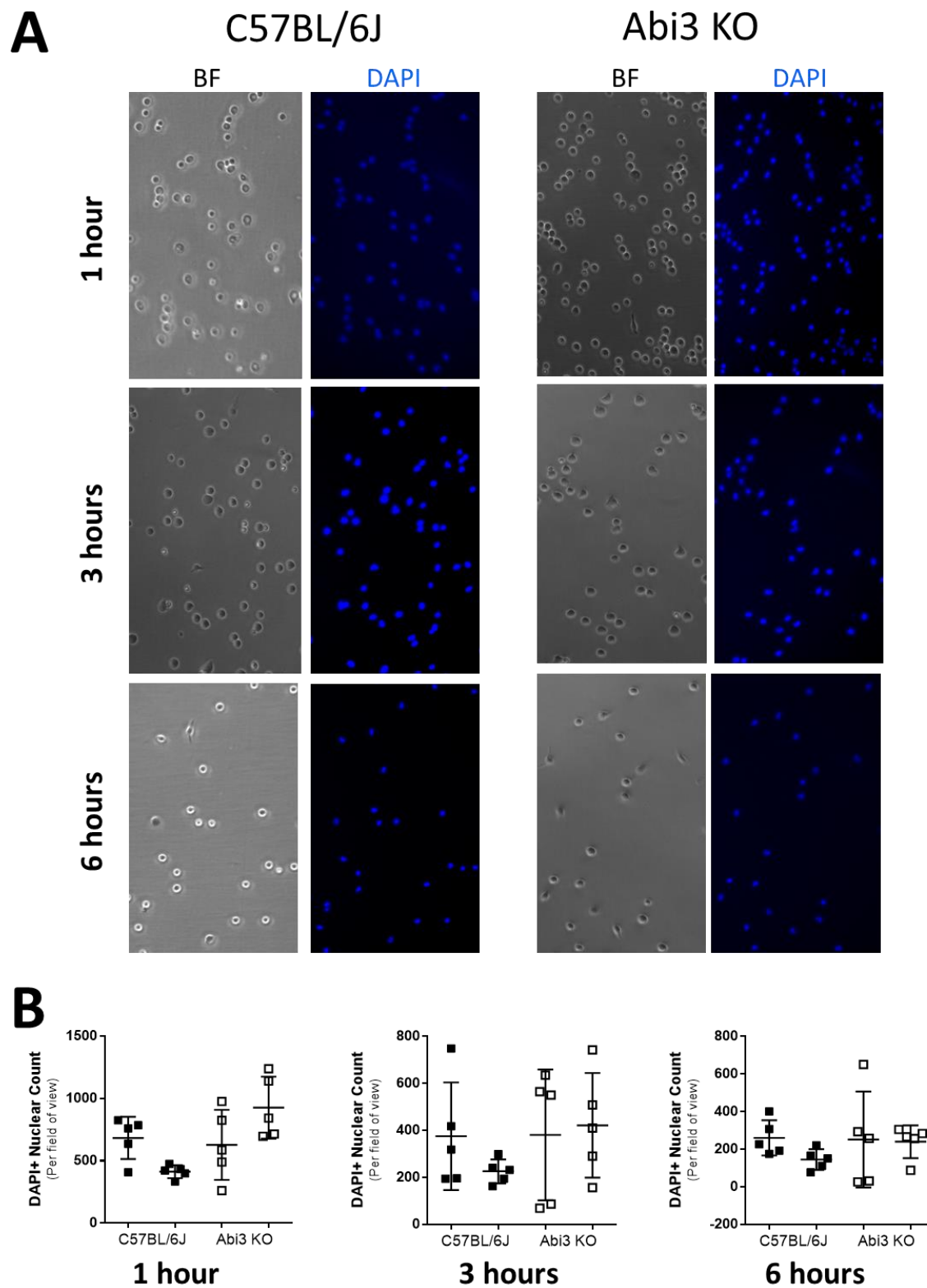


Figure 6.8 Assessing the impact of ABI3 KO on lavage cell adhesion- Part I A Here cells from the peritoneal cavity were isolated before being plated at equal density and cultured for 1, 3 and 6 hour(s)- top to bottom respectively. At the end of each timepoint any non-adherent cells were washed away during several PBS

washes. The images shown here are brightfield and DAPI images taken on the EVOS microscope at 20X magnification. **B** The cells that remained were fixed and stained with DAPI so that the number of adherent cells could be assessed from microscope images and the number of DAPI+ nuclei counted using Image J. Five pictures were taken of each well to provide an accurately assess any changes to cell adhesion caused by ABI3 KO. The results of these ImageJ counts are shown here, where each mouse is shown separately. Each datapoint represents the number of nuclei present in an individual image. At 1 hour the ABI3 KO lavages seem to have a higher mean cell number than the C57BL/6 controls, suggesting that they might be more adherent/resistant to PBS washing. However, this was not as apparent at the later 3 hour timepoint and any difference appears to be lost after 6 hours in culture. The horizontal bars indicate the mean value and the error bars denote the standard deviation. This experiment was repeated once with n=2 ABI3 KO mice and n=2 C57BL/6 male mice, all aged 11-14 weeks.

While there was no overt differences according to genotype of the cellsthere was a significant difference in the number of cells counted at each timepoint (One-way ANOVAs; Figure 6.8C $P < 0.0001$ and Figure 6.8D $P = 0.0009$). As the number of adhered cells appeared to be lower at the later timepoints it was possible that earlier timepoints (15 -30 minutes) would give a better representation of the role of Abi3 in pMØ cell adhesion, based on a similar assay [245].

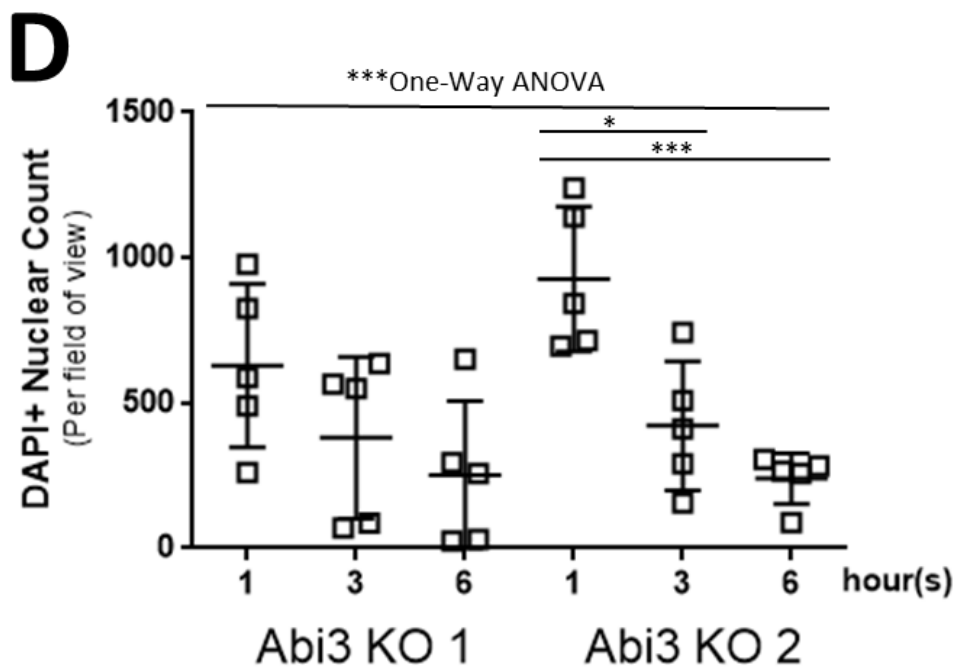
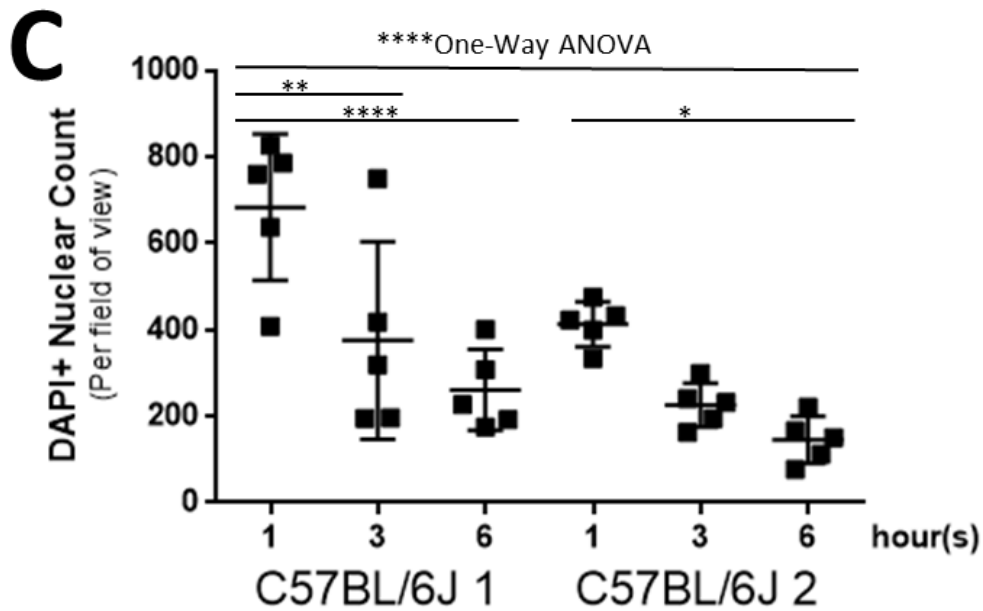


Figure 6.8 Assessing the impact of ABI3 KO on lavage cell adhesion- Part II C In the C57BL/6J mice the number of nuclei per field of view was different between the assessed timepoints. One-way ANOVA ($P < 0.0001$) and Sidak's multiple comparison test confirmed there were significantly different nuclear counts between 1 hour and 6 hour timepoints for both mice ($P \leq 0.0001$ and $P \leq 0.05$ respectively). There was only a significant difference between the 1 hour and 3 hour timepoints for one of the mice. **D** Comparing the nuclei numbers per image at each timepoint in Abi3 KO mice. Again, the number of adhered cells significantly differ between each timepoint, one-way ANOVA ($P = 0.0009$). Sidak's multiple comparison test showed there were only significant differences across the timepoints for one mouse, where there were significantly different

*nuclei numbers between 1 and 6 hours and 1 and 3 hours ($P \leq 0.001$ and $P \leq 0.05$ respectively). As mentioned above the horizontal bars indicate the mean value and the error bars denote the standard deviation. This experiment was repeated once with $n=2$ ABI3 KO mice and $n=2$ C57BL/6J male mice, all aged 11-14 weeks. *denotes a P-value of ≤ 0.05 , ** $P \leq 0.01$, *** $P \leq 0.001$ and $P \leq 0.0001$.*

Phagocytosis is another function of M ϕ s that requires changes to the actin cytoskeleton, as reviewed in [392]. Hence zymosan phagocytosis in Abi3 KO and C57BL/6J pM ϕ was assessed using imaging cytometry. In this experiment cells were extracted from the peritoneal cavity of mice and plated at an equal density of cells and allowed to adhere before receiving FITC-labelled zymosan and incubated for 30 minutes. The cells were then harvested, fixed and stained for pM ϕ markers F4/80 and Tim4 and run on the Amnis Imagestream MkII[®] imaging cytometer. All analysis was performed using the “internalization wizard” in the IDEAS[®] software, detailed below. Figure 6.9 shows the plots used to separate F4/80⁺Tim4^{high} and F4/80⁺Tim4^{low} pM ϕ for downstream analysis, including representative images for each gate used.

The first step in this analysis was to isolate cells from other debris, such as apoptotic cells or unbound zymosan (Figure 6.9A). Then focused cells were then selected (Figure 6.9B) before the two pM ϕ populations were gating using F4/80 and Tim4 staining intensity.

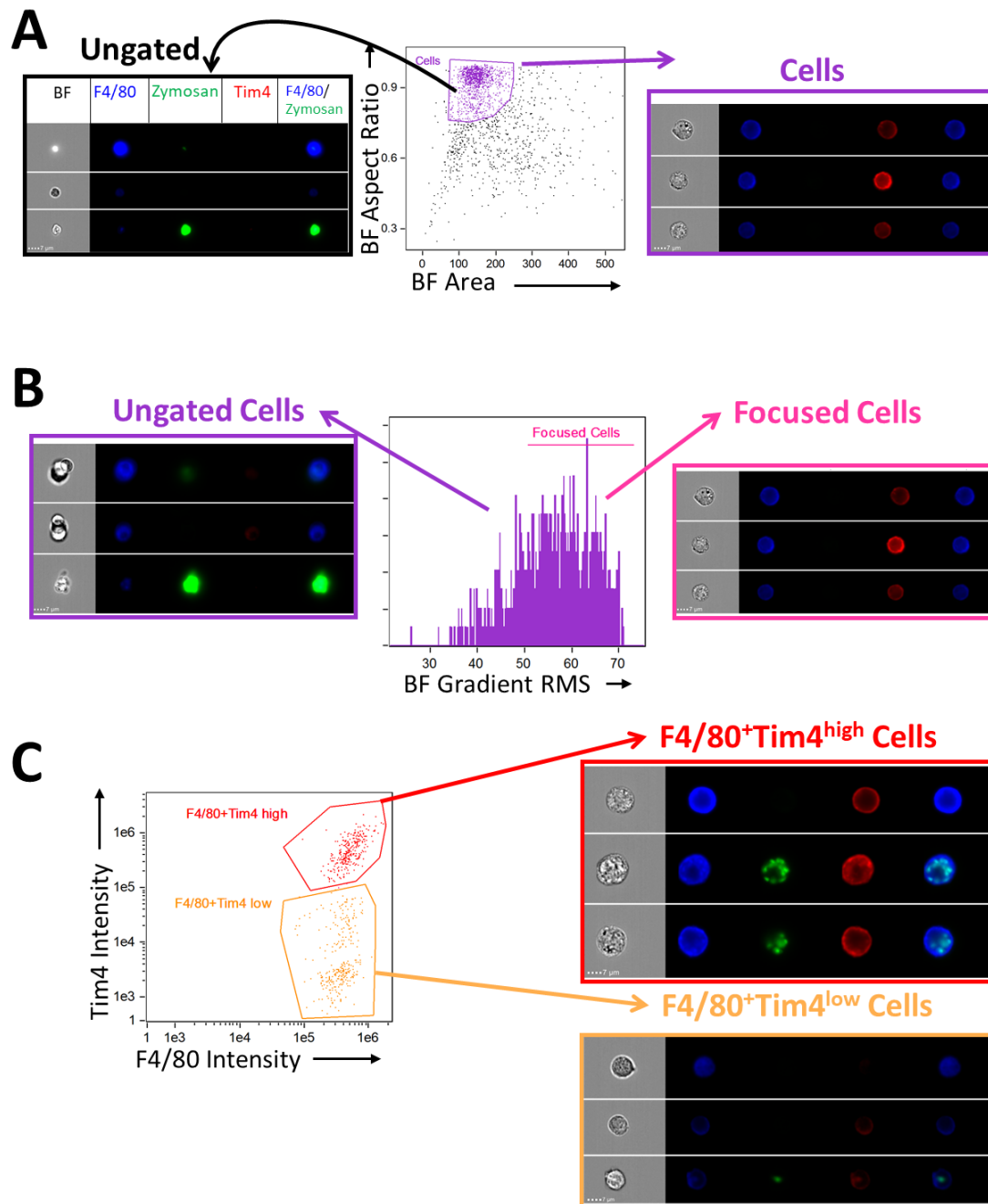


Figure 6.9 Exemplar Images from the ABI3 KO Phagocytosis experiment. In all these image galleries F4/80 staining is stained blue, Tim4 is coloured red and zymosan particles are labelled with FITC in green. These images were all taken using the 60X lens on the imaging cytometer. A These image galleries show that any dots outside of the cell gate (purple) were apoptotic cells or unbound zymosan (black). B Focused cells were then selected (pink gate). Unfocused cells were excluded from further analysis. C F4/80 and Tim4 antibody staining were then used to select F4/80⁺Tim4^{high} pMØ (red) and F4/80⁺Tim4^{low} pMØ (orange). This analysis was performed using the IDEAS® software.

Based in this analysis it was confirmed that there were no overt differences in the proportion of each pMØ subset between the Abi3 KO and C57BL/6J genotypes (Figure 6.10A).

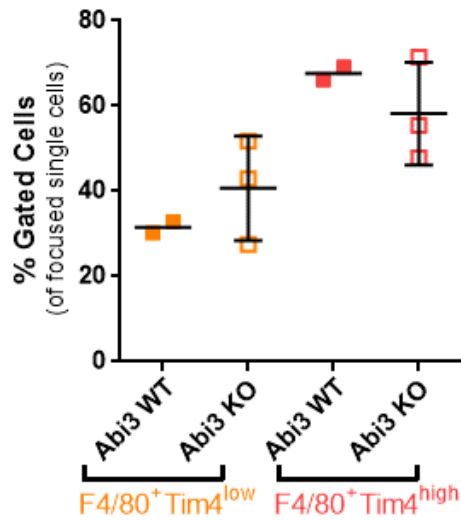


Figure 6.10 Shows the F4/80+Tim^{high} and F4/80+Tim^{low} populations in each sample. A Quantitative summary of the percentage of the sub-types of pMØ populations from each sample as a percentage of all focused cells. There are no vast differences to the percentage of F4/80+Tim4^{low} (orange) cells in the C57BL/6J and ABI3 KO lavages. There were no large differences in the proportion of F4/80+Tim4^{high} cells (red). The mice used in this experiment were 13-week-old males n=2 C57BL/6J and n=3 ABI3 KO. The mean values are indicated by horizontal bar and the standard deviation by the error bars. This experiment was performed once.

The proportion of pMØ that had phagocytosed zymosan was then calculated using the gating shown below in Figure 6.11A. As shown by the representative images, this analysis was used to separate zymosan positive cells from pMØ that have not ingested any particles. The zymosan positive pMØ were further divided into cells which had engulfed low, mid or high amounts of zymosan particles.

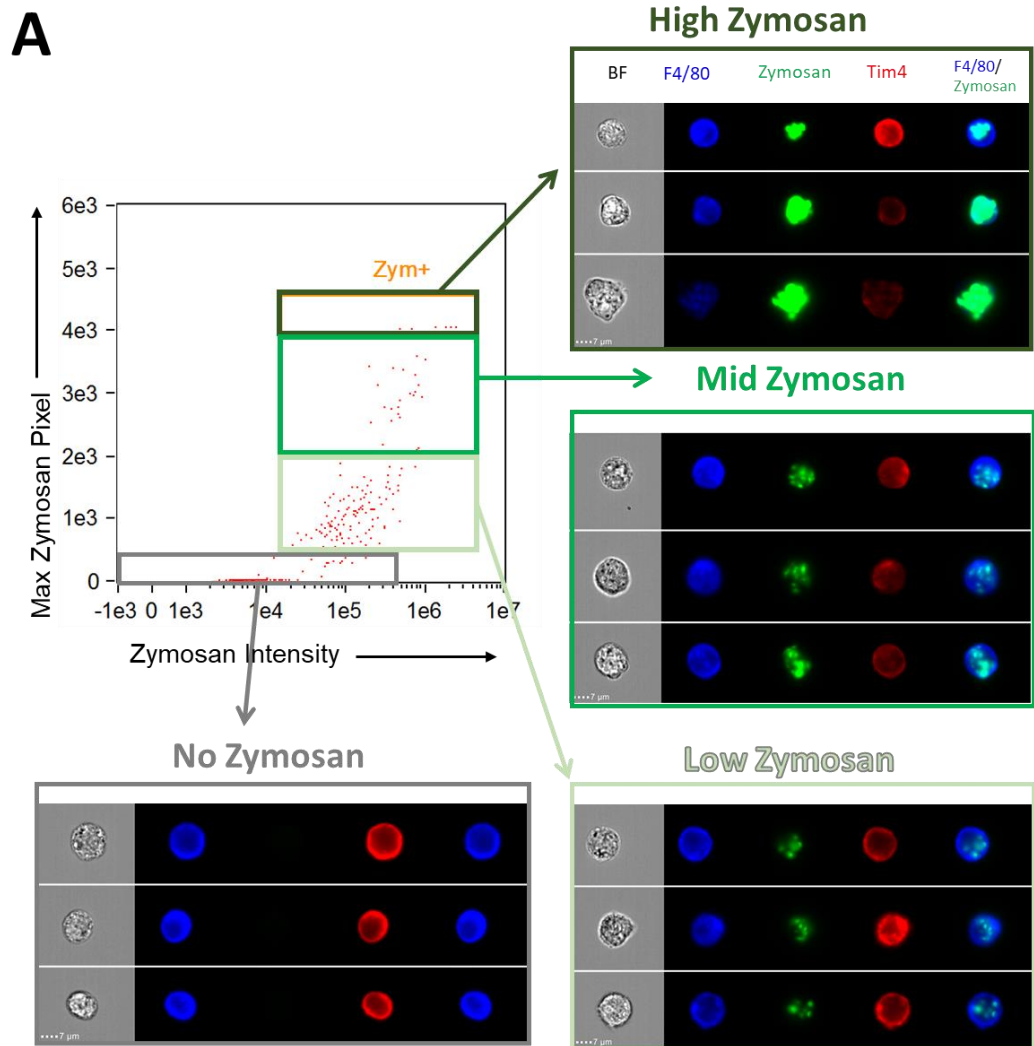


Figure 6.11 Gating used in analysis to identify pMΦ that had phagocytosed zymosan, including exemplar images- Part I A The zymosan positive cells were further sub-divided into low, middle and high for this analysis. Again all cells were imaged using the 60X magnification lens and F4/80 is stained blue, Tim4 is coloured red and zymosan particles are labelled with FITC in green.

The graphical summary of this analysis is shown in Figure 6.11B-C below. Briefly the percentage of zymosan positive cells appeared to be higher in the C57BL/6J mice compared to the Abi3 KO mice in both the F4/80⁺Tim4^{high} and F4/80⁺Tim4^{low} pMΦ subsets (Figure 6.11B). However this change was only statistically different in the F4/80⁺Tim4^{high} pMΦ (One-Way ANOVA with Sidak's Multiple Comparison test P≤0.05). When the zymosan positive cells were split into low, mid and high, depending on the number of internalised particles. There were no overt differences in the proportion of pMΦ in each subset between the genotypes (Figure 6.11D). There was a similar percentages of low/mid/high zymosan+ cells each mouse irrespective of the Tim4^{low}/Tim4^{high} pMΦ subset.

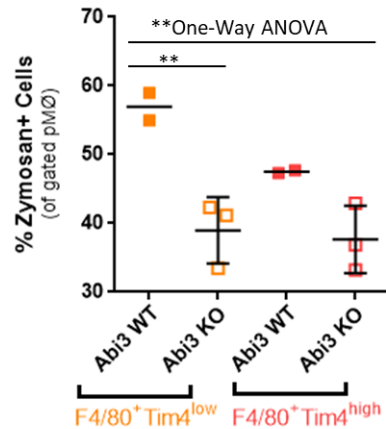
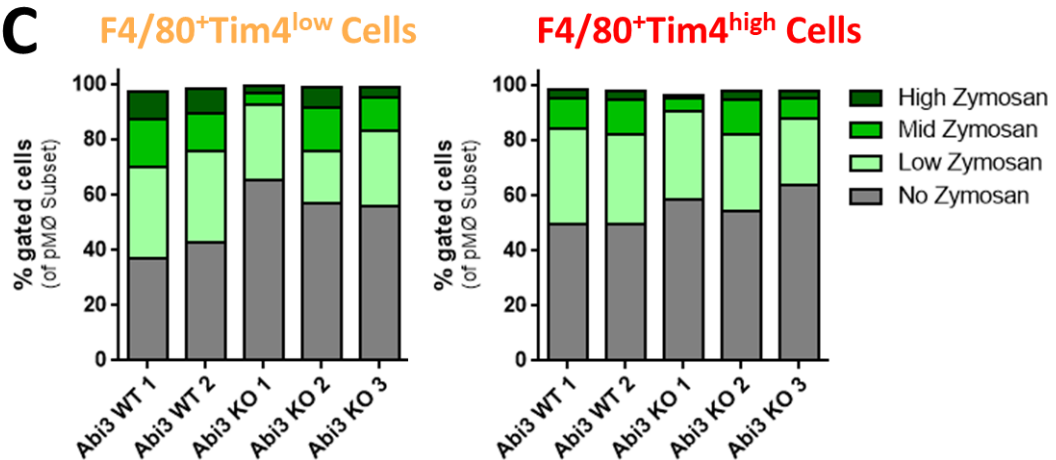
B**C**

Figure 6.11 Gating used in analysis to identify pMØ that had phagocytosed zymosan, including exemplar images- Part II B There was a significant difference between the number of zymosan+ cells (**One-way ANOVA $P=0.0077$) Sidak's multiple comparison test showed that this significance was mainly due to the lower level of phagocytosis in the $F4/80^+Tim4^+$ pMØ when compared to the $F4/80^+Tim4^{low}$ and not the genotype of the mice. There was a significant difference between the proportion of cells phagocytosed by the C57BL/6J and Abi3 KO $F4/80^+Tim4^{high}$ pMØ (** $P<0.01$), though the mean values on the graph suggest this is not a large change. **C** Breakdown of the zymosan negative and positive cells which were separated according to the amount of particles that were internalised within the cell. Here it seems that $Tim4^{low}$ pMØ have a larger proportion of cells with mid and high amounts of zymosan compared to $Tim4^{high}$ pMØ. There does not appear to be any difference caused by the genotype of these mice. Again in **B** and **C** the horizontal bars denote the mean while the error bars indicate the standard deviation. This was experiment was performed once in 13-week-old male mice ($n=2$ C57BL/6J and $n=3$ Abi3 KO).

The final step in this IDEAS® analysis was to calculate the internalisation ratio. This ratio was calculated by comparing the intensity of the zymosan signal within the cell boundary compared to the signal from the entire cell. A positive ratio indicates a larger the amount of zymosan particles have been internalised within the cell (Figure 6.12A).

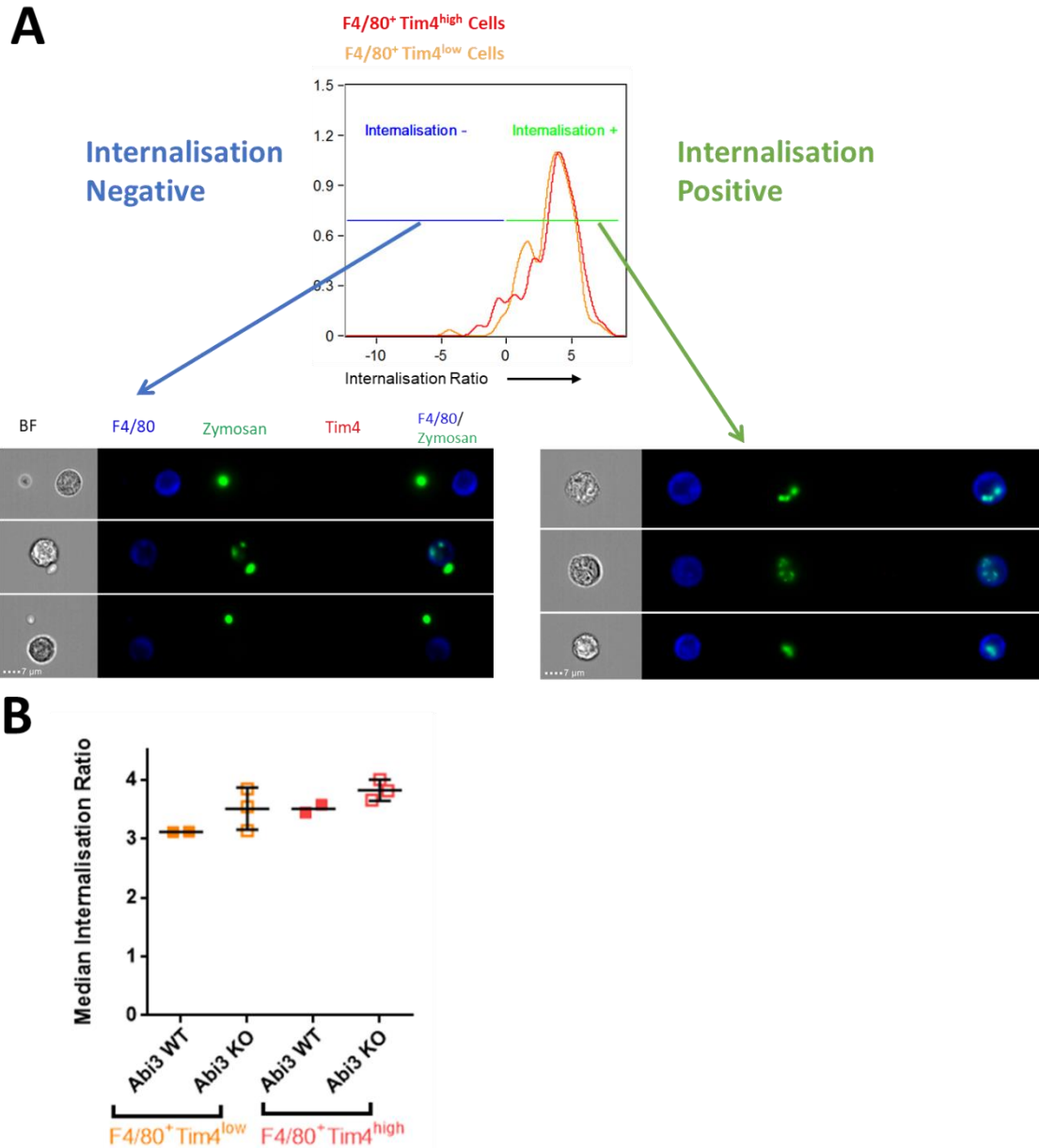


Figure 6.12 Internalisation ratio calculations and summary. **A** Shows an example of the internalisation ratio plotted for both the F4/80⁺Tim4^{high} (red) and F4/80⁺Tim4^{low} (orange) sub-sets, which was calculated from the zymosan positive cells. Cells which had phagocytosed zymosan have a positive value and are gated in green, whereas cells which had not engulfed zymosan were gated in blue. This can be seen in the representative images where F4/80 expression is shown in blue and zymosan in green. **B** The median internalisation ratios for each sample. A positive value indicates that most pMφ had phagocytosed zymosan. There was no significant difference between the genotypes in each pMφ subset (***)One-way ANOVA P= 0.0821). These graphs were based on data gathered from 13-week-old male mice (C57BL/6 n=2 and Abi3 KO n=3). The means are indicated by a horizontal bar the error bars indicate the standard deviation.

As summarised in Figure 6.12B the internalisation ratio did not differ between C57BL/6J and Abi3 KO mice, though there was a significant difference in the number of zymosan positive cells in the F4/80⁺Tim4^{low} pMφ population (One-way ANOVA P=0.0077).

Taken together this indicated that a lack of Abi3 expression likely resulted in a reduced number of phagocytotic pMØ, though these changes only reached statistical significance in the F4/80⁺Tim4^{low} pMØ subset. As the internalisation ratios did not appear different between the two genotypes, suggesting that a lack of Abi3 does not impact the rest of the phagocytic process. Given that the LacZ β-galactosidase assays suggest that Abi3 may only be expressed in a portion of pMØ it was possible that Abi3 KO does impact the internalisation as well but these defects are masked by the rest of the pMØ population.

In conclusion this section demonstrates that Abi3 was removed in the Abi3 KO mice, at the genomic and mRNA level, and LacZ β-galactosidase was expressed in these mice. There were no major changes to the number of pMØ in these mice or any overt deficits to the adhesion. While the percentage of zymosan positive pMØ was lower in each Abi3 KO pMØ subset, they were still able to phagocytose zymosan. Given that LacZ β-galactosidase expression analysis (Figure 6.4 and Figure 6.5) suggested that Abi3 might not be expressed in all pMØ it is possible that the pMØ lacking Abi3 could have defective adhesion and phagocytosis but this is hidden by the rest of the pMØ population. Including a LacZ stain in this assay could help clarify this. Overall these results suggested that until Abi3/LacZ expression can be assessed in *ex vivo* pMØ, it may be that the impact of removing Abi3 would be best studied in a cell line, where Abi3 expression was expected to be more uniform.

6.2.2 Establishing MØP Cell Lines

To study the impact of Abi3 KO *in vitro* in cells MØP cell lines were developed from the bones of Abi3 WT and Abi3 KO mice. All this data was from one pair of MØP cell lines that originated from a pair of MØP cell lines made from 8-week-old female Abi3 KO and Abi3 WT mice in parallel (n=1 mouse per MØP cell line). After these cell lines had been made (as described in section 2.4.6) the lines were assessed by PCR and qPCR to confirm Abi3 was absent in the Abi3 KO mice.

Figure 6.13A summarises where the primer pairs should bind in Abi3 gene. Exon 8 was intact in both the Abi3 WT and Abi3 KO mice and would therefore be expected to produce a PCR band from the exon 8 primers (blue). Only genomic DNA taken from the Abi3 WT MØP cell line produced a PCR band from the primers targeting exons 5-7 (red). These primers were used in PCR reactions with template genomic DNA that was extracted from either the Abi3 WT and Abi3 KO MØP cell lines. The resulting PCRs confirmed that while exon 8 is present in both cell lines exons 5-7 were only measured in Abi3 WT MØP cells (Figure 6.13B).

Once established these conditionally-immortalised MØP cell lines are maintained with GM-CSF and oestrogen in the culture media to ensure survival. Once these factors have been removed from the culture media, MØP cells can be differentiated over 3-4 days using GM-CSF to make dendritic-like cells or using M-CSF to gain cells phenotypically similar to Bone-Marrow Derived MØs (BMDM) [304]. *Abi3* gene expression was assessed in WT and KO undifferentiated MØP cells, GM-CSF differentiated MØP cells and M-CSF differentiated MØP cells using qPCR. Figure 6.13C showed that relative *Abi3* expression was significantly different across the experimental samples (One-way ANOVA $P < 0.0001$). Moreover, this graph showed that *Abi3* mRNA expression was higher in GM-CSF and M-CSF differentiated *Abi3* WT MØP cells compared to undifferentiated cells (*Post-hoc* analysis with Tukey's multiple comparison $P \leq 0.001$). This increase in *Abi3* expression was not seen in *Abi3* KO MØP cells which minimal *Abi3* expression, as expected.

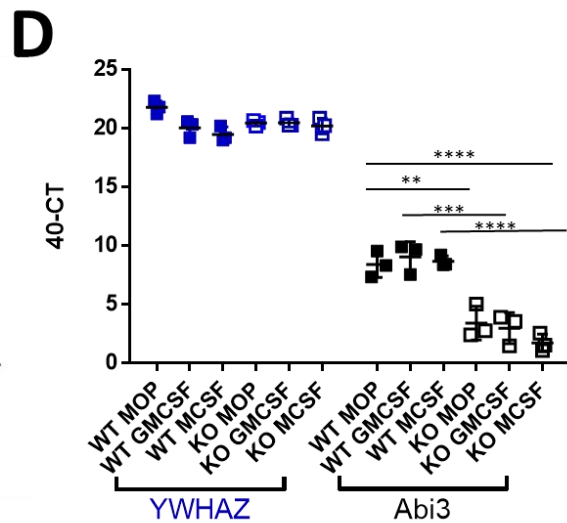
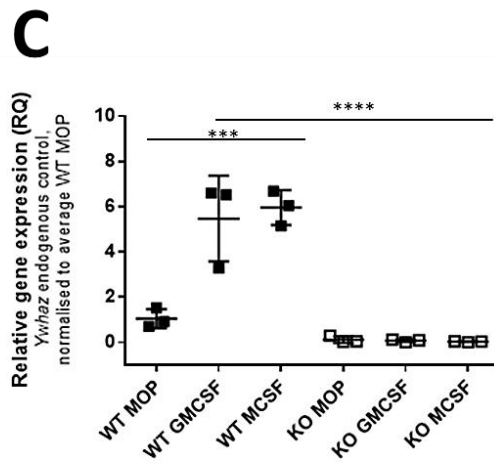
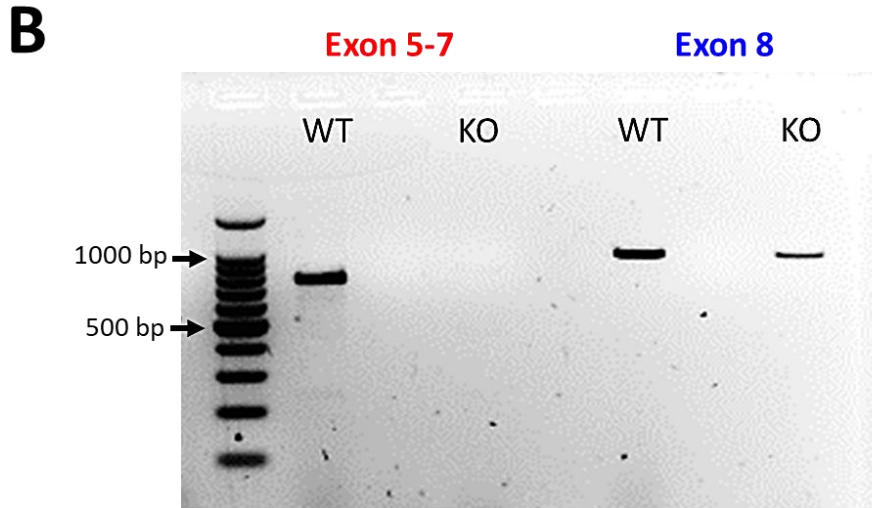
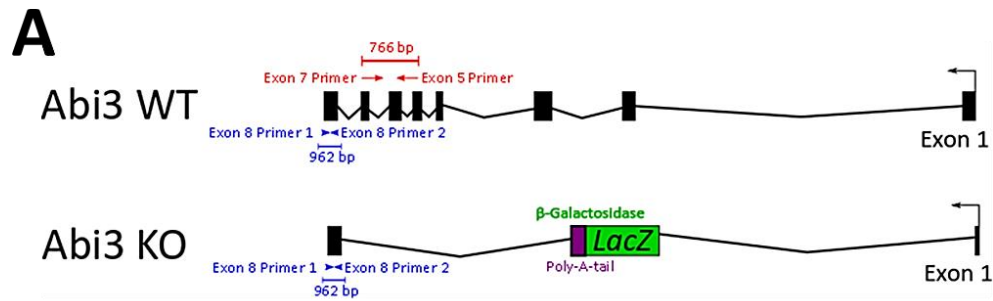


Figure 6.13 Confirmation of *Abi3* KO in MØP Cell Lines. **A** Maps showing primer binding sites in both the WT *ABI3* sequence (transcript variant 1; NCBI Reference NM_025659.4) and KO *ABI3* sequence (MGI reference 1913860#21465). Primers targeting exon 5 and 7 of the *ABI3* gene (highlighted in red) are only present in the WT sequence. In the *ABI3* KO mice exons 1-7 have been replaced with a *LacZ* reporter (coloured in green). Exon 8 remains intact in both the *ABI3* WT and KO mice and therefore the primers, shown in blue, should be able to amplify a PCR band in both the WT and KO mice. **B** Shows the resulting PCRs using genomic DNA for exon 5-7 (left) and exon 8 (right) with the Promega 100bp Ladder. This PCR gel shows that *ABI3* exon 8 was

present in both the *Abi3* WT and *Abi3* KO MØP cell lines while exons 5-7 are not present in the *Abi3* KO cell line. **C** The relative gene expression following qPCR analysis of *ABI3* expression in both WT (filled) and KO (empty) cell lines that were either undifferentiated (MØP) cells, GM-CSF differentiated cells or M-CSF differentiated cells. Here it can be seen that WT undifferentiated MØP cells have a relatively low expression of *Abi3* mRNA compared to GM-CSF or M-CSF differentiated MØP cells. *Abi3* mRNA was not detected in any of the undifferentiated or differentiated KO MØP cells. **D** Plots the 40 – CT values from the qPCR data. Here it can be seen that the endogenous control gene *Ywhaz* (blue) is highly expressed in all samples, whereas *Abi3* mRNA (black) is only present in the WT cell lines whereas the 40 - CT values in the KO cell lines are all under 2 which is very close to the limit of detection and is therefore considered not to be expressed. Each datapoint in plots **C** and **D** result from n=3 separate experiments. The means are indicated by a horizontal line and are surrounded by standard deviation error bars. The P-values are indicated using asterisks where ** $P \leq 0.01$ *** $P \leq 0.001$ and **** $P \leq 0.0001$.

The endogenous housekeeper gene *Ywhaz* was highly expressed in all MØP cells. The *Abi3* 40 – CT values show a *Abi3* expression was significantly different between the genotypes in undifferentiated and M-CSF/GM-CSF differentiated MØP cells (One-way ANOVA $P < 0.0001$).

Multiple comparisons analysis (Tukey's) showed *Abi3* expression was higher in undifferentiated, GM-CSF and M-CSF differentiated WT MØP cells compared to their matched *Abi3* KO MØP sample ($P \leq 0.01$, $P \leq 0.001$ and $P \leq 0.0001$ respectively).

Expression of the *LacZ* β -galactosidase reporter was also assessed in these MØP cells. Given that *Abi3* mRNA expression was higher in differentiated cells β -galactosidase expression was measured in M-CSF differentiated MØP cells (M-CSF MØPs), as these were also the more biologically relevant cell type. M-CSF MØPs were incubated the immunohistochemistry β -galactosidase staining kit (Sigma) for 1 hour (Figure 6.14A-top) and overnight (Figure 6.14A-bottom). There was no detectable blue stain, indicating the presence of *LacZ* β -galactosidase, in either the *Abi3* WT (WT) or *Abi3* KO (KO) differentiated MØP cells. A higher percentage of *LacZ* β -galactosidase activity was measured as fluorescent processed FDG in *Abi3* KO M-CSF MØP cells using flow cytometry, compared to *Abi3* WT M-CSF MØP cells (Figure 6.14B), though it was expressed in a minority of cells. Therefore, the *LacZ* reporter did not appear to be fully functional in *Abi3* KO M-CSF MØP cells.

In summary, these results indicated that exons 5-7 were not present in the *Abi3* KO MØP cell line and that *Abi3* mRNA did not appear to be expressed in this cell line. In the *Abi3* WT MØP cell line *Abi3* mRNA was lowly expressed in undifferentiated cells and expression increased following MØP cell differentiation with either GM-CSF or M-CSF. The lack of a ubiquitous *LacZ* β -galactosidase expression in the *Abi3* KO M-CSF MØP cells could be a result of processing required to create these cell lines. Despite this qPCR indicated that *Abi3* mRNA should be expressed at the protein level in differentiated *Abi3* WT MØP cells but not in *Abi3* KO MØP cells, and therefore the MØP cells are a useful *in vitro* model.

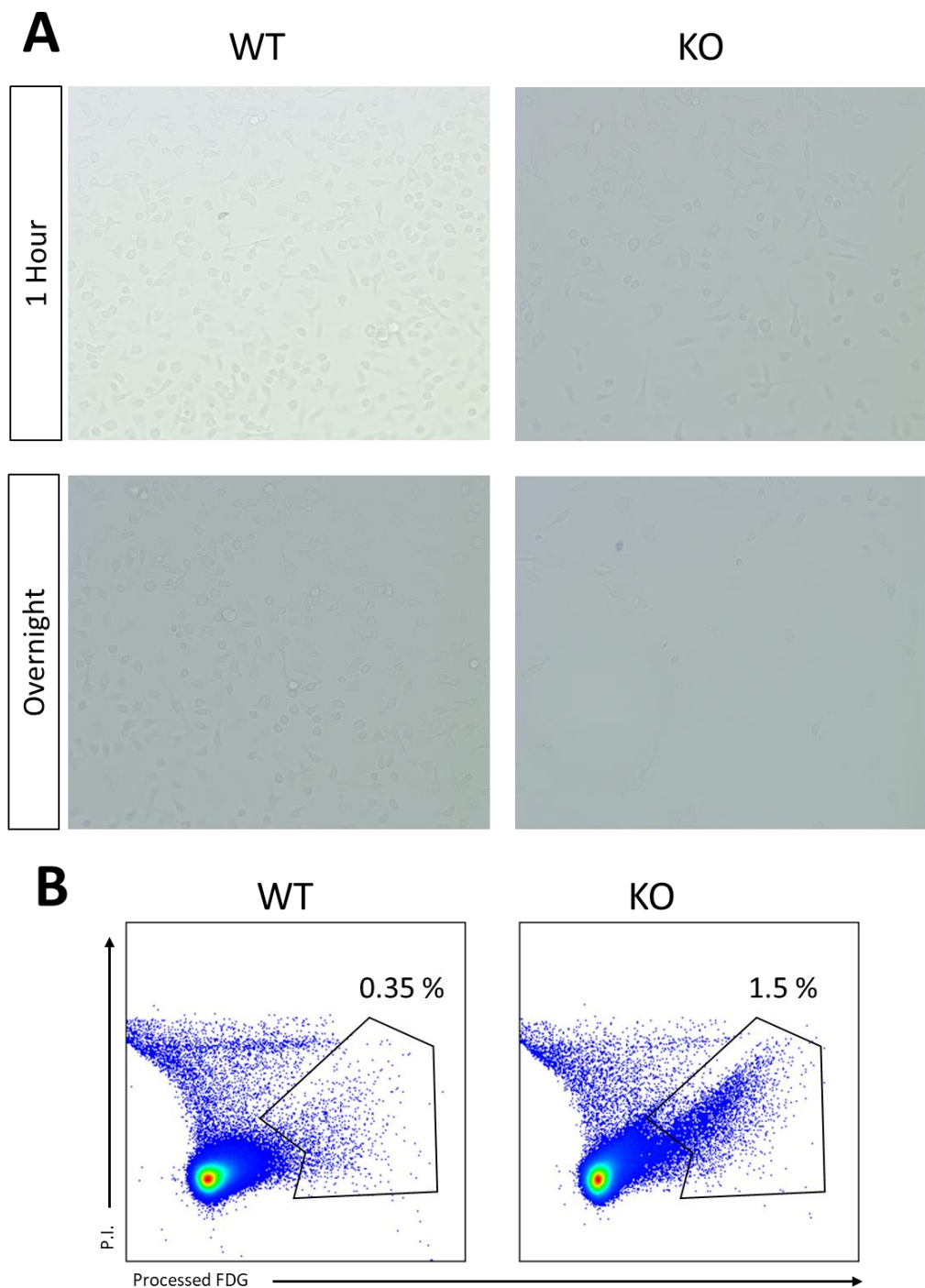


Figure 6.14 Determining if the LacZ reporter can be detected in M-CSF differentiated MØP cells. **A** Shows the resulting pictures of β -galactosidase immunohistochemistry staining kit (Sigma) after both an hour of incubation (top panel) with the staining reagents and following an overnight incubation (bottom panel). As you can see there is no visible blue staining that would indicate a strong expression of LacZ. A positive control image taken of ABI3 KO lavage cells treated with the staining solution for two hours can be seen in Figure 6.5A. Pictures were taken using the 20X magnification on the Zeiss Apotome Axio-Observer microscope. **B** Flow cytometry plots of M-CSF differentiated MØP cells that have undergone staining with the LacZ Flow

Cytometry kit (Life Technologies). If the LacZ β -galactosidase was present then the FDG is processed to give a fluorescent signal similar to FITC. Propidium Iodide, P.I. was used as a live/dead stain, meaning that dead cells will have a stronger signal. The plots show that LacZ is not detected in the whole population of ABI3 KO M-CSF MØP cells, and the signal does not appear to be hugely strong. All of these experiments were only performed once, as the removal of ABI3 has been confirmed by other experiments.

6.2.2.1 Basic Phenotyping of MØP Cell Lines

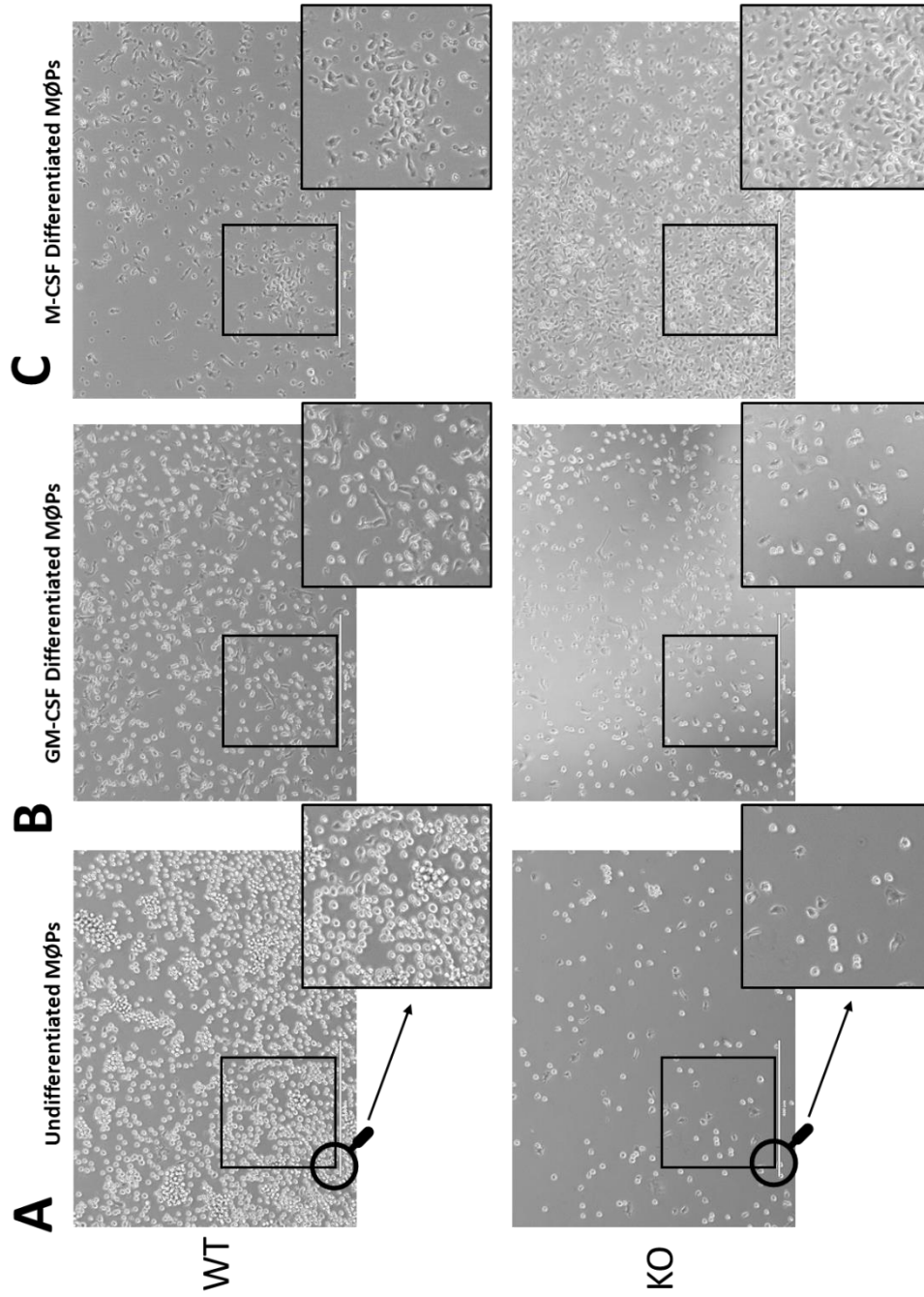
After Abi3 knock-out had been confirmed by qPCR in the Abi3 KO MØP cell line, the basic phenotype of the Abi3 WT and Abi3 KO MØP cell lines was assessed to investigate if a lack of Abi3 resulted in overt morphological changes.

Figure 6.15 shows bright-field images of undifferentiated MØP cells (Figure 6.15A) and MØP cells that had been differentiated with GM-CSF or M-CSF for 4 days (Figure 6.15B and Figure 6.15C respectively). These images confirmed that there were no obvious differences in the morphology of these Abi3 WT MØP cells and Abi3 KO MØP cells. However, when looking at the expanded portion of the images in the images below there were some subtle differences between these culture images. There seem to be fewer number of cells in the undifferentiated Abi3 MØP cells (Figure 6.15A). The GM-CSF differentiated cells (Figure 6.15B) were the most similar between the genotypes.

In M-CSF differentiated MØP cells (Figure 6.15C) there was a greater density of differentiated cells Abi3 KO, and both cultures had some dead/undifferentiated cells (non-adherent). Figure 6.16A-D shows that under while the density of M-CSF differentiated cells can vary depending on which part of the plate the images were taken and the density at which MØP cells were seeded, for the most part there were only subtle differences in the numbers of M-CSF differentiated and dead/undifferentiated cells between the genotype. When the seeding density of the MØP cells was reduced there was a reduced number of undifferentiated/dead cells and an increased number of M-CSF differentiated cells, especially in the Abi3 WT cell line (data not shown).

Overall in these cell lines the removal of Abi3 did not appear to have a large impact on the size or shape of either the undifferentiated MØPs or GM-CSF/M-CSF differentiated MØP cells. However there did appear to be some changes to the number of undifferentiated and differentiated cells between the Abi3 WT and Abi3 KO cell lines, which will be further explored in Section 6.2.2.2.

Figure 6.15 Morphological Characterisation of AB13 WT and KO MØP cell lines. A Pictures of undifferentiated MØP cells from both WT and KO lines following 4 days in culture. There were no observable differences in cell morphology between the two cell lines. There did appear to be a larger number of cells in the WT cultures compared to the KO MØP cell line. B WT and KO MØP cells following 4 days in culture with GM-CSF differentiation media. Again there were no obvious differences in morphology between the WT and KO cells. C MØP cells following differentiation with M-CSF supplemented media for 4 days. Both the WT and KO M-CSF differentiated cells appear to have a similar morphology. However there did appear to be an increased number of differentiated MØP cells in the KO compared to the WT, and a large number of dead cells in both M-CSF differentiated cultures. All Pictures were taken on EVOS microscope (live technologies) at 10X magnification, each white scale bar indicates 400µM. The black square indicates an exemplar region which were further



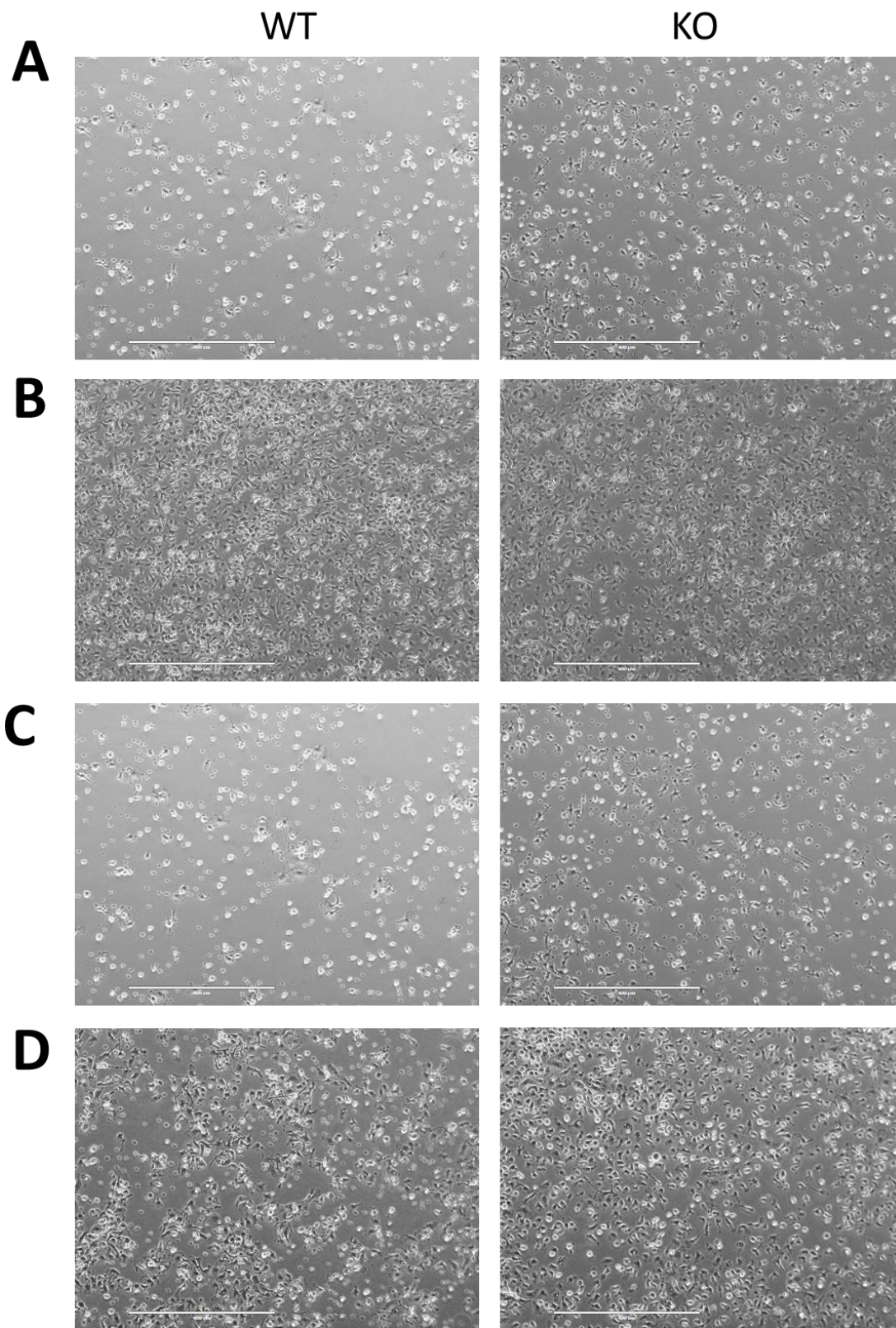


Figure 6.16 Additional images of M-CSF Differentiated MØPs. These EVOS images taken using the 10X magnification lens show that despite variation in the numbers of differentiated cells between different cultures the Abi3 WT cells and Abi3 KO cells appeared similar. A 1×10^6 MØP cells were seeded and

differentiated in a 6-well plate for 4 days. **B** Another 1×10^6 M ϕ P cells were seeded and differentiated in a 6-well plate for 4 days. **C** 5×10^5 M ϕ P cells were differentiated for 4 days in a 6-well plate. **D** 5×10^6 M ϕ P cells were differentiated for 3 days in a 15mm^2 tissue culture plate. All the white scale-bars in these images are $400 \mu\text{M}$ in size.

The next step in the basic phenotypic analysis of the Abi3 WT and Abi3 KO M ϕ P cell lines was to investigate the expression of several key receptors in these undifferentiated and differentiated M ϕ P cells. Based on previous work in the lab [151] the receptors selected for analysis were CD11b, CD45, CD11c and MHCII. Figure 6.17 shows example flow plots taken from one of these experiments where Abi3 WT M ϕ P cells are indicated in grey, and Abi3 KO M ϕ P cells by a dotted line. Overall MHCII expression did not appear to be altered by a lack of Abi3. In GM-CSF (Figure 6.17B) and M-CSF differentiated cells (Figure 6.17C) the CD45 expression was not largely changed between the WT and KO genotypes. In GM-CSF differentiated cells CD11c expression did not appear to be altered by a lack of Abi3. However, there were some alterations to CD11b receptor expression caused by ABI3 removal expression, which appeared to be slightly higher in undifferentiated M ϕ P cells and lower M-CSF differentiated cells. This experiment was repeated on three separate occasions.

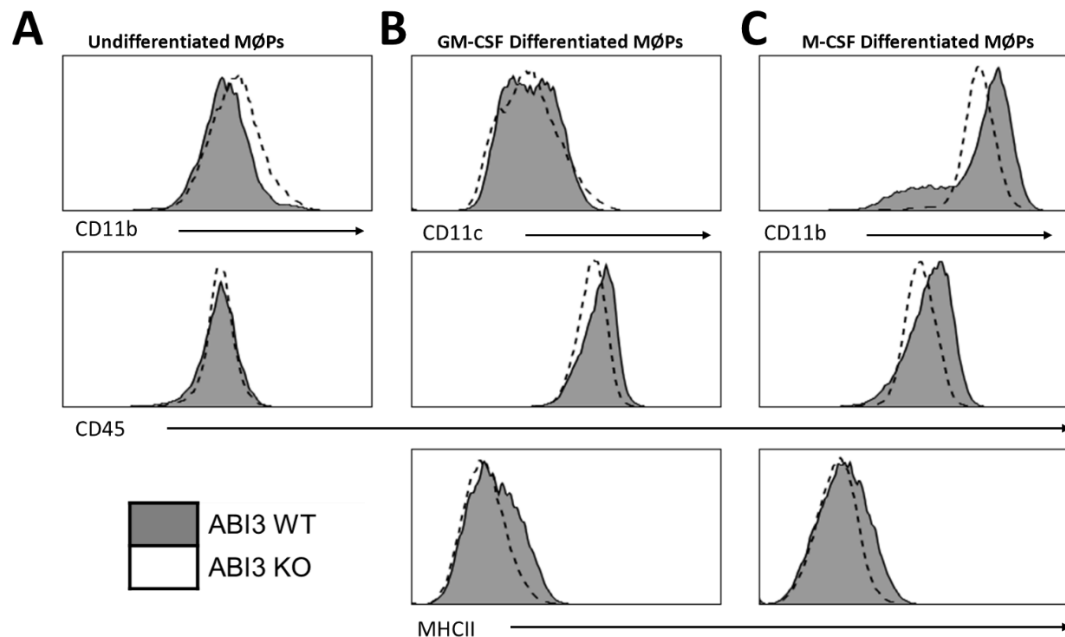


Figure 6.17 Characterisation of ABI3 WT and KO M ϕ P cell lines Receptor Expression. **A** CD11b and CD45 receptor expression were measured on undifferentiated M ϕ P cells and assessed via flow cytometry. There were no remarkable differences in CD11b expression between the WT (grey filled plot) or the KO (clear plot with dotted line) and no difference in CD45 expression between the two cell lines. **B** WT and KO GM-CSF differentiated M ϕ P cells were stained with CD11c, CD45 and MHCII antibodies. Again there were no vast differences in the Median Fluorescent Intensity (MFI) readings between the WT and KO GM-CSF differentiated cells for any receptor. **C** CD11b, CD45 and MHCII receptor expression was also measured on

WT and KO MØP cells differentiated with M-CSF. There were no notable differences in receptor expression between the Abi3 WT and KO differentiated cells. The histograms displayed in this figure are representative of 3 independent biological replicates (n=3).

Therefore, the receptor was normalised to Abi3 WT Median Fluorescent Intensity values (MFI) values from each experiment (Figure 6.18). Figure 6.18A suggested that CD11b expression was different between Abi3 WT and Abi3 KO undifferentiated MØPs did not meet statistical significance (Two-tailed Paired T-test; $P=0.0532$). There were overt changes to CD45 expression in undifferentiated Abi3 KO MØP cells (Figure 6.18A). In GM-CSF differentiated MØP cells (Figure 6.18B) there were no large genotype differences in CD11c, CD45 or MHCII receptor expression. Figure 6.18C shows that CD45 and MHCII expression in these M-CSF differentiated MØP cells was similar in both the Abi3 WT and Abi3 KO cells. Though the mean CD11b expression appeared similar to Abi3 KO M-CSF differentiated cells compared to Abi3 WT cells there was a large variation in the Abi3 WT M-CSF differentiated MØP cells between experiments.

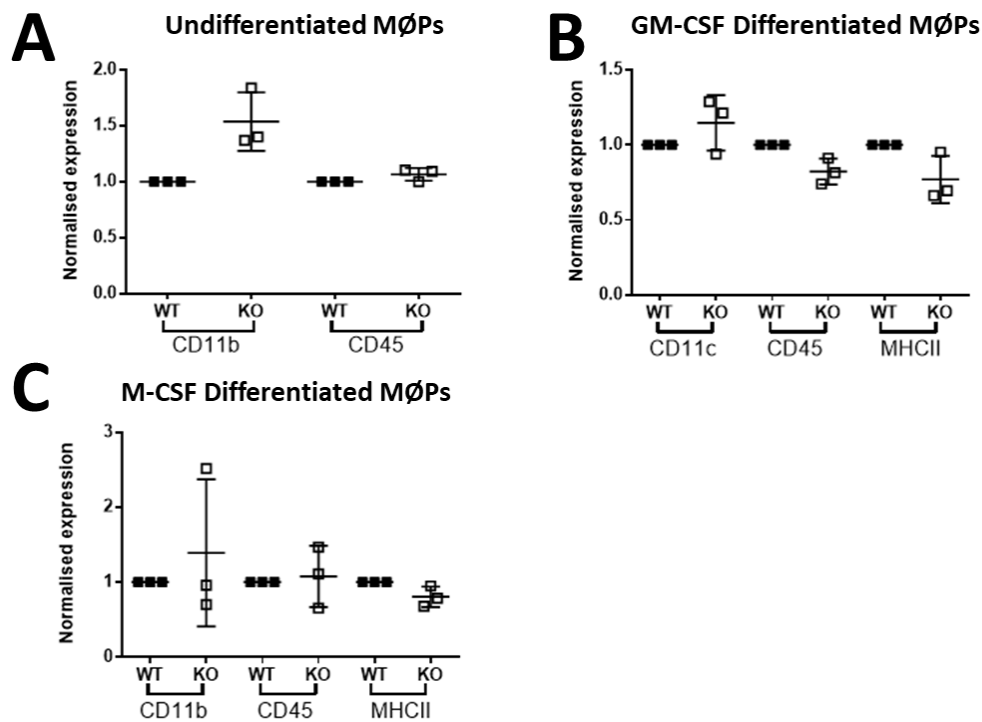


Figure 6.18 Summary of Receptor Expression in WT and KO MØP Cells. **A** Normalised expression was calculated by dividing the Abi3 KO Median Fluorescent Intensity (MFI) by the relative Abi3 WT for each experiment. CD11b receptor expression was not significantly different between WT and KO cells (Two-tailed Paired t-test, $P=0.0532$) whereas there were no visible differences in CD45 expression (Two-tailed Paired t-test, $P=0.1865$). **B** In GM-CSF differentiated WT and ABI3 KO cells there did not appear to be a difference in CD11c, CD45 and MHCII receptor expression ((Two-tailed Paired t-test, $P=0.3695$, $P=0.1173$ and $P=0.1499$ respectively). There did appear to be more variation in CD11c receptor expression in WT cells than there was in CD45 or MHCII receptor expression. **C** Again there was no significant difference in CD11b, CD45 or MHCII

receptor expression in WT M-CSF differentiated cells compared to ABI3 KO M-CSF differentiated MØP cells (Two-Tailed Paired t-test, $P=0.5607$, $P=0.7743$ and $P=0.1304$ respectively). Though there was some variation in CD11b receptor expression in these cells. The datapoints on the graphs represent three separate experiments ($n=3$) the mean indicated by a horizontal line and the error bars denote the standard deviation.

In summary, there were some subtle variations in the appearance of Abi3 WT and Abi3 KO undifferentiated and differentiated MØP cells this appeared to be a result of difference cell numbers rather than any obvious changes to the morphology of individual cells. This was especially apparent in the M-CSF differentiated cells. With regards to receptor expression neither CD45 nor MHCII receptor expression were altered in the Abi3 KO MØP cell lines, and CD11c expression was also similar in GM-CSF differentiated cells. Abi3 KO MØPs appeared to have higher levels of CD11b receptor expression though this did not reach statistical significance. This was perhaps unexpected as Figure 6.13C-D show *Abi3* mRNA expression was not very high in undifferentiated MØP cells, suggesting Abi3 KO MØP cells should not have any large-scale phenotypic changes resulting from a loss of Abi3. As all of these experiments were performed from one Abi3 WT and one Abi3 KO MØP cell line, meaning these changes would need to be validated in MØP cell lines derived from other mice before these CD11b changes could be considered meaningful.

6.2.2.2 Assessing Proliferation in MØP Cell Lines

During the course of the MØP cell phenotyping experiments above the MØP cell lines were maintained in MØP culture media (standard RPMI media with 10 ng/mL GM-CSF and 1 μ M oestrogen). It was observed that the culture media used to maintain the Abi3 WT (WT) MØP cell line changed colour faster than the media in the Abi3 KO (KO) MØP cell line. Figure 6.19 presents pictures of this anecdotal evidence where both MØP cell lines were seeded at the same density and maintained in the same volume of media for a prolonged period of time. In these experiments the phenol red in the RPMI media acted as a pH indicator and becomes orange/yellow as the acidity of the media increases [393]. The most likely cause of this acidity-related colour change was thought to be an increased CO₂ production resulting from a higher number of cells.

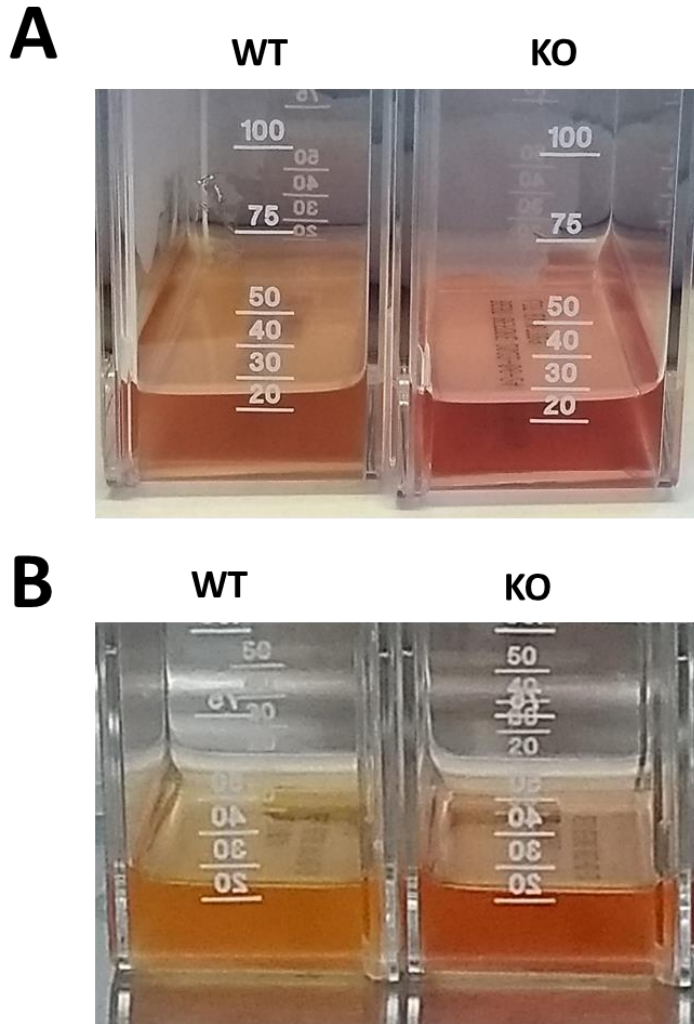


Figure 6.19 Colour changes in ABI3 KO and WT media suggest there could be altered proliferation. A Cells were seeded at a density of 1×10^6 for 3 days and supplemented with an equal volume of cell media. The media of the WT MØP cell line had a more orange colour, indicating an increase in CO_2 production which was most likely caused by cell proliferation. **B** Here the MØP cells for both the WT and ABI3 KO lines were seeded at 2×10^6 cells in 20mL of media. To maintain the cultures the MØP cell media was regularly changed, meaning equal volumes were removed and replaced, for 6 days. Again the media in the WT cell line appeared to show an increase in CO_2 which alters the colour of the phenol red to become a orange/yellow colour.

This raised the question of whether Abi3 KO MØP cell lines had an altered proliferation compared to the Abi3 WT MØPs. Moreover several reports have suggested that forced over-expression of Abi3 alters proliferation in multiple cancer cell lines [295]. Therefore, proliferation was assessed in both MØP cell lines using Ki67 and phospho-histone H3 (phh3) antibody staining. Figure 6.20A shows the approach taken to gate out the stages of the cell cycle using DAPI nuclear staining and Ki67 antibody staining. As indicated by the diagram to the right of Figure 6.20A any cells outside the G_0 phase of the cell cycle should be ki67 positive whereas the phh3 antibody staining binds to

cells in the prophase portion of the M-phase of the cell cycle [394]. Figure 6.20B shows representative ki67 and phh3 staining plots for undifferentiated Abi3 WT and Abi3 KO MØPs from one experimental replicate.

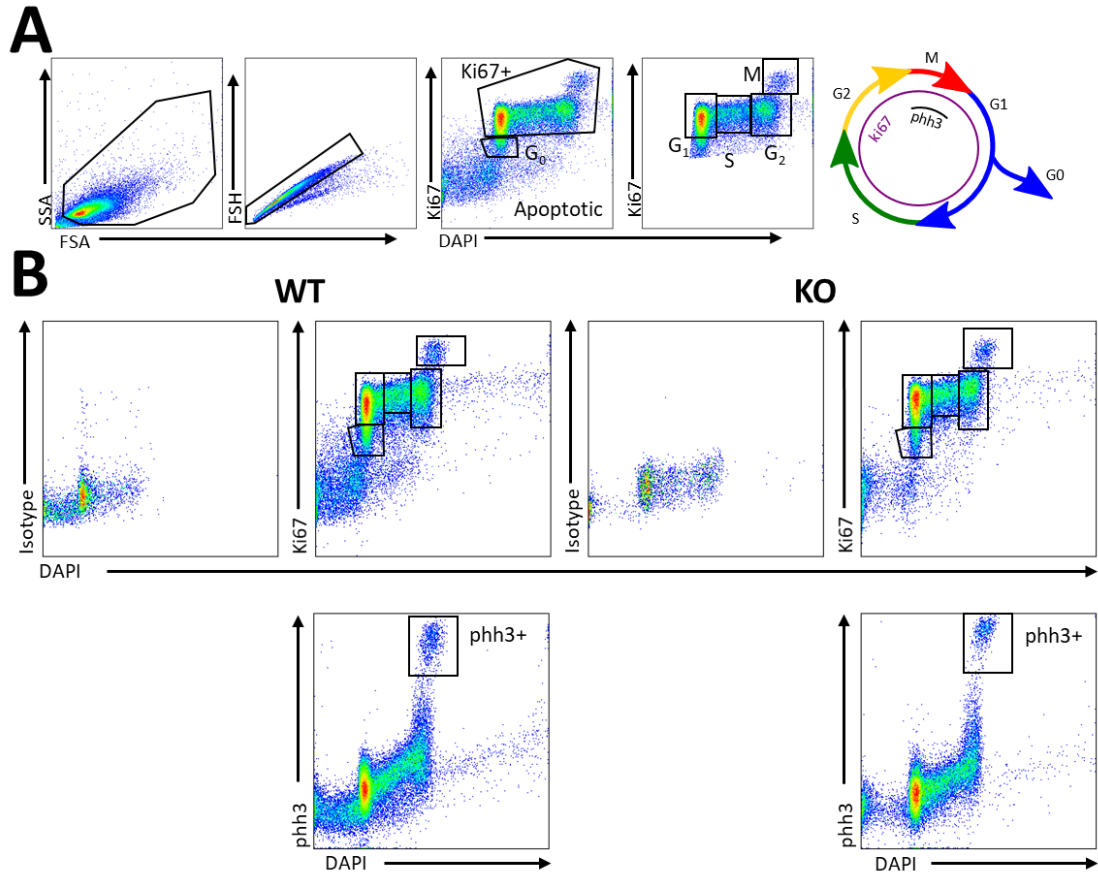


Figure 6.20 Assessing WT and ABI3 KO MØP cell proliferation by flow cytometric analysis of ki67 and phh3 staining- Part I **A** The gating strategy used in the Ki67 staining. First cells were separated from the debris, before singlets were selected. Using DAPI and Ki67 staining cells were separated into G₀ and Ki67+ gates. Ki67+ cells were then further subdivided into G₁, S, G₂ and M phases of the cell cycle as shown in the final flow plot. **B** The top panel shows the isotype and Ki67 staining against DAPI in both ABI3 WT and KO MØP cell lines, where there were no discernible differences between the two genotypes. The bottom panel shows phh3 staining against DAPI in the same cells.

The cell numbers were determined using the MUSE® Cell Analyser. Figure 21C shows that the cell numbers were consistently lower in the Abi3 KO MØP cells compared to Abi3 WT MØPs. These cell counts were normalised to the number of Abi3 WT MØP cells in each experiment (Figure 6.20C right) to allow for statistical analysis. This analysis confirmed that Abi3 KO MØPs have a significantly lower cell number compared to Abi3 WT cells (One-tailed paired T-test P=0.0024).

However, the percentage of G₀, G₁, S, G₂ and M phases both of these MØP cell lines were not significantly different (Figure 6.20D; Two-Way ANOVA, $_{int}$ P-value=0.8116). When the Ki67 positive

cells (G₁, S, G₂ and M phase) were separately graphed (Figure 6.20E) there was again no overt differences in the percentage of cells in each gate between the Abi3 KO and Abi3 WT MØP cell lines. The percentage of Ki67/phh3 double positive cells (Figure 6.20F) were not significantly different in the Abi3 KO or Abi3 WT MØP cell lines (Two-tailed Mann-Whitney Test, P=0.6857).

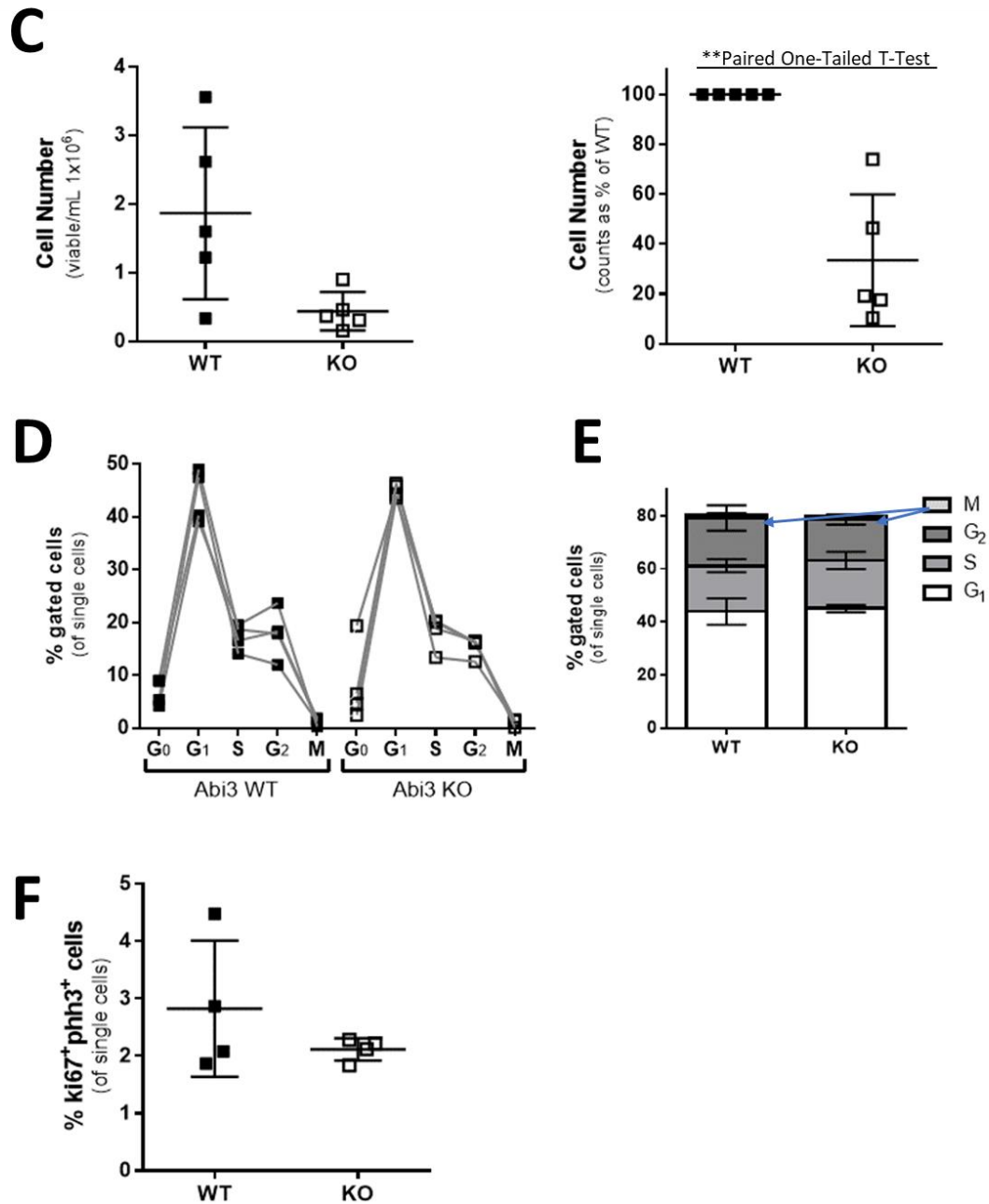


Figure 6.20 Assessing WT and ABI3 KO MØP cell proliferation by flow cytometric analysis of Ki67 and phh3 staining- Part II C Left The number of viable cells per mL for each proliferation experiment harvest, and one unrelated experiment, (n=5 total) where MØP cells were cultured at the same density for the same amount of time in the same volume of media. In each linked replicate (black line) the Abi3 KO MØP cells (empty

square) had a lower cell number than Abi3 WT MØP cells (black square). The mean values for the WT and KO MØP cell lines could not be tested for significance with a standard T-test due to a difference in the variances. Right The WT cell counts (filled squares) were normalised to 100% and the relative number of ABI3 KO cells (empty squares). Here it can be clearly seen that Abi3 KO MØP cells had significantly lower cell number compared to their WT counterparts (**One-tailed paired T-test $P=0.0024$) D The proportions of G_0 and Ki67+ cells, expressed as a percentage of all single cells, for each of the 4 experiments ($n=4$). Overall there did not appear to be a difference between the percentage of cells in either G_0 (unfilled squares) or Ki67+ cells (filled squares). E The percentage of G_1 , S, G_2 and M gated cells of all the Ki67+ gated cells. Again there were no large scale differences in any of the populations analysed when comparing the WT and ABI3 KO cell lines. The proportion of cells in M-phase is relatively small, hence the position has been indicated with a blue arrow. F The percentage of double-positive Ki67+phh3+ cells of all single cells. These cells expressed both Ki67 and phh3 which both mark cells in M phase, this phh3 antibody specifically marks prophase. Two-Tailed Mann-Whitney Test showed there were not any significant differences in the percentage of M-phase cells between WT and KO MØP cell lines (exact $P=0.6857$). On these graphs the mean is indicated by a horizontal line and the error bars denote the standard deviation across all the experiments ($n=5$ for cell counts and $n=4$ for ki67/phh3 staining).

This suggests that while there were differences in the number of Abi3 KO and Abi3 WT MØP cells this was not due to any obvious changes to proliferation, as assessed by Ki67 staining. However Ki67 antibody staining is not the most sensitive measure of proliferation. As evidenced in Figure 6.21A below, allowing 5-ethynyl-2'-deoxyuridine (EdU) to be incorporated into dividing MØP cells where it preferentially binds cells in the S-phase of the cell cycle and then staining the Click-iT™ EdU kit (Thermofisher) produced a much clearer signal than Ki67 staining, and did not require an isotype background control [380]. The 10 μ M dose of EdU used in these experiments was based on the manufacturer's guidelines and MØP cells were treated with EdU for 3 and 6 hours. These cells were stained with DAPI before being run on the flow cytometer. Figure 6.21A shows that there were few EdU positive (EdU+) cells in the untreated MØP cells, and the EdU+ (S-phase) cells were clearly separated. The proportion of MØP cells in S-phase from both repeats of this experiment were quantified, as shown in Figure 6.21B. This graph does suggest a reduced percentage of EdU+ cells in the Abi3 KO MØP cell line, though was based on one experiment so the results must be interpreted with some caution.

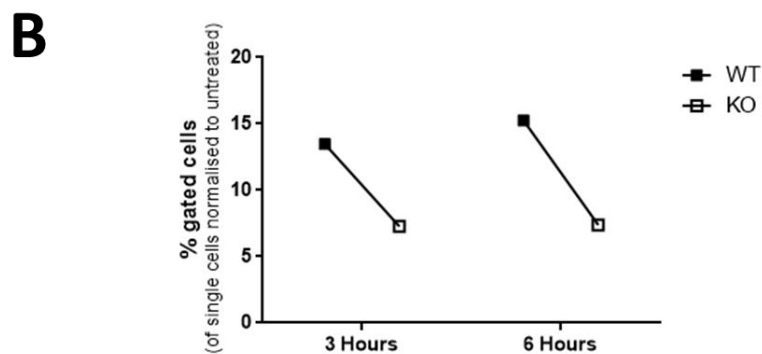
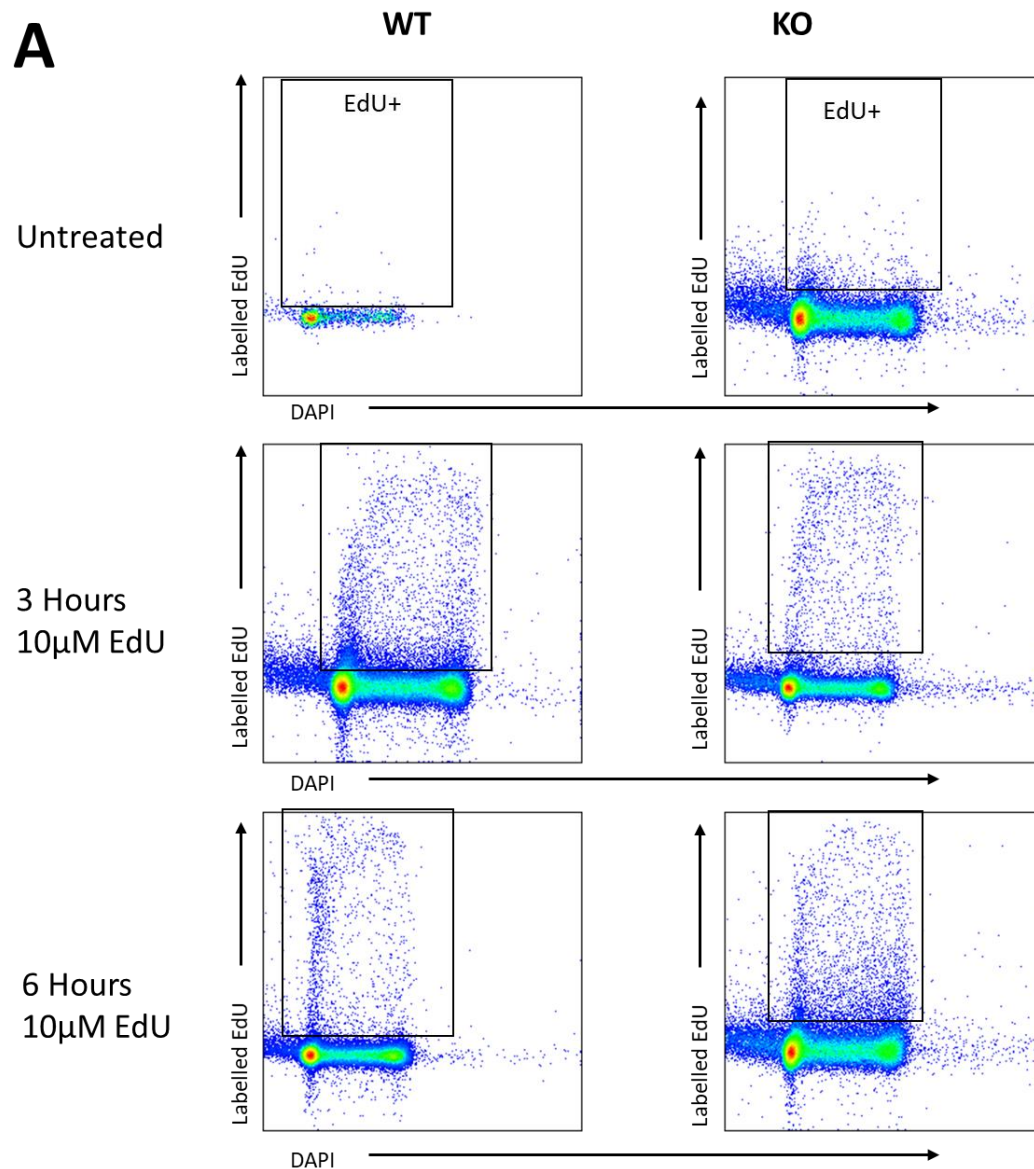


Figure 6.21 Results of EdU stimulation in WT and ABI3 KO MØP cells at multiple timepoints. A The results of one EdU time course as analysed by flow cytometry where the plots show DAPI staining against EdU staining. In both the untreated MØP cell samples there are very few EdU+ events. The other samples shown in this figure were treated with 10µM EdU for 3 hours (middle plots) and 6 hours (lower plots). Here it can be seen that there was an increased number of EdU positive cells. **B** Summarises the percentage of EdU+ cells at

each timepoint for one pilot experiment. Here it can be seen that there may have been a reduction in the S-phase of these cells (EdU+).

As the proliferation of these MØP cell lines is dependent on the level of GM-CSF cytokine, the time between the cultures being fed and the cells being harvested could be an important factor in assessing proliferation. To ensure media replenishment was not causing any bias in the results these cultures were fed with equal volumes of media at the same time every day and equal samples were taken from the cultures 6 hours later. NIM-DAPI staining was used to assess the nuclei of these cells and this experiment was repeated over three days.

Though both MØP cultures were seeded at the same density, Figure 6.22A shows that the number of Abi3 KO MØP cells was initially lower than in Abi3 WT MØP cell samples. However over the three timepoints the cell number did not significantly differ (Friedman's Test $P > 0.999$). Figure 6.22B shows representative nuclear DAPI staining profiles for Abi3 WT MØP cells (grey) and Abi3 KO MØP cells (outline), including the gating that was used to analyse the percentage of cells in each phase of the cell cycle. There were no differences in the percentage of MØP cells in the G1, S and G2M phases of the cell cycle between the Abi3 WT and Abi3 KO cell lines (Figure 6.22C, Friedman's Test $P = 0.1667$).

Overall, this data indicated that while Abi3 KO MØP cells appear to have a lower number than Abi3 WT MØP cells this was not due to any overt changes to the proliferation of these MØP cell lines. This was surprising as qPCR analysis suggests that *Abi3* mRNA was not highly expressed in undifferentiated MØP cells, raising the question why the removal of Abi3 would affect proliferation of these cells. It could be that Abi3 is expressed at the protein level in these MØP cells, though this has not yet been confirmed. Therefore proliferation was assessed in M-CSF differentiated MØP cells, which are known to have a higher *Abi3* mRNA expression and are a more biologically relevant model to study as they represent BMDM.

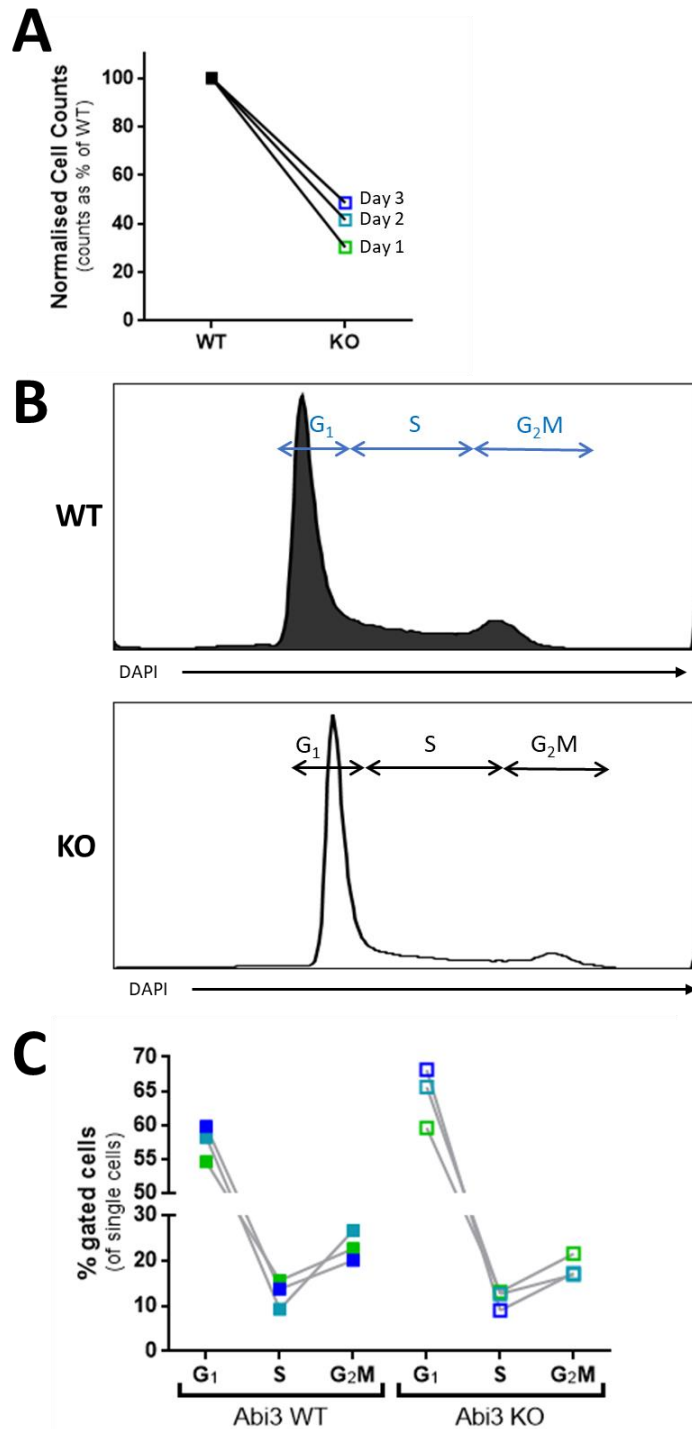


Figure 6.22 NIM-DAPI analysis of serial MØP cell samples. This experiment aimed to see if there were consistent differences in the WT and ABI3 MØP cell cycle. To do this the cell lines were seeded at the same density before being consistently fed at the same time of day, and a sample taken from the cultures 6 hours after feeding. The cell number was then determined using the MUSE cell counter before NIM-DAPI buffer was used to extract the nuclei and stain them with DAPI. **A** This graph denotes the cell counts taken from each experiment, expressed as a percentage to normalise between experiments. Here there was a lower number of ABI3 KO MØP cells in comparison to WT cell numbers at the start of this experiment despite the cultures being seeded at the same density. Over all three timepoints the cell number did not significantly change

*between the genotypes (Friedman's Test $P > 0.999$). **B** Example histograms showing the DAPI staining intensity at one timepoint, as well as the gating strategy used to identify the stages of the cell cycle in analysis. In this example there did seem to be a higher proportion of WT MØP cells in the S/G₂/M phases of the cell cycle compared to the ABI3 KO DAPI staining. **C** Graphical summary of all 3 timepoints of this NIM-DAPI time course in MØP cells. There were no significant differences at between the genotypes at each timepoint (Friedman's Test $P = 0.1667$).*

To ensure that the proliferation continued in these M-CSF differentiated MØP cells, even after differentiation, the cultures were supplemented daily with M-CSF in standard RMPI media. Figure 6.23A shows a representative ki67 and phh3 data plots following flow cytometric analysis. Compared to the MØP cell ki67/phh3 staining (Figure 6.20B) there was a much smaller percentage of cells undergoing division, which was expected due to the terminal differentiation of the MØP cells despite the daily M-CSF supplementation.

In 3 out of 4 replicates there was a relatively lower number of Abi3 KO M-CSF differentiated cells compared to Abi3 WT (Figure 6.23B), further experiments would be required to determine if this datapoint should be excluded as an erroneous result and not having true biological meaning. The percentage of cells in the G₀ or Ki67 positive (G₁/S/G₂/M) phase of the cell cycle were similar in both the Abi3 WT and Abi3 KO M-CSF differentiated MØPs (Figure 6.23C). When the G₁/S/G₂/M phases of the cell cycle were graphed separately there were no overt differences (Figure 6.23D). Again, when the percentage of cells that stained for both Ki67 and phh3, indicating they were in the prophase portion of M-phase, did not significantly differ between Abi3 WT and Abi3 KO M-CSF differentiated MØP cells (Two-tailed Unpaired T-tests $P = 0.6326$).

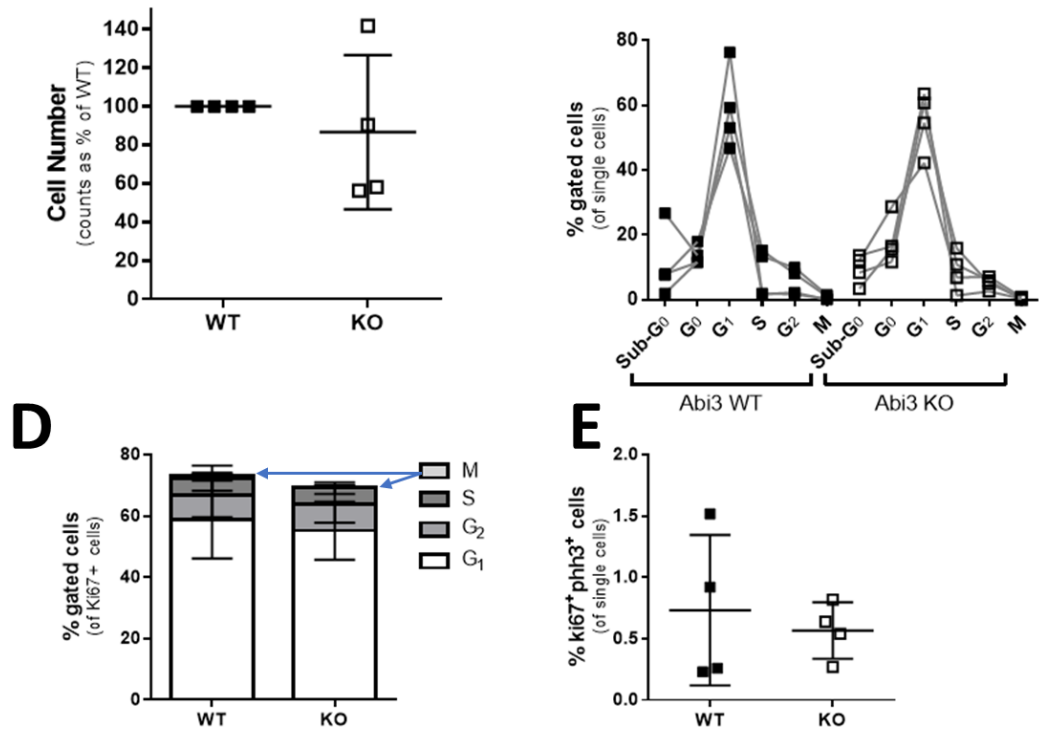


Figure 6.23 Proliferation as analysed by Ki67 staining in M-CSF differentiated MØP cells. **A** These flow plots show an example of isotype and Ki67 staining against DAPI nuclear staining. The gating strategy used to separate out the stages of the cell cycle in analysis. The second row of plots show the *phh3*⁺ staining, a marker of cells in M phase, against DAPI staining. These plots suggest there might be subtle differences in the proportion of cells in each phase of the cell cycle, though this has been quantified below. **B** Here the results of the cell counts taken from the M-CSF differentiated MØP at the time the cells were harvested. Overall there seem to be a lower number of ABI3 KO cells compared to WT cells, *n* 3 out of 4 replicates (Two-Tailed Paired T-Test, *P*=0.5524). **C** The graph shows the results of the 4 biological replicates (*n*=4) where Ki67 staining was assessed in M-CSF differentiated MØP cells. Here there did not appear to be any observable differences in the proportion of cells in the G₀ phase or the overall proportion that were ki67⁺. **D** When the ki67⁺ cells were subdivided for further analysis it appeared that in the ABI3 KO differentiated cells had no altered percentages in the G₁/S/G₂/M phase compared to their WT counterparts. Blue arrows highlight the position of the M phase data in the bar. **E** Here the proportion of WT and KO differentiated cells in the prophase part of M-phase are shown, as denoted by Ki67⁺phh3⁺ cells. Again there seemed to be a trend where there are fewer ABI3 KO cells in prophase compared to WT cells though this was not consistent across all replicates, and did not reach statistical significance (Unpaired Two-Tailed T-Test, *P*=0.6326). The data shown in these graphs are the result of 4 independent experiments (*n*=4). The flow plots shown in part A are representative of these experiments. These cultures were given M-CSF supplemented media daily to ensure that proliferation continued throughout differentiation. The mean values are indicated by horizontal lines or the bar, and the error bars denote the standard deviation.

The more sensitive EdU staining was also used to assess proliferation in these cultures. The flow cytometry plots in Figure 6.24A show that EdU positive cells were much easier to separate from non-dividing cells. In these two separate experiments, Figure 6.24B, there was no clear pattern between the Abi3 WT and Abi3 KO M-CSF differentiated MØP cells. It is possible that further repeats of this experiment would clarify if there are any differences in proliferation between the

Abi3 KO and Abi3 WT M-CSF MØP cells. Taken together this section suggests that there were differences in the number of Abi3 KO and Abi3 WT MØP cells, and though these differences may not be present in M-CSF differentiated MØP cells. Proliferation was assessed using multiple flow cytometry based assays and there was no overt differences between the two MØP cell lines. To ensure these changes were not an artefact from making the MØP cell lines these experiments would need to be repeated in another set of independently derived MØP cell lines from a different set of mice.

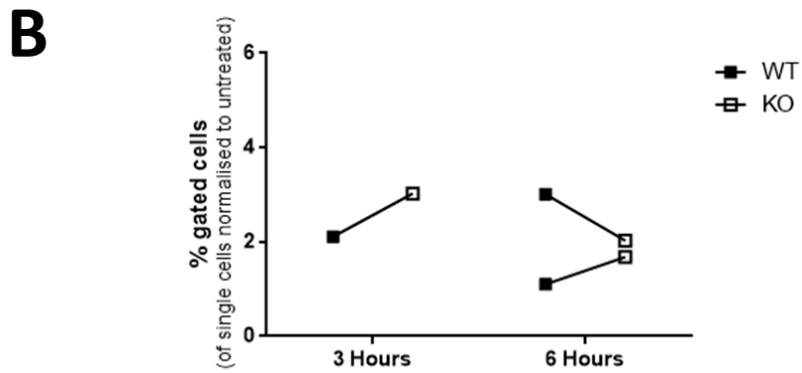
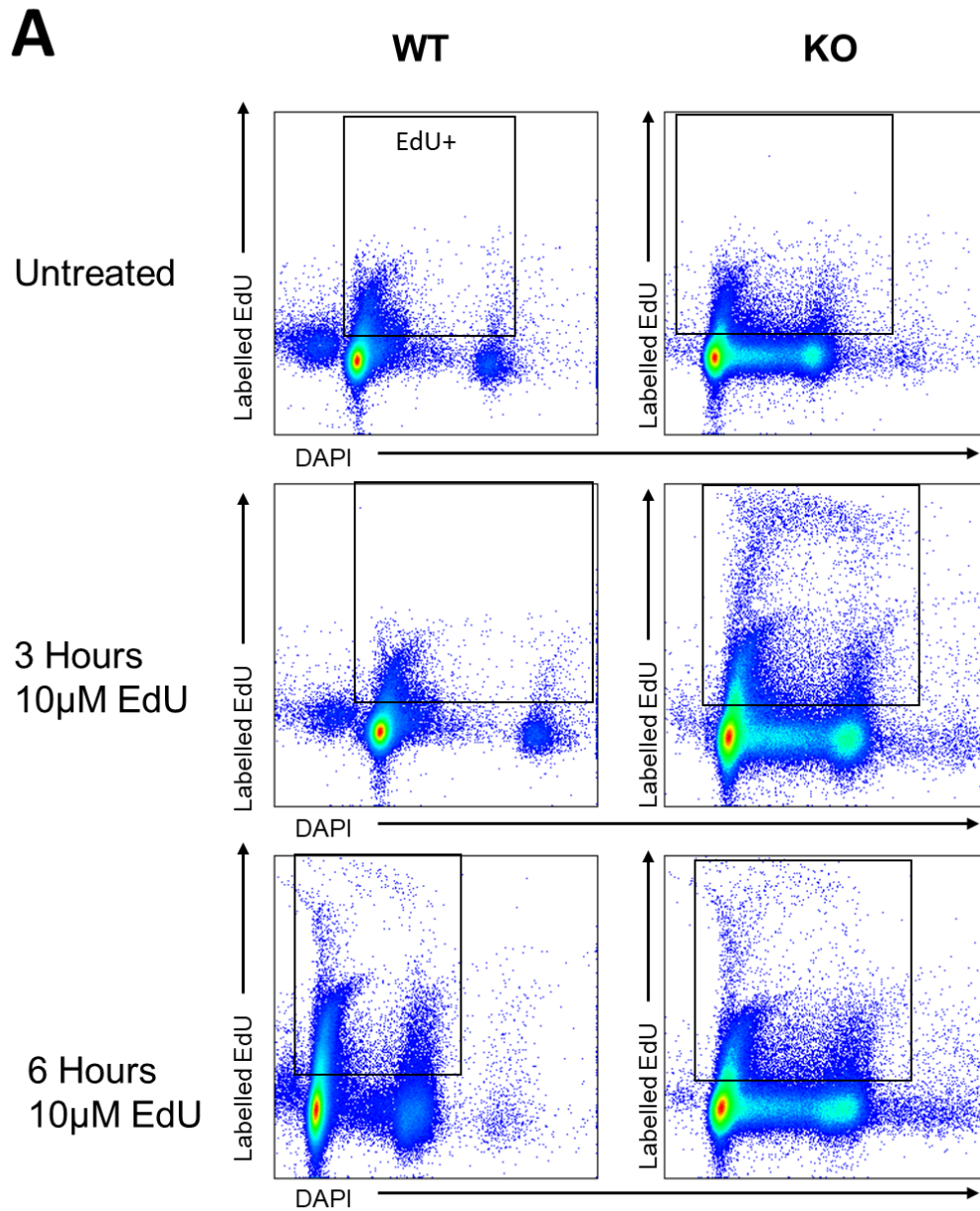


Figure 6.24 WT and ABI3 KO M-CSF differentiated M ϕ P cells treated with EdU. **A** Representative flow plots showing DAPI against EdU staining in untreated WT and ABI3 KO differentiated cells (top panel), as well as

cells exposed to 10 μ M of EdU for 3 hours (middle panel) or 6 hours (bottom panel). The EdU staining was clearly detected in all the EdU treated samples and not present in the untreated samples. **B** A graphical summary of the percentage of EdU+ cells, normalised to the untreated samples, across all treatment variations. The results presented in this graph were taken from two independent experiments (n=2), though one replicate at the 3 hour timepoint was removed due to unclear DAPI staining. There did appear to be some variation between the proportion of EdU+ differentiated WT cells compared to ABI3 KO but there enough variation between the repeats which suggests it would benefit from further repeats.

6.2.2.3 Assessing M-CSF stimulation responses in M ϕ P Cell Lines

As discussed in Section 6.1 of this chapter reductions in WAVE2 and Abi1 expression have been shown to impact the ability of M ϕ s to produce F-actin protrusions following stimulation with M-CSF [289]. Other work has shown that Abi3 has an inhibitory action on WAVE2 preventing it from translocating to the cell surface [245,284]. Therefore the impact of Abi3 knock-out on this M-CSF stimulated actin protrusions was assessed using M-CSF differentiated M ϕ P cells in the assay similar to the one developed by [289]. Briefly, after differentiation M-CSF was removed from the Abi3 WT/Abi3 KO M ϕ P culture media for 4 hours, where serum was also depleted for the last hour. The cells were then stimulated with 20 ng/mL M-CSF for 5 minutes before being stained for F-actin, with phalloidin, and the nuclear marker DAPI (Figure 6.25A).

The steps used to analyse the phalloidin staining in ImageJ are shown in Figure 6.25B. Briefly, the brightness and contrast was optimised and cells that were too close to be considered separately by the automated analysis were separated using a black line. The phalloidin images with DAPI counterstaining were used here to ensure cells were correctly separated. A threshold was applied to remove any non-specific background staining and any gaps within the cell boundary were filled. Finally, several measurements of each cell were made using the “Analyse Particles” function to gain information about the morphology including area, perimeter, circularity, aspect ratio (AR), roundness and solidity. The final four features in this list were calculated using the equations listed in Table 6.1, as described in the ImageJ user guide [395].

Feature	Calculation
Circularity	$4\pi \times \frac{[\text{Area}]}{[\text{Perimeter}]^2}$
Aspect Ratio	$\frac{\text{Major Axis}}{\text{Minor Axis}}$
Roundness	$4 \times \frac{[\text{Area}]}{\pi \times \text{Major Axis}^2}$
Solidity	$\frac{[\text{Area}]}{[\text{Convex Area}]}$

Table 6.1 Equations used to calculate the shape descriptor features in ImageJ.

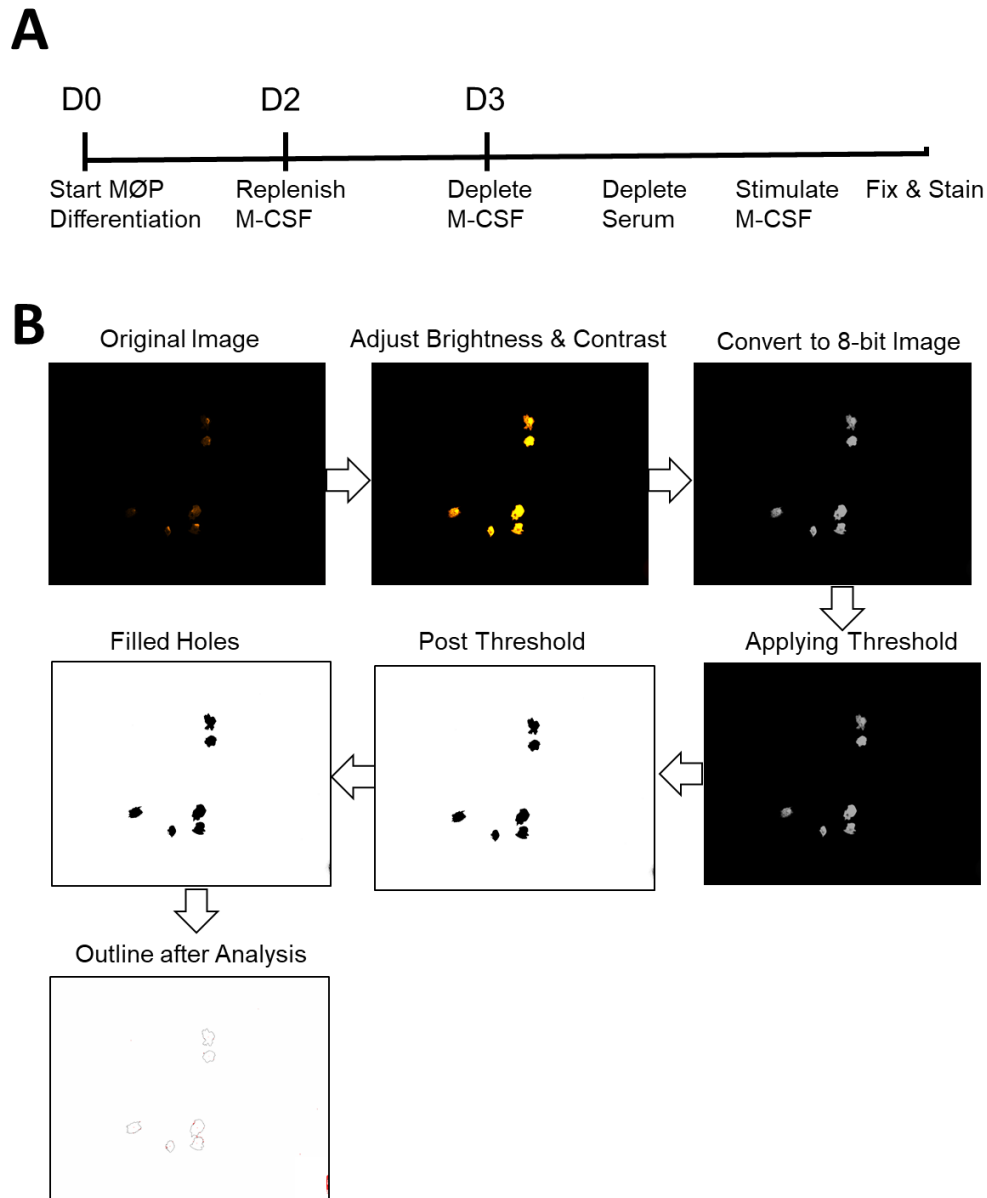
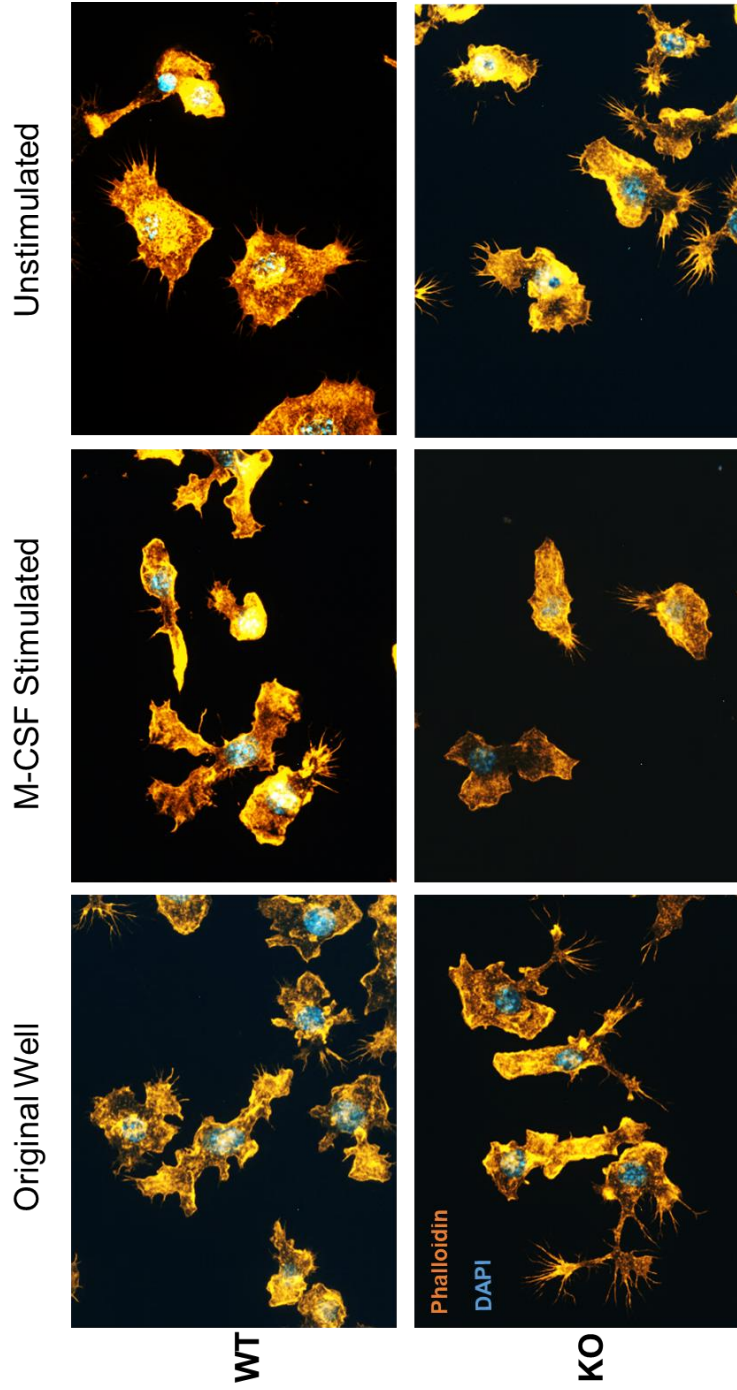


Figure 6.25 M-CSF Depletion Assay Set-up and Analysis. **A** The timeline used for each M-CSF depletion experiment. As shown in the timeline MØP cells were differentiated for 3 days, where cells were supplemented with M-CSF on day 2 of culture. Once differentiated (3 days later) M-CSF supplemented media was removed from the appropriate wells and replaced with standard RPMI medium. Cells were returned to the incubator for 3 hours. Following this M-CSF depletion step the serum was then removed from the desired cells and the cells returned to the incubator for a further hour. The appropriate M-CSF differentiated cells were then stimulated with 20ng/mL M-CSF for 5 minutes before cells were washed and fixed with paraformaldehyde. These cells were then stained with phalloidin and DAPI to identify the cytoskeleton and nucleus respectively. **B** The process used to assess the shape of the cells in ImageJ analysis. The phalloidin images were exported as TIFF images and imported into ImageJ. The brightness and contrast was adjusted on each image and black lines were drawn to separate any cells that were too close to be differentiated automatically. Composite images with DAPI nuclear staining were used here to help identify individual cells. Following this the images were converted to an 8-bit Image before an automatic threshold was applied to remove all the background. The binary "fill holes" function was used to ensure there were no gaps within the cell boundary. Finally each cell was analysed and the outline image of all the cells were saved.

In each experiment the cells were differentiated in an 8-well chamber slide (see section 2.5.4). Both the Abi3-WT and Abi3 KO M-CSF differentiated MØP cells had one 'original' well where cells were not depleted of M-CSF or serum. Each genotype also had an 'unstimulated' well where the M-CSF MØP cells were depleted of both M-CSF and serum but were not re-stimulated with M-CSF. This experiment was repeated four times, though during the third repeat there was an experimental error that meant the 'original' samples were excluded from further analysis.

Figure 6.26 shows a selection of exemplar images from one complete experiment taken at a higher magnification (63X) to better show cell morphology. M-CSF MØP cells in the original wells that were not experimentally manipulated had a more branched morphology. The images taken of 'unstimulated' cells that were starved of M-CSF and serum had a more rounded morphology. M-CSF stimulation appeared to partially restore the branched morphology of cells. There were no overt differences between the Abi3 WT and Abi3 KO M-CSF MØPs in these images. These cells were then analysed in ImageJ to provide a more unbiased assessment of changes of morphology. A minimum of 30 cells were assessed from the 5 pictures were taken in different areas of each well.

Figure 6.26 Exemplar picture of cell morphology in the M-CSF depletion assay. For each experiment one "original" well was not depleted of either M-CSF or serum to show what the original M-CSF differentiated MØP cells. These pictures were taken at 63X magnification with the Zeiss Axio Observer Microscope to provide examples of changes to cell morphology. Phalloidin AF666 (orange) was used to highlight the cytoskeletal structure of the cells and DAPI staining (blue) shows the location of the nucleus.



The values resulting from this ImageJ analysis were analysed as individual experiments (Figure 6.28) and where all four replicates were pooled (Figure 6.27). Given the standardized experimental set-up and analysis the values from each of these replicates were combined to provide a more powerful assessment. Figure 6.27 Non-parametric Kruskal-Wallis tests confirmed the medians were significantly different between some of groups in all parameters assessed. This was followed with a Dunn's multiple comparison test to interpret which groups were being affected, the P-values given below are all from this *post-hoc* analysis. Within both genotypes the median areas were significantly different between the stimulated and unstimulated cells ($P \leq 0.05$ in Abi3 WT and $P \leq 0.001$ in Abi3 KO). Both M-CSF stimulated ($P \leq 0.0001$) and unstimulated ($P \leq 0.05$) samples differed between the Abi3 WT and KO differentiated MØP cells (Figure 6.27A). This suggests the area of the cells was being changed by M-CSF stimulation and that a lack of Abi3 results in a moderately larger area.

The perimeter of the differentiated MØP cells was different in Abi3 KO and Abi3 WT M-CSF stimulated groups ($P \leq 0.0001$). The genotype of the cells also significantly impacted the perimeter of the unstimulated cells ($P \leq 0.002$). The graph suggest that the perimeter was higher in Abi3 KO differentiated cells compared to Abi3 WT (Figure 6.27B).

The circularity and solidity follow the same pattern in the M-CSF differentiated Abi3 WT cells, where the median is highest in the M-CSF stimulated samples lower in the unstimulated cells. These differences were found to be significant in both Abi3 WT groups ($P \leq 0.001$ for both), but not in the Abi3 KO groups. There was no significant difference between the circularity and solidity of the original Abi3 WT and Abi3 KO MØP cells, though the genotypes did cause significant differences to these parameters following M-CSF stimulation ($P \leq 0.001$ in circularity and $P \leq 0.05$ in solidity) as shown in Figure 6.27C and Figure 6.27F respectively. Circularity differed by genotype following M-CSF withdrawal ($P \leq 0.01$).

The aspect ratio appeared to be unchanged by the experimental manipulation, though it was significantly different in the original M-CSF MØP cells (Figure 6.27D; $P \leq 0.01$). A similar pattern was seen in the roundness of the cells, where only the original cells have significantly different values (Figure 6.27E; $P \leq 0.001$).

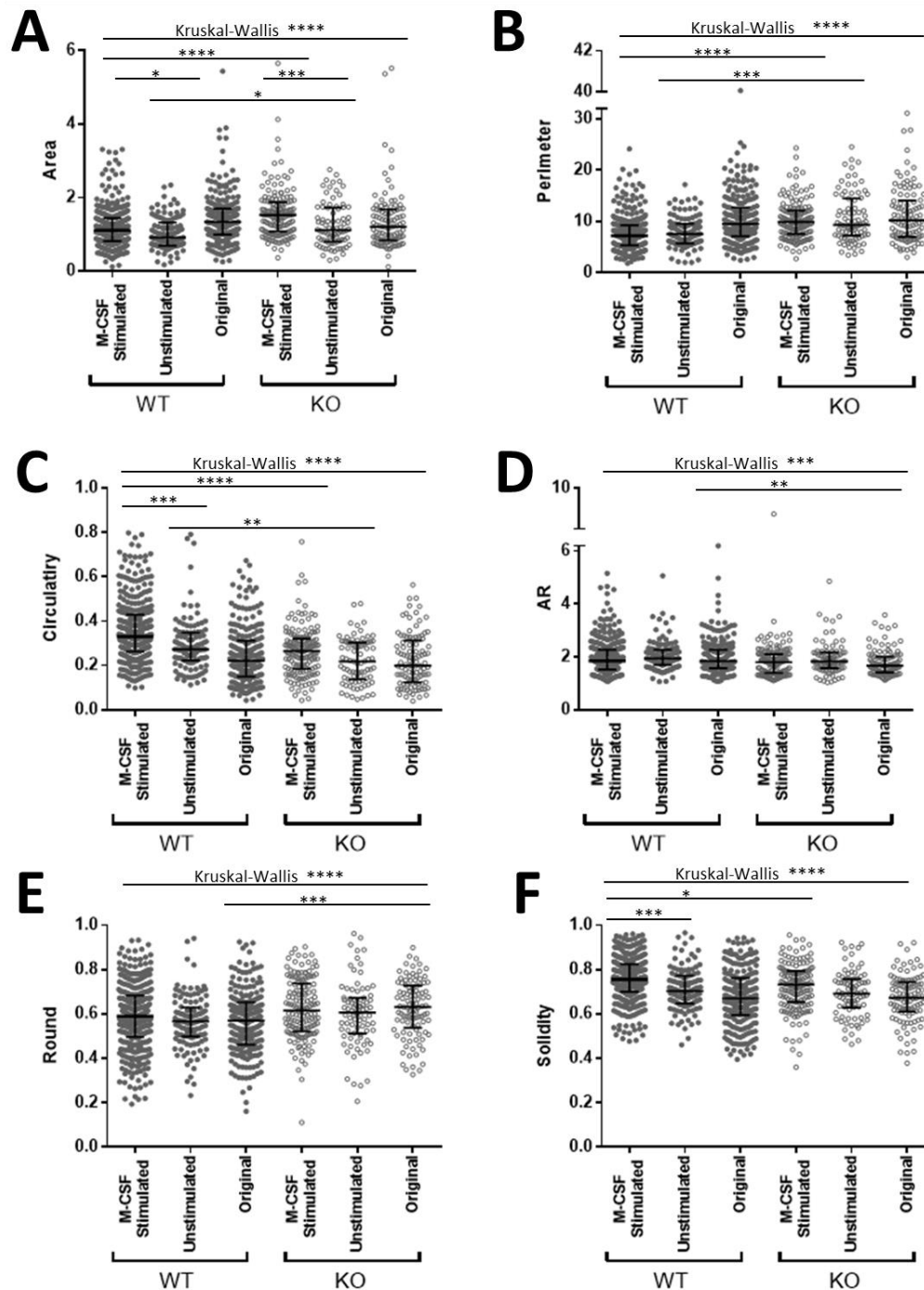


Figure 6.27 Summary of parameters analysed in M-CSF depletion assay. ImageJ was used to assess several parameters in both WT (filled) and ABI3 KO (empty), each dot represents an individual cell from one of the 4 replicate samples ($n=4$) which are shown together here, except the original samples where the dataset was $n=3$. The black horizontal bar denotes the median and the error bars show the inter-quartile range. There were no overt differences to cell morphology between the ABI3 KO and WT response to M-CSF withdrawal/stimulation. However there were several subtler differences present in this analysis. **A** The first parameter that was investigated was the area of the cell a non-parametric ANOVA confirmed there were differences between the medians (Kruskal-Wallis test gave an approximate P -value of <0.0001). Post-hoc

analysis with a Dunn's multiple comparison test confirmed the areas did not meaningfully differ between the original WT and ABI3 KO M-CSF differentiated MØP cells. *Abi3* WT cells that were stimulated with M-CSF have a slightly larger area than unstimulated cells ($P \leq 0.05$), though this increase in area was more apparent in the ABI3 KO cells ($P \leq 0.001$). The median values of the unstimulated and M-CSF stimulated cells both differ according to genotype, $P \leq 0.0001$ and $P \leq 0.05$ respectively. **B** A Kruskal-Wallis statistical test confirmed that the median perimeter of the cells was affected in this experiment, giving an approximate P-value of < 0.0001 . Again Dunn's multiple comparison test confirmed the perimeter is not statistically different in both original samples. In each separate genotype the depletion and subsequent stimulation had little effect on the perimeter. However the perimeter did differ between the genotypes. M-CSF stimulated and unstimulated *Abi3* KO and WT cells had statistically different perimeters ($P \leq 0.0001$ and $P \leq 0.001$ respectively). **C** Circularity was significantly altered between the groups (Kruskal-Wallis test approximate P-value of < 0.0001). The WT M-CSF stimulated cells appeared to be more circular than their respective controls (Dunn's multiple comparison test $P \leq 0.001$). In the KO M-CSF cells the circularity was not significantly different between the stimulated and unstimulated cells. However, the circularity differs between the genotypes in both the unstimulated ($P \leq 0.01$) and M-CSF stimulated ($P \leq 0.0001$) cells. **D** Though there were no dramatic differences in the Aspect Ratio (AR) differences across any of the samples the medians of some groups were still significantly different (Kruskal-Wallis test gave an approximate P-value of 0.0002). Post-hoc analysis showed the only significant difference was between the original M-CSF MØP cells ($P \leq 0.01$). **E** The roundness of the cell was determined to be the inverse of the aspect ratio. A Kruskal-Wallis test suggested there were differences between the experimental groups, approximate P-value of < 0.0001 . Here the ABI3 KO cells seem to have a consistently higher "roundness" index than the WT control cells (Dunn's multiple comparison test $P \leq 0.001$), though the M-CSF depletion/stimulation did not appear to influence this parameter. **F** The solidity of these cells also differed in this experiment (Kruskal-Wallis $P < 0.0001$). For both genotypes the M-CSF stimulated cells have a moderately higher solidity compared to the unstimulated samples, though this was only statistically significant in the WT cells ($P \leq 0.001$). The WT and KO M-CSF stimulated samples were significantly different ($P \leq 0.05$). In all the above figures Kruskal-Wallis tests were used to compare the group medians and followed by a post-hoc analysis with paired Dunn's multiple comparison tests. * $P \leq 0.05$ ** $P \leq 0.01$ *** $P \leq 0.001$ and **** $P \leq 0.0001$.

The analysis in Figure 6.28 suggests that the differences between *Abi3* KO and *Abi3* WT differentiated cells following M-CSF stimulation were subtle, and therefore the experimental pattern was also investigated. For the most part the means of each replicate followed the same experimental pattern observed when all samples were combined. To third replicate was excluded from this analysis due to the lack of 'original' control samples. On average these measurements the *Abi3* WT M-CSF differentiated MØP cell lines appeared to have greater morphological changes in response to M-CSF withdrawal and stimulation than *Abi3* KO cells.

The area (Figure 6.28A) was significantly different between genotypes in the M-CSF stimulated cells (Two-Way ANOVA $\text{int}P < 0.0001$, followed by Tukey's Multiple Comparison $P \leq 0.001$). The perimeter significantly differed between the genotypes in both the unstimulated and M-CSF stimulated groups (Figure 6.28B, Two-Way ANOVA $\text{int}P < 0.0001$, followed by Tukey's Multiple Comparison $P \leq 0.05$ and $P \leq 0.0001$ respectively).

The circularity was increased in the WT M-CSF MØP cells following M-CSF stimulation (Two-Way ANOVA $\text{int}P < 0.0001$, Tukey's Multiple Comparison $P \leq 0.0001$) though this response appeared to be attenuated in the KO M-CSF stimulated cells (Tukey's analysis $P \leq 0.01$). Figure 6.28D and Figure

6.28E show that the AR and round parameters did not provide much information about experimental changes but suggest that there was a subtle difference between the genotypes in the original samples (Two-Way ANOVA intP=0.0021 and P <0.0001 respectively, Tukey's Multiple Comparison P≤0.05 for both parameters)

The solidity (Figure 6.28F) appeared to be increased in both genotypes following M-CSF stimulation, though this was only reached significance in the Abi3 WT M-CSF differentiated MØP cells (Two-Way ANOVA intP<0.0001, followed by Tukey's Multiple Comparison P≤0.0001).

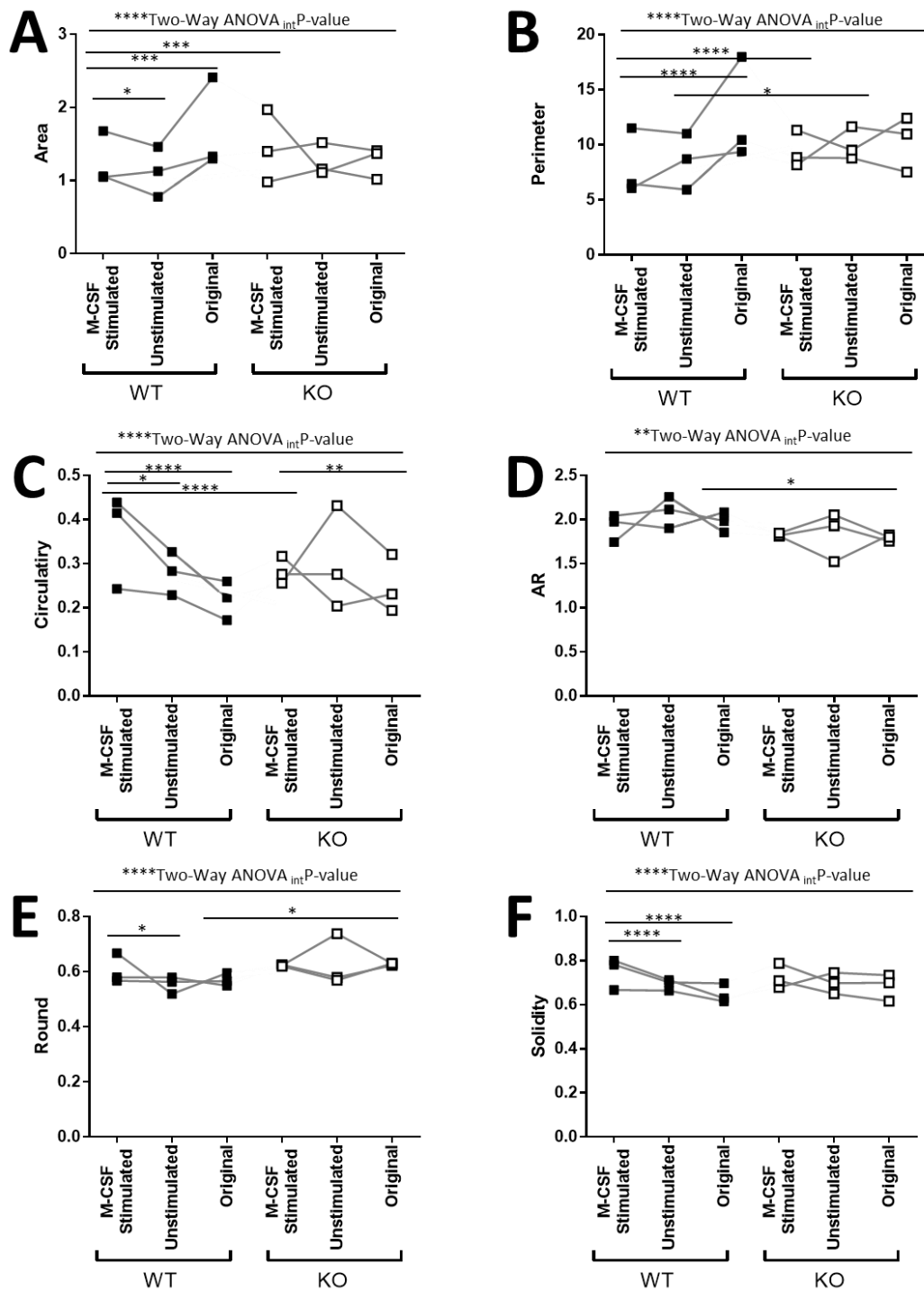


Figure 6.28 Experimental pattern of each replicate in M-CSF depletion assay. Each dot represents the mean WT (filled) and ABI3 KO (empty) value from each of the 3 replicate samples ($n=3$). Each replicate is connected with a grey line. **A** The area was significantly different between the experimental groups (Two-Way ANOVA $intP < 0.0001$). M-CSF stimulated WT cells were significantly different compared to the WT unstimulated and WT original samples (Tukey's Multiple Comparison, $P \leq 0.05$ and $P \leq 0.001$ respectively). The KO cells had a slightly larger area after M-CSF stimulation compared to WT stimulated cells ($P \leq 0.001$). **B** The perimeter did significantly differ (Two-Way ANOVA $intP < 0.0001$), Tukey's multiple comparison tests suggested the genotype

differences were between M-CSF stimulated ($P \leq 0.001$) and unstimulated ($P \leq 0.05$) groups **C** In both the WT and KO samples the circularity was altered (Two-Way ANOVA $_{int}P < 0.0001$). Tukey's analysis confirmed that in both genotypes the M-CSF stimulated samples were different from the original samples ($P \leq 0.001$ in WT and $P \leq 0.01$ in KO). The circularity appeared to be significantly lower in the M-CSF stimulated KO cells compared to WT cells ($P \leq 0.0001$). **D** The AR was largely unchanged by M-CSF stimulation, though there was a difference in the original samples (Two-Way ANOVA $_{int}P = 0.0021$, followed by Tukey's Multiple Comparison $P \leq 0.05$) in the majority of WT replicates whereas it was reduced following M-CSF stimulation in three of the four replicates. **E** Again the roundness did significantly differ (Two-Way ANOVA $_{int}P < 0.0001$), though the only difference between the genotypes was in the original samples ($P \leq 0.05$) **F** In both WT and KO cells the solidity of the cells was increased following M-CSF stimulation, though this only reached significance in the WT cells (Two-Way ANOVA $_{int}P < 0.0001$, followed by Tukey's Multiple Comparison $P \leq 0.0001$). In all the above figures a two-way ANOVA was used to compare the means and followed by a Tukey's multiple comparison tests. The interaction P-value ($_{int}P$ -value) is shown. * $P \leq 0.05$ ** $P \leq 0.01$ *** $P \leq 0.001$ and **** $P \leq 0.0001$.

To summarise this Section, M-CSF stimulation did induce some subtle changes to M-CSF differentiated MØP cell morphology though WT M-CSF seem to have a more dynamic response to M-CSF, which is more visible in Figure 6.28. Future experiments could restrict analysis to assess area, perimeter and circularity parameters. Overall this assay showed there were minor differences between the Abi3 WT and Abi3 KO MØP cell lines and their responses to M-CSF stimulation, though the biological relevance of these results will be discussed in the next section.

6.3 Discussion

This chapter highlights that much work is still needed to elucidate the complete function of *Abi3* in M \emptyset . The experiments in Section 6.2.1.1 confirmed that at in the *Abi3* KO mice exons 5-7 were disrupted and cannot be detected by PCR in either primary pM \emptyset or immortalised bone marrow M \emptyset P cells (Figure 6.3B and Figure 6.13B respectively). When *Abi3* mRNA expression was assessed by qPCR in pM \emptyset and M \emptyset P cells it was barely detectable in *Abi3* KO mice compared to control mice (Figure 6.6 and Figure 6.13C respectively). The removal of *Abi3* at the protein level in these *Abi3* mice could not be assessed due to a lack of specific commercially available antibodies (data not shown). Currently a specific antibody is being developed in-house by immunising these *Abi3* KO mice with part of the *Abi3* protein.

Moreover, the *LacZ* β -galactosidase reporter inserted into these *Abi3* KO mice can be detected in a subset of pM \emptyset by both flow cytometry (Figure 6.4) and IHC (Figure 6.5). In the M-CSF differentiated M \emptyset P cells β -galactosidase expression was detected in a small proportion of *Abi3* KO cells by flow cytometric analysis in (Figure 6.14B), despite qPCR analysis suggesting *Abi3* mRNA was expressed in these differentiated cells (Figure 6.13C-D).

There are three main reasons why *LacZ* β -galactosidase might not stain the entire pM \emptyset or M-CSF differentiated M \emptyset P population. The first possibility is that the entire population does express β -galactosidase but at a low level and therefore the staining was not sensitive enough to detect all levels of expression. The IHC staining kit suggests that extending the length of the incubation time and replacing the staining solution in this time can increase the β -galactosidase staining signal. However, as the flow cytometry β -galactosidase kit is more sensitive it should detect minimal enzyme activity.

The second possibility was that *Abi3* may not be highly expressed at the protein level in the entire cell population under physiological conditions. The single cell sequencing data from a WT *Gata6*^{tm2.1Sad/J} mouse (Figure 6.1B) suggested that *Abi3* mRNA is not expressed in the entire pM \emptyset population at the same level. This cannot be confirmed at the protein level until the development of a specific *Abi3* antibody.

The third explanation was that the deletion of most of the *Abi3* exon and the insertion of the *LacZ* β -Galactosidase sequence disrupted gene regulatory elements, meaning that the *LacZ*/ β -galactosidase expression is potentially dissimilar from the natural *Abi3* protein expression in these cells. Again, antibody staining is required to confirm this.

Taken together this data suggests that until percentage of Abi3 positive pM \emptyset or M-CSF differentiated M \emptyset Ps can be confirmed at the protein level in the Abi3 WT mice the accuracy of the *LacZ* β -galactosidase expression in the Abi3 KO mice cannot be confirmed. As microglia are thought to have a higher expression of Abi3 (Figure 6.1A) they may provide a better measure of *LacZ* β -galactosidase reporter expression than pM \emptyset .

As pM \emptyset are a much more accessible M \emptyset population than microglia they were used in several pilot experiments investigating if Abi3 KO had any substantial effects on M \emptyset function. In these experiments pM \emptyset from Abi3 KO mice, which were made on a C57BL/6NJ background, were compared to pM \emptyset from C57BL/6J due to a lack of available Abi3 WT mice. There are some known differences phenotypic comparison of these C57BL/6J and C57BL/6NJ mice though the white blood cell counts do not appear to majorly differ between these strain sub-types [396].

No differences were found in the number of pM \emptyset , or the proportion of Tim4^{low}/Tim4^{high} pM \emptyset between Abi3 KO and C57BL/6J controls (Figure 6.7E-H) or between the three matched Abi3 KO and Abi3 WT mice assessed (Figure 6.7A-D). Further repeats directly comparing Abi3 KO and Abi3 WT mice would be needed to confirm there are no differences to the pM \emptyset populations caused by Abi3 KO.

The first pilot experiment aimed to see if pM \emptyset adhesion was compromised by a lack of Abi3. Analysis of DAPI staining suggest adhesion to a standard tissue culture plate was not affected at any of the three timepoints (Figure 6.8). The second pilot experiment investigated zymosan phagocytosis where a small reduction in the percentage of Abi3 KO pM \emptyset phagocytosing zymosan was observed (Figure 6.11B), though this was only significant in F4/80⁺Tim4^{low} pM \emptyset . This data was taken from one experiment where only one dose of zymosan and one timepoint were assessed. Future experiments could utilise the imaging cytometer to investigate the rate of zymosan phagocytosis over time in these Abi3 KO and Abi3 WT mice and could even include comparing phagocytosis of opsonised and un-opsonised zymosan. While previous work in the literature suggests WAVE2, of which Abi3 is a part, does not play a role in Fc γ receptor mediated phagocytosis [289] the impact on other receptor-driven forms of phagocytosis has not been published. Moreover, both of these pilot experiments would be improved with β -Galactosidase staining in the Abi3 KO or Abi3 antibody staining, as if only a subset of pM \emptyset strongly express Abi3 then it may make it harder to detect if the phenotype of the Abi3 KO cells are altered.

Section 6.2.2 provided a basic phenotyping of M \emptyset P cell lines derived from these Abi3 KO and Abi3 WT mice. The only noticeable differences between the lines was a slightly lower CD11b expression

(Figure 6.18) and a reduced cell number (Figure 6.20C and Figure 6.22A) in undifferentiated MØP cells. The cell numbers in M-CSF differentiated MØP cells were not as noticeably different between the *Abi3* WT and *Abi3* KO cells (Figure 6.23B). This result was unexpected given that *Abi3* mRNA was not highly expressed in the undifferentiated cells (Figure 6.13C-D), though the amount of *Abi3* in the undifferentiated and differentiated MØP cells has yet to be confirmed at the protein level.

The differences in MØP cell number were not obviously resulting from an altered rate of proliferation in these cells. Flow cytometric analysis of Ki67 and phh3 antibody staining did not differ between the two genotypes (Figure 6.20 and Figure 6.23), though further repeats of the EdU proliferation experiments (Figure 6.21 and Figure 6.24) are needed to verify this result. The colour changes to the media (Figure 6.19) could be a result of an increased cell death in the *Abi3* KO MØP cell line or an altered metabolism. This could be assessed in several ways including using live cell microscopy to track these cells in culture or testing these MØP cell lines with an (3-(4,5-dimethylthiazol-2-yl)-2,5-diphenyltetrazolium bromide) tetrazolium (MTT) assay, which is converted to a detectable dye by cells that are metabolically active, and is therefore used to indirectly measure the viability of cells [397].

Overall the first step would be to ensure these differences were not an artefact of the individual MØP cell lines but a true biological effect. This would be done by creating multiple *Abi3* KO and *Abi3* WT MØP cell lines, from both male and female mice, and repeating the experiments in these independent cell lines. Meanwhile proliferation, apoptosis and metabolism could be assessed in freshly isolated pMØ to determine the impact of *Abi3* KO, though the population of *LacZ* expressing pMØ would need to be assessed. As the β -galactosidase flow kits requires live cells it was not possible to combine this assay with proliferation staining, which requires cells to be permeabilised. Most of the work investigating the role of *Abi3* in cell proliferation was performed in cancer cell lines where forced *Abi3* over-expression reduced proliferation [295], which might not reflect the true physiological function of *Abi3*.

Section 6.2.2.3 showed the impact of *Abi3* removal on cytoskeletal actin formation following M-CSF stimulation. Previous work has shown that M-CSF starvation in the BAC1.2F5 murine MØ cell line results in cells with a rounder morphology, whereas M-CSF stimulation causes f-actin protrusions resulting in a less circular morphology [389]. Moreover, it has been suggested that this M-CSF driven f-actin formation is dependent on the *Abi1*/WAVE2 complex [289]. When either *Abi1* or WAVE2 were reduced by siRNA the RAW cells had a rounder morphology following M-CSF

stimulation [289]. Abi1 and Abi3 are thought to work antagonistically, where Abi3 inhibits WAVE2 phosphorylation and translocation to the membrane [245,284,293,294]. This led to the prediction that M-CSF MØP lacking Abi3 would have a larger number of f-actin protrusions following M-CSF stimulation [289], as summarised in Figure 6.29.

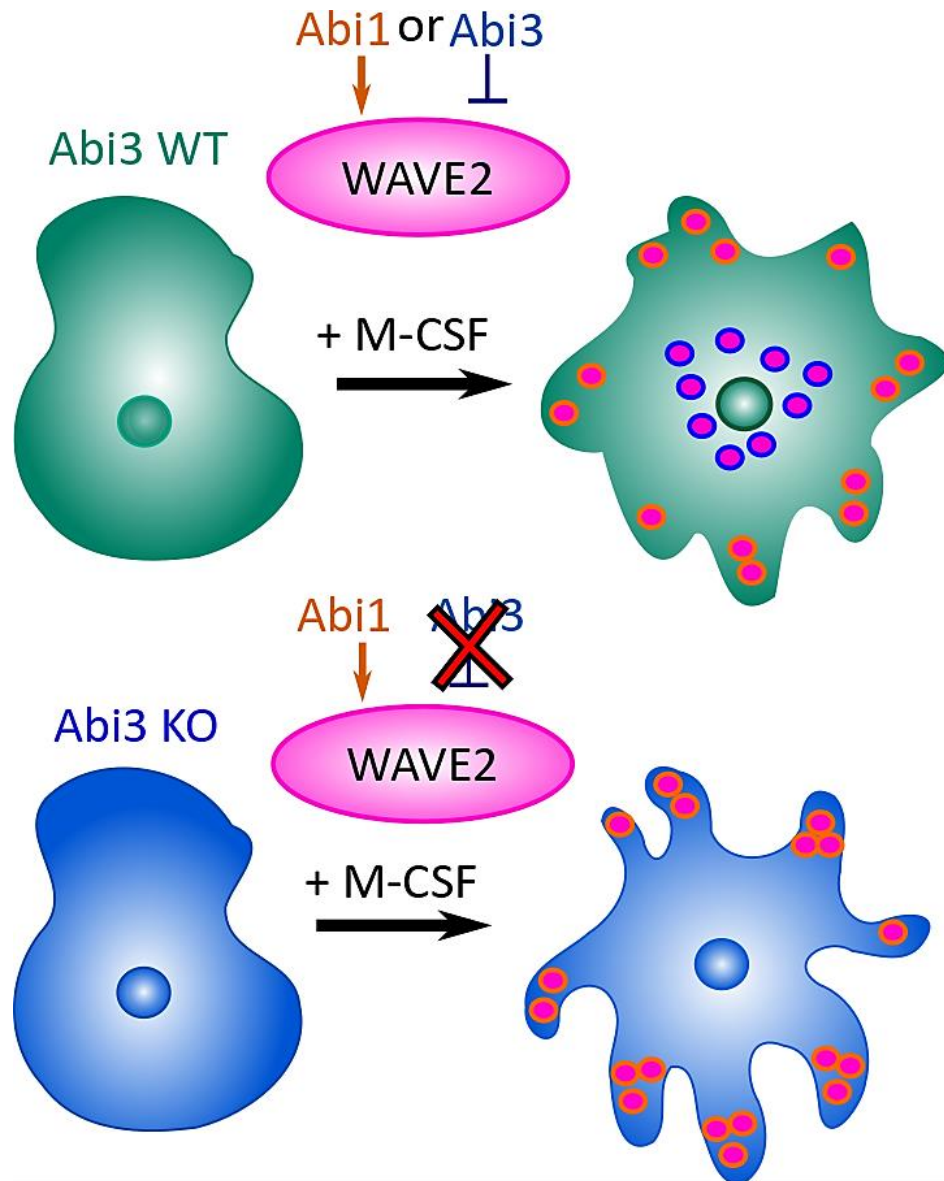


Figure 6.29 Graphical hypothesis of the impact of Abi3 KO on M-CSF depletion assay based on insights from the literature. While M-CSF withdrawal causes a more circular morphology, M-CSF stimulation increased the number of f-actin protrusions, and this M-CSF response is mediated by Abi1 (orange) phosphorylation of WAVE2 (fuchsia) to allow translocation, and Abi3 (blue) has a mutually exclusive function from Abi1 [245,284,289,389]. Therefore it was hypothesised that in these M-CSF differentiated MØP cells, which express Abi3, take longer to develop these f-actin protrusions. The Abi3 KO M-CSF differentiated MØP cells lack the Abi3-mediated inhibition of WAVE2 and were therefore expected to have a larger morphology with more actin protrusions.

Briefly, Figure 6.27 and Figure 6.28 showed that the *Abi3*-WT differentiated MØP cells appeared to be more responsive to M-CSF stimulation than *Abi3* KO cells. While *Abi3* KO MØP cells appeared to have a larger area and perimeter following M-CSF stimulation, though the changes seemed to vary between experiments. The circularity and solidity seemed to provide much more robust changes to morphology in this assay. These analyses suggest that WT M-CSF differentiated MØPs had an increasingly circular and solid following M-CSF stimulation, which was not seen to the same extent in KO cells. As M-CSF stimulation is thought to induce a ramified morphology with the *Abi1*/*WAVE2* complex it suggests that *WAVE2* translocation might be more inhibited in the WT cells which robustly express *Abi3* when differentiated (Figure 6.13). However many questions remained unanswered. For example, does *Abi3* affect *WAVE2* translocation following M-CSF stimulation? Moreover it is possible that morphology changes might be masked by the heterogeneity of the cells. Again, these results should be interpreted with some caution as the needs to be repeated in other *Abi3* WT/KO MØP cell lines and could even be optimised to assess the impact of M-CSF stimulation in *ex vivo* pMØ.

6.3.1 Conclusions and future work

In conclusion this work suggested that the *Abi3* KO mice will provide a useful tool in elucidating the role of *Abi3* in MØ function, as so far most studies have relied on forced over-expression of *Abi3* [245,284,294]. While in pilot pMØ experiments a lack of *Abi3* did not appear to have much of an impact on MØ number, adhesion or proliferation these experiments were not optimal, due to a lack of matched *Abi3* WT mice.

In immortalised MØP cell lines derived from individual female *Abi3* WT and *Abi3* KO mice there did appear to be some differences which require further investigation once new MØP cell lines have been derived. Rather than solely focusing on how *Abi3* KO impacts proliferation, apoptosis and cell metabolism should also be assessed. However proliferation studies should not be abandoned as recent work by Moraes *et al.* 2017 showed *Abi3* links *WAVE2* to the PI3K/AKT signalling pathway, in forced *Abi3* over-expression in thyroid carcinoma cell lines [294]. Previous work has suggested that PI3K and *WAVE* signalling could be responsible for actin cytoskeletal changes that occur during the cell cycle [292] Proliferation should also be assessed in freshly isolated pMØ to determine the impact of *Abi3* KO. Other work investigating the role of *Abi3* in cell proliferation was performed in cancer cell lines where forced *Abi3* over-expression reduced proliferation [295].

As previously mentioned *WAVE2* staining should be included in the M-CSF depletion/stimulation assay in the M-CSF differentiated MØP cells. If there were still morphological differences in the

Abi3 KO mice compared to Abi3 WT following M-CSF stimulation in subsequent MØP lines then this assay could be performed in freshly isolated pMØ and microglia.

Moreover, several papers have suggested that Abi1, another protein in the same family as Abi3, is increased in an inflammatory setting. IHC assessment of Abi1 expression following *in vitro* TNF α stimulation in a human colon cancer cell line (HDC-9) showed stimulation increased Abi1 levels [398]. In a mouse melanoma cell line (B16F1) platelet-derived growth factor increased Abi1 levels which was detectable by immunoprecipitation (IP) from 5 minutes after stimulation [293]. However this was not seen with all stimulants, as M-CSF stimulation in RAW cells changed the localisation of Abi1 but not the amount of Abi1 protein, as detected by IP [289].

Currently Abi3 protein expression has not been measured following an immune cell challenge in MØ. However, even without a specific anti-mouse Abi3 antibody the Abi3 KO mice could be used to investigate if there are any changes to the activation of the *Abi3* promoter following stimulation. If Abi3 KO *LacZ*/ β -galactosidase activity is representative of Abi3 protein staining in Abi3 WT pMØ cells then the flow cytometric assay could be combined with an immune challenge, such as LPS, to see if the percentage of fluorescent cells is altered. This could also be assessed in pMØ from Abi3 WT mice with or without a mild immune challenge, though pMØ would need to be sorted using flow cytometry before assessing *Abi3* mRNA expression by performing qPCR analysis on both stimulated and unstimulated pMØ. A more appropriate immune challenge for microglia would be fluorescently labelled amyloid- β oligomers.

Though this chapter has focused on the role of Abi3 in MØ rather than how Abi3 might impact microglia function in health and AD. Given the high levels of *Abi3* mRNA expression in microglia (Figure 6.1A) it is possible that Abi3 has a different function in microglia. In the literature Abi3 has been shown to be one of the genes controlled by homeostatic TGF- β signalling in microglia [154]. Preliminary work by another PhD student in the lab suggests that there are a greater number of microglia in these Abi3 KO mice which have a more amoeboid morphology, indicative of a more reactive state [43] (Simonazzi 2019, unpublished). The potential impact Abi3 might have in AD pathology is being investigated by breeding the Abi3 KO and Abi3 WT mice to the human APP knock-in AD mouse model (APP^{NL-G-F}) as published in [399].

The assays developed in this chapter can easily be applied to the primary culture system developed in Chapter 4 or freshly isolated microglia. Therefore, going forward the impact of Abi3 removal can be assessed both *in vitro* to determine subtle changes to WAVE2 signalling as well as looking at *in vivo* changes to microglia physiology in health and AD model mice

Chapter 7 General Discussion

7.1 Introduction

The broad objective of this thesis was to better understand how two GWAS genes, *Spi1* and *Abi3* can independently impact microglia/MØ physiology, providing insight as to how the function of microglia might be altered in AD. A recent review by Sarlus *et al.* (2017) highlighted that many of the GWAS genes discussed in section 1.4.4 converge onto a few common pathways [226]. In microglia, these pathways are thought to impact several key physiological functions including endocytosis, motility and phagocytosis, as reviewed in [226], suggesting the function of these pathways may be altered in AD. For example, the work in this thesis suggests the levels of both *Spi1*/PU.1 and *Abi3* were able to individually impact phagocytosis, despite likely acting at opposing ends of this biological pathway. The following sections will reintroduce the AD associated risk genes studied in this thesis.

7.1.1 *Spi1*/PU.1

The first LOAD associated risk gene investigated in this thesis was *SPI1*, which encodes the PU.1 transcription factor. The role of PU.1 in microglia has been well studied given that it is essential for the survival and function of several MØ populations [6–8]. Moreover, Gosselin *et al.* 2014 suggested that in mice PU.1 acts at active chromatin regions with other tissue-specific binding partners to aid in establishing a unique microglia identity, which was disparate from other MØ populations [153]. This work has also been validated in human microglia, where potential PU.1 binding sites were found in over half of the regions of accessible chromatin [156]. Taken together these analyses implied *Spi1* was one the most highly expressed transcription factors controlling expression of many genes in both mouse and human microglia.

SPI1 has been identified as a LOAD risk gene [4] and has been purported to be at the centre of a hub of AD risk proteins [5]. This is unsurprising given that other AD-risk genes have *SPI1*/PU.1 binding sites upstream of their promoters [230,231]. Several potential AD therapeutics, CSF1R inhibitors and the HDAC inhibitor Valproic Acid, are thought to indirectly impact PU.1 [73,90–92,279]. CSF1R inhibitors are thought to slow disease progression in AD model mice by reducing the number microglia [73,90–92]. In a recent clinical trial the HDAC inhibitor Valproic Acid was found to accelerate disease progression [318]. In human mixed-glia cultures VPA has been shown to reduce microglial phagocytosis of A β ₁₋₄₂ [281]. As Valproic Acid is thought to hyperacetylate Histone 3 and Histone 4 residues and block access to catalytic HDAC site [282] and its effects are not specific to PU.1. However, *in vitro* microglia studies have shown directly lowering PU.1 results in a reduced phagocytic capacity [230,232]. This led to concerns that drugs reducing PU.1 might

impact the number or function peripheral MØ populations, compromising the peripheral innate immune system. Therefore, this thesis set out to identify which microglia genes are affected by physiologically-relevant alterations in *Spi1* expression. The gene changes from the *Spi1* RNA-Seq datasets were then mapped to functional pathways. The *Spi1* over-expression dataset may even highlight problematic pathways in AD pathology.

An initial objective of this study was to see if microglial PU.1 could be down-regulated following removal of the *Spi1* -14 kB URE, as freshly isolated microglia have been shown to better represent *in vivo* microglia than those in long-term culture [154,155]. In parallel to this work TGF- β was used to develop *in vitro* cultures with a physiology more representative of *in vivo* microglia. These cultures were able to cope with lentiviral infection that reduced and increase Spi1/PU.1 protein. RNA was isolated from the microglia of these cultures where *Spi1* expression had been manipulated and sequenced to see the impact on the microglial transcriptome.

7.1.2 Abi3

The second LOAD associated risk gene investigated in this thesis was *ABI3*, which has been shown to bind to WAVE2 to form part of the Wave Regulatory Complex (WRC) [245,284]. This complex enables cells to reform their actin cytoskeleton in MØ migration and endocytosis [400,401]. WAVE2 has been specifically shown to form small actin protrusions called podosomes in response to M-CSF [289]. As previously mentioned, Abi1 phosphorylates WAVE2 which enables the WRC to translocate to the plasma membrane enabling podosome formation. Meanwhile Abi3 cannot phosphorylate WAVE2 and is thought to act in a functionally exclusive manner to Abi1 [245,293].

Recently identified, the LOAD associated risk SNP (rs616338^T) results in a missense mutation where phenylalanine replaces the serine at position 209 (S209F) in *ABI3* [5]. This SNP was associated with AD risk in an independent cohort [402]. *ABI3/Abi3* mRNA is highly expressed in microglia, though is present in other MØs [248,387,403]. *In silico* analyses suggested Abi3 is part of the network of microglia genes upregulated in AD [402] and ABI3 protein expression has been confirmed in post-mortem human microglia samples [244,291].

The exact role of Abi3 in microglia/MØ function remains largely unknown. As Abi3 appears to inhibit actin cytoskeleton changes [245] it raises the question how high levels of Abi3 may be important for microglia physiology. Most studies investigating ABI3 have focused on forcing ABI3 over-expression in cancer cells, which reduced tumour growth and suppressed cell motility *in vitro* [11,295] and is potentially regulated by the PI3K/AKT pathway [294]. However many of these studies forcibly increased Abi3 which might not represent the physiological function of Abi3.

Hence, another aim in this thesis was to better understand the role of the Abi3 protein in MØ function. This was done using primary MØs isolated from the newly developed Abi3 KO mice and conditionally-immortalised cell lines derived from these mice. As these mice had not been previously investigated, indeed the viability of Abi3-deficiency was unknown, they first needed to undergo a basic phenotypic analysis which included confirming Abi3 was removed in these mice. More specific cytoskeletal changes were then assessed in these MØ and cell lines to better understand how Abi3 regulates microglial functions that rely on alterations to the cytoskeleton such as phagocytosis.

7.2 Main Findings

The following sections will discuss the main findings from each of the results chapters in relation to what is currently understood in the field.

7.2.1 Removal of the -14 kB *Spi1*-URE did not impact trMØ PU.1 expression

The first thesis chapter showed the results of removing the -14 kB *Spi1*-URE (URE) with Cx3cr1 restricted Cre expression on PU.1 protein expression in pMØ and microglia. Previously published work showed removing this URE resulted in an ~80 % PU.1 reduction in total bone-marrow and splenic MØ [260,298]. Analysis of open chromatin and H3K27ac modifications undertaken in this suggested the URE was open to other DNA-binding factors in MØ populations including microglia. Contrary to expectations, this thesis did not find a significant difference in pMØ and microglial PU.1 expression following Cre mediated removal of the URE, in both *ex vivo* and *in vitro* experiments.

While this appears to conflict with published work there were several possible explanations for this disparity, some of which were excluded, as discussed section 3.3. In short, the function of the Cre lentivirus and Cx3cr1-Cre^{CONST} mice was confirmed. It was confirmed that the URE was removed at the genomic level in Spi1-CONST mice but not in Spi1-ERT mice. Despite this PU.1 protein levels were similar in Spi1-ERT, Spi1-CONST and Cx3cr1-Cre^{CONST} mice, suggesting that the URE removal was not impacting PU.1 expression. An *in vivo* pilot experiment suggested this is also not because the URE is only functional in an inflammatory context in adult mice.

This meant that other explanations must be considered. Firstly, there are several criticisms of the work published around the role of the URE in MØ. A transgenic mouse strain where a GFP reporter was inserted under the -14 kB *Spi1* URE promoter [268] suggested the URE was activated in splenic myeloid cells [298]. However, the impact of removing this URE in MØs has not been reported. The

original paper only mentioned PU.1 was reduced in total bone marrow, and did not state if the myeloid population was impacted [260]. The subsequent paper in 2006 utilised slightly different mice, where the neomycin cassette had been removed from the *Spi1*-URE floxed set-up. This paper stated that the reduction of *Spi1* mRNA expression was not affected by the presence/absence of the neomycin cassette, though this data was not shown and it was not stated if this was seen at the protein level [298]. Thus it appears that the work in this thesis measuring the impact on PU.1 after removing the URE in trMØs may not be directly in conflict with the published literature as this has not been thoroughly assessed by others.

Secondly, as discussed in section 1.5, myeloid cells have several mechanisms that help maintain a high PU.1 expression. When Runx1 binds to both the -14 kB URE and the -10.3 kB enhancer sites PU.1 is highly expressed [266]. When C/EBP α binds at the -14 kB URE it rearranges the chromatin to open transcription factor binding sites at the -12 kB enhancer that also increase PU.1 expression in myeloid cells [270]. Moreover, when Ikaros co-binds with PU.1 at the -10.3 kB, -12.2 kB and -14 kB *Spi1* enhancer sites it promotes PU.1 expression [269]. Overall this suggests the regulation of the PU.1 transcription factor in myeloid cells is highly complex. As the *Spi1*-CONST mice lack the -14 kB URE but still express PU.1 it suggests that the -14 kB URE is not essential for basal PU.1 expression in pMØ or microglia.

Thirdly, the original paper bred the *Spi1* URE floxed mice to another mouse strain where Cre was expressed in germline cells to ensure the resultant offspring ubiquitously lacked the -14 kB URE from the start of development [260,404]. In this thesis, Cre expression was restricted to Cx3cr1 expressing cells, namely myeloid cells [146] and previous work in Cx3cr1^{gfp/+} reporter mice indicates that Cx3cr1 expression can be detected in CD11b⁺ 'microglia' from embryonic day 9.5 [88]. Given Cx3cr1 is expressed early on in development it is unlikely that PU.1 was not reduced in *Spi1*-CONST mice because Cre was expressed after a URE-dependent window in development. However, by restricting Cre expression to Cx3cr1⁺ cells this ensured B-cells were not impacted in *Spi1*-ERT/*Spi1*-CONST mice. Therefore it could be that the reduction in bone-marrow PU.1 observed by Rosenbauer *et al.* (2004) were due to the impact of URE removal in B-cells [260]. The results of the subsequent paper supports this as mice lacking the URE had a reduced number of B-cells, and *Spi1* expression was reduced in CD45⁺ bone marrow cells [298]. While this could have been investigated further, aim of this thesis was to reduce PU.1 expression in microglia, under the conditions investigated, hence the *Spi1*-URE floxed model was not suitable for the aims of this thesis.

7.2.2 *In vitro* Microglia Model

Another aim of Chapter 4 was to design and evaluate an *in vitro* microglia culture model where PU.1 protein could be reduced and increased using custom lentiviruses. These experiments confirmed that the *Spi1* shRNA lentivirus was able to reduce the amount of PU.1 protein, compared to a NS shRNA control lentivirus, in primary microglia cultures. The *Spi1* shRNA lentivirus was shown to modestly reduce PU.1 in pMØ *in vivo*. Moreover, as this model provided more flexibility so PU.1 protein expression was also increased in microglia infected with a lentivirus containing the *Spi1* coding sequence (*Spi1* pSIEW) compared to an empty vector control (pSIEW).

To ensure the microglia cultures represented *in vivo* microglia as much as possible the cultures were supplemented with the TGF- β cytokine. TGF- β has been shown to help maintain several key homeostatic genes in cultured microglia [154,155]. A protocol was optimised that allowed for efficient lentiviral infection and microglia cultures to be supplemented with TGF- β . The findings in this thesis mostly supported the proposal that TGF- β maintained expression of key microglia genes *in vitro*. Section 4.2.2 demonstrated that TGF- β increased *P2ry12*, *Tmem119*, *Sall1*, *Fcrls*, *Siglech* and *Cd34* expression, in accordance with published work [154], though the level of expression did vary between replicates. This variation in TGF- β gene expression is likely due to variation in the primary cultures or an artefact of assessing changes to gene transcription by qPCR alone. The addition of lentivirus to this culture system partially reduced the TGF- β -increases on microglial gene expression. Given that TGF- β has been shown to produce an anti-viral response in other cell types it is not unexpected that TGF- β may impact the efficiency of lentiviral infection [30, reviewed in 31]. Overall, even with lentivirus infection TGF- β still increased expression of some microglia genes, listed above, compared to cultures supplemented with M-CSF alone. Therefore in the final 21-day culture protocol TGF- β was added to the cultures on day 5 and lentiviruses after 10 days in culture.

Three limitations are noted in this 21-day culture model. First, the microglia were cultured with M-CSF to maintain cell survival instead of IL-34. Both M-CSF and IL-34 signal through the CSF1R [405], though IL-34 can bind two additional receptors, Syndecan-1 and Receptor-type protein-tyrosine phosphatase ζ [406,407]. Murine RNA-Seq data suggests that *Csf1r* is predominantly expressed in

microglia and CSF1R knock-out mice lack microglia the CSF1R is thought to be the most essential receptor [88,248].

In mice IL-34 signalling affects more microglia in the cortex, hippocampus and olfactory bulb [408] and regional *IL-34* expression changes with age [409]. However both M-CSF and IL-34 maintained microglia *in vitro* [155] and *in vivo* [86,87]. *In vitro* M-CSF is commonly used to culture microglia [154,339] and an in-house protocol using M-CSF had been developed by another PhD student [410]. Future experiments could compare IL-34 and M-CSF in the culture model developed in this thesis to see if the microglia transcriptome is altered.

Secondly, the brains were not perfused and microglia were sorted by CD11b and CD45 expression alone, which means there could be potential contamination from monocytes that had differentiated into microglia-like cells *in vitro* (MDML) [411]. A pilot experiment suggested perfusion had little impact on the percentage of monocytes but did diminish the viability of the cells (data not shown). While *Tmem119* is purportedly present on native microglia and not peripheral microglia-like cells [108] other work suggests bone-marrow derived microglia also express *Tmem119* when cultured with M-CSF [412]. This thesis showed *Tmem119* was not expressed at a high enough level for flow cytometric sorting. This was not unexpected as *Tmem119* has been shown to be quickly lost after microglia are removed from the brain [155], it follows that *Tmem119* would be lower in cultured microglia. Also even if *Tmem119* had been used to sort microglia, it does not exclude the possibility that other CNS myeloid populations were present in these cultures [134]. Despite these criticisms CD11b and CD45 expression are commonly used to sort microglia cells.

Thirdly, as this thesis relied on lentiviruses to reduce and increase PU.1 expression there were concerns that these viruses could impact the mRNA profile of the microglia. However even if microglia were directly transfected with an siRNA or an shRNA these constructs can be recognised as viral RNA by Toll-like Receptor (TLR) 3 and TLR7-TLR9 resulting in an interferon (IFN) response in innate immune cells, as reviewed in [340]. To minimise the impact of the experimental viruses on the transcriptome of the microglia appropriate control viruses were used. This meant that in analysis the shRNA/virus induced changes would be mostly removed when the viruses were compared to their respective controls, Non-Silencing (NS) shRNA for *Spi1* shRNA and empty vector pSIEW for *Spi1* pSIEW.

To summarise, the results provided here provide further support the importance of TGF- β signalling maintaining microglia gene expression. Moreover, the *Spi1* shRNA virus was shown to be

effective in reducing PU.1 protein in M-CSF/TGF- β cultured microglia, ~65 % reduction, as well as having modest effects *in vivo* pM \emptyset (40-50 % reduction). The *Spi1* pSIEW virus was also shown to increase PU.1 protein levels in infected M-CSF only microglia cultures by between 50-200 %. With both these viruses the PU.1 protein was only moderately changed to try and better represent physiological changes that could be induced by a risk SNP. The expectation was that mRNA-Seq analysis of these microglia with altered PU.1 levels could provide a superior understanding of which biological pathways are impacted by physiological relevant PU.1 changes.

7.2.3 *Spi1* RNA-seq Results and Validation

The results of this chapter indicate that there was a “core” set of 162 microglia genes sensitive to the amount of *Spi1*/PU.1 (where $P \leq 0.05$), which is in line with other work suggesting PU.1 acts at several transcription sites in a concentration-dependent manner [9,10]. Another finding was the identification of a set of 122 genes ($P \leq 0.05$) that appeared to only be up-regulated in the *Spi1* over-expression dataset, the implications of which will be discussed in section 7.2.3.2. *In Silico* pathway analyses indicated that multiple pathways relating to the cell cycle and DNA damage were likely activated in the *Spi1* knock-down RNA-Seq dataset. The most significantly activated pathways in the *Spi1* over-expression RNA-Seq dataset were related to the IFN signalling pathways and the bacterial/viral immune response. As discussed in the preceding section, there were concerns that these virus-related pathways might be present in these samples as an artefact of the experimental design. However, this is likely to be a true biological effect as these pathways were thought to be deactivated in the *Spi1* knock-down dataset. Secondly, similar pathways were activated in a myeloid progenitor cell line where PU.1 expression could be conditionally induced [413]. Thirdly, PU.1 can bind to the IFN Regulator Factor 4 (IRF-4) and the IFN Consensus Binding Protein (ICSBP) to induce activity of the IL-1 β promoter in M \emptyset cell lines [277].

To ensure the accuracy of the RNA-Seq data PU.1, Iba-1 and P2ry12 were measured at the protein level. Both PU.1 and Iba-1 protein levels were reduced in *Spi1* shRNA infected microglia compared to NS shRNA infected controls, as observed in the *Spi1* knock-down dataset. P2ry12 appeared to be reduced in P2ry12^{high} *Spi1* shRNA infected microglia. The *Spi1* pSIEW virus resulted in a level of increased PU.1 protein, Iba-1 and P2ry12 were not obviously altered. Taken together these results indicate that the RNA-Seq datasets do represent *Spi1* virus dependent changes at the protein level.

Since the advent of this thesis, two *in vitro* papers have been published where PU.1 has been manipulated in microglia [230,233]. In short, Huang *et al.* (2017) reduced and increased PU.1 in

the BV-2 mouse microglia cell line while Rustenhoven *et al.* (2018) used a PU.1 siRNA to reduce PU.1 protein in primary human mixed glia cultures. The reduction in PU.1 protein in this thesis (~65 %) was comparable to Rustenhoven *et al.* (~60 %) in the validation cultures and more moderate than Huang *et al.* 2017 (~80 %). The PU.1 over-expression was not quantified in Huang *et al.* 2017 though in this thesis PU.1 expression was increased between 50-200 %.

As summarised in Table 7.1 there are several differences in the experimental approaches taken in both studies. Firstly, the *in vitro* microglia models were different. The work in this thesis was performed in primary microglia cultures supplemented with TGF- β which were sorted before RNA-Seq and are much more representative of *in vivo* microglia than the BV-2 cell line used by Huang *et al.* (2017) [154,230]. While Rustenhoven *et al.* (2018) used primary human glia cultures, neither microglia or cells with a reduced PU.1 were purified before microarray analyses. Moreover, these cultures were derived from patients with medial temporal epilepsy which is known to induce an inflammatory microglial phenotype, reviewed in [42], and might not represent normal microglial physiology.

Secondly, using RNA-Seq to assess mRNA changes has multiple advantages over a Microarray or qPCR approach, a major advantage being that RNA-Seq data is not limited by prior knowledge of mRNA sequences and can be re-analysed following other discoveries [371]. To summarise, while the methodology of these papers is not without criticism the approaches still led to meaningful results and have overcome the lack of Spi1/PU.1 transgenic mouse models. The next few sections will describe the results of the functional experiments performed in this thesis.

Experimental Parameters		This Thesis (unpublished)	Huang et al. 2017	Rustenhoven et al. 2018
Species?		Mouse	Mouse	Human
Cell Type?		Primary Mixed Glia Cultures with TGF- β	BV-2 Microglia Cell Line	Primary Mixed Glial Cultures (Patients undergoing neurosurgery)
PU.1 Manipulations?		Knock-down and Over-expression	Knock-down and Over-expression	Knock-down only
Method of PU.1 Manipulation?		Lentivirus infection with <i>Spi1</i> shRNA (\downarrow) and <i>Spi1</i> pSIEW (\uparrow)	Lipofectamine transfection with <i>Spi1</i> shRNA (\downarrow) and FLAG-PU.1 (\uparrow)	Lipofectamine transfection with <i>Spi1</i> siRNA (\downarrow)
Time between transfection/infection and analysis?		11 days	2 days	7 days
Sorted before RNA extraction?		Yes, GFP+ microglia	Yes, GFP+	No
mRNA Analysis				
Method of Transcriptome Assessment?		RNA-Sequencing	qPCR	Gene Microarray
Number of genes assessed		3,077 in Knock-down and 346 in Over-expression*	49 in both	180
Assessed <i>Spi1</i> mediated mRNA Changes (method)?		Yes (RNA-Seq and qPCR)	Yes (qPCR)	Yes (microarray and qPCR)
<i>Spi1</i> mRNA significantly reduced by Knock-down?*		No	Yes	No
<i>Spi1</i> mRNA significantly increased by Over-expression?*		Yes	Yes	N/A
Confirmed PU.1 protein Changes?		Yes, Flow Cytometry	Yes, Western Blot	Yes, Immunofluorescence
PU.1 significantly reduced by Knock-down?*		Yes	Yes	Yes
PU.1 significantly increased by Over-expression?*		Yes	No Data	N/A
Functional Assessments				
GO/Pathway Analysis Used (details)?		Yes (IPA and DAVID)	No	Yes (DAVID)
Comparison to human AD data (details)?		Yes (IGAP data)	No	Yes (Nanosting RNA from mid-frontal gyrus 8 AD cases and 8 AD controls)
Proliferation? (method)		Yes (Flow Cytometric analysis of ki67/DAPI staining)	No	N/A but noted no difference in microglia cell number in <i>Spi1</i> siRNA
Phagocytosis? (method)		Yes (Imaging Cytometry, labelled zymosan)	Yes (Flow Cytometry, labelled zymosan)	N/A

Table 7.1 Comparison of papers manipulating PU.1 expression in cultured microglia. *Where a P-value of ≤ 0.05 were taken to be significant

7.2.3.1 *Spi1* Knock-Down Dataset

The functional assays were selected based on the results of clustering and pathway analysis of the RNA-Seq datasets, as shown in Chapter 6, to determine the impact of an altered PU.1 on microglia function. Given the *Spi1* RNA-Seq dataset implied pathways related to the control of the cell cycle or the DNA damage/repair response were up-regulated, ki67 was used to assess proliferation in these cells (Figure 7.1). Some studies have already shown that differentiating MØ increase their levels of PU.1 by lengthening cell cycle [257], though this may not apply in adult microglia [165] which are a self-renewing population. PU.1 has also been shown to be part of the in M-CSF dependent proliferation of mature MØ and microglia [255,271,414]. The impact of PU.1 knock-down on microglia phagocytosis was also assessed in this model as PU.1 has been shown to bind to the Fcγ Receptor promoter and the CD11b promoter [272,415], both of which are key receptors in the phagocytotic process [183].

7.2.3.1.1 Assessment of Proliferation

While the work in this thesis did not find any significant differences in microglia proliferation caused by *Spi1* shRNA infection, as assessed by ki67 flow cytometric analysis, there did appear to be a slight increase in the proportion of ki67+ cells overall. This was slightly unexpected given the *Spi1* knock-down RNA-Seq pathway analysis and reports in the literature that *in vivo* CSF1R inhibitors blocked neurodegenerative disease-related microgliosis [73,416] and M-CSF stimulation can increase PU.1 protein and microglia proliferation [271]. While PU.1 is important in M-CSF dependent MØ/microglia proliferation [255,271,414] none of these studies assessed proliferation as a direct consequence of reducing PU.1 protein. Additionally, in this experimental model microglia were cultured with TGF-β to better represent homeostatic microglia. Several studies have shown that TGF-β suppresses microglia proliferation [341,342] which is not surprising given that *in vivo* microglia proliferate at a slow rate, as discussed in section 1.4.1. Future experiments could assess proliferation by EdU staining in this culture model both with and without the addition of TGF-β.

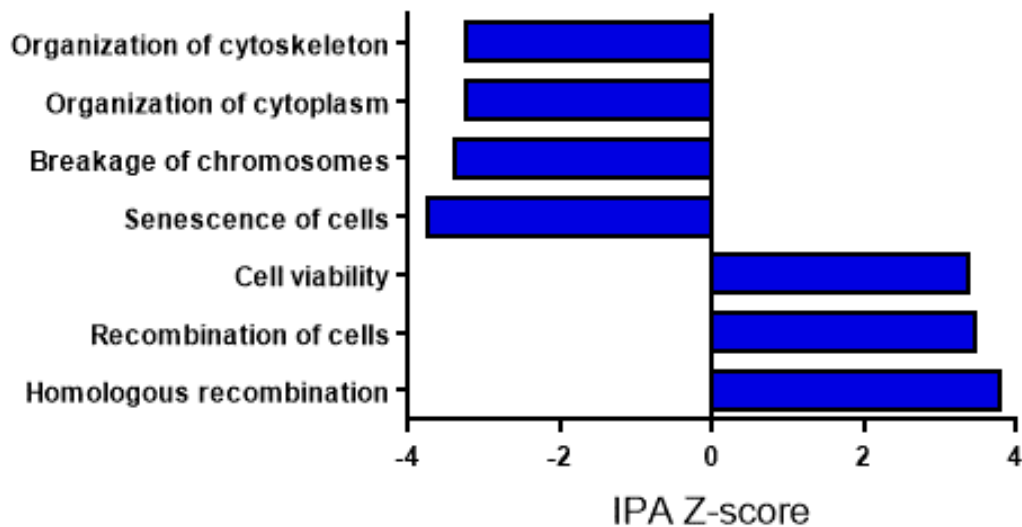


Figure 7.1 Z-Score of Cell-Cycle IPA Disease/Function Pathways in the *Spi1* Knock-Down dataset. A positive Z-Score indicates that a pathway is activated and a negative Z-Score indicates that a pathway is less active. Overall this *in silico* analysis suggests that the cell cycle/DNA repair mechanisms are altered by *Spi1* knock-down.

As the pathway analysis in this thesis also implicated cell cycle checkpoint and chromosomal replication pathways there were concerns *Spi1* shRNA infected microglia were failing to undergo correct cytokinesis. DAPI staining in these microglia failed to prove that there was a difference in the percentage of cells with multiple nuclei which would indicate a failure in cytokinesis. However, the microglia were infected with lentivirus for 10 days it is possible that microglia which fail to correctly divide undergo apoptosis are quickly phagocytosed by the remaining microglia. Some support comes from Smith *et al.* (2013) who noted there was a reduced number of microglia in human mixed glia cultures where PU.1 was reduced by ~70 % [232]. While another paper produced by the same group observed no difference between the number of microglia in the PU.1 siRNA cultures, this work was limited as neither the PU.1 or the scrambled control had a reporter and therefore uninfected microglia were not be excluded from the analysis. In summary, these results suggest that more research on this topic needs to be undertaken before the association between the PU.1 reduction and the cell cycle related pathways becomes apparent. One potential experiment would be to track microglia in cultures following infection with either NS shRNA and *Spi1* shRNA lentivirus using microscopy.

7.2.3.1.2 Phagocytosis

In this study *Spi1* shRNA infected microglia were found to have a lower percentage of cells associated with zymosan than NS shRNA infected microglia. This PU.1 mediated reduction in phagocytosis has been previously observed *in vitro* in BV-2 cells and human microglia [230,232], though the reductions seen in this thesis seem milder than those observed in primary human

microglia cultures ~10 % compared to ~40 %. This is likely due to experimental differences, as the human microglia were cultured with A β ₁₋₄₂ for 24 hours whereas this thesis mouse microglia cultures were incubated with zymosan for 1 hour. Moreover microglia can internalise A β ₁₋₄₂ through mechanisms other than phagocytosis [417]. Several other reports indicate that PU.1 likely has a role in microglial phagocytosis. Analysis of the BV-2 cell line indicated there were a number of potential PU.1 binding sites in genes in the Fc γ -receptor mediated phagocytosis and endocytosis pathways [319]. Rustenhoven *et al.* (2018) identified actin filament binding and several vesicle transport pathways that were impacted in microglia with an siRNA reduced PU.1 expression [233].

7.2.3.2 *Spi1* Over-Expression Dataset

The work in this thesis was also designed to determine the effect of increasing the *Spi1*/PU.1 on the microglia transcriptome. *Spi1* mRNA has been shown to be higher in the brains of PS19, APP/PS1 and CK-P25 AD mouse models [70,73,418] in the temporal cortex of AD PM tissue compared to controls [73]. These studies isolated mRNA from whole tissue, so it is unknown if *Spi1*/PU.1 expression was increased in individual microglia or as a consequence of AD microgliosis or an influx of monocytes cells [82, reviewed in 83].

The *SPI1* AD-risk associated SNP (rs1377416) was found to increase reporter expression when inserted upstream of PU.1 in the BV-2 cell line [70]. The opposite was seen in a *SPI1* SNP (rs1057233^g) that is thought to cause a lower level of *SPI1* expression and has been linked with a lower risk of AD and a later age of AD onset [230]. ChIP-Seq of histone modifications in CK-p25 AD mice and hippocampal grey matter of AD patients suggested that the immune response was enriched, and there were more potential PU.1 binding sites in many of the promoter/enhancer regions in this set [70]. This has been supported by others who have found *SPI1* binding motifs in open chromatin regions upstream of AD risk genes in human microglia [231]. Huang *et al.* (2017) suggested several LOAD risk SNPs impacted PU.1 binding motifs [230]. The top 18 genes identified by Sierksma *et al.* (2019) in the human-APP/PS1 mouse 'conserved risk' set were thought to have adjacent *Spi1* binding sites [278]. Taken together these results suggest that *Spi1* controls the expression of multiple genes related to AD risk.

The current study found that in the *Spi1* over-expression RNA-seq dataset the number of genes in the IFN and PRR signalling pathways were higher than would be expected due to random chance especially after comparison to control lentiviruses. Moreover *in silico* analyses suggests the IFN pathway was more active in the *Spi1* over-expression and less active in the *Spi1* knock-down dataset, suggesting the pathway activation might be moderated by the levels of PU.1 rather than

viral infection. In the high *Spi1* RNA-Seq dataset IFN response genes *Irf7*, *Irf3* and *Stat1* were identified as potential up-regulators of these changes. Activation of IFN genes has been detected in APP/PS1 (*Stat2*, *Stat1* and *irf7*) and CK-p25 (*irf7*) AD model mice [278,420]. PU.1 has been shown to bind to the IFN family members IRF-4 and ICSBP to regulate IL-1 β secretion as part of the inflammatory response [277]. Moreover, Minogue *et al.* (2014) showed that 24-month-old APP/PS1 had higher cortical expression of *Ifny* mRNA and higher phosphorylated (activated) STAT1 than wild-type littermates suggesting an activation of interferon pathways. On a cellular level there were a higher number of CD11b and IFN γ receptor double-positive cells in APP/PS1 transgenic mice [120].

Clustering analysis suggested there were a distinct set of genes that were only detected in the *Spi1* over-expression dataset. Pathway analysis of these clusters suggested that PU.1 influences the expression of genes contributing to antigen presentation and activation of various immune pathways (Figure 7.2). In a recent review Schetters *et al.* (2018) concluded that in AD and other neurodegenerative diseases microglia have increased major histocompatibility complex class II (MHCII) expression [421]. Bioinformatic analysis undertaken by Rustenhoven *et al.* 2018 suggested that *Spi1*/PU.1 could link the innate and adaptive immune systems [233]. Sierksma *et al.* (2019) saw the MHC response and the adaptive immune response pathways were significantly upregulated in 'common' genes that were common to APP/PS1 mice and a human AD dataset were shown to be [278].

21 of the most significantly changed genes in the *Spi1* over-expression dataset significantly associated with their orthologues in the human IGAP dataset. 6 of these genes are known to be involved with the IFN/viral response (*Ifit2*, *Oas1* and *Oas2*) or activation of the adaptive immune response (*Pecam1*, *Rnf144b* and *Trem14*) [363,364,367–369].

In summary these results suggest that increasing *Spi1*/PU.1 expression in microglia resulted in an activation of IFN pathways and MHCII-driven antigen presentation pathways. Given that a high level of *Spi1* in myeloid cells is thought to be a risk factor for LOAD [70,230] it suggests that in AD pathology microglia activation might be partially mediated by *Spi1*. Moreover, these results suggest the *Spi1* driven changes to the microglia transcriptome are conserved between mice and humans.

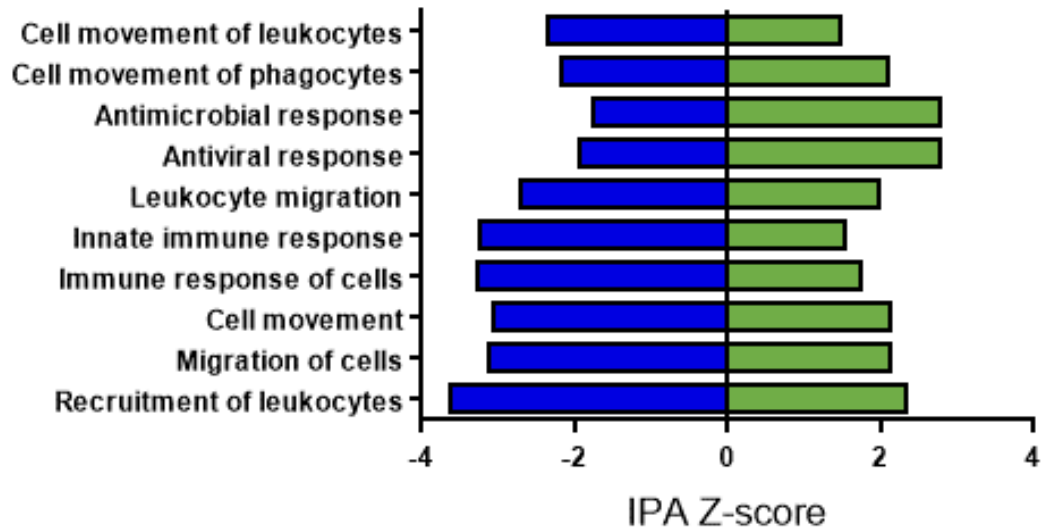


Figure 7.2 Z-Score of Cell-Cycle IPA Disease/Function Pathways in both RNA-Seq dataset. All of the chemotaxis/immune response pathways may be regulated by *Spi1*, as these pathways appear deactivated in the *Spi1* knock-down dataset (blue, negative score) and activated in *Spi1* over-expression dataset (green, positive score). Further work is required to see if MHCII expression results for most of these changes or if other chemokines are also changed by *Spi1*.

Microglia are known to have higher MHCII expression in AD which is indicative of a more reactive phenotype [422–424]. IFN γ stimulation of the hippocampus causes upregulation of MHCII within 24 hours *in vivo* [425] and *in vitro* this activation allows microglia to stimulate CD4⁺ T-cells [426]. In another type of antigen presenting cell, called dendritic cells, PU.1 binds the promoter of a MHCII regulating protein (CITA-pII) increasing its expression [427]. *In silico* analysis of the *Spi1* over-expression RNA-Seq dataset showed that *ccl2* was increased (data not shown), which is key in recruiting monocytes to the CNS [95]. This suggests that increased *Spi1* may drive microglia to express MHCII to activate antigen presentation pathways and leukocyte migration.

When IFN γ was virally over-expressed in APP-TgCRND8 model mice there was an increase in complement and microglia activation, resulting in a higher number of monocytes in the CNS [119]. The outcome of the IFN γ over-expression was a reduced number of A β plaques in these mice compared to controls, suggesting IFN γ might be helpful in preventing some AD pathology [119].

When *Spi1* was over-expressed the BV-2 microglial cell line phagocytosis was increased [230]. Given that this thesis showed MHCII and other bacteria/virus recognition pathways it would be interesting to investigate how *Spi1* over-expression alters microglia phenotype. Further work could also investigate if an increased *Spi1* affected microglia alone or affected the behaviour of other cells through their secretome.

7.2.4 The role of Abi3 in MØ function

The next section aimed to assess the importance of Abi3 protein expression in MØ function, given that a mutation in the ABI3 protein has been linked to AD risk [5,402]. Moreover *ABI3* expression has been shown to be part of the network of microglia genes upregulated in AD [402]. While implication that *ABI3* is part of a network of microglia genes altered in AD pathology of interest, there is a lack of information about the function of ABI3 in MØ. Current reports suggest that Abi3 acts in an opposing manner to Abi1, preventing WAVE2 from interacting with the actin cytoskeleton in response to M-CSF [245,284]. The recent development of Abi3 KO mice [299] provided an unparalleled opportunity to study the impact of Abi3 on MØ function by comparing these mice lacking Abi3 to wild-type controls. First, this thesis observed that the Abi3 KO mice were able to produce viable offspring with no obvious physical defects. Subsequent experiments verified Abi3 KO mice express the *LacZ*/ β -galactosidase reporter under the control of the Abi3 promoter in some pMØ and lack Abi3 exon 2-7 at the genomic level.

An interesting finding about Abi3 expression in pMØ was that it appeared to be strongly expressed in a subset of pMØ under resting conditions. This might explain why in pilot adhesion and phagocytosis experiments, both mediated through changes to the actin cytoskeleton, the loss of Abi3 did not overtly impact these MØ functions. These experiments were designed to investigate if Abi3 KO had a glaring impact on MØ function, and it could be that a more refined approach is needed because the loss of Abi3 has a subtler effect on MØ adhesion or phagocytosis. Future work could include assessing phagocytosis over time or with different doses of zymosan and assessing adhesion in a similar manner to the spreading assay performed by Sekino *et al.* 2015 [245].

One unanticipated finding was that during the growth of the conditionally immortalised CD117+ bone marrow precursor (MØP) cell lines derived from the Abi3 KO mice appeared to have a lower cell number compared to MØP cells from an age and sex matched Abi3 WT cell line, which was first observed by a media colour change and confirmed by cell count data. Flow cytometric assessment of proliferation by ki67, pph3 and EdU staining was not able to confirm that this difference in cell number was caused by an altered rate of proliferation. In M-CSF differentiated MØP cells, which have a higher *Abi3* mRNA expression than MØP precursors, the difference in KO and WT cell numbers was not as extreme. Following M-CSF stimulation in these M-CSF MØP cells the Abi3 KO cells were found to have a larger area and were less circular than WT cells. A possible explanation for these results is that in the Abi3 KO cells, Abi3 was not inhibiting the WAVE2 complex, allowing for a greater/faster actin rearrangement following M-CSF stimulation than Abi3

WT cells [289,389]. The data gathered using these MØP cell lines must be interpreted with some caution because these experiments were performed on one set of Abi3 WT and Abi3 KO MØP cell lines, these experiments should be replicated in multiple sets of MØP lines before can determine this is a true biological effect.

These findings provide further support for the hypothesis that Abi3 KO can cause changes to actin cytoskeleton formation in MØ, as previous work in thyroid cancer cells has shown that high ABI3 expression can reduce proliferation and inhibit cancer cell migration [11,295]. There is abundant room for further progress in determining the role of Abi3 in MØ and microglia function. Colleagues continue to investigate Abi3 and WAVE2 localisation in these MØP cell lines and assessing the morphology of microglia in the brains of these Abi3 KO mice.

7.3 Conclusions

This thesis aimed to assess the impact of alterations to Abi3 or *Spi1*/PU.1 have on MØ phenotype, to better understand how these AD risk genes may alter the physiology of these cells.

As a transcription factor *Spi1* can alter many genes in microglia [230,231,319], though a few studies have investigated the impact of altering the *Spi1*/PU.1 dose on the microglia transcriptome [230,233] the methods of assessing these changes were not as advantageous as RNA-Seq. The amount of PU.1 in freshly isolated microglia from transgenic mice lacking the -14 kB *Spi1* URE did not differ from mice where the URE was intact. This model was therefore unsuitable to measure PU.1 dependent changes to the microglia transcriptome, and led to the development of an *in vitro* culture model where PU.1 was manipulated in primary microglia. This led to the identification of a gene list that were controlled by different PU.1 levels in microglia.

The present study contributes to the existing knowledge of how the amount of *Spi1* impacts the transcriptome of microglia, through the production of *Spi1* knock-down and *Spi1* over-expression RNA-Seq datasets. Previous work has suggested that AD is thought to be mediated small contributions from multiple genes [317] and analysis of MØ and microglia chromatin suggested *SPI1* may bind at the regulatory regions of other AD risk genes [230,231,278] controlling the gene expression. The current findings add to a growing body of literature suggesting that *Spi1*/PU.1 alone can cause transcriptional changes in microglia. This study has generated a list of microglia genes which are controlled by PU.1 in a concentration dependent manner. Approaches such as these could lead to better understanding of AD aetiology and the development of better therapeutics targeting more microglia specific pathways.

The work of this thesis was limited as the microglia used to generate these datasets were from *in vitro* manipulations and not freshly isolated from transgenic mice where *Spi1* has been manipulated. Recent work in the literature has shown that microglia quickly lose expression some of the homeostatic receptors and while this loss can be partially ameliorated by TGF- β supplementation in the culture media it is not a perfect way to compensate for the loss of signals from the CNS milieu [154,155,428]. However given that the findings of the *Spi1* manipulations in microglia correlate to the human IGAP dataset [3] and are supported by others in the literature working with freshly isolated microglia from AD mouse models [278] or primary human microglia [233] suggests this model was representative of *in vivo* changes.

Despite its exploratory nature, this study offers some insight into how *Spi1* might drive an effector/interferon response in microglia. Pathway analysis of these results suggested that pathways altered by an increased PU.1 include activation of the adaptive immune response via microglia MHCII and IFN response, which has been supported by others [233,278]. These results intimate that the upregulation of MHCII in AD [422–424] might be part of a *Spi1* driven activation of microglia to help ameliorate AD pathology [97,98,122]. Datasets like these might yield more clues into specific pathway controlled by *Spi1* and if these pathways are also linked to AD risk or a failed attempt to recruit beneficial cells. While such analyses are outside the scope of this thesis, the datasets produced from this work provides a detailed map of microglial genes under control of PU.1.

The work also contributes to the existing knowledge on the role of *Abi3* in M ϕ in several ways. Firstly, the validity of the *Abi3* KO mouse model was confirmed via PCR, qPCR and *LacZ* reporter expression in both M ϕ P cell lines and *ex vivo* pM ϕ s. It was found that *Abi3* only appeared to be expressed by a subset of pM ϕ s, though this finding still needs to be validated with *Abi3* antibody staining. Secondly, the removal of *Abi3* did not obviously impact the number of pM ϕ *in vivo* or overtly impact adhesion and caused a subtle reduction in phagocytosis in *ex vivo* experiments, though if *Abi3* is only expressed by a subset of pM ϕ then these experiments should be repeated to confirm this.

Thirdly, work in the conditionally immortalised bone marrow precursor (M ϕ P) cell lines suggested that *Abi3* expression increases following differentiation with M-CSF or GM-CSF. There were no overt differences to the expression of key M ϕ surface receptors CD45 and MHCII. In the undifferentiated cells lacking *Abi3* loss might result in a reduced cell number and altered CD11b expression, though this has yet to be observed in multiple M ϕ P cell lines.

Finally, preliminary experiments investigating actin cytoskeletal rearrangement, combined with work done by others, indicated that in MØ the removal of Abi3 inhibition could result in a faster/greater WAVE2 response to M-CSF stimulation [245,284,289]. Whilst this study would need an antibody to confirm changes to Abi3 localisation and levels currently commercially available antibodies are not specific to Abi3 (data not shown), thus Abi3 removal was only confirmed at the genomic and mRNA level. This thesis has only examined the function of Abi3 in a few MØ functions that require actin cytoskeletal changes which might differ in microglia which express higher levels of *Abi3* [248].

7.4 Future perspectives

Several opportunities exist for further research. For example, a greater understanding of the role of the different regulatory elements of *Spi1* in different immune cell types, especially trMØ, would be of great help to allow for the development of transgenic mouse lines where PU.1 is lower exclusively in MØ. It would be interesting to assess the level of PU.1 protein in the pMØ and microglia subsets in the *Spi1^{tm1.3Dgt}/J* mice, where the -14 kB *Spi1* URE is supposedly ubiquitously removed, which are now commercially available. The enhancer landscape could also be investigated in these mutant mice to see if the ATAC-Seq and H3K27ac profiles differed from wild-type mice.

The results of this study suggested that the *in vitro* lentiviral infection of microglia culture system developed in this thesis could be a useful tool in investigating the function of conserved LOAD genes on microglia gene expression. While this model was limited as it cannot fully mimic the complex *in vivo* environment [154,155], useful preliminary data to study the effect of AD risk genes and SNP variants, for which there are no transgenic mice available, could be obtained.

Based on bioinformatic analysis of the RNA-Seq datasets, a natural progression of the *Spi1* shRNA and *Spi1* pSIEW viruses in this model would be to validate changes in molecules in the MHCII antigen presentation pathway and cytokine profile. Though this study was unable to analyse the effect that an increased PU.1 expression may have *in vivo* as transgenic mice over-expressing *Spi1* in microglia are still being developed. Further research might explore how a higher level of *Spi1* in microglia might impact their morphology, receptor expression, function and if immune cell trafficking is altered. The impact of *Spi1* on AD pathology could then be assessed by breeding *Spi1* over-expressing mice to AD model mice. While PU.1 could be manipulated in AD transgenic mice now by injecting the lentiviruses developed in this thesis it would likely require many trials to optimise viral delivery. Chapter 4 showed the PU.1 shRNA viruses were modestly effective at

infecting pMØ of mice that had received intra-peritoneal injections of this virus, and microglia are a much harder cell type to access w=for lentiviral injections.

The precise pathways which are under the control of PU.1 in a dose dependent manner have yet to be elucidated. A more in-depth bioinformatic of these results could reveal more information about how the amount of PU.1 regulates gene expression in microglia, and how this might contribute to AD pathology. Throughout the analysis microglia with a higher expression of the GFP reporter have a greater change to PU.1 protein levels. Therefore, it would be interesting to perform single cell sequencing on microglia cultures infected with *Spi1* pSIEW, to see the extent of the PU.1 dependency on the transcription of these genes. For example, is there a *Spi1* mRNA threshold that must be reached to induce *Irf7* gene transcription? A preliminary way to assess this would be to separately sort GFP^{high} and GFP^{low} *Spi1* pSIEW infected microglia and measure changes to *Spi1*/PU.1 and *Irf7* a selection of other genes.

Another possible area of future research would be to use the *Spi1* knock-down and *Spi1* over-expression datasets to inform *in silico* drug target prediction. While this has already been done in human microglia with a lower PU.1 expression [233] the RNA-Seq datasets generated in this thesis have a greater amount of information, both from the *Spi1* over-expression dataset but also a higher number of genes in the *Spi1* knock-down dataset.

More broadly, additional research is needed to understand how the *Spi1* related LOAD risk SNPs rs1057233^g and rs1377416 alter the level of PU.1 protein in microglia [70,230]. This could be done in an *in vitro* culture system where the mutations are inserted into murine microglia using CRISPR-Cas9 system [330]. Another approach would be to differentiate microglia from individuals with the *Spi1* risk SNPs using one of the models making microglia-like cells from induced pluripotent stem cells (iPSC) [429,430]. These iPSC/macrophage derived microglia have been used by others to investigate how AD risk genes and risk SNPs impact microglia phenotype [56,362,431]. Work is currently undertaken differentiating iPSC cells with different rs1057233 genotypes into microglia *in vitro* [432].

To extend the Abi3 work some of the M-CSF stimulation results first need to be validated in another set of MØP cell lines and in more primary pMØ samples and microglia. WAVE2, Abi3 and Arp2/3 immunofluorescent staining should also be included in this assay to better assess the underlying changes [289]. Given that Abi1 is suspected to bind both WAVE and WASP family members the interaction of Abi3 with the other WAVE/WASP family members should also be assessed [433]. Further research needs to examine more closely the links between Abi3 KO and

cell number, especially in the MØP cell lines. It would be interesting to assess the effects *Abi3* expression on cell migration and inflammation given that both these functions require changes to the actin cytoskeleton. The scope of this study was limited in terms of investigating the function of *Abi3* in microglia, which express more *Abi3* than pMØ [248]. Research investigating the role of *Abi3* in microglia is being carried out by colleagues. They are also looking for functional differences between the wild-type (S209) and AD risk variants of *ABI3* (F209) over-expressed in a cell line [5].

Taken together, these findings show further support that microglia should be targeted in AD therapeutically, and that while impact of individual risk genes might vary the impact on microglia physiology should still be investigated.

References

1. Knapp PM, Guerchet M, McCrone M, Prina P, Comas-Herrera M, Wittenberg A, et al. Dementia UK Update. 2014.
2. Jones L, Holmans PA, Hamshere ML, Harold D, Moskvina V, Ivanov D, et al. Genetic Evidence Implicates the Immune System and Cholesterol Metabolism in the Aetiology of Alzheimer's Disease. *PLoS One*. 2010 Nov 15;5(11):13950.
3. Lambert JC, Ibrahim-Verbaas CA, Harold D, Naj AC, Sims R, Bellenguez C, et al. Meta-analysis of 74,046 individuals identifies 11 new susceptibility loci for Alzheimer's disease. *Nat Genet*. 2013;45(12):1452–8.
4. Escott-Price V, Bellenguez C, Wang LS, Choi SH, Harold D, Jones L, et al. Gene-wide analysis detects two new susceptibility genes for Alzheimer's disease. *PLoS One*. 2014;9(6):94661.
5. Sims R, van der Lee SJ, Naj AC, Bellenguez C, Badarinarayan N, Jakobsdottir J, et al. Rare coding variants in *PLCG2*, *ABI3*, and *TREM2* implicate microglial-mediated innate immunity in Alzheimer's disease. *Nat Genet*. 2017;49(9):1373–84.
6. Scott EW, Fisher RC, Olson MC, Kehrl E, Simon MC, Singh H. PU.1 functions in a cell-autonomous manner to control the differentiation of multipotential lymphoid-myeloid progenitors. *Immunity*. 1997;6:437–47.
7. McKercher SR, Torbett BE, Anderson KL, Henkel GW, Vestal DJ, Baribault H, et al. Targeted disruption of the PU.1 gene results in multiple hematopoietic abnormalities. *EMBO J*. 1996;15(20):5647–58.
8. Beers DR, Henkel JS, Xiao Q, Zhao W, Wang J, Yen AA, et al. Wild-type microglia extend survival in PU.1 knockout mice with familial amyotrophic lateral sclerosis. *PNAS*. 2006 Oct 24;103(43):16021–6.
9. Kamath MB, Houston IB, Janovski A J, Zhu X, Gowrisankar S, Jegga A G, et al. Dose-dependent repression of T-cell and natural killer cell genes by PU.1 enforces myeloid and B-cell identity. *Leukemia*. 2008;22:1214–25.
10. Pham TH, Minderjahn J, Schmidl C, Hoffmeister H, Schmidhofer S, Chen W, et al. Mechanisms of in vivo binding site selection of the hematopoietic master transcription factor PU.1. *Nucleic Acids Res*. 2013;41(13):6391–402.
11. Ichigotani Y, Yokozaki S, Fukuda Y, Hamaguchi M, Matsuda S. Forced expression of NESH suppresses motility and metastatic dissemination of malignant cells. *Cancer Res*. 2002;62:2215–9.
12. Stelzmann RA, Schnitzlein HN, Murtagh FR. An English Translation of Alzheimer's 1907 Paper "Über eine eigenartige Erkrankung der Hirnrinde." *Clin Anat*. 1995;8:429–31.
13. Cummings J, Lee G, Ritter A, Zhong K. Alzheimer's disease drug development pipeline: 2018. *Alzheimer's Dement Transl Res Clin Interv*. 2018;4:195–214.
14. Perl DP. Neuropathology of Alzheimer's Disease. *Mt Sinai J Med*. 2010;77(1):32–42.
15. Levy-Lahad E, Wasco W, Poorkaj P, Romano DM, Oshima J, Pettingell WH, et al. Candidate Gene for the Chromosome 1 Familial Alzheimer's Disease Locus. *Science* (80-). 1995;269:973–6.

16. Rossor MN, Newman S, Frackowiak RSJ, Lantose P, Kennedy AM. Alzheimer's Disease Families with Amyloid Precursor Protein Mutations. *Ann N Y Acad Sci.* 1993;695:198–202.
17. Sherrington R, Rogaev EI, Liang Y, Rogaeva EA, Levesque G, Ikeda M, et al. Cloning of a gene bearing missense mutations in early-onset familial Alzheimer's disease. *Nature.* 1995 Jun;375:754–60.
18. Svedružić ŽM, Popović K, Smoljan I, Šendula-Jengić V. Modulation of γ -secretase activity by multiple enzyme-substrate interactions: Implications in Pathogenesis of Alzheimer's Disease. *PLoS One.* 2012;7(3).
19. Van Helmond Z, Miners JS, Kehoe PG, Love S. Oligomeric A β in Alzheimer's disease: Relationship to plaque and tangle pathology, apoe genotype and cerebral amyloid angiopathy. *Brain Pathol.* 2010;20(2):468–80.
20. Hardy J, Selkoe DJ. The Amyloid Hypothesis of Alzheimer's Disease: Progress and Problems on the Road to Therapeutics. *Science (80-).* 2002;297:353–6.
21. Selkoe DJ. Alzheimer's Disease: Genes, Proteins, and Therapy. *Physiol Rev.* 2001 Apr 1;81(2):741–66.
22. Kaye R, Lasagna-Reeves CA. Molecular mechanisms of amyloid oligomers toxicity. *Alzheimer's Dis Adv a New Century.* 2013;33:67–78.
23. Moreno F, Avila J, Hernández F, Pérez M, Santa-María I. Tau Phosphorylation, Aggregation, and Cell Toxicity. *J Biomed Biotechnol.* 2006;2006:1–5.
24. Lauriola M, Rabinovici GD, Sosa N, O'Neil JP, Bejanin A, Schonhaut DR, et al. Tau pathology and neurodegeneration contribute to cognitive impairment in Alzheimer's disease. *Brain.* 2017;140(12):3286–300.
25. Braak H, Tredici K Del. Spreading of tau pathology in sporadic Alzheimer's disease along cortico-cortical top-down connections. *Cereb Cortex.* 2018;28(9):3372–84.
26. Fu H, Hussaini SA, Wegmann S, Profaci C, Daniels JD, Herman M, et al. 3D Visualization of the temporal and spatial spread of tau pathology reveals extensive sites of tau accumulation associated with neuronal loss and recognition memory deficit in aged tau transgenic mice. *PLoS One.* 2016;11(7):1–20.
27. Kametani F, Hasegawa M. Reconsideration of amyloid hypothesis and tau hypothesis in Alzheimer's disease. *Front Neurosci.* 2018;12(25):1–11.
28. Wu JW, Hussaini SA, Bastille IM, Rodriguez GA, Mrejeru A, Rilett K, et al. Neuronal activity enhances tau propagation and tau pathology in vivo. 2016;19(8):1085–91.
29. Fu H, Rodriguez GA, Herman M, Emrani S, Nahmani E, Barrett G, et al. Tau Pathology Induces Excitatory Neuron Loss, Grid Cell Dysfunction, and Spatial Memory Deficits Reminiscent of Early Alzheimer's Disease. *Neuron.* 2017;93:533–41.
30. Morris M, Maeda S, Vossel K, Mucke L. The Many Faces of Tau. *Neuron.* 2011;70(3):410–26.
31. Roberson ED, Scarce-Levie K, Palop JJ, Yan F, Cheng IH, Wu T, et al. Reducing Endogenous Tau Ameliorates Amyloid- β Induced Deficits in an Alzheimer's Disease Mouse Model. *Science (80-).* 2007;316:750–4.
32. Nuriel T, Angulo SL, Khan U, Ashok A, Chen Q, Figueroa HY, et al. Neuronal hyperactivity

due to loss of inhibitory tone in APOE4 mice lacking Alzheimer's disease-like pathology. *Nat Commun.* 2017;8(1464):1–14.

33. Huang Y, Mucke L. Alzheimer Mechanisms and Therapeutic Strategies. *Cell.* 2012;148(6):1204–22.
34. Cabrejo L, Guyant-Marechal L, Laquerriere A, Vercelletto M, Fourniere FD La, Thomas-Anterion C, et al. Phenotype associated with APP duplication in five families. *Brain.* 2006;129:2966–76.
35. Amatniek JC, Hauser WA, Delcastillo-castaneda C, Jacobs DM, Marder K, Bell K, et al. Incidence and Predictors of Seizures in Patients with Alzheimer's Disease. *Epilepsia.* 2006;47(5):867–72.
36. Vossel KA, Beagle AJ, Rabinovici GD, Shu H, Lee SE, Naasan G, et al. Seizures and Epileptiform Activity in the Early Stages of Alzheimer Disease. *JAMA Neurol.* 2013;70(9):1158–66.
37. Palop JJ, Chin J, Roberson ED, Wang J, Thwin MT, Bien-Ly N, et al. Aberrant Excitatory Neuronal Activity and Compensatory Remodeling of Inhibitory Hippocampal Circuits in Mouse Models of Alzheimer's Disease. *Neuron.* 2007;55(5):697–711.
38. Minkeviciene R, Rheims S, Dobszay MB, Zilberter M, Hartikainen J, Fulop L, et al. Amyloid β -Induced Neuronal Hyperexcitability Triggers Progressive Epilepsy. *J Neurosci.* 2009;29(11):3453–62.
39. Busche MA, Eichhoff G, Adelsberger H, Abramowski D, Wiederhold K, Haass C, et al. Clusters of Hyperactive Neurons Near Amyloid Plaques in a Mouse Model of Alzheimer's Disease. *Science (80-).* 2008;321:1686–90.
40. Martinez-Losa M, Tracy TE, Ma K, Verret L, Clemente-Perez A, Khan AS, et al. Nav1.1-Overexpressing Interneuron Transplants Restore Brain Rhythms and Cognition in a Mouse Model of Alzheimer's Disease. *Neuron.* 2018;98(1):75-89.e5.
41. Béchade C, Cantaut-Belarif Y, Bessis A. Microglial control of neuronal activity. *Front Cell Neurosci.* 2013;7(32):1–7.
42. Hiragi T, Ikegaya Y, Koyama R. Microglia after Seizures and in Epilepsy. *Cells.* 2018;7(26):1–12.
43. Kettenmann H, Hanisch U-K, Noda M, Verkhratsky A. Physiology of Microglia. *Physiol Rev.* 2011;91:461–553.
44. Kaindl AM, Degos V, Peineau S, Gouadon E, Chhor V, Loron G, et al. Activation of Microglial N-Methyl-D-Aspartate Receptors Triggers Inflammation and Neuronal Cell Death in the Developing and Mature Brain. *Ann Neurol.* 2012;72:536–49.
45. Justin TR, Josh MM, Adam DB, Charles EH, Melinda P, Bethany a G, et al. CX3CR1 deficiency leads to impairment of hippocampal cognitive function and synaptic plasticity. *J Neurosci.* 2011;31(45):16241–50.
46. Costello DA, Lyons A, Denieffe S, Browne TC, Cox FF, Lynch MA. Long term potentiation is impaired in membrane glycoprotein CD200-deficient mice: A role for toll-like receptor activation. *J Biol Chem.* 2011;286(40):34722–32.
47. Pascual O, Achour S Ben, Rostaing P, Triller A, Bessis A. Microglia activation triggers

- astrocyte-mediated modulation of excitatory neurotransmission. *PNAS*. 2012;109(4):197–205.
48. Fine SM, Angel RA, Perry SW, Epstein LG, Rothstein JD, Dewhurst S, et al. Tumor Necrosis Factor α Inhibits Glutamate Uptake by Primary Human Astrocytes. *J Biol Chem*. 1996;271(26):15303–6.
 49. Ventura MT, Casciaro M, Gangemi S, Buquicchio R. Immunosenescence in aging: Between immune cells depletion and cytokines up-regulation. *Clin Mol Allergy*. 2017;15(21):1–8.
 50. Ryan NS, Rossor MN. Correlating familial Alzheimer's disease gene mutations with clinical phenotype. *Biomark Med*. 2010;4(1):99–112.
 51. Gatz M, Reynolds CA, Fratiglioni L, Johansson B, Mortimer JA, Berg S, et al. Role of Genes and Environments for Explaining Alzheimer's Disease. *Arch Gen Psychiatry*. 2006;63:168–74.
 52. Kim J, Basak J, Holtzman D. The role of Apolipoprotein E in Alzheimer's disease. *Neuron*. 2009;63(3):287–303.
 53. Slooter IArjen JC, Cruts M, Kalmijn S, Hofman A, Breteler MMB, Van Broeckhoven, Christine van Duijn CM. Risk Estimates of Dementia by Apolipoprotein E Genotypes From a Population-Based Incidence Study: The Rotterdam Study. *Arch Neurol*. 1998;55:964–8.
 54. Singh PP, Singh M, Mastana SS. APOE distribution in world populations with new data from India and the UK. *Ann Hum Biol*. 2006;33(3):279–308.
 55. Mahley RW. Apolipoprotein E: Cholesterol Transport Protein with Expanding Role in Cell Biology. *Science* (80-). 1988;240:622–30.
 56. Lin YT, Seo J, Gao F, Feldman HM, Wen HL, Penney J, et al. APOE4 Causes Widespread Molecular and Cellular Alterations Associated with Alzheimer's Disease Phenotypes in Human iPSC-Derived Brain Cell Types. *Neuron*. 2018;98:1141–54.
 57. Chung W-S, Verghese PB, Chakraborty C, Joung J, Hyman BT, Ulrich JD, et al. Novel allele-dependent role for APOE in controlling the rate of synapse pruning by astrocytes. *PNAS*. 2016;113(36):10186–91.
 58. Krasemann S, Madore C, Cialic R, Baufeld C, Calcagno N, El Fatimy R, et al. The TREM2-APOE Pathway Drives the Transcriptional Phenotype of Dysfunctional Microglia in Neurodegenerative Diseases. *Immunity*. 2017;47:566–81.
 59. Lambert JC, Heath S, Even G, Campion D, Sleegers K, Hiltunen M, et al. Genome-wide association study identifies variants at CLU and CR1 associated with Alzheimer's disease. *Nat Genet*. 2009;41(10):1094–100.
 60. Harold D, Abraham R, Hollingworth P, Sims R, Gerrish A, Hamshere ML, et al. Genome-wide association study identifies variants at CLU and PICALM associated with Alzheimer's disease. *Nat Genet*. 2009;41:1088–93.
 61. Corneveaux JJ, Myers AJ, Allen AN, Pruzin JJ, Huentelman MR, Engel A, et al. Association of CR1, CLU and PICALM with Alzheimer's disease in a cohort of clinically characterized and neuropathologically verified individuals. *Hum Mol Genet*. 2010;19(6):3295.
 62. Carrasquillo MM, Belbin O, Hunter TA, Ma L, Bisceglia GD, Zou F, et al. Replication of CLU, CR1, and PICALM associations with Alzheimer's disease. *Arch Neurol*. 2010;67(8):961–4.

63. Naj AC, Jun G, Beecham GW, Wang LS, Vardarajan BN, Buross J, et al. Common variants at MS4A4/MS4A6E, CD2AP, CD33 and EPHA1 are associated with late-onset Alzheimer's disease. *Nat Genet.* 2011;43(5):436–43.
64. Hollingworth P, Harold D, Sims R, Gerrish A, Lambert JC, Carrasquillo MM, et al. Common variants at ABCA7, MS4A6A/MS4A4E, EPHA1, CD33 and CD2AP are associated with Alzheimer's disease. *Nat Genet.* 2011;43(5):429–36.
65. Marioni RE, Harris SE, Zhang Q, McRae AF, Hagenaars SP, Hill WD, et al. GWAS on family history of Alzheimer's disease. *Transl Psychiatry.* 2018;8(1):8–14.
66. Kunkle BW, Grenier-Boley B, Sims R, Bis JC, Damotte V, Naj AC, et al. Genetic meta-analysis of diagnosed Alzheimer's disease identifies new risk loci and implicates A β , tau, immunity and lipid processing. *Nat Genet.* 2019;51:414–30.
67. Escott-Price V, Shoai M, Pither R, Williams J, Hardy J. Polygenic score prediction captures nearly all common genetic risk for Alzheimer's disease. *Neurobiol Aging.* 2017;49(214):7–11.
68. Jones L, Lambert JC, Wang LS, Choi SH, Harold D, Vedernikov A, et al. Convergent genetic and expression data implicate immunity in Alzheimer's disease. *Alzheimer's Dement.* 2015;11:658–71.
69. Karch CM, Jeng AT, Nowotny P, Cady J, Cruchaga C, Goate AM. Expression of Novel Alzheimer's Disease Risk Genes in Control and Alzheimer's Disease Brains. *PLoS One.* 2012;7(11):e50976.
70. Gjoneska E, Pfenning AR, Mathys H, Quon G, Kundaje A, Tsai LH, et al. Conserved epigenomic signals in mice and humans reveal immune basis of Alzheimer's disease. *Nature.* 2015;518:365–9.
71. Heppner FL, Ransohoff RM, Becher B. Immune attack: the role of inflammation in Alzheimer's disease. *Nat Rev Neurosci.* 2015;16:358–72.
72. Wegiel J, Wisniewski HM. The complex of microglial cells and amyloid star in three-dimensional reconstruction. *Acta Neuropathol.* 1990;81(2):116–24.
73. Olmos-Alonso A, Schettters STTT, Sri S, Askew K, Mancuso R, Vargas-Caballero M, et al. Pharmacological targeting of CSF1R inhibits microglial proliferation and prevents the progression of Alzheimer's-like pathology. *Brain.* 2016 Jan 8;139:891–907.
74. Perry VH, Teeling J. Microglia and macrophages of the central nervous system: the contribution of microglia priming and systemic inflammation to chronic neurodegeneration. *Semin Immunopathology.* 2013 Sep;35:601–12.
75. Edison P, Donat CK, Sastre M. In vivo imaging of glial activation in Alzheimer's disease. *Front Neurol.* 2018;9:625.
76. Notter T, Coughlin JM, Sawa A, Meyer U. Reconceptualization of translocator protein as a biomarker of neuroinflammation in psychiatry. *Mol Psychiatry.* 2018;23:36–47.
77. Wegiel J, Wang K, Imaki H, Rubenstein R, Wronska A, Osuchowski M, et al. The role of microglial cells and astrocytes in fibrillar plaque evolution in transgenic APPSW mice. *Neurobiol Aging.* 2001;22:49–61.
78. Grathwohl SA, Kälin RE, Bolmont T, Prokop S, Winkelmann G, Kaeser SA, et al. Formation

- and maintenance of Alzheimer's disease β -amyloid plaques in the absence of microglia. *Nat Neurosci*. 2009;12(11):1361–3.
79. Meyer-Luehmann M, Spires-Jones TL, Prada C, Garcia-Alloza M, de Calignon A, Rozkalne A, et al. Rapid appearance and local toxicity of amyloid- β plaques in a mouse model of Alzheimer's disease. *Nature*. 2008 Feb 7;451:720–4.
 80. Wolf Y, Yona S, Kim K-W, Jung S. Microglia, seen from the CX3CR1 angle. *Front Cell Neurosci*. 2013;7(26):1–9.
 81. Koning N, Swaab DF, Hoek RM, Huitinga I. Distribution of the immune inhibitory molecules CD200 and CD200R in the normal central nervous system and multiple sclerosis lesions suggests neuron-glia and glia-glia interactions. *J Neuropathol Exp Neurol*. 2009;68(2):159–67.
 82. Barclay AN, Wright GJ, Brooke G, Brown MH. CD200 and membrane protein interactions in the control of myeloid cells. *Trends Immunol*. 2002;23(6):285–90.
 83. Fuhrmann M, Bittner T, Jung CKE, Burgold S, Page RM, Mitteregger G, et al. Microglial Cx3cr1 knockout prevents neuron loss in a mouse model of Alzheimer's disease. *Nat Neurosci*. 2010 Apr;13(4):411–3.
 84. Hoek RM, Ruuls SR, Murphy CA, Wright GJ, Goddard R, Zurawski SM, et al. Down-Regulation of the Macrophage Lineage Through Interaction with OX2 (CD200). *Science (80-)*. 2000;290:1768–71.
 85. Downer EJ, Cowley TR, Lyons A, Mills KHG, Berezin V, Bock E, et al. A novel anti-inflammatory role of NCAM-derived mimetic peptide, FGL. *Neurobiol Aging*. 2010;31:118–28.
 86. Węgiel J, Wiśniewski HM, Dziewiątkowski J, Tarnawski M, Kozielski R, Trenkner E, et al. Reduced number and altered morphology of microglial cells in colony stimulating factor-1-deficient osteopetrotic op/op mice. *Brain Res*. 1998;804:135–9.
 87. Wang Y, Szretter KJ, Vermi W, Gilfillan S, Rossini C, Cella M, et al. IL-34 is a tissue-restricted ligand of CSF1R required for the development of Langerhans cells and microglia. *Nat Immunol*. 2012;13(8):753–60.
 88. Ginhoux F, Greter M, Leboeuf M, Nandi S, See P, Gokhan S, et al. Fate mapping analysis reveals that adult microglia derive from primitive macrophages. *Science (80-)*. 2010;330:841–5.
 89. Elmore MRP, Najafi AR, Koike MA, Dagher NN, Spangenberg EE, Rice RA, et al. Colony-stimulating factor 1 receptor signaling is necessary for microglia viability, unmasking a microglia progenitor cell in the adult brain. *Neuron*. 2014;82:380–97.
 90. Dagher NN, Najafi AR, Kayala KMN, Elmore MRP, White TE, Medeiros R, et al. Colony-stimulating factor 1 receptor inhibition prevents microglial plaque association and improves cognition in 3xTg-AD mice. *J Neuroinflammation*. 2015;12(139):1–14.
 91. Sosna J, Philipp S, Albay RI, Reyes-Ruiz JM, Baglietto-Vargas D, LaFerla FM, et al. Early long-term administration of the CSF1R inhibitor PLX3397 ablates microglia and reduces accumulation of intraneuronal amyloid, neuritic plaque deposition and pre-fibrillar oligomers in 5XFAD mouse model of Alzheimer's disease. *Mol Neurodegener*. 2018;13:1–11.

92. Spangenberg EE, Lee RJ, Najafi AR, Rice RA, Elmore MRP, Blurton-Jones M, et al. Eliminating microglia in Alzheimer's mice prevents neuronal loss without modulating amyloid- β pathology. *Brain*. 2016;139:1265–81.
93. Priller J, Flügel A, Wehner T, Boentert M, Haas CA, Prinz M, et al. Targeting gene-modified hematopoietic cells to the central nervous system: Use of green fluorescent protein uncovers microglial engraftment. *Nat Med*. 2001;7(12):1356–61.
94. Simard AR, Rivest S. Bone marrow stem cells have the ability to populate the entire central nervous system into fully differentiated parenchymal microglia. *FASEB J*. 2004;18(9):998–1000.
95. Mildner A, Schmidt H, Nitsche M, Merkler D, Hanisch UK, Mack M, et al. Microglia in the adult brain arise from Ly6ChiCCR2+ monocytes only under defined host conditions. *Nat Neurosci*. 2007;10(12):1544–53.
96. Kennedy DW, Abkowitz JL. Kinetics of central nervous system microglial and macrophage engraftment: Analysis using a transgenic bone marrow transplantation model. *Blood*. 1997;90(3):986–93.
97. Baruch K, Rosenzweig N, Kertser A, Deczkowska A, Sharif AM, Spinrad A, et al. Breaking immune tolerance by targeting Foxp3(+) regulatory T cells mitigates Alzheimer's disease pathology. *Nat Commun*. 2015;6:7967.
98. Baruch K, Deczkowska A, Rosenzweig N, Tsitsou-Kampeli A, Sharif AM, Matcovitch-Natan O, et al. PD-1 immune checkpoint blockade reduces pathology and improves memory in mouse models of Alzheimer's disease. *Nat Med*. 2016 Feb;22(2):135–7.
99. Rosenzweig N, Dvir-szternfeld R, Tsitsou-kampeli A, Keren-shaul H, Ben-yehuda H, Weill-raynal P, et al. PD-1/PD-L1 checkpoint blockade harnesses monocyte-derived macrophages to combat cognitive impairment in a tauopathy mouse model. *Nat Commun*. 2019;10(465):1–15.
100. Berner O, Mittal K, Strominger I, Nemirovsky A, Monsonogo A, Elyahu Y, et al. The Choroid Plexus Functions as a Niche for T-Cell Stimulation Within the Central Nervous System. *Front Immunol*. 2018;9(May):1–15.
101. Engelhardt B, Coisne C. Fluids and barriers of the CNS establish immune privilege by confining immune surveillance to a two-walled castle moat surrounding the CNS castle. *Fluids Barriers CNS*. 2011;8(1):1–9.
102. Malm TM, Koistinaho M, Parepalo M, Vatanen T, Ooka A, Karlsson S, et al. Bone-marrow-derived cells contribute to the recruitment of microglial cells in response to β -amyloid deposition in APP/PS1 double transgenic Alzheimer mice. *Neurobiol Dis*. 2004;18(1):134–42.
103. Simard AR, Soulet D, Gowing G, Julien JP, Rivest S. Bone marrow-derived microglia play a critical role in restricting senile plaque formation in Alzheimer's disease. *Neuron*. 2006;49(4):489–502.
104. Terada K, Hickman SE, Geula C, El Khoury J, Means TK, Toft M, et al. Ccr2 deficiency impairs microglial accumulation and accelerates progression of Alzheimer-like disease. *Nat Med*. 2007;13(4):432–8.
105. Naert G, Rivest S. CC Chemokine Receptor 2 Deficiency Aggravates Cognitive Impairments

- and Amyloid Pathology in a Transgenic Mouse Model of Alzheimer's Disease. *J Neurosci*. 2011;31(16):6208–20.
106. Martin E, Boucher C, Fontaine B, Delarasse C. Distinct inflammatory phenotypes of microglia and monocyte-derived macrophages in Alzheimer's disease models: effects of aging and amyloid pathology. *Aging Cell*. 2017;16(1):27–38.
 107. Holtzman DM, Ulrich JD, Hole JT, Yuan P, Shi Y, Wang Y, et al. TREM2-mediated early microglial response limits diffusion and toxicity of amyloid plaques. *J Exp Med*. 2016;213(5):667–75.
 108. Bennett ML, Bennett FC, Liddelow SA, Ajami B, Zamanian JL, Fernhoff NB, et al. New tools for studying microglia in the mouse and human CNS. *PNAS*. 2016 Feb 16;113(8):2738–46.
 109. Montagne A, Zhao Z, Zlokovic B V. Alzheimer's disease: A matter of blood-brain barrier dysfunction? *J Exp Med*. 2017;214(11):3151–69.
 110. Montagne A, Barnes SR, Sweeney MD, Halliday MR, Sagare AP, Zhao Z, et al. Blood-Brain Barrier Breakdown in the Aging Human Hippocampus. *Neuron*. 2015;85(2):296–302.
 111. van de Haar HJ, Burgmans S, Jansen JFA, Osch MJP van, Buchem MA van, Muller M, et al. Blood-Brain Barrier Leakage in Patients with Early Alzheimer Disease. *Radiology*. 2017;282(2):615–615.
 112. Nation DA, Sweeney MD, Montagne A, Sagare AP, D'Orazio LM, Pachicano M, et al. Blood–brain barrier breakdown is an early biomarker of human cognitive dysfunction. *Nat Med*. 2019;25(February).
 113. Ryu JK, McLarnon JG. A leaky blood-brain barrier, fibrinogen infiltration and microglial reactivity in inflamed Alzheimer's disease brain. *J Cell Mol Med*. 2009;13(9 A):2911–25.
 114. Zenaro E, Piacentino G, Constantin G. The blood-brain barrier in Alzheimer's disease. *Neurobiol Dis*. 2017;107:41–56.
 115. Kunis G, Baruch K, Rosenzweig N, Kertser A, Miller O, Berkutzki T, et al. IFN- γ -dependent activation of the brain's choroid plexus for CNS immune surveillance and repair. *Brain*. 2013;136:3427–40.
 116. Baruch K, Deczkowska A, David E, Castellano JM, Miller O, Kertser A, et al. Aging-induced type I interferon response at the choroid plexus negatively affects brain function. *Science (80-)*. 2014;346(6205):89–93.
 117. Deczkowska A, Matcovitch-Natan O, Tsitsou-Kampeli A, Ben-Hamo S, Dvir-Szternfeld R, Spinrad A, et al. Mef2C restrains microglial inflammatory response and is lost in brain ageing in an IFN-I-dependent manner. *Nat Commun*. 2017;8(717):1–11.
 118. Lavin Y, Winter D, Blecher-Gonen R, David E, Keren-Shaul H, Merad M, et al. Tissue-Resident Macrophage Enhancer Landscapes Are Shaped by the Local Microenvironment. *Cell*. 2014 Dec;159:1312–26.
 119. Chakrabarty P, Ceballos-Diaz C, Dickson D, Janus C, Beccard A, Golde TE, et al. IFN- γ Promotes Complement Expression and Attenuates Amyloid Plaque Deposition in Amyloid Precursor Protein Transgenic Mice. *J Immunol*. 2010;184(9):5333–43.
 120. Minogue AM, Jones RS, Kelly RJ, McDonald CL, Connor TJ, Lynch MA. Age-associated dysregulation of microglial activation is coupled with enhanced blood-brain barrier

- permeability and pathology in APP/PS1 mice. *Neurobiol Aging*. 2014 Jun;35:1442–52.
121. Schwartz M, Kipnis J, Rivest S, Prat A. How Do Immune Cells Support and Shape the Brain in Health, Disease, and Aging? *J Neurosci*. 2013;33(45):17587–96.
 122. Marsh SE, Abud EM, Lakatos A, Karimzadeh A, Yeung ST, Davtayan H, et al. The adaptive immune system restrains Alzheimer's disease pathogenesis by modulating microglial function. *PNAS*. 2016;113:1316–25.
 123. Togo T, Akiyama H, Iseki E, Kondo H, Ikeda K, Kato M, et al. Occurrence of T cells in the brain of Alzheimer's disease and other neurological diseases. *J Neuroimmunol*. 2002;124(1–2):83–92.
 124. Ribocco-Lutkiewicz M, Sodja C, Haukenfrers J, Haqqani AS, Ly D, Zachar P, et al. A novel human induced pluripotent stem cell blood-brain barrier model: Applicability to study antibody-triggered receptor-mediated transcytosis. *Sci Rep*. 2018;8(1):1–17.
 125. Cecchelli R, Aday S, Sevin E, Almeida C, Culot M, Dehouck L, et al. A Stable and Reproducible Human Blood-Brain Barrier Model Derived from Hematopoietic Stem Cells. *PLoS One*. 2014;9(6):e99733.
 126. Engelhart MJ, Geerlings MI, Meijer J, Kiliaan A, Ruitenberg A, Swieten JC van, et al. Inflammatory Proteins in Plasma and the Risk of Dementia. *Arch Neurol*. 2004;61:668–72.
 127. Drake C, Boutin H, Jones MS, Denes A, McColl BW, Selvarajah JR, et al. Brain inflammation is induced by co-morbidities and risk factors for stroke. *Brain Behav Immun*. 2011 Aug 16;25:1113–22.
 128. Holmes C, Cunningham C, Zotova E, Woolford J, Dean C, Kerr S, et al. Systemic inflammation and disease progression in Alzheimer's disease. *Neurology*. 2009;73:768–74.
 129. Chou RC, Kane M, Ghimire S, Gautam S, Gui J. Treatment for Rheumatoid Arthritis and Risk of Alzheimer's Disease: A Nested Case-Control Analysis. *CNS Drugs*. 2016;30:1111–20.
 130. Butchart J, Brook L, Hopkins V, Teeling J, Püntener U, Culliford D, et al. Etanercept in Alzheimer disease: A randomized, placebo-controlled, double-blind, phase 2 trial. *Neurology*. 2015;85:2161–8.
 131. Alzforum. Alzforum Therapeutics Database [Internet]. 2019 [cited 2019 Jan 4]. Available from: <https://www.alzforum.org/therapeutics>
 132. Hoogland ICM, Houbolt C, van Westerloo DJ, van Gool WA, van de Beek D. Systemic inflammation and microglial activation: systematic review of animal experiments. *J Neuroinflammation*. 2015;12:114–27.
 133. Cunningham C, Champion S, Lunnon K, Murray CL, Woods JFC, Deacon RMJ, et al. Systemic Inflammation Induces Acute Behavioral and Cognitive Changes and Accelerates Neurodegenerative Disease. *Biol Psychiatry*. 2009;65:304–12.
 134. Goldmann T, Wieghofer P, Jordão MJC, Prutek F, Hagemeyer N, Frenzel K, et al. Origin, fate and dynamics of macrophages at central nervous system interfaces. *Nat Immunol*. 2016;17(7):797–805.
 135. Hawkes CA, McLaurin J. Selective targeting of perivascular macrophages for clearance of β -amyloid in cerebral amyloid angiopathy. *PNAS*. 2009;106(4):1261–6.

136. Mildner A, Schlevogt B, Kierdorf K, Böttcher C, Erny D, Kummer MP, et al. Distinct and Non-Redundant Roles of Microglia and Myeloid Subsets in Mouse Models of Alzheimer's Disease. *J Neurosci*. 2011 Aug 3;31(31):11159–71.
137. Liddel SA, Guttenplan KA, Clarke LE, Bennett FC, Bohlen CJ, Schirmer L, et al. Neurotoxic reactive astrocytes are induced by activated microglia. *Nature*. 2017;541:481–7.
138. Serrano-Pozo A, Gómez-Isla T, Growdon JH, Frosch MP, Hyman BT. A phenotypic change but not proliferation underlies glial responses in Alzheimer's disease. *Am J Pathol*. 2013;182:2332–44.
139. Orre M, Kamphuis W, Osborn LM, Jansen AHP, Kooijman L, Bossers K, et al. Isolation of glia from Alzheimer's mice reveals inflammation and dysfunction. *Neurobiol Aging*. 2014;35:2746–60.
140. Gomez-Arboledas A, Davila JC, Sanchez-Mejias E, Navarro V, Nuñez-Diaz C, Sanchez-Varo R, et al. Phagocytic clearance of presynaptic dystrophies by reactive astrocytes in Alzheimer's disease. *Glia*. 2018;66:637–53.
141. Jeong H-K, Ji K, Min K, Joe E-H. Brain Inflammation and Microglia: Facts and Misconceptions. *Exp Neurobiol*. 2013 Jun 27;22(2):59–67.
142. Sidoryk-Wegrzynowicz M, Wegrzynowicz M, Lee E, Bowman AB, Aschner M. Role of Astrocytes in Brain Function and Disease. *Toxicol Pathol*. 2011;39:115–23.
143. Metchnikoff E. *Leçons sur la pathologie comparée de l'inflammation* Faites à l'Institut Pasteur. Paris: Masson; 1892.
144. Gordon S, Martinez-Pomares L. Physiological roles of macrophages. *Eur J Physiol*. 2017;469:365–74.
145. Davies LC, Jenkins SJ, Allen JE, Taylor PR. Tissue-resident macrophages. *Nat Immunol*. 2013;14(10):986–95.
146. Jung S, Aliberti J, Graemmel P, Sunshine MJ, Kreutzberg GW, Sher A, et al. Analysis of Fractalkine Receptor CX3CR1 Function by Targeted Deletion and Green Fluorescent Protein Reporter Gene Insertion. *Mol Cell Biol*. 2000;20(11):4106–14.
147. Yona S, Kim K-W, Wolf Y, Mildner A, Varol D, Breker M, et al. Fate mapping reveals origins and dynamics of monocytes and tissue macrophages under homeostasis. *Immunity*. 2013 Jan 24;38:79–91.
148. Gautier EL, Shay T, Miller J, Greter M, Jakubzick C, Ivanov S, et al. Gene-expression profiles and transcriptional regulatory pathways that underlie the identity and diversity of mouse tissue macrophages. *Nat Immunol*. 2012;13(11):1118–28.
149. Okabe Y, Medzhitov R. Tissue biology perspective on macrophages. *Nat Immunol*. 2016 Jan;17(1):9–17.
150. Gautier EL, Yvan-Charvet L. Understanding macrophage diversity at the ontogenic and transcriptomic levels. *Immunol Rev*. 2014;262(1):85–95.
151. Rosas M, Davies LC, Giles PJ, Liao C-T, Kharfan B, Stone TC, et al. The transcription factor Gata6 links tissue macrophage phenotype and proliferative renewal. *Science* (80-). 2014;344:645–8.

152. Buttgereit A, Lelios I, Yu X, Vrohlig M, Krakoski NR, Gautier EL, et al. Sall1 is a transcriptional regulator defining microglia identity and function. *Nat Immunol*. 2016;17(12):1397–406.
153. Gosselin D, Link VM, Romanoski CE, Fonseca GJ, Eichenfield DZ, Spann NJ, et al. Environment Drives Selection and Function of Enhancers Controlling Tissue-Specific Macrophage Identities. *Cell*. 2014 Dec;159:1327–40.
154. Butovsky O, Jedrychowski MP, Moore CS, Cialic R, Lanser AJ, Gabriely G, et al. Identification of a unique TGF- β -dependent molecular and functional signature in microglia. *Nat Neurosci*. 2014 Jan;17(1):131–43.
155. Bohlen CJ, Bennett FC, Tucker AF, Collins HY, Mulinyawe SB, Barres BA. Diverse Requirements for Microglial Survival, Specification, and Function Revealed by Defined-Medium Cultures. *Neuron*. 2017;94:759–73.
156. Gosselin D, Skola D, Coufal NG, Holtman IR, Schlachetzki JCM, Sajti E, et al. An environment-dependent transcriptional network specifies human microglia identity. *Science* (80-). 2017;356(1248):1–11.
157. Douvaras P, Sun B, Wang M, Kruglikov I, Lallo G, Zimmer M, et al. Directed Differentiation of Human Pluripotent Stem Cells to Microglia. *Stem Cell Reports*. 2017;8(6):1516–24.
158. Satoh J ichi, Kino Y, Asahina N, Takitani M, Miyoshi J, Ishida T, et al. TMEM119 marks a subset of microglia in the human brain. *Neuropathology*. 2016;36(1):39–49.
159. Barron KD. The Microglial Cell. A historical review. *J Neurol Sci*. 1995;134:57–68.
160. Ginhoux F, Lim S, Hoeffel G, Low D, Huber T. Origin and differentiation of microglia. *Front Cell Neurosci*. 2013;7(45):1–14.
161. Matcovitch-Natan O, Winter DR, Giladi A, Vargas Aguilar S, Spinrad A, Sarrazin S, et al. Microglia development follows a stepwise program to regulate brain homeostasis. *Science* (80-). 2016;353(6301):789.
162. Erö C, Gewaltig M-O, Keller D, Markram H. A Cell Atlas for the Mouse Brain. *Front Neuroinform*. 2018;12(November):1–16.
163. De Biase LM, Schuebel KE, Fufeld ZH, Jair K, Hawes IA, Cimbri R, et al. Local Cues Establish and Maintain Region-Specific Phenotypes of Basal Ganglia Microglia. *Neuron*. 2017;95(2):341-356.e6.
164. Bruttger J, Karam K, Wörtge S, Regen T, Marini F, Hoppmann N, et al. Genetic Cell Ablation Reveals Clusters of Local Self-Renewing Microglia in the Mammalian Central Nervous System. *Immunity*. 2015 Jul 21;43:92–106.
165. Askew K, Li K, Olmos-Alonso A, Garcia-Moreno F, Liang Y, Richardson P, et al. Coupled Proliferation and Apoptosis Maintain the Rapid Turnover of Microglia in the Adult Brain. *Cell Rep*. 2017;18:391–405.
166. Tay TL, Mai D, Dautzenberg J, Fernández-Klett F, Lin G, Sagar S, et al. A new fate mapping system reveals context-dependent random or clonal expansion of microglia. *Nat Neurosci*. 2017;20(6):793–803.
167. Fügen P, Hefendehl JK, Veeraraghavalu K, Wendeln A-C, Schlosser C, Obermüller U, et al. Microglia turnover with aging and in an Alzheimer’s model via long-term in vivo single-cell

- imaging. *Nat Neurosci.* 2017;20(10):1371–6.
168. Réu P, Khosravi A, Bernard S, Mold JE, Salehpour M, Alkass K, et al. The Lifespan and Turnover of Microglia in the Human Brain. *Cell Rep.* 2017;20:779–84.
 169. Kierdorf K, Prinz M. Factors regulating microglia activation. *Front Cell Neurosci.* 2013;7(April):44.
 170. Nimmerjahn A, Kirchhoff F, Helmchen F. Resting microglial cells are highly dynamic surveillants of brain parenchyma in vivo. *Science* (80-). 2005 May;308:1314–8.
 171. Davalos D, Grutzendler J, Yang G, Kim J V, Zuo Y, Jung S, et al. ATP mediates rapid microglial response to local brain injury in vivo. *Nat Neurosci.* 2005;8(6):752–8.
 172. Cardona AE, Piro EP, Sasse ME, Kostenko V, Cardona SM, Dijkstra IM, et al. Control of microglial neurotoxicity by the fractalkine receptor. *Nat Neurosci.* 2006;9(7):917–24.
 173. Hickman SE, Kingery ND, Ohsumi TK, Borowsky ML, Wang L, Means TK, et al. The microglial sensome revealed by direct RNA sequencing. *Nat Neurosci.* 2013 Dec;16(12):1896–905.
 174. Hirbec H, Marmai C, Duroux-Richard I, Roubert C, Esclangon A, Croze S, et al. The microglial reaction signature revealed by RNAseq from individual mice. *Glia.* 2018;1–16.
 175. Illes P, Ribeiro JA. Molecular physiology of P2 receptors in the central nervous system. *Eur J Pharmacol.* 2004;483:5–17.
 176. Haynes SE, Hollopeter G, Yang G, Kurpius D, Dailey ME, Gan W-B, et al. The P2Y12 receptor regulates microglial activation by extracellular nucleotides. *Nat Neurosci.* 2006;9(12):1512–9.
 177. Noda M, Doi Y, Liang J, Kawanokuchi J, Sonobe Y, Takeuchi H, et al. Fractalkine attenuates excitotoxicity via microglial clearance of damaged neurons and antioxidant enzyme heme oxygenase-1 expression. *J Biol Chem.* 2011;286(3):2308–19.
 178. Eyo UB, Peng J, Swiatkowski P, Mukherjee A, Bispo A, Wu L-J. Neuronal Hyperactivity Recruits Microglial Processes via Neuronal NMDA Receptors and Microglial P2Y12 Receptors after Status Epilepticus. *J Neurosci.* 2014;34(32):10528–40.
 179. Nolte C, Möller T, Walter T, Kettenmann H. Complement 5a controls motility of murine microglial cells in vitro via activation of an inhibitory G-protein and the rearrangement of the actin cytoskeleton. *Neuroscience.* 1996;73(4):1091–107.
 180. Mazaheri F, Snaidero N, Kleinberger G, Madore C, Daria A, Werner G, et al. TREM2 deficiency impairs chemotaxis and microglial responses to neuronal injury. *EMBO Rep.* 2017;18(7):1186–98.
 181. Tvrdik P, Kalani MYS. In vivo imaging of microglial calcium signaling in brain inflammation and injury. *Int J Mol Sci.* 2017;18(2366):1–18.
 182. Siddiqui TA, Lively S, Vincent C, Schlichter LC. Regulation of podosome formation, microglial migration and invasion by Ca²⁺-signaling molecules expressed in podosomes. *J Neuroinflammation.* 2012;9(250):1–16.
 183. Goodridge HS, Underhill DM, Touret N. Mechanisms of Fc Receptor and Dectin-1 Activation for Phagocytosis. *Traffic.* 2012;13:1062–71.

184. Sierra A, Abiega O, Shahraz A, Neumann H. Janus-faced microglia: beneficial and detrimental consequences of microglial phagocytosis. *Front Cell Neurosci.* 2013;7(6):1–22.
185. Hillaireau H, Couvreur P. Nanocarriers' entry into the cell: relevance to drug delivery. *Cell Mol Life Sci.* 2009 Sep;66(17):2873–96.
186. Fu R, Shen Q, Xu P, Luo J, Tang Y. Phagocytosis of Microglia in the Central Nervous System Diseases. *Mol Neurobiol.* 2014;49:1422–34.
187. Takahashi K, Rochford CD, Neumann H. Clearance of apoptotic neurons without inflammation by microglial triggering receptor expressed on myeloid cells-2. *J Exp Med.* 2005;201(4):647–57.
188. Fiebich BL, Batista CRA, Saliba SW, Yousif NM, de Oliveira ACP. Role of Microglia TLRs in Neurodegeneration. *Front Cell Neurosci.* 2018;12(329):1–10.
189. Fellner L, Irschick R, Schanda K, Reindl M, Klimaschewski L, Poewe W, et al. Toll-like receptor 4 is required for α -synuclein dependent activation of microglia and astroglia. *Glia.* 2013;61:349–60.
190. Ulvestad E, Williams K, Vedeler C, Antel J, Nyland H, Mørk S, et al. Reactive microglia in multiple sclerosis lesions have an increased expression of receptors for the Fc part of IgG. *J Neurol Sci.* 1994;121:125–31.
191. Hong S, Beja-Glasser VF, Nfonoyim BM, Frouin A, Li S, Ramakrishnan S, et al. Complement and microglia mediate early synapse loss in Alzheimer's mouse models. *Science (80-).* 2016;352(6286):712–6.
192. Reichert F, Rotshenker S. Complement-receptor-3 and scavenger-receptor-AI/II mediated myelin phagocytosis in microglia and macrophages. *Neurobiol Dis.* 2003;12(1):65–72.
193. Beccari S, Diaz-Aparicio I, Sierra A. Quantifying Microglial Phagocytosis of Apoptotic Cells in the Brain in Health and Disease. *Curr Protoc Immunol.* 2018;e49.
194. Paglinawan R, Malipiero U, Schlapbach R, Frei K, Reith W, Fontana A. TGF- β Directs Gene Expression of Activated Microglia to an Anti-Inflammatory Phenotype Strongly Focusing on Chemokine Genes and Cell Migratory Genes. *Glia.* 2003;44:219–31.
195. Czubala MA, Finsterbusch K, Ivory MO, Mitchell JP, Ahmed Z, Shimauchi T, et al. TGF β Induces a SAMHD1-Independent Post-Entry Restriction to HIV-1 Infection of Human Epithelial Langerhans Cells. *J Invest Dermatol.* 2016;136:1981–9.
196. Letterio J, Roberts AB. Regulation of immune responses by TGF- β . *Annu Rev Immunol.* 1998;16:137–61.
197. Casano AM, Peri F. Microglia: Multitasking Specialists of the Brain. *Dev Cell.* 2015;32:469–77.
198. Bianchin MM, Martin KC, De Souza AC, De Oliveira MA, De Mello Rieder CR. Nasu-Hakola disease and primary microglial dysfunction. *Nat Rev Neurol.* 2010;6(9):1–2.
199. Marin-Teva JL, Dusart I, Colin C, Gervais A, Rooijen N Van, Mallat M. Microglia Promote the Death of Developing Purkinje Cells. *Neuron.* 2004;41:535–47.
200. Ueyama T, Lennartz MR, Noda Y, Kobayashi T, Shirai Y, Rikitake K, et al. Superoxide Production at Phagosomal Cup/Phagosome through β I Protein Kinase C during Fc γ R-

- Mediated Phagocytosis in Microglia. *J Immunol.* 2004;173(7):4582–9.
201. Brown GC, Vilalta A. How microglia kill neurons. *Brain Res.* 2015;1628:288–97.
 202. Paolicelli RC, Bolasco G, Pagani F, Maggi L, Scianni M, Panzanelli P, et al. Synaptic Pruning by Microglia Is Necessary for Normal Brain Development. *Science* (80-). 2011;333:1456–9.
 203. Stevens B, Allen NJ, Vazquez LE, Howell GR, Christopherson KS, Nouri N, et al. The Classical Complement Cascade Mediates CNS Synapse Elimination. *Cell.* 2007;131:1164–78.
 204. Filipello F, Morini R, Corradini I, Zerbi V, Canzi A, Michalski B, et al. The Microglial Innate Immune Receptor TREM2 Is Required for Synapse Elimination and Normal Brain Connectivity. *Immunity.* 2018;48:1–13.
 205. Lehrman EK, Wilton DK, Litvina EY, Umemori H, Chen C, Lehrman EK, et al. CD47 Protects Synapses from Excess Microglia-Mediated Pruning during Development. *Neuron.* 2018;100:120–34.
 206. Tremblay M-È, Lowery RL, Majewska AK. Microglial Interactions with Synapses Are Modulated by Visual Experience. *PLoS Biol.* 2010;8(11):e1000527.
 207. Schafer DP, Lehrman EK, Kautzman AG, Koyama R, Mardinly AR, Yamasaki R, et al. Microglia Sculpt Postnatal Neural Circuits in an Activity and Complement-Dependent Manner. *Neuron.* 2012;74:691–705.
 208. Sierra A, Encinas JM, Deudero JJP, Chancey JH, Enikolopov G, Overstreet-Wadiche LS, et al. Microglia shape adult hippocampal neurogenesis through apoptosis-coupled phagocytosis. *Cell Stem Cell.* 2010;7:483–95.
 209. Cunningham CL, Martínez-Cerdeno V, Noctor SC. Microglia Regulate the Number of Neural Precursor Cells in the Developing Cerebral Cortex. *J Neurosci.* 2013;33(10):4216–33.
 210. Ueno M, Fujita Y, Tanaka T, Nakamura Y, Kikuta J, Ishii M, et al. Layer V cortical neurons require microglial support for survival during postnatal development. *Nat Neurosci.* 2013;16(5):543–51.
 211. Squarzoni P, Oller G, Hoeffel G, Pont-lezica L, Rostaing P, Low D, et al. Microglia Modulate Wiring of the Embryonic Forebrain. *Cell Rep.* 2014;8:1271–9.
 212. Arnoux I, Audinat E. Fractalkine Signaling and Microglia Functions in the Developing Brain. *Neural Plast.* 2015;2015(689404):1–18.
 213. Wake H, Moorhouse AJ, Jinno S, Kohsaka S, Nabekura J. Resting Microglia Directly Monitor the Functional State of Synapses In Vivo and Determine the Fate of Ischemic Terminals. *J Neurosci.* 2009;29(13):3974–80.
 214. Hayashi Y, Ishibashi H, Hashimoto K, Nakanishi H. Potentiation of the NMDA Receptor-Mediated Responses Through the Activation of the Glycine Site by Microglia Secreting Soluble Factors. *Glia.* 2006;53:660–8.
 215. Parkhurst CN, Yang G, Ninan I, Savas JN, Yates JR, Lafaille JJ, et al. Microglia promote learning-dependent synapse formation through brain-derived neurotrophic factor. *Cell.* 2013;155:1596–609.
 216. Rymo SF, Gerhardt H, Sand FW, Lang R, Uv A, Betsholtz C. A Two-Way Communication between Microglial Cells and Angiogenic Sprouts Regulates Angiogenesis in Aortic Ring

Cultures. *PLoS One*. 2011;6(1):e15846.

217. Ding X, Gu R, Zhang M, Ren H, Shu Q, Xu G, et al. Microglia enhanced the angiogenesis, migration and proliferation of co-cultured RMECs. *BMC Ophthalmol*. 2018;18(1):249–51.
218. Fantin A, Vieira JM, Gestri G, Denti L, Schwarz Q, Prykhodzhiy S, et al. Tissue macrophages act as cellular chaperones for vascular anastomosis downstream of VEGF-mediated endothelial tip cell induction. *Blood*. 2010;116(5):829–40.
219. Arnold T, Betsholtz C. The importance of microglia in the development of the vasculature in the central nervous system. *Vasc Cell*. 2013;5(4):1–7.
220. Takagi S, Furube E, Nakano Y, Morita M, Miyata S. Microglia are continuously activated in the circumventricular organs of mouse brain. *J Neuroimmunol*. 2017;0165–5728(17):1–13.
221. Ousman SS, Kubes P. Immune surveillance in the central nervous system. *Nat Neurosci*. 2012;15(8):1096–102.
222. Pan XD, Zhu YG, Lin N, Zhang J, Ye QY, Huang HP, et al. Microglial phagocytosis induced by fibrillar β -amyloid is attenuated by oligomeric β -amyloid: Implications for Alzheimer's disease. *Mol Neurodegener*. 2011;6(45):1–17.
223. Keren-Shaul H, Spinrad A, Weiner A, Matcovitch-Natan O, Dvir-Szternfeld R, Ulland TK, et al. A Unique Microglia Type Associated with Restricting Development of Alzheimer's Disease. *Cell*. 2017;169:1276–90.
224. Yin Z, Raj D, Saiepour N, Van Dam D, Brouwer N, Holtman IR, et al. Immune hyperreactivity of A β plaque-associated microglia in Alzheimer's disease. *Neurobiol Aging*. 2017;55:115–22.
225. Guerreiro R, Wojtas A, Bras J, Minerva Carrasquillo ER, Majounie E, Cruchaga C, et al. TREM2 variants in Alzheimer's disease. *N Engl J Med*. 2013;368:117–27.
226. Hansen D V, Hanson JE, M S. Microglia in Alzheimer's disease. *J Cell Biol*. 2018;217(2):1–13.
227. Griciuc A, Serrano-Pozo A, Parrado AR, Lesinski AN, Asselin CN, Mullin K, et al. Alzheimer's disease risk gene CD33 inhibits microglial uptake of amyloid beta. *Neuron*. 2013 May 22;78(4):631–43.
228. Rathore N, Ramani SR, Pantua H, Payandeh J, Bhangale T, Wuster A, et al. Paired Immunoglobulin-like Type 2 Receptor Alpha G78R variant alters ligand binding and confers protection to Alzheimer's disease. *PLoS Genet*. 2018;14(11):e1007427.
229. Magno L, Lessard CB, Martins M, Cruz P, Katan M, Chakrabaty P, et al. Alzheimer's disease Phospholipase C-gamma-2 (PLCG2) protective variant is a functional hypermorph. *Alzheimer's Res Ther*. 2018;11(16):1–21.
230. Huang K, Marcora E, Pimenova AA, Narzo AF Di, Kapoor M, Jin SC, et al. A common haplotype lowers SPI1 (PU.1) expression in myeloid cells and delays age at onset for Alzheimer's disease. *Nat Neurosci*. 2017;20:1052–61.
231. Tansey KE, Cameron D, Hill MJ. Genetic risk for Alzheimer's disease is concentrated in specific macrophage and microglial transcriptional networks. *Genome Med*. 2018;10(14):1–10.
232. Smith AM, Gibbons HM, Oldfield RL, Bergin PM, Mee EW, Faull RLM, et al. The transcription

- factor PU.1 is critical for viability and function of human brain microglia. *Glia*. 2013 Jun 1;61:929–42.
233. Rustenhoven J, Smith AM, Smyth LC, Jansson D, Scotter EL, Swanson ME V., et al. PU.1 regulates Alzheimer's disease-associated genes in primary human microglia. *Mol Neurodegener*. 2018;13:44.
234. Corneveaux JJ, Myers AJ, Allen AN, Pruzin JJ, Ramirez M, Engel A, et al. Association of CR1, CLU and PICALM with Alzheimer's disease in a cohort of clinically characterized and neuropathologically verified individuals. *Hum Mol Genet*. 2010;19(16):3295–301.
235. Ando K, Brion JP, Stygelbout V, Suain V, Authelet M, Dedecker R, et al. Clathrin adaptor CALM/PICALM is associated with neurofibrillary tangles and is cleaved in Alzheimer's brains. *Acta Neuropathol*. 2013;125:861–78.
236. Xiao Q, Gil S, Yan P, Wang Y, Han S, Gonzales E, et al. Role of Phosphatidylinositol Clathrin Assembly Lymphoid-Myeloid Leukemia (PICALM) in Intracellular Amyloid Precursor Protein (APP) Processing and Amyloid Plaque Pathogenesis. *J Biol Chem*. 2012;287(25):21279–89.
237. Zhong L, Chen XF, Zhang ZL, Wang Z, Shi XZ, Xu K, et al. DAP12 stabilizes the C-terminal fragment of the triggering receptor expressed on myeloid cells-2 (TREM2) and protects against LPS-induced pro-inflammatory response. *J Biol Chem*. 2015;290(25):15866–77.
238. Kamen LA, Levinsohn J, Swanson JA. Differential Association of Phosphatidylinositol 3-Kinase, SHIP-1, and PTEN with Forming Phagosomes. *Mol Biol Cell*. 2007;18:2463–72.
239. Bao M, Hanabuchi S, Facchinetti V, Du Q, Bover L, Plumas J, et al. CD2AP/SHIP1 Complex Positively Regulates Plasmacytoid Dendritic Cell Receptor Signaling by Inhibiting the E3 Ubiquitin Ligase Cbl. *J Immunol*. 2012;189(2):786–92.
240. Ubelmann F, Burrenha T, Salavessa L, Gomes R, Ferreira C, Moreno N, et al. Bin 1 and CD2AP polarise the endocytic generation of beta-amyloid. *EMBO Rep*. 2017;18(1):102–22.
241. Calafate S, Flavin W, Verstreken P, Moechars D. Loss of Bin1 Promotes the Propagation of Tau Pathology. *Cell Rep*. 2016;17:931–40.
242. Kajihito H, Saito K, Tsujita K, Kontani K, Araki Y, Kurosu H, et al. RIN3: a novel Rab5 GEF interacting with amphiphysin II involved in the early endocytic pathway. *J Cell Sci*. 2003;116(20):4159–68.
243. Chapuis J, Hansmannel F, Gistelincq M, Mounier A, Cauwenberghe C Van, Kolen K, et al. Increased expression of BIN1 mediates Alzheimer genetic risk by modulating tau pathology. *Mol Psychiatry*. 2013;18:1225–34.
244. Satoh J, Kino Y, Yanaizu M, Tosaki Y, Sakai K, Ishida T, et al. Microglia express ABI3 in the brains of Alzheimer's disease and Nasu-Hakola disease. *Intractable Rare Dis Res*. 2017;6(4):262–8.
245. Sekino S, Kashiwagi Y, Kanazawa H, Takada K, Baba T, Sato S, et al. The NESH/Abi-3-based WAVE2 complex is functionally distinct from the Abi-1-based WAVE2 complex. *Cell Commun Signal*. 2015;13(41):1–15.
246. Lloberas J, Soler C, Celada A. The key role of PU.1/SPI-1 in B cells, myeloid cells and macrophages. *Immunol Today*. 1999 Apr;20(4):184–9.

247. Klemsz MJ, McKercher SR, Celada A, Van Beveren C, Maki RA. The macrophage and B cell-specific transcription factor PU.1 is related to the ets oncogene. *Cell*. 1990;61:113–24.
248. Heng TSP, Painter MW, Elpek K, Lukacs-Kornek V, Mauermann N, Turley SJ, et al. The immunological genome project: Networks of gene expression in immune cells. *Nat Immunol*. 2008;9(10):1091–4.
249. DeKoter RP, Singh H. Regulation of B lymphocyte and macrophage development by graded expression of PU.1. *Science* (80-). 2000 May;288:1439–41.
250. Back J, Dierich A, Bronn C, Kastner P, Chan S. PU.1 determines the self-renewal capacity of erythroid progenitor cells. *Blood*. 2004;103(10):3615–23.
251. Back J, Allman D, Chan S, Kastner P. Visualizing PU.1 activity during hematopoiesis. *Exp Hematol*. 2005;33:395–402.
252. Heinz S, Benner C, Spann N, Bertolino E, Lin YC, Laslo P, et al. Simple Combinations of Lineage-Determining Transcription Factors Prime cis-Regulatory Elements Required for Macrophage and B Cell Identities. *Mol Cell*. 2010;38:576–89.
253. Mak KS, Funnell APW, Pearson RCM, Crossley M. PU.1 and haematopoietic cell fate: Dosage matters. *Int J Cell Biol*. 2011;808524:1–6.
254. Walton MR, Gibbons H, MacGibbon GA, Sirimanne E, Saura J, Gluckman PD, et al. PU.1 expression in microglia. *J Neuroimmunol*. 2000 May;104:109–15.
255. Celada A, Borrás FE, Soler C, Lloberas J, Klemsz M, Beveren C van, et al. The Transcription Factor PU.1 Is Involved in Macrophage Proliferation. *J Exp Med*. 1996;184:61–9.
256. Zhang DE, Hetherington CJ, Chen HM, Tenen DG. The macrophage transcription factor PU.1 directs tissue-specific expression of the macrophage colony-stimulating factor receptor. *Mol Cell Biol*. 1994;14(1):373–81.
257. Kueh HY, Champhekar A, Nutt SL, Elowitz MB, Rothenberg E V. Positive Feedback Between PU.1 and the Cell Cycle Controls Myeloid Differentiation. *Science* (80-). 2013 Aug 8;341:670–3.
258. Scott EW, Simon MC, Anastasi J, Singh H. Requirement of transcription factor PU.1 in the development of multiple hematopoietic lineages. *Science* (80-). 1994 Sep;265:1573–7.
259. Houston IB, Kamath MB, Schweitzer BL, Chlon TM, DeKoter RP. Reduction in PU.1 activity results in a block to B-cell development, abnormal myeloid proliferation, and neonatal lethality. *Exp Hematol*. 2007;35(7):1056–68.
260. Rosenbauer F, Wagner K, Kutok JL, Iwasaki H, Le Beau MM, Okuno Y, et al. Acute myeloid leukemia induced by graded reduction of a lineage-specific transcription factor, PU.1. *Nat Genet*. 2004;36(6):624–30.
261. Sharrocks AD. The ETS-domain transcription factor family. *Nat Rev Mol Cell Biol*. 2001;2:827–37.
262. Pio F, Kodapani R, Ni CZ, Shepard W, Klemsz M, McKercher SR, et al. New insights on DNA recognition by ets proteins from the crystal structure of the PU.1 ETS domain-DNA complex. *J Biol Chem*. 1996;271(38):23329–37.
263. Zhang P, Behre G, Pan J, Iwama A, Wara-aswapati N, Radomska HS, et al. Negative cross-

- talk between hematopoietic regulators: GATA proteins repress PU.1. *PNAS*. 1999 Jul 20;96:8705–10.
264. Hu Z, Gu X, Baraoidan K, Ibanez V, Sharma A, Kadkol SH, et al. RUNX1 regulates corepressor interactions of PU.1. *Blood*. 2011;117(24):6498–508.
 265. Jin H, Li L, Xu J, Zhen F, Zhu L, Liu PP, et al. Runx1 regulates embryonic myeloid fate choice in zebrafish through a negative feedback loop inhibiting Pu.1 expression. *Blood*. 2012;119(22):5239–49.
 266. Zarnegar MA, Chen J, Rothenberg E V. Cell-Type-Specific Activation and Repression of PU.1 by a Complex of Discrete, Functionally Specialized cis-Regulatory Elements. *Mol Cell Biol*. 2010;30(20):4922–39.
 267. Li Y, Okuno Y, Zhang P, Radomska HS, Chen H, Iwasaki H, et al. Regulation of the PU. 1 gene by distal elements. *Blood*. 2001;98(10):2958–65.
 268. Okuno Y, Huang G, Rosenbauer F, Evans EK, Radomska HS, Iwasaki H, et al. Potential Autoregulation of Transcription Factor PU . 1 by an Upstream Regulatory Element. *Mol Cell Biol*. 2005;25(7):2832–45.
 269. Zarnegar MA, Rothenberg E V. Ikaros represses and activates PU.1 cell-type-specifically through the multifunctional Sfp1 URE and a myeloid specific enhancer. *Oncogene*. 2012 Oct 25;31:4647–54.
 270. Leddin M, Perrod C, Hoogenkamp M, Ghani S, Assi S, Heinz S, et al. Two distinct auto-regulatory loops operate at the PU.1 locus in B cells and myeloid cells. *Blood*. 2011;117(10):2827–38.
 271. Smith AM, Gibbons HM, Oldfield RL, Bergin PM, Mee EW, Curtis MA, et al. M-CSF increases proliferation and phagocytosis while modulating receptor and transcription factor expression in adult human microglia. *J Neuroinflammation*. 2013 Jan 17;10(85):1–15.
 272. Pahl HL, Scheibe RJ, Zhang DE, Chen HM, Galson DL, Maki RA, et al. The proto-oncogene PU.1 regulates expression of the myeloid-specific CD11b promoter. *J Biol Chem*. 1993;268(7):5014–20.
 273. Anderson KL, Nelson SL, Perkin HB, Smith KA, Klemsz MJ, Torbett BE. PU.1 is a Lineage-specific Regulator of Tyrosine Phosphatase CD45. *J Biol Chem*. 2001;276(10):7637–42.
 274. Yeh H, Ikezu T. Transcriptional and Epigenetic Regulation of Microglia in Health and Disease. *Trends Mol Med*. 2018;25(2):96–111.
 275. Ghisletti S, Barozzi I, Mietton F, Polletti S, De Santa F, Venturini E, et al. Identification and Characterization of Enhancers Controlling the Inflammatory Gene Expression Program in Macrophages. *Immunity*. 2010;32:317–28.
 276. Das A, Kim SH, Arifuzzaman S, Yoon T, Chai JC, Lee YS, et al. Transcriptome sequencing reveals that LPS-triggered transcriptional responses in established microglia BV2 cell lines are poorly representative of primary microglia. *J Neuroinflammation*. 2016;13(182):1–18.
 277. Marecki S, Riendeau CJ, Liang MD, Fenton MJ. PU.1 and Multiple IFN Regulatory Factor Proteins Synergize to Mediate Transcriptional Activation of the Human IL-1 β Gene. *J Immunol*. 2001;166:6892–6838.
 278. Sierksma A, Lu A, Salta E, Mancuso R, Zoco J, Blum D, et al. Novel Alzheimer risk genes

determine the microglia response to amyloid- β but not to TAU pathology. bioRxiv (preprint). 2019;491902.

279. Laribee RN, Klemsz MJ. Loss of PU.1 Expression Following Inhibition of Histone Deacetylases. *J Immunol.* 2001;167:5160–6.
280. Smith AM, Gibbons HM, Dragunow M. Valproic acid enhances microglial phagocytosis of amyloid- β 1-42. *Neuroscience.* 2010;169(1):505–15.
281. Gibbons HM, Smith AM, Teoh HH, Bergin PM, Mee EW, Faull RLM, et al. Valproic acid induces microglial dysfunction, not apoptosis, in human glial cultures. *Neurobiol Dis.* 2011;41:96–103.
282. Gottlicher M, Minucci S, Zhu P, H.Kramer O, Schimpf A, Giavara S, et al. Valproic acid defines a novel class of HDAC inhibitors inducing differentiation of transformed cells. *EMBO J.* 2001;20(24):6969–78.
283. (DZNE) GC for ND. Clinical Trial to Determine Tolerable Dosis of Vorinostat in Patients With Mild Alzheimer Disease [Internet]. NIH Clinical Trials Database. 2017. Available from: <https://clinicaltrials.gov/ct2/show/NCT03056495>
284. Hirao N, Sato S, Gotoh T, Maruoka M, Suzuki J, Matsuda S, et al. NESH (Abi-3) is present in the Abi/WAVE complex but does not promote c-Abl-mediated phosphorylation. *FEBS Lett.* 2006;580:6464–70.
285. Uhlemann R, Gertz K, Boehmerle W, Schwarz T, Nolte C, Freyer D, et al. Actin dynamics shape microglia effector functions. *Brain Struct Funct.* 2016;221(5):2717–34.
286. Ichigotani Y, Fujii KEI, Hamaguchi M, Matsuda S. In search of a function for the E3B1/Abi2/Argbp1/NESH family. *Int J Mol Med.* 2002;9:591–5.
287. Vincent C, Siddiqui TA, Schlichter LC. Podosomes in Migrating Microglia: Components and Matrix Degradation. *J Neuroinflammation.* 2012;9:190–204.
288. Takenawa T, Miki H. WASP and WAVE family proteins: key molecules for rapid rearrangement of cortical actin filaments and cell movement. *J Cell Sci.* 2001;114(10):1801–9.
289. Kheir WA, Gevrey J-C, Yamaguchi H, Isaac B, Cox D. A WAVE2-Abi1 complex mediates CSF1-induced F-actin-rich membrane protrusions and migration in macrophages. *J Cell Sci.* 2005;118:5369–79.
290. Miyazaki K, Matsuda S, Ichigotani Y, Takenouchi Y, Hayashi K, Fukuda Y, et al. Isolation and characterization of a novel human gene (NESH) which encodes a putative signaling molecule similar to e3B1 protein. *Biochim Biophys Acta.* 2000;1493:237–41.
291. Sjöstedt E, Fagerberg L, Hallström BM, Häggmark A, Mitsios N, Nilsson P, et al. Defining the human brain proteome using transcriptomics and antibody-based profiling with a focus on the cerebral cortex. *PLoS One.* 2015;10:1–20.
292. Kotula L. Abi1, a critical molecule coordinating actin cytoskeleton reorganization with PI-3 kinase and growth signaling. *FEBS Lett.* 2012;586:2790–4.
293. Leng Y, Zhang J, Badour K, Arpaia E, Freeman S, Cheung P, et al. Abelson-interactor-1 promotes WAVE2 membrane translocation and Abelson-mediated tyrosine phosphorylation required for WAVE2 activation. *PNAS.* 2005;102(4):1098–103.

294. Moraes L, Zanchin NIT, Cerutti JM. ABI3, a component of the WAVE2 complex, is potentially regulated by PI3K/AKT pathway. *Oncotarget*. 2017;8(40):67769–81.
295. Latini FRM, Hemerly JP, Freitas BCG, Oler G, Riggins GJ, Cerutti JM. ABI3 ectopic expression reduces in vitro and in vivo cell growth properties while inducing senescence. *BMC Cancer*. 2011;11(11):1–12.
296. Latini FRM, Hemerly JP, Oler G, Riggins GJ, Cerutti JM. Re-expression of ABI3-binding protein suppresses thyroid tumor growth by promoting senescence and inhibiting invasion. *Endocr Relat Cancer*. 2008;15:787–99.
297. Bae J, Sung BH, Cho IH, Kim S-M, Song WK. NESH Regulates Dendritic Spine Morphology and Synapse Formation. *PLoS One*. 2012;7(4):e34677.
298. Rosenbauer F, Owens BM, Yu L, Tumang JR, Steidl U, Kutok JL, et al. Lymphoid cell growth and transformation are suppressed by a key regulatory element of the gene encoding PU.1. *Nat Genet*. 2006;38(1):27–37.
299. The Jackson Laboratory. B6N(Cg)-Abi3tm1.1(KOMP)Vlclg/J Strain Page [Internet]. [cited 2019 Feb 20]. Available from: <https://www.jax.org/strain/028180>
300. Office UH. Animals (Scientific Procedures) Act 1986. 1986.
301. The Jackson Laboratory. Spi1tm1.3Dgt/J Strain Page [Internet]. [cited 2019 Mar 15]. Available from: <https://www.jax.org/strain/006083>
302. Schneider U, Schwenk H-U, Bornkamm G. Characterization of EBV-genome negative “null” and “T” cell lines derived from children with acute lymphoblastic leukemia and leukemic transformed non-Hodgkin lymphoma. Vol. 19, *International journal of cancer*. New York, NY ; 1977. p. 621–6.
303. DuBridg RB, Tang P, Hsia HC, Leong PM, Miller JH, Calos MP. Analysis of mutation in human cells by using an Epstein-Barr virus shuttle system. *Mol Cell Biol*. 1987 Jan 1;7:379–87.
304. Rosas M, Osorio F, Robinson MJ, Davies LC, Dierkes N, Jones S a., et al. Hoxb8 conditionally immortalised macrophage lines model inflammatory monocytic cells with important similarity to dendritic cells. *Eur J Immunol*. 2011;41:356–65.
305. Raschke WC, Baird S, Ralph P, Nakoinz I. Functional Macrophage Cell Lines Transformed By Abelson Leukemia-Virus. *Cell*. 1978;15:261–7.
306. The Jackson Laboratory. Body Weight Information For C57BL/6J [Internet]. [cited 2019 Mar 4]. Available from: <https://www.jax.org/jax-mice-and-services/strain-data-sheet-pages/body-weight-chart-000664>
307. Molecular Probes. FluoReporter® lacZ Flow Cytometry Kits [Internet]. Product Information. 2003 [cited 2019 Mar 4]. p. 1–5. Available from: <https://www.thermofisher.com/document-connect/document-connect.html?url=https%3A%2F%2Fassets.thermofisher.com%2FTFS-Assets%2FLSG%2Fmanuals%2Fmp01930.pdf&title=Rmx1b1JlcG9ydGVyICZsdDtpJmd0O2xhY1ombHQ7L2kmZ3Q7IEZsb3cgQ3l0b21ldHJ5IEtpdHM=>
308. Moore CB, Guthrie EH, Huang MT, Taxman DJ. Short Hairpin RNA (shRNA): Design, Delivery, and Assesment of Gene Knockdown. *Methods Mol Biol*. 2010;629:141–58.

309. Davies LC. Homeostasis, Control of Macrophage. Cardiff University; 2014.
310. Davies LC. Control of Macrophage Homeostasis. Cardiff University; 2014.
311. Mizuguchi H, Xu Z, Ishii-Watabe A, Uchida E, Hayakawa T. IRES-Dependent Second Gene Expression Is Significantly Lower Than Cap-Dependent First Gene Expression in a Bicistronic Vector. *Mol Ther.* 2000;1(4):376–82.
312. Love MI, Huber W, Anders S. Moderated estimation of fold change and dispersion for RNA-seq data with DESeq2. *Genome Biol.* 2014 Dec;15(12):550.
313. Huang DW, Sherman BT, Lempicki RA. Systematic and integrative analysis of large gene lists using DAVID bioinformatics resources. *Nat Protoc.* 2009;4(1):44–57.
314. Broad Institute. Morpheus Software [Internet]. [cited 2019 Feb 9]. Available from: <https://software.broadinstitute.org/morpheus>
315. Herrero J. How to get all the orthologous genes between two species [Internet]. Ensembl Blog. 2009 [cited 2018 Nov 20]. Available from: <http://www.ensembl.info/2009/01/21/how-to-get-all-the-orthologous-genes-between-two-species/>
316. De Leeuw CA, Mooij JM, Heskes T, Posthuma D. MAGMA : Generalized Gene-Set Analysis of GWAS Data. *PLoS Computational Biol.* 2015;11(4):1–19.
317. Escott-Price V, Sims R, Bannister C, Harold D, Vronskaya M, Majounie E, et al. Common polygenic variation enhances risk prediction for Alzheimer’s disease. *Brain.* 2015;138:3673–84.
318. Fleisher AS, Truran D, Mai JT, Langbaum JBS, Aisen PS, Cummings JL, et al. Chronic divalproex sodium use and brain atrophy in Alzheimer disease. *Neurology.* 2011;77:1263–71.
319. Satoh J, Asahina N, Kitano S, Kino Y. A Comprehensive Profile of ChIP-Seq-Based PU.1/Spi1 Target Genes in Microglia. *Gene Regul Syst Bio.* 2014;8:127–39.
320. Buenrostro J, Wu B, Chang H, Greenleaf W. ATAC-seq: A Method for Assaying Chromatin Accessibility Genome-Wide. *Curr Protoc Mol Biol.* 2016;109:1–10.
321. Creyghton MP, Cheng AW, Welstead GG, Kooistra T, Carey BW, Steine EJ, et al. Histone H3K27ac separates active from poised enhancers and predicts developmental state. *PNAS.* 2010 Dec;107(50):21931–6.
322. Mei S, Qin Q, Wu Q, Sun H, Zheng R, Zang C, et al. Cistrome Data Browser: a data portal for ChIP-Seq and chromatin accessibility data in human and mouse. *Nucleic Acids Res.* 2017 Oct 26;45(D1):D658–62.
323. Yoshida H, Lareau CA, Ramirez RN, Rose SA, Maier B, Wroblewska A, et al. The cis-Regulatory Atlas of the Mouse Immune System. *Cell.* 2019 Feb;176(4):897–912.
324. Czimmerer Z, Daniel B, Horvath A, Ruckerl D, Nagy G, Kiss M, et al. The Transcription Factor STAT6 Mediates Direct Repression of Inflammatory Enhancers and Limits Activation of Alternatively Polarized Macrophages. *Immunity.* 2018 Jan;48:75–90.
325. Choukallah M-A, Song S, Rolink AG, Burger L, Matthias P. Enhancer repertoires are reshaped independently of early priming and heterochromatin dynamics during B cell

- differentiation. *Nat Commun.* 2015 Oct;6:8324.
326. Iwata S, Mikami Y, Sun H-W, Brooks SR, Jankovic D, Hirahara K, et al. The Transcription Factor T-bet Limits Amplification of Type I IFN Transcriptome and Circuitry in T Helper 1 Cells. *Immunity.* 2017 Jun;46(6):983–91.
 327. Furey TS, Kent WJ, Roskin KM, Sugnet CW, Zahler AM, Pringle TH, et al. The Human Genome Browser at UCSC. *Genome Res.* 2002;12:996–1006.
 328. Kent WJ. BLAT-The BLAST-like alignment tool. *Genome Res.* 2002;12:656–64.
 329. Torlakovic E, Tierens A, Dang HD, Delabie J. The Transcription Factor PU.1, Necessary for B-Cell Development Is Expressed in Lymphocyte Predominance, But Not Classical Hodgkin's Disease. *Am J Pathol.* 2001 Nov 27;159:1807–14.
 330. Platt RJ, Chen S, Zhou Y, Yim MJ, Swiech L, Kempton HR, et al. CRISPR-Cas9 knockin mice for genome editing and cancer modeling. *Cell.* 2014;159:440–55.
 331. Fonseca MI, Chu SH, Hernandez MX, Fang MJ, Modarresi L, Selvan P, et al. Cell-specific deletion of C1qa identifies microglia as the dominant source of C1q in mouse brain. *J Neuroinflammation.* 2017;14(48):1–15.
 332. Joo M, Park GY, Wright JG, Blackwell TS, Atchison ML, Christman JW. Transcriptional Regulation of the Cyclooxygenase-2 Gene in Macrophages by PU.1. *J Biol Chem.* 2004;279(8):6658–65.
 333. Zhou X, Gao X-P, Fan J, Liu Q, Anwar KN, Frey RS, et al. LPS activation of Toll-like receptor 4 signals CD11b/CD18 expression in neutrophils. *AJP Lung Cell Mol Physiol.* 2004;288:655–62.
 334. Jian W, Yan B, Huang S, Qiu Y. Histone deacetylase 1 activates PU.1 gene transcription through regulating TAF9 deacetylation and transcription factor IID assembly. *FASEB J.* 2017;31:4104–16.
 335. Laribee RN, Klemsz MJ. Histone H4 HDAC activity is necessary for expression of the PU.1 gene. *Biochim Biophys Acta - Gene Struct Expr.* 2005;1730:226–34.
 336. Nerlov C, Querfurth E, Kulesa H, Graf T. GATA-1 interacts with the myeloid PU.1 transcription factor and represses PU.1-dependent transcription. *Blood.* 2000 Apr 15;95(8):2543–51.
 337. Balcaitis S, Weinstein JR, Li S, Chamberlain JS, Möller T. Lentiviral transduction of microglial cells. *Glia.* 2005;50:48–55.
 338. Gomez-Nicola D, Riecken K, Fehse B, Perry VH. In-vivo RGB marking and multicolour single-cell tracking in the adult brain. *Sci Rep.* 2015;4(7520):1–10.
 339. Ponomarev ED, Novikova M, Maresz K, Shriver LP, Dittel BN. Development of a culture system that supports adult microglial cell proliferation and maintenance in the resting state. *J Immunol Methods.* 2005 May;300:32–46.
 340. Meng Z, Lu M. RNA interference-induced innate immunity, off-target effect, or immune adjuvant? *Front Immunol.* 2017;8(331):1–7.
 341. Suzumura A, Sawada M, Yamamoto H, Marunouchi T. Transforming growth factor-beta suppresses activation and proliferation of microglia in vitro. *J Immunol.* 1993;151:2150–8.

342. Ma D, Doi Y, Jin S, Li E, Sonobe Y, Takeuchi H, et al. TGF- β induced by interleukin-34-stimulated microglia regulates microglial proliferation and attenuates oligomeric amyloid- β neurotoxicity. *Neurosci Lett*. 2012;529:86–91.
343. Sevilla L, Zaldumbide A, Carlotti F, Dayem MA, Pognonec P, Boulukos KE. Bcl-xL Expression Correlates with Primary Macrophage Differentiation, Activation of Functional Competence, and Survival and Results from Synergistic Transcriptional Activation by Ets2 and PU.1. *J Biol Chem*. 2001;276(21):17800–7.
344. Ridinger-Saison M, Evanno E, Gallais I, Rimmelé P, Selimoglu-Buet D, Sapharikas E, et al. Epigenetic silencing of Bim transcription by Spi-1/PU.1 promotes apoptosis resistance in leukaemia. *Cell Death Differ*. 2013;20(9):1268–78.
345. Karpurapu M, Wang X, Deng J, Park H, Xiao L, Sadikot RT, et al. Functional PU.1 in macrophages has a pivotal role in NF- κ B activation and neutrophilic lung inflammation during endotoxemia. *Blood*. 2011;118(19):5255–66.
346. Kozera B, Rapacz M. Reference genes in real-time PCR. *J Appl Genet*. 2013;54:391–406.
347. Sanders R, Mason DJ, Foy CA, Huggett JF. Considerations for accurate gene expression measurement by reverse transcription quantitative PCR when analysing clinical samples. *Anal Bioanal Chem*. 2014;406:6471–83.
348. Konishi H, Kobayashi M, Kunisawa T, Imai K, Sayo A, Malissen B, et al. Siglec-H is a microglia-specific marker that discriminates microglia from CNS-associated macrophages and CNS-infiltrating monocytes. *Glia*. 2017;65:1927–43.
349. Condello C, Yuan P, Schain A, Grutzendler J. Microglia constitute a barrier that prevents neurotoxic protofibrillar A β 42 hotspots around plaques. *Nat Commun*. 2015;6(6176):1–14.
350. Wilson MD, Cheung J, Martindale DW, Scherer SW, Koop BF. Comparative analysis of the paired immunoglobulin-like receptor (PILR) locus in six mammalian genomes: duplication, conversion, and the birth of new genes. *Physiol Genomics*. 2006;27:201–18.
351. Mildner A, Huang H, Radke J, Stenzel W, Priller J. P2Y12 receptor is expressed on human microglia under physiological conditions throughout development and is sensitive to neuroinflammatory diseases. *Glia*. 2017;65:375–87.
352. Ito D, Imai Y, Ohsawa K, Nakajima K, Fukuuchi Y, Kohsaka S. Microglia-specific localisation of a novel calcium binding protein, Iba1. *Mol Brain Res*. 1998;57:1–9.
353. Sasaki Y, Ohsawa K, Kanazawa H, Kohsaka S, Imai Y. Iba1 is an actin-cross-linking protein in macrophages/microglia. *Biochem Biophys Res Commun*. 2001;286:292–7.
354. Ohsawa K, Imai Y, Kanazawa H, Sasaki Y, Kohsaka S. Involvement of Iba1 in membrane ruffling and phagocytosis of macrophages/microglia. *J Cell Sci*. 2000;113:3073–84.
355. Ohsawa K, Imai Y, Sasaki Y, Kohsaka S. Microglia/macrophage-specific protein Iba1 binds to fimbriin and enhances its actin-bundling activity. *J Neurochem*. 2004;88:844–56.
356. Imai Y, Kohsaka S. Intracellular signaling in M-CSF-induced microglia activation: Role of Iba1. *Glia*. 2002;40:164–74.
357. Minett T, Classey J, Matthews FE, Fahrenhold M, Taga M, Brayne C, et al. Microglial immunophenotype in dementia with Alzheimer's pathology. *J Neuroinflammation*. 2016;13(135):1–10.

358. Hopperton KE, Mohammad D, Trépanier MO, Giuliano V, Bazinet RP. Markers of microglia in post-mortem brain samples from patients with Alzheimer's disease: A systematic review. *Mol Psychiatry*. 2018;23:177–98.
359. Shiratori I, Ogasawara K, Saito T, Lanier LL, Arase H. Activation of Natural Killer Cells and Dendritic Cells upon Recognition of a Novel CD99-like Ligand by Paired Immunoglobulin-like Type 2 Receptor. *J Exp Med*. 2004;199(4):525–33.
360. Tato CM, Joyce-Shaikh B, Banerjee A, Chen Y, Sathe M, Ewald SE, et al. The myeloid receptor PILR β mediates the balance of inflammatory responses through regulation of IL-27 production. *PLoS One*. 2012;7(3):e31680.
361. Karch CM, Ezerskiy LA, Bertelsen S, Albert MS, Albin RL, Apostolova LG, et al. Alzheimer's disease risk polymorphisms regulate gene expression in the ZCWPW1 and the CELF1 loci. *PLoS One*. 2016;11(e0148717):1–22.
362. Ryan KJ, White CC, Patel K, Xu J, Olah M, Replogle JM, et al. A human microglia-like cellular model for assessing the effects of neurodegenerative disease gene variants. *Sci Transl Med*. 2017;9(7635):1–12.
363. Siegfried A, Berchtold S, Manncke B, Deuschle E, Reber J, Ott T, et al. IFIT2 Is an Effector Protein of Type I IFN-Mediated Amplification of Lipopolysaccharide (LPS)-Induced TNF- α Secretion and LPS-Induced Endotoxin Shock. *J Immunol*. 2013;191:3913–21.
364. Choi UY, Kang JS, Hwang YS ahng, Kim YJ. Oligoadenylate synthase-like (OASL) proteins: dual functions and associations with diseases. *Exp Mol Med*. 2014;47(e144):1–6.
365. Montine TJ, Milatovic D, Gupta RC, Valyi-Nagy T, Morrow JD, Breyer RM. Neuronal oxidative damage from activated innate immunity is EP2 receptor-dependent. *J Neurochem*. 2002;83:463–70.
366. Liang X, Wang Q, Hand T, Wu L, Breyer RM, Montine TJ, et al. Deletion of the Prostaglandin E2 EP2 Receptor Reduces Oxidative Damage and Amyloid Burden in a Model of Alzheimer's Disease. *J Neurosci*. 2005;25(44):10180–7.
367. Muller WA, Weigl SA, Deng X, Phillips DM. PECAM-1 Is Required for Transendothelial Migration of Leukocytes. *J Exp Med*. 1993;178:449–60.
368. Ariffin JK, Kapetanovic R, Schaale K, Gatica-Andrades M, Blumenthal A, Schroder K, et al. The E3 ubiquitin ligase RNF144B is LPS-inducible in human, but not mouse, macrophages and promotes inducible IL-1 β expression. *J Leukoc Biol*. 2016;100:155–61.
369. Hemmi H, Zaidi N, Wang B, Matos I, Fiorese C, Lubkin A, et al. Trem14, an Ig superfamily member, mediates presentation of several antigens to T cells in vivo, including protective immunity to HER2 protein. *J Immunol*. 2012;188(3):1147–55.
370. Lopez-Garcia J, Periyasamy M, Thomas RS, Christian M, Leao M, Jat P, et al. ZNF366 is an estrogen receptor corepressor that acts through CtBP and histone deacetylases. *Nucleic Acids Res*. 2006;34(21):6126–36.
371. Kukurba KR, Montgomery SB. RNA Sequencing and Analysis. *Cold Spring Harb Protoc*. 2015;11:951–69.
372. Sioud M. RNA interference and innate immunity. *Adv Drug Deliv Rev*. 2007;59:153–63.
373. Brass AL, Zhu AQ, Singh H. Assembly requirements of PU.1–Pip (IRF-4) activator complexes:

- inhibiting function in vivo using fused dimers. *EMBO J.* 1999;18(4):977–91.
374. Burdette D, Haskett A, Presser L, Mcrae S, Iqbal J, Waris G. Hepatitis C virus activates interleukin-1 β via caspase-1-inflammasome complex. *J Gen Virol.* 2012;93:235–46.
 375. Taylor JM, Moore Z, Minter MR, Crack PJ. Type-I interferon pathway in neuroinflammation and neurodegeneration: focus on Alzheimer's disease. *J Neural Transm.* 2018;125(5):797–807.
 376. Wu S-Y, Watabe K. The roles of microglia, macrophages in tumor progression of brain cancer and metastatic disease. *Front Biosci.* 2017;22:1805–29.
 377. Fu X, Fu N, Guo S, Yan Z, Xu Y, Hu H, et al. Estimating accuracy of RNA-Seq and microarrays with proteomics. *BMC Genomics.* 2009;10(161):1–9.
 378. Schonheit J, Kuhl C, Gebhardt ML, Klett FF, Riemke P, Scheller M, et al. PU.1 Level-Directed Chromatin Structure Remodeling at the *Irf8* Gene Drives Dendritic Cell Commitment. *Cell Rep.* 2013;3:1617–28.
 379. Ungerback J, Hosokawa H, Wang X, Strid T, Williams BA, Sigvardsson M, et al. Pioneering, chromatin remodeling, and epigenetic constraint in early T-cell gene regulation by SPI1 (PU.1). *Genome Res.* 2018;28:1508–19.
 380. Pereira PD, Serra-Caetano A, Cabrita M, Bekman E, Braga J, Rino J, et al. Quantification of cell cycle kinetics by EdU (5-ethynyl-2'-deoxyuridine)-coupled-fluorescence-intensity analysis. *Oncotarget.* 2017;8(25):40514–32.
 381. Hayashi MT, Karlseder J. DNA damage associated with mitosis and cytokinesis failure. *Oncogene.* 2013;32(39):4593–601.
 382. Lee W Bin, Choi WY, Lee DH, Shim H, Kim-Ha J, Kim YJ. OAS1 and OAS3 negatively regulate the expression of chemokines and interferon-responsive genes in human macrophages. *BMB Rep.* 2019;52(2):133–8.
 383. Dansokho C, Ait Ahmed D, Aid S, Toly-Ndour C, Chaigneau T, Calle V, et al. Regulatory T cells delay disease progression in Alzheimer-like pathology. *Brain.* 2016;139(4):1237–51.
 384. Sala Frigerio C, Wolfs L, Fattorelli N, Thrupp N, Voytyuk I, Schmidt I, et al. The Major Risk Factors for Alzheimer's Disease: Age, Sex, and Genes Modulate the Microglia Response to A β Plaques. *Cell Rep.* 2019;27(4):1293-1306.e6.
 385. Liu S-Y, Sanchez DJ, Aliyari R, Lu S, Cheng G. Systematic identification of type I and type II interferon-induced antiviral factors. *Proc Natl Acad Sci.* 2012;109(11):4239–44.
 386. Hansen D V, Hanson JE, Sheng M. Microglia in Alzheimer's disease. *JCB.* 2017;217(2):459–72.
 387. Zhang Y, Chen K, Sloan SA, Bennett ML, Scholze AR, O'Keefe S, et al. An RNA-Sequencing Transcriptome and Splicing Database of Glia, Neurons, and Vascular Cells of the Cerebral Cortex. *J Neurosci.* 2014;34(36):11929–47.
 388. Boocock CA, Jones GE, Stanley ER, Pollard JW. Colony-stimulating factor-1 induces rapid behavioural responses in the mouse macrophage cell line, BAC1.2F5. *J Cell Sci.* 1989;93:447–56.
 389. Webb SE, Pollard JW, Jones GE. Direct observation and quantification of macrophage

- chemoattraction to the growth factor CSF-1. *J Cell Sci.* 1996;109:793–803.
390. Isaac BM, Ishihara D, Nusblat LM, Gevrey JC, Dovas A, Condeelis J, et al. N-WASP has the ability to compensate for the loss of WASP in macrophage podosome formation and chemotaxis. *Exp Cell Res.* 2010;316:3406–16.
391. Linehan E, Dombrowski Y, Snoddy R, Fallon PG, Kissenpfennig A, Fitzgerald DC. Aging impairs peritoneal but not bone marrow-derived macrophage phagocytosis. *Aging Cell.* 2014;13(4):699–708.
392. García-García E, Rosales C. Signal transduction during Fc receptor-mediated phagocytosis. *J Leukoc Biol.* 2002;72:1092–108.
393. Held P. Using Phenol Red to Assess pH in Tissue Culture Media. BioTek: Application Note. 2018.
394. Dai J, Sultan S, Taylor SS, Higgins JMG. The kinase haspin is required for mitotic histone H3 Thr 3 phosphorylation and normal metaphase chromosome alignment. *Genes Dev.* 2005;19(4):472–88.
395. Tiago Ferreira, Rasband W. Section 30.7 Set Measurements [Internet]. Image J User Guide (version IJ 1.46r). 2012 [cited 2019 Feb 19]. Available from: <https://imagej.nih.gov/ij/docs/guide/146-30.html#sec:Analyze-Menu>
396. Simon MM, Greenaway S, White JK, Fuchs H, Gailus-Durner V, Wells S, et al. A comparative phenotypic and genomic analysis of C57BL/6J and C57BL/6N mouse strains. *Genome Biol.* 2013;14(7):R82.
397. Riss T, Moravec R, Niles A, Sittampalam G, Coussens N, Brimacombe K. Cell Viability Assays. [Internet]. Assay Guidance Manual [Internet]. [cited 2019 Feb 20]. Available from: <https://www.ncbi.nlm.nih.gov/books/NBK144065/>
398. Steinestel K, Brüderlein S, Steinestel J, Märkl B, Schwerer MJ, Arndt A, et al. Expression of abelson interactor 1 (Abi1) correlates with inflammation, kras mutation and adenomatous change during colonic carcinogenesis. *PLoS One.* 2012;7(7):e40671.
399. Saito T, Matsuba Y, Mihira N, Takano J, Nilsson P, Itohara S, et al. Single App knock-in mouse models of Alzheimer’s disease. *Nat Neurosci.* 2014;17(5):661–3.
400. Takenawa T, Suetsugu S. The WASP-WAVE protein network: Connecting the membrane to the cytoskeleton. *Nat Rev Mol Cell Biol.* 2007;8(1):37–48.
401. Mendoza MC. Phosphoregulation of the WAVE regulatory complex and signal integration. *Semin Cell Dev Biol.* 2013;24:272–9.
402. Conway OJ, Carrasquillo MM, Wang X, Bredenberg JM, Reddy JS, Strickland SL, et al. ABI3 and PLCG2 missense variants as risk factors for neurodegenerative diseases in Caucasians and African Americans. *Mol Neurodegener.* 2018;13(53):1–12.
403. Zhang Y, Sloan SA, Clarke LE, Caneda C, Plaza CA, Blumenthal PD, et al. Purification and Characterization of Progenitor and Mature Human Astrocytes Reveals Transcriptional and Functional Differences with Mouse. *Neuron.* 2016;89:37–53.
404. Schwenk F, Baron U, Rajewsky K. A cre-transgenic mouse strain for the ubiquitous deletion of loxP-flanked gene segments including deletion in germ cells. *Nucleic Acids Res.* 1995;23(24):5080–1.

405. Lin H, Lee E, Hestir K, Leo C, Huang M, Bosch E, et al. Discovery of a Cytokine and Its Receptor by Functional Screening of the Extracellular Proteome. *Science* (80-). 2008;320:807–11.
406. Segaliny AI, Brion R, Mortier E, Maillason M, Cherel M, Jacques Y, et al. Syndecan-1 regulates the biological activities of interleukin-34. *Biochim Biophys Acta*. 2015;1853:1010–21.
407. Nandi S, Cioce M, Yeung YG, Nieves E, Tesfa L, Lin H, et al. Receptor-type protein-tyrosine phosphatase ζ is a functional receptor for interleukin-34. *J Biol Chem*. 2013;288(30):21972–86.
408. Greter M, Lelios I, Pelczar P, Hoeffel G, Price J, Leboeuf M, et al. Stroma-Derived Interleukin-34 Controls the Development and Maintenance of Langerhans Cells and the Maintenance of Microglia. *Immunity*. 2012;37(6):1050–60.
409. Wei S, Nandi S, Chitu V, Yeung Y-G, Yu W, Huang M, et al. Functional overlap but differential expression of CSF-1 and IL-34 in their CSF-1 receptor-mediated regulation of myeloid cells. *J Leukoc Biol*. 2010;88:495–505.
410. Wheat R. Complement-Mediated Microglial Priming: An In Vitro Study. Cardiff University; 2016.
411. Jobst S, Reza P, Wottge H-U. Blood monocytes and spleen macrophages differentiate into microglia-like cells on monolayers of astrocytes: Morphology. *Glia*. 1994;12:245–58.
412. Kawanishi S, Takata K, Iteazono S, Nagayama H, Konoya S, Chisaki Y, et al. Bone-Marrow-Derived Microglia-Like Cells Ameliorate Brain Amyloid Pathology and Cognitive Impairment in a Mouse Model of Alzheimer's Disease. *J Alzheimer's Dis*. 2018;64:563–85.
413. Weigelt K, Lichtinger M, Rehli M, Langmann T. Transcriptomic profiling identifies a PU.1 regulatory network in macrophages. *Biochem Biophys Res Commun*. 2009;380:308–12.
414. Reddy MA, Yang B-S, Yue X, Barnett CJK, Ross IL, Sweet MJ, et al. Opposing Actions of c-ets/PU.1 and c-myb Protooncogene Products in Regulating the Macrophage-specific Promoters of the Human and Mouse Colony-stimulating Factor-1 Receptor (c-fms) Genes. *J Exp Med*. 1994;180:2309–19.
415. Eichbaum QG, Iyer R, Raveh DP, Mathieu C, Ezekowitz AB. Restriction of interferon γ responsiveness and basal expression of the myeloid human Fc γ R1b gene is mediated by a functional PU.1 site and a transcription initiator consensus. *J Exp Med*. 1994;179:1985–96.
416. Gómez-Nicola D, Fransen NL, Suzzi S, Perry VH. Regulation of Microglial Proliferation during Chronic Neurodegeneration. *J Neurosci*. 2013 Feb 6;33(6):2481–93.
417. Mandrekar S, Jiang Q, Lee CYD, Koenigsnecht- J, Holtzman DM, Landreth GE. Microglia Mediate the Clearance of Soluble A β through Fluid Phase Macropinocytosis. *J neurosci*. 2009;29(13):4252–62.
418. Litvinchuk A, Wan Y, Swartzlander DB, Chen F, Cole A, Propson NE, et al. Complement C3aR Inactivation Attenuates Tau Pathology and Reverses an Immune Network Deregulated in Tauopathy Models and Alzheimer's Disease. *Neuron*. 2018;100:1337–53.
419. Hickman SE, Khoury J El. Mechanisms of Mononuclear Phagocyte Recruitment in Alzheimer's Disease. *CNS Neurol Disord Drug Targets*. 2010;9(2):168–73.

420. Mathys H, AdaiKKan C, Gao F, Ransohoff RM, Regev A, Mathys H, et al. Temporal Tracking of Microglia Activation in Neurodegeneration at Single-Cell Resolution Article Temporal Tracking of Microglia Activation in Neurodegeneration at Single-Cell Resolution. *CellReports*. 2017;21(2):366–80.
421. Schettters STT, Gomez-Nicola D, Garcia-Vallejo JJ, Van Kooyk Y. Neuroinflammation: Microglia and T cells get ready to tango. *Front Immunol*. 2018;8(1905):1–11.
422. McGeer PL, Itagaki S, Tago H, McGeer EG. Reactive microglia in patients with senile dementia of the Alzheimer type are positive for the histocompatibility glycoprotein HLA-DR. *Neurosci Lett*. 1987;79:195–200.
423. Rogers J, Luber-Narod J, Styren SD, Civin WH. Expression of immune system-associated antigens by cells of the human central nervous system: Relationship to the pathology of Alzheimer's disease. *Neurobiol Aging*. 1988;9:339–49.
424. Parachikova A, Agadjanyan MG, Cribbs DH, Blurton-Jones M, Perreau V, Rogers J, et al. Inflammatory changes parallel the early stages of Alzheimer disease. *Neurobiol Aging*. 2007;28(12):1821–33.
425. Gottfried-blackmore A, Kaunzner UW, Gottfried-blackmore A, Kaunzner UW, Felger JC, Mcewen BS, et al. Correction for Graham et al., Phylogenetic structure in tropical hummingbird communities. *Proc Natl Acad Sci*. 2009;107(1):513–513.
426. Byram SC. CD4-Positive T Cell-Mediated Neuroprotection Requires Dual Compartment Antigen Presentation. *J Neurosci*. 2004;24(18):4333–9.
427. Ryosuke M, Kazumi K, Nobuhiro N, Mutsuko H, Keiko M, Ko O, et al. Role of PU.1 in MHC class II expression via CIITA transcription in plasmacytoid dendritic cells. *PLoS One*. 2016;11(4):1–13.
428. Abutbul S, Shapiro J, Szaingurten-solodkin I, Levy N, Carmy Y, Baron R, et al. TGF- β Signaling Through SMAD2 / 3 Induces the Quiescent Microglial Phenotype Within the CNS Environment. 2012;1171(April):1160–71.
429. Takata K, Kozaki T, Lee CZW, Thion MS, Otsuka M, Lim S, et al. Induced-Pluripotent-Stem-Cell-Derived Primitive Macrophages Provide a Platform for Modeling Tissue-Resident Macrophage Differentiation and Function. *Immunity*. 2017;47(1):183-198.e6.
430. Leone C, Le Pavec G, Meme W, Porcheray F, Samah B, Dormont D, et al. Characterization of human monocyte-derived microglia-like cells. *Glia*. 2006 Aug;54(3):183–92.
431. Abud EM, Ramirez RN, Martinez ES, Healy LM, Nguyen CHH, Newman SA, et al. iPSC-Derived Human Microglia-like Cells to Study Neurological Diseases. *Neuron*. 2017;94(2):278-293.e9.
432. Goate AM. Understanding the mechanism of SPI1 dependent Alzheimer disease risk [Internet]. NIH Grantome. 2016 [cited 2019 Mar 1]. Available from: <http://grantome.com/grant/NIH/RF1-AG054011-01>
433. Innocenti M, Gerboth S, Rottner K, Lai FPL, Hertzog M, Stradal TEB, et al. Abi1 regulates the activity of N-WASP and WAVE in distinct actin-based processes. *Nat Cell Biol*. 2005;7(10):969–76.

Appendices

List of 162 Genes Controlled by level of PU.1

Symbol	Ensembl_ID	Spi1 KD Log ₂ FC	Spi1 OE Log ₂ FC	Symbol	Ensembl_ID	Spi1 KD Log ₂ FC	Spi1 OE Log ₂ FC
Mx1	ENSMUSG00000000386	-2.265	1.355	Ddx60	ENSMUSG00000037921	-2.145	1.422
Pparg	ENSMUSG00000000440	-2.164	1.707	Igfbp9	ENSMUSG00000037995	-1.534	0.884
Zfp385a	ENSMUSG00000000552	-0.673	0.577	Rnf144b	ENSMUSG00000038068	-2.503	3.951
Ckb	ENSMUSG00000001270	-0.913	0.826	Parp12	ENSMUSG00000038507	-0.758	0.897
Irf9	ENSMUSG00000002325	-0.699	0.546	Jarid2	ENSMUSG00000038518	-0.501	0.554
Arhgef40	ENSMUSG00000004562	-0.549	0.430	Rap1gap2	ENSMUSG00000038807	-1.424	1.055
Hap1	ENSMUSG00000006930	-2.379	1.240	Garnl3	ENSMUSG00000038860	-1.357	1.240
Kcnd1	ENSMUSG00000009731	-1.906	2.075	Isg20	ENSMUSG00000039236	-1.484	1.787
Ifi35	ENSMUSG00000010358	-0.997	0.931	Znfx1	ENSMUSG00000039501	-1.517	0.969
Phf21b	ENSMUSG00000016624	-1.577	1.483	Fgl2	ENSMUSG00000039899	-0.975	0.935
Dhx58	ENSMUSG00000017830	-1.456	1.381	Tbc1d16	ENSMUSG00000039976	-0.765	0.819
Il12rb2	ENSMUSG00000018341	-1.592	1.609	Stat2	ENSMUSG00000040033	-1.263	0.958
Slc13a3	ENSMUSG00000018459	-3.454	2.143	Plcb2	ENSMUSG00000040061	-1.236	1.047
Slc25a22	ENSMUSG00000019082	-0.901	0.626	Ddx58	ENSMUSG00000040296	-1.396	1.172
Fyn	ENSMUSG00000019843	-1.648	0.874	Olfir56	ENSMUSG00000040328	-0.895	1.031
Tmcc3	ENSMUSG00000020023	-1.576	1.076	Trim41	ENSMUSG00000040365	-0.579	0.373
Cmpk2	ENSMUSG00000020638	-3.684	2.102	Xaf1	ENSMUSG00000040483	-1.456	1.403
Rsad2	ENSMUSG00000020641	-2.779	2.171	Matn1	ENSMUSG00000040533	-4.697	2.004
Xylt2	ENSMUSG00000020868	-1.029	0.695	Oasl1	ENSMUSG00000041827	-2.864	2.288
Rtn1	ENSMUSG00000021087	-2.234	2.749	Rapgef5	ENSMUSG00000041992	-1.550	1.372
Evl	ENSMUSG00000021262	-1.177	0.774	Inka1	ENSMUSG00000042106	-1.743	1.037
Degs2	ENSMUSG00000021263	-1.218	0.855	Ljph	ENSMUSG00000044626	-3.101	1.923
Parp9	ENSMUSG00000022906	-1.198	1.004	Tlr1	ENSMUSG00000044827	-1.545	0.882
Mx2	ENSMUSG00000023341	-1.634	1.367	Ifit2	ENSMUSG00000045932	-3.539	2.073
Mmp25	ENSMUSG00000023903	-5.663	3.080	Tmem150b	ENSMUSG00000046456	-0.918	0.813
Bysl	ENSMUSG00000023988	-0.336	0.309	Irgm1	ENSMUSG00000046879	-1.524	1.056
Eif2ak2	ENSMUSG00000024079	-1.049	0.620	Ust	ENSMUSG00000047112	-0.903	0.997
Sectm1a	ENSMUSG00000025165	-3.205	2.931	C130026i21Rik	ENSMUSG00000052477	-1.693	1.790
Dnase1l3	ENSMUSG00000025279	-6.927	4.837	St6galnac3	ENSMUSG00000052544	-4.139	3.151
Irf7	ENSMUSG00000025498	-2.760	2.283	Clec12a	ENSMUSG00000053063	-2.185	1.480
Rdh10	ENSMUSG00000025921	-0.754	1.066	Slamf8	ENSMUSG00000053318	-3.133	1.494
Stat1	ENSMUSG00000026104	-0.897	1.084	Smagp	ENSMUSG00000053559	-1.764	1.573
Sp100	ENSMUSG00000026222	-1.278	1.173	H2-T24	ENSMUSG00000053835	-1.938	1.576
Ifi211	ENSMUSG00000026536	-2.242	1.424	Slc39a8	ENSMUSG00000053897	-1.392	0.859
Ifih1	ENSMUSG00000026896	-1.801	1.093	Sifn5	ENSMUSG00000054404	-1.582	1.807
Fcna	ENSMUSG00000026938	-1.670	4.989	Rab39	ENSMUSG00000055069	-2.729	1.362
Ube2l6	ENSMUSG00000027078	-0.999	1.259	Armc7	ENSMUSG00000057219	-0.693	1.099
Gatm	ENSMUSG00000027199	-1.252	0.869	Trim30d	ENSMUSG00000057596	-1.751	0.928
Sema6d	ENSMUSG00000027200	-1.639	1.538	Ptp4a3	ENSMUSG00000059895	-0.972	0.882
Dusp2	ENSMUSG00000027368	-2.109	1.845	Tor3a	ENSMUSG00000060519	-1.527	1.028
Zbp1	ENSMUSG00000027514	-1.610	1.556	Blnk	ENSMUSG00000061132	-1.770	1.320
Ifi44	ENSMUSG00000028037	-2.202	2.482	Ifit3b	ENSMUSG00000062488	-3.159	2.358
Gbp3	ENSMUSG00000028268	-1.500	1.089	Kdr	ENSMUSG00000062960	-1.588	1.589
Gbp2	ENSMUSG00000028270	-1.204	1.069	Rnf183	ENSMUSG00000063851	-1.953	1.768
Pdlim5	ENSMUSG00000028273	-1.098	1.145	Trim12a	ENSMUSG00000066258	-0.772	0.574
Usp24	ENSMUSG00000028514	-0.347	0.268	Ifi208	ENSMUSG00000066677	-4.717	3.199
Gbp9	ENSMUSG00000029298	-1.233	1.221	Oasl1g	ENSMUSG00000066861	-1.768	1.534
Rilpl1	ENSMUSG00000029392	-0.685	0.665	Phf11d	ENSMUSG00000068245	-2.734	1.302
Oasl2	ENSMUSG00000029561	-2.115	1.629	Irgm2	ENSMUSG00000069874	-1.051	1.038
Oasl1b	ENSMUSG00000029605	-1.584	1.536	Sp110	ENSMUSG00000070034	-1.014	0.838
Herc6	ENSMUSG00000029798	-1.927	1.141	Rnf213	ENSMUSG00000070327	-1.089	1.074
Usp18	ENSMUSG00000030107	-1.941	1.842	Lilra5	ENSMUSG00000070873	-2.263	1.878
Cd69	ENSMUSG00000030156	-2.185	1.412	Nfxl1	ENSMUSG00000072889	-0.723	0.767
Etnk1	ENSMUSG00000030275	-0.634	0.433	Ifi213	ENSMUSG00000073491	-3.928	2.431
Siglece	ENSMUSG00000030474	-1.771	1.066	Gm4951	ENSMUSG00000073555	-2.655	1.938
Sez6l2	ENSMUSG00000030683	-2.145	1.424	Ifit3	ENSMUSG00000074896	-2.737	2.314
Acer3	ENSMUSG00000030760	-0.382	0.406	Gm11545	ENSMUSG00000075611	-2.770	2.208
Adgrg1	ENSMUSG00000031785	-1.375	1.477	Trim30c	ENSMUSG00000078616	-3.280	2.262
Ifi30	ENSMUSG00000031838	-0.768	0.890	Sifn1	ENSMUSG00000078763	-5.672	2.541
Hsbp1	ENSMUSG00000031839	-0.861	0.433	Igtp	ENSMUSG00000078853	-0.951	1.085
Fhl3	ENSMUSG00000032643	-0.645	0.705	Ifi47	ENSMUSG00000078920	-1.031	1.075
Oasl3	ENSMUSG00000032661	-1.965	1.822	Gbp4	ENSMUSG00000079363	-1.678	1.753
Oasl2	ENSMUSG00000032690	-2.235	1.772	Phyh1d	ENSMUSG00000079484	-0.776	0.703
Rtp4	ENSMUSG00000033355	-1.732	1.951	Gm12250	ENSMUSG00000082292	-1.448	1.466
Igf2bp2	ENSMUSG00000033581	-1.518	1.113	Gm15550	ENSMUSG00000084325	-2.350	2.283
Parp14	ENSMUSG00000034422	-1.918	1.054	Dhx58os	ENSMUSG00000085604	-1.340	1.486
Gbp8	ENSMUSG00000034438	-1.662	1.513	Gm5970	ENSMUSG00000085977	-3.024	1.552
Ifit1	ENSMUSG00000034459	-2.101	1.977	Gm11707	ENSMUSG00000086481	-2.250	2.385
Cacna1a	ENSMUSG00000034656	-2.548	1.447	Pou3f1	ENSMUSG00000090125	-4.436	3.070
Cd207	ENSMUSG00000034783	-4.493	3.251	Ifi203-ps	ENSMUSG00000090222	-2.023	1.252
Art3	ENSMUSG00000034842	-2.279	1.274	Gm6548	ENSMUSG00000091549	-1.145	0.629
Cxcl10	ENSMUSG00000034855	-2.161	1.427	Mir6381	ENSMUSG00000098871	-1.206	1.297
Sifn8	ENSMUSG00000035208	-1.831	1.034	Gm28177	ENSMUSG00000101628	-0.912	1.117
Ccl12	ENSMUSG00000035352	-1.815	1.735	Gbp5	ENSMUSG00000105504	-1.859	1.201
Ccr3	ENSMUSG00000035448	-7.643	3.444	Gm20559	ENSMUSG00000106734	-1.570	1.062
Tdrd7	ENSMUSG00000035517	-0.669	0.568	Gm43068	ENSMUSG00000107075	-2.495	1.733
Isg15	ENSMUSG00000035692	-1.303	1.908	Gm43197	ENSMUSG00000107215	-1.319	0.840
Pml	ENSMUSG00000036986	-0.682	0.566	Gm43198	ENSMUSG00000107222	-1.482	0.843
Slc12a9	ENSMUSG00000037344	-2.064	0.806	Gm44148	ENSMUSG00000107736	-1.851	1.889
Fbxw17	ENSMUSG00000037816	-0.823	0.745	Gm45193	ENSMUSG00000108112	-1.957	1.251
Ifi206	ENSMUSG00000037849	-3.942	2.354	A930037H05Rik	ENSMUSG00000109408	-1.104	1.141